



<https://theses.gla.ac.uk/>

Theses Digitisation:

<https://www.gla.ac.uk/myglasgow/research/enlighten/theses/digitisation/>

This is a digitised version of the original print thesis.

Copyright and moral rights for this work are retained by the author

A copy can be downloaded for personal non-commercial research or study,
without prior permission or charge

This work cannot be reproduced or quoted extensively from without first
obtaining permission in writing from the author

The content must not be changed in any way or sold commercially in any
format or medium without the formal permission of the author

When referring to this work, full bibliographic details including the author,
title, awarding institution and date of the thesis must be given

Enlighten: Theses

<https://theses.gla.ac.uk/>
research-enlighten@glasgow.ac.uk

OSCILLATING FOIL PROPULSION

by

Peter Shung Kin Lai, B.Sc.

Submitted as a Thesis for the Degree of Doctor of Philosophy, Department of
Naval Architecture and Ocean Engineering, University of Glasgow.

January 1990

© Peter S. K. Lai, 1990
Great Britain

ProQuest Number: 11007328

All rights reserved

INFORMATION TO ALL USERS

The quality of this reproduction is dependent upon the quality of the copy submitted.

In the unlikely event that the author did not send a complete manuscript and there are missing pages, these will be noted. Also, if material had to be removed, a note will indicate the deletion.



ProQuest 11007328

Published by ProQuest LLC (2018). Copyright of the Dissertation is held by the Author.

All rights reserved.

This work is protected against unauthorized copying under Title 17, United States Code
Microform Edition © ProQuest LLC.

ProQuest LLC.
789 East Eisenhower Parkway
P.O. Box 1346
Ann Arbor, MI 48106 – 1346

DECLARATION

Except where reference is made to the work of others, this thesis is believed to be original.

DEDICATION

To my wife, Marie, and my parents

ACKNOWLEDGEMENT

I wish to thank the Science and Engineering Research Council, Marine Technology Directorate (MTD Ltd.), for providing financial support for this work. The work was carried out from 1986 to 1989 in the Department of Naval Architecture and Ocean Engineering, the University of Glasgow.

My sincere gratitude also goes to Professor D. Faulkner, Head of Department, for allowing me to carry out this research and for his encouragement .

I am deeply indebted to Professor Neil Bose, formerly lecturer in the Department and my previous supervisor, for initiating this research, his continuing support, enthusiastic discussions, valuable suggestions, constructive guidance and advice, and his encouragement.

I would like to express my true gratitude to Dr. R. C. McGregor for his supervision, valuable discussion and advice, and encouragement over the last two years. In particular, I would like to acknowledge his efforts in extending the contract which made the completion of this work possible and his enthusiasm.

In addition, I would like to thank Dr. A. M. Ferguson, formerly the Superintendent of the Hydrodynamics Laboratory, for his supervision before he retired.

I also wish to express my thanks to Mr. N. S. Miller, formerly senior lecturer in the department, for reading my thesis and his valuable comments.

The excellent work of the technicians in the Hydrodynamics Laboratory in building the models and test rig, and in assisting with the model test is truly appreciated. In particular, I would like to express my grateful thanks to Messrs. R. B. Christison, B. Reilly, G. Dunning, D. Nicholson, J. Aitken, D. Sinclair, P. Miller, J. Gillan and A. Khan (formerly electronic technician in the laboratory). My hearty thanks also goes to Dr. A. Incecik (Superintendent), the researchers, and staff of the Hydrodynamics Laboratory.

Finally, I am deeply indebted forever to my wife, Marie, and my parents for their continuous encouragement and support.

CONTENTS

	Page
DECLARATION	I
DEDICATION	II
ACKNOWLEDGEMENT	III
CONTENTS	IV
LIST OF FIGURES	XIV
LIST OF TABLES	XXIV
NOMENCLATURE	XXVII
SUMMARY	XL

CHAPTER ONE

INTRODUCTION

1.0	SHIP PROPULSION	1
2.0	THE PROPULSION SYSTEM OF AQUATIC ANIMALS	2
2.1	Mode of Swimming	3
3.0	OSCILLATING FOIL PROPULSION	5
4.0	THE BACKGROUND AND OBJECTIVE OF THE STUDY	7
4.1	Aims of Research	8
5.0	CONTENT OF THESIS	8
5.1	Two-Dimensional Oscillating Foil Propeller	9
5.2	Flexible Fin Propeller	9
5.3	Rotary Foil Propeller	11
5.4	Application and Conclusion	12

PART I : TWO-DIMENSIONAL OSCILLATING FOIL PROPELLER

CHAPTER TWO

HYDRODYNAMIC FORCE AND MOMENTS ACTING ON A TWO DIMENSIONAL OSCILLATING FOIL

1.0	INTRODUCTION	17
2.0	BOUNDARY CONDITIONS	18
3.0	THE TWO-DIMENSIONAL AEROFOIL IN STEADY FLOW	19
4.0	QUASI-STEADY APPROACH FOR A TWO-DIMENSIONAL OSCILLATING FOIL	21
5.0	BASIC ASSUMPTIONS IN TWO-DIMENSIONAL LINEARISED OSCILLATING FOIL THEORY	22
6.0	APPLICATION OF THE ACCELERATION POTENTIAL IN THE UNSTEADY OSCILLATING FOIL PROBLEM	23
6.1	The Kinematic Boundary Conditions	24
6.2	Force and Moment Due to Vertical Oscillation	26
6.3	Force and Moment Due to Rotational Oscillation	29
6.4	Total Force and Moment Due to Combined Motions of Vertical Translation and Angular Rotation	30
7.0	APPLICATION OF VELOCITY POTENTIAL IN THE UNSTEADY OSCILLATING FOIL PROBLEM	31
7.1	Non-Circulatory Flow	32
7.2	Circulatory Flow	33
7.3	Total Lift and Moment	36
8.0	COMPARISON BETWEEN METHODS	36
9.0	LEADING EDGE SUCTION FORCE	38
10.0	CONCLUDING REMARKS	39

CHAPTER THREE

PERFORMANCE OF A TWO-DIMENSIONAL OSCILLATING FOIL PROPELLER

1.0	INTRODUCTION	44
2.0	OUTLINE OF THE THEORETICAL MODEL	45
2.1	The Lifting Force and Moment at the Rotating Centre	46
2.2	Leading Edge Suction Force	47
2.3	Propulsive Thrust and Propulsive Efficiency	48
3.0	PARAMETRIC STUDIES OF THE PERFORMANCE OF A TWO-DIMENSIONAL OSCILLATING FOIL PROPELLER	49
4.0	RESULTS AND DISCUSSIONS	51
4.1	Propulsive Thrust Coefficient and Efficiency for Various Phase Shift Values (β)	51
4.2	The Propulsive Thrust and Efficiency when $\beta = 90^\circ$	53
4.3	Variation of Propulsive Thrust Throughout an Oscillating Cycle when $\beta = 90^\circ$	54
5.0	CONCLUSIONS	55

PART II : FLEXIBLE FIN PROPELLER

CHAPTER FOUR

THEORETICAL MODEL OF THE FLEXIBLE FIN PROPELLER

1.0	INTRODUCTION	90
2.0	OUTLINE OF THE THEORETICAL MODEL	93
3.0	LINEARISED UNSTEADY OSCILLATING FOIL THEORY	93
4.0	LARGE-DEFLECTION BEAM THEORY	97
4.1	A Constant Cross-Section Flexible Cantilever with an	98

	External Force System Acting at its Free End	
4.2	A Flexible Cantilever with a Linear variation in Cross- Section and an External Force System Acting at Its Free End	100
4.3	Computation Method	101
4.4	Comparison with Small Deflection Beam Theory	104
5.0	DYNAMIC EQUILIBRIUM	106
6.0	CONCLUDING REMARKS	109

CHAPTER FIVE

THEORETICAL PERFORMANCE OF FLEXIBLE FIN PROPELLER

1.0	INTRODUCTION	121
2.0	NON-DIMENSIONAL PARAMETERS	122
3.0	RANGE OF ANALYSIS	124
4.0	RESULTS AND DISCUSSION	125
4.1	The Effect of Stiffness of the Flexible Bar	125
4.2	The Effect of Taper Ratio of the Flexible Bar	127
4.3	The Effect of Aspect ratio	128
4.4	The Effect of Foil Shape (Rectangular and Elliptical)	129
5.0	CONCLUSIONS	129

CHAPTER SIX

THE MODEL AND THE TESTING RIG FOR A FLEXIBLE FIN PROPELLER

1.0	INTRODUCTION	145
2.0	THE DESIGN OF THE TESTING RIG AND THE MODEL	145
2.1	The Driving Unit	146

2.2	The Sinusoidal Oscillator	146
2.3	The Wire and Pulley System	147
2.4	The Three Bar System	147
2.5	The Propulsive Force Measuring Arm	148
2.6	The Flexible Bars and the Foil Clamp	148
2.7	The Enclosing Strut	148
3.0	FUNCTIONS OF INDIVIDUAL COMPONENTS OF THE TEST RIG	149
3.1	The Conversion from Linear Displacement into Angular Displacement	149
3.2	The Angular Sinusoidal Oscillation	151
3.3	The Motion of the Connecting Bar (BC)	152
4.0	THE DYNAMOMETER	153
4.1	The Measurement of Propulsive Thrust	153
4.2	The Measurement of Input Power	154
4.3	The Friction Factors K_{out} and K_{in}	156
4.4	The Speed Tachometer	157
5.0	CONCLUSIONS	157

CHAPTER SEVEN

EXPERIMENTAL PERFORMANCE OF THE FLEXIBLE FIN PROPELLER

1.0	INTRODUCTION	167
2.0	THE FLEXIBLE FIN PROPELLER MODEL	168
2.1	The Bending Moduli of the Flexible Bars	168
2.2	The Flexible Bar	169
2.3	The Foil	170
3.0	DATA COLLECTION AND ANALYSIS	170
4.0	THE FLOW VELOCITY AROUND THE OSCILLATING FOIL	173

5.0	FRICIONAL LOSS TEST	175
6.0	THE PERFORMANCE OF THE PROPELLER AT FORWARD SPEEDS	176
6.1	Testing Conditions	177
6.2	Net Propulsive Thrust and Input Power	177
6.3	Propulsive Thrust Coefficient	178
6.4	Propulsive Efficiency	180
7.0	THE PERFORMANCE OF THE FLEXIBLE FIN PROPELLER AT ZERO SPEED	182
8.0	FULL SCALE PROPELLER	183
9.0	CONCLUSIONS	184

CHAPTER EIGHT

STRESS ANALYSIS AND MATERIAL SELECTION FOR THE FLEXIBLE BAR

1.0	INTRODUCTION	214
2.0	OUTLINE OF THE THEORETICAL APPROACH	215
3.0	PARAMETRIC STUDIES AND DISCUSSION	217
3.1	The Effect of Reduced Frequency	218
3.2	The Effect of Angular Oscillating Function	218
3.3	The Effect of Stiffness of the Flexible Bar	218
3.4	The Effect of Taper Ratio	219
3.5	The Effect of Aspect Ratio and Foil Shape (Rectangular & Elliptical)	219
3.6	The Effect of Thickness Function	220
4.0	FULL SCALE PROPELLER	221
5.0	THE MATERIAL OF THE FLEXIBLE BAR	222
5.1	Glass Fibre Reinforced Plastics	224
5.2	Carbon Fibre Reinforced Plastics	225

5.3	Hybrid Fibre Reinforced Plastics	228
6.0	CONCLUSIONS	230

CHAPTER NINE

ON WAVE PROPULSION WITH A FLEXIBLE FIN PROPELLER

1.0	INTRODUCTION	247
2.0	THE DEMONSTRATION TEST	249
2.1	The Model and the Experimental Apparatus	249
2.2	Results and Discussion	250
3.0	THE EXPERIMENTAL INVESTIGATION OF WAVE PROPULSION WITH A FLEXIBLE FIN PROPELLER	251
3.1	The Model	251
3.2	The Set up of the Experiment and Analysis	252
3.3	The Non-Dimensional Parameters	254
3.4	Testing Conditions	256
3.5	Motion Response of the Model in Waves	256
3.6	Resistance of the Model and Propulsive Thrust Generated by the Flexible Fin Propeller in Waves	257
3.7	The Effect of Depth of Submergence of the Flexible Fin Propeller	259
4.0	CONCLUSIONS	260

PART III : ROTARY FOIL PROPELLER

CHAPTER TEN

EXPERIMENTAL PERFORMANCE OF A TROCHOIDAL PROPELLER WITH HIGH ASPECT RATIO BLADES

1.0	INTRODUCTION	279
2.0	THE PROPELLER MODEL AND DYNAMOMETER	281
3.0	DATA COLLECTION AND ANALYSIS OF EXPERIMENTAL RECORDS	282
4.0	FLOW VELOCITY AT THE PROPELLER	283
5.0	FRICTIONAL LOSS TESTS	284
6.0	PROPELLER PERFORMANCE TESTS IN FORWARD MOTION	285
6.1	The Propulsive Thrust Coefficient	286
6.2	The Driving Torque Coefficient	287
6.3	The Propulsive Efficiency	287
7.0	PROPELLER PERFORMANCE TEST IN REVERSE MOTION	288
7.1	The Propulsive Thrust Coefficient	288
7.2	The Driving Torque Coefficient	289
7.3	The Propulsive Efficiency	289
8.0	PROPELLER PERFORMANCE AT ZERO SPEED	289
9.0	FULL SCALE PROPELLER	290
10.0	CONCLUSIONS	291

**PART IV : APPLICATION OF OSCILLATING FOIL PROPELLERS
& GENERAL CONCLUSIONS**

CHAPTER ELEVEN

APPLICATION OF OSCILLATING FOIL PROPULSION

1.0	INTRODUCTION	310
2.0	PARTICULARS OF SHIP EXAMPLES	312
3.0	FULL SCALE PROPELLERS	314
3.1	Two-Dimensional Oscillating Propeller	314
3.2	Flexible Fin Propeller	315
3.3	Rotary Foil Propeller	320
4.0	ARRANGEMENT OF OSCILLATING FOIL PROPELLERS FOR MONOHULLS	323
4.1	Two-Dimensional Oscillating Foil Propeller	323
4.2	Flexible Fin Propeller	324
4.3	Rotary Foil Propeller	325
5.0	ARRANGEMENT OF AN OSCILLATING FOIL PROPELLER ON A SWATH SHIP	325
5.1	Two-Dimensional Oscillating Foil propeller	325
5.2	Flexible Fin Propeller	326
5.3	Rotary Foil Propeller	326
6.0	NATURAL FREQUENCY OF THE FLEXIBLE FIN PROPELLER	326
7.0	THE DRIVING MECHANISM	328
7.1	Two-Dimensional Oscillating Foil Propeller	328
7.2	Flexible Fin Propeller	329
7.3	Rotary Foil Propeller	330
8.0	WAVE PROPULSION WITH A FLEXIBLE FIN PROPELLER	330

9.0	ENGINEERING ECONOMY ON THE APPLICATION OF OSCILLATING FOIL PROPULSION	332
9.1	Two-Dimensional Oscillating Foil Propeller	334
9.2	Flexible Fin propeller	337
9.3	Rotary Foil Propeller	340
10.0	CONCLUSIONS	342

CHAPTER TWELVE

GENERAL CONCLUSIONS

1.0	INTRODUCTION	363
2.0	TWO-DIMENSIONAL OSCILLATING FOIL PROPELLER	363
3.0	FLEXIBLE FIN PROPELLER	366
4.0	ROTARY FOIL PROPELLER	369
5.0	FUTURE DEVELOPMENTS	371

REFERENCES	373
-------------------	------------

APPENDIX I

LIST OF FIGURES

CHAPTER ONE

	Page
Fig. 1.1 Modes of Swimming	13
Fig. 1.2 Four Different Modes of Swimming	14
Fig. 1.3 The "Aqueon" Inner Space Vehicle	14
Fig. 1.4 Three Types of Oscillating Foil Propeller	15

CHAPTER TWO

Fig. 2.1 Two Dimensional Aerofoil in Steady Flow	41
Fig. 2.2 Conformal Representation of a Thin Aerofoil	41
Fig. 2.3 The Theodorsen's Function $C(k) = F + i G$	42
Fig. 2.4 Sign Convention of Theodorsen's Theory	43
Fig. 2.5 Conformal Mapping of the Aerofoil and the Circulation in the Wake	43

CHAPTER THREE

Fig. 3.1 A Two Dimensional Oscillating Foil Propeller	57
Fig. 3.2 The Force System Acting on an Oscillating Foil	57
Fig. 3.3 The Propulsive Thrust Coefficient when $\theta = 0.2$	58
Fig. 3.4 The Propulsive Thrust Coefficient when $\theta = 0.4$	60
Fig. 3.5 The Propulsive Thrust Coefficient when $\theta = 0.6$	62
Fig. 3.6 The Propulsive Thrust Coefficient when $\theta = 0.8$	64
Fig. 3.7 The Propulsive Efficiency when $\theta = 0.2$	66
Fig. 3.8 The Propulsive Efficiency when $\theta = 0.4$	68
Fig. 3.9 The Propulsive Efficiency when $\theta = 0.6$	70
Fig. 3.10 The Propulsive Efficiency when $\theta = 0.8$	72

Fig. 3.11	The Propulsive Thrust Coefficient ($\theta = 0.6, k = 0.8$)	74
Fig. 3.12	The Hydromechanical Efficiency ($a = 0.75 c, k = 0.8$)	74
Fig. 3.13	Propulsive Efficiency of a 2-D foil and a Rectangular Foil with $AR = 7.0$	75
Fig. 3.14	Thrust Coefficient and Efficiency of a 2-D Foil with Rotating Centre at L.E.	76
Fig. 3.15	Thrust Coefficient and Efficiency of a 2-D Foil with Rotating Centre at 0.25 Chord	77
Fig. 3.16	Thrust Coefficient and Efficiency of a 2-D Foil with Rotating Centre at Mid-Chord	78
Fig. 3.17	Thrust Coefficient and Efficiency of a 2-D Foil with Rotating Centre at 0.75 Chord	79
Fig. 3.18	Thrust Coefficient and Efficiency of a 2-D Foil with Rotating Centre at T.E.	80
Fig. 3.19	The Propulsive Thrust Coefficient in a Cycle when $\theta = 0.2$	81
Fig. 3.20	The Propulsive Thrust Coefficient in a Cycle when $\theta = 0.4$	83
Fig. 3.21	The Propulsive Thrust Coefficient in a Cycle when $\theta = 0.6$	85
Fig. 3.22	The Propulsive Thrust Coefficient in a Cycle when $\theta = 0.8$	87

CHAPTER FOUR

Fig. 4.1	The Flexible Fin Propeller	111
Fig. 4.2	The Unsteady Lifting Functions	112
Fig. 4.3	The Unsteady Lifting Functions	113
Fig. 4.4	The Propulsive Thrust Coefficient and Efficiency of an Oscillating Foil with Aspect Ratio = 8.0 and $a = 0.5$	114
Fig. 4.5	The Efficiency of an Oscillating Foil with Aspect Ratio = 7.0, $\theta = 0.8$ and $a = 1.0$	115
Fig. 4.6	The Deflection of a Flexible Cantilever	116
Fig. 4.7	The Flow Chart of the Dynamic Equilibrium Search	117
Fig. 4.8	Heaving and Pitching Motion of an Oscillating Foil	118

Fig. 4.9	The Oscillation of Flexible Bar of a Flexible Fin Propeller	119
----------	---	-----

CHAPTER 5.0

Fig. 5.1	Propulsive Thrust Coefficient for Different Stiffness Functions AR = 4.0	132
Fig. 5.2	The Efficiency for Different Stiffness Functions AR = 4.0	133
Fig. 5.3	The Propulsive Thrust Coefficients for Different Taper Ratios $\xi = 6.0$, AR = 4.0	134
Fig. 5.4	The Propulsive Thrust Coefficients for Different Taper Ratios $\xi = 12.0$, AR = 4.0	135
Fig. 5.5	The Efficiency for Different Taper Ratios $\xi = 6.0$, AR = 4.0	136
Fig. 5.6	The Efficiency for Different Taper Ratios $\xi = 12.0$, AR = 4.0	137
Fig. 5.7	The Propulsive Thrust Coefficients for Different Aspect Ratios $\xi = 12.0$	138
Fig. 5.8	The Efficiency for Different Aspect Ratios $\xi = 12.0$	139
Fig. 5.9	Propulsive Thrust Coefficients for Rectangular and Elliptical Foils $\xi = 12.0$, AR = 4.0	140
Fig. 5.10	Propulsive Efficiency for Rectangular and Elliptical Foils $\xi = 12.0$, AR = 4.0	141
Fig. 5.11	The Performance of different Foil Shapes, $\xi = 6.0$, $\zeta = 3.0$, AR = 4.0	142
Fig. 5.12	The Amplitudes of Heave and Pitch for Different Stiffness Functions $\zeta = 3.0$, $k = 0.6$ and AR = 4.0	143
Fig. 5.13	The Tip Deflections for Different Taper Ratios	144

CHAPTER SIX

Fig. 6.1	General Arrangement of the Flexible Fin Propeller Model	158
Fig. 6.2	Diagrammatic Arrangement of the Flexible Fin Propeller Model	159

Fig. 6.3	The Driving Unit of the Test Rig	160
Fig. 6.4	The Sinusoidal Oscillator	160
Fig. 6.5	The Arrangement of the LVDT for Measuring the Angular Oscillating Motion	161
Fig. 6.6	Comparison of the Measured Angular Oscillation and the Cosine Function	162
Fig. 6.7	Arrangement of Calibration of the Propulsive Thrust Measuring Arm	163
Fig. 6.8	Calibration of Propulsive Thrust Measuring Arm	164
Fig. 6.9a	The Measurement of the Input Power	165
Fig. 6.9b	Arrangement of Calibration of Input Thrust Measurement	165
Fig. 6.10	Calibration of the Measured Moment Acting at the Pivot	166

CHAPTER SEVEN

Fig. 7.1	The Flexible Fin Propeller Model	187
Fig. 7.2	Thickness Distribution of BAR-SO, BAR-ST and BAR-XST	187
Fig. 7.3	Deflection of a Flexible Cantilever	187
Fig. 7.4	Deflection Measured in the Bending Test	188
Fig. 7.5	Thickness Distribution of BAR-R and BAR-B	189
Fig. 7.6	The Foil for the Flexible Fin Propeller Model	189
Fig. 7.7	The Diagrammatic Arrangement of the Flexible Fin Propeller Model Test	190
Fig. 7.8	An Example of Chart Records for the Performance Test with Forward Speed	191
Fig. 7.9	Calibration of the Flow Meter (STREAMFLO)	192
Fig. 7.10	Five Positions for Flow Velocity Calibration	193
Fig. 7.11	Flow Velocity Behind the Fairing Strut	194
Fig. 7.12	Flow Velocity Profile Behind the Fairing Strut	195
Fig. 7.13	Mean Flow Velocity Behind the Fairing Strut Vs Free Stream Velocity	195

Fig. 7.14	An Example of Chart Records for the Frictional Loss Test	196
Fig. 7.15	Mean Propulsive Thrust Recorded in the Frictional Loss Test	197
Fig. 7.16	Mean Input Power Measured in Frictional Loss Test	198
Fig. 7.17	Comparison of the Records of Propulsive Thrust Between the Performance Test and the Frictional Loss Test	199
Fig. 7.18	The Propulsive Thrust Coefficient for Different Stiffness Functions, where : Aspect Ratio = 4.0, Taper Ratio = 0.37	200
Fig. 7.19	The Propulsive Thrust Coefficient for Different Stiffness Functions; where : Aspect Ratio = 4.0, Taper Ratio = 0.3	201
Fig. 7.20	Comparisons of Propulsive Thrust Coefficient for Different Taper Ratios with Similar Stiffness Functions	202
Fig. 7.21a	The Propulsive Thrust Coefficient for Different Stiffness Functions when $k = 0.6$	203
Fig. 7.21b	The Propulsive Thrust Coefficient for Different Angular Oscillating Function when $k = 0.6$	203
Fig. 7.22	The Propulsive Thrust Coefficient for Different Stiffness Functions where : Aspect Ratio = 4.0, $\zeta = 3.5$	204
Fig. 7.23	The Propulsive Efficiency for Different Stiffness Functions where : Aspect Ratio = 4.0, Taper Ratio = 0.37	205
Fig. 7.24	The Propulsive Efficiency for Different Stiffness Functions where : Aspect Ratio = 4.0, Taper Ratio = 0.30	206
Fig. 7.25	Comparison of Propulsive Efficiency for Different Taper Ratios with Similar Stiffness Function when $\zeta = 7.0$	207
Fig. 7.26	The Propulsive Thrust Coefficient in Bollard Pull Condition	207
Fig. 7.27	The Propulsive Thrust Generated in Bollard Pull Condition by BAR-R	208
Fig. 7.28	Comparison of Propulsive Thrust Between Bollard Pull Condition and Forward Speed Condition	208

CHAPTER EIGHT

Fig. 8.1	Stress Distribution Along the Flexible Bar within an Oscillating Cycle	233
Fig. 8.2	Stress Function for Different Stiffness Function : AR = 4.0	234
Fig. 8.3	Stress Function for Different Taper Ratios : AR = 4.0, $\xi = 6.0$	235
Fig. 8.4	Stress Function for Different Taper Ratios : AR= 4.0, $\xi = 12.0$	236
Fig. 8.5	Stress Function for Different Angular Oscillating Functions : $\xi = 12.0$	237
Fig. 8.6	Stress Function for Different Stiffness Functions : $\zeta = 3.0$	237
Fig. 8.7	Comparison of Stress Distribution Along Bars with Constant Cross-Section (TR = 0.0) and Linear Variation in Thickness (TR = 0.6)	238
Fig. 8.8	Stress Distribution Along Flexible Bars	238
Fig. 8.9	Stress Function for Different Taper Ratios : $\zeta = 3.0$	239
Fig. 8.10	The Percentage of Stress Function Drops for Different taper Ratios	239
Fig. 8.11	Stress Function for Different Aspect Ratio : $\xi=12, \zeta = 3.0$	240
Fig. 8.12	Stress Function for Rectangular & Elliptical Foils : $\xi=12, \zeta = 3.0$	240
Fig. 8.13	Stress Functions for Different Thickness Functions : $k = 0.2, \xi=12, \zeta = 3.0$	241
Fig. 8.14	Material Selection Chart : Modulus (E) Vs Strength	242
Fig. 8.15	Comparison Between Different Fibre Arrangement in GRP	243
Fig. 8.16	The Fatigue S-N Diagram for Various Stages of Failure in Chopped Strand Mat - Polyester Resin Laminate	244
Fig. 8.17	The Histogram of the Ratio of Fatigue Strength at 10^7 cycles to Ultimate Strength for 20 Published Results	244
Fig. 8.18	Fatigue Strength S-N Diagram for Unidirectional 'E' Glass (62% by vol.) with Epoxy	245
Fig. 8.19	Normalised Flexural Fatigue Results for Unidirectional, High	245

Modulus Carbon Fibre with Polyester Resin

Fig. 8.20	Fatigue Behaviour of Unidirectional High Strength Carbon Fibre Reinforced Plastics (SP313)	246
Fig. 8.21	Comparison of the Fatigue Behaviour of Quasi-Isotropic Carbon/Glass Hybrid Composites	246

CHAPTER NINE

Fig. 9.1	Linden's Wave Propulsion Device	262
Fig. 9.2	Jakobsen's Wave Motor	262
Fig. 9.3	The Ship Model with the Springs and Foil System	263
Fig. 9.4	The 0.33 m Yacht Model with Flexible Fin Propeller	263
Fig. 9.5	The Arrangement of the Model Test	264
Fig. 9.6a	The Speed of Model with and without Flexible Fin Propeller	265
Fig. 9.6b	The Net Speed of the Model	265
Fig. 9.7	The Three Quarter Ton Racing Yacht Model with Flexible Fin Propeller	266
Fig. 9.8	The Thickness Distribution of the Flexible Bar	266
Fig. 9.9	The Arrangement of the Mounting of the Flexible Fin Propeller	267
Fig. 9.10	The General Arrangement of the Model Test	268
Fig. 9.11	The Diagrammatic Arrangement of the Wave Propulsion Test	269
Fig. 9.12	Example of Times Series Records of Motion Response and Encounter Wave	270
Fig. 9.13	Example of Wave Records	271
Fig. 9.14	Time Series Data and Its Frequency Spectrum	272
Fig. 9.15	Example of Frequency Spectra of Motion Response and Encounter Wave	273
Fig. 9.16	The Motion Response of the Model in Head Sea ($Fr = 0.13$)	274
Fig. 9.17	The Motion Response of the Model in Head Sea ($Fr = 0.18$)	274

Fig. 9.18	The Motion Response of the Model in Head Sea ($Fr = 0.33$)	275
Fig. 9.19a	The Resistance of the Model in Head Sea ($Fr = 0.13$)	275
Fig. 9.19b	Propulsive Thrust Coefficient ($Fr = 0.13$)	275
Fig. 9.20a	The Resistance of the Model in Head Sea ($Fr = 0.18$)	276
Fig. 9.20b	Propulsive Thrust Coefficient ($Fr = 0.18$)	276
Fig. 9.21a	The Resistance of the Model in Head Sea ($Fr = 0.33$)	276
Fig. 9.21b	Propulsive Thrust Coefficient ($Fr = 0.33$)	276
Fig. 9.22	The Motion Response of the Model in Head Sea, $Fr = 0.18$, Depth = 1.5c	277
Fig. 9.23a	The Resistance of the Model in Head Sea, $Fr = 0.18$, Depth = 1.5 c	277
Fig. 9.23b	Propulsive Thrust Coefficient, $Fr = 0.18$	277

CHAPTER TEN

Fig. 10.1	Mechanical Arrangement of Rotary Foil Propeller Model	293
Fig. 10.2	Propeller Boat	294
Fig. 10.3	The Rotary Foil Propeller and the Supporting Frame	295
Fig. 10.4	The Rotary Foil Propeller Model with the Propeller Boat	295
Fig. 10.5	Side View of Propeller Depicting the Form of the Blade Oscillation	296
Fig. 10.6	Rotary Foil Propeller Blade (Blade Section : NACA-16 Series)	297
Fig. 10.7	The Diagrammatic Arrangement of the Rotary Foil Propeller Model Test	298
Fig. 10.8	The Flow Velocity Calibration (Output Volt. Vs Flow Vel.)	299
Fig. 10.9	The Location of the Points for Flow Velocity Calibration	300
Fig. 10.10	The Relationship between the Actual Flow Velocity and the Free Stream Velocity	301
Fig. 10.11	Flow Velocity Profile Alongside Propeller Boat at Propeller Axis Position	302
Fig. 10.12	Torque Associated with Frictional Losses within Propeller	302

Model	
Fig. 10.13 Thrust Coefficient of Propeller Operating at Forward Speed	303
Fig. 10.14 Total and Frictional Torque Coefficients of Propeller Operating at Forward Speed	303
Fig. 10.15 Torque Coefficient of Propeller Operating at Forward Speed	304
Fig. 10.16 Efficiency of Propeller Operating at Forward Speed	305
Fig. 10.17 Thrust Coefficient of Propeller Operating in Reverse	305
Fig. 10.18 Total and Friction Torque Coefficients of Propeller Operating in Reverse	306
Fig. 10.19 Torque Coefficient of Propeller Operating in Reverse	306
Fig. 10.20 Efficiency of Propeller Operating in Reverse	307
Fig. 10.21 Thrust Coefficient of Propeller at Zero Speed	308
Fig. 10.22 Torque Coefficient of Propeller at Zero Speed	308

CHAPTER ELEVEN

Fig. 11.1 The Arrangement of Two-Dimensional Oscillating Foil Propeller (Horizontal)	348
Fig. 11.2 The Arrangement of Two-Dimensional Oscillating Foil Propeller (Vertical)	349
Fig. 11.3 The Arrangement of Flexible Fin Propeller	350
Fig. 11.4 The Arrangement of Rotary Foil Propeller	351
Fig. 11.5 The Arrangement of Rotary Foil Propeller with SWATH	352
Fig. 11.6 Modeling of the Flexible Fin Propeller in Myklestad's Method	353
Fig. 11.7 Frequency Vs Reciprocal of Receptance Curve	353
Fig. 11.8 The Change of Natural Frequency with Changes in the Net Weight of the Foil	353
Fig. 11.9 Crank Mechanism of the Oscillating Foil	354
Fig. 11.10 Driving Mechanism of the Oscillating Foil Developed by Marine Technology Centre, Norway.	354

Fig. 11.11	The Driving Mechanism of Flexible Fin Propeller	355
Fig. 11.12	The Oscillating Motion of the Driving Bar (DA) of Flexible Fin Propeller	356
Fig. 11.13	Angular Oscillating Motion at the Pivot Generated by the Proposed Driving Mechanism	357
Fig. 11.14	Percentage of Occurrence of Wave Period (Sea + Swell) at 5 miles East of Barra	358
Fig. 11.15	The Arrangement of a Passive Flexible Fin Propeller at Stern	358
Fig. 11.16	The Present Value of Fuel Saving in a 15 Year Life Time	359
Fig. 11.17	The Breakeven Cost of the Oscillating Foil Propeller Presented in Percentage of the Cost of Existing Screw Propeller	360
Fig. 11.18	The Breakeven Cost of the Oscillating Foil Propeller with the Fluctuation of Oil Price	361
Fig. 11.19	The Breakeven Cost of the Flexible Fin Propeller at Different Interest Rates	361
Fig. 11.20	The Net Saving of a Flexible Fin Propeller with Aspect Ratio 4.0 at 75% of the Cost of Existing Screw Propeller with Fluctuation of Oil Price	362
Fig. 11.21	The Net Saving of a Flexible Fin Propeller with Aspect Ratio 10.0 at 75% of the Cost of Existing Screw Propeller with Fluctuation of Oil Price	362

LIST OF TABLES

CHAPTER FOUR

	Page
Table 4.1 The Constants of Curve-Fit Polynomial Equations for F_A of Different Aspect Ratios	120
Table 4.2 The Constants of Curve-Fit Polynomial Equations for $-G_A$ of Different Aspect Ratios	120

CHAPTER SIX

Table 6.1 The Distance of Centres of Holes to the Centre of Flange	149
Table 6.2 The Relationship Between the Holes, Angular Oscillating Amplitude and X_d	150
Table 6.3 Results from the Calibration of the Propulsive Thrust Measuring Arm	154

CHAPTER SEVEN

Table 7.1 The Estimated Bending Modulus of Flexible Bar (SO)	209
Table 7.2 The Estimated Bending Modulus of Flexible Bar (ST)	210
Table 7.3 The Estimated Bending Modulus of Flexible Bar (XST)	211
Table 7.4 The Particulars of the Flexible Bars	170
Table 7.5 The Offset Table for the Wing Section NACA-16-012	212
Table 7.6 Typical ASCII Data File	213
Table 7.7 The Stiffness Functions (ξ) for Different Flexible Bars with Different Incoming Velocity	177

CHAPTER EIGHT

Table 8.1	Mechanical Properties of Unidirectional Glass Fibre Reinforcement Plastic with 50% by Volume	223
Table 8.2	Mechanical Properties of High Strength Carbon Fibre Reinforced Plastics	227

CHAPTER NINE

Table 9.1	Principal Dimension of the 0.33m Yacht Model	249
Table 9.2	Dimensions of the Blade	249
Table 9.3	Principal Particulars of the 3/4 ton Yacht Model	251
Table 9.4	The Particulars of the Flexible Bar	252
Table 9.5	Reduction in Motion Response and Resistance	260

CHAPTER ELEVEN

Table 11.1	Principal Particulars of Ships	313
Table 11.2	Particulars of the Two-Dimensional Oscillating Propellers	315
Table 11.3	The Particulars of Flexible Fin Propellers	316
Table 11.4	Particulars of the Flexible Bars of the Propellers	318
Table 11.5	Particulars of the Flexible Fin Propeller with Aspect Ratio of 10	319
Table 11.6	The Particulars of Rotary Fin Propellers	321
Table 11.7	The Particulars of a SWATH ship	322
Table 11.8	The Particulars of Existing Screw Propellers and Engines	332
Table 11.9	The Drops of Breakeven Cost at Different Interest Rate and Different Extra Maintenance Cost	335
Table 11.10	The Breakeven Prices of Oscillating Foil Propeller with an Overall Efficiency of 0.75 at Different Interest Rates	336
Table 11.11	The Breakeven Cost of Oscillating Foil Propeller with an	336

Overall Efficiency of 0.75 at Different Interest Rates
(An Extra-Maintenance Cost of 5% is Included)

Table 11.12 The Breakeven Price of Rotary Foil Propeller with an
Overall Efficiency of 0.73 at Different Interest Rates

341

[The table content is extremely faint and illegible due to low contrast and scan quality. It appears to be a table with multiple columns and rows, likely containing numerical data related to the breakeven price of rotary foil propellers under various interest rates.]

NOMENCLATURE

PART I TWO-DIMENSIONAL OSCILLATING PROPELLER

CHAPTER TWO

$C(k)$	=	Theodorsen function ($C(k) = F + iG$)
C_L	=	lift coefficient
C_{Lc}	=	lift coefficient due to the circulatory flow
C_{Lp}	=	lift coefficient with quasi-steady assumption
C_M	=	moment coefficient
F	=	real part of Theodorsen function
F_S	=	leading edge suction force
F_x	=	force in x-direction
F_y	=	force in y-direction
G	=	imaginary part of Theodorsen function
$K_0(ik)$	=	modified Bessel Function of the second kind of order zero
$K_1(ik)$	=	modified Bessel Function of the second kind of order one
L	=	lift
L_a	=	lift force due to the non-circulatory flow
L_c	=	lift force due to the circulatory flow
M_a	=	moment at the rotating centre
M_{aa}	=	moment at the rotating centre due to the non-circulatory flow
M_{ac}	=	moment at the rotating centre due to the circulatory flow
$M_{1/2}$	=	moment about mid-chord point
P_l	=	pressure at the lower foil surface
P_u	=	pressure at the upper foil surface
U	=	steady flow velocity
a	=	the distance between the centre of rotation and the mid-chord point

b	=	half chord
c	=	chord
k	=	reduced frequency
l	=	lift force of a foil element
l_a	=	lift force of a foil element due to the non-circulatory flow
l_c	=	lift force of a foil element due to the circulatory flow
p	=	pressure acting on a foil element
t	=	time
v_i	=	induced velocity
$w(z)$	=	complex potential
y_o	=	non-dimensional amplitude of heave
ΔP	=	different in pressure between upper and lower foil surfaces
Δt	=	time delay factor
α	=	angle between the centre line of the foil section and the steady flow direction (angle of attack)
α_o	=	the amplitude of pitch
α_e	=	equivalent of angle of attack
ϵ_o	=	the angle of zero lift
ρ	=	density of fluid
ϕ	=	acceleration potential
φ_α	=	velocity potential represents the effect of angle of attack
$\varphi_{\dot{\alpha}}$	=	velocity potential represents the effect of pitching velocity
$\varphi_{\dot{y}}$	=	velocity potential represents the effect of heaving velocity
ω	=	oscillating frequency
Γ	=	vorticity
Φ	=	strength of vorticity
$\dot{}$	=	first derivative with respect to time (t)

.. = second derivative with respect to time (t)

CHAPTER THREE

C_T = propulsive thrust coefficient $\left(\frac{\bar{F}_T}{\frac{1}{2} \rho \omega^2 y_o^2} \right)$

C_{TS} = propulsive thrust coefficient contributed by the leading edge suction
force $\left(\frac{\bar{F}_S}{\frac{1}{2} \rho \omega^2 y_o^2} \right)$

F = real part of Theodorsen function

F_S = leading edge suction force

F_T = propulsive thrust

G = imaginary part of Theodorsen function

L = lift

L_R = real part of the lift force

L_I = imaginary part of the lift force

M_a = moment at the rotating centre

M_{aR} = real part of the moment at the rotating centre

M_{aI} = imaginary part of the moment at the rotating centre

T = period

U = advance speed

a = distance between rotating centre and mid-chord point

b = half chord

c = chord

k = reduced frequency

s = span

t = time

y = vertical displacement

y_o = amplitude of heave

α	=	angular displacement
α_o	=	the amplitude of pitch
β	=	phase lag between heave and pitch
θ	=	feathering parameter
ρ	=	density of fluid
ω	=	oscillating frequency
\Re	=	real part of the equation
-	=	mean

PART II FLEXIBLE FIN PROPELLER

CHAPTER FOUR

C_A	=	unsteady lifting function ($C_A = F_A + i G_A$)
E	=	bending modulus
F_A	=	real part of unsteady lifting function
F_H	=	horizontal force
F_V	=	vertical force
F_S	=	leading edge suction force
G_A	=	imaginary part of unsteady-lifting function
I	=	section modulus
I_σ	=	section modulus at any point σ
L	=	lift
L_o	=	length of the cantilever
M	=	bending moment
M_a	=	moment at the rotating centre
M_o	=	moment acting at the free end of cantilever
R	=	radius of curvature
U	=	advance speed

a	=	the distance between the centre of rotation and the mid-chord point
b	=	half chord
c	=	chord
k	=	reduced frequency
s	=	span
t	=	time
t_1	=	sectional thickness at the free end
t_2	=	sectional thickness at the fixed end
t_σ	=	sectional thickness of the beam at point σ
w	=	width of the beam
y	=	vertical displacement
y_c	=	calculated amplitude of heave
y_e	=	estimated amplitude of heave
Δx	=	tip deflection in x-direction
Δy	=	tip deflection in y-direction
α	=	angular displacement
α_c	=	calculated amplitude of pitch
α_e	=	estimated amplitude of pitch
β	=	phase lag between heave and pitch
β_c	=	calculated phase lag between heave and pitch
β_e	=	estimated phase lag between heave and pitch
δ_x	=	non-dimensional parameter of tip deflection in x-direction
δ_y	=	non-dimensional parameter of tip deflection in y-direction
δ_ϕ	=	non-dimensional parameter of tip rotation
ε	=	continuation parameter
θ_A	=	oscillating angle at the pivot
θ_{Ao}	=	amplitude of angular oscillation at the pivot
μ	=	non-dimensional parameter of flexibility

ρ	=	density of fluid
σ	=	location along the beam
ϕ	=	slope of deflection
ϕ_t	=	slope of deflection at the free end
ω	=	oscillating frequency
$\dot{}$	=	first derivative with respect to time (t)
$\ddot{}$	=	second derivative with respect to time (t)
\prime	=	first derivative with respect to σ
$\prime\prime$	=	second derivative with respect to σ

CHAPTER FIVE

AR	=	aspect ratio
C_T	=	propulsive thrust coefficient $\left(\frac{F_T}{\frac{1}{2} \rho U^2 S} \right)$
E	=	bending modulus of the flexible bar
I	=	section modulus of the flexible bar
L_o	=	length of the cantilever
S	=	foil area
TR	=	taper ratio $\left(\frac{t_2 - t_1}{t_m} \right)$
U	=	advance speed
c	=	chord
k	=	reduced frequency
s	=	span
t_1	=	sectional thickness at the free end
t_2	=	sectional thickness at the fixed end
t_m	=	mean sectional thickness at the fixed end

- ζ = angular oscillating function $\left(\zeta = \frac{L_o \theta_{Ao}}{b}\right)$
 θ_{Ao} = amplitude of angular oscillation at the pivot
 λ = non-dimensional pitch parameter $\left(\frac{\alpha_o}{\theta_{Ao}}\right)$
 ξ = stiffness function $\left(\xi = \frac{EI}{\rho U^2 S L_o^2}\right)$
 ρ = density of fluid
 τ = non-dimensional heave amplitude $\left(\frac{y_o}{L_o \theta_{Ao}}\right)$
 ω = oscillating frequency

CHAPTER SIX

- F_H = propulsive thrust at the pivot of the flexible fin propeller
 F_{in} = input thrust measured by the load cell on the three bar system
 F_{out} = propulsive thrust measured by the load cell on the propulsive thrust measuring arm
 K_{in} = constant factors from calibration
 K_{out} = constant factors from calibration
 M_A = moment applied to the pivot
 x_d = vertical displacement of hinge B
 l_1 = moment arm of the propulsive thrust between the pivot and the hinge D of the propulsive thrust measuring arm
 l_2 = moment arm of the measured propulsive thrust at the load cell between the hinge D and the load cell
 l_3 = horizontal distance between bar BC of the three bar system and the pivot
 l_o = length of bar AB and CD of the three bar system
 l_s = distance between the centre of pulley of the LVDT system and the hinge C when bar CD is in horizontal position

- l_x = distance between the pulley of the LVDT system and the hinge C when bar CD is at an angle of θ_A to horizontal
 Δl = recorded displacement by LVDT
 θ_A = oscillating angle at the pivot
 θ_{Ao} = amplitude of angular oscillation at the pivot
 $\dot{}$ = first derivative with respect to time (t)

CHAPTER SEVEN

- AR = aspect ratio
 C_T = propulsive thrust coefficient
 C_{Tb} = propulsive thrust coefficient in the bollard pull condition

$$\left(\frac{F_{Tb}}{\frac{1}{2} \rho (L_o \omega)^2 S} \right)$$

 E = bending modulus of the flexible bar
 F_H = propulsive thrust at the pivot of the flexible fin propeller
 F_T = mean propulsive thrust at the pivot of flexible fin propeller within an oscillating cycle
 F_{Tb} = mean propulsive thrust in the bollard pull condition
 F_V = vertical loading
 I_m = mean section modulus of the flexible bar
 L_o = length of the flexible bar
 M_A = moment applied to the pivot
 N = number of oscillating cycles
 S = foil area
 T = period
 TR = taper ratio
 U = advance speed

k	=	reduced frequency
t_1	=	thickness at the free end of flexible beam
t_2	=	thickness at the fixed end of flexible beam
t_m	=	mean thickness of the flexible beam
Δx	=	tip deflection in x-direction
Δy	=	tip deflection in y-direction
ζ	=	angular oscillating function
η	=	propulsive efficiency
θ_A	=	oscillating angle at the pivot
θ_{Ao}	=	amplitude of oscillating angle at the pivot
ξ	=	stiffness function
ρ	=	density of fluid
τ	=	non-dimensional heaving amplitude of the oscillating foil
ω	=	oscillating frequency
$\dot{}$	=	first derivative with respect to time (t)

CHAPTER EIGHT

AR	=	aspect ratio
E	=	bending modulus
I	=	section modulus
I_m	=	mean section modulus
L_o	=	length of the cantilever
M	=	bending moment
TR	=	taper ratio
f	=	stress
f_{max}	=	maximum stress acting on the beam within an oscillating cycle
k	=	reduced frequency

q	=	$\rho U^2 S$
w	=	width of the bar
\bar{y}	=	distance from the neutral axis to the surface of beam
ζ	=	angular oscillating function
ξ	=	stiffness function
ρ	=	density of fluid
σ	=	location along the beam
ϕ	=	slope of deflection
Λ	=	stress function $\left(\frac{f_{\max}}{E} \times 10^3 \right)$
ϑ	=	thickness function $\left(\frac{t_m}{L_o} \times 10^3 \right)$

CHAPTER NINE

AR	=	aspect ratio
B_{WL}	=	beam of waterline
B_{\max}	=	maximum beam
E	=	bending modulus
Fr	=	Froude Number $\left(\frac{U}{\sqrt{g L_{WL}}} \right)$
I_m	=	mean sectional modulus
L_{WL}	=	length of waterline
L_{OA}	=	overall length
TR	=	taper ratio
S_3	=	heave coefficient
S_5	=	pitch coefficient
U	=	advance speed
Z_o	=	heave amplitude of model

a_o	=	wave amplitude
c	=	chord
g	=	gravitational constant
s	=	span
t	=	thickness of the foil
t_1	=	thickness at the free end of flexible beam
t_2	=	thickness at the fixed end of flexible beam
t_m	=	mean thickness of the flexible beam
λ	=	wave length
λ_c	=	encounter wave length ratio
λ_e	=	encounter wave length
v	=	non-dimensional speed $\left(\frac{U}{a_o \omega_w}\right)$
ϕ_o	=	pitch amplitude
ω_c	=	wave frequency coefficient
ω_e	=	encounter wave coefficient
ω_{ew}	=	encounter wave frequency
ω_w	=	wave frequency
Θ	=	wave slope

PART III ROTARY FOIL PROPELLER

CHAPTER TEN

A_s	=	swept area (2Rs)
J	=	advance ratio $\left(\frac{U\pi}{\Omega R}\right)$
Q	=	torque
Q_c	=	torque coefficient $\left(\frac{Q}{\rho \Omega^2 R^3 A_s}\right)$

R	=	radius of rotation of the blades
T	=	thrust
T_c	=	thrust coefficient $\left(\frac{T}{\rho \Omega^2 R^2 A_s}\right)$
U	=	advance speed
s	=	span of the blade
β	=	pitch angle of the blade
β_{\max}	=	pitch angle of the blade
η	=	propulsive efficiency
θ_R	=	rotation angle
ρ	=	density of fluid
Ω	=	rotation speed

PART IV APPLICATION OF OSCILLATING FOIL PROPELLERS & GENERAL CONCLUSIONS

CHAPTER ELEVEN

AR	=	aspect ratio
AR_e	=	effective aspect ratio
B	=	beam of ship
BHP	=	brake horse power
C_{FFP}	=	cost of flexible fin propeller
C_B	=	block coefficient
D_T	=	draft
Fr	=	Froude number
J	=	advance ratio
L_o	=	length of flexible bar
L_{pp}	=	length between perpendicular

P_E	=	effective power
P_T	=	thrust power
R	=	radius of rotation of the blades
T_c	=	thrust coefficient
TR	=	taper ratio
S	=	foil area or swept area for rotary foil propeller
$SPWF$	=	series present worth factor
V	=	service speed
b	=	half chord
c	=	chord
int	=	interest rate
k	=	reduced frequency
s	=	span
t	=	thrust deduction fraction
t_m	=	mean thickness of the flexible bar
w	=	wake fraction
w_b	=	width of the flexible bar
y_o	=	amplitude of heave
α_o	=	amplitude of pitch
β_{max}	=	pitch angle of the blade
ζ	=	angular oscillating function
θ_{Ao}	=	amplitude of angular oscillation at the pivot
λ_c	=	encounter wave length ratio
ξ	=	stiffness function
ω	=	oscillating frequency
Λ	=	stress function
Ω	=	rotation speed
ϑ	=	thickness function

SUMMARY

In this thesis, an investigation on the use of oscillating foil propulsion for marine vehicle as an alternate effective propulsion system is presented. Three different oscillating foil propellers, namely: two-dimensional oscillating foil propeller; flexible fin propeller; and rotary foil propeller, have been studied.

The thesis is made up of four parts : one related to each type of propeller and one on the application of oscillating foil propellers along with general conclusions.

Two-Dimensional Oscillating Foil Propeller

A review on the hydrodynamic forces and moments acting on a two-dimensional oscillating foil is presented. The equations for estimating the force system have been extended to cover different phase lags between heave and pitch and to calculate the force system at a particular instant of time within an oscillating cycle. The sensitivity of the propulsive thrust coefficient and the hydromechanical efficiency has been investigated for a range of different parameters. The operating condition for optimum performance is identified.

Flexible Fin Propeller

The theoretical model of the flexible fin propeller, which has been set up by combining linearised unsteady foil theory and large deflection beam theory, is described. Non-dimensional parameters are established to study the performance of this type of propeller. A flexible fin propeller model and its test rig was designed and built. The model was tested in the Hydrodynamics Laboratory at the Department of Naval Architecture and Ocean Engineering, the University of Glasgow. The performance of the propeller was examined at both forward and zero speeds. Results have been compared with theoretical predictions. Conclusions on the performance of the flexible fin propeller are drawn based on the theoretical predictions and experimental results. The stress acting on the flexible bar has been computed and discussed. The selection of material has been discussed and promising materials identified.

The feasibility of using flexible fin propellers for wave propulsion to absorb wave energy and convert it into propulsive thrust has been studied. A one-fifth scale model of a three quarter ton racing yacht with a flexible fin propeller model mounted at the stern was tested. At a low Froude number, there is a significant reduction in the motion response and in the required thrust around the resonance zone, where the encounter wave length is equal to the ship length.

Rotary Foil Propeller

A three bladed propeller model with high-aspect ratio blades was tested in forward and reverse directions and zero speed conditions. The experimental results on the performance of the model at forward speed have been compared to that predicted by Bose [1987] using multiple stream tube theory and discussed.

Application of Oscillating Foil Propeller and General Conclusions

The practical application of three oscillating foil propellers and economic studies of their operation have been studied and discussed. Three ship examples with the same Froude number but different in sizes and a high speed craft have been used in these studies. Three types of oscillating foil propeller are designed for each ship example. The required stern hull form and the driving mechanism have been discussed. The application of the flexible fin propeller in wave propulsion has been demonstrated. The natural frequency of a full scale flexible fin propeller was calculated and found to be much higher than the optimum driving frequencies in the operating condition.

The net present value method has been applied in the economic studies where breakeven conditions, different interest rates, fluctuation of oil price, and different additional maintenance costs have been considered.

The main conclusions of this research have been drawn up and are presented. Recommendation on the design of these propeller are also made.

CHAPTER 1

INTRODUCTION

1.0 SHIP PROPULSION

On this beautiful planet, Earth, about two-thirds of the surface is covered by water. The blue oceans, rivers and streams separate lands into continents and islands. In the earliest days, man learnt to travel across streams on floating pieces of wood and propelled with oars by manpower. Then, vessels were propelled by combining wind propulsion and rowing. According to Comstock [1977], Toogood & Hayes, in 1661, held a patent of the first propulsive device for ships driven by mechanical power, which was a pump; and water was accelerated by the pumping action and this was used for propulsion. This formed the foundation of the later development of jet propulsion for high speed craft (e.g. hydrofoils). Later, the first steam ship equipped with paddle wheels, Charlotte Dundas, was built and operated in Scotland in 1801. This paddle wheel system was far from effective for ship propulsion.

A more effective and reliable device, the screw propeller, was proposed in 1680 by Hook and its first application came in 1836. The paddle wheel was in due course superseded by the screw propeller. The screw propeller quickly developed to dominate the ship propulsion systems for years and is still the main propulsion system in modern marine vehicles. However, the practical propulsive efficiency of screw propellers is normally about 0.6 to 0.7. For small ships, the efficiency may be even lower. A number of devices have been used to improve the propulsive effectiveness of the screw propeller such as the controllable pitch propeller, ducted propeller (shroud or nozzle), Mitsui integrated duct system, tip vortex free propeller (propeller with end plates), Grim vane wheel, contra-rotating propellers, tandem propellers, swirl and Schneekluth wake distributor duct. These devices are discussed in detail by Dumpleton [1986]. Recently, propeller boss cap fins [Gearhart and McBride 1989] have been developed

for improving efficiency. However, there is no unique solution for the improvement of the propulsive efficiency of the screw propeller.

2.0 THE PROPULSION SYSTEM OF AQUATIC ANIMALS

People have always been amazed by the high swimming speed of fishes and cetacean mammals. For example, a 2m tunny fish can swim at a top speed of 40 knots [Lighthill 1977]. A dolphin can support its body out of the water by oscillating its tail. The thrust generated by the oscillating tail is high. These animals live in a world with a strong predator-prey relationship and "survival of the fittest" makes propulsive effectiveness essential to them. As their lives depend on capturing other marine organisms or being captured, swimming speed and efficiency is closely linked to the matter of live and death. For a minority group, different protective systems are used to escape from being captured. Biologists deeply believe the "convergent evolution" and fishes evolve to a form with higher survival capability and better swimming efficiency.

The drag and power output of the muscles of a dolphin were calculated and compared by Gray [1936]; a large discrepancy was found between the available power from the muscles and that required to achieve the swimming speed. This became known as "Gray's Paradox". He concluded that, unless the muscle generates an amazingly high power, it is impossible for a dolphin to achieve its swimming speed. This finding stimulated research on the swimming efficiency of fishes and cetacean mammals. Gray himself made a large contribution to the study of fish locomotion [Gray 1968]. The development of research on the thrust, drag and power of swimming fishes and a literature review are described by Peachey [1981]. In the sixties and early seventies, Lighthill [1960, 1969, 1970 and 1971] and Wu [1971 a, b and c] made significant contributions to the theoretical model of fish propulsion from the hydrodynamic point of view.

Investigations on the hydrodynamic performance of an oscillating lunate fin have been carried out. Chopra & Kambe [1977] applied the Davies [1965] method of

finding the loading distribution on an oscillating wing to investigate the propulsive thrust and efficiency of different foil shapes which included lunate shape and efficiency above 0.9 was found. Lan [1979] applied his unsteady quasi-vortex-lattice method to study the performance of an oscillating arrow shaped foil. Cheng & Murillo [1983] used a curved lifting line to model the lunate tail and applied the asymptotic unsteady lifting line theory to calculate the lift distribution of an oscillating lunate tail. Bose and Lien [1989] used a quasi-non-linear theoretical approach with measurements from an immature fin whale to illustrate the performance of the flukes in propulsion.

Humans deeply believe the propulsion system used by fast fishes and cetacean mammals is an effective system. However, neither fishes nor cetacean mammals have a propulsion method similar to a screw propeller.

2.1 Mode of Swimming

There are different modes of fish swimming. Examples of different modes of motion are shown in fig. 1.1 [Hoar & Randall 1978]. The vertical axis shows the part of body and fins (shaped) which generates propulsive thrust. The horizontal axis describes the motions from undulation (wave form motion) to oscillation (rigid fan-like motion). The shaded area is the part which generates propulsive thrust. Breder [1926] divided the swimming motion, where propulsive thrust come from the body and caudal fin, into three classes : anguilliform, carangiform and ostraciiform.

The anguilliform is a pure undulatory swimming motion that involves the majority of the body in generating the propulsive thrust. The oscillating wave length to the body length is short; the best example is the swimming motion of an eel. The ostraciiform is a rigid oscillation where the caudal fin flaps like a fan with pendulum motion. The anguilliform and ostraciiform are two extreme modes of motion. The motion between anguilliform and ostraciiform is the carangiform. Since the term, carangiform, covers a wide range of motion, it has been further divided into three different classes : subcarangiform, carangiform and thunniform as shown in fig. 1.1.

These swimming modes are compared and listed in detail by Hoar & Randall [1978, table II p.13]. In fig. 1.2, the swimming modes of anguilliform, subcarangiform, carangiform and thunniform are illustrated.

After millions of years of convergent evolution, fast fishes and cetacean mammals possess a similar mode of swimming motion (thunniform) and similar caudal fin shape (a high-aspect-ratio lunate tail). The best examples are the tunny fish, dolphins, swordfish and whales. These aquatic animals followed different evolutionary routes, indeed dolphins and whales are mammals, but they have ended up with similar propulsion systems. They are either fast swimmers or required large propulsive thrust making effective propulsion essential.

For the thunniform mode of swimming, the wave length of the undulating motion is large and is about one to two body lengths. The undulations are confined to the peduncle and tail. The body shape is streamlined with extreme narrow-necking of the peduncle. The aspect ratio of the caudal fin is high and lunate. The centre part of the fin always lead the tips of the fin. When the tail is at the upper or lower most positions, the lagging of the tips prevents the total loss of propulsive thrust at these parts of the cycle as mentioned by Lunde [1982].

The body motion is reduced to a minimum in thunniform swimming and is concentrated on the posterior portion, as shown in fig. 1.2. The swimming path of thunniform is straighter [Fierstine & Walters 1968]. The caudal fin heaves and pitches with a 90° phase difference. The fin is parallel to the forward motion at the top of the upward stroke. As the fin moves down, it pitches downward and maximum pitching angle occurs when the fin passes the body axis. The fin comes to zero pitch position again at the bottom of the downward stroke. The whole process is reversed when the fin moves upward.

3.0 OSCILLATING FOIL PROPULSION

A number of inventions on novel ship propulsion systems had been proposed. Recent work [Tsutahara & Kimura 1987] on applying the mechanism of hovering flight of small insects, termed "Weis-Fogh Mechanism" [Weis-Fogh 1973 and Lighthill 1973] has also been carried out. A similar device with driving mechanism has been proposed by Brown [1986]. The system is made up of two vertical surface piercing wings which oscillates 180° out of phase to each other.

A large number of inventions have been stimulated from the swimming of fishes. Most of these inventions are closer to the ostraciiform where propulsive thrust is generate by either rigid or flexible flaps. Bjelvucic [1907] invented a system which was made up of one or more pairs of elastic horizontal wings and connected on a vertical shaft which was rapidly reciprocated up and down. Therefore the wings flapped and generated propulsive thrust. Hotchkiss [1947] proposed a flapper with a rubber diapham which can be used to utilise wave energy or direct driven by manpower or engine. The diapham of the flapper formed a concavity when the flapper moved through the water. Warner's invention [1963] was very similar to that of Bjelvucic [1907]. Tipaldi [1980] proposed a rigid paddle shaped plate which was connected directly on a pivot and oscillated up and down by manpower. Ramsay-Whale [1980] proposed vertical flexible flaps which were hand operated and oscillated sideways. Although the ostraciiform possesses the following advantages,

- i) The main body motion is rigid and stable, and
- ii) a straighter course is achieved,

low efficiency is expected. Thunniform swimming is expected to have high efficiency and also possesses the above advantages. From the view point of ship propulsion, thunniform swimming is the most suitable.

In 1895, Linden obtained a patent [Linden 1895] for converting wave energy

into propulsive energy with a flap activated by the ship response in waves. In Norway [Jakobsen 1981 and 1982] and Japan [Isshiki et al. 1982, 1984 and 1986], research has been carried out using foil systems to convert wave energy into propulsion energy. Owing to the ship motion in waves, the foil heaves and pitches.

Active fin propulsion systems for ships has been developed in parallel to that of wave propulsion. Scherer [1968] established a semi-linear large amplitude oscillating foil theory and the result was compared with experiment on an oscillating foil with aspect ratio 3 and applied to the design of a shallow-draft boat. Chopra [1976] developed a more sophisticated theory on the large amplitude oscillation of a two-dimensional foil. Potze [1986] looked at optimum sculling propulsion and interaction between two oscillating foils.

An active foil propulsion system with springs has been developed by Jakobsen [1983 and 1988] and the Marine Technology Centre, Norway [Lai 1988]. The fin was oscillated vertically and the pitching motion was provided by a spring system. A similar system was tested in Sweden [Bergman & Gothberg 1985] and a high efficiency of 0.75 was measured in this test.

Research on propulsion systems with a flexible foil has also been carried out. Katz and Weihs [1978] had developed a mathematical model for a two-dimensional oscillating foil with chordwise flexibility. Kudo et al. [1984] looked at the performance of rigid and partially elastic oscillating foils by using linearized theory. Kubota et al. [1984] proposed a non-linear theory for the performance of an oscillating foil and studied its application to ship propulsion and found that higher efficiency but lower thrust can be obtained in a partially elastic foil. A partially elastic oscillating foil was fitted on a ship model and tested and an efficiency of 0.65 was found. In Russia, Strekalov [1986] proposed a propulsion system with elastic oscillating wings driven by a crank system. Both forward and reverse thrusts can be generated by this system. Experiments [Isshiki et al. 1987] were performed on a boat with a low-aspect-ratio fin; the oscillation was provided by a crank shaft system similar to that of Strekalov's

machine. An outboard system was also tested.

A swimming aid using oscillating foil propulsion and driven by human power has been developed as shown in fig. 1.3 [Unitex Marine Limited, 1989]. The manufacturer claimed that with the system it is possible to generate a mean thrust in excess of 40 kg and can be used to tow three persons.

4.0 THE BACKGROUND AND OBJECTIVE OF THE STUDY

The characteristics and performance of an oscillating foil system are different for each of the individual systems. From the inspiration of thunniform swimming, three different oscillating foil propulsion systems were proposed at the beginning of the study. These propellers are termed the two-dimensional oscillating foil propeller, flexible fin propeller and rotary foil propeller as shown in fig. 1.4. Their particulars are listed as follows.

1) Two-Dimensional Oscillating Foil Propeller

The active foil is held between two enclosing end struts which house the driving mechanism as shown in fig. 1.4a. These enclosing struts provide an end shielding effect which reduces the pressure loss at the tips of the foil. Theoretically, if there is no pressure leakage through the tips, the flow across the foil is two-dimensional and propulsive efficiency is increased.

2) Flexible Fin Propeller

This propeller is an imitation of the fish tail thunniform motion. A hydrofoil is connected to a pivot through a flexible bar as shown in fig. 1.4b. The foil heaves and pitches as a result of applying an angular oscillation at the pivot. Owing to the flexibility of the connecting bar, a phase lag is obtained between heaving and pitching. This method is first mentioned by Gray [1968, p 25]. Bose et al.[1986] proposed a research

project using this as a ship propulsion device and received a Science and Engineering Research Council research grant to study the device in detail.

3) Rotary Foil Propeller

This is a multi-bladed propeller where blades with high-aspect-ratio are mounted on a rotating drum. These blades also oscillate about their rotating axes, as shown in fig. 1.4b. This is a type of trochoidal propeller with high aspect ratio blades. The foil heaves and pitches as a result of the rotation of the drum and the angular oscillation about its rotating axis. The surface of the rotating drum provides a mirror image which increases the effective aspect ratio of the blades.

4.1 Aims of Research

The aim of this research is to investigate the use of these propellers for propulsion of marine vehicles. The main objectives of this work are to :

- 1) study the hydromechanical performance of these propellers by theoretical and experimental investigation;
- 2) investigate the application of these propellers to ship propulsion based on the hydromechanical performance; and,
- 3) set down recommendations for design.

5.0 CONTENT OF THESIS

The content is made up of four parts namely,

- i) the two-dimensional oscillating foil propeller,
- ii) the flexible fin propeller,
- iii) the rotary foil propeller, and
- iv) the application and economic studies and main conclusions.

5.1 Two-Dimensional Oscillating Foil Propeller

In Chapter 2, the hydrodynamic forces and moments acting on a two-dimensional oscillating foil are reviewed. As an introduction to the subject, a quasi-steady approach is discussed. Two-dimensional linearized unsteady foil theory based on approaches using the acceleration potential [Biot 1940, Lai 1988a] and velocity potential [Theodorsen 1935] are presented and compared. The leading edge suction force is also discussed. The force system acting on an oscillating foil is made up of a lift force, leading edge suction force and pitching moment at the rotation centre.

The equations for estimating the force system [Lai 1988b] are extended to cover different phase lags between heave and pitch and to calculate the forces and moment at a particular instant of time within an oscillating cycle. This is described in Chapter 3. The sensitivity of the propulsive thrust coefficient and efficiency is investigated for different parameters. The variation of the propulsive thrust throughout an oscillating cycle is studied when the pitching motion lags the heaving motion by 90° . Optimum performance is expected to occur at low reduced frequency with phase lags around 90° , high values of the feathering parameter and a location of rotation centre between the mid-chord and the three quarter chord point.

5.2 Flexible fin Propeller

A theoretical model of flexible fin propeller with rectangular foil [Lai 1989] has been set up by combining linearized unsteady foil theory and large deflection beam theory. This is presented in Chapter 4. The force system acting on a rectangular foil with finite aspect ratio is described. The three-dimensional effect is included by using the unsteady-lifting functions for rectangular and elliptical wings [Jones 1940, Drischler 1956]. Good agreement is found between the results of the present method and that from Chopra & Kambe [1977] and Lan [1979]. As the connecting bar is flexible, a large deflection beam theory has been applied. A second order differential

equation has been formulated with a force system acting at the free end of a flexible cantilever and this is solved by a numerical method. The model has also been set up to investigate a flexible fin propeller in which the connecting bar is constant in width but has a linear variation in thickness.

Parametric studies [Lai 1989] have been carried out using this theoretical model. A number of non-dimensional parameters have been set up to study their effect on hydromechanical performance in Chapter 5. These parameters represent the flexibility of the connecting bar, amplitude of angular oscillation at the pivot, the relationship between the oscillating frequency and forward speed and aspect ratio of the foil. Propulsive thrust increases as the stiffness of the bar increases, but the efficiency decreases. Higher thrust is obtained when the angular oscillating amplitude increases. Efficiency increases as the aspect ratio increases.

A flexible fin propeller model and its test rig was designed and built. The design of the rig is described in Chapter 6 and the construction drawings [Lai 1988c] are shown in Appendix I. The objective of the rig is to convert the rotation into a sinusoidal angular oscillation and transfer this to drive the model at the pivot. The dynamometer is also integrated into the rig. The objective functions were checked and confirmed to meet the design criteria.

The experimental investigation [Lai 1989a] on the performance of the flexible fin propeller has also been carried out as shown in Chapter 7. A flexible fin propeller model with a wooden rectangular foil, with aspect ratio was four and the cross section was NACA 16-012, was tested in the Hydrodynamics Laboratory at the Department of Naval Architecture and Ocean Engineering, University of Glasgow. Incoming flow velocity at the foil and frictional loss in the driving mechanism were investigated. The performance of the model was tested at both forward and zero speed conditions. Experimental results in the forward speed condition have been compared to the theoretical predictions. At low angular oscillating amplitude, good agreement is found between experiment and theory for both propulsive thrust and efficiency. High

efficiency is also obtained at low angular oscillating amplitudes. A high efficiency of 0.7 was found in the experiments.

The stress acting on the bar is computed by using a theoretical model and this is discussed in Chapter 8. In this chapter, the maximum working stress of a flexible fin propeller for a 66 m ship is used to discuss the selection of material and study fatigue life. High strength carbon fibre reinforced plastic possesses the required fatigue strength and suitable mechanical properties. Hybrid carbon-glass fibre reinforced plastic is a more cost-effective material which still possesses a promising fatigue strength and mechanical properties.

The feasibility of using a flexible fin propeller for wave propulsion to absorb wave energy and convert this into ship propulsive thrust has been studied and presented in Chapter 9. A simplified flexible fin propeller with no power supply was mounted on a 0.33 m yacht model and tested in the small demonstration tank [Lai & McGregor 1989]. The model advanced forward in waves with the propeller and drifted backward without the propeller and the idea was confirmed. A larger scale of model test was carried out in the main tank of the Hydrodynamics Laboratory. A one-fifth scale model of a three-quarter ton racing yacht and a flexible fin propeller with rectangular foil at an aspect ratio 4.0 was used in this investigation. The resistance and motion response for the model with and without the propeller were measured and compared for different wave conditions and forward speeds. There is a significant reduction in motion response and resistance around the resonance zone, where the encounter wave length is equal to the ship length, with a passive flexible fin propeller fitted on the stern at a low Froude number.

5.3 Rotary Foil Propeller

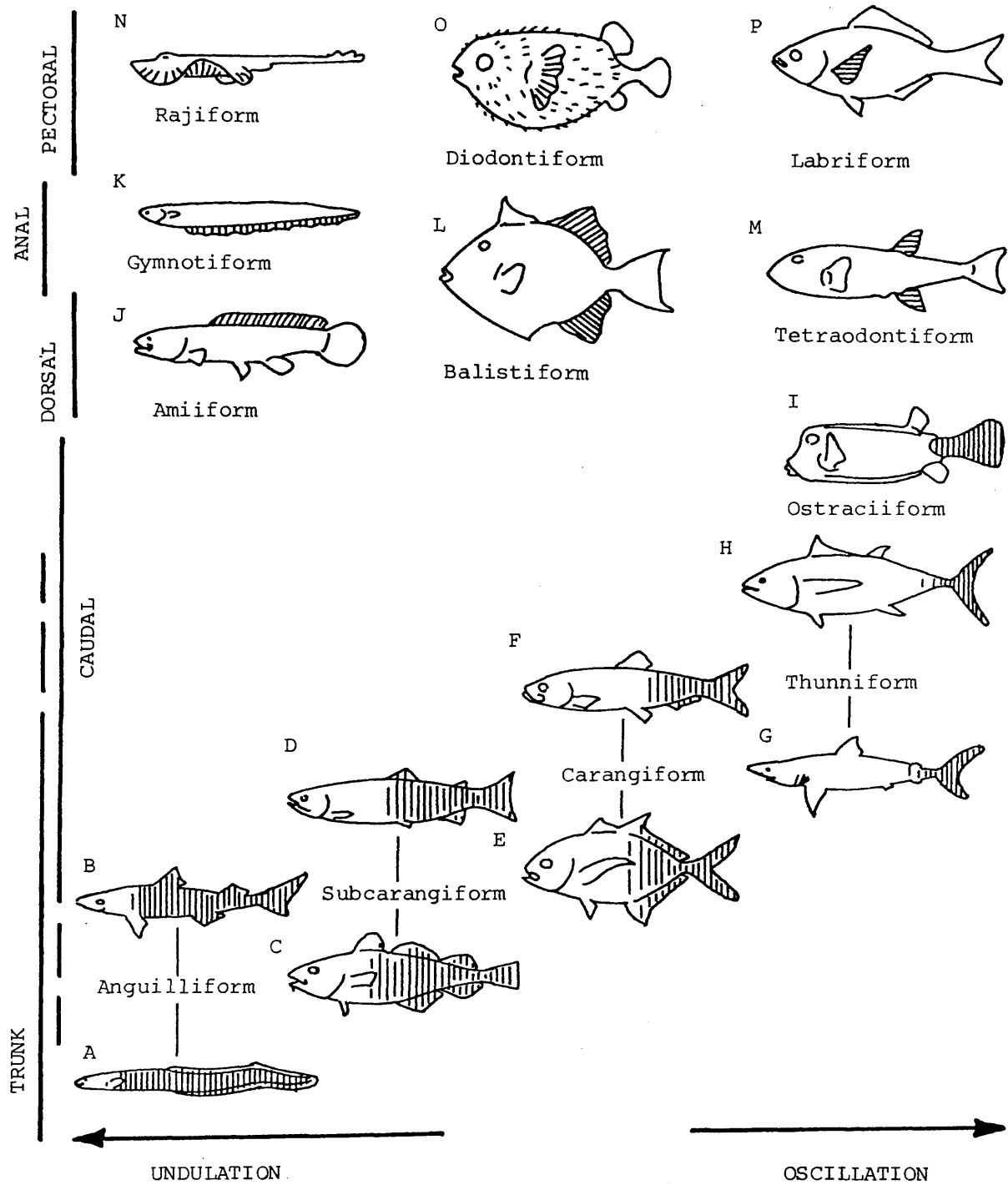
A trochoidal propeller model with high-aspect ratio blades, which is designated as a rotary foil propeller [Bose 1987], was tested in the testing tank of the laboratory. The model is a three-bladed model with an effective aspect ratio of 10. The performance

of the propeller was tested in forward and reverse direction and zero speed conditions. The results are presented in Chapter 10. The flow velocity around the blades and frictional loss in the driving mechanism were also investigated. The experimental results on the performance of the model at forward speed are compared to that predicted by Bose [1987] using multiple stream tube theory. A high propulsive efficiency of 0.8 was found in the calm water test with forward speed.

5.4 Application and Conclusion

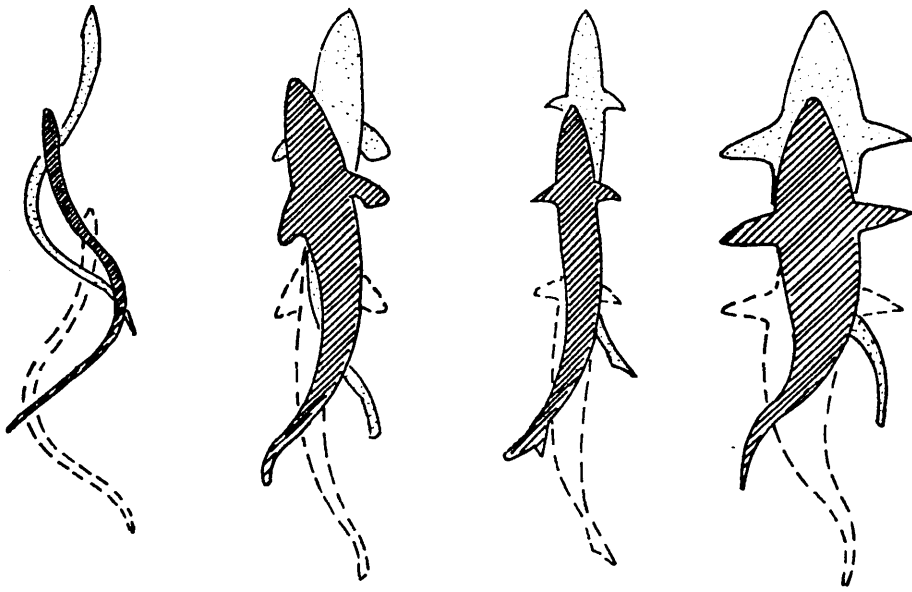
The practical application and economic studies of the operation of these propellers in actual marine service have been analysed using data and programs based the previous studies and are presented in Chapter 11. Three ships with a similar Froude number around 0.25 but different in size together with a high speed craft have been used in this study. Three types of oscillating foil propeller were designed for each ship example and these are discussed. Suitable hull forms for different propellers are also proposed in this chapter. The corresponding driving mechanism and arrangements are discussed. The natural frequency of a full scale flexible fin propeller was calculated and compared to the operating condition. The application of wave propulsion with a flexible fin propeller is also demonstrated. The net present value method is applied in the economic studies where break even conditions, fluctuation of oil price, different interest rates and different additional maintenance costs are considered. Recommendations on the application of these oscillating foil propellers, from the economic point of view, have been made.

Conclusions are given at the end of each chapter. In Chapter 12, the conclusions and findings of this thesis are summarised and future development on this subject is suggested.



- | | | | |
|---|--------------------------|---|--------------------------------|
| A | <i>Anguilla anguilla</i> | I | <i>Ostracion tuberculatum</i> |
| B | <i>Squalus acanthias</i> | J | <i>Amia calva</i> |
| C | <i>Gadus morhua</i> | K | <i>Gymnotus carapo</i> |
| D | <i>Salmo gairdneri</i> | L | <i>Balistes capriscus</i> |
| E | <i>Caranx hippos</i> | M | <i>Lagocephalus laevigatus</i> |
| F | <i>Clupea harengus</i> | N | <i>Raja undulata</i> |
| G | <i>Isurus glaucus</i> | O | <i>Diodon holocanthus</i> |
| H | <i>Thunnus albacares</i> | P | <i>Cymatogaster aggregata</i> |

Fig. 1.1 Modes of Swimming



a) Anguilliform b) Subcarangiform c) Carangiform d) Thunniform

	1 st Location
	2 nd Location
	3 rd Location

Fig. 1.2 Four Different Modes of Swimming (Hoar & Randall 1978)

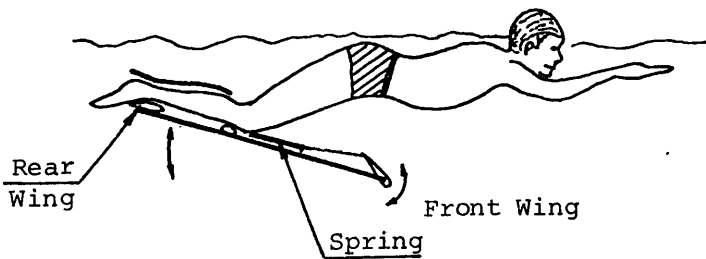
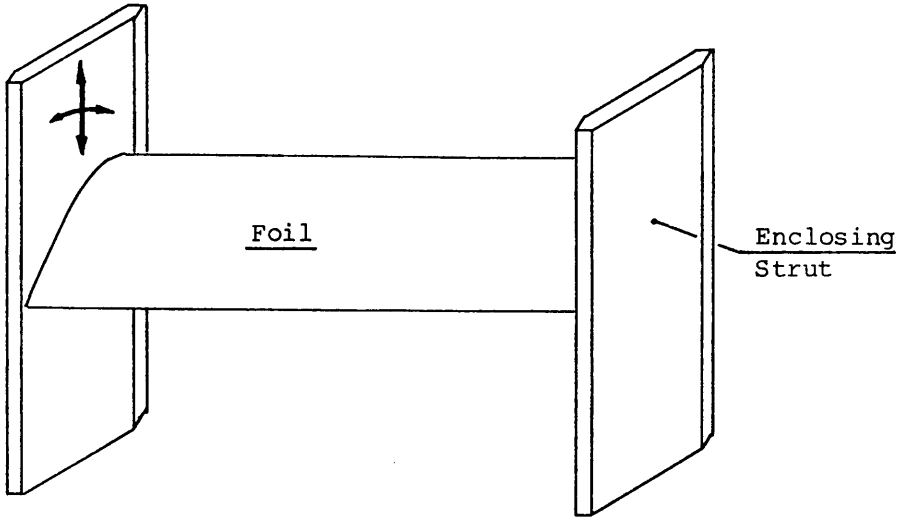
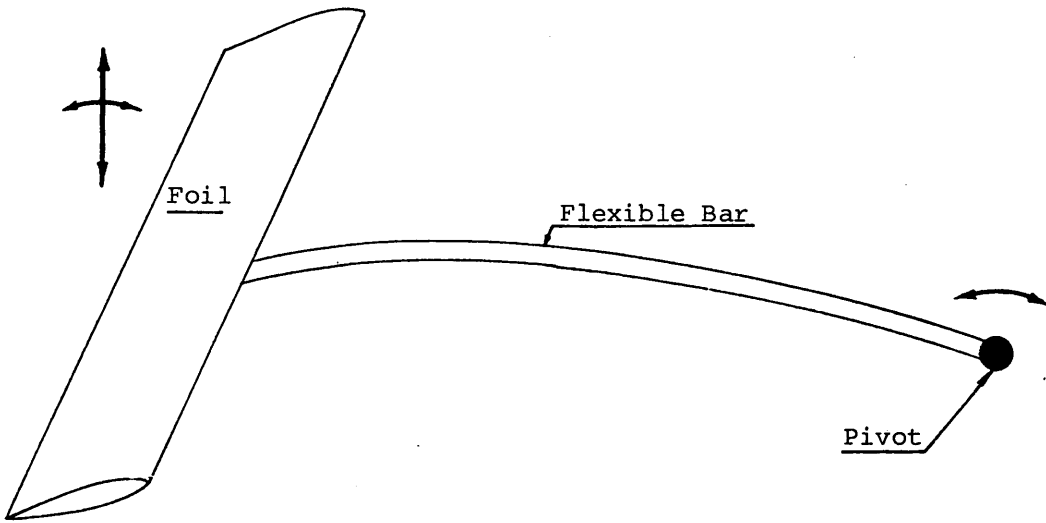


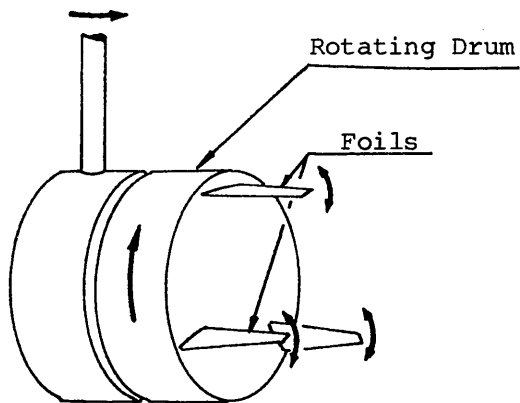
Fig. 1.3 The "Aqueon" Inner Space Vehicle (Unitex Marine Ltd. 1989)



a) Two-Dimensional Oscillating Foil Propeller



b) Flexible Fin Propeller



c) Rotating Foil Propeller

Fig. 1.4 Three Types of Oscillating Foil Propeller

PART I

A TWO-DIMENSIONAL OSCILLATING FOIL PROPELLER

A two-dimensional oscillating foil propeller is investigated in this part. This propeller is made up of an oscillating foil and two side struts which enclose the tips of the foil. In the ideal condition, no flow occurs across the gap between the foil and struts. The flow across the foil is a two-dimensional one. The hydrodynamic force system acting on a 2-dimensional oscillating foil is discussed in chapter two. The performance of this type of propeller is investigated in chapter three. An optimum motion is recommended as a result of this investigation.

CHAPTER 2

HYDRODYNAMIC FORCE AND MOMENTS ACTING ON A TWO DIMENSIONAL OSCILLATING FOIL

1.0 INTRODUCTION

When a foil oscillates in a fluid domain with a speed of advance, hydrodynamic forces and moments are generated and these act on the foil. In this chapter, the force system acting on an oscillating two dimensional foil is discussed. The force system can be calculated using a quasi-steady approach or an unsteady foil theory. In this chapter, both the quasi-steady approach and the unsteady lifting foil theory are presented and compared.

The quasi-steady approach is only suitable for a low frequency oscillation where the unsteadiness is not important. For higher oscillating frequencies, an unsteady lifting foil theory should be used. As an introduction to the quasi-steady approach, an aerofoil in a steady flow is briefly discussed here. Bose [1987] applied a similar quasi-steady approach in the multiple stream-tube theory to study the performance of a trochoidal propeller.

In unsteady lifting foil theory, linearised assumptions are used. Two-dimensional linearised theory was first developed in the 1930's for studying the flutter problems of aeroplane wings. Recently, Kyojuka et al. [1988] developed a linearised theory to include the effect of foil thickness. His results showed that thickness effects are not important.

Two dimensional linearised unsteady foil theory has been developed by a number of authors [Glauert 1929, Wagner 1925, Theodorsen 1935, von Karman and Sears 1938, Biot 1940]. In particular, Theodorsen [1935] developed the theory using

velocity potentials and applied it to study the flutter problem of an oscillating foil. Von Karman and Sears [1938] calculated the lift and moment forces based on the rate of change of momentum of vortex pairs in the system. Biot [1940] applied the acceleration potential in calculating the force system.

In this chapter, Biot's method based on the acceleration potential is shown. Application of the acceleration potential was first introduced by Prantl [1936]. Biot extended it and applied it to an unsteady oscillating foil with a vertical oscillation. Then Fung [1969] further extended the theory to include pitching oscillations. Based on the acceleration potential, Lighthill [1970] developed a theory to estimate the propulsive thrust and efficiency of a two-dimensional oscillating foil. In addition, Theodorsen's theory [1935] is presented. Comparisons are made between these two approaches. The quasi-steady approach is compared to linearised unsteady foil theory. The leading edge suction force is discussed.

Although the approaches to the unsteady oscillating foil theory are different, the final equations to calculate the force system are the same. The oscillating motion introduces a modified angle of attack with a downwash angle at the three-quarter chord point. In unsteady foil theory, the equivalent angle of attack is further modified by a complex function known as the Theodorsen Function and this introduces a time delay factor.

2.0 BOUNDARY CONDITIONS

The boundary conditions in aerofoil problems are set out below.

- 1) **Kinematic Boundary Condition** :-The fluid must not penetrate the aerofoil surface. Therefore the flow must be tangential to the solid surface of the foil at all times.

- 2) **The Kutta flow off condition** :- This condition at the trailing edge must be satisfied. The Kutta condition states that for an inviscid fluid there must be no flow around the sharp trailing edge and the fluid must flow off the trailing edge smoothly. The

flow velocity is finite.

- 3) Radiation Condition (Far Field Condition) :- At infinity, the velocity disturbance decreases to zero. This means that the velocity potential tends to a constant. The acceleration of the fluid particles decreases to zero.

3.0 THE TWO DIMENSIONAL AEROFOIL IN STEADY FLOW

When a steady flow with speed U acts on an aerofoil with an angle of attack α , there is a lift force generated [Glauert 1942, Schlichting and Truckenbrodt 1979, Abbott and Von Doenhoff 1959]. The lift force is generated by the pressure difference on the lower and upper surfaces and the lift production is related to the circulation of the flow in the near field, as shown in fig. 2.1.

$$dL = (P_l - P_u)dA = \Delta P dA \quad - 2.1$$

The difference in pressure (ΔP) is related to the changes of flow velocity on the upper and lower surface of the foil by the Bernoulli Equation. The vorticity is related to lift by the Kutta-Joukowski equation

$$dL = \rho U \Gamma(x) dx \quad - 2.2$$

The flow around a thin profile is obtained by superposition of a steady flow with a distribution of potential vortices. Since the camber of the aerofoil is assumed to be small, the vortices are assumed to be distributed along the X - axis. The vertical component [Glauert 1942] of the induced velocity at a point (x) is

$$v_i(x) = \int_0^c \frac{\Gamma(\xi)d\xi}{2\pi(\xi - x)} \quad - 2.3$$

Therefore the slope of the uniform stream is $(\alpha + v_i/ U)$. According to the

kinematic boundary condition, the slope of the flow stream will be equal to the slope of the aerofoil surface (dY/dx). Therefore ,

$$\alpha + \frac{v_i}{U} = \frac{dY}{dx} \quad - 2.4$$

The vorticity at point x is expressed as a series [Glauert 1942]

$$\Gamma(x) = 2U \left[A_0 \cot \frac{\theta}{2} + \sum_1^{\infty} A_n \sin n\theta \right] \quad - 2.5$$

As shown in Glauert [1942], by applying this eqn. into eqn. 2.3 and the boundary condition in eqn. 2.4, the lift force generated by a 2-dimensional aerofoil with a steady angle of attack, α , is found as

$$L = \rho U \int_0^c \Gamma(x) dx = \frac{1}{2} \rho c U^2 C_L \quad - 2.6$$

where $C_L = 2\pi(\alpha + \epsilon_0)$ - 2.7

Similarly, the pitching moment about the leading edge is

$$M = - \int_0^c \rho U x \Gamma(x) dx = \frac{1}{2} \rho c^2 U^2 C_M \quad - 2.8$$

where, $C_M = \left(\mu_0 - \frac{\pi}{2} \epsilon_0 \right) - \frac{C_L}{4}$; - 2.9

ϵ_0 is the negative value of the angle of the zero lift, the term in the equation for C_M , $\{\mu_0 - 0.5\pi\epsilon_0\}$ is the moment coefficient at zero lift; and the lift force acts at the quarter (0.25) chord point. Both ϵ_0 and μ_0 depend on the section shape of the aerofoil. From eqn. 2.7, the theoretical lift slope, is

$$\frac{dC_L}{d\alpha} = 2\pi$$

- 2.10

4.0 QUASI-STEADY APPROACH FOR A TWO-DIMENSIONAL OSCILLATING FOIL

Quasi-steady theory [Fung 1969] can be used as a first approach to the oscillating foil problem. The results are valid so long as values of the oscillating frequency are low but they become less reliable as the frequency increases.

The following assumptions are applied in the quasi-steady approach.

- (i) The hydrodynamic characteristics of an aerofoil with variable linear and angular velocities are assumed to be equal to that of an aerofoil with a constant linear and angular velocity at those instantaneous values.
- (ii) As a thin aerofoil with small camber is considered, the surface of the aerofoil differs only infinitesimally from that of a flat plate. A flat plate is used here for the analysis. At any instant of time, the inclination of the flow velocity to the profile is constant and equal to the actual inclination.
- (iii) The Kutta-Joukowski equation, eqn. 2.2, is assumed to be applicable in the unsteady condition.
- (iv) It is assumed that the equation for the vertical component of induced velocity at a point, eqn. 2.3, is still valid.

In this approach, only the lift force and moment originating from circulation is included. Let the flat plate be in a steady stream with velocity U along the x -axis and consider that the plate oscillates in two degrees of freedom with a vertical translation (y)

and a rotation (α) about the centre of rotation (O).

The vertical velocity component at a point x is

$$-\dot{y} + b(a - x)\dot{\alpha} \quad - 2.11$$

The instantaneous slope of the flat plate is α . According to the boundary condition (1), the vertical velocity of the fluid particle at x must satisfy the following equation

$$\frac{v_i}{U} = -\alpha - \frac{\dot{y}}{U} + \frac{b(a - x)\dot{\alpha}}{U} \quad - 2.12$$

The equations in the previous section are applicable by substituting eqn. 2.12 for dY/dx in eqn 2.4. By a similar approach, the lift coefficient (C_L) and the moment coefficient are defined as,

$$C_{Lq} = 2\pi \left[\alpha + \frac{\dot{y}}{U} + \frac{\dot{\alpha}}{U} b \left(\frac{1}{2} - a \right) \right] \quad - 2.13$$

$$C_M = -\frac{b}{4} \frac{\pi}{U} \dot{\alpha} - \frac{1}{4} C_L \quad - 2.14$$

Since the thin aerofoil is assumed to be a flat plate, the term ϵ_0 in eqns. 2.7 and 2.9 is equal to zero.

5.0 BASIC ASSUMPTIONS IN TWO-DIMENSIONAL LINEARISED OSCILLATING FOIL THEORY

The assumptions in this linearised theory are as follows.

1. As with the previous section, a thin aerofoil with small camber is replaced by an

infinitely thin plate with the same chord length and a rounded leading edge where the leading edge suction force acts.

2. The heave and pitch motions are assumed to have small amplitudes and the normal component of velocity of the plate is small compared to the advance velocity U . Second order terms in the equations of motion are assumed to be small and negligible. Surging motion of the foil is also neglected.
4. The Kutta condition around the trailing edge holds.
5. The wake behind the aerofoil is assumed to be a thin surface without thickness. Since small amplitude oscillations are assumed, the wake surface lies on the x -axis.
6. The flow is non-viscous and irrotational.

The lift and moment acting upon a two-dimensional oscillating foil can be interpreted from physical considerations of the change of momentum [Von Karman and Sears 1938]. When the aerofoil oscillates, the circulation around the foil changes continuously. Hence, it leaves a continuous sheet of vortex lines in the wake. These vortices influence the circulation around the foil. The system is made up of vortex pairs (i.e. a vortex in the wake and a vortex representing the circulation around the foil) shed at different times. The sum of the momentum of these vortex pairs is the total momentum of the system. Therefore the rate of change of momentum at any instant determines the magnitude of the lift.

6.0 APPLICATION OF THE ACCELERATION POTENTIAL IN THE UNSTEADY OSCILLATING FOIL PROBLEM

The velocity potential is discontinuous across that wake. However, the acceleration potential is still continuous [Biot 1940]. The advantage of the continuity of the acceleration potential provides a simpler approach to the calculation of forces on an

unsteady oscillating foil.

According to the Euler's equation of motion in an ideal fluid,

$$\rho \frac{D\bar{u}}{Dt} = - \text{grad } p \quad - 2.15$$

which indicates an acceleration vector,

$$\bar{a} = \frac{D\bar{u}}{Dt} = \text{grad } \phi \quad - 2.16$$

The value (ϕ) is termed an acceleration potential. The relationship between the acceleration potential and the pressure is therefore

$$\rho \phi = - p \quad - 2.17$$

The pressure distribution on the surface of an oscillating foil can be found by estimating the acceleration potential in the fluid. In an incompressible fluid, the acceleration potential also satisfies Laplace's Equation ($\nabla^2 \phi = 0$).

This potential will be determined by satisfying the kinematic boundary condition that the acceleration normal to the aerofoil is given by the acceleration of the aerofoil. The Kutta condition states that the velocity at the trailing edge must be finite and there is no pressure discontinuity at the trailing edge. Therefore the condition can be satisfied by choosing an acceleration potential which is continuous at the trailing edge.

6.1 The Kinematic Boundary Conditions

The flow velocity (u, v) at a point (x) on the aerofoil is described as $u=U +u'$ and $v= v'$. u' and v' are the perturbation velocities which are assumed to be much

smaller than U as a result of the small amplitude assumptions.

By the small amplitude assumptions, the oscillation provides a vertical motion (Y) only at every point and the surging motion (X) is neglected.

Let the velocity of the foil at a point (x) be $\bar{v}_1' = \left(0, \frac{dY}{dt}\right)$,

the flow velocity at the same point be $\bar{v}_2' = (U + u', v')$, and

the normal vector at the surface be $\bar{n} = \left(-\frac{dY}{dt}, 1\right)$.

According to the kinematic boundary condition,

$$\bar{v}_1' \cdot \bar{n} = \bar{v}_2' \cdot \bar{n} \quad - 2.18$$

By neglecting the second order of small quantities in the equations of motion, the flow velocity and acceleration are,

$$v' = \frac{dY}{dt} + U \frac{dY}{dx} = \frac{DY}{Dt}, \text{ and} \quad - 2.19$$

$$a_y' = \frac{D^2Y}{Dt^2} = \frac{d^2Y}{dt^2} + 2U \frac{d^2Y}{dx dt} + U^2 \frac{d^2Y}{dx^2} \quad - 2.20$$

The corresponding acceleration potential ϕ' of the flow must satisfy the following equation,

$$\frac{d\phi'}{dy} = a_y' = \frac{dv'}{dt} + U \frac{dv'}{dx} \quad - 2.21$$

Let the oscillation be a sinusoidal function, where

$$\phi' = \phi(x,y) e^{i\omega t}, u' = u(x,y) e^{i\omega t} \text{ and } v' = v(x,y) e^{i\omega t} \quad - 2.22$$

Then eqn. 2.21 is transformed into

$$\frac{d}{dy} \phi(x,y) = i \omega v(x,y) + U \frac{dv(x,y)}{dx} \quad - 2.23$$

Equation 2.23 is solved as an ordinary linear differential equation using the boundary condition (3) [Biot 1940], $v = 0$ when $x = -\infty$, and

$$v(x, y) = \frac{1}{U} e^{-i\omega\left(\frac{x}{U}\right)} \int_{-\infty}^x \frac{d\phi(\xi, y)}{dy} e^{i\omega\left(\frac{\xi}{U}\right)} d\xi \quad - 2.24$$

6.2 Force And Moment Due To Vertical Oscillation

Let the vertical oscillation be a sinusoidal motion, given by

$$Y = y_0 b e^{i\omega t} \quad - 2.25$$

where y_0 is a non-dimensional function, b is the half chord. A non-dimensional parameter is used to represent the unsteadiness, called the reduced frequency, k , where

$$k = \frac{\omega b}{U} \quad - 2.26$$

In this section, the half chord length is taken as unity and

$$k = \frac{\omega}{U} \quad - 2.27$$

Using eqns 2.19 and 2.20,

$$v' = \frac{DY}{Dt} = iU k y_o e^{iUkt} \quad - 2.28$$

$$a_y' = \frac{D^2Y}{Dt^2} = -U^2 k^2 y_o e^{iUkt} \quad - 2.29$$

The section of a thin aerofoil is transformed into a unit circle in the ζ -plane, as shown in fig. 2.2. The relationship between the z -plane and the ζ -plane is

$$z = \frac{1}{2} \left[\zeta + \frac{1}{\zeta} \right] \quad \text{and} \quad \zeta = z + \sqrt{z^2 - 1} \quad - 2.30$$

The relationship of the vertical component of the acceleration ($a_y'(x,0,t)$) of the aerofoil in the z -plane and the normal component of the acceleration ($a_n'(r=1, \theta = \cos^{-1}\xi, t)$) of the circle in the ζ -plane is

$$a_y'(x,0,t) \sin\theta = a_n'(r=1, \theta = \cos^{-1}\xi, t) \quad - 2.31$$

The normal component of the acceleration on the aerofoil (in the z -plane) and on the circle (in the ζ -plane) is

$$a_n' (|\zeta| = 1) = -U^2 k^2 y_o \sin \theta \quad - 2.32$$

In order to set up the form of the complex acceleration potential of an oscillating foil, two sink-source doublets are used. A sink-source doublet is placed at the leading edge (i.e. $\zeta = -1$) while the other is at the mid-chord point (i.e. $\zeta = 0$).

By applying the conformal mapping technique and the kinematic boundary condition, Biot [1940] set up the corresponding acceleration potential as

$$\phi = -2iU^2 y_o C(k) \frac{\sin \theta_1}{r_1} + U^2 k^2 y_o \frac{\sin \theta}{r} \quad - 2.33$$

where $C(k) = \frac{K_1(ik)}{K_1(ik) + K_0(ik)} = F + iG$, and

$K_0(ik)$ = the modified Bessel Function [Watson 1922] of the second kind of order zero

$K_1(ik)$ = the modified Bessel Function [Watson 1922] of the second kind of order one

The values of F and G are plotted in the fig. 2.3

Since the acceleration potential ϕ is equal but opposite on the upper and lower surfaces, the lift distribution (l) is equal to $-2p$ (eqn. 2.17). By putting

$$r = 1, \text{ and } r_1 = 2 \cos \theta_1, \text{ as shown in fig. 2.2,}$$

the corresponding lift force is

$$l = 2 \rho U^2 y_o \left[-i k C(k) \tan \frac{\theta}{2} + k^2 \sin \theta \right] \quad - 2.34$$

At the trailing edge, $\theta = \pi$, the value l is zero and the equation satisfies the Kutta flow-off condition. The total lift can be obtained by integration

$$L = \int_{-1}^1 l dx = \int_0^\pi l \sin \theta d\theta = \pi \rho U^2 y_o k^2 \left[1 - \frac{2i}{k} C(k) \right] \quad - 2.35$$

The moment about the origin (mid-chord) is

$$M_{1/2} = - \int_{-1}^1 l x dx = \int_0^{\pi} l \cos \theta \sin \theta d\theta$$

therefore $M_{1/2} = - \pi \rho U^2 i y_o k C(k)$ - 2.36

6.3 Force And Moment Due To Rotational Oscillation

Let the rotational oscillation be a sinusoidal motion, where

$$\alpha = \alpha_o e^{iUkt},$$
 - 2.37

and the rotating centre is at the origin (mid-chord). The vertical motion due to the rotational motion is

$$Y = - \alpha_o x e^{iUkt}$$
 - 2.38

Similarly to eqns. 2.19 and 2.20, the vertical velocity and the acceleration are,

$$v' = \frac{DY}{Dt} = - \alpha_o U e^{ikUt} (ikx + 1)$$
 - 2.39

$$a_y' = \frac{D^2Y}{Dt^2} = \alpha_o U^2 k e^{iUkt} (kx - 2i)$$
 - 2.40

The kinematic boundary conditions are set up using the velocity and acceleration stated in eqns.2.39 & 2.40. As in the previous section, the lift force acting on the foil undergoing rotational oscillation, as shown in [Fung 1969], is

$$L = \pi \rho U^2 k \left\{ i + \left[i + \frac{2}{k} \right] C(k) \right\} \alpha_o e^{iUkt} \quad - 2.41$$

The total moment about the mid-chord is,

$$M_{\frac{1}{2}} = \frac{1}{2} \pi \rho U^2 k \left\{ -i + \frac{k}{4} + \left(i + \frac{2}{k} \right) C(k) \right\} \alpha_o e^{iUkt} \quad - 2.42$$

6.4 Total Force and Moment due to Combined Motions of Vertical Translation and Angular Rotation

The total lift force of the combined oscillations is the summation of eqns. 2.35 and 2.41 and is shown as follows,

$$L = \pi \rho U^2 y_o k^2 \left[1 - \frac{2i}{k} C(k) \right] e^{iUkt} + \pi \rho U^2 k \left\{ i + \left[i + \frac{2}{k} \right] C(k) \right\} \alpha_o e^{iUkt} \quad - 2.43$$

Similarly, the total moment about the mid-chord position is,

$$M_{1/2} = \left\{ -\pi \rho U^2 y_o i k C(k) + \frac{1}{2} \pi \rho U^2 k \left[-i + \frac{k}{4} + \left(i + \frac{2}{k} \right) C(k) \right] \alpha_o \right\} e^{iUkt} \quad - 2.44$$

Since vertical translation and angular rotation are sinusoidal oscillations, the displacement, velocity and acceleration have the following relationships :

$$\begin{aligned} \text{the vertical displacement} & \quad y = y_o e^{iUkt}; \\ \text{the vertical velocity} & \quad \dot{y} = iUk y_o e^{iUkt}; \end{aligned} \quad - 2.45$$

$$\begin{aligned}
\text{the vertical displacement} \quad & \ddot{y} = -U^2 k^2 y_o e^{iUkt}; \\
\text{the angular displacement} \quad & \alpha = \alpha_o e^{iUkt}; \\
\text{the angular velocity} \quad & \dot{\alpha} = iUk \alpha_o e^{iUkt}; \\
\text{the angular acceleration} \quad & \ddot{\alpha} = -U^2 k^2 \alpha_o e^{iUkt}.
\end{aligned}
\tag{2.46}$$

In order to present the equations for lift and moment in a more general form, the relationships in eqns. 2.45 & 2.46 are used and the semi-chord length (b) is put back into the equations. The total lift force is

$$L = -\pi \rho b^2 (\ddot{y} - U \dot{\alpha}) - 2 \pi \rho U b C(k) \left[\dot{y} - \frac{b}{2} \dot{\alpha} - U \alpha \right]
\tag{2.47}$$

Similarly, eqn. 2.44 becomes,

$$M_{1/2} = -\rho \pi b^3 \left[\frac{U}{2} \dot{\alpha} + \frac{b}{8} \ddot{\alpha} \right] + \rho \pi U b^2 \left[-\dot{y} + \frac{\dot{\alpha}}{2} b + U \alpha \right] C(k)
\tag{2.48}$$

7.0 APPLICATION OF VELOCITY POTENTIAL IN THE UNSTEADY OSCILLATING FOIL PROBLEM

Based on the velocity potential approach, Theodorsen [1935] calculated the forces and moment on a two-dimensional foil which heaves and pitches about a rotation centre (O), fig. 2.4. In this approach, the potentials are treated separately in two classes: non-circulating flow potential; and, circulating flow potential. The first term represents the added mass of the foil when it oscillates; the second term represents forces induced by the vorticity in the wake and around the foil.

7.1 Non-Circulatory Flow

In non-circulatory flow, three velocity potentials are defined to represent the effect of angle of attack (α), heaving velocity and pitching velocity. These velocity potentials are,

$$\begin{aligned} \phi_{\alpha} &= U\alpha b\sqrt{1-x^2}, \quad \phi_{\dot{y}} = \dot{y} b\sqrt{1-x^2}, \text{ and} \\ \phi_{\dot{\alpha}} &= \dot{\alpha} b^2\left(\frac{1}{2}x - a\right)\sqrt{1-x^2} \end{aligned} \quad - 2.49$$

The local pressure (p) at a point (x) on the foil surface due to non-circulatory flow is found by using Bernoulli Equation as

$$p = -\rho \left(\frac{v_x^2}{2} + \frac{d\phi}{dt} \right), \quad - 2.50$$

where the local velocity $v_x = U \pm \frac{d\phi}{dx}$ (\pm for upper and lower surfaces)

Therefore the net pressure at a point (x) between the upper and lower surface of the foil is

$$l_a = -2\rho \left(U \frac{d\phi}{dx} + \frac{d\phi}{dt} \right) \quad - 2.51$$

By integrating the pressure over the whole chord, the lift force is found. The integration is carried out by introducing the individual velocity potentials, eqn. 2.49. Similarly, the moment acting at the rotating centre is calculated by integrating the pressure times its moment arm. The corresponding lift force and moment are,

$$L_a = -\rho b^2 \pi (U \dot{\alpha} + \ddot{y} - b a \dot{\alpha}) \quad - 2.52$$

$$M_{aa} = -\rho b^2 \pi \left[-U^2 \alpha + \left(\frac{1}{8} + a^2 \right) b^2 \ddot{\alpha} - b a \ddot{y} - U \dot{y} \right] \quad - 2.53$$

7.2 Circulatory Flow

The aerofoil is mapped into a circle by conformal mapping. The relationship between the z -plane and ζ -plane are the same as stated in eqns. 2.30, where $z = (x,y)$ and $\zeta = (X,Y)$, and

$$\begin{aligned} X_o &= x_o + \sqrt{x_o^2 - 1} \text{ on the } x \text{ axis,} \\ X &= x \text{ and } Y = \sqrt{1 - x^2} \text{ on the circle.} \end{aligned} \quad - 2.54$$

When the foil oscillates, vortices are generated in the wake. The velocity potential, which is induced by a vortex element $-\Delta\Gamma$ at $(X_o, 0)$, around the circle in ζ -plane (fig. 2.5), is

$$\phi_{\Gamma\zeta} = \frac{\Delta\Gamma}{2\pi} \left[\tan^{-1} \left(\frac{Y}{X - X_o} \right) - \tan^{-1} \left(\frac{Y}{X - \frac{1}{X_o}} \right) \right] \quad - 2.55$$

In the z -plane, eqn. 2.55 becomes

$$\phi_{\Gamma z} = \frac{\Delta\Gamma}{2\pi} \tan^{-1} \left(\frac{\sqrt{1 - x^2} \sqrt{x_o^2 - 1}}{1 - x x_o} \right) \quad - 2.56$$

Since the foil advances at a speed U through the fluid domain, the point x_o is considered to travel at a speed of U in the opposite direction. Therefore

$$\frac{d\phi_{\Gamma z}}{dt} = \frac{d\phi_{\Gamma z}}{dx_o} \frac{dx_o}{dt} = \frac{d\phi_{\Gamma z}}{dx_o} U, \quad - 2.57$$

Eqn. 2.51 becomes,

$$l_c = -2\rho U \left(\frac{d\phi_{\Gamma z}}{dx} + \frac{d\phi_{\Gamma z}}{dx_o} \right) \quad - 2.58$$

where
$$\frac{d\phi_{\Gamma z}}{dx} = \frac{\Delta\Gamma}{2\pi} \left[\frac{\sqrt{x_o^2 - 1}}{\sqrt{1 - x^2}} \frac{1}{(x_o - x)} \right],$$

and
$$\frac{d\phi_{\Gamma z}}{dx_o} = \frac{\Delta\Gamma}{2\pi} \left[\frac{\sqrt{1 - x^2}}{\sqrt{x_o^2 - 1}} \frac{1}{(x_o - x)} \right] \quad -2.59$$

The effect of $\Delta\Gamma$ at x_o on the foil is found by integrating these two terms over the chord length. The corresponding lift force is found by integrating the wake surface from the trailing edge ($x=1$) to infinity.

If the strength of the vorticity is Φ and $\Delta\Gamma = \Phi dx_o$.

$$L_c = -\rho U b \int_1^{\infty} \frac{x_o}{\sqrt{x_o^2 - 1}} \Phi dx_o \quad - 2.60$$

The moment acting at the rotating centre is found in a similar way,

$$M_{ac} = -2\rho U b^2 \int_{-1}^{\infty} \int_{-1}^1 \left(\frac{d\phi_{\Gamma z}}{dx} + \frac{d\phi_{\Gamma z}}{dx_o} \right) (x - a) dx \Phi dx_o \quad - 2.61$$

$$M_{ac} = -\rho U b^2 \int_1^{\infty} \left\{ \frac{1}{2} \sqrt{\frac{x_o + 1}{x_o - 1}} - \left(a + \frac{1}{2} \right) \frac{x_o}{\sqrt{x_o^2 - 1}} \right\} \Phi dx_o$$

In order to find the strength of the vorticity, Φ , the Kutta condition is applied. The flow velocity at the trailing edge is finite and

$$\frac{\partial}{\partial x}(\varphi_\alpha + \varphi_{\dot{y}} + \varphi_{\dot{\alpha}} + \varphi_\Gamma) = \text{finite} \quad - 2.62$$

The following relationship, as shown by Theodorsen [1935], is set as

$$\frac{1}{2\pi} \int_1^\infty \frac{\sqrt{x_o + 1}}{\sqrt{x_o - 1}} \Phi dx_o = U\alpha + \dot{y} + b\left(\frac{1}{2} - a\right)\dot{\alpha} \quad -2.63$$

Substituting eqn. 2.63 into 2.60, the lift

$$L_c = -2\pi\rho Ub \left[U\alpha + \dot{y} + b\dot{\alpha}\left(\frac{1}{2} - a\right) \right] \frac{\int_1^\infty \frac{x_o}{\sqrt{x_o^2 - 1}} \Phi dx_o}{\int_1^\infty \frac{\sqrt{x_o + 1}}{\sqrt{x_o - 1}} \Phi dx_o} \quad - 2.64$$

If the strength Φ is changing sinusoidally and the distance between the first vortex and the foil is infinity,

$$\Phi = \Phi_o e^{-ikx_o}$$

$$\text{and } \frac{\int_1^\infty \frac{x_o}{\sqrt{x_o^2 - 1}} \Phi dx_o}{\int_1^\infty \frac{\sqrt{x_o + 1}}{\sqrt{x_o - 1}} \Phi dx_o} = \frac{\int_1^\infty \frac{x_o}{\sqrt{x_o^2 - 1}} e^{-ikx_o} dx_o}{\int_1^\infty \frac{\sqrt{x_o + 1}}{\sqrt{x_o - 1}} e^{-ikx_o} dx_o} = \frac{K_1(ik)}{K_1(ik) + K_o(ik)} = C(k) \quad - 2.65$$

Therefore, the lift force due to circulating flow

$$L_c = -2\pi\rho Ub \left[U\alpha + \dot{y} + b\dot{\alpha}\left(\frac{1}{2} - a\right) \right] C(k) \quad - 2.66$$

Similarly, the moment is

$$M_{ac} = 2\pi \rho U b^2 \left[U\alpha + \dot{y} + b\dot{\alpha} \left(\frac{1}{2} - a \right) \right] \left[\frac{1}{2} - \left(a + \frac{1}{2} \right) C(k) \right]$$

- 2.67

7.3 Total Lift and Moment

The lift force and moment acting at the rotating centre of a two-dimensional oscillating foil is found by summing up the forces and moment induced by the non-circulatory and circulatory flow. The lift force

$$L = L_a + L_c$$

$$= -\rho b^2 \pi (U\dot{\alpha} + \ddot{y} - ba\ddot{\alpha}) - 2\pi \rho U b C(k) \left\{ U\alpha + \dot{y} + b \left(\frac{1}{2} - a \right) \dot{\alpha} \right\}$$

- 2.68

$$M_a = M_{aa} + M_{ac}$$

$$= -\rho b^2 \pi \left[\left(\frac{1}{2} - a \right) U b \dot{\alpha} + b^2 \left(\frac{1}{8} + a^2 \right) \ddot{\alpha} - a b \ddot{y} \right]$$

$$+ 2\pi \rho U b^2 \pi \left(a + \frac{1}{2} \right) C(k) \left\{ U\alpha + \dot{y} + b \left(\frac{1}{2} - a \right) \dot{\alpha} \right\}$$

- 2.69

8.0 COMPARISON BETWEEN METHODS

The final equations from the two previous approaches were compared. The sign conventions used in these two approaches are different. In order to compare the final equations, the sign conventions of the acceleration potential approach are changed as follows,

- i) clockwise rotation is positive, and
- ii) anti-clockwise moment is positive.

Equations 2.47 and 2.48 from the acceleration potential approach are the same as eqns 2.68 and 2.69 when the rotating centre is at the mid-chord point ($a=0$). A similar comparison was carried out for the theory described by von Karman & Sears [1938]. Although the approaches are different, the final equations for calculating the force and moment are the same.

The circulating term in eqn. 2.68 is rearranged into a more common form as,

$$L_c = \frac{1}{2} \rho U^2 (2b) C_{Lc} \quad - 2.70$$

where $C_{Lc} = 2 \pi \alpha_e$

$$\alpha_e = \left[\alpha + \frac{\dot{y}}{U} + \frac{b}{U} \left(\frac{1}{2} - a \right) \dot{\alpha} \right] C(k) \quad - 2.71$$

The terms inside the bracket are the same as that in eqn. 2.13 of the quasi-steady approach. These terms inside the square brackets are regarded as an equivalent angle of attack, as if the foil was operating in steady flow. The oscillating motion induces a modification to the steady angle of attack by a downwash angle of the oscillating flow at the three-quarter chord point. The resultant downward velocity comprises the vertical translation velocity at the 3/4 chord point and the rotating velocity at the same point about the rotating centre (O).

The effect of unsteadiness on the circulation term is the effect of the Theodorsen function (i.e. $C(K) = F + iG$). The lift force is proportional to the magnitude of this complex function, which changes with the reduced frequency, k . It induces a time delay factor (Δt) on the equivalent angle of attack (α_e), where

$$\Delta t = \frac{1}{\omega} \left[\tan^{-1} \frac{G}{F} \right] \quad -2.72$$

The heaving velocity and the angular pitching velocity are calculated at a time $(t - \Delta t)$ to obtain the lift force at time (t) . In addition, the non-circulatory terms and the vorticity in the wake are not included when calculating the lift force and its corresponding moment by the quasi-steady approach. Unsteady effects are small when the reduced frequency, k , is small: when k approaches zero, $C(k)$ approaches one.

9.0 LEADING EDGE SUCTION FORCE

There is another important contribution to the force system acting on the foil. This comes from the suction force acting on the rounded leading edge. When an incoming flow passes an aerofoil, the local flow velocity at the leading edge is fast and there is a pressure drop. Therefore a suction force (F_S) results which acts parallel to the plane of the aerofoil.

In inviscid flow, the lift force acts perpendicularly to the incoming flow, as proved by thin aerofoil theory. The lift force comes from the pressure difference between the upper and the lower surfaces of the foil, which are normal to the plane of the aerofoil. Therefore there is a component of lift which acts parallel to the incoming flow which is equal to $L \tan \alpha$.

In steady conditions, this force component ($L \tan \alpha$) is cancelled by the component of the suction force [Durand et al. 1943] (i.e. $F_S \cos \alpha$). As the component of the suction force (i.e. $F_S \sin \alpha$), which acts perpendicularly to the flow, is much smaller than the lift force at small α , its effect is neglected. The lift force still acts perpendicular to the incoming flow. In unsteady conditions, this assumption does not hold. Both forces, the horizontal component of lift force ($L \tan \alpha$) and the suction force (F_S), should be considered.

In steady flow, the Blasius's formula [Robinson and Laurmann 1956] gives

$$F_x + i F_y = \frac{1}{2} \rho i \int_s w(z)^2 dz \quad - 2.73$$

where $w(z)$ is the complex potential. If the integration is concentrated around a small circle surrounding the leading edge and the radius approaches zero,

$$F_x + i F_y = \frac{1}{2} \rho i \int_s w(z)^2 dz = -i \pi \rho C^2 \quad -2.74$$

where $C = U\sqrt{c} \sin \alpha$ and the suction force $F_S = -F_Y = \pi \rho C^2$

Since this phenomenon is the same for steady and unsteady conditions, the leading edge (L.E.) suction force of an oscillating foil takes the instantaneous steady flow value. Lighthill [1970] shows the mean L.E. suction force of a two-dimensional oscillating foil. Here, the corresponding instantaneous value can be expressed as

$$F_S = \rho \pi C_o^2 \quad - 2.75$$

$$\text{where } C_o = \sqrt{c} \left\{ \left[U\alpha + \dot{y} + \dot{\alpha}b\left(\frac{1}{2} - a\right) \right] C(k) - \frac{b}{2} \dot{\alpha} \right\}$$

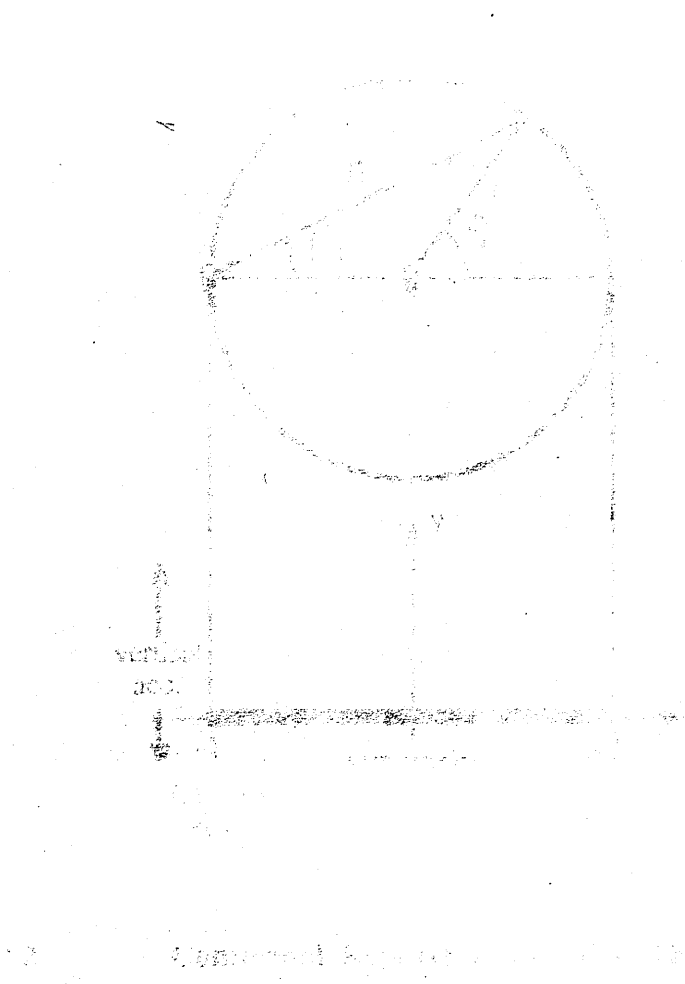
10.0 CONCLUDING REMARKS

From this study, the following concluding remarks may be made.

- 1) In spite of different approaches, two-dimensional linearised unsteady foil theory results in the same equations for calculating the lift force and pitching moment.
- 2) In the quasi-steady approach, the angle of attack is modified by a downwash

angle at the three quarter chord point. The effect of unsteadiness is included in the unsteady foil theory. It includes the force and moment generated by the added mass of the oscillating foil and the equivalent angle of attack is further modified by the Theodorsen function. This function approaches 1.0 when the reduced frequency approaches zero.

- 3) In the unsteady oscillating foil theory, the force system acting on an oscillating foil system is made up of a lift force, leading edge suction force and the pitching moment about the rotating centre. Thus a basis has been established for the analysis of experimental work on oscillating foils.



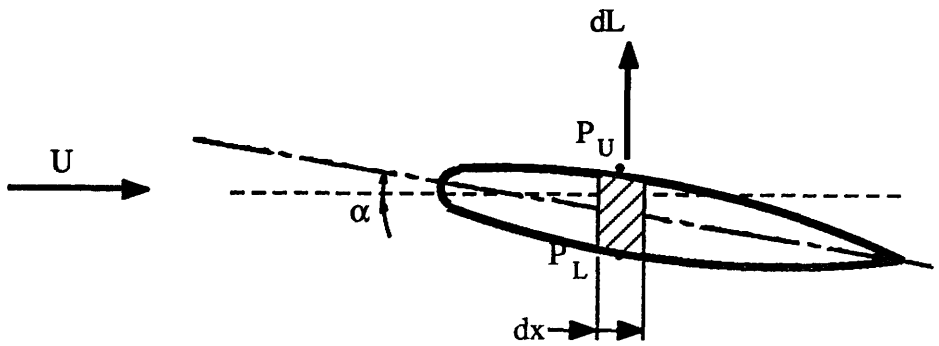


Fig. 2.1 Two Dimensional Aerofoil in Steady Flow

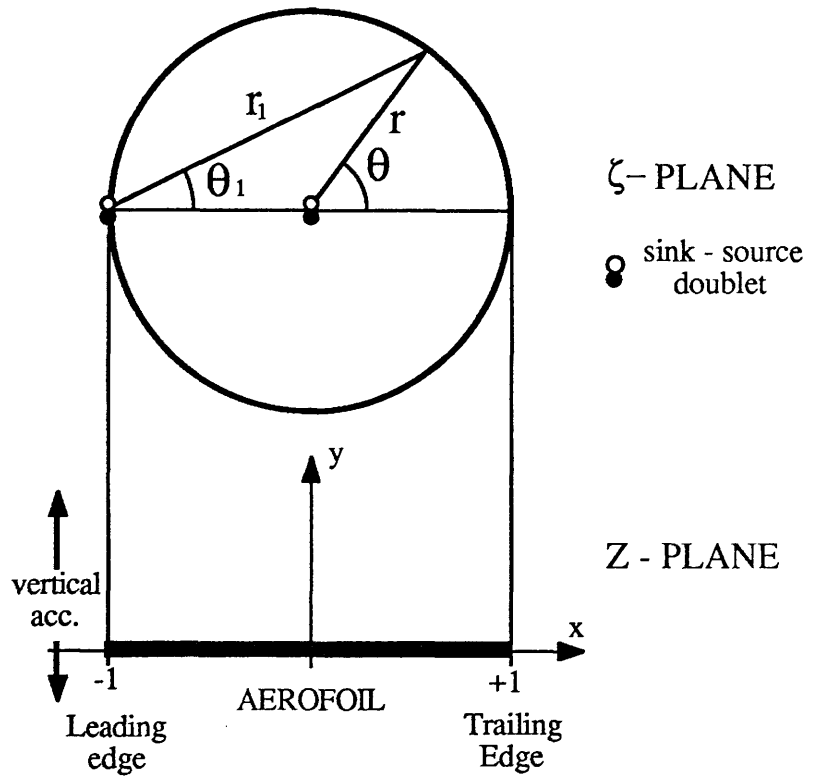
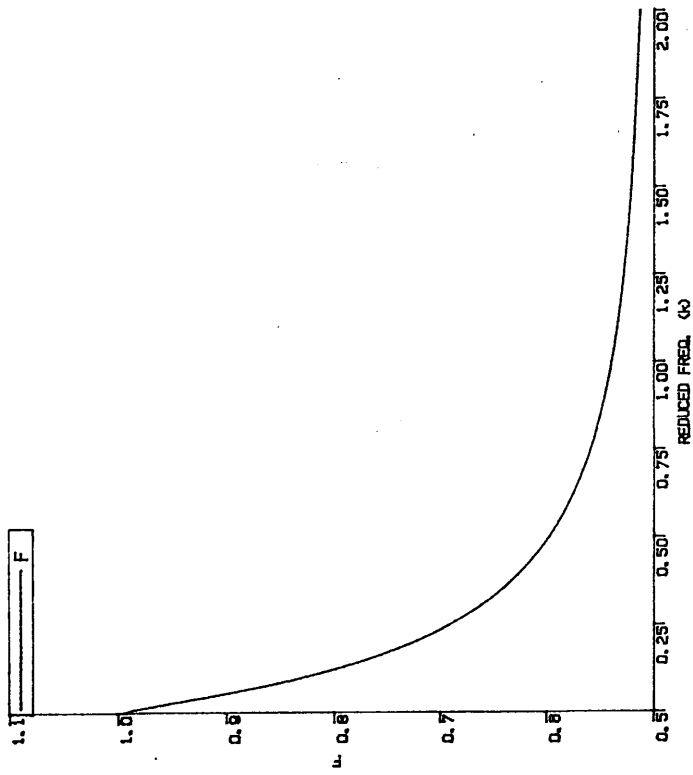
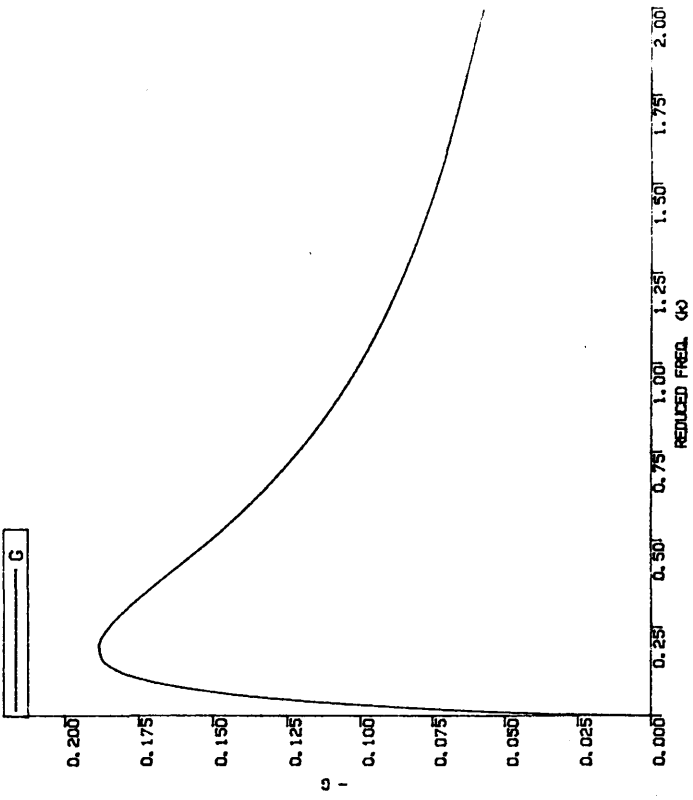


Fig. 2.2 Conformal Representation of a Thin Aerofoil



(a) THE REAL PART (F)



(b) THE IMAGINARY PART (G)

Fig. 2.3 The Theodorsen's Function $C(k) = F + i G$

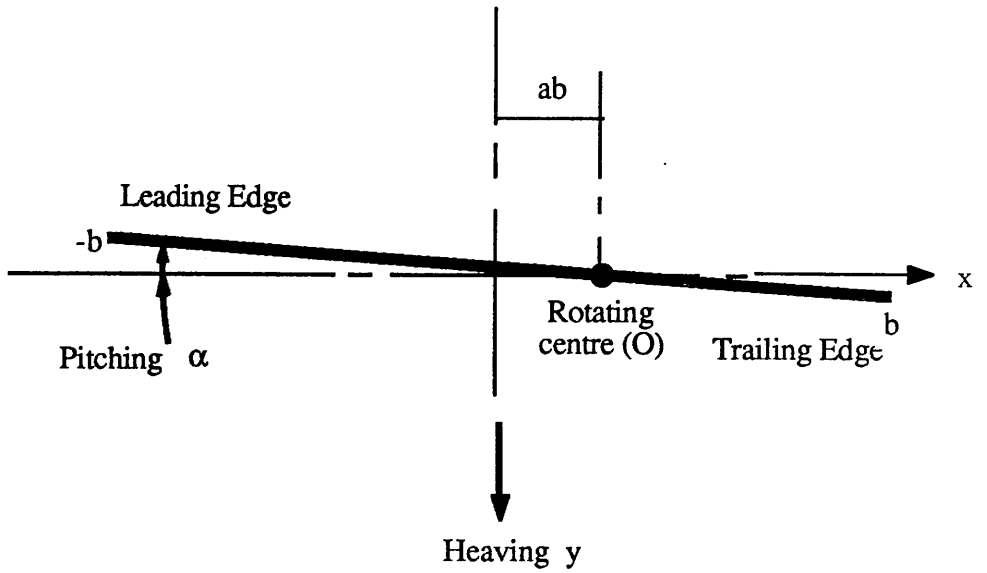


Fig. 2.4 Sign Convention of Theodorsen's Theory

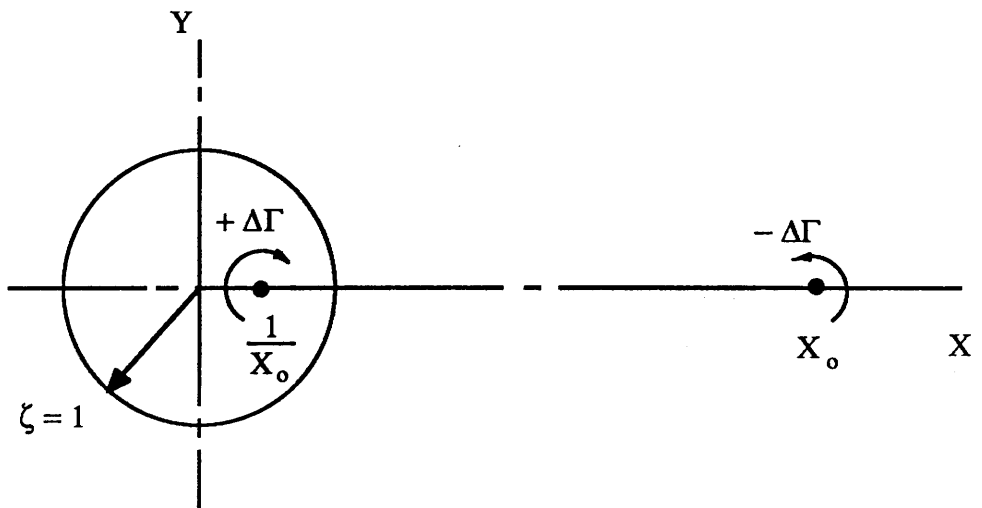


Fig. 2.5 Conformal Mapping of The Aerofoil and the Circulation in the Wake

CHAPTER 3

PERFORMANCE OF A TWO-DIMENSIONAL OSCILLATING FOIL PROPELLER

1.0 INTRODUCTION

A two-dimensional oscillating foil propeller is made up of an oscillating foil and two struts at both tips of the foil which enclose the oscillating foil, as shown in fig. 1. The foil oscillation is completely under the control of mechanical devices. Therefore the foil can heave and pitch at specified phase lags and pitch about any specified centre of rotation.

In an ideal condition, there is no pressure leakage through the gap between the enclosing struts and the tips of the foil. The flow across the foil is two-dimensional. The theory presented in Chapter 2 can be used to study the performance of this propeller. The equations based on the Theodorsen theory are extended to take the phase lag between heaving and pitching into account and they were developed to investigate the variation of the forces within an oscillating cycle.

A parametric study of propulsive thrust and efficiency has been done and this is presented in this chapter. The object of this study is to investigate the effect of different parameters on performance. An investigation of the propulsive thrust coefficient and efficiency was carried out. The impact of different phase lags on the propulsive thrust coefficient and efficiency are investigated in section 4.1. The propulsive thrust and efficiency, when the phase lag between pitching and heaving is 90° , is computed and presented in the section 4.2. The variation of propulsive thrust throughout a cycle is also studied for the same phase lag at 90° .

Results of propulsive thrust and efficiency at a phase lag of 90° are compared to Lighthill's results [1970]. The two results are the same. This gives further support to the first conclusion in Chapter 2. The propulsive efficiency for different phase lags are compared to results from numerical unsteady-lifting-surface theory [Lan 1979] for a rectangular foil with aspect ratio 7. The results are similar. Good agreement is found at high reduced frequency, three dimensional effects are weak in this condition. James [1975] and Cheng [1975] also found this result in their studies of unsteady-lifting-line theory using the asymptotic approach. In these two references, this is described as a consequence of the self-averaging effect of the periodic vorticity in the far wake. As a result of this study, optimum performance is expected in a condition when the phase lags between heaving and pitching are 90° and at low reduced frequencies. The corresponding feathering parameter is around 0.5 to 0.6 and the centre of rotation is located between the mid-chord and the three-quarter chord point.

2.0 OUTLINE OF THE THEORETICAL MODEL

As the oscillating foil is enclosed by two side struts, the pressure leakage from the foil tips is minimised. In ideal conditions, there is no leakage between the foil tips and the struts. The flow across the oscillating foil is two-dimensional. Two-dimensional linearised unsteady-lifting-foil theory as given in Chapter 2 is applied to the performance of a two-dimensional oscillating foil propeller. Heaving and pitching motions of the foil are sinusoidal and a phase lag (β) exists between these motions. The relationships are listed as follows:

$$\begin{aligned}
 \text{vertical displacement} & \quad y = y_o e^{i\omega t}; \\
 \text{vertical velocity} & \quad \dot{y} = i\omega y_o e^{i\omega t}; \\
 \text{vertical acceleration} & \quad \ddot{y} = -\omega^2 y_o e^{i\omega t}; \\
 \text{angular displacement} & \quad \alpha = \alpha_o e^{i(\omega t - \beta)}; \\
 \text{angular velocity} & \quad \dot{\alpha} = i\omega \alpha_o e^{i(\omega t - \beta)}; \\
 \text{angular acceleration} & \quad \ddot{\alpha} = -\omega^2 \alpha_o e^{i(\omega t - \beta)}.
 \end{aligned}
 \tag{3.1}$$

The force system acting on the oscillating foil is made up of a lift force, leading edge suction force and pitching moment acting at the rotating centre (O).

2.1 The Lifting Force and Moment at the Rotating Centre

The lift and moment are found from eqns. 2.68 and 2.69. By using the relationships in eqn. 3.1, these two equations are rearranged as a complex number with a time factor $e^{i\omega t}$. The magnitude of the lift force at any instant of time (t) is the real part of this complex number including the time factor. Therefore, the lift force at any instant of time (t) is

$$\begin{aligned} L &= \Re (L_R + iL_I)e^{i\omega t} \\ &= L_R \cos \omega t - L_I \sin \omega t \end{aligned} \quad - 3.2$$

where

$$\begin{aligned} L_R &= -\rho b^2 \pi (U \omega \alpha_o \sin \beta - \omega^2 y_o + b a \omega^2 \alpha_o \cos \beta) \\ &\quad - 2\pi\rho U b \left\{ F \left[U \alpha_o \cos \beta + b \left(\frac{1}{2} - a \right) \omega \alpha_o \sin \beta \right] \right. \\ &\quad \left. - G \left[\omega y_o - U \alpha_o \sin \beta + b \left(\frac{1}{2} - a \right) \omega \alpha_o \cos \beta \right] \right\} \end{aligned} \quad - 3.3$$

and

$$\begin{aligned} L_I &= -\rho b^2 \pi (U \omega \alpha_o \cos \beta - b a \omega^2 \alpha_o \sin \beta) \\ &\quad - 2\pi\rho U b \left\{ G \left[U \alpha_o \cos \beta + b \left(\frac{1}{2} - a \right) \omega \alpha_o \sin \beta \right] \right. \\ &\quad \left. + F \left[\omega y_o - U \alpha_o \sin \beta + b \left(\frac{1}{2} - a \right) \omega \alpha_o \cos \beta \right] \right\} \end{aligned}$$

Similarly, the moment acting about the rotating centre (O) at any instant of time (t) is,

$$\begin{aligned} M_a &= \Re (M_{aR} + iM_{aI})e^{i\omega t} \\ &= M_{aR} \cos \omega t - M_{aI} \sin \omega t \end{aligned} \quad - 3.4$$

where

$$\begin{aligned}
 M_{aR} = & -\rho b^2 \pi \left[\left(\frac{1}{2} - a \right) U b \omega \sin \beta \alpha_o - b^2 \left(\frac{1}{8} + a^2 \right) \alpha_o \omega^2 \cos \beta + \omega^2 y_o a b \right] \\
 & + 2\rho U b^2 \pi \left(a + \frac{1}{2} \right) \left\{ F \left[U \alpha_o \cos \beta + b \left(\frac{1}{2} - a \right) \omega \alpha_o \sin \beta \right] \right. \\
 & \left. - G \left[\omega y_o - U \alpha_o \sin \beta + b \left(\frac{1}{2} - a \right) \omega \alpha_o \cos \beta \right] \right\}
 \end{aligned}$$

and,

$$\begin{aligned}
 M_{aI} = & -\rho b^2 \pi \left[\left(\frac{1}{2} - a \right) U b \omega \cos \beta \alpha_o + b^2 \left(\frac{1}{8} + a^2 \right) \alpha_o \omega^2 \sin \beta \right] \\
 & + 2\rho U b^2 \pi \left(a + \frac{1}{2} \right) \left\{ G \left[U \alpha_o \cos \beta + b \left(\frac{1}{2} - a \right) \omega \alpha_o \sin \beta \right] \right. \\
 & \left. + F \left[\omega y_o - U \alpha_o \sin \beta + b \left(\frac{1}{2} - a \right) \omega \alpha_o \cos \beta \right] \right\}
 \end{aligned} \tag{3.5}$$

2.2 Leading Edge Suction Force

The instantaneous value of leading edge suction force is calculated by using eqn. 2.75 :

$$F_s = \rho \pi C_o^2 \tag{3.6}$$

C_o is rearranged as

$$\begin{aligned}
 C_o &= \Re (C_{oR} + i C_{oI}) e^{i\omega t} \sqrt{c} \\
 &= (C_{oR} \cos \omega t - C_{oI} \sin \omega t) \sqrt{c}
 \end{aligned} \tag{3.7}$$

where

$$\begin{aligned}
 C_{oR} &= F \left[U \alpha_o \cos \beta + \omega \alpha_o b \left(\frac{1}{2} - a \right) \sin \beta \right] \\
 &\quad - G \left[\omega y_o - U \alpha_o \sin \beta + \omega \alpha_o b \left(\frac{1}{2} - a \right) \cos \beta \right] \\
 &\quad - \frac{b}{2} \omega \alpha_o \sin \beta
 \end{aligned} \tag{3.8}$$

$$C_{o_I} = G \left[U \alpha_o \cos \beta + \omega \alpha_o b \left(\frac{1}{2} - a \right) \sin \beta \right] \\ + F \left[\omega y_o - U \alpha_o \sin \beta + \omega \alpha_o b \left(\frac{1}{2} - a \right) \cos \beta \right] \\ - \frac{b}{2} \omega \alpha_o \cos \beta$$

The leading edge suction force at a particular instant of time (t) is calculated by using eqns. 3.6 to 3.8.

2.3 Propulsive Thrust and Propulsive Efficiency

The force system acting on an oscillating foil is presented in fig. 3.2. This is made up of a lift force, L, with horizontal component $L \tan \alpha$, a moment acting at the rotating centre (O) and leading edge suction force (F_S). The forces are computed by using the equations developed in the previous section.

The propulsive thrust is $F_T = F_S \cos \alpha + L \tan \alpha$. Since small amplitudes are assumed, the angle, α , is small and the cosine term is equal to 1.

The propulsive thrust is $F_T = F_S + L \alpha$ - 3.9

The mean propulsive thrust $\bar{F}_T = \frac{\int_{t=0}^{t=T} F_T dt}{T}$

The power input to the system is that required to drive the foil in heave and pitch. This is the sum of the total vertical force times the vertical oscillating velocity and the moment about the rotating centre (O) times the angular rotating velocity. The output of the system is the propulsive thrust times advance speed (U). Efficiency is calculated by integrating these two values over an oscillating cycle :

$$\eta = \frac{\text{OUTPUT}}{\text{INPUT}} = \frac{\int_{t=0}^{t=T} (F_T \cdot U) dt}{\int_{t=0}^{t=T} (L\dot{y} + M_a \dot{\alpha}) dt} \quad - 3.10$$

3.0 PARAMETRIC STUDIES OF THE PERFORMANCE OF A TWO-DIMENSIONAL OSCILLATING FOIL PROPELLER

A computer program (UNSTOS) was written to compute the propulsive thrust and efficiency. NAG routine (D01GAF) was used to integrate the input power and propulsive thrust throughout a whole cycle and hence find the mean value of the propulsive thrust. Gill and Miller's method [Gill and Miller 1972] using third-order finite-difference formulae with error estimates is applied in this NAG routine.

The performance of this propeller was studied for a range of different parameters. These parameters are listed as follows.

- 1) Reduced Frequency (k). This non-dimensional coefficient represents the ratio of the time to advance a distance equal to the semi-chord to the period of oscillation. This parameter is

$$k = \frac{\omega c}{2U} \quad - 3.11$$

and it quantifies the degree of unsteadiness.

- 2) Feathering Parameter (θ). This parameter was introduced by Lighthill [1970] and it represents the ratio of maximum pitching angle (i.e. α_o) to the slope of the path of the oscillating foil. The feathering parameter is

$$\theta = \frac{U\alpha_o}{\omega y_o} \quad - 3.12$$

It gives an idea of the relationship between pitching motion and heaving motion.

- 3) Rotating Centre (O). This is the distance of the rotating centre from the leading edge.
- 4) Phase Difference (β). This is the phase lag between pitching and heaving motions.
- 5) Propulsive thrust coefficient (C_T). This is a non-dimensional parameter for mean propulsive thrust

$$C_T = \frac{\bar{F}_T}{\frac{1}{2} \rho \omega^2 y_0^2 S} \quad - 3.13$$

Parametric studies were carried out for a range of :

- (i) reduced frequencies (k) between 0.005 and 1.0;
- (ii) feathering parameters (θ) between 0.0 and 0.8 with an increment of 0.2;
- (iii) positions of rotating centre (O) from leading edge to trailing edge with an increment of 0.25 chord length; and
- (iv) phase lags (β) between heaving and pitching from zero to 180 degrees.

When the reduced frequency is zero, there is no oscillation. A reduced frequency of 0.005 is chosen as the lowest value of reduced frequency in this study.

4.0 RESULTS AND DISCUSSIONS

4.1 Propulsive Thrust Coefficient and Efficiency for Various Phase Shift Values (β)

The propulsive thrust coefficient and efficiency for different phase lags (i.e. $\beta = 0^\circ$ to 180°) between heaving and pitching are shown in figs. 3.3 to 3.6 and in fig. 3.7 to 3.10 respectively for different feathering parameters. Since high efficiency is obtained at low reduced frequency, the performance is studied at closer intervals for reduced frequencies below 0.2. The propulsive thrust coefficient and efficiency at k values of 0.005, 0.1 and 0.2 are presented in fig. a, while the results of a range of reduced frequency between 0.2 and 1.0 with an increment of 0.2 are shown in fig. b of figs. 3.3 to 3.10.

Propulsive thrust is more sensitive to change of phase angle (β) for high feathering parameters : compare figure 3.6 with 3.3. When the feathering parameter is high, the propulsive thrusts are negative for some values of phase difference (β). This is true when the rotating centre is close to the leading edge or trailing edge and reduced frequency ≥ 0.4 . When the rotating centre is located between mid-chord and the three-quarter-chord point, the propulsive thrusts are all positive for various phase lags (β) throughout the whole range of θ . When the rotating centre is at the leading edge and reduced frequency > 0.2 , the propulsive thrust coefficient decreases as the phase angle (β) increases and vice versa when the rotating centre is at trailing edge. At low reduced frequency ≤ 0.2 , a trough of the propulsive thrust curve is obtained around 90° phase lag for all locations of rotating centre. The variation of propulsive thrust is much less sensitive to the location of the rotating centre when the phase difference is near to 90° . An example of this phenomenon is shown in fig. 3.11.

High efficiency is located at low reduced frequencies. When the reduced frequency approaches to zero, the efficiency approaches to 1.0. Generally an increase

of reduced frequency decreases the efficiency (see fig. 3.7). The efficiency is nearly constant for low pitching motion (i.e. θ low). When the magnitude of the pitching oscillation increases (i.e. θ high), the variation for different phase lags is much more significant. A sample condition is presented in fig. 3.12. The efficiency drops to zero for some values of phase difference (β) as shown in fig. 3.9 and fig. 3.10. These drops correspond to the negative values of the propulsive thrust in fig. 3.5 and 3.6.

In Lan [1979, fig. 5], the efficiency of an oscillating rectangular foil with an aspect ratio 7.0, reduced frequencies of 0.15 and 0.75 and a feathering parameter of 0.8 are presented for various phase differences. The sign convention of phase lags in Lan [1979] and the present method are different. The theoretical results from [Lan 1979] are reconstructed according to the present phase definition used here and then they are compared to the results from the present method in fig. 3.13. The two methods give similar results. This is because the flow around a rectangular foil with large aspect ratio is very close to the two-dimensional condition. There is good agreement between the two sets of results at high reduced frequencies. However, a discrepancy is shown when the reduced frequency is small. James [1975] (and also found independently by Cheng [1975]) showed that three dimensional effects on an unyawed, straight oscillating wing are weak when

$$k_s = \frac{\omega s}{2U} \gg 1 \quad - 3.14$$

Since the aspect ratio is 7, the k_s values are 1.05 and 5.25 for $k = 0.15$ and 0.75 respectively. The self-averaging phenomenon is also confirmed here.

The peak in the efficiency curves shifts from a phase lag higher than 90° to a value lower than 90° as the rotating centre moves downstream as shown in fig. 3.9. This is more significant when the feathering parameter is high. When the rotating centre is located at the three-quarter-chord point, peak values are achieved at a value of phase lag equal to 90° . High efficiencies are concentrated in a range where the phase lag is around 90° .

The caudal fin motions of fish and mammals are described by Gray [1968], Lighthill [1977] and Lang & Dcybell [1963]. The motion of a porpoise was recorded by Lang and is presented in Lang & Dcybell [1963, fig. 17]. When the fin moves to the top of the upward stroke, the fin is horizontal (i.e. $\alpha = 0$). When the fin moves down and passes the horizontal axis, the pitching angle of the fin is maximum and pitches toward the direction of motion (i.e. α is maximum). The fin comes back to horizontal again when it moves down to the lowest point. A similar motion is observed in the upstroke. This is an oscillation where the pitching motion lags the heaving motion by 90° . The present studies explain why some fast fishes and cetacean mammals adopt this carangiform swimming.

4.2 The Propulsive Thrust and Efficiency when $\beta = 90^\circ$

The propulsive thrust coefficient (C_T), the coefficient of the thrust component contributed by the leading edge suction force (C_{TS}) and efficiency (η) were calculated, when the phase difference is 90° , for variations of feathering parameters (θ), reduced frequency (k) and position of the rotating centre (O). The results are presented in fig. 3.14 to 3.18. The results were compared with the published results in [Lighthill 1970, in fig.4] and good agreement is obtained. The results from this approach, which is generated based on Theodorsen theory, match with the results from Lighthill's theory. This also validates the computational method and the computer program (UNSTOS).

When the foil performs a pure heaving oscillation at forward speed, the leading edge suction force is the only force contributing to propulsive thrust. This is because the other component, which is contributed by the lift force, is zero when α is zero.

In general, the propulsive thrust decreases as the feathering parameter increases, as shown in fig. 3.14a to 3.18a. When the rotating centre (O) is near the leading edge, the main component of propulsive thrust comes from the lift force. The suction force becomes more dominant when the rotating centre moves backward. When the location

of the rotating centre is aft of the mid-chord and the feathering parameter is high, the lift-force component (i.e. $L \tan \alpha$) is negative and the propulsive thrust comes mainly from the suction-force component. In this condition, the added mass term (i.e. the first term in eqn. 2.68) contributes a negative value and the lift force is negative.

The efficiency drops as the reduced frequency increases, as shown in fig. 14c to 18c. In general, the efficiency decreases as the feathering parameter decreases. When the rotating centre moves backward, the values become less sensitive to the increment of the reduced frequency.

4.3 Variation of Propulsive Thrust Throughout an Oscillating Cycle when $\beta=90^\circ$

In fig. 3.19 to 3.22, the variation of the propulsive thrust coefficient throughout an oscillating cycle for the same condition (i.e. $\beta = 90^\circ$) is presented. Similarly to section 4.1, propulsive thrusts at low reduced frequencies are presented in fig. a and results for higher reduced frequency ($k \geq 0.2$) are presented in fig. b. The oscillating frequency of the propulsive thrust is twice the oscillating frequency of the oscillating motion. When the value of the feathering parameter is small and the rotating centre is near the leading edge, the propulsive thrust is positive throughout the whole cycle. However, when the feathering parameter increases and the reduced frequency is high, the propulsive thrust coefficient is negative for part of the cycle. This also means that the system produces drag rather than propulsive thrust. The duration of the negative thrust increases as the rotating centre moves downstream. In order to prevent this drag occurring, it is preferable that the rotating centre be located further forward and it is recommended that it should be between the mid-chord point and the three-quarter-chord point.

5.0 CONCLUSIONS

The following main conclusions can be drawn based on the numerical results generated in the course of this study. The conclusions apply to a two-dimensional oscillating foil with small amplitude oscillations in non-viscous flow.

- 1) The variation of the propulsive thrust coefficient is much smaller and much less sensitive for different positions of rotating centre when the phase lag is 90° than at other phase lags. When the pitching motion is large (i.e. θ is high), the propulsive thrust becomes negative for some phase angles (β); in these conditions the foil may produce a drag instead of a propulsive thrust.
- 2) Efficiency approaches 1.0 when the reduced frequency approaches zero. High efficiency occurs at low reduced frequency. The variation of propulsive efficiency with changing phase angle is large for high values of feathering parameter. The peak value of the efficiency is higher at a higher feathering parameter. The efficiency drops to zero in response to the zero value of propulsive thrust for some phase angles (β) when the feathering parameter is high and the rotating centre is located near to the leading or trailing edge. High efficiency is concentrated in an area around $\beta=90^\circ$. From this conclusion and the previous one, a phase angle where pitching lags heaving by 90° shows advantages for both propulsive thrust and efficiency.
- 3) For the 90° phase lag, the efficiency increases as the feathering parameter increases when the rotating centre is located aft of the mid-chord point. However the propulsive thrust drops as the feathering parameter increases. The component of propulsive thrust that is contributed by lift is dominant when the rotating centre is near to the leading edge. When the rotating centre moves downstream towards the trailing edge, the contribution from leading-edge suction becomes dominant. However a high suction force may not be

realised in practice owing to separation of the flow.

- 4) The propulsive thrust coefficient oscillates at a frequency twice that of the oscillating frequency. For a phase lag of 90° , the propulsive thrust is negative for part of an oscillating cycle when the feathering parameter and reduced frequency are high. The system produces a drag instead of a thrust in this particular situation. In order to avoid this, the feathering parameter should be kept smaller than 0.6 and the rotating centre should be in front of the three quarter chord point.

- 5) Although drag occurs in part of the oscillating cycle when the pitching axis is located near the trailing edge, high efficiency is obtained. However, the propulsive efficiency drops to zero for some other phase angles (β) in this condition. In order to avoid the drag produced by the system and zero efficiency for some phase angles (β), the rotating centre should be located between the mid-chord and the three quarter chord point.

Overall optimum performance is expected to occur for,

- i) phase lags around 90° ,
- ii) low reduced frequency,
- iii) high values of the feathering parameter, and
- iv) a location of the rotating centre between the mid-chord and the three quarter chord point.

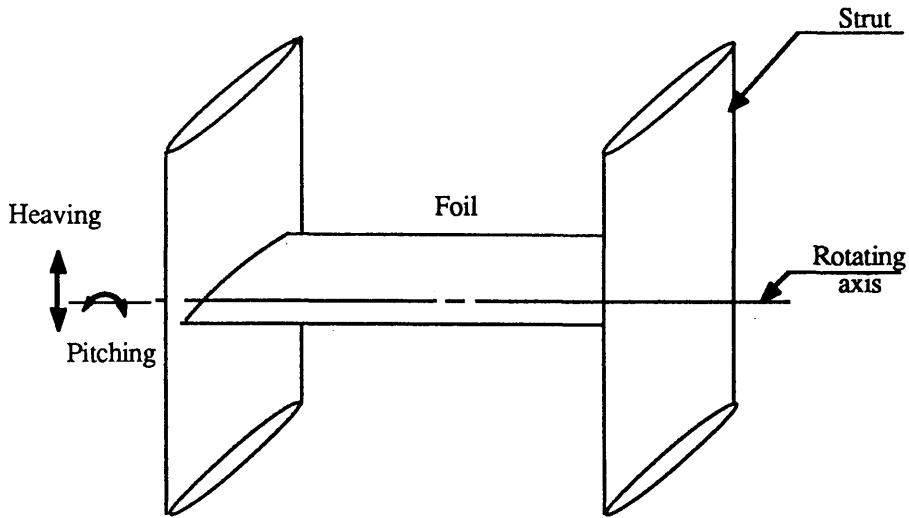


Fig. 3.1 A Two-Dimensional Oscillating Foil Propeller

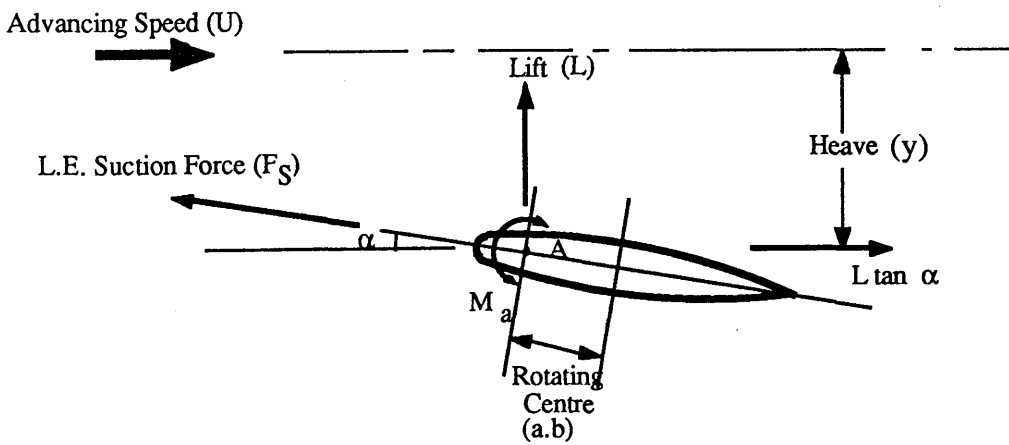
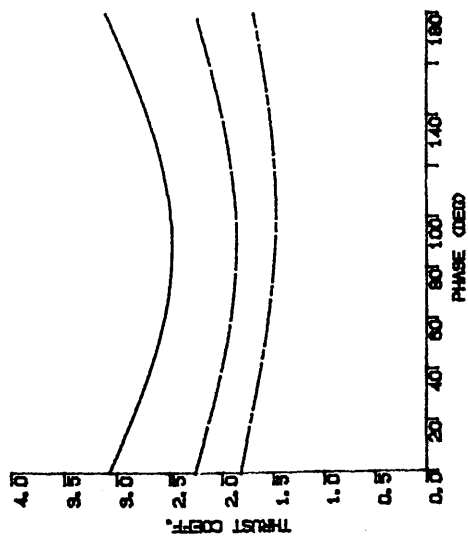
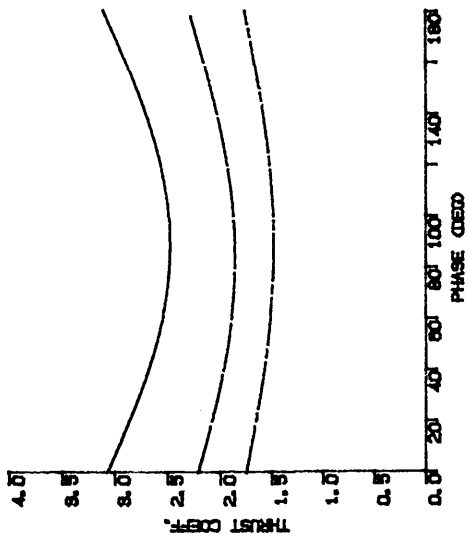


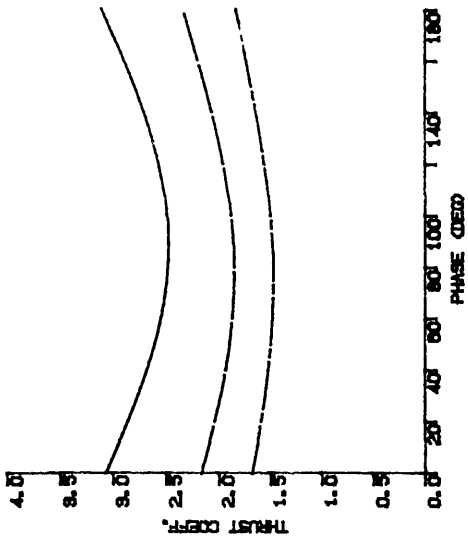
Fig. 3.2 The Force System Acting on an Oscillating Foil



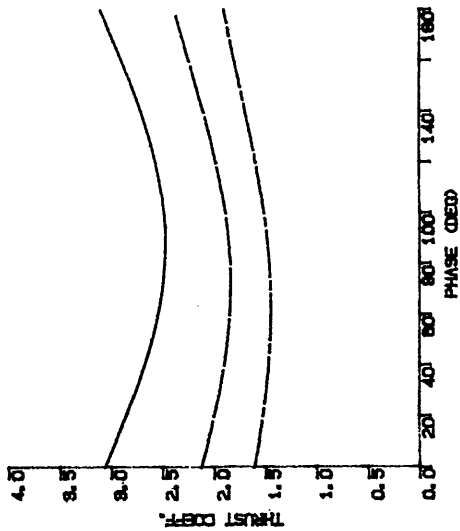
Rotating Centre = L. E.



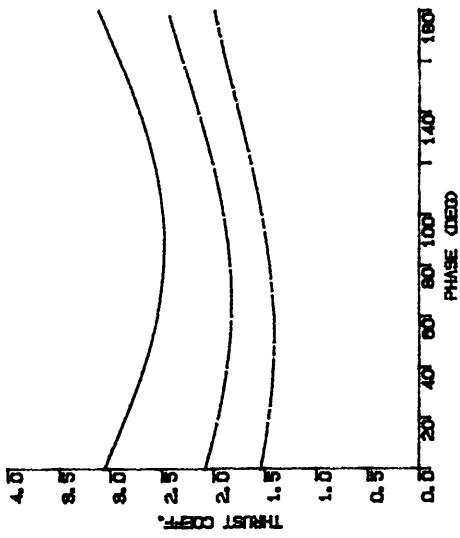
Rotating Centre = 0.25c



Rotating Centre = 0.5c



Rotating Centre = 0.75c



Rotating Centre = T. E.

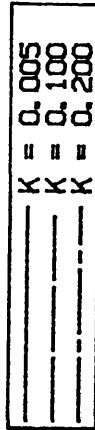
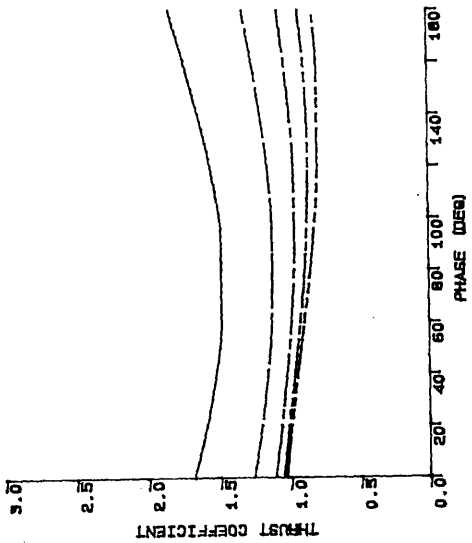
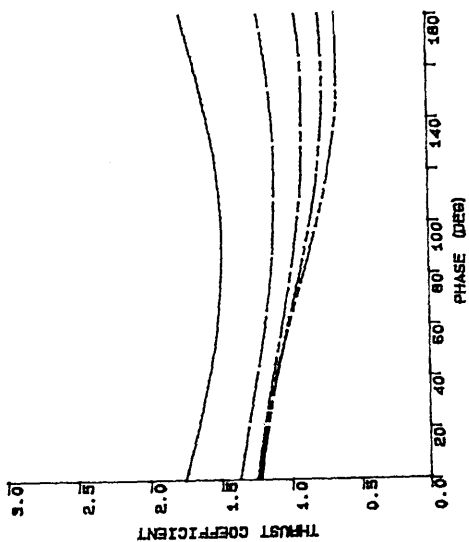


Fig. 3.3a The Propulsive Thrust Coefficient when $\theta = 0.2$

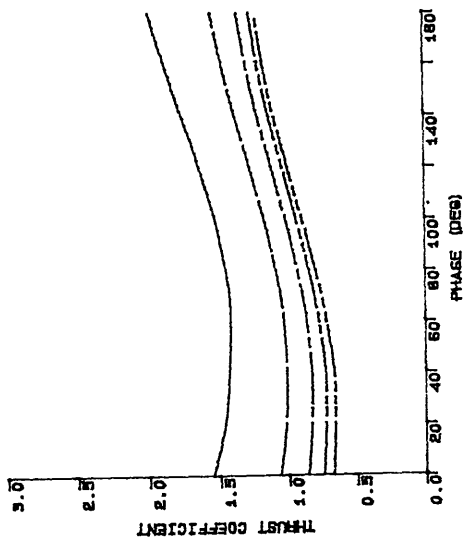


Rotating Centre = 0.5c

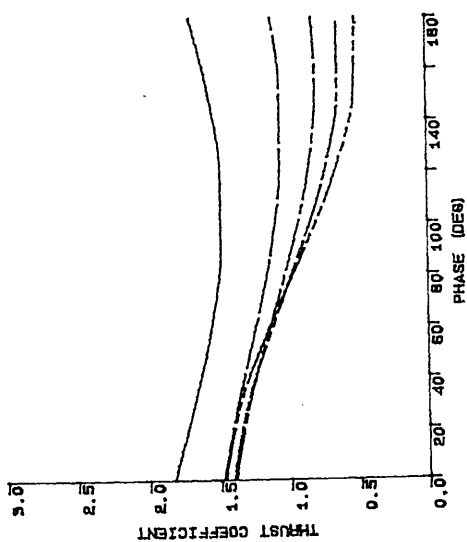
—	K = 0.2
- - -	K = 0.4
—	K = 0.6
- - -	K = 0.8
—	K = 1.0



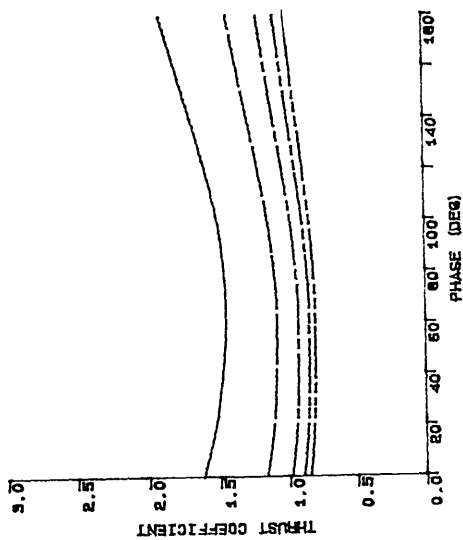
Rotating Centre = 0.25c



Rotating Centre = T. E.

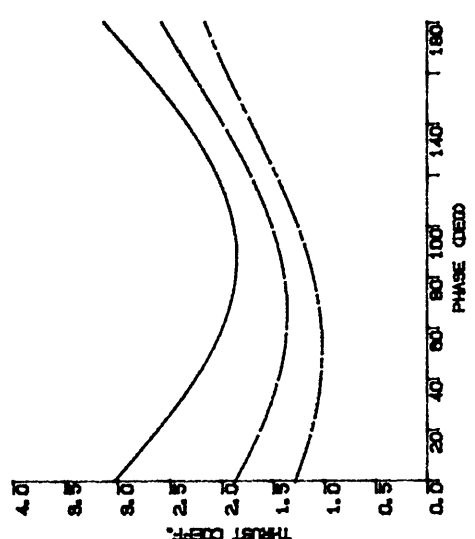
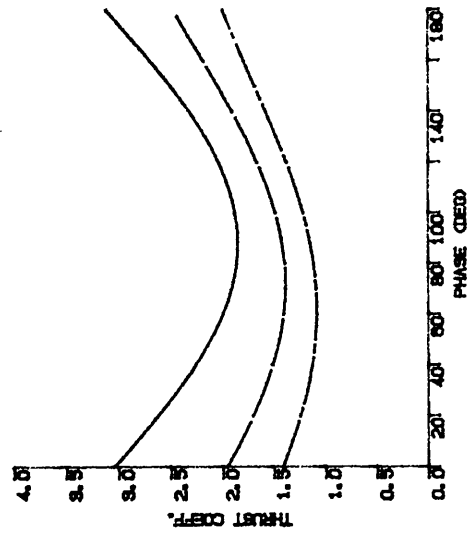
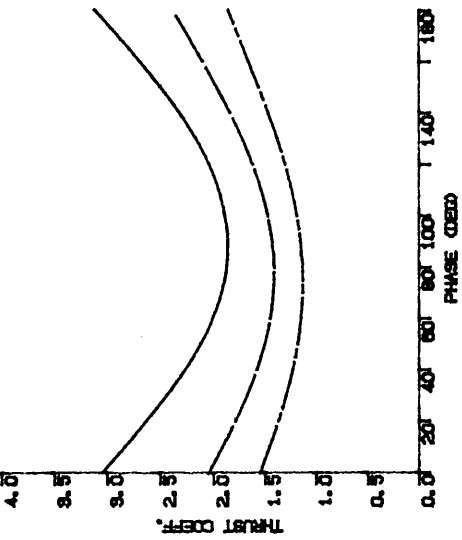
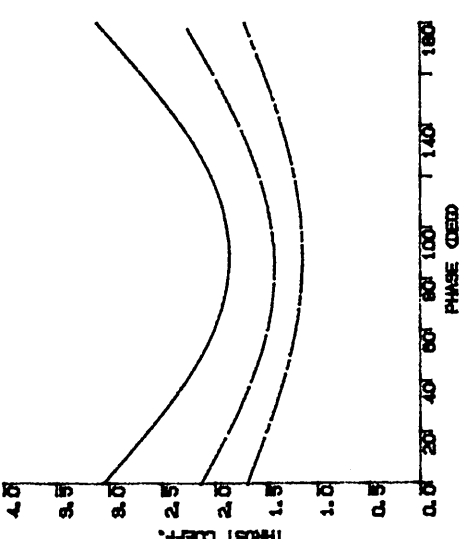
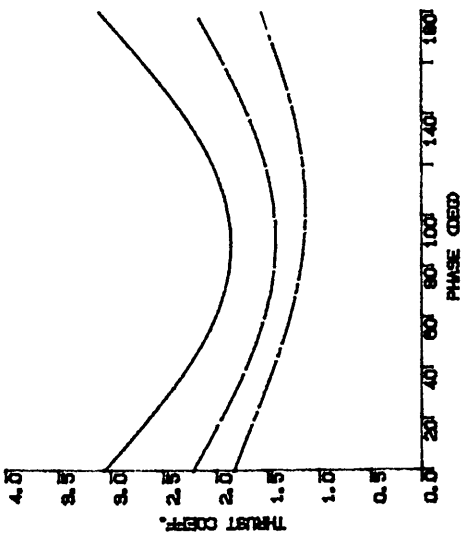


Rotating Centre = L. E.



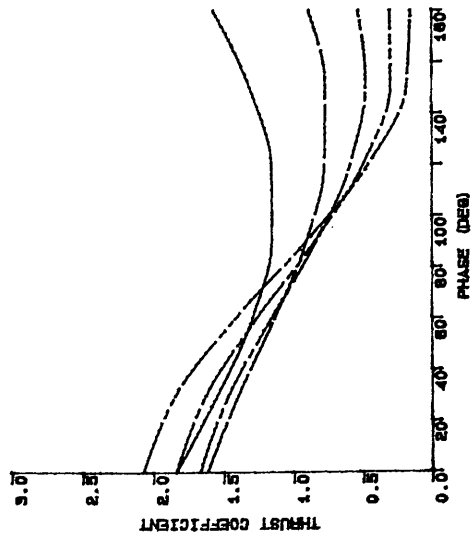
Rotating Centre = 0.75c

Fig. 3.3b The Propulsive Thrust Coefficient when $\theta = 0.2$

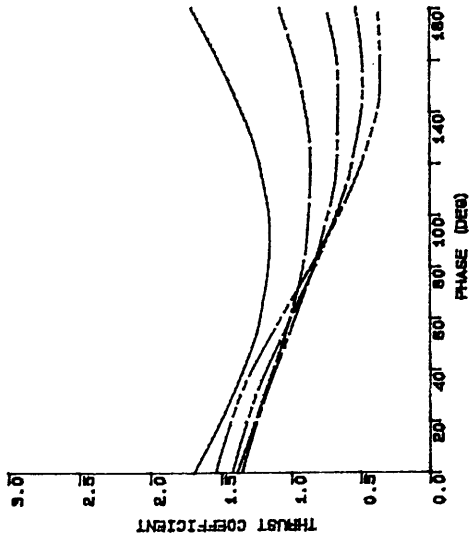


—	K = 0.005
- - -	K = 0.100
---	K = 0.200

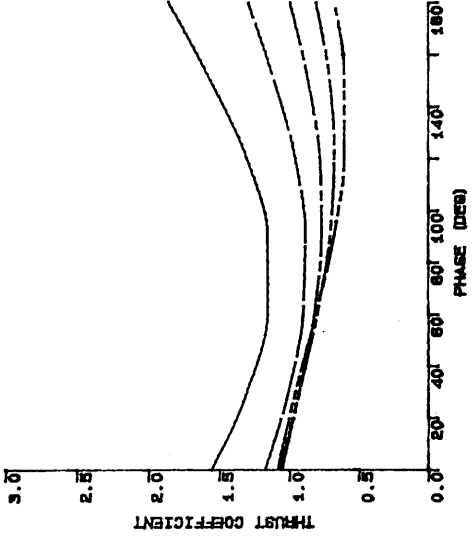
Fig. 3.4a The Propulsive Thrust Coefficient when $\theta = 0.4$



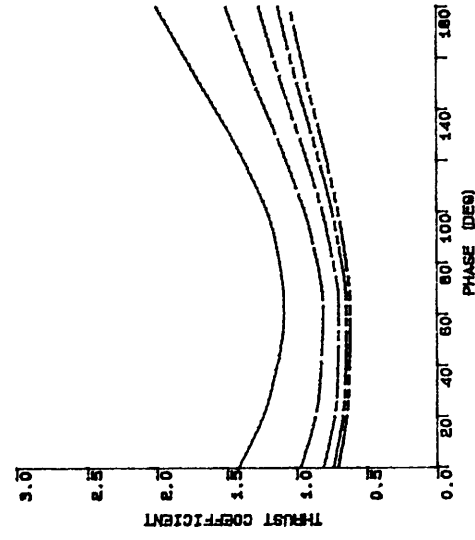
Rotating Centre = L. E.



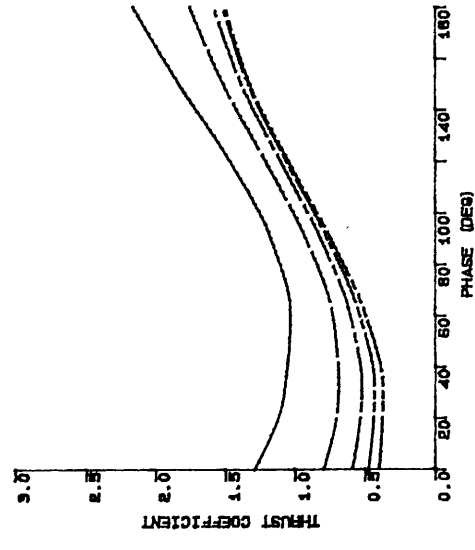
Rotating Centre = 0.25c



Rotating Centre = 0.5c



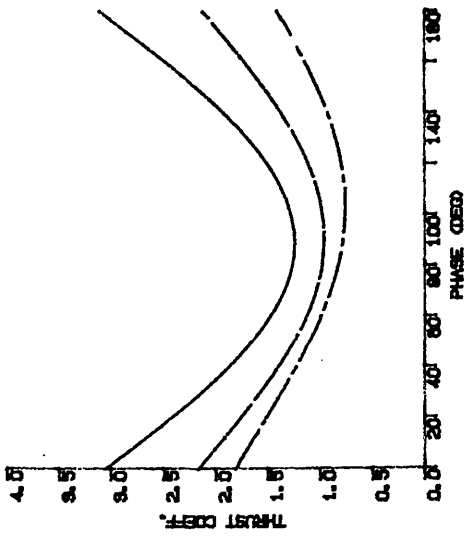
Rotating Centre = 0.75c



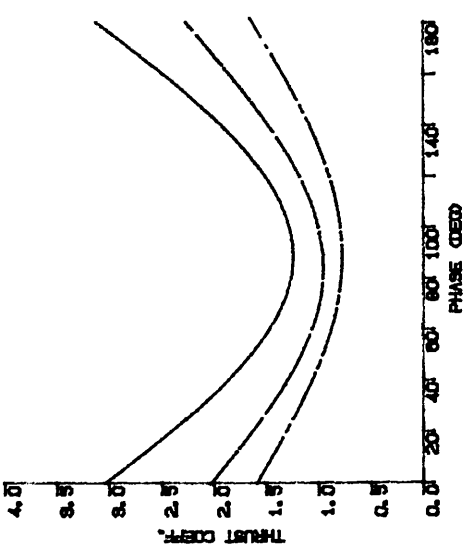
Rotating Centre = T. E.

—	K = 0.2
—	K = 0.4
—	K = 0.6
- - -	K = 0.8
- - -	K = 1.0

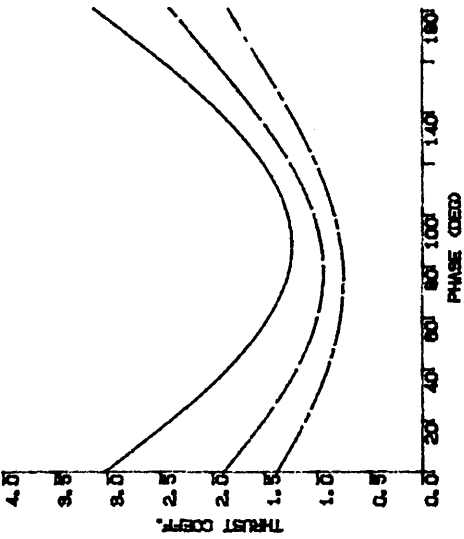
Fig. 3.4b The Propulsive Thrust Coefficient when $\theta = 0.4$



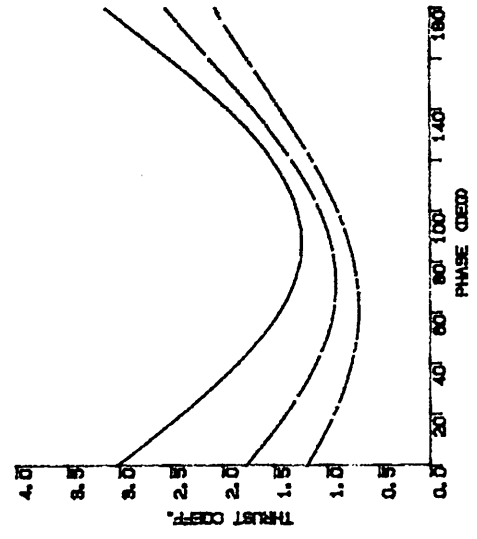
Rotating Centre = L. E.



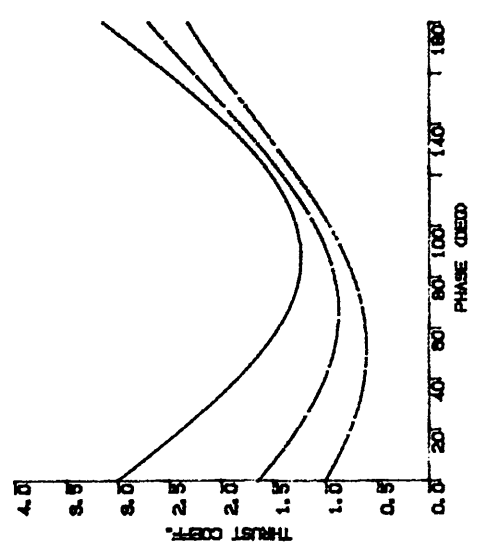
Rotating Centre = 0.25c



Rotating Centre = 0.5c



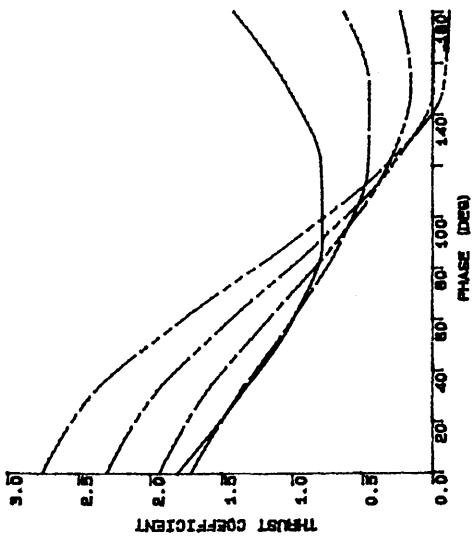
Rotating Centre = 0.75c



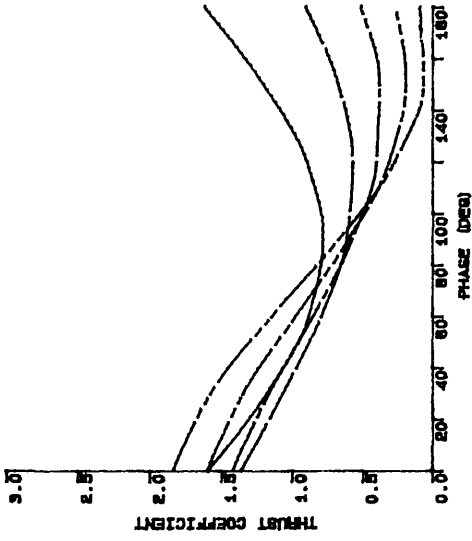
Rotating Centre = T. E.

—	K = 0.005
- - -	K = 0.100
- · -	K = 0.200

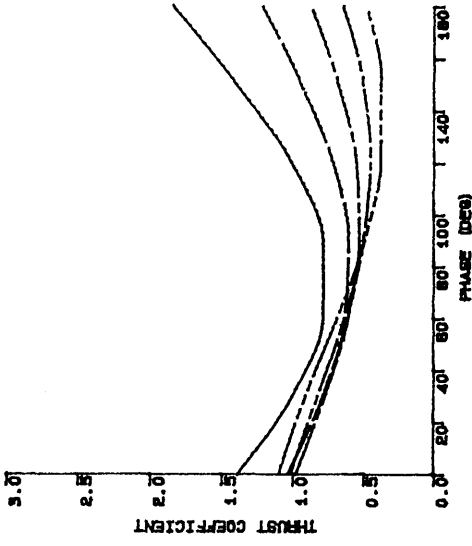
Fig. 3.5a The Propulsive Thrust Coefficient when $\theta = 0.6$



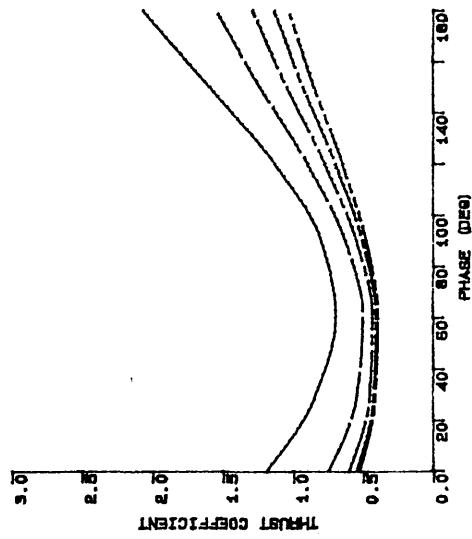
Rotating Centre = L. E.



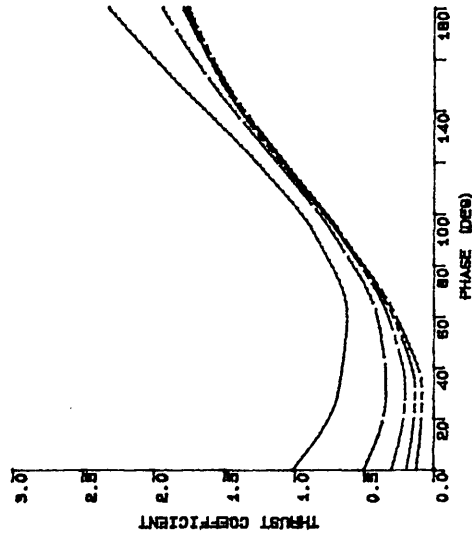
Rotating Centre = 0.25c



Rotating Centre = 0.5c



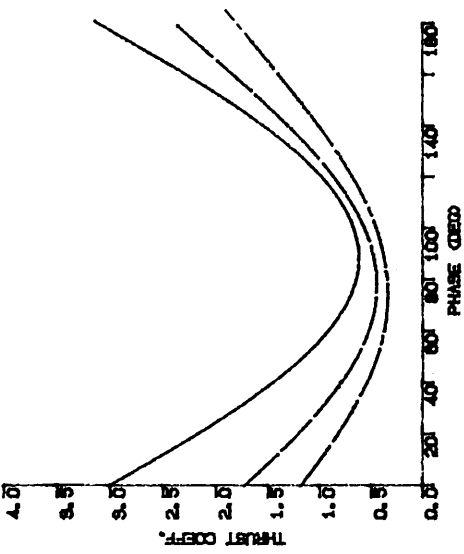
Rotating Centre = 0.75c



Rotating Centre = T. E.

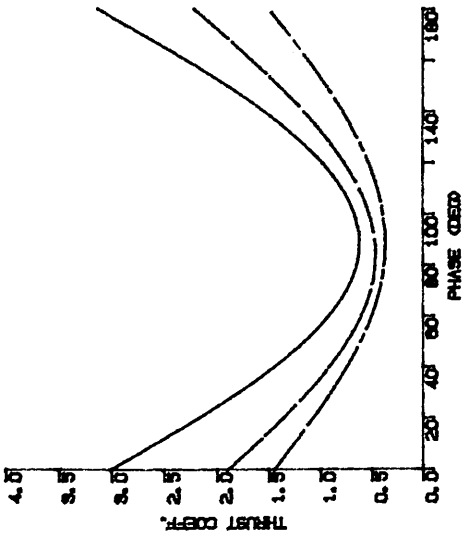
—	K = 0.2
- - -	K = 0.4
—	K = 0.6
- - -	K = 0.8
—	K = 1.0

Fig. 3.5b The Propulsive Thrust Coefficient when $\theta = 0.6$

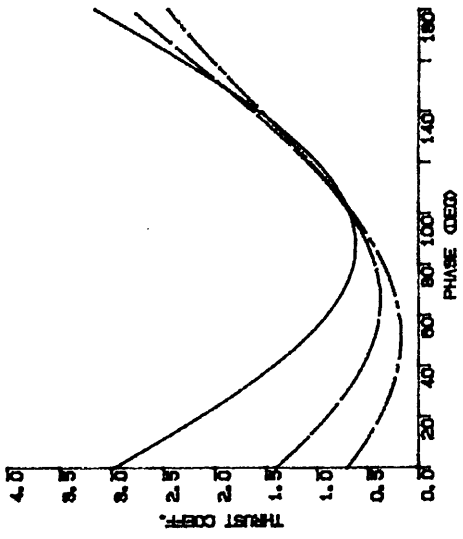


Rotating Centre = 0.5c

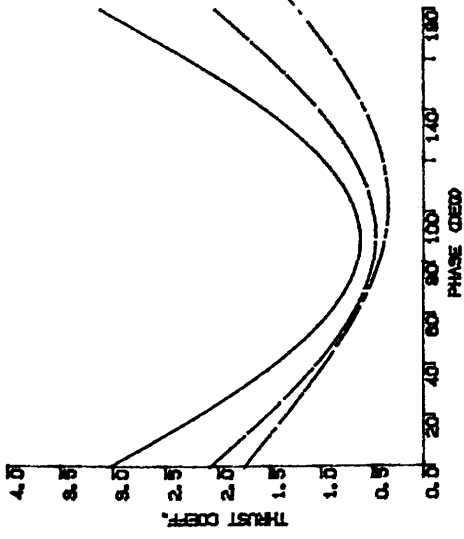
—	K = 0.005
- - -	K = 0.100
- · - ·	K = 0.200



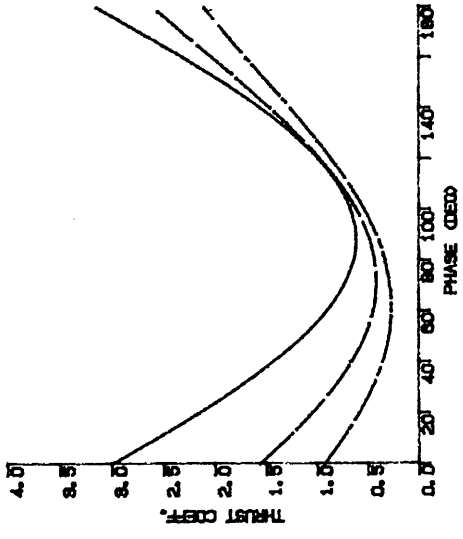
Rotating Centre = 0.25c



Rotating Centre = T. E.

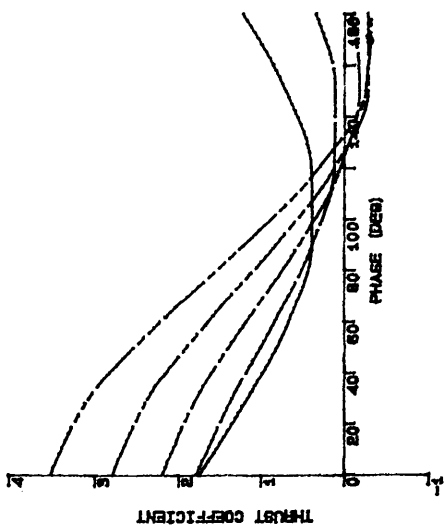


Rotating Centre = L. E.

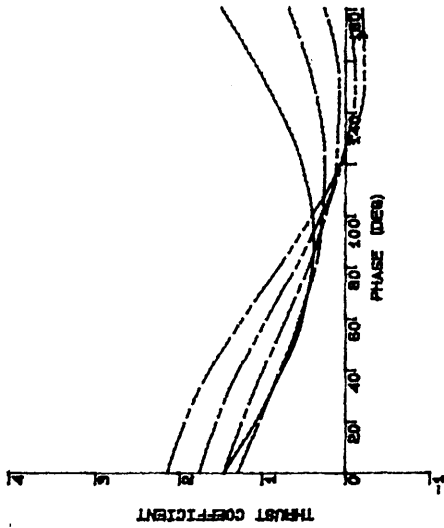


Rotating Centre = 0.75c

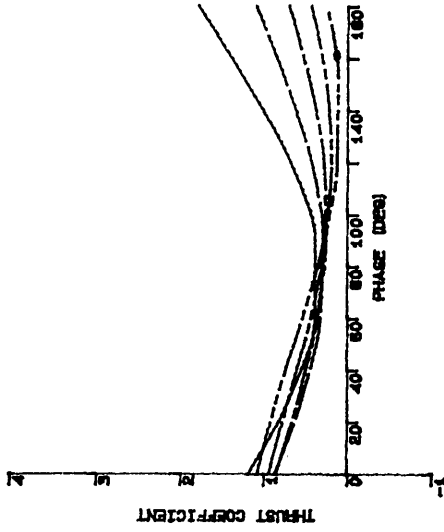
Fig. 3.6a The Propulsive Thrust Coefficient when $\theta = 0.8$



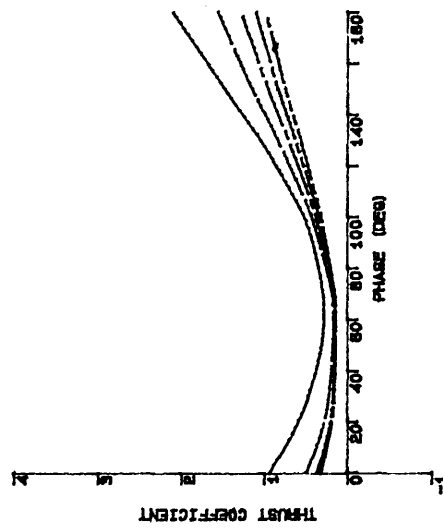
Rotating Centre = L. E.



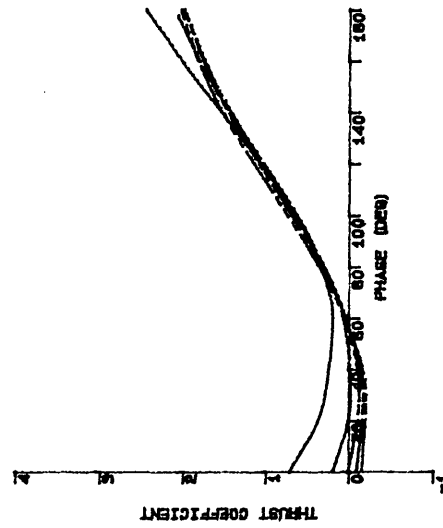
Rotating Centre = 0.25c



Rotating Centre = 0.5c



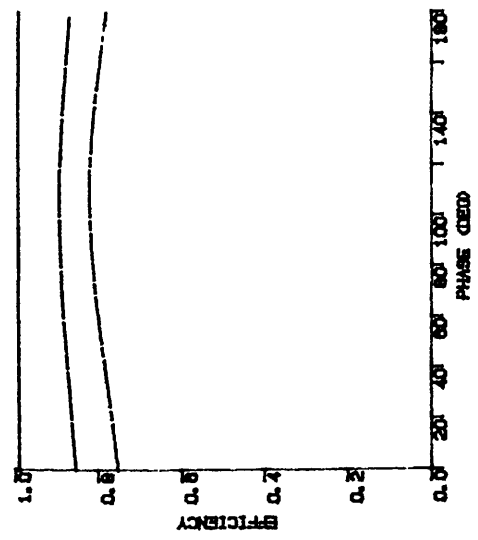
Rotating Centre = 0.75c



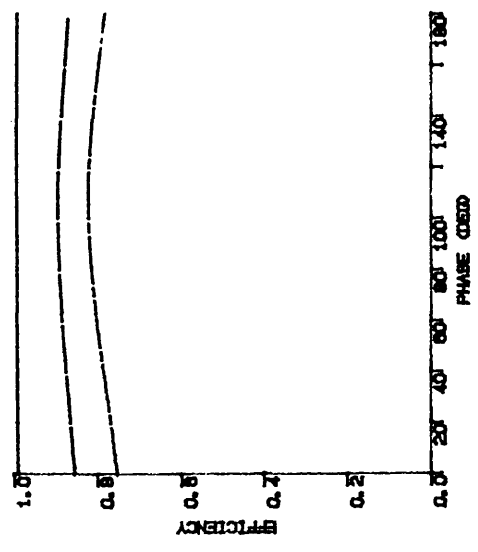
Rotating Centre = T. E.

—	K = 0.2
- - -	K = 0.4
· · ·	K = 0.6
— · —	K = 0.8
- - -	K = 1.0

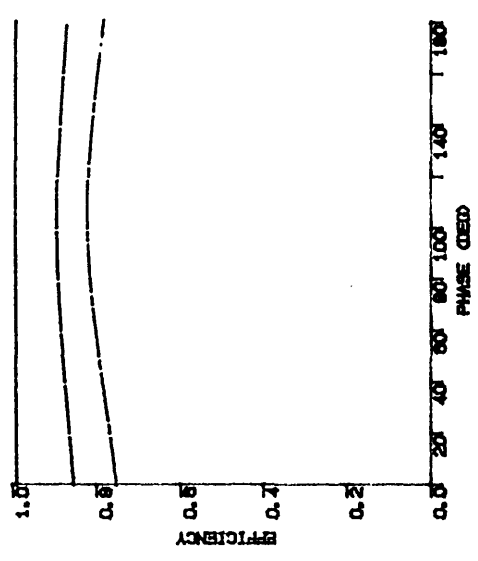
Fig. 3.6b The Propulsive Thrust coefficient when $\theta = 0.8$



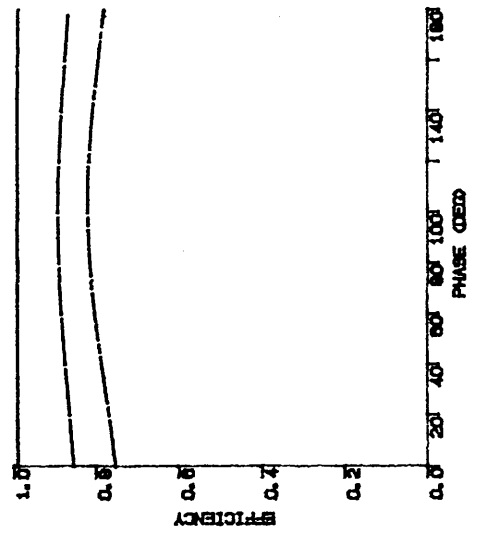
Rotating Centre = L. E.



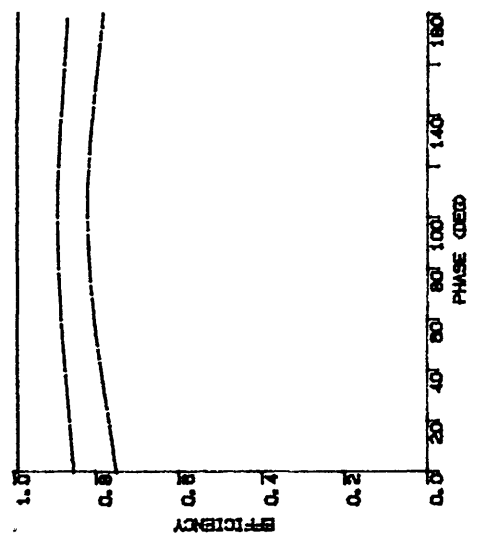
Rotating Centre = 0.25c



Rotating Centre = 0.5c



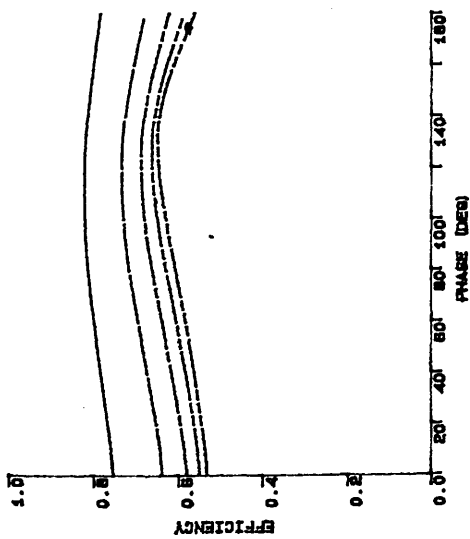
Rotating Centre = 0.75c



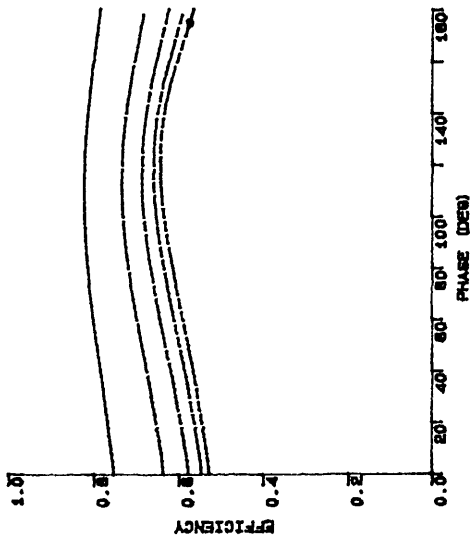
Rotating Centre = T. E.



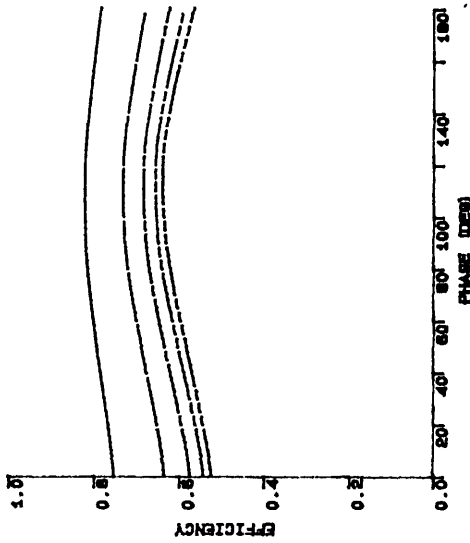
Fig. 3.7a The Propulsive Efficiency when $\theta = 0.2$



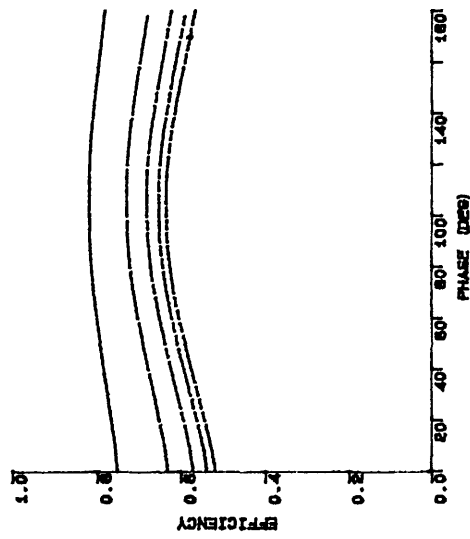
Rotating Centre = L. E.



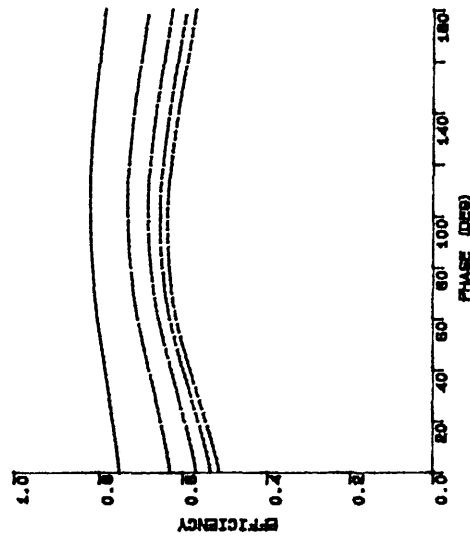
Rotating Centre = 0.25c



Rotating Centre = 0.5c



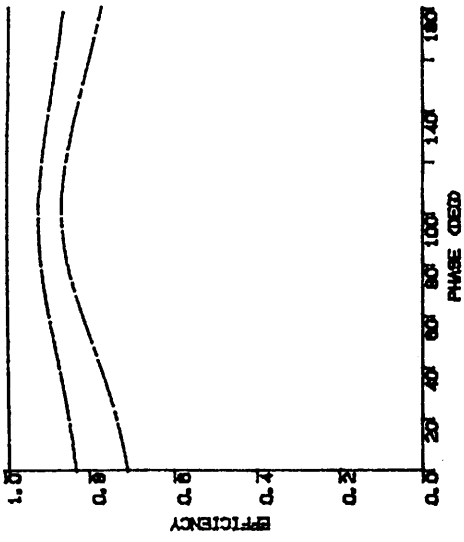
Rotating Centre = 0.75c



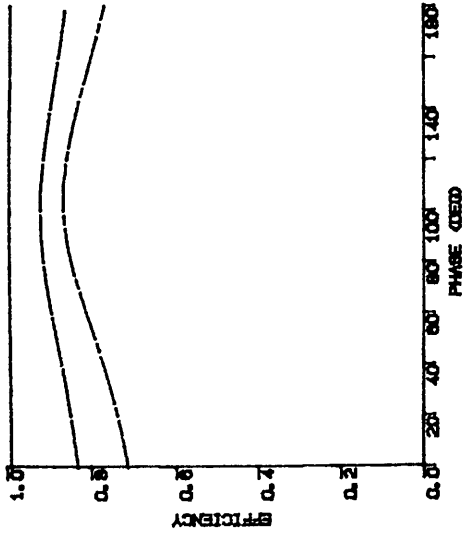
Rotating Centre = T. E.

—	K = 0.2
—	K = 0.4
—	K = 0.6
—	K = 0.8
—	K = 1.0

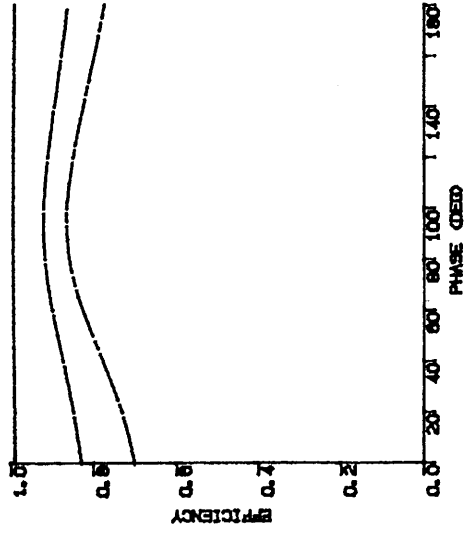
Fig. 3.7b The Propulsive Efficiency when $\theta = 0.2$



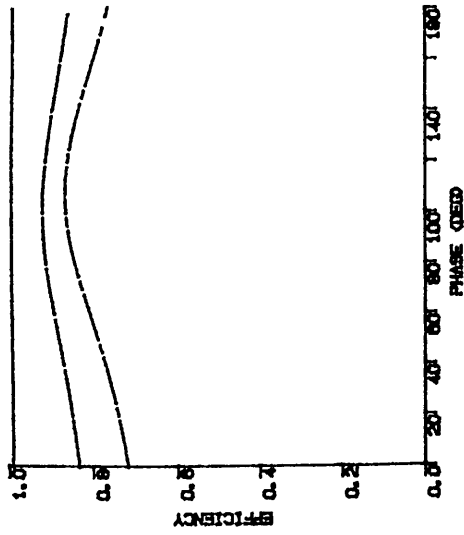
Rotating Centre = 0.5c



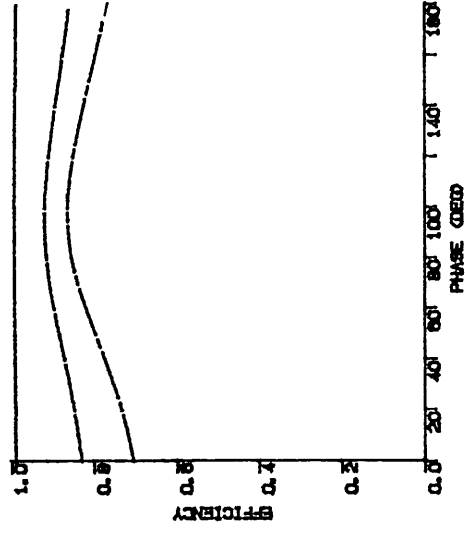
Rotating Centre = 0.25c



Rotating Centre = T. E.

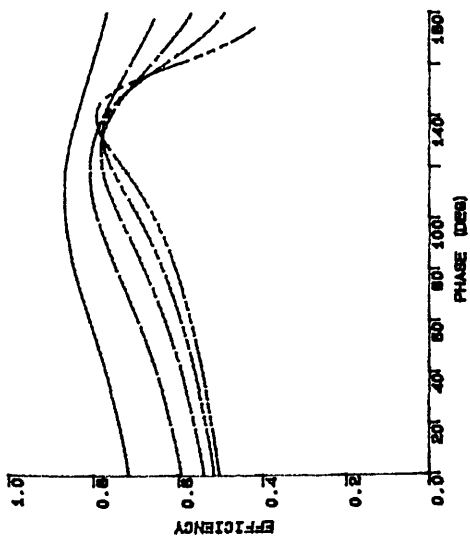


Rotating Centre = L. E.

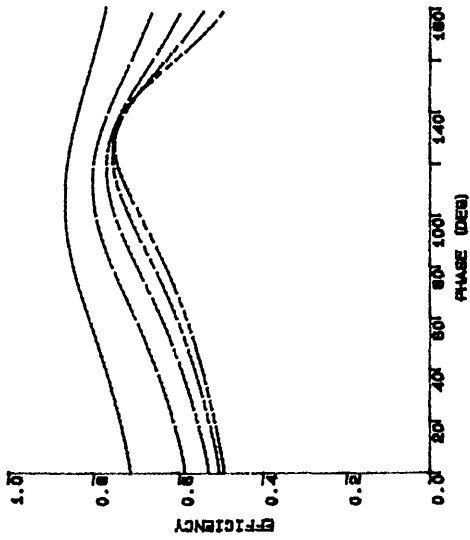


Rotating Centre = 0.75c

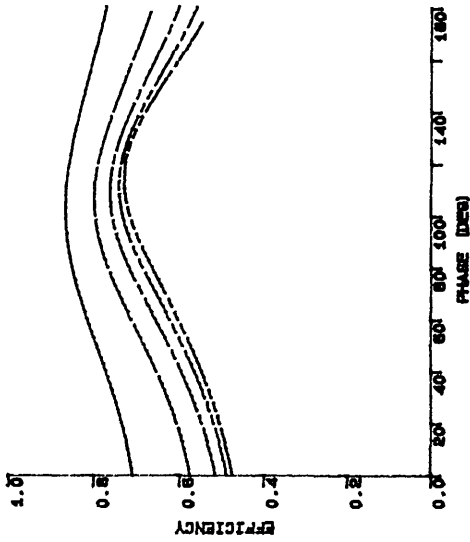
Fig. 3.8a The Propulsive Efficiency when $\theta = 0.4$



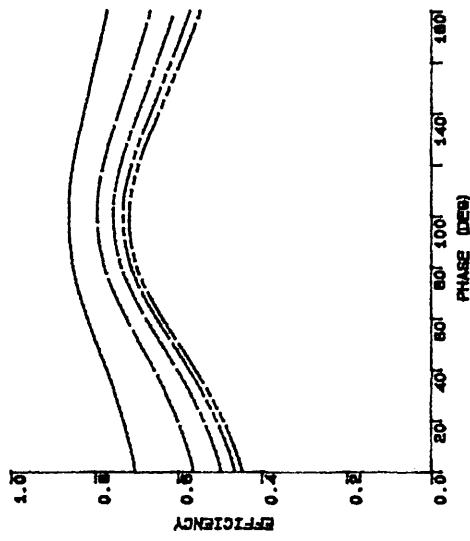
Rotating Centre = L. E.



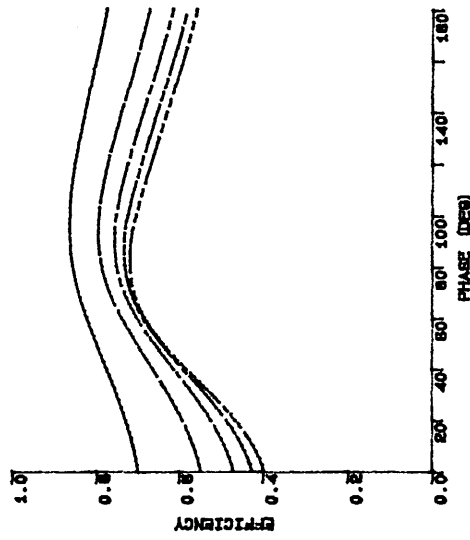
Rotating Centre = 0.25c



Rotating Centre = 0.5c



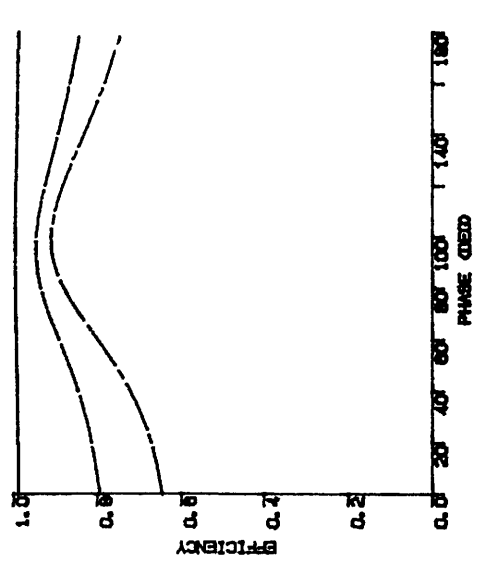
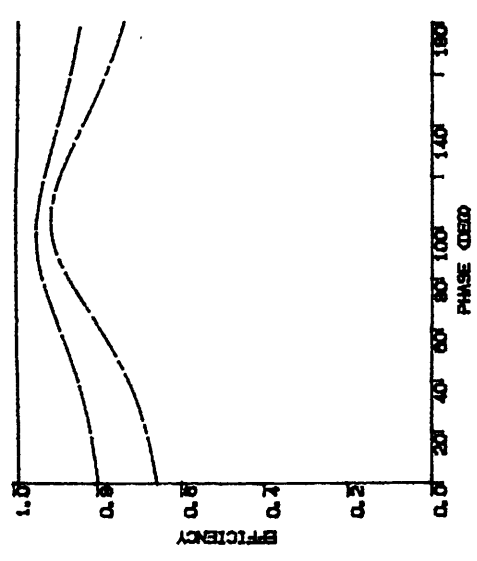
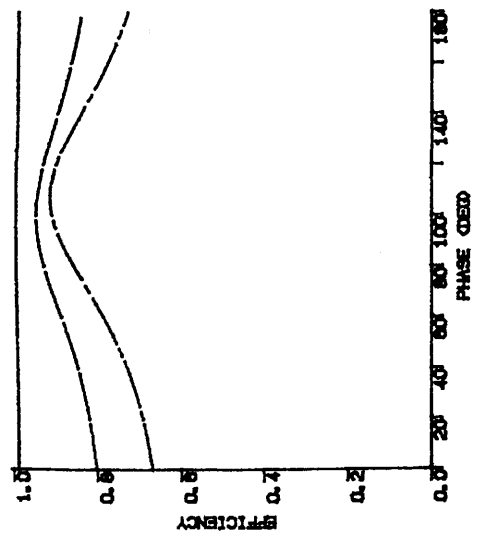
Rotating Centre = 0.75c



Rotating Centre = T. E.

—	K = 0.2
—	K = 0.4
—	K = 0.6
- - -	K = 0.8
- - -	K = 1.0

Fig. 3.8b The Propulsive Efficiency when $\theta = 0.4$



Rotating Centre = L. E.

Rotating Centre = 0.25c

Rotating Centre = 0.5c

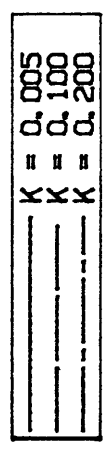
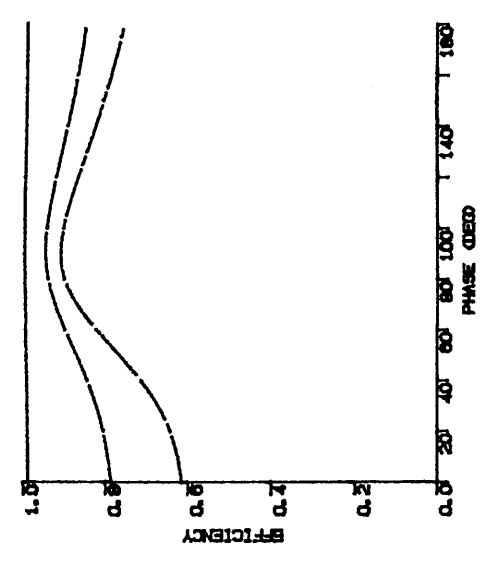
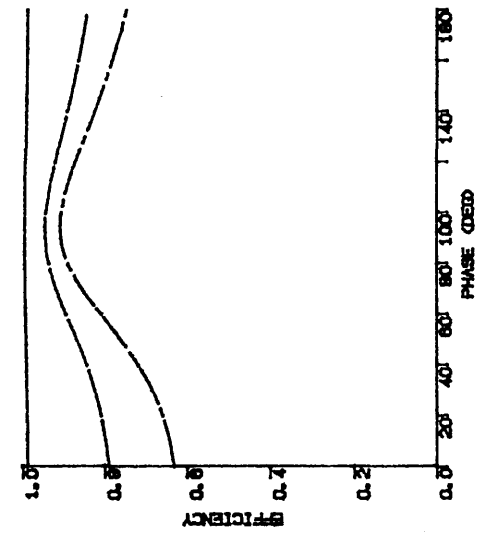
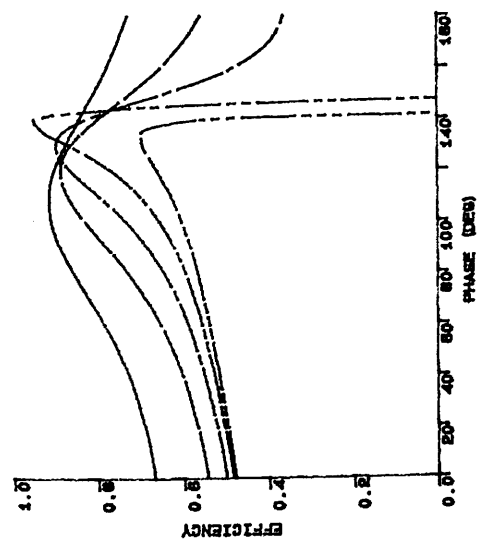
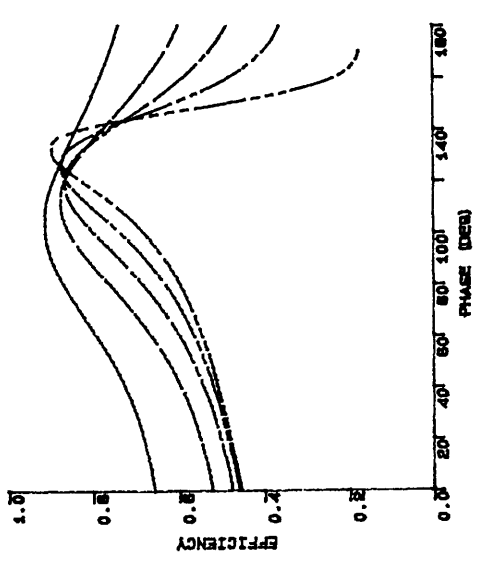


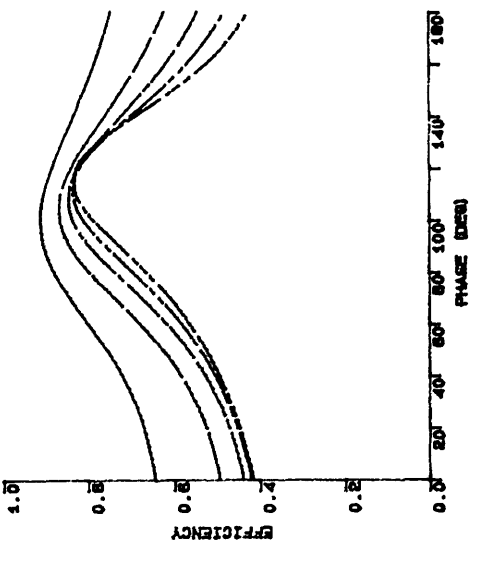
Fig. 3.9a The Propulsive Efficiency when $\theta = 0.6$



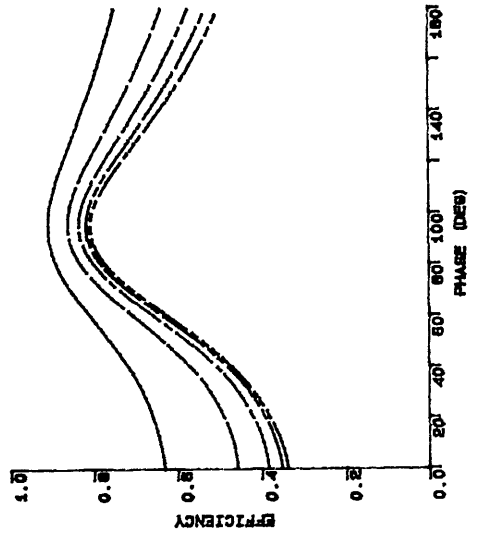
Rotating Centre = L. E.



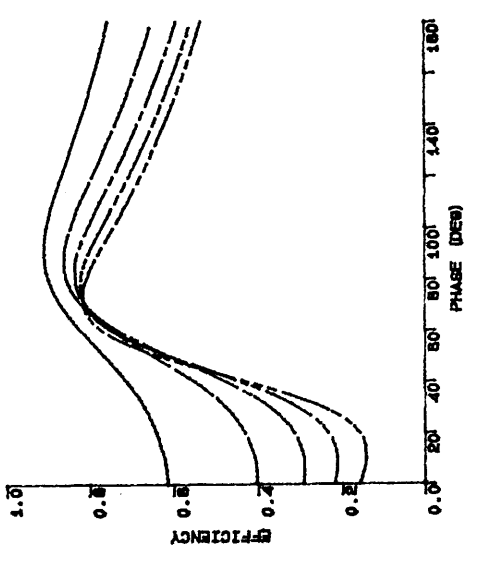
Rotating Centre = 0.25c



Rotating Centre = 0.5c



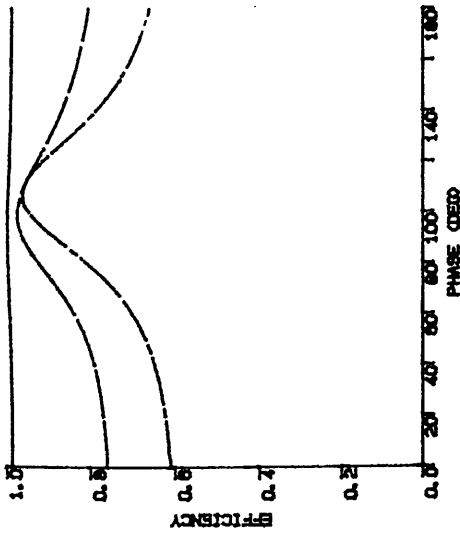
Rotating Centre = 0.75c



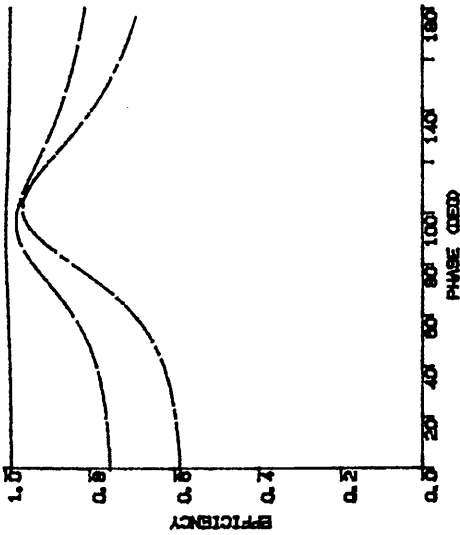
Rotating Centre = T. E.

—	K = 0.2
—	K = 0.4
—	K = 0.6
- - -	K = 0.8
- - -	K = 1.0

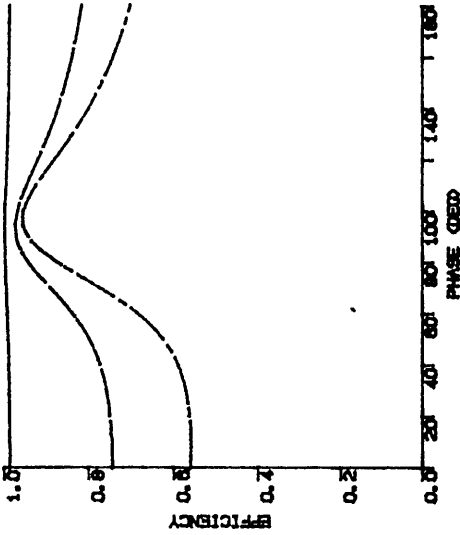
Fig. 3.9b The Propulsive Efficiency when $\theta = 0.6$



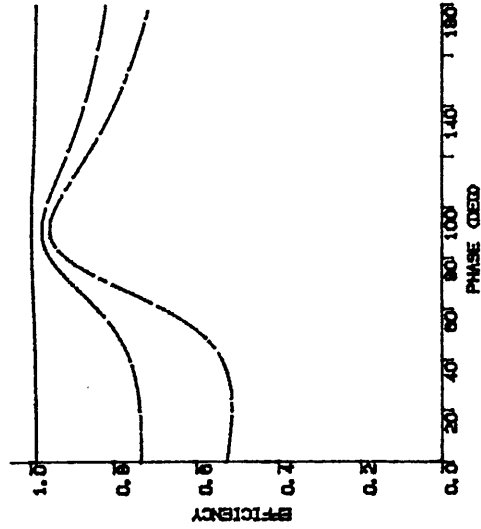
Rotating Centre = L. E.



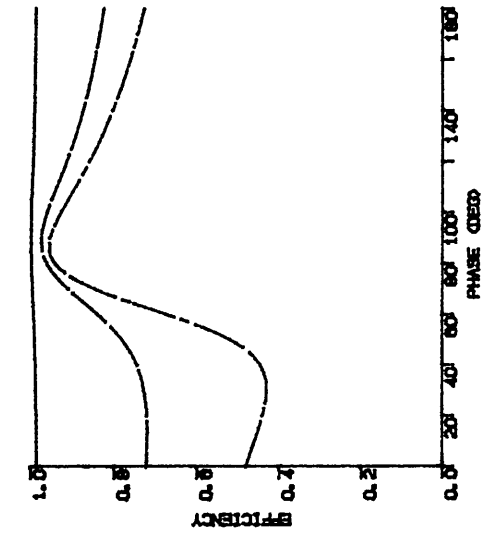
Rotating Centre = 0.25c



Rotating Centre = 0.5c



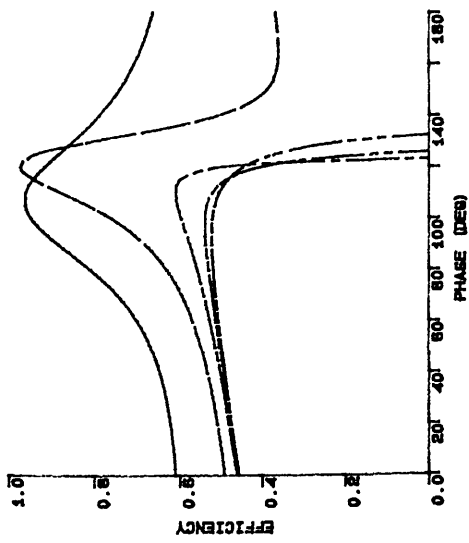
Rotating Centre = 0.75c



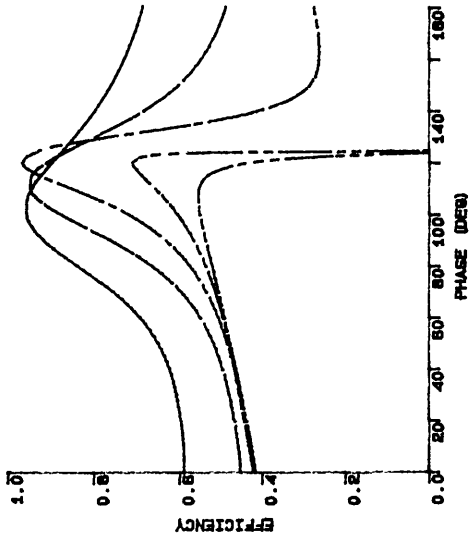
Rotating Centre = T. E.



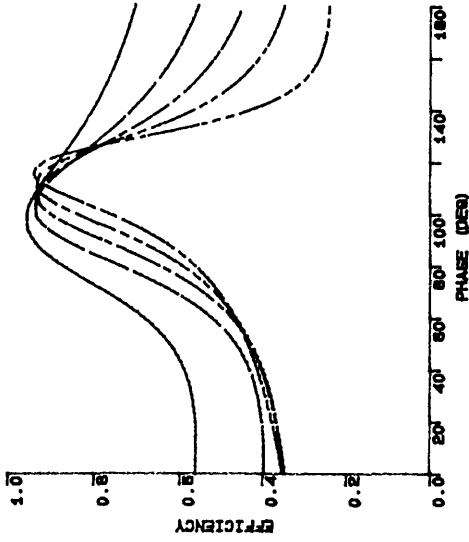
Fig. 3.10a The Propulsive Efficiency when $\theta = 0.8$



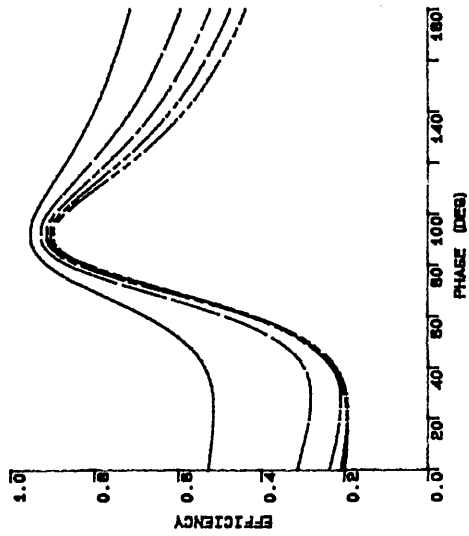
Rotating Centre = L. E.



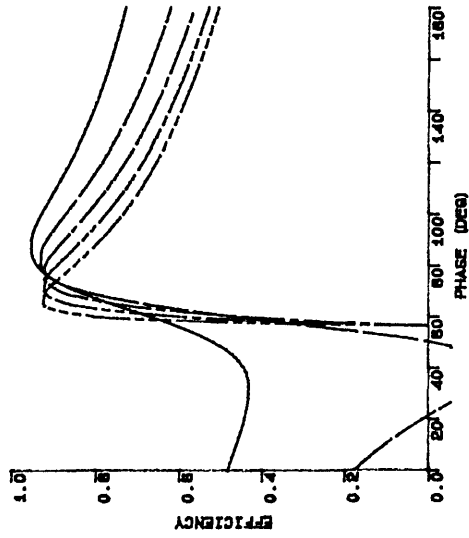
Rotating Centre = 0.25c



Rotating Centre = 0.5c



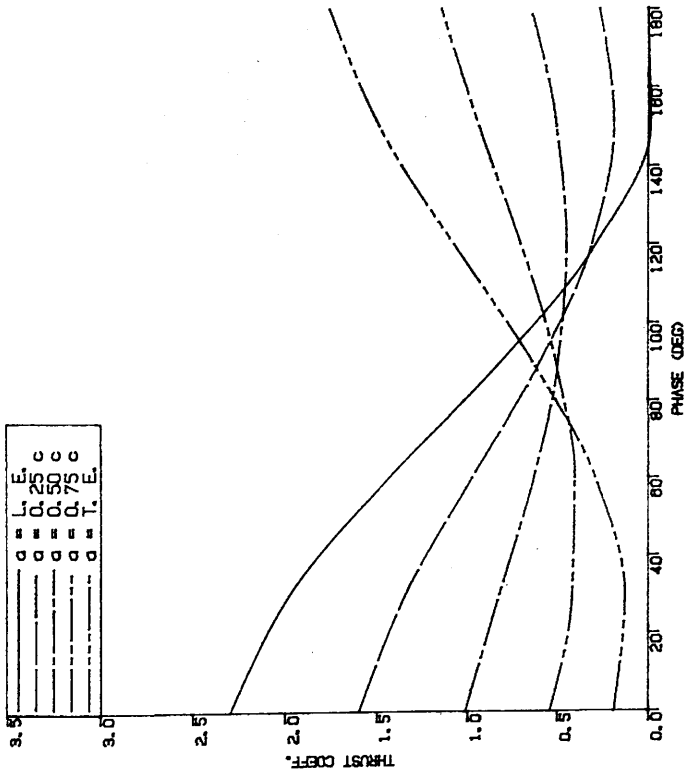
Rotating Centre = 0.75c



Rotating Centre = T. E.

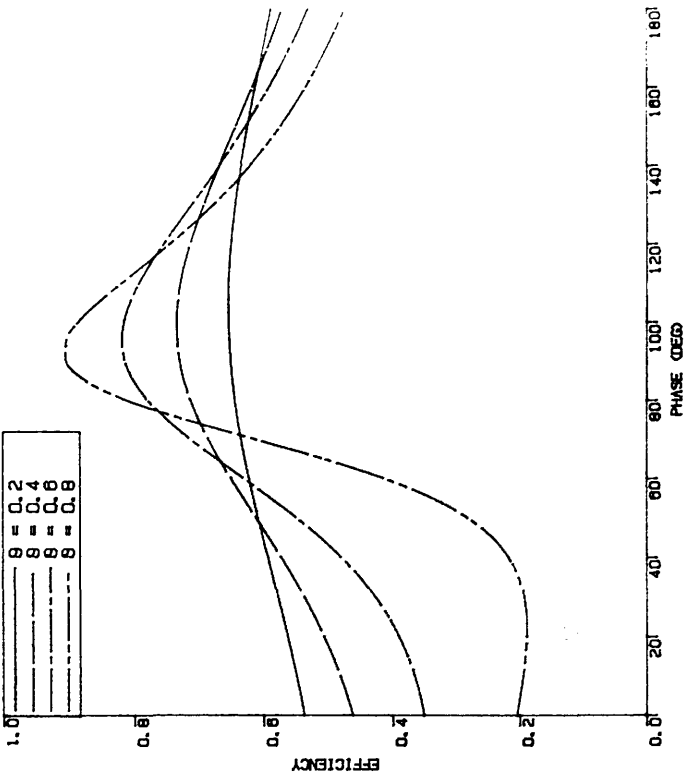
—	K = 0.2
- - -	K = 0.4
· · ·	K = 0.6
— · —	K = 0.8
- - -	K = 1.0

Fig. 3.10b The Propulsive Efficiency when $\theta = 0.8$



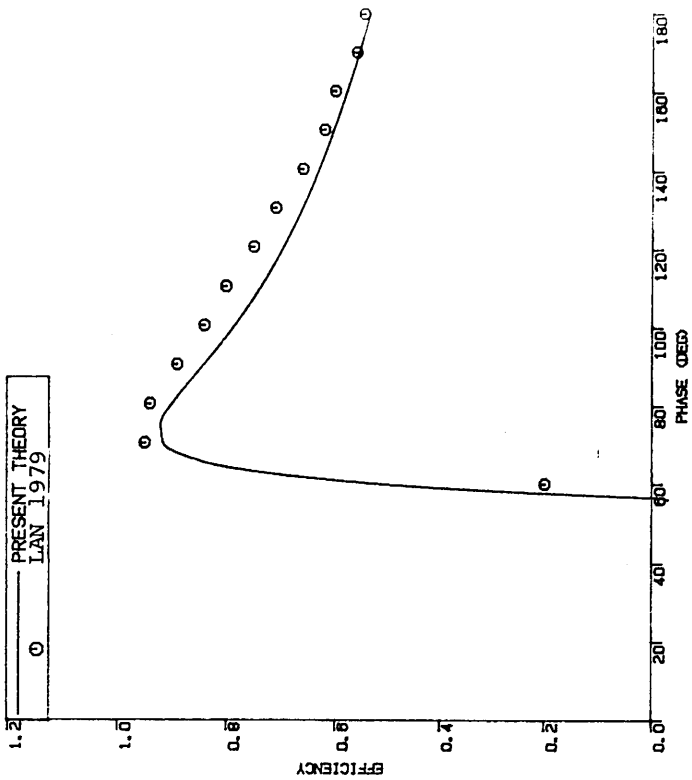
THE PROPULSIVE THRUST COEFF.
 ($\theta = 0.6, k = 0.8$)

Fig. 3.11

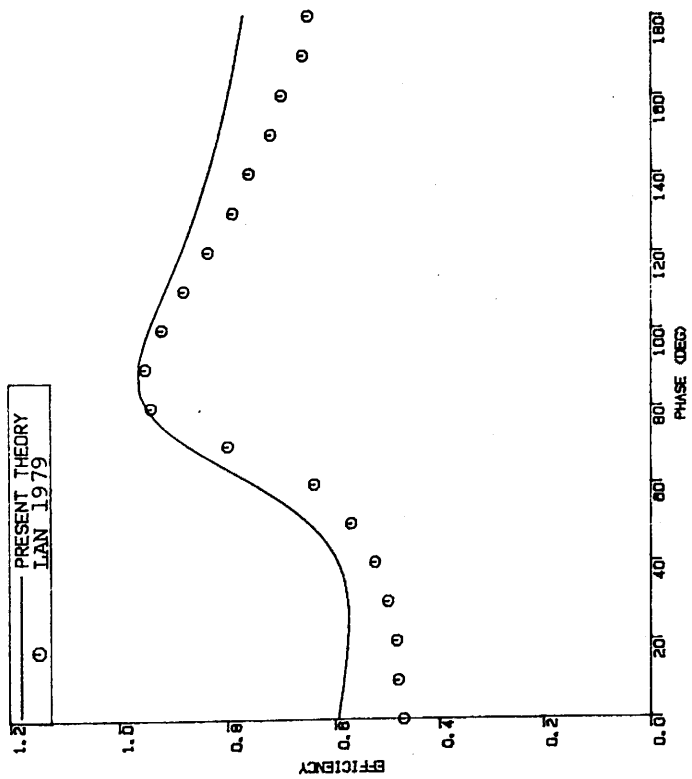


THE HYDROMECHANICAL EFFICIENCY
 ($\alpha = 0.75c, k = 0.8$)

Fig. 3.12

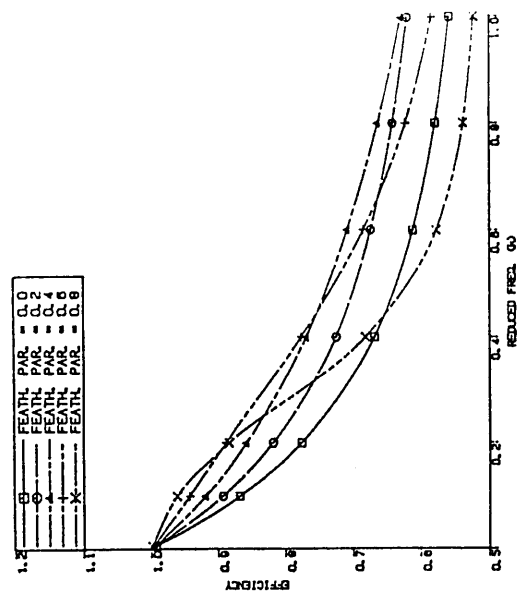


(a) $k = 0.15$

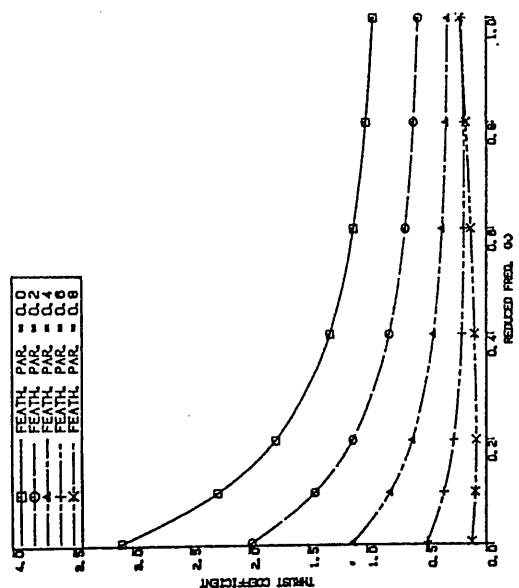


(b) $k = 0.75$

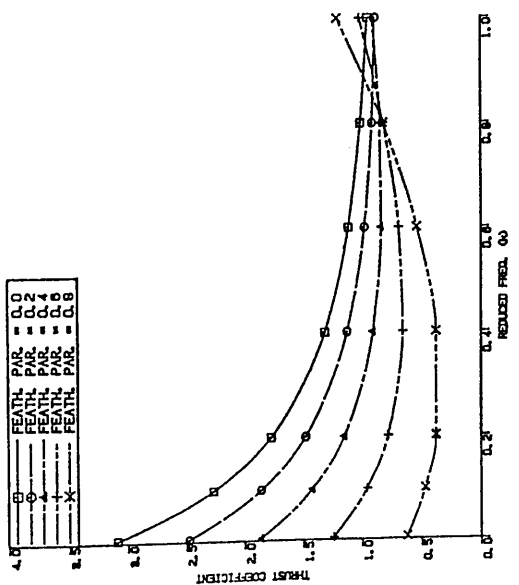
Fig. 3.13 Propulsive Efficiency of a 2-D foil and a Rectangular Foil with AR = 7.0



THE EFFICIENCY (ROTATING CENTRE AT LEADING EDGE)

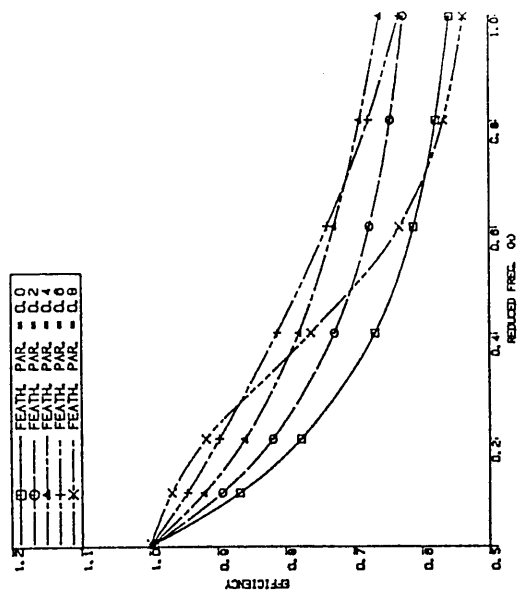


THE THRUST COEFF. (SUCTION) (ROTATING CENTRE AT L. E.)

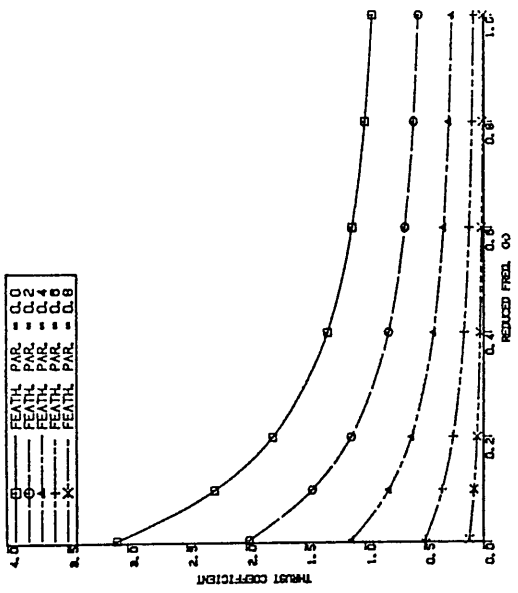


THE THRUST COEFF. (ROTATING CENTRE AT LEADING EDGE)

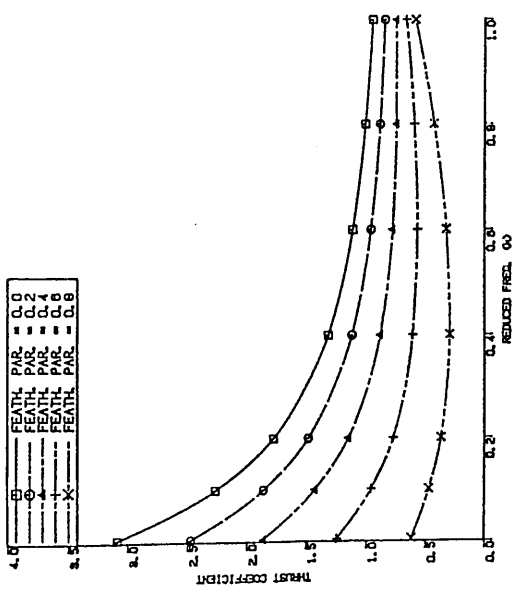
Fig. 3.14 Thrust Coefficient and Efficiency of a 2-D foil with Rotating Centre at L. E.



THE EFFICIENCY (ROTATING CENTRE AT 0.25 CHORD)

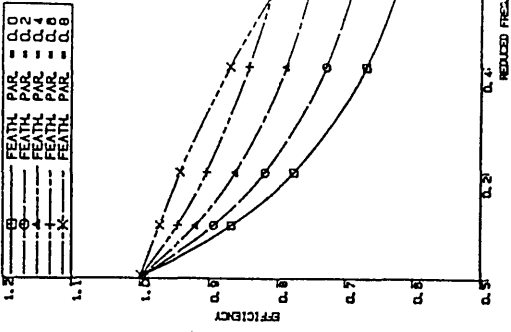


THE THRUST COEFF. (SUCTION) (ROTATING CENTRE AT 0.25 C)

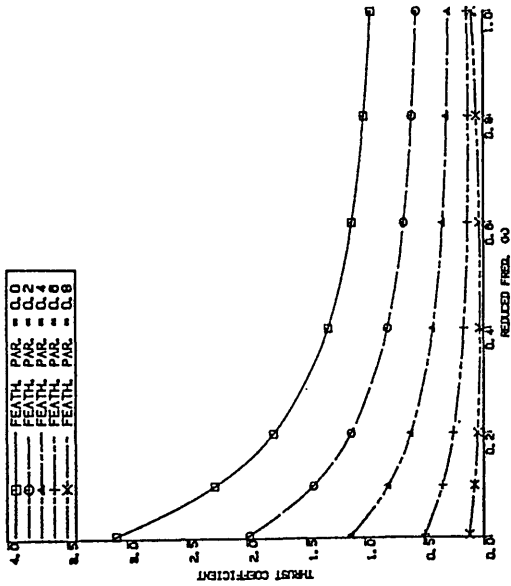


THE THRUST COEFF. (ROTATING CENTRE AT 0.25 CHORD)

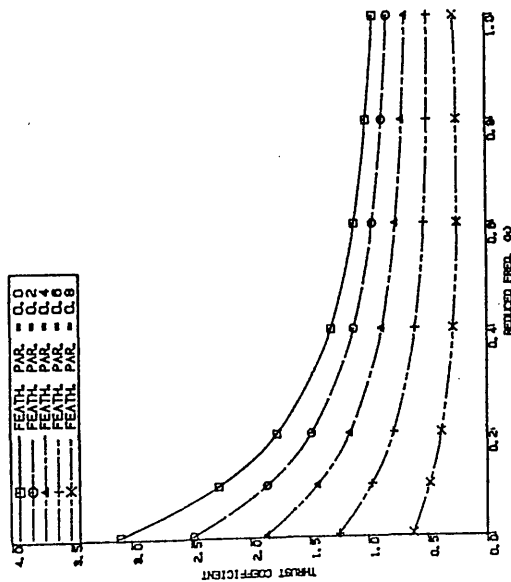
Fig. 3.15 Thrust Coefficient and Efficiency of a 2-D Foil with Rotating Centre at 0.25 Chord



THE EFFICIENCY (ROTATING CENTRE AT MID-CHORD)

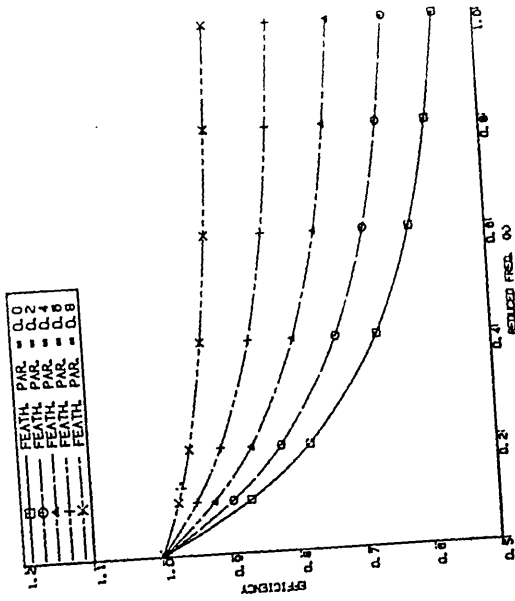


THE THRUST COEFF. (SUCTION) (ROTATING CENTRE AT MID-CHORD)

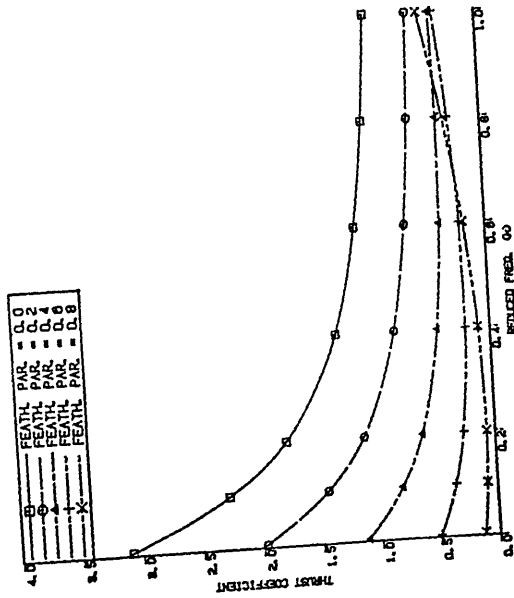


THE THRUST COEFF. (ROTATING CENTRE AT MID-CHORD)

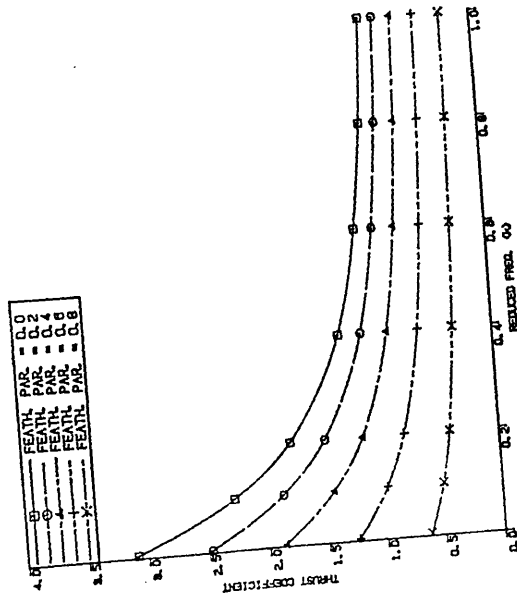
Fig. 3.16 Thrust Coefficient and Efficiency of a 2-D Foil with Rotating Centre at Mid-Chord



THE EFFICIENCY (ROTATING
CENTRE AT 0.75 CHORD)

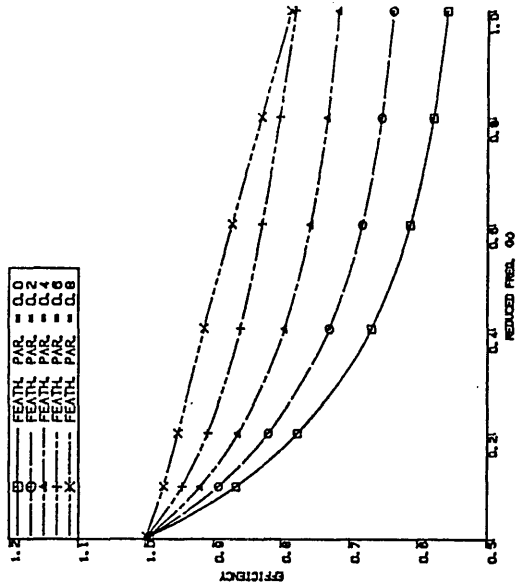


THE THRUST COEFF. (SUCTION)
(ROTATING CENTRE AT 0.75 C)

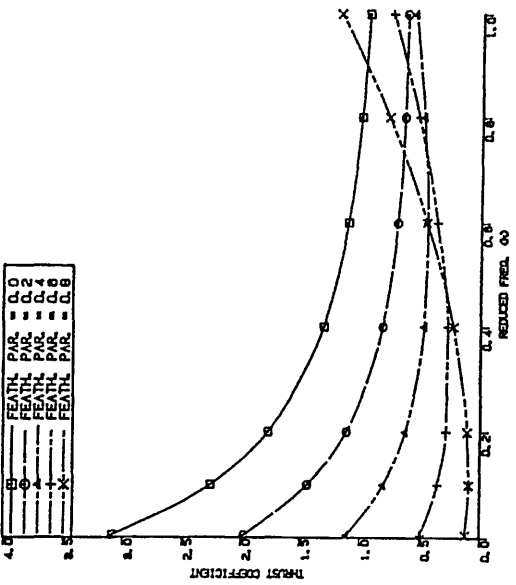


THE THRUST COEFF. (ROTATING
CENTRE AT 0.75 CHORD)

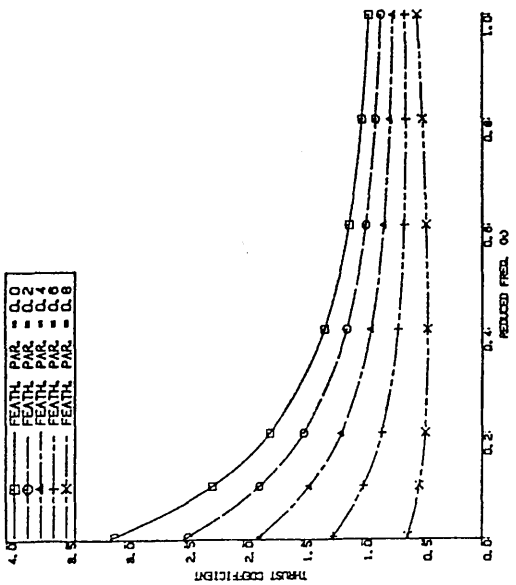
Fig. 3.17 Thrust Coefficient and Efficiency of a 2-D Foil with Rotating Centre at 0.75 Chord



THE EFFICIENCY (ROTATING CENTRE AT TRAILING EDGE)

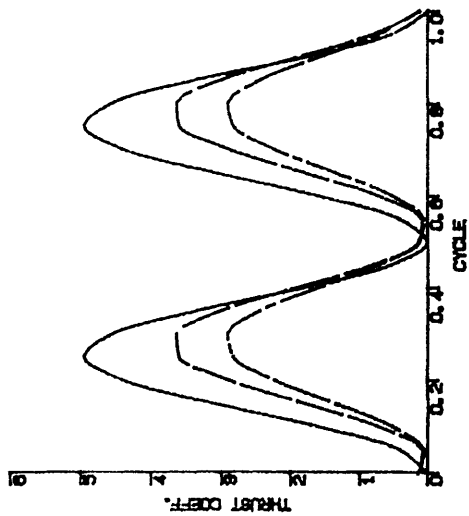


THE THRUST COEFF. (SUCTION) (ROTATING CENTRE AT T. E.)

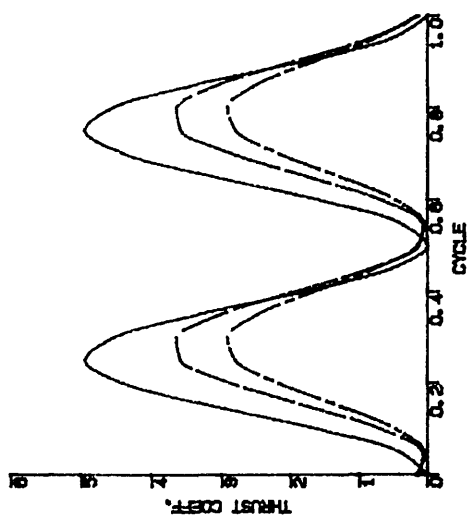


THE THRUST COEFF. (ROTATING CENTRE AT TRAILING EDGE)

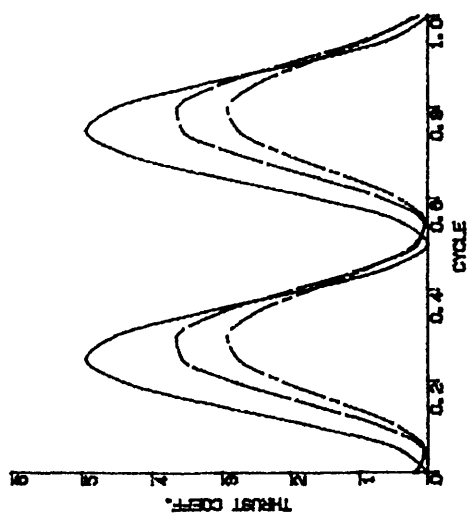
Fig. 3.18 Thrust Coefficient and Efficiency of a 2-D Foil with Rotating Centre at T. E.



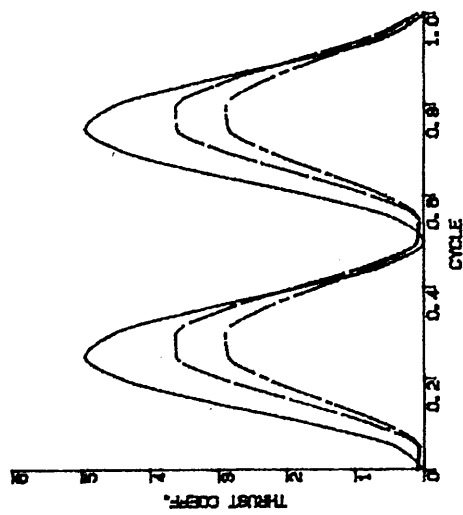
Rotating Centre = 0.5c



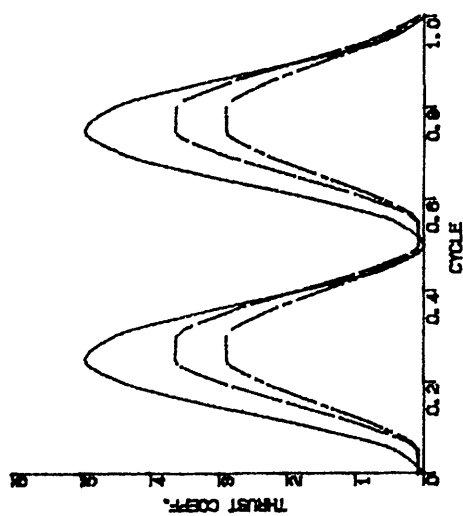
Rotating Centre = 0.25c



Rotating Centre = L. E.



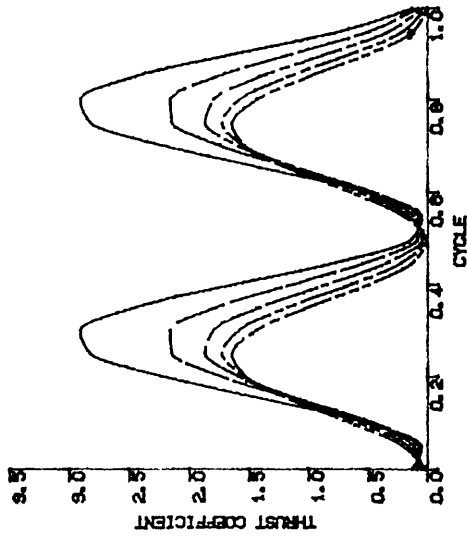
Rotating Centre = 0.75c



Rotating Centre = T. E.

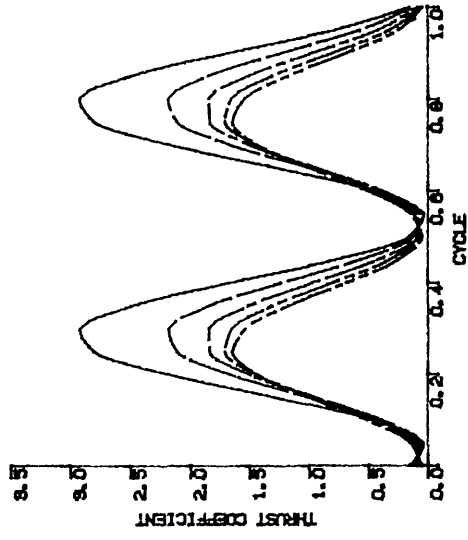
—	K = 0.005
- - -	K = 0.100
- · -	K = 0.200

Fig. 3.19a The Propulsive Thrust Coefficient in a Cycle when $\theta = 0.2$

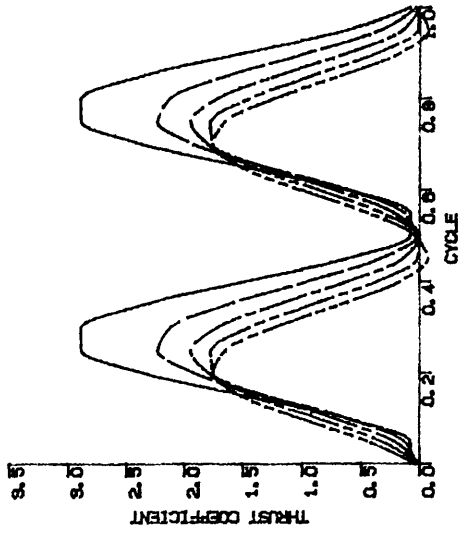


Rotating Centre = 0.5c

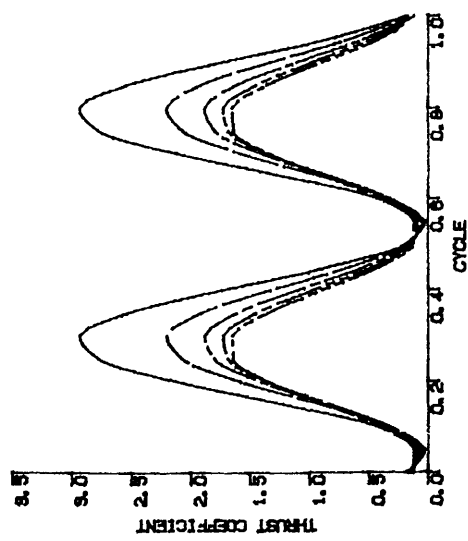
—	K = 0.2
- - -	K = 0.4
— · —	K = 0.6
- - -	K = 0.8
—	K = 1.0



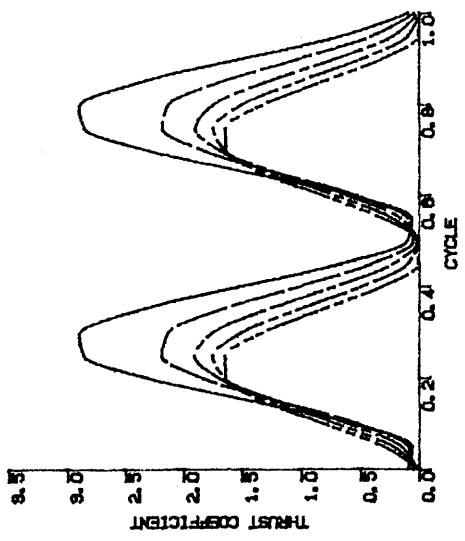
Rotating Centre = 0.25c



Rotating Centre = T. E.

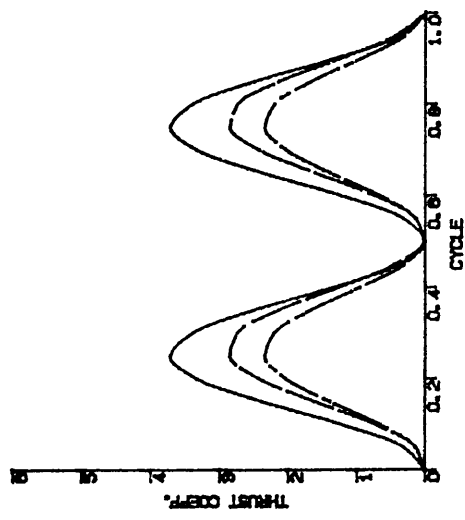
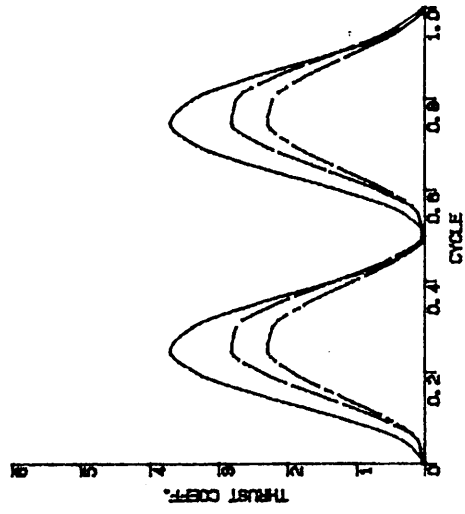
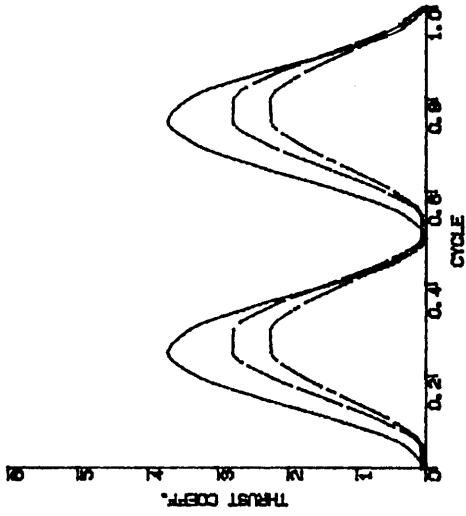
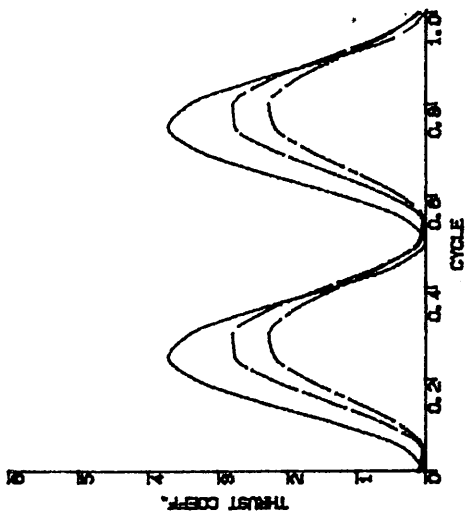
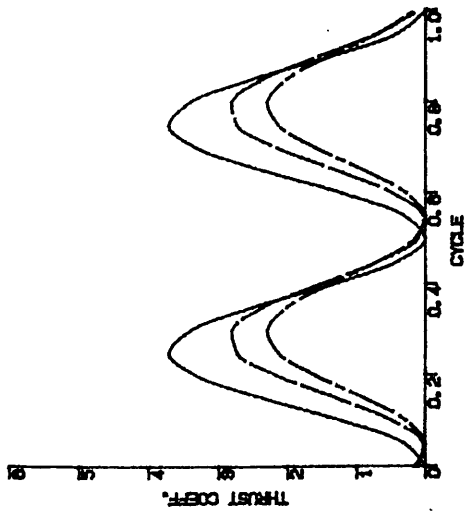


Rotating Centre = L. E.



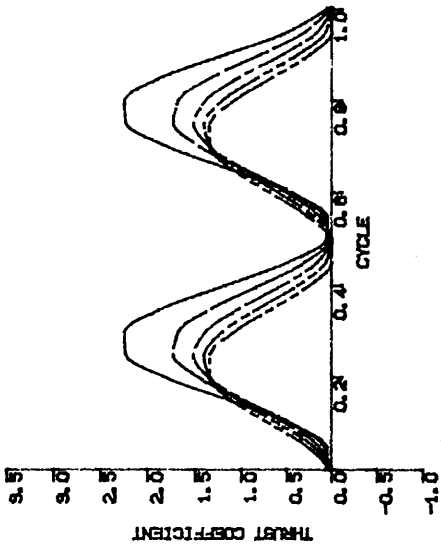
Rotating Centre = 0.75c

Fig. 3.19b The Propulsive Thrust Coefficient in a Cycle when $\theta = 0.2$

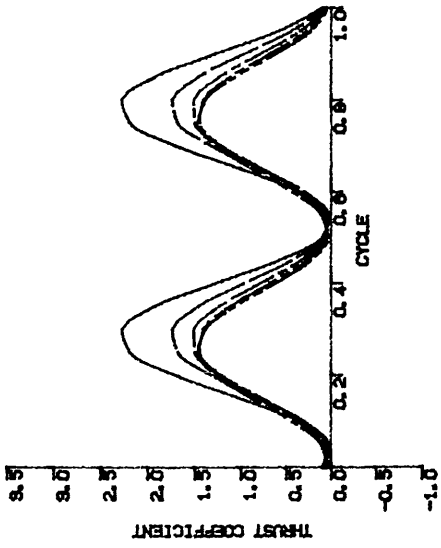


—	K = 0.005
- - -	K = 0.100
---	K = 0.200

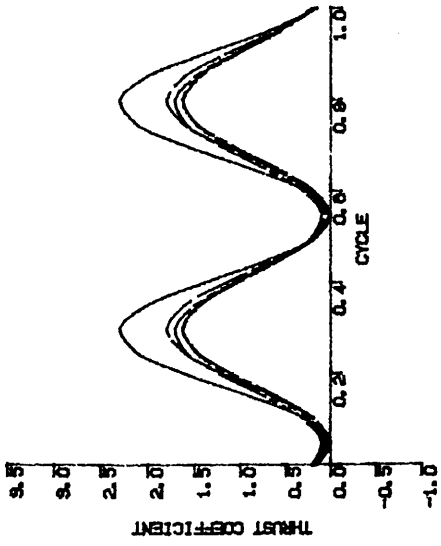
Fig. 3.20a The propulsive Thrust Coefficient in a Cycle when $\theta = 0.4$



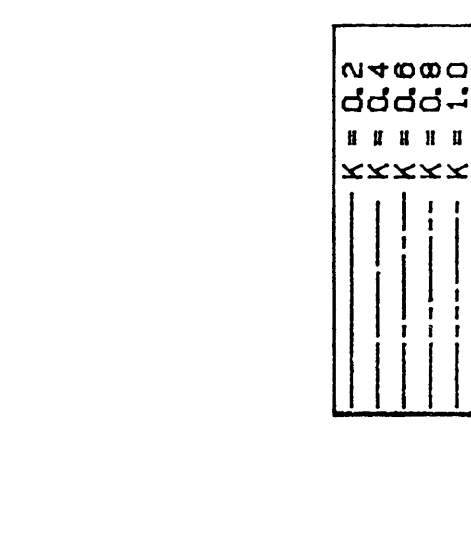
Rotating Centre = 0.5c



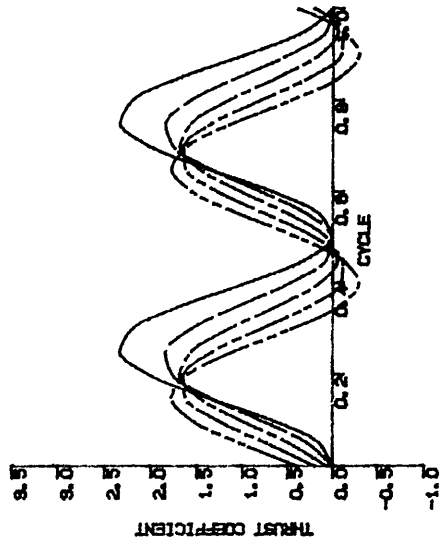
Rotating Centre = 0.25c



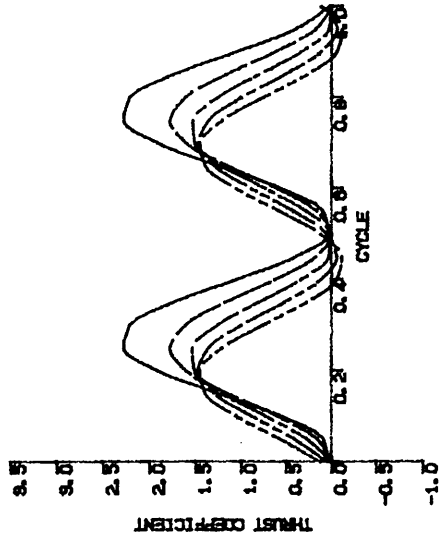
Rotating Centre = L. E.



Rotating Centre = T. E.

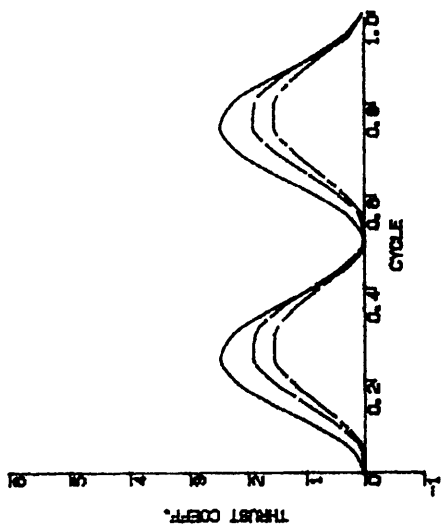


Rotating Centre = 0.75c

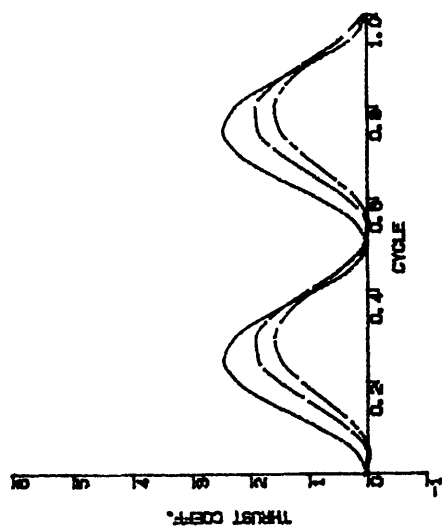


—	K = 0.2
—	K = 0.4
—	K = 0.6
—	K = 0.8
—	K = 1.0

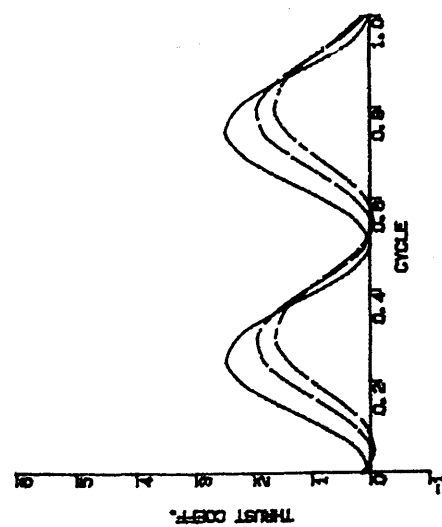
Fig. 3.20b The Propulsive Thrust Coefficient in a cycle when $\theta = 0.4$



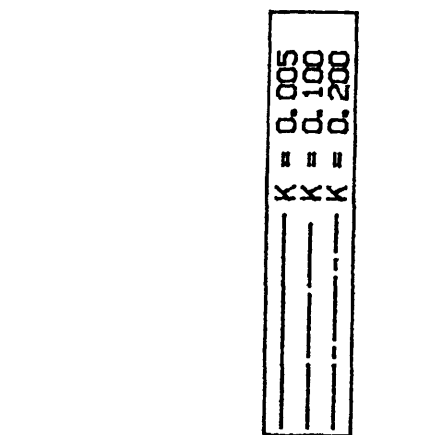
Rotating Centre = 0.5c



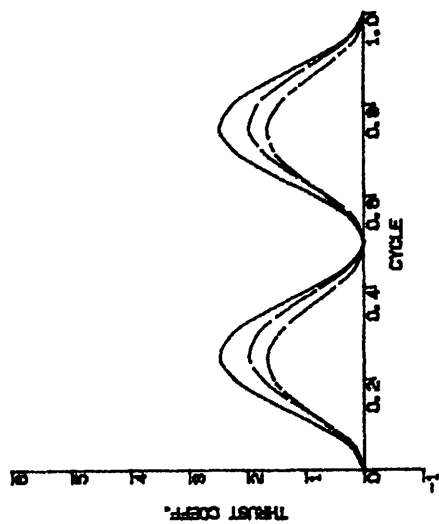
Rotating Centre = 0.25c



Rotating Centre = L. E.



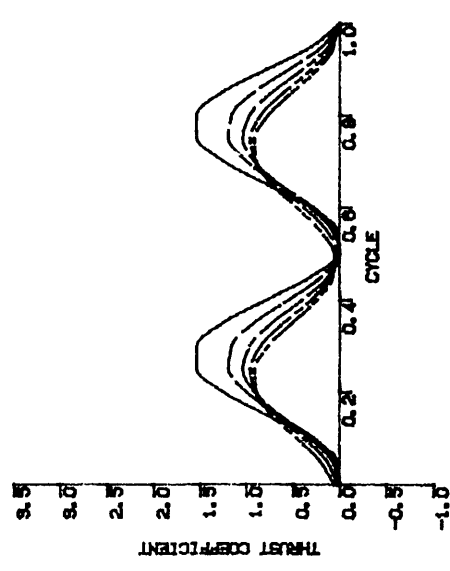
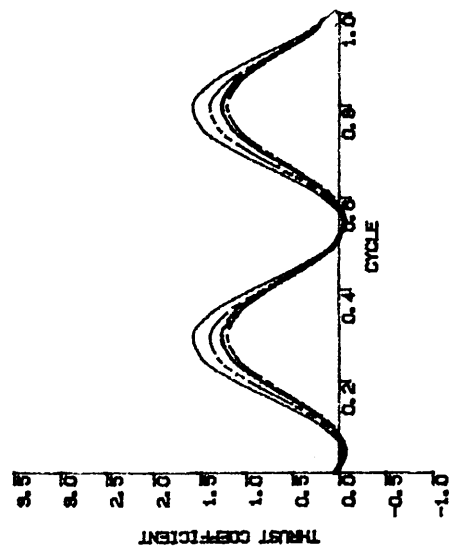
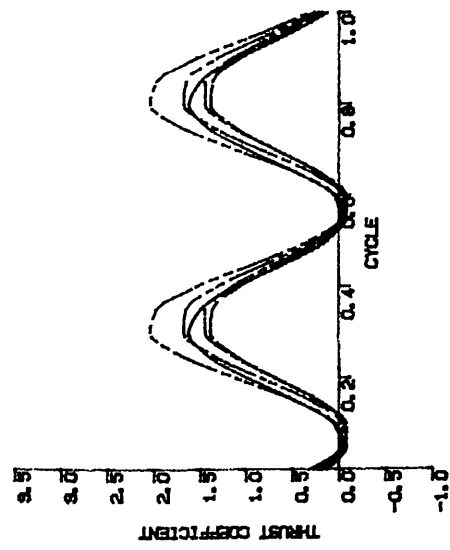
Rotating Centre = T. E.



Rotating Centre = 0.75c

—	K = 0.005
- - -	K = 0.100
- · -	K = 0.200

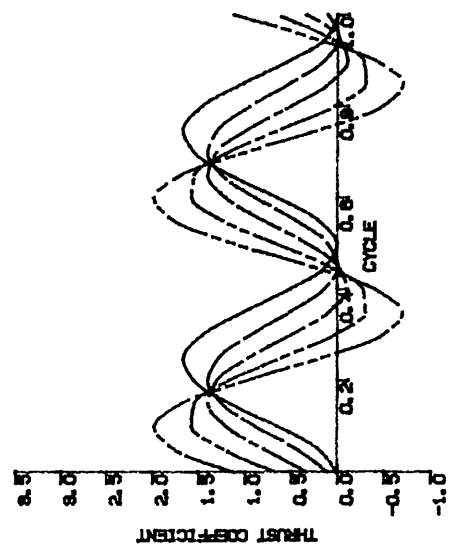
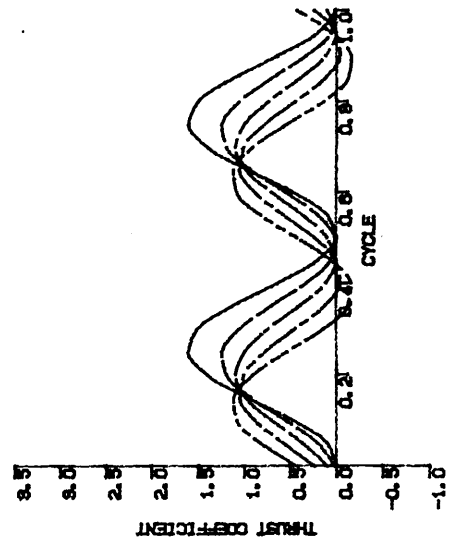
Fig. 3.21a The Propulsive Thrust Coefficient in a Cycle when $\theta = 0.6$



Rotating Centre = L. E.

Rotating Centre = 0.25c

Rotating Centre = 0.5c

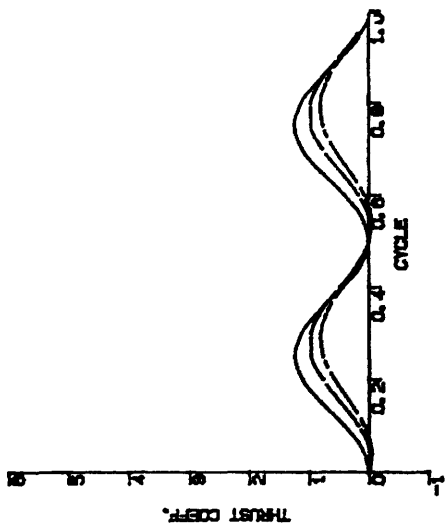


—	K = 0.2
- - -	K = 0.4
— · —	K = 0.6
- - -	K = 0.8
— · —	K = 1.0

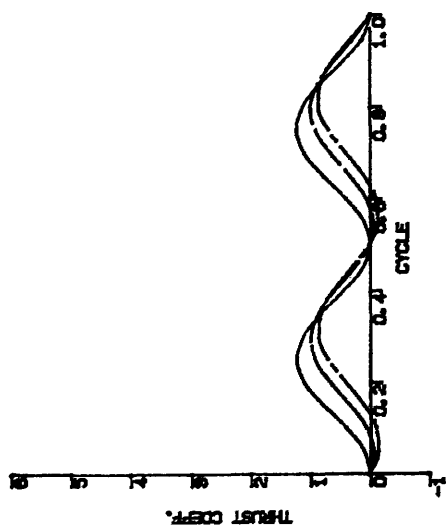
Rotating Centre = 0.75c

Rotating Centre = T. E.

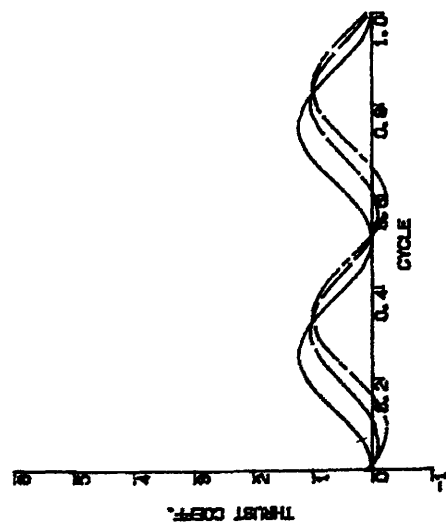
Fig. 3.21b The Propulsive Thrust Coefficient in a Cycle when $\theta = 0.6$



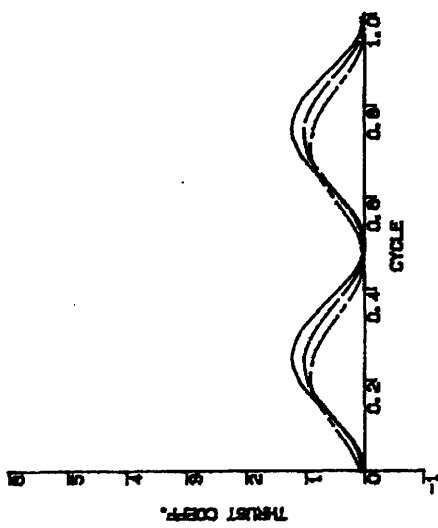
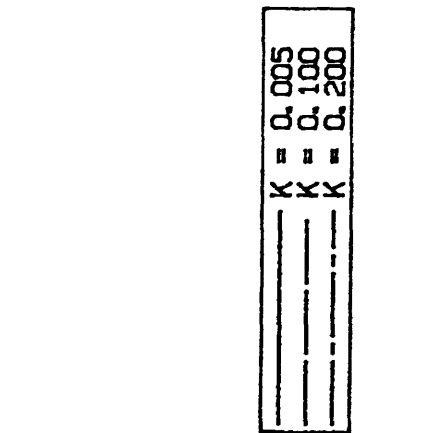
Rotating Centre = 0.5c



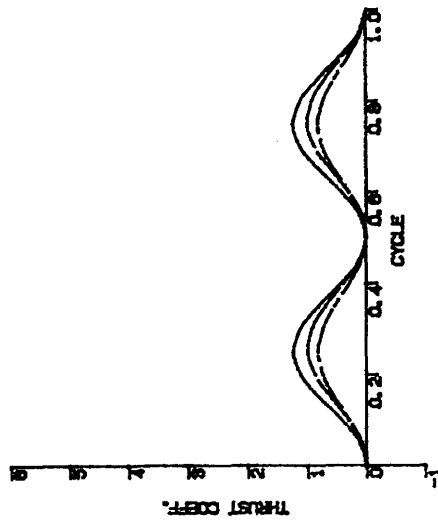
Rotating Centre = 0.25c



Rotating Centre = L. E.

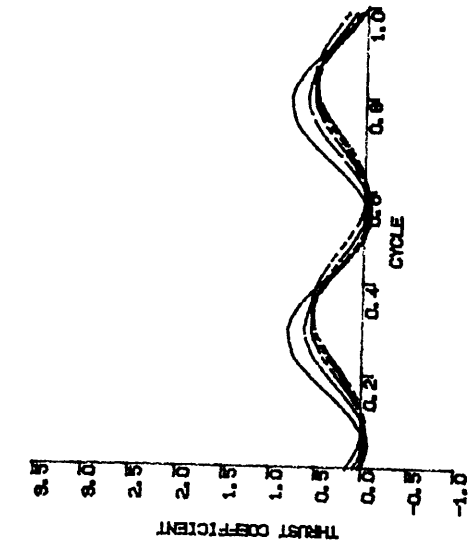


Rotating Centre = T. E.



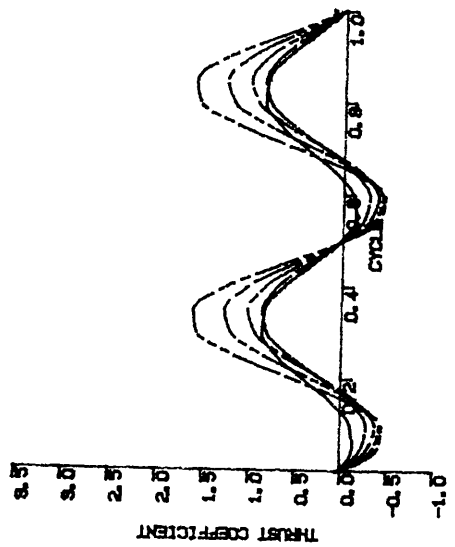
Rotating Centre = 0.75c

Fig. 3.22a The Propulsive Thrust Coefficient in a cycle when $\theta = 0.8$

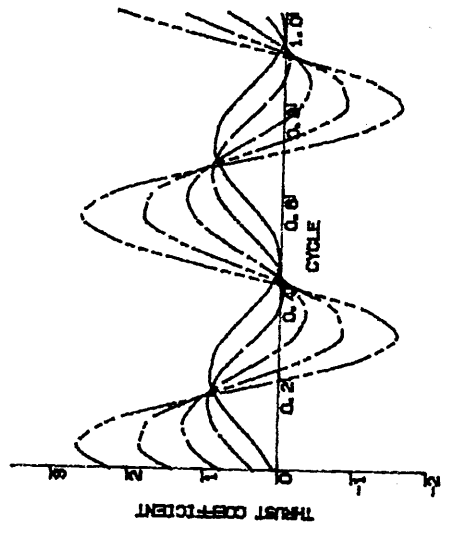


Rotating Centre = 0.5c

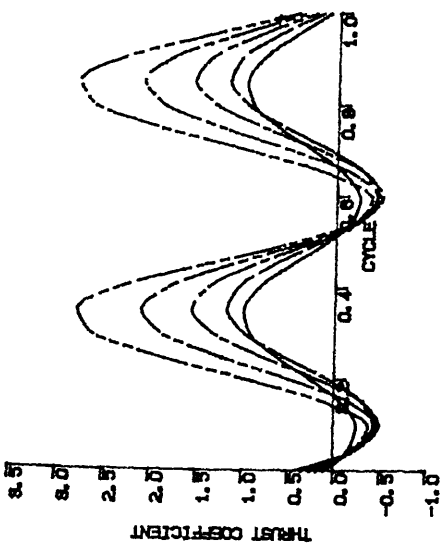
—	K = 0.2
—	K = 0.4
—	K = 0.6
—	K = 0.8
—	K = 1.0



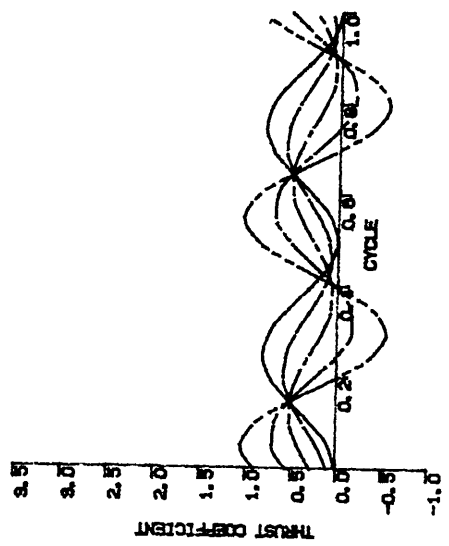
Rotating Centre = 0.25c



Rotating Centre = T. E.



Rotating Centre = L. E.



Rotating Centre = 0.75c

Fig. 3.22b The Propulsive Thrust Coefficient in a Cycle when $\theta = 0.8$

PART II

A FLEXIBLE FIN PROPELLER

A flexible fin propeller is investigated in this part. This propeller is made up of an aerofoil which is connected to a pivot through a flexible bar. The foil heaves and pitches as a result of applying an angular oscillation at the pivot. The theoretical model is described in the chapter 4. The performance of the propeller is studied by using the theoretical model and is discussed in chapter 5. A flexible fin propeller model and its test rig were designed and built and are described in chapter 6. In chapter 7, the experimental investigation of its performance is discussed. In chapter 8, the stress acting on the flexible bar is investigated and the criteria for the selection of material for this bar is presented. The study on wave propulsion using the flexible fin propeller is shown in chapter 9.

CHAPTER 4

THEORETICAL MODEL OF THE FLEXIBLE FIN PROPELLER

1.0 INTRODUCTION

In the evolution of these fish and mammals, high aspect ratio aerofoil shaped tails and carangiform swimming developed. Carangiform swimming is where the maximum lateral body movement is at the tail. This natural effective propulsive method has inspired the development of oscillating foil propulsion. A propulsion system was developed in this study by simulating fish tail motions. The system is called a flexible fin propeller.

A flexible fin propeller comprises an aerofoil shaped blade which is linked to a pivot through a flexible bar (fig. 4.1a). The foil performs a combined heaving and pitching motion as a result of the introduction of a sinusoidal oscillation at the pivot. The flexibility of the connecting bar provides a phase lag between the heaving and pitching. The amplitudes of heave and pitch also depend on the flexibility of this connecting bar. A force system with a net propulsive thrust is generated by the oscillating foil when it advances through a fluid.

A theoretical model has been set up by combining linearised unsteady-lifting-foil theory and large-deflection beam theory. Firstly, the force system acting on an oscillating foil is described. The unsteady-lifting-surface theory of a wing of infinite aspect ratio was first investigated in the 1940's when W. P. Jones [1943, 1945a, and 1945b] and R. T. Jones [1940] made a significant contribution to this field. Lawrence [1951 and 1952] developed an unsteady-lifting-surface theory for low aspect ratio wings. In the middle 70's, numerical solutions for analysing unsteady-lifting-surface theory [Chopra 1974a, Chopra 1974b, Chopra and Kambe 1977, Lan 1979] were employed to investigate the performance of a lunata tail. Chopra & Kambe applied

Davies' [1965] method in finding the loading distribution on a wing to calculate the propulsive thrust and hydromechanical efficiency of different foil shapes. Lan extended his steady Quasi-Vortice-Lattice method [Lan 1974] to establish an unsteady-lifting-surface theory applying Richardson's [1960] velocity potential for doublets in unsteady flow.

There have been a number of developments [eg. James 1975, Cheng 1975, Ahmadi and Widnall 1985, Ahmadi and Widnall 1986, Wilmott 1988] on unsteady-lifting-line theory using the method of matched asymptotic expansions. Wilmott [1988] presented an unsteady-lifting-line theory using matched asymptotic expansions. Ahmadi & Widnall [1985, 1986] developed a lifting line theory for a large aspect ratio wing oscillating at low frequency. Cheng & Murillo [1984] applied lifting line theory to study lunate tails with a curved centre line. Wilmott [1988] stated that the developed lifting line theories, with the exception of Ahmadi's work, have been either inadequate, incorrect or based on invalid assumptions. In addition, lifting-line theory requires a foil shape with a slow variation of chord length in the spanwise direction. Its application is not suitable to a blunt wing tip such as a rectangular foil or a tapered wing. In the case of unsteady-lifting-surface theories, long computer times can be a problem when solving the boundary-value problem for the velocity potential, which models the ideal attached flow across an aerofoil.

In the present study, unsteady-lifting-functions for different aspect ratios of a rectangular oscillating foil are used. These functions were calculated by W. P. Jones [1943, 1945a and 1945b] and R. T. Jones [1940] using lifting surface theories. Scherer [1968] applied the unsteady-lifting-function of an elliptical foil to his study. The propulsive thrust and efficiency are calculated using the unsteady-lifting-functions and they are then compared to the results of Chorpa & Kambe [1977] and Lan [1979]. Good agreement is found. The computer time is expected to be shorter than that using unsteady-lifting-surface theory. Since an iterative procedure is required to find the equilibrium condition, which will be described later in section 5, a short computing time for calculating the force system is essential.

The flexible bar between the foil and the pivot point is an essential part of the design. As the flexibility of this is expected to be high, a beam theory which takes large deflections into account, is required.

Large-deflection beam theory was first investigated in the middle of the twentieth century. The condition with a concentrated load acting at the free end of a cantilever was first investigated by Barten [1944 and 1945] and Bishopp and Drucker [1945]. Seames et al. [1957] and Mitchell [1959] gave solutions for straight and curved beams. Frish-Fay [1961, 1962] introduced a new approach to the solution for a large deflection beam. In the solution, a second order differential equation was derived for a force system with vertical and horizontal forces acting at the free end. Elliptic functions were used to obtain the solution of this differential equation. Seide [1984] considered a simply supported beam subject to an end moment.

Here, a flexible cantilever with a force system, which is made up of vertical and horizontal forces and moment acting at the free end, is considered. A second order differential equation with corresponding boundary conditions is set up. This second order differential equation is solved numerically using a finite difference technique: NAG routine (D02RAF) is used.

This method has been extended to consider a flexible cantilever with a linear variation in cross-section. In the present study, the cross-section of the flexible cantilever is assumed to be rectangular. A linear variation in thickness throughout the whole length with a constant width is investigated. Based on this idea, equations can be modified to handle different cross-sections of flexible bar when the variation is a continuous function of length, e.g. a cantilever with circular cross section and linear variation in diameter. An example condition with zero free end moment and constant cross-section is considered. The calculated tip deflections are compared with the results using Frish-Fay's method. Good agreement is found.

The hydrodynamic force system depends on the oscillation of the foil and hence the deflection of the flexible bar. The deflection also depends on the force acting on the bar. Owing to this inter-relationship, an iterative search method was used to get the equilibrium condition. The performance of the flexible fin propeller is calculated from this equilibrium condition. This method is presented in section 5.

2.0 OUTLINE OF THE THEORETICAL MODEL

The flexible fin propeller is represented by an oscillating flexible cantilever with a force system acting at its free end (fig. 4.1b). This force system comprises a vertical force, F_V , a horizontal force, F_H , and a free end bending moment, M_a . The performance of the flexible fin propeller is investigated in the time domain. The oscillating cycle is divided into 20 time intervals. The force system and deflection of the flexible cantilever is calculated at every time step. The computation starts with an estimated foil motion. This estimated motion is assumed to be a sinusoidal motion with certain amplitudes of heave and pitch separated by a phase difference. Based on this estimated motion, the force system at every time step is calculated using linearised unsteady oscillating foil theory. According to this dynamic force system, the deflection of the flexible cantilever is calculated. The tip deflection of the flexible beam, at every time interval, is combined to form a continuous motion throughout an oscillating cycle. The computed motion is compared to the estimated motion and a new estimated motion is found. Convergence of this iterative procedure is achieved when there is no practical difference between the computed motion and the estimated motion. A dynamic equilibrium condition is reached. The mean propulsive thrust, input power and propulsive efficiency are estimated from this condition.

3.0 LINEARISED UNSTEADY OSCILLATING FOIL THEORY

The force system acting on an oscillating foil, which is heaving and pitching in a uniform flow, is estimated using two-dimensional linearised theory with a three-

dimensional correction. The two-dimensional linearised unsteady-lifting-foil theory is presented in chapter two. The lift and moment at the centre of rotation at a distance, a , from the mid-chord point for a two-dimensional foil are formulated in eqns. 2.68 and 2.69 respectively. The corresponding leading edge suction force is also computed by eqn. 2.75.

Jones [1943, 1945a and 1945b] presented an unsteady-lifting-surface theory for a rectangular foil to calculate the hydrodynamic forces acting on an oscillating foil. This theory is based on an exact mathematical solution and an unsteady-lifting-function (C_A) was calculated to include the three-dimensional effect, which is

$$C_A = F_A + iG_A \quad - 4.1$$

This unsteady-lifting-function is similar to the Theodorsen Function ($C(k)$) in two-dimensional theory.

Jones [1940] calculated unsteady-lifting-functions for elliptical foils with aspect ratios 3 and 6. These functions are also presented by Jones [1940] as empirical formulae as follows,

$$F_A + iG_A = 0.600 - 0.170 \frac{ik}{ik + 0.540} \text{ for aspect ratio} = 3;$$

and
$$F_A + iG_A = 0.740 - 0.267 \frac{ik}{ik + 0.381} \text{ for aspect ratio} = 6.$$

- 4.2

Based on these results, unsteady-lifting-functions for elliptical aerofoils with different aspect ratios were curve fitted and presented as empirical formulae by Scherer [1968]

$$F_A = 1 - \frac{c_1 k^2}{k^2 + c_2^2}; \text{ and, } G_A = - \frac{c_1 c_2 k}{k^2 + c_2^2} \quad - 4.3$$

where $c_1 = 0.5 \left(\frac{AR}{AR + 2.32} \right)$,

and $c_2 = 0.181 + \frac{0.772}{AR}$.

- 4.4

Drischler [1956] presented unsteady-lifting-functions for rectangular foils with aspect ratios of 4 and 6. The unsteady-lifting-functions presented in [Scherer 1968, Jones 1940, Drischler 1956] were normalised from their steady state values by a factor, Ψ , where

$$\Psi = \frac{AR}{AR + 2}$$

- 4.5

Here, the actual values of unsteady-lifting-functions without the values of Ψ are plotted in figs. 4.2 a and b together with the Theodorsen function for two-dimensional flow. These functions are plotted against a parameter, $1/AR$, for different reduced frequencies, k . These values are curve fitted so that the unsteady-lifting-functions for intermediate aspect ratios can be estimated. These functions are reorganized and plotted against the reduced frequency. In fig. 4.3a & b, unsteady-lifting-functions for rectangular foils with aspect ratios 4 to 10 and the Theodorsen functions are shown. These functions were curve fitted into fourth order and seventh order polynomial equations for the real part (F_A) and imaginary part (G_A) respectively, where

$$F_A = a_0 + a_1 k + a_2 k^2 + a_3 k^3 + a_4 k^4, \text{ and}$$

$$G_A = b_0 + b_1 k + b_2 k^2 + b_3 k^3 + b_4 k^4 + b_5 k^5 + b_6 k^6 + b_7 k^7$$

-4.6

The constants (a_0, a_1, \dots, a_4 and b_0, b_1, \dots, b_7) for different aspect ratio are presented in table 4.1 and 4.2 at the end of this chapter for F_A and G_A respectively.

Based on these functions, the hydrodynamic forces and moment acting on a rectangular oscillating foil with finite span are formulated. The lift force is given by

$$L = -\pi \rho b^2 s (U\dot{\alpha} + \ddot{y} - ba\ddot{\alpha}) - 2\pi \rho UbsC_A \left[U\alpha + \dot{y} + b\left(\frac{1}{2} - a\right)\dot{\alpha} \right], \quad - 4.7$$

the pitching moment at the rotating centre by

$$M_a = -\rho b^3 s \left[\pi \left(\frac{1}{2} - a\right) U\dot{\alpha} + \pi b \left(\frac{1}{8} + a^2\right) \ddot{\alpha} - a\pi \ddot{y} \right] + 2\rho U b^2 s \pi \left(a + \frac{1}{2} \right) C_A \left[U\alpha + \dot{y} + b\left(\frac{1}{2} - a\right)\dot{\alpha} \right], \quad - 4.8$$

and the leading edge suction force by

$$F_s = \rho \pi C_o^2$$

$$C_o = \sqrt{cs} \left\{ \left[U\alpha + \dot{y} + \dot{\alpha}b\left(\frac{1}{2} - a\right) \right] C_A - \frac{b}{2}\dot{\alpha} \right\} \quad - 4.9$$

A sinusoidal motion is assumed. The relationship stated in eqn. 3.1 is used. As with eqns. 3.2 to 3.8, eqns.4.7-4.9 are rearranged into complex equations with a time factor $e^{i\omega t}$. The magnitude of forces and moment at any instant of time (t) are the real parts of these equations, taking the the time factor into account.

The force system generated by an oscillating foil at any instant of time (t) comprises a vertical force (F_V), a horizontal force (F_H) and a moment (M_a) about its rotating centre at a distance of (a) from the mid-chord, where

$$F_V = L + F_s \sin \alpha, \quad - 4.10$$

$$\text{and } F_H = F_s \cos \alpha + L \tan \alpha \quad - 4.11$$

The propulsive thrust coefficient (C_T) and efficiency (η), as shown in eqn. 3.13 and 3.10 respectively, of an oscillating rectangular foil with an aspect ratio of 8 and a rotating centre at the three-quarter-chord point were calculated for :

- i) a range of reduced frequencies (k);
- ii) feathering parameters (θ) of 0.0 and 0.8;
- iii) phase lag (β) between heaving and pitching of 90° .

The results were compared to the published results of Chopra and Kambe's lifting surface method [1977] and Lan's quasi-vortex-lattice method [1979] and the comparison is shown in fig. 4.4.

The hydromechanical efficiency of an oscillating rectangular foil with aspect ratio 7 and rotating centre at the trailing edge were calculated for a feathering parameter of 0.8, a range of phase lags from 0° to 180° and reduced frequencies of 0.15 and 0.75. The results are compared with the published results from [Lan 1979] and are shown in fig. 4.5. In fig. 4.4 and 4.5, Chopra's and Lan's theory shows a good agreement with the present method.

4.0 LARGE-DEFLECTION BEAM THEORY

The fundamental beam theory (Euler's "law of elastica") stated that the bending moment at a point on a beam is proportional to the change in curvature induced by the external loadings, as

$$\frac{EI}{R} = M \quad - 4.12$$

where

$$\frac{1}{R} = \frac{d\phi}{d\sigma} = \frac{\frac{d^2y}{dx^2}}{\left[1 + \left(\frac{dy}{dx}\right)^2\right]^{3/2}} \quad - 4.13$$

as shown in fig. 4.6.

In normal engineering materials (e.g. steel), the bending modulus (E) is usually high and the slope induced by external loadings is small. Therefore the squared term of

(dy/dx) is assumed to be negligible. In addition, the deflection in the x-direction (i.e. Δx in fig. 4.6) is also neglected. Therefore, the change of curvature is

$$\frac{d\phi}{d\sigma} \approx \frac{d^2y}{dx^2} \quad - 4.14$$

When the flexibility of the beam increases, these assumptions are unsatisfactory. The square term of the deflected slope is no longer small and negligible. The change in length of moment arm (i.e. $L - \Delta x$) is essential in estimating the bending moment at the fixed end.

4.1 A Constant Cross-Section Flexible Cantilever with an External Force System Acting at its Free End

In the present section, a forcing system, which comprises a vertical force, a horizontal force and a free end moment, acting at the free end of a low stiffness cantilever is considered; the beam has constant cross-section (i.e. I constant). According to eqn.4.12,

$$EI \frac{d\phi}{d\sigma} = F_V (L_o - x - \Delta x) + F_H (\Delta y - y) + M_o \quad - 4.15$$

Equation 4.15 is further differentiated with respect to σ , giving

$$\frac{d^2\phi}{d\sigma^2} = - \frac{F_V}{EI} \frac{dx}{d\sigma} - \frac{F_H}{EI} \frac{dy}{d\sigma} \quad - 4.16$$

For the element $d\sigma$, as shown in fig. 4.6,

$$\frac{dx}{d\sigma} = \cos \phi \quad - 4.17$$

$$\frac{dy}{d\sigma} = \sin \phi \quad - 4.18$$

Equation 4.16 becomes,

$$\frac{d^2\phi}{d\sigma^2} = -\frac{F_V}{EI} \cos \phi - \frac{F_H}{EI} \sin \phi \quad - 4.19$$

The boundary conditions of this differential equation (eqn. 4.19) are,

- 1) the slope induced by the loading is zero at the fixed end (i.e. when $\sigma=0$, $\phi=0$);
- 2) at the free end, when σ equals to the full length L_0 ,

$$EI \frac{d\phi}{d\sigma} = M_0. \quad - 4.20$$

The problem is solved using finite difference techniques. The solution gives the values of ϕ and $d\phi/d\sigma$ for the corresponding σ position.

The deflected shape of the cantilever can be generated using the relationship stated in the eqns. 4.17 and 4.18. The x and y values at corresponding σ position are computed by,

$$x = \int_0^{\sigma} \cos \phi \, d\sigma \quad - 4.21$$

$$y = \int_0^{\sigma} \sin \phi \, d\sigma$$

The results are checked using the fundamental equation (i.e. eqn. 4.12) with the calculated tip deflections. At the fixed end, eqn. 4.12 is rearranged as follows,

$$EI \frac{d\phi}{d\sigma} = F_V (L_o - \Delta x) + F_H \Delta y + M_o \quad - 4.22$$

By putting the computed tip deflection values of $d\phi/d\sigma$, Δx and Δy into this equation, the LHS and RHS of equation should be equal.

4.2 A Flexible Cantilever with a Linear Variation in Cross-Section and an External Force System Acting at its Free End

When the cross-section varies along the length, the second moment of inertia is a function of σ . The following equations are set up for a flexible cantilever with a constant width and a linear taper in thickness. However, a similar idea can be applied to other forms of beam, e.g. round sections with a linear variation in diameter. The section modulus at any point of the flexible bar is

$$I_\sigma = \frac{wt_\sigma^3}{12} \quad - 4.23$$

$$\text{where } t_\sigma = t_2 - \frac{\sigma}{L_o} (t_2 - t_1) \quad - 4.24$$

Since the sectional modulus is a function of σ , further differentiation of eqn.4.15 is different from eqn 4.16. The R.H.S. of eqn. 4.19 still holds, but the L.H.S. of the equation is changed to,

$$\text{LHS} = \frac{Ew}{12} \left\{ t_\sigma^2 \cdot \frac{d^2\phi}{d\sigma^2} - \frac{3(t_2 - t_1)}{L_o} \cdot t_\sigma \cdot \frac{d\phi}{d\sigma} \right\} \quad - 4.25$$

Therefore, eqn. 4.19 is changed to,

$$\frac{d^2\phi}{d\sigma^2} = \left\{ \frac{12}{Ew} (-F_V \cos \phi - F_H \sin \phi) + \frac{3(t_2 - t_1)}{L_o} t_\sigma \cdot \frac{d\phi}{d\sigma} \right\} \frac{1}{t_\sigma^3} \quad - 4.26$$

When t_1 equals t_2 , these equations are the same as the ones in previous section. As with the previous section, the deflected shape of the flexible bar is calculated by using the same boundary conditions and a similar approach.

4.3 Computation Method

A computer subroutine (BEAM) has been written using the above equations; NAG routine (D02RAF) [1988] was used to solve the second order differential equation (i.e. eqn. 4.26) using a finite difference technique with Newton iteration. The subroutine was programmed for a beam with linear variation in cross-section as described in section 4.4.2

In order to use the NAG routine, eqn 4.26 is rearranged into a more general format as,

$$\phi'' = A \cos \phi + B \sin \phi + C \phi' \quad - 4.27$$

where

$$A = -\frac{F_V}{Ew} \cdot \frac{12}{t_\sigma^3}$$

$$B = -\frac{F_H}{Ew} \cdot \frac{12}{t_\sigma^3} \quad - 4.28$$

$$C = \frac{3}{L} \cdot \frac{(t_2 - t_1)}{t_\sigma}$$

Let

$$\phi'_1 = f_1(\sigma, \phi_1, \phi_2) = \phi_2$$

$$\phi'_2 = f_2(\sigma, \phi_1, \phi_2) = A \cos \phi_1 + B \sin \phi_1 + C \phi_2 \quad - 4.29$$

where

$$\phi_1 = \phi, \quad \phi_2 = \phi' \quad \text{and} \quad \phi'_2 = \phi'' \quad - 4.30$$

The boundary conditions mentioned in the previous sections are rearranged into the NAg required format, where

$$g_i(\phi(\text{fix}), \phi(\text{free})) = 0 \quad i = 1, 2 \quad - 4.31$$

The 1st boundary condition was applied to the fixed end, where the slope at the fixed end is zero (i.e. $\phi_1(\text{fix}) = 0$).

$$g_1(\phi(\text{fix}), \phi(\text{free})) = \phi_1(\text{fix}) = 0 \quad - 4.32$$

The 2nd boundary condition (i.e. eqn.4.20) was applied to the free end, where

$$\phi_2(\text{free}) = \frac{M_o}{EI} \quad - 4.33$$

and
$$g_2(\phi(\text{fix}), \phi(\text{free})) = \phi_2(\text{free}) - \frac{M_o}{EI} = 0 \quad - 4.34$$

Jacobian matrices were used for the Newton iteration. These Jacobian matrices are

$$\left[\frac{df_i}{d\phi_j} \right], \left[\frac{dg_i}{d\phi_j(\text{fix})} \right] \text{ and } \left[\frac{dg_i}{d\phi_j(\text{free})} \right] \quad i=1, 2 \text{ and } j = 1, 2$$

where

$$\left[\frac{df_i}{d\phi_j} \right] = \begin{bmatrix} \frac{df_1}{d\phi_1} & \frac{df_2}{d\phi_1} \\ \frac{df_1}{d\phi_2} & \frac{df_2}{d\phi_2} \end{bmatrix} = \begin{bmatrix} 0, & -A \sin \phi_1 + B \cos \phi_1 \\ 1, & 0 \end{bmatrix} \quad - 4.35$$

$$\left[\frac{dg_i}{d\phi_j(\text{fix})} \right] = \begin{bmatrix} \frac{dg_1}{d\phi_1(\text{fix})}, & \frac{dg_2}{d\phi_1(\text{fix})} \\ \frac{dg_1}{d\phi_2(\text{fix})}, & \frac{dg_2}{d\phi_2(\text{fix})} \end{bmatrix} = \begin{bmatrix} 1, & 0 \\ 0, & 0 \end{bmatrix} \quad - 4.36$$

and

$$\left[\frac{dg_i}{d\phi_j(\text{free})} \right] = \begin{bmatrix} \frac{dg_1}{d\phi_1(\text{free})}, & \frac{dg_2}{d\phi_1(\text{free})} \\ \frac{dg_1}{d\phi_2(\text{free})}, & \frac{dg_2}{d\phi_2(\text{free})} \end{bmatrix} = \begin{bmatrix} 0, & 0 \\ 0, & 1 \end{bmatrix} \quad - 4.37$$

When the deflection of the flexible bar is large and the tip slope (ϕ_2) is greater than 90° , the Newton iteration fails to converge. In this NAG routine (D02RAF), a continuation facility can be used to help the convergence. The program was written to use this facility. A continuation parameter (ϵ) was introduced into the eqn. 4.29 as

$$\phi_2 = f_2(\sigma, \phi_1, \phi_2) = A \cos \phi_1 + \epsilon(B \sin \phi_1 + C \phi_2) \quad - 4.38$$

When ϵ is zero, the vertical force is the only force in the forcing system. The iteration is started with $\epsilon = 0$ and ends with an exact solution when $\epsilon = 1$. This converges faster when there is only a vertical force. The continuation parameter (ϵ) was tried with the equation with vertical force as well. However, it did not help the convergence. Equation 4.35 becomes,

$$\left[\frac{df_i}{d\phi_j} \right] = \begin{bmatrix} \frac{df_1}{d\phi_1}, & \frac{df_2}{d\phi_1} \\ \frac{df_1}{d\phi_2}, & \frac{df_2}{d\phi_2} \end{bmatrix} = \begin{bmatrix} 0, & -A \sin \phi_1 + \epsilon B \cos \phi_1 \\ 1, & 0 \end{bmatrix} \quad - 4.39$$

The following Jacobian matrices are required for the continuation facility of the NAg routine D02RAF,

$$\left[\frac{df_i}{d\epsilon} \right] = \left[\frac{df_1}{d\epsilon}, \frac{df_2}{d\epsilon} \right] = [0, B \sin \phi_1 + C \phi_2] \quad - 4.40$$

and

$$\left[\frac{dg_i}{d\epsilon} \right] = \left[\frac{dg_1}{d\epsilon}, \frac{dg_2}{d\epsilon} \right] = [0, 0] \quad - 4.41$$

The outputs of this routine are the slope (ϕ) and the value of the first derivative of ϕ with respect to σ for the corresponding σ location. The whole length of the flexible bar is divided into number of segments (minimum number 50). Another NAg routine (D01GAF) is used to integrate eqn. 4.21 to find the coordinates of the tip deflections. Trapezoidal integration was also used to provide the coordinate of the deflected shape of the beam. Since the number of segments is high, good agreement is found in the tip deflections between these two methods.

In order to validate this computation, results of an example condition calculated using the present program is compared to the one from Frish-Fay's method [1961, 1962]. The flexible cantilever with a vertical force (30.5N) and a horizontal force (8.5N) acting at the free end is considered. The bending modulus is $40 \times 10^9 \text{ Nm}^{-2}$ and a constant sectional modulus is $2.485 \times 10^{-9} \text{ m}^4$. The length of the cantilever is one metre. The same tip deflections, Δx and Δy , are found from both methods as 0.006m and 0.104m.

4.4 Comparison with Small Deflection Beam Theory

In this section, a cantilever with a concentrated vertical loading acting at its free end is analysed. Tip deflections calculated using the present method are compared to the

ones estimated by the conventional approach which assumes small deflections.

The results are presented in terms of non-dimensional parameters. The non-dimensional parameter of the tip deflection in the y -direction is

$$\delta_y = \frac{\Delta y}{L_o} \quad - 4.42$$

Similarly, the non-dimensional parameter of the tip deflection in the x-direction is

$$\delta_x = \frac{\Delta x}{L_o} \quad - 4.43$$

The non-dimensional parameter of the tip rotation (i.e. the slope at the free end) is

$$\delta_\phi = \frac{\phi_t}{\pi} \quad - 4.44$$

A non-dimensional parameter, which represents the flexibility of the bar, is introduced as

$$\mu = \frac{F_v L_o^2}{EI} \quad - 4.45$$

A comparison of vertical tip deflections, between the small deflection theory and the present theory, is shown in fig. 4.7a. Similarly, the horizontal tip deflections and the tip rotations are presented in figs. 4.7b and 4.7c respectively.

When the μ value is below 0.5, there is no significant difference between these two theories. However, when the μ value increases, the difference becomes significant.

Take for example, a cantilever with a constant thickness of 2 mm, 50 mm width and length 500 mm. If made from steel with a bending modulus of 200 GNm⁻², it gives a μ value of 0.37; on the other hand, if made from unidirectional fibre glass with a bending modulus of 36 GNm⁻², its μ value is 2.04. A significant discrepancy between the two theories is obtained in the case of the fibre glass cantilever. The small deflection assumptions fail and large-deflection theory should be used.

5.0 DYNAMIC EQUILIBRIUM

The whole system, which comprises the foil and the flexible cantilever, is designed to oscillate sinusoidally about pivot A, as shown in fig. 4.1b, where

$$\begin{aligned}\theta_A &= \theta_{Ao} \cos \omega t \\ \dot{\theta}_A &= -\omega \theta_{Ao} \sin \omega t \\ \ddot{\theta}_A &= -\omega^2 \theta_{Ao} \cos \omega t\end{aligned}\quad - 4.46$$

The magnitudes of the hydrodynamic forces and moment acting on the foil, and the flexible bar, depend on the amplitudes of heave and pitch and the phase lag between them. These amplitudes and phase lags depend on the deflected shape of the flexible cantilever during an oscillating cycle. Conversely, the deflected shape depends on the forces acting on the system. Owing to this relationship, an iterative procedure is used to find the equilibrium condition where the force system generated by an oscillating foil with a specified motion deflects the oscillating flexible bar to provide the same motion. In the present study, this condition is termed a dynamic equilibrium. The performance of the flexible fin propeller is estimated from this dynamic equilibrium condition.

A computer program (MAIN) was written to calculate the propulsive thrust and efficiency of a flexible fin propeller with a rectangular foil. The force system is calculated in subroutine UNSTOS. The deflected shape of the flexible cantilever is computed by subroutine BEAM.

The program flow chart is shown in fig. 4.8. The computation starts with an estimated motion. This estimated motion is a sinusoidal motion with rotating axis at the leading edge and specified amplitudes of heave (y_e), pitch (α_e) and phase lag (β_e) between them. The whole oscillating cycle is divided into 20 time intervals. The force system at every time step is calculated by using the method presented in section 3 of this chapter. Two axis systems have been used, as shown in fig. 4.1b. These axis systems are

- 1) a global axis system where the X-Y axes are parallel to horizontal and vertical axes and which advance with a forward speed U in the direction of the negative X-axis,
- 2) an instantaneous body axis system where the X_T axis is at an angle of θ_A to the horizontal at a specified time (t) and the Y_T axis is perpendicular to the X_T axis.

The force system is converted into the instantaneous body axes at the corresponding time step by,

$$\begin{bmatrix} F_v \\ F_H \end{bmatrix} \begin{bmatrix} \cos \theta_A & \sin \theta_A \\ -\sin \theta_A & \cos \theta_A \end{bmatrix} = \begin{bmatrix} F_{vT} \\ F_{HT} \end{bmatrix} \quad - 4.47$$

The deflected shapes of the flexible cantilever are calculated in the instantaneous body axis system using the theory presented in section 4. The deflected shape of the cantilever is then converted back into the global axis system in a similar manner to eqn. 4.43. The transformation matrix is

$$\begin{bmatrix} y_T \\ x_T \end{bmatrix} \begin{bmatrix} -\sin \theta_A & \cos \theta_A \\ \cos \theta_A & \sin \theta_A \end{bmatrix} = \begin{bmatrix} y \\ x \end{bmatrix} \quad - 4.48$$

The deflected slope at the free end, ϕ_T , is also converted into the global axis system using

$$\alpha = \phi_T + \theta_A \quad - 4.49$$

This value (α) is the pitch angle of the oscillating foil at that particular time step.

A continuous motion is formed by combining the tip deflections at every time step. The y and α values at the free end also form a series of heaving and pitching motions of the foil. An example is shown in fig. 4.9. The maximum values of y and α may not be exactly located at any particular time step. To find the maximum y value, three points in the region of maximum values are fitted into a quadratic equation, where

$$y = at^2 + bt + c \quad - 4.50$$

and a , b and c are constant.

The actual maximum point will be located when,

$$\frac{dy}{dt} = 2at + b = 0 \quad - 4.51$$

The maximum α value, α_c , and its location are found in a similar manner. The phase lag, β_c , is calculated by comparing the locations of the peak values of y_c and ϕ_c .

The calculated values (y_c , ϕ_c and β_c) are compared with the estimated values (y_e , ϕ_e and β_e) and a new estimated motion is obtained, if the difference between corresponding values is greater than 0.001. The new specified amplitudes of the motion and phase lag are estimated as follows,

$$\begin{array}{ll} \text{new estimated} & y_e = y_c + C(y_e - y_c) \\ \text{new estimated} & \alpha_e = \alpha_c + C(\alpha_e - \alpha_c) \\ \text{new estimated} & \beta_e = \beta_c + C(\beta_e - \beta_c) \end{array} \quad - 4.52$$

The factor C is a constant for the step size of each iteration and depends on the flexibility of the cantilever (usually < 0.5). Convergence of this iterative procedure is assumed when the differences between the estimated and computed amplitudes and phase lags are less than 0.001.

During the iterative process, the calculated motion may not be a sinusoidal motion. However, the best fit sinusoidal motion is assumed. When the equilibrium condition is found, the motion of the foil is usually a sinusoidal motion. This is true when the oscillating amplitudes are small. When the oscillating amplitude increases, the deflection of the flexible beam becomes larger and larger. The converged motion of the foil differs to some extent from sinusoidal at high angular oscillating function and high oscillating frequency. When the bar comes to an extreme of deflection, where the oscillation is no longer a smooth motion, the iteration fails to converge.

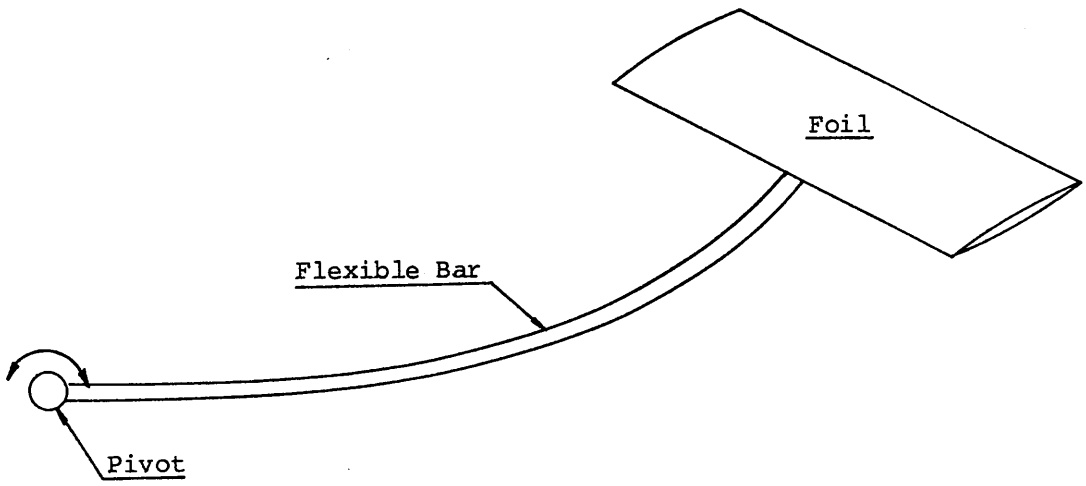
An example of the deflected shape of the cantilever in an oscillating cycle is presented in a 3-D figure, shown in fig. 4.10. The axis T shows the time t . The $X-T$ plane is shaded to highlight the neutral plane. Each curve shows the shape of the cantilever at that particular instant of time.

6.0 CONCLUDING REMARKS

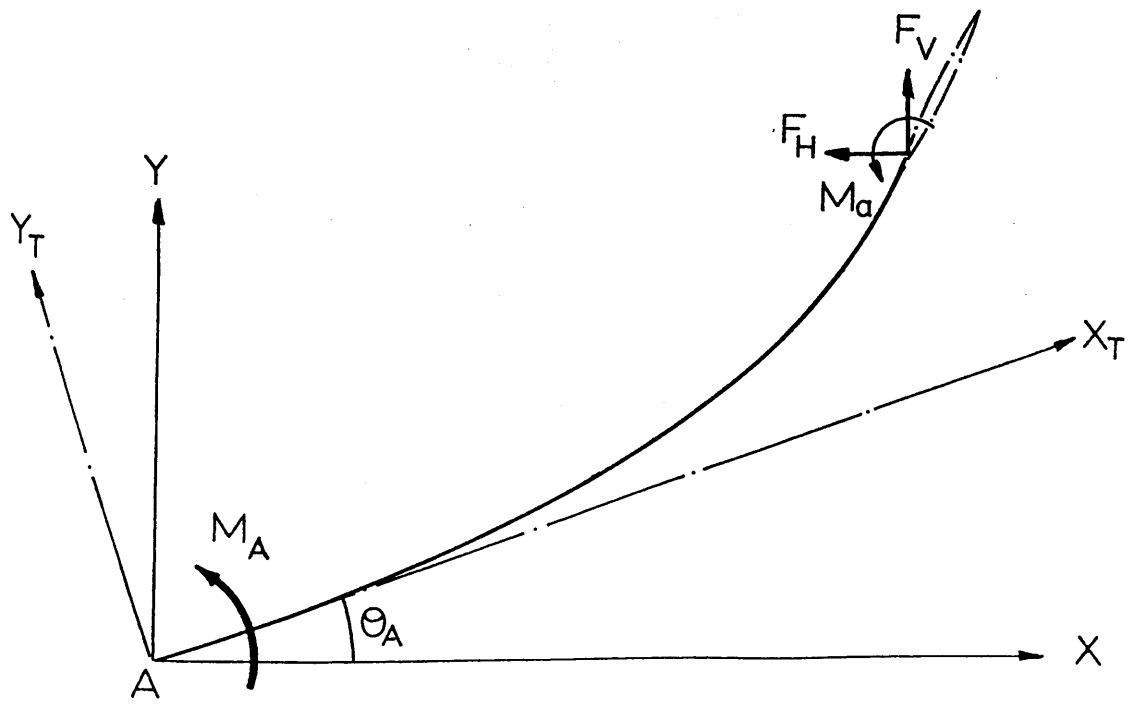
A theoretical model of a flexible fin propeller has been developed based on linearised unsteady-lifting-foil theory and large-deflection beam theory. Results from the present method using unsteady-lifting-functions to calculate the force system are compared to the published results of Chopra's and Lan's unsteady-lifting-surface theory. A large-deflection beam theory is developed to calculate the deflection of a flexible cantilever with a force system, which is made up of vertical and horizontal forces and a moment acting at the free end. The theory is extended to cover a linear variation in cross section of the flexible bar. In order to compare the results with Frish-Fay's method, an example with constant cross-section and a force system which only

comprises a vertical and horizontal forces, is used. The calculated tip deflections from the two methods are the same. From these comparisons with published results, the present method is found to be accurate and reliable for use in further calculations.



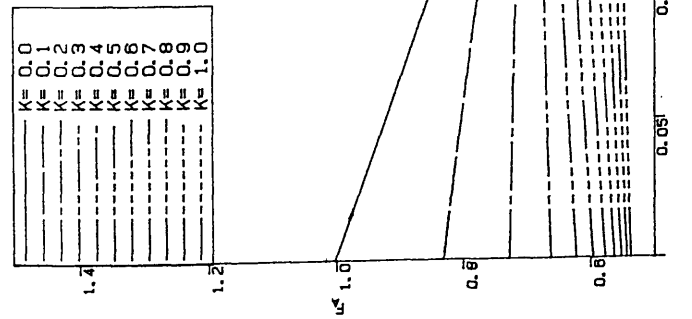


(a)

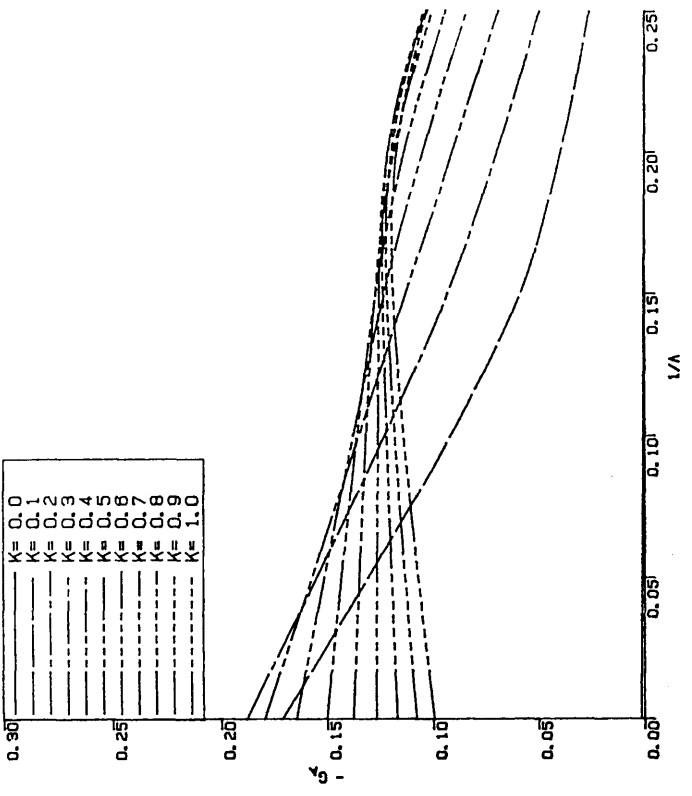


(b)

Fig.4.1 The Flexible Fin Propeller

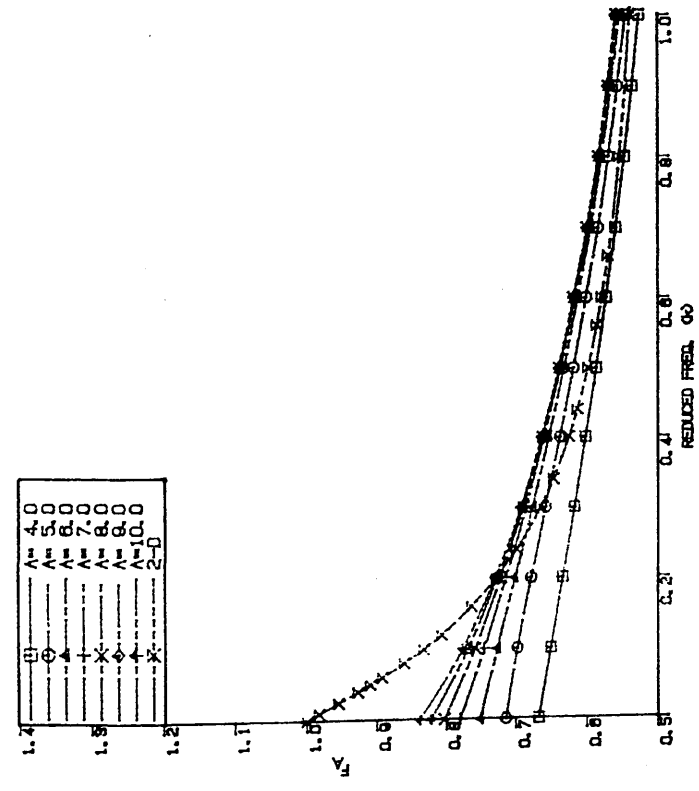


(a) The Real Part (F_A)

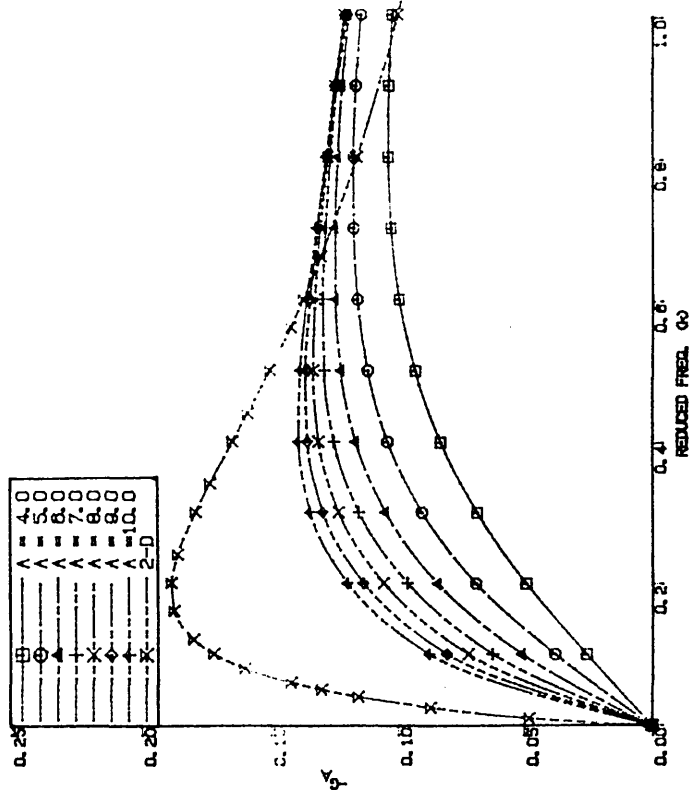


(b) The Imaginary Part (G_A)

Fig. 4.2 The Unsteady Lifting Functions



(a) THE REAL PART (F_A)



(b) THE IMAGINARY PART (G_A)

THE UNSTEADY LIFTING FUNCTIONS

Fig. 4.3

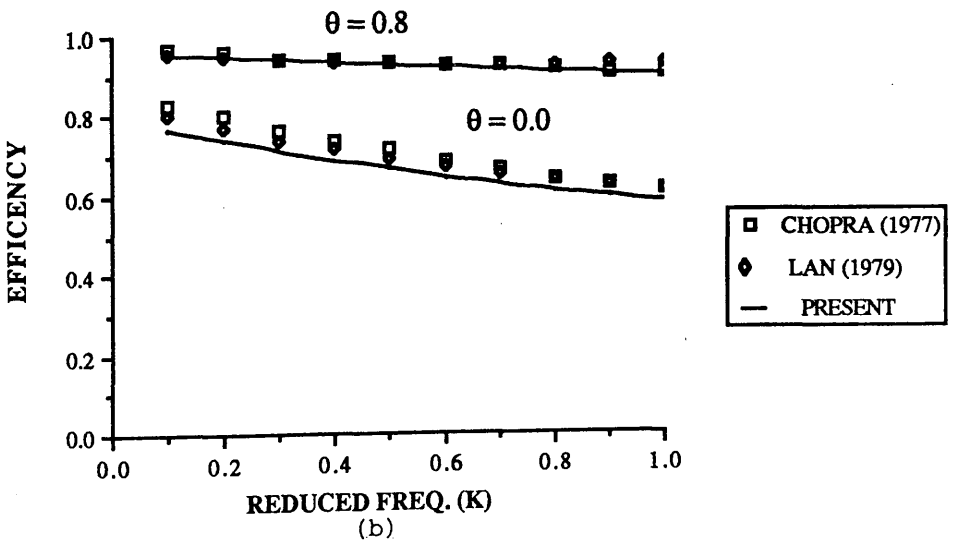
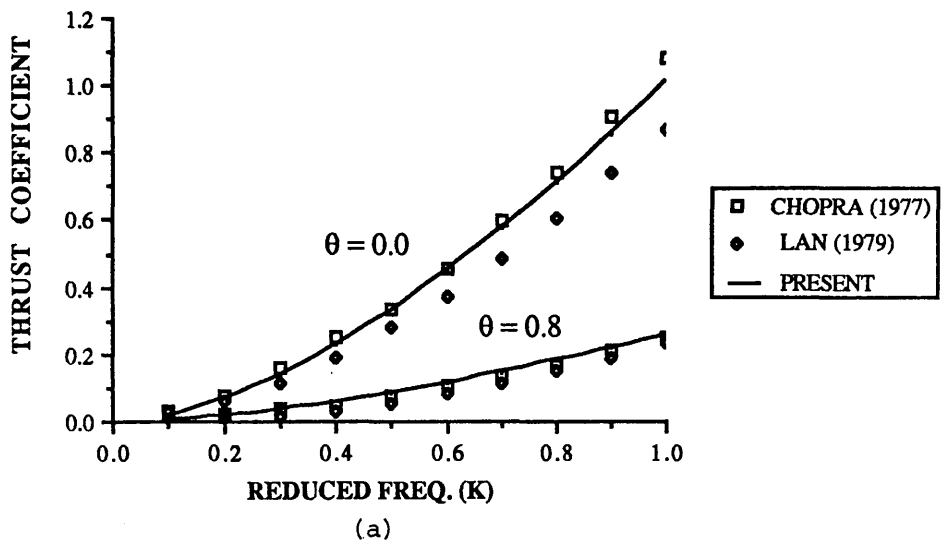


Fig. 4.4 The Propulsive Thrust Coefficient and Efficiency of an Oscillating Foil With Aspect Ratio = 8.0 and $a = 0.5$

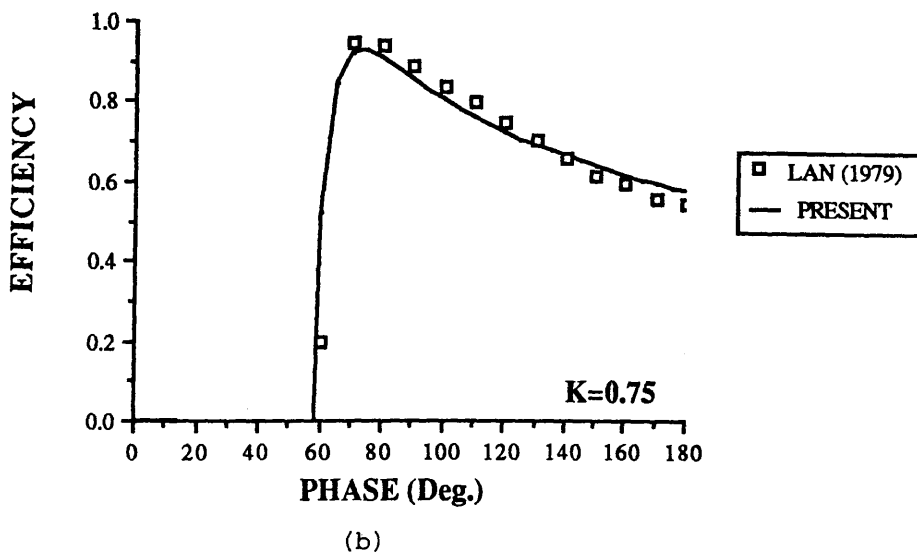
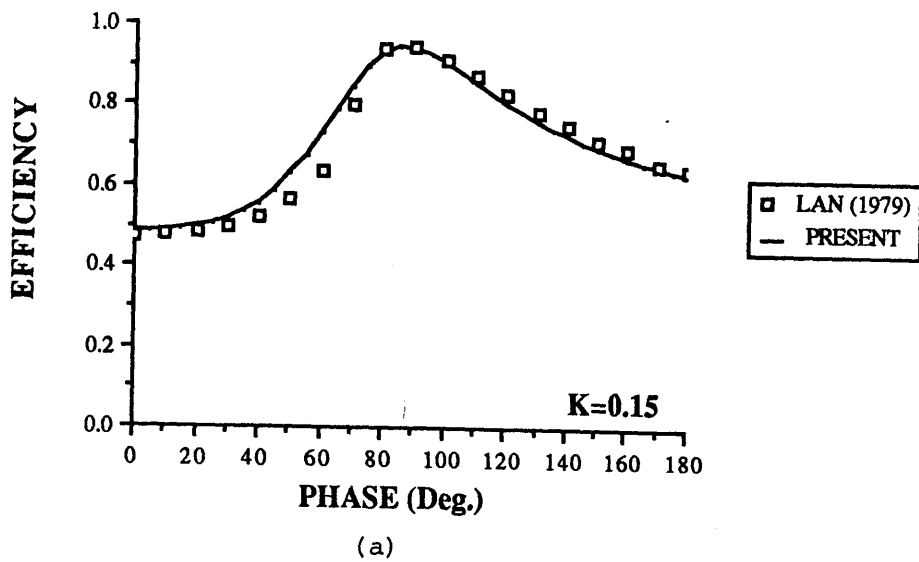
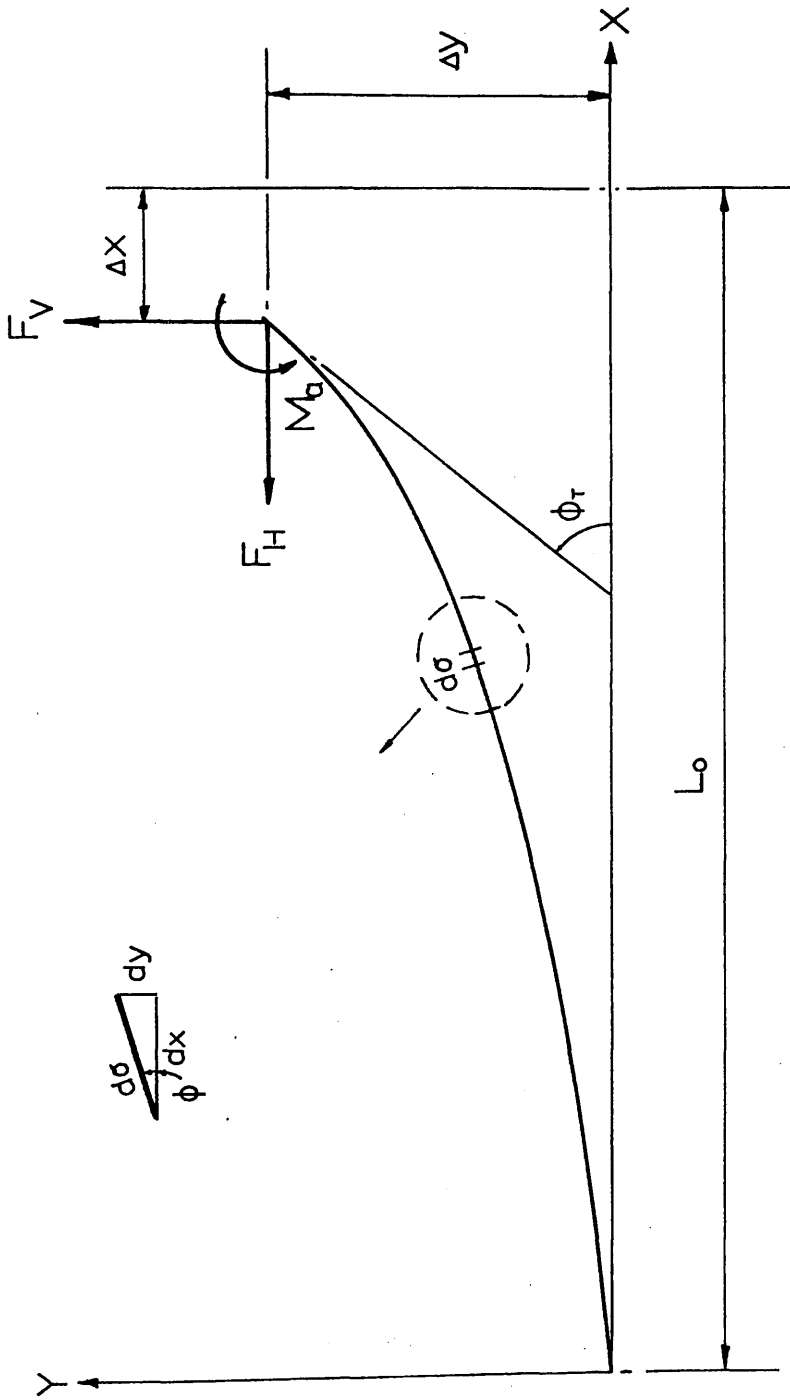
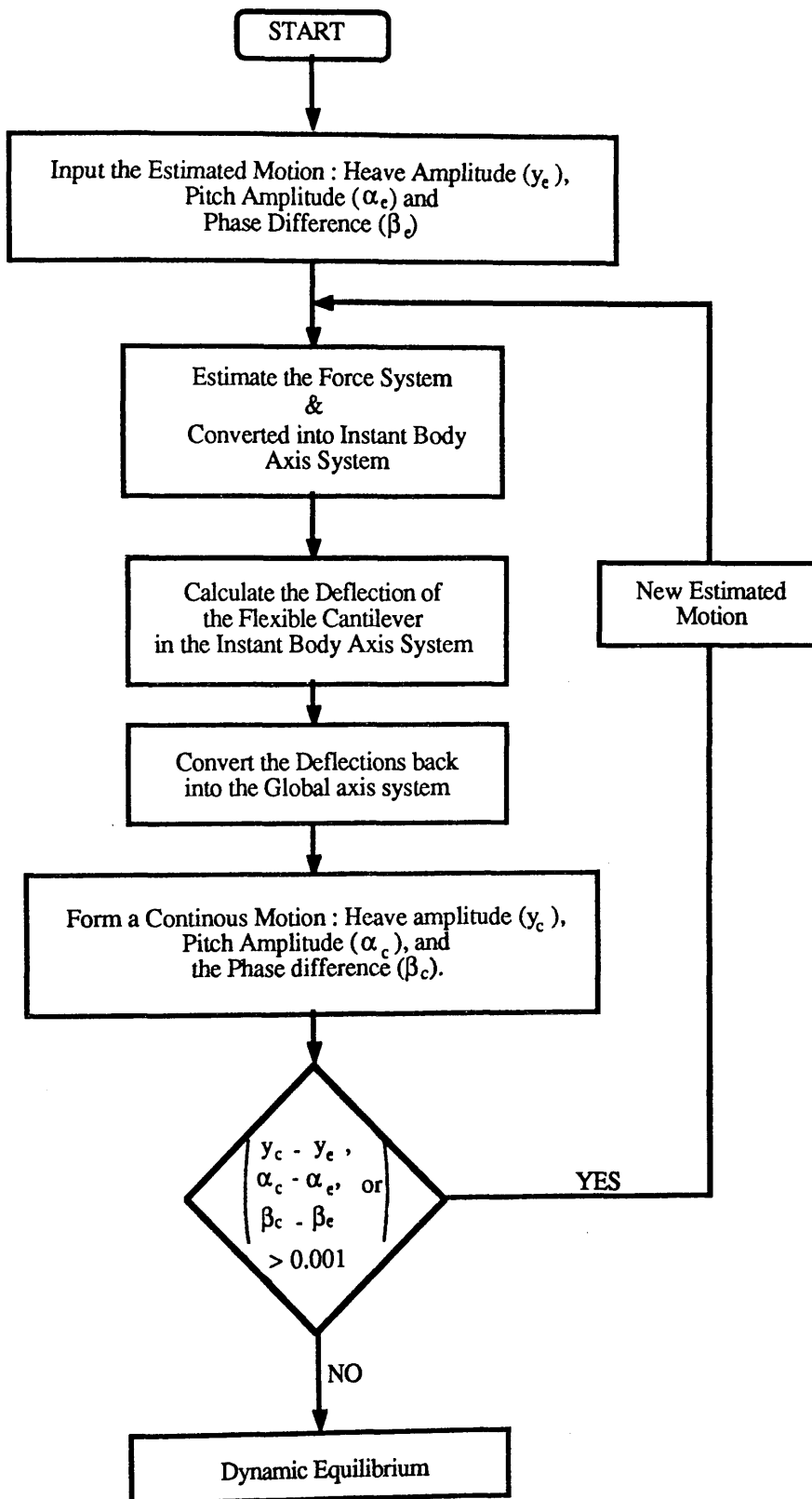


Fig. 4.5 The Efficiency of an Oscillating Foil with Aspect Ratio = 7.0, $\theta = 0.8$ and $a=1.0$



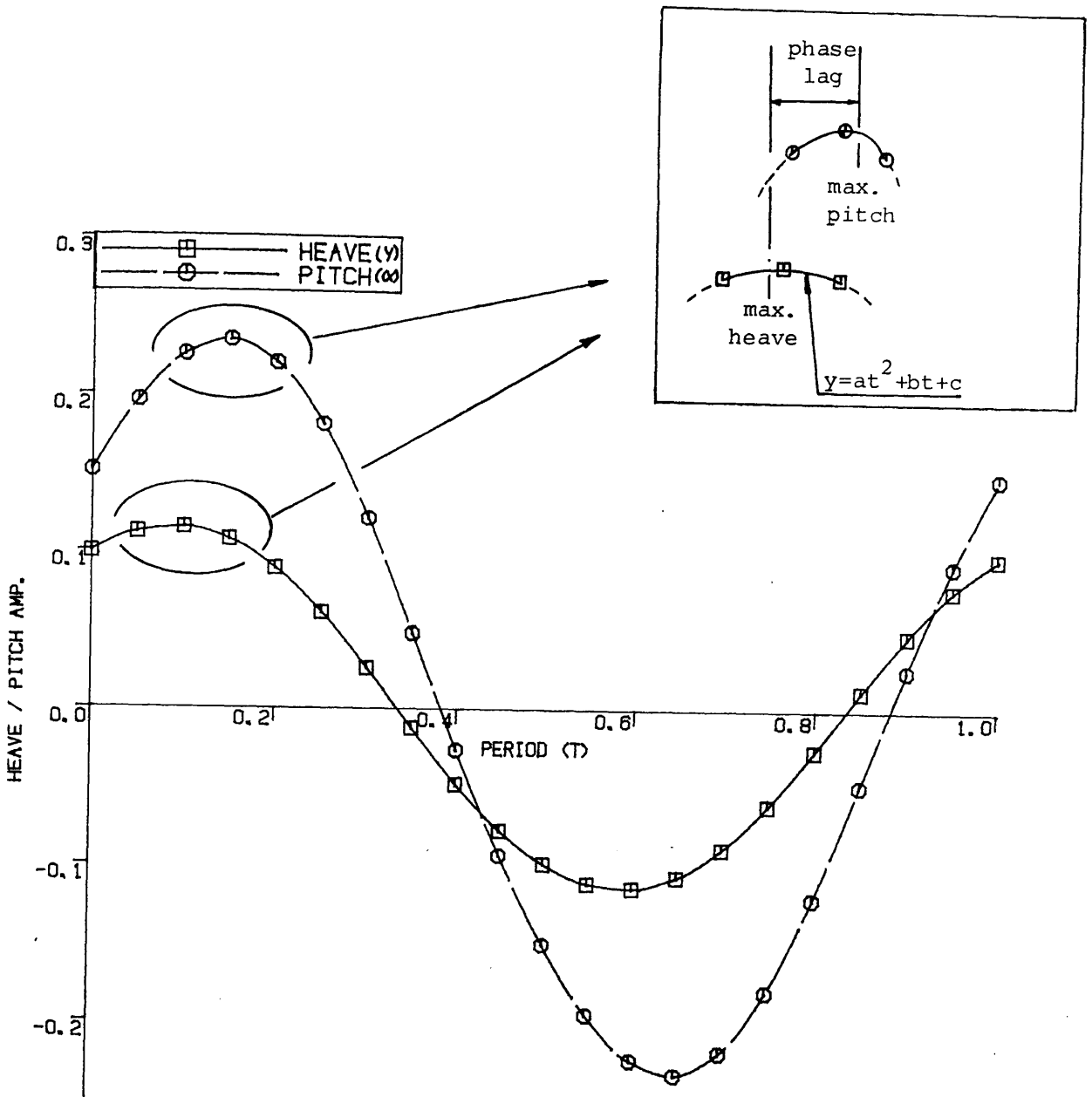
The Deflection of a Flexible Cantilever

Fig. 4.6



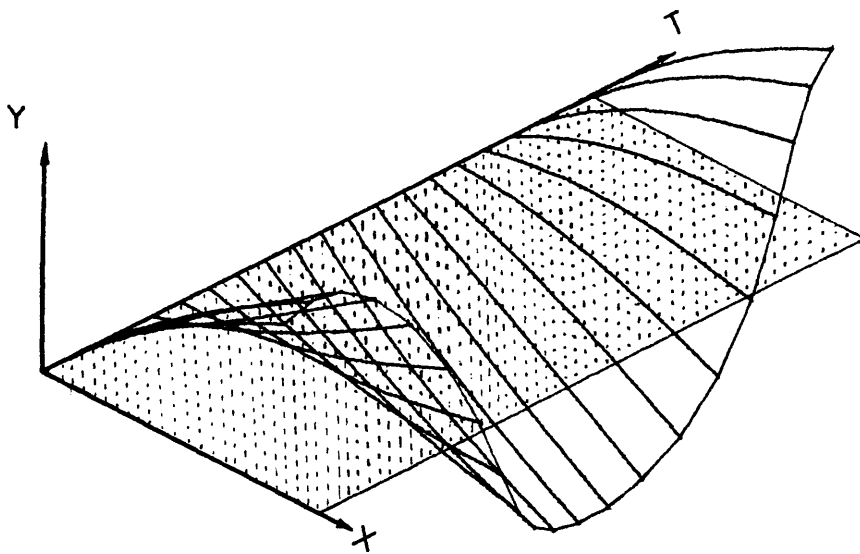
The Flow Chart of The Dynamic Equilibrium Search

Fig. 4.7



HEAVING AND PITCHING MOTION
OF AN OSCILLATING FOIL

Fig. 4.8



THE OSCILLATION OF FLEXIBLE
BAR OF A F. F. PROPELLER

Fig. 4.9

ASPECT RATIO	4.00	5.00	6.00	7.00
a0	6.679013967514 E-01	7.142567038536 E-01	7.508097887039 E-01	7.797173857689 E-01
a1	-1.71759066753 E-01	-1.513129621744 E-01	-2.463268637657 E-01	-3.671703934669 E-01
a2	2.045092172921 E-03	-1.920446604490 E-01	-4.561357945204 E-02	1.925612539053 E-01
a3	3.890443220735 E-02	2.728279232979 E-01	1.503675580025 E-01	-7.095959782600 E-02
a4	-1.077902317047 E-02	-9.877797216177 E-02	-5.623483657837 E-02	2.243596129119 E-02

ASPECT RATIO	8.00	9.00	10.00
a0	8.029161691666 E-01	8.218252062798 E-01	8.375545144081 E-01
a1	-4.865802526474 E-01	-5.964658260345 E-01	-6.952595710754 E-01
a2	4.426451921463 E-01	6.821801662445 E-01	8.991806507111 E-01
a3	-3.069924712181 E-01	-5.389682054520 E-01	-7.467548251152 E-01
a4	1.060604304075 E-01	1.899777203798 E-01	2.636939287186 E-01

Table 4.1 The Constants of Curve-Fit Polynomial Equations for F_A of Different Aspect Ratios

$$F_A = a_0 + a_1 k + a_2 k^2 + a_3 k^3 + a_4 k^4$$

ASPECT RATIO	4.0	5.0	6.0	7.0
b0	3.000591823366 E-04	4.970561712980 E-04	6.988482200541 E-04	8.060263333400 E-04
b1	2.607675790787 E-01	3.872943818569 E-01	6.032140851021 E-01	8.238742351532 E-01
b2	1.550274156034 E-02	1.063275933266 E-01	-1.087452530861 E+00	-2.592340946198 E+00
b3	-5.967847108841 E-01	-2.612686395645 E+00	8.918799757957 E-01	6.039940834045 E+00
b4	6.852017045021 E-01	6.085954666138 E+00	-3.106171190739 E-01	-1.062124061584 E+01
b5	-3.290469050407 E-01	-7.044991493225 E+00	1.397726684809 E-02	1.200035476685 E+01
b6	7.829380035400 E-02	4.260344505310 E+00	1.955903507769 E-02	-7.409246921539 E+00
b7	-1.163394097239 E-02	-1.067842245102 E+00	-1.166108716279 E-02	1.879057288170 E+00

Table 4.2 The Constants of Curve-Fit Polynomial Equations for $-G_A$ of Different Aspect Ratios

ASPECT RATIO	8.0	9.0	10.0
b0	9.126188815571 E-04	1.018312061206 E-03	1.126972376369 E-03
b1	1.023193240166 E+00	1.202691912651 E+00	1.359584331512 E+00
b2	-4.03005522919 E+00	-5.383697032928 E+00	-6.622944831848 E+00
b3	1.101433658600 E+01	1.581788921356 E+01	2.040798950195 E+01
b4	-2.043891525269 E+01	-3.007941055298 E+01	-3.964269638062 E+01
b5	2.312157630920 E+01	3.419300842285 E+01	4.551979446411 E+01
b6	-1.410532283783 E+01	-2.085814094543 E+01	-2.793933677673 E+01
b7	3.535683631897 E+00	5.227654457092 E+00	7.036804676056 E+00

$$-G_A = b_0 + b_1 k + b_2 k^2 + b_3 k^3 + b_4 k^4 + b_5 k^5 + b_6 k^6 + b_7 k^7$$

CHAPTER 5

THEORETICAL PERFORMANCE OF A FLEXIBLE FIN PROPELLER

1.0 INTRODUCTION

In this chapter, parametric studies are presented which use the theoretical model described in Chapter 4. The model of a flexible fin propeller with an oscillating rectangular foil is investigated. There are eleven factors which affect the performance of a flexible fin propeller. Therefore, a number of non-dimensional parameters were set up to link the related factors. These parameters include stiffness function, angular oscillating function, reduced frequency, taper ratio and aspect ratio. The effect of different stiffnesses of the flexible beam, oscillating frequency, angular oscillating amplitude and aspect ratio of the oscillating foil on propulsive thrust and efficiency are investigated and discussed. Flexible beams of different taper ratios with a linear variation in cross section were also studied. The performance of a flexible fin propeller with an elliptical foil is compared to that with a rectangular foil.

Propulsive thrust increases as stiffness of the connecting beam increases, but propulsive efficiency drops. Higher propulsive thrust is obtained by increasing angular oscillating amplitude at the pivot. The effect of aspect ratio on propulsive thrust is not significant; however, efficiency is improved significantly by increasing aspect ratio. Different taper ratios of the flexible beam have little effect on propulsive efficiency. A flexible fin propeller with an elliptical foil generates higher propulsive thrust coefficients than that with a rectangular foil. Higher efficiency is obtained by using an elliptical foil at lower reduced frequencies and vice versa at high reduced frequencies.

2.0 NON-DIMENSIONAL PARAMETERS

The performance of the flexible fin propeller depends on a number of factors.

These are :

- 1) advance velocity (U);
- 2) oscillating frequency (ω);
- 3) foil area (S);
- 4) span (s) of the foil;
- 5) chord (c) of the foil;
- 6) bending modulus (E) of the flexible bar;
- 7) section modulus (I) of the flexible bar;
- 8) length (L_0) of the flexible bar; and,
- 9) angular oscillating amplitude at the pivot (θ_A).

For a flexible bar with variation in cross section throughout its length, the changes in cross-section particulars are also included. In the present study, a flexible flat bar with constant width and linear variation in thickness is considered. For this, two other factors are included:

- 10) thickness (t_1) at the free end of the flexible bar; and,
- 11) thickness (t_2) at the fixed end of the flexible bar.

To study the effect of these factors on the performance of a flexible fin propeller, non-dimensional parameters were formed to link the related factors together. These parameters are listed below.

- 1) Stiffness Function (ξ). The performance of a flexible fin propeller depends on the oscillation of the foil and hence deflection of the flexible bar. The deflection

of this bar depends on the external loading acting on it. A stiffer cantilever under a larger external loading behaves in a similar manner to a less stiff bar under a smaller loading. Since the force system acting on the bar is a function of advance velocity and foil area, the physical characteristics of the bar can be normalised by these two factors. The maximum deflected slope of a cantilever under a load at its free end is a function of (L_o^2/EI) . Therefore, this parameter is set up as

$$\xi = \frac{EI}{qL_o^2} \quad , \text{ where } q = \rho U^2 S \quad - 5.1$$

As the value of ξ increases, the stiffness of the bar increases for a given aerofoil and forward speed.

- 2) Angular Oscillating Function (ζ). The amplitude of heave of the oscillating foil is a function of the angular oscillating amplitude (θ_{Ao}) at the pivot and the length of the flexible bar.

$$\zeta = \frac{L_o \theta_{Ao}}{b} \quad - 5.2$$

This function represents a non-dimensional parameter related to the heaving amplitude of the foil.

- 3) Reduced Frequency (k). This parameter, which is developed in chapter 3 (eqn. 3.11), quantifies the degree of unsteadiness.
- 4) Taper ratio (TR). This ratio shows the difference of the thickness at the free end and the fixed end of the flexible bar. The bar is flat with a constant width and linear variation in thickness.

$$TR = \frac{t_2 - t_1}{t_m} \quad - 5.3$$

When this ratio is zero, the thickness of the bar is constant.

- 5) Aspect ratio (AR). This is the aspect ratio of the oscillating rectangular foil.

$$AR = \frac{s}{c} = \frac{s^2}{S} \quad - 5.4$$

- 6) Propulsive Thrust Coefficient (C_T). The mean propulsive thrust, F_T , over an oscillating cycle is presented in a non-dimensional form as,

$$C_T = \frac{F_T}{\frac{1}{2}\rho U^2 S} \quad - 5.5$$

- 7) Non-Dimensional Heave amplitude (τ). A non-dimensional parameter is used to present the heave amplitude, y_o , of the oscillating foil

$$\tau = \frac{y_o}{L_o \theta_{Ao}} = \frac{y_o}{b} \frac{1}{\zeta} \quad - 5.6$$

- 8) Non-Dimensional Pitch Parameter (λ). The pitch angle, α_o , is represented by the non-dimensional parameter.

$$\lambda = \frac{\alpha_o}{\theta_{Ao}} \quad - 5.7$$

3.0 RANGE OF ANALYSIS

Propulsive thrust coefficient (C_T) and efficiency (η) of a flexible fin propeller with an aspect ratio of 4.0 were calculated for a range of reduced frequencies from 0.2 to 0.6. They are presented in figs. 5.1 a, b and c and 5.2a , b and c. Results were

found for different stiffness functions (ξ) of 3.0, 6.0, 9.0 and 12.0. The results for three angular oscillating functions (ζ) of 3.0, 5.0 and 7.0 are presented in figures a, b and c respectively.

The effect of different taper ratios on propulsive thrust and efficiency were studied for two stiffness functions (ξ) of 6.0 and 12.0 over the same range of reduced frequencies and angular oscillating functions. The propulsive thrust coefficients for a stiffness function of 6.0 and 12.0 are presented in figs. 5.3 and 5.4 and corresponding efficiencies are shown in figs 5.5 and 5.6 respectively. A range of taper ratios from 0.0 to 0.6 with an increment of 0.2 was investigated.

The effect of the aspect ratio of the oscillating foil on performance was also studied. Three aspect ratios of 4.0, 7.0 and 10.0 were studied for a propeller in conjunction with a stiffness function of 12.0. Calculations were done for the same range of reduced frequencies and angular oscillating functions. Corresponding propulsive thrust coefficients and efficiencies are presented in figs. 5.7 and 5.8.

The performance of a flexible fin propeller with an elliptical foil is compared to results with a rectangular foil. Comparisons of propulsive thrust coefficient and efficiency between these two foil shapes with an aspect ratio of four and a stiffness function of 12.0 for the same range of angular oscillating functions and reduced frequencies are shown in figs. 5.9 and 5.10 respectively. The performance at a lower stiffness function, $\xi = 6.0$, and an angular oscillating function of 3.0 was calculated and is shown in fig. 5.11.

4.0 RESULTS AND DISCUSSION

4.1 The Effect of Stiffness of the Flexible Bar

Propulsive thrust is increased by increasing the stiffness of the flexible bar (fig. 5.1). Propulsive thrust increases as the oscillating amplitude of the foil increases.

Decrease in stiffness of the connecting bar tends to reduce oscillating amplitude throughout the whole oscillating cycle and hence the propulsive thrust. To demonstrate this effect, the non-dimensional heaving amplitude (τ) and pitching amplitude (λ) of the oscillating foil under the condition when $\zeta = 3.0$, $k = 0.6$ and the aspect ratio of the foil equal to 4.0 for different stiffness functions are calculated and presented in fig. 5.12 a and b respectively. The oscillating amplitude increases as the stiffness function increases. However the rate of increase in the oscillating amplitude decreases as the stiffness function increases. This is because the effect of external loading on the deflection of the beam decreases as the stiffness increases. Therefore the differences in propulsive thrust coefficient are smaller between bars with $\xi = 9$ and 12 than those between bars with $\xi = 3$ and 6. The condition with a reduced frequency of 0.6 and an angular oscillating function of 3.0 is used as an example (fig. 5.1a). The propulsive thrust coefficient increases 85% by increasing the stiffness function from 3.0 to 6.0 and a further 35 % when the stiffness function increases to 9.0. A smaller increase in propulsive thrust coefficient of 14 % is obtained by increasing the stiffness function to 12.0.

Propulsive thrust increases as the angular oscillating function increases. This is because swept area and oscillating amplitude of the foil increases as the angular oscillating function increases. Also propulsive thrust increases as reduced frequency increases.

Efficiency increases as the stiffness decreases (fig. 5.2). Efficiency is not sensitive to the oscillating frequency when the angular oscillating functions are small (fig. 5.2a). Variation of stiffness has only a little effect on propulsive efficiency at low angular oscillating function. Propulsive efficiencies for a range of stiffness function from 3.0 to 12.0 are between 0.6 and 0.65 when $\zeta = 3.0$. The effect of stiffness function on efficiency increases as the angular oscillating function increases. The hydrodynamic force system acting on the flexible fin propeller is larger at higher angular oscillating amplitudes and because of this the effects of stiffness function on both propulsive thrust coefficient and efficiency are larger. When the angular oscillating

function equals 7.0, the efficiency increases towards 1.0 at high reduced frequencies (fig. 5.2c). At this high angular oscillating function and for high reduced frequencies, large deflections occur in the flexible beam and the converged oscillation of the foil from the dynamic equilibrium search is not a pure sinusoidal motion. The sinusoidal assumption fails in this zone. The rise of the efficiency curve in this area is not realistic (fig. 5.2c). When the angular oscillating functions are large, non-linear terms become dominant. In this condition, flow separation on the foil surface may occur and cause dynamic stall [McCroskey 1977, 1981, and 1982, Carr 1988]. Both propulsive thrust and efficiency will drop when dynamic stall occurs. In addition, the theory which is based on a linearised assumption (Chapter 2), fails when the oscillating amplitude is large. The predicted performance at large angular oscillating functions should be treated with some caution.

4.2 The Effect of Taper Ratio of the Flexible Bar

The effects of taper ratio on tip deflections under pure static vertical loads was studied. The results are shown in fig. 5.13a, b and c. The results are present in a non-dimensional parameters. These non-dimensional parameters are :

- i) $\delta_x = \frac{\Delta x}{L_o}$;
- ii) $\delta_y = \frac{\Delta y}{L_o}$;
- iii) $\delta_\phi = \frac{\phi_t}{\pi}$; and,
- iv) $\mu = \frac{F_v L_o^2}{EI}$ (see fig. 4.6).

Deflections increase as the taper ratio increases; increasing taper ratio increases flexibility.

The effects of taper ratio on propulsive thrust and efficiency have been studied

for two different stiffness functions. Propulsive thrust coefficients for connecting bars with stiffness functions of $\xi = 6$ and 12 are shown in fig. 5.3 and 5.4 respectively. The effect of increasing taper ratio on propulsive thrust has the same tendency as decreasing the stiffness function. The propulsive thrust coefficient decreases as taper ratio increases. This effect is greater when the stiffness function is lowered. However, the magnitude of the propulsive thrust is not sensitive to small changes in taper ratio.

Propulsive efficiencies for connecting bars with stiffness functions $\xi = 6$ and 12 are shown in fig. 5.5 and 5.6 respectively. The effect of taper ratio on propulsive efficiency is very small. When the angular oscillating function is small, there is practically no effect on the efficiency. This is because efficiency is not sensitive to changes in flexibility.

4.3 Effect of Aspect Ratio

Propulsive thrust coefficients and propulsive efficiency for different aspect ratios are presented in fig. 5.7 and 5.8 respectively for a flexible bar with a stiffness function of 12. To study the effect of aspect ratio of the foil, a similar foil area is used for all foils. Three aspect ratios were studied : 4.0, 7.0 and 10.0.

The effect of aspect ratio on propulsive thrust is small. There is practically no difference in propulsive thrust between aspect ratios of 7.0 and 10.0 at this stiffness function. The difference is larger between 4.0 and 7.0. The effect of three-dimensional flow is small for a high-aspect-ratio foil and higher propulsive thrust per unit foil area is obtained at higher aspect ratios.

Propulsive efficiency is improved by increasing aspect ratio (fig. 5.8). The maximum propulsive efficiency is increased by 17% by increasing the aspect ratio from 4.0 to 7.0 when the angular function is 3.0; a further increase of 5 % is obtained by increasing the aspect ratio to 10.0.

The effect of aspect ratio on the hydrodynamic forces is reflected by the unsteady lifting functions (F_A and G_A) (see section 3 of Chapter 4). The differences in the unsteady lifting functions between aspect ratios of 4.0 and 7.0 are larger than those between 7.0 and 10.0. This is reflected in the propulsive thrust and efficiency.

4.4 The Effect of Foil Shape (Rectangular and Elliptical)

The hydrodynamic force system of an oscillating elliptical foil is estimated by using a similar approach to the one for an oscillating rectangular foil. The unsteady lifting functions for an elliptical foil [Scherer 1968, Jones 1940] are used. The performance of the propeller with an elliptical foil is calculated by using the same theoretical model described in chapter 4. The mean chord of the elliptical foil, which is the foil area (S) divided by the span (s), is used in calculating the reduced frequency and angular oscillating function. The propulsive thrust coefficients generated by propellers with rectangular and elliptical foils of aspect ratio 4.0 and the stiffness function 12.0, are shown in fig. 5.9. The flexible fin propeller with an elliptical foil generates a higher propulsive thrust. At low reduced frequency, the differences between the rectangular foil and elliptical foil are small. However, the differences increase as the reduced frequency increases. In fig. 5.10, the corresponding efficiencies are shown. The efficiency of the propeller with an elliptical foil is higher than the one with rectangular foil at low reduced frequency and vice versa at high reduced frequencies. Similar trends are obtained at a lower stiffness function; the results for a stiffness function $\xi = 6.0$ are shown in figs. 5.11.

5.0 CONCLUSIONS

A series of parametric studies were carried out by using the theoretical model of a flexible fin propeller. The following conclusions are drawn from the investigation.

- 1) Propulsive thrust coefficients increase as the stiffness of the flexible beam increases. The increment in propulsive thrust coefficient is larger when the

stiffness function is low. When $\zeta=3$ and $k=0.6$, the propulsive thrust coefficient increases by 85% for an increase in stiffness function from 3.0 to 6.0 but only by 6% when the stiffness function changes from 9.0 to 12.0.

- 2) The hydrodynamic force system is a function of oscillating frequency and propulsive thrust increases as reduced frequency increases.
- 3) Swept area and oscillating amplitude of the foil increase as the angular oscillating function increases and as a result the propulsive thrust increases.
- 4) Propulsive efficiency is not sensitive to changes in reduced frequency and stiffness function when the angular oscillating function is small. At a low angular oscillating function of 3.0, the propulsive efficiency of a flexible fin propeller with an aspect ratio of 4.0 lies between 0.6 and 0.65 for a range of reduced frequencies between 0.2 and 0.6 and stiffness functions between 3.0 and 12.0.
- 5) For high values of the angular oscillating function, the hydrodynamic forces acting on the system are larger and the variation of propulsive thrust coefficient and efficiency in response to the change of stiffness function are also larger.
- 6) The propulsive thrust coefficient decreases as taper ratio of a connecting bar with linear variation in cross-section increases. The effect of increasing taper ratio on the propulsive thrust has the same tendency as a decrease in stiffness function. The effect is larger for a flexible bar than a stiff bar. However, in terms of magnitude, the effect on propulsive thrust is small.
- 7) There is no significant effect of taper ratio on propulsive efficiency. There is practically no difference in propulsive efficiency for different taper ratios between 0.0 to 0.6, when the angular oscillating function is 3.0.
- 8) Higher propulsive thrust per unit area is obtained for higher aspect ratios.

However, there is no significant difference in propulsive thrust coefficient for aspect ratios between 7.0 and 10.0. Although the effect of aspect ratio on propulsive thrust is not large, propulsive efficiency is improved by increasing the aspect ratio of the foil. When the angular oscillating function is 3.0, the efficiency is increased from 0.65 to 0.76 (17%) by increasing the aspect ratio from 4.0 to 7.0 and a further improvement of 5% to 0.79 is obtained by increasing the aspect ratio to 10.0.

- 9) A flexible fin propeller with an elliptical foil generates higher propulsive thrust coefficients than one with a rectangular foil. Higher efficiency is obtained by using an elliptical foil at lower reduced frequencies and vice versa at high reduced frequencies.

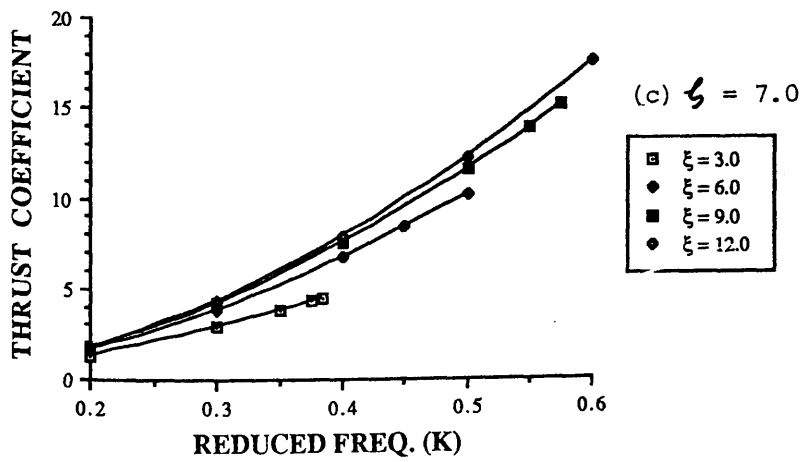
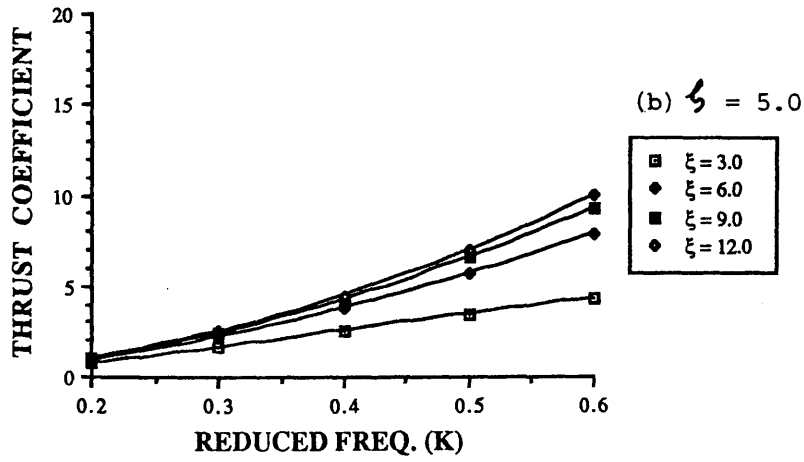
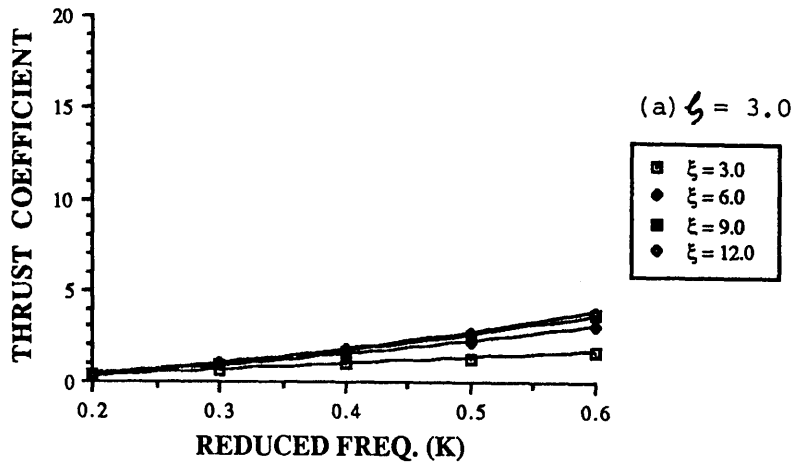


Fig. 5.1 Propulsive Thrust Coefficient for Different Stiffness Functions, AR= 4.0

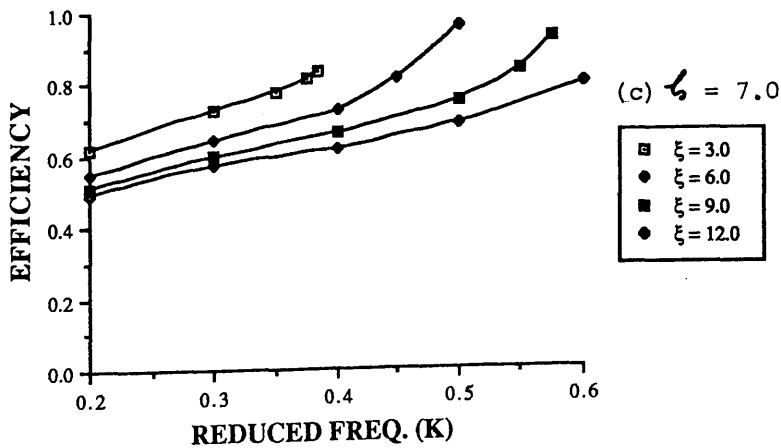
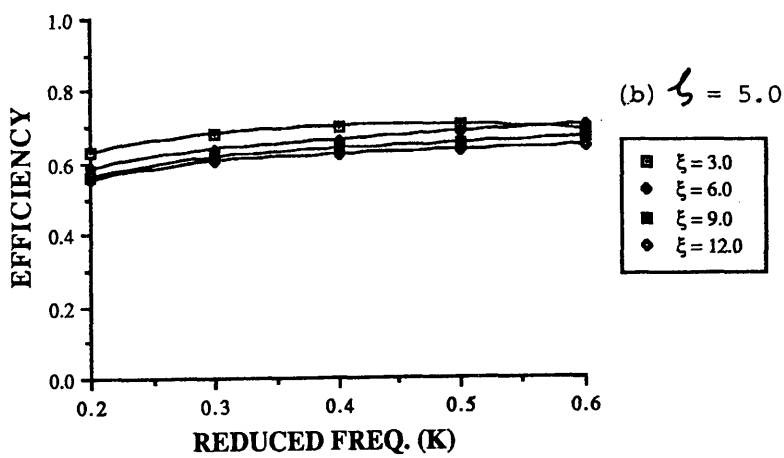
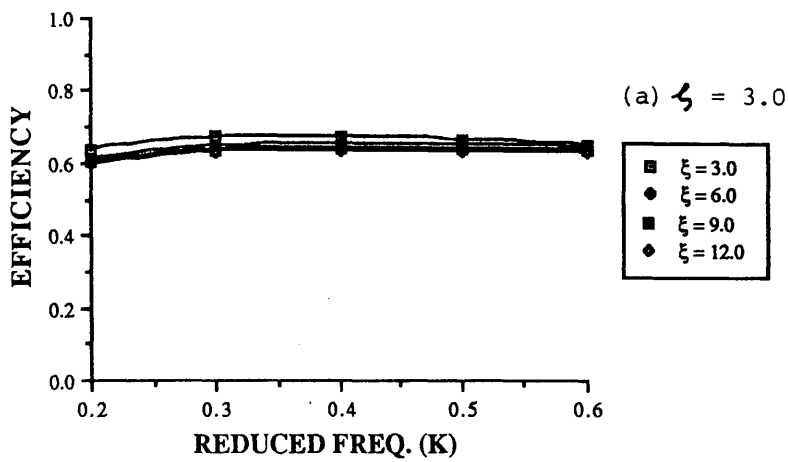


Fig. 5.2 The Efficiency for Different Stiffness Functions; AR= 4.0

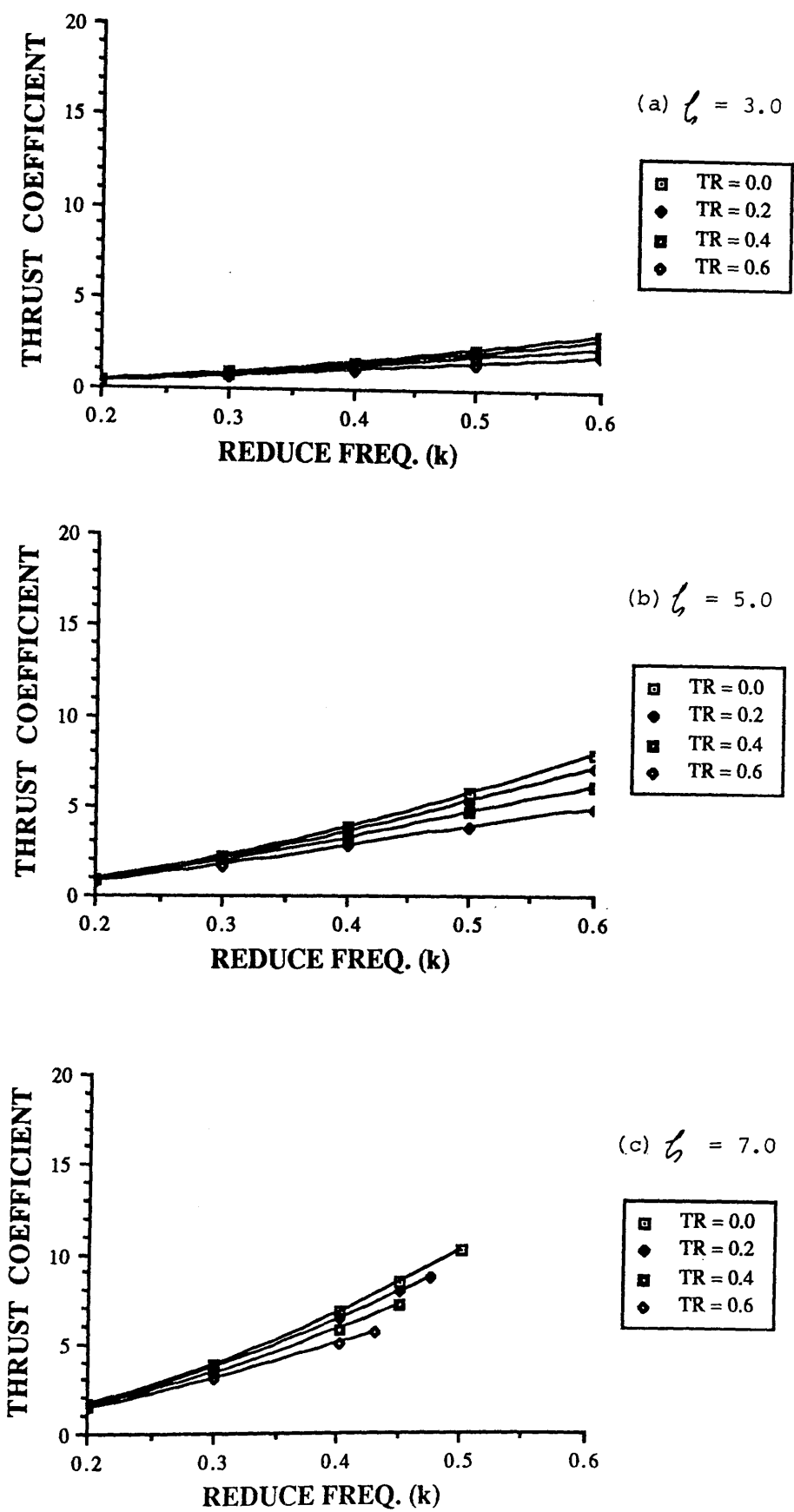


Fig. 5.3 The Propulsive Thrust Coefficients for Different Taper Ratio

$\xi = 6.0, AR = 4.0$

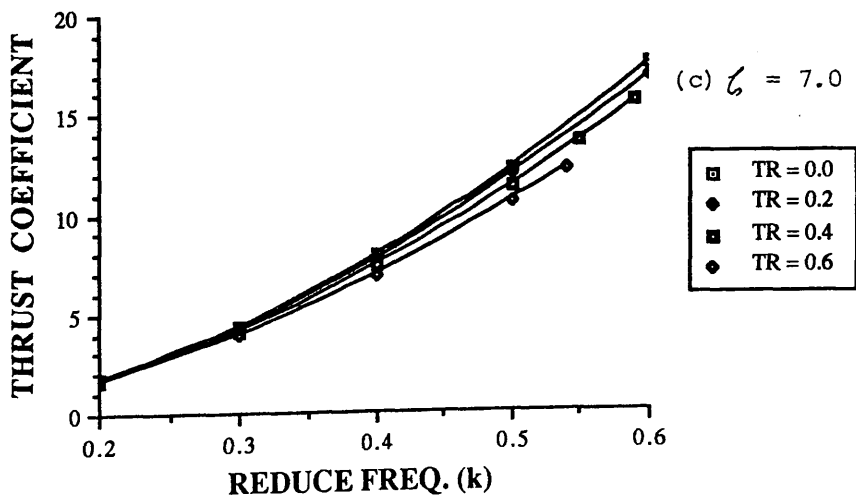
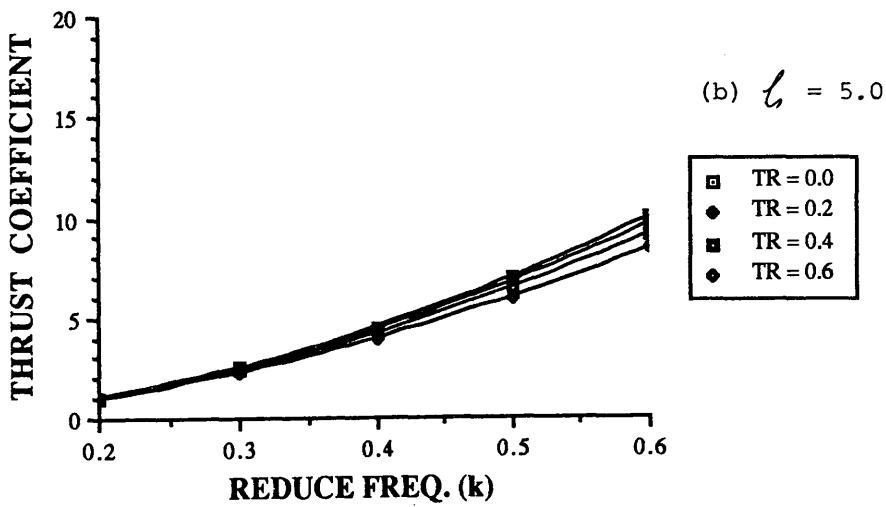
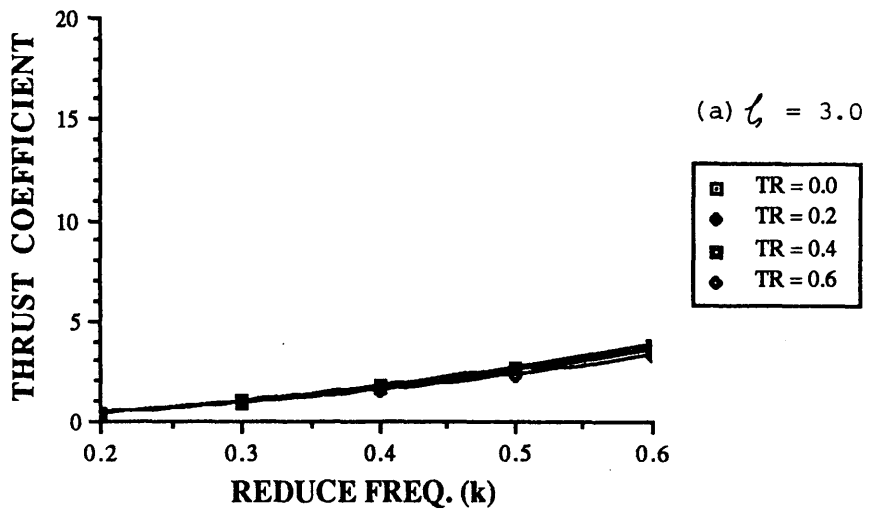


Fig. 5.4 The Propulsive Thrust Coefficients for Different Taper Ratios

$\zeta = 12.0, AR = 4.0$

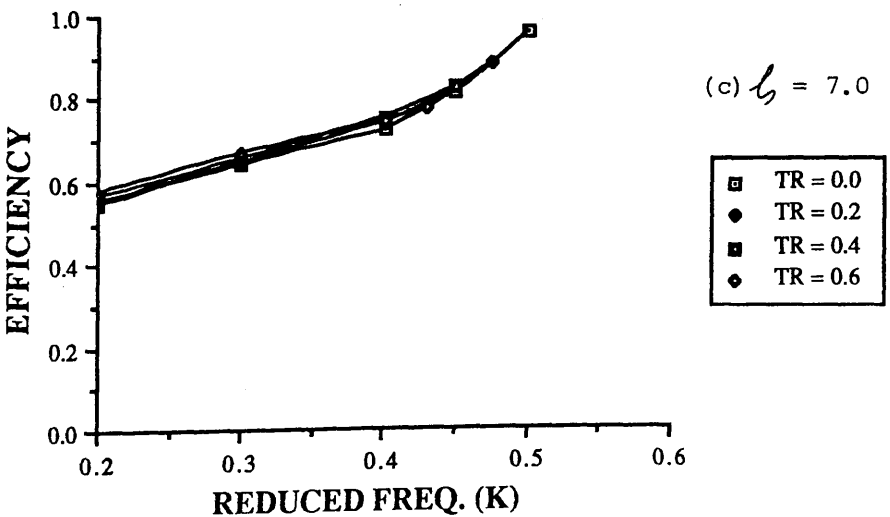
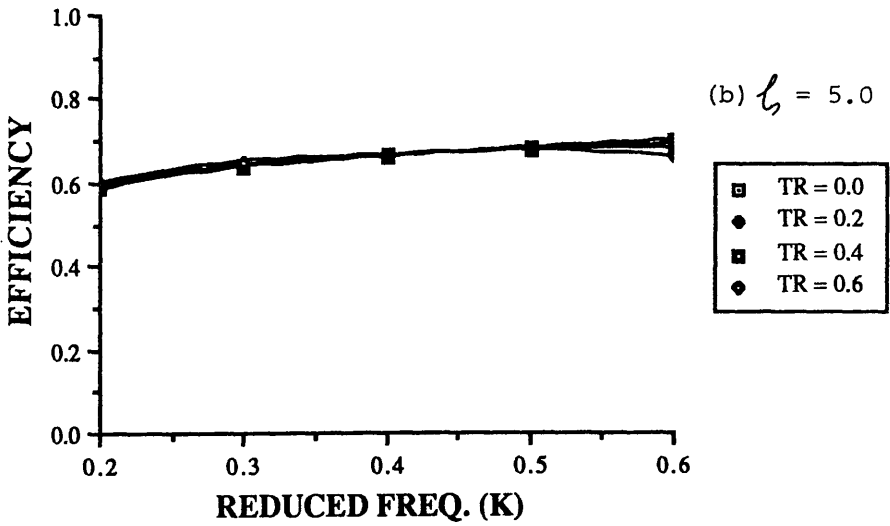
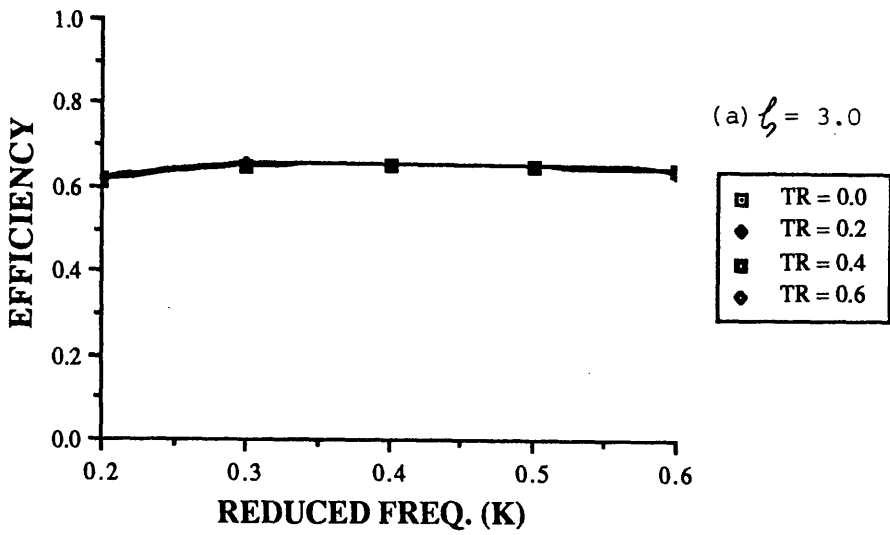


Fig. 5,5 The Efficiency for Different Taper Ratios $\xi = 6.0$, AR= 4.0

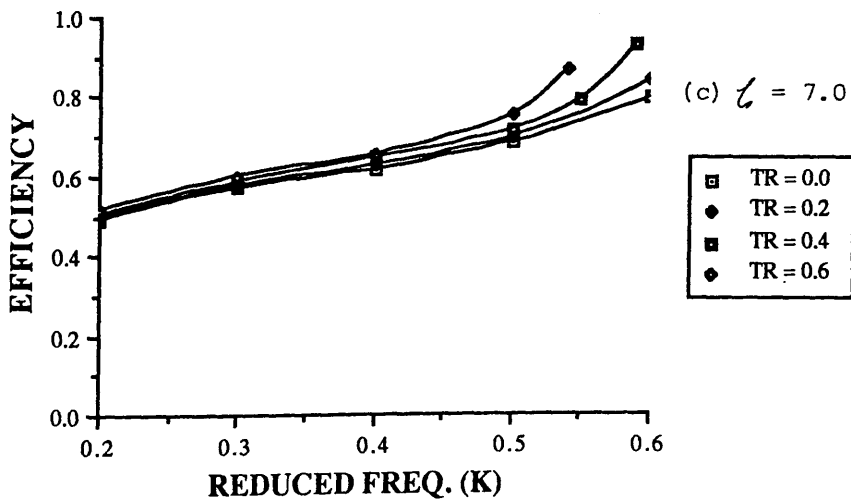
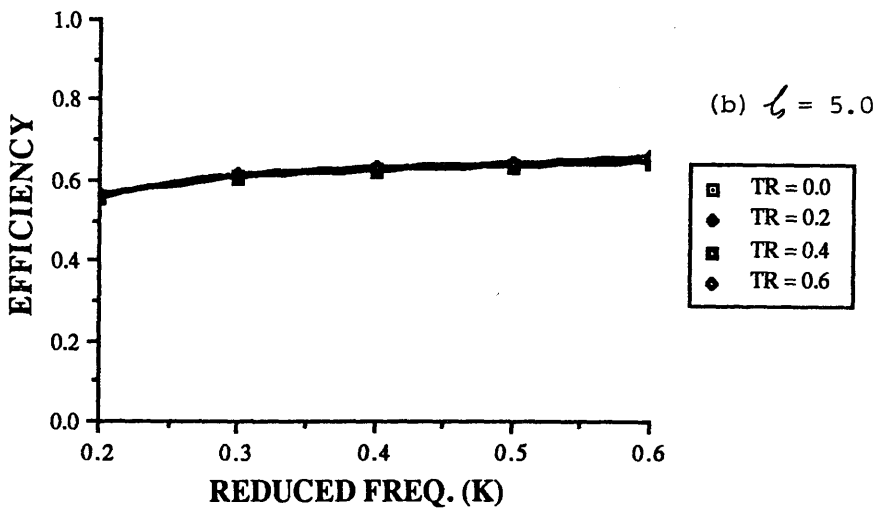
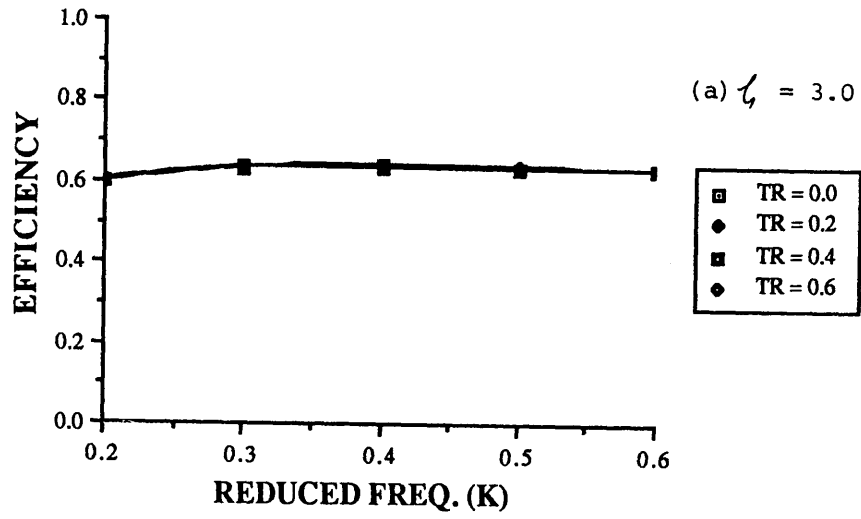


Fig. 5.6 The Efficiency for Different Taper Ratios $\zeta = 12.0$, AR = 4.0

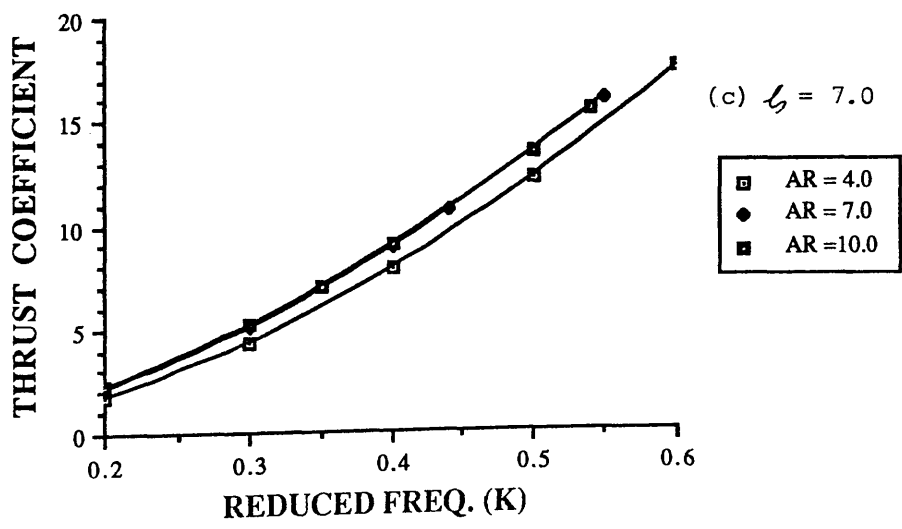
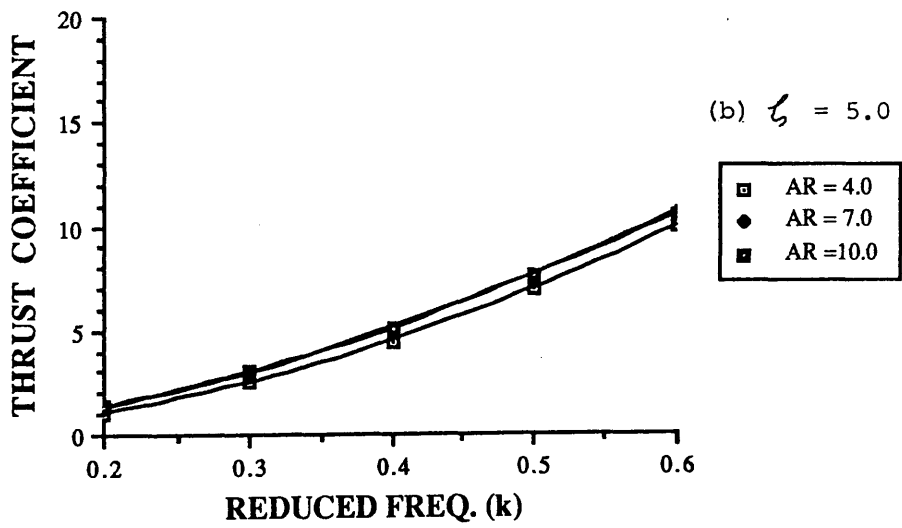
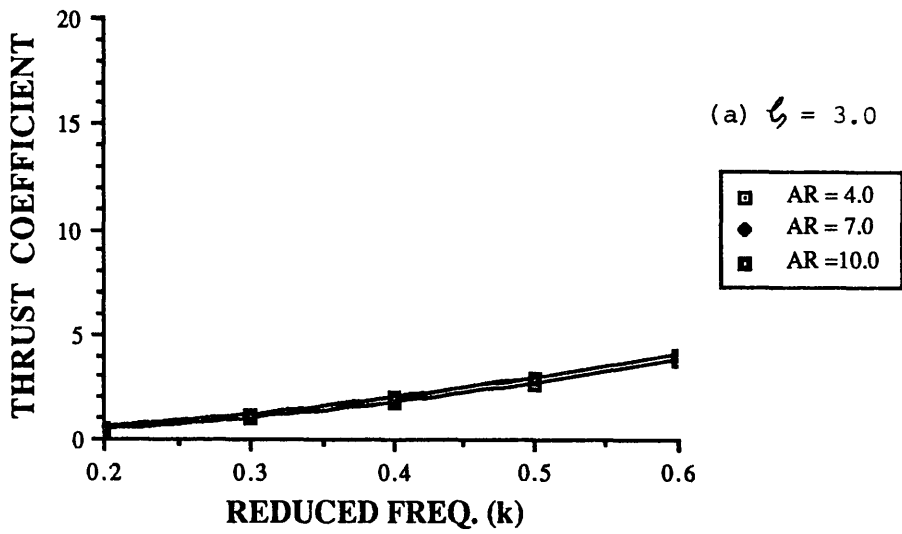


Fig. 5.7 The Propulsive Thrust Coefficients for Different Aspect Ratios

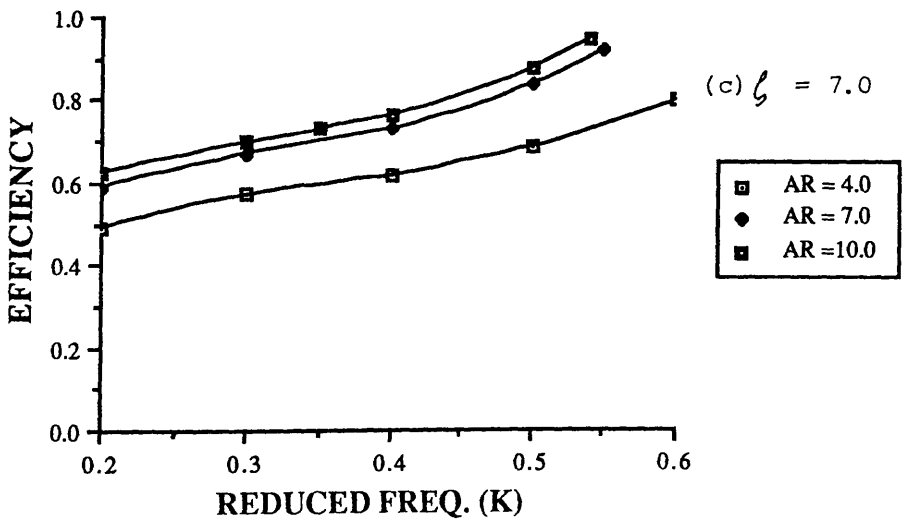
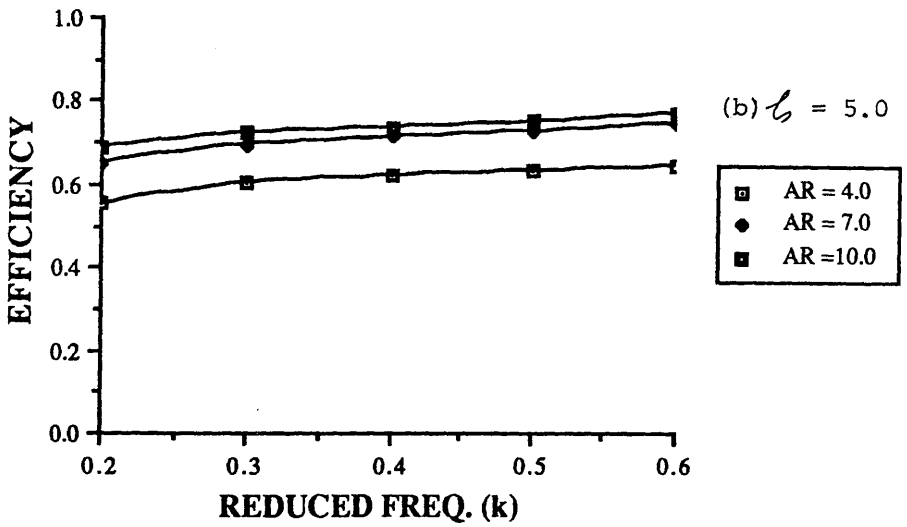
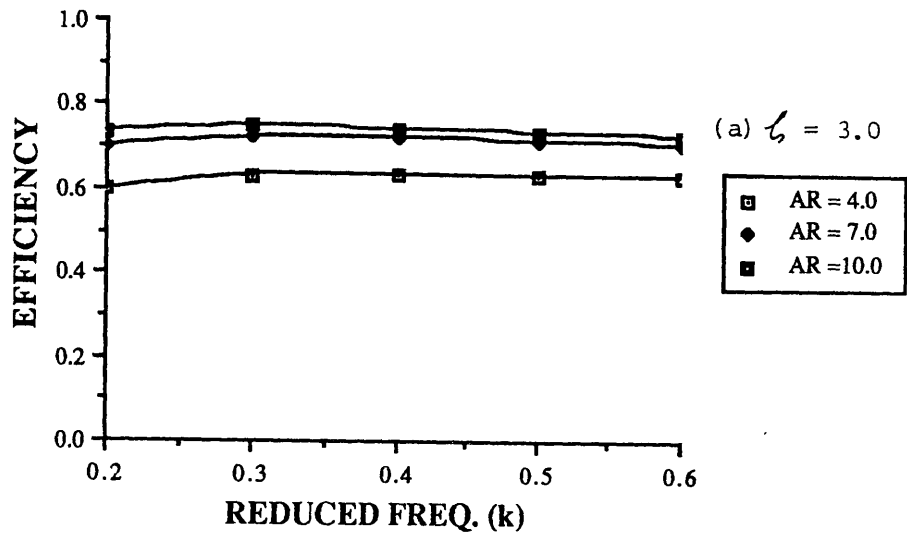


Fig. 5.8 The Efficiency for Different Aspect Ratios $\xi = 12.0$

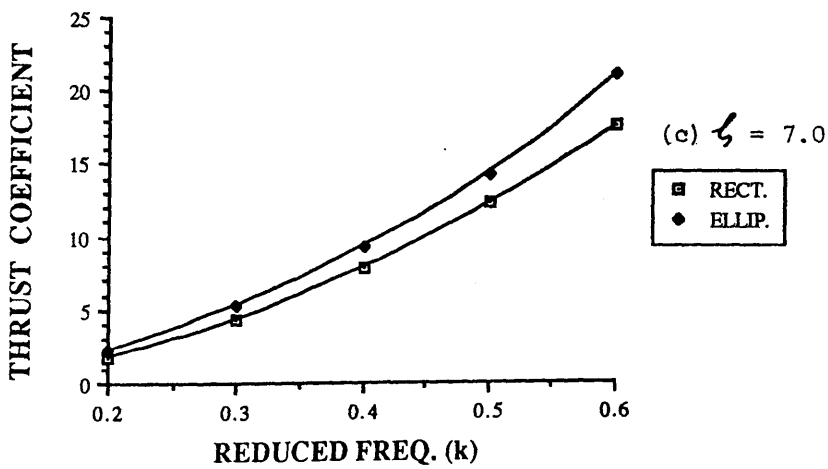
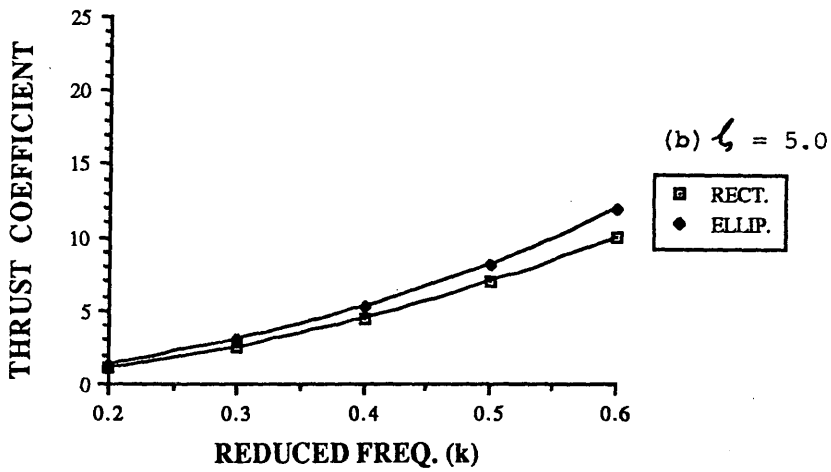
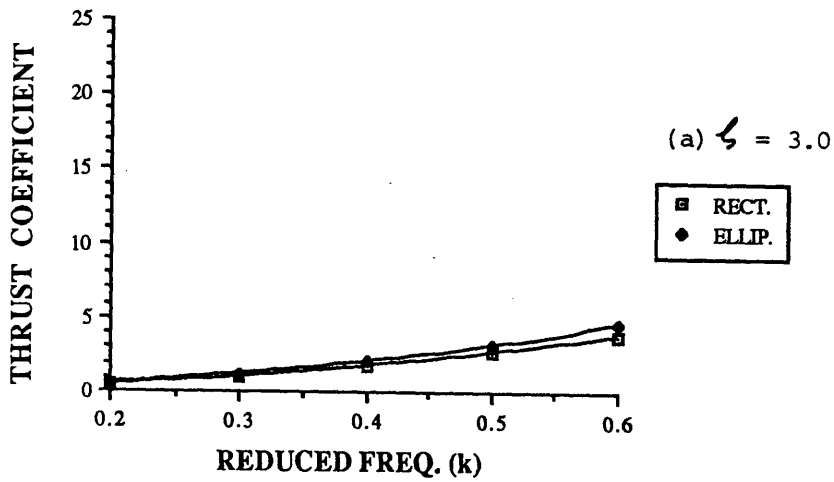


Fig. 5.9 Propulsive Thrust Coefficients for Rectangular and Elliptical Foils : $\zeta = 12.0$, AR = 4.0

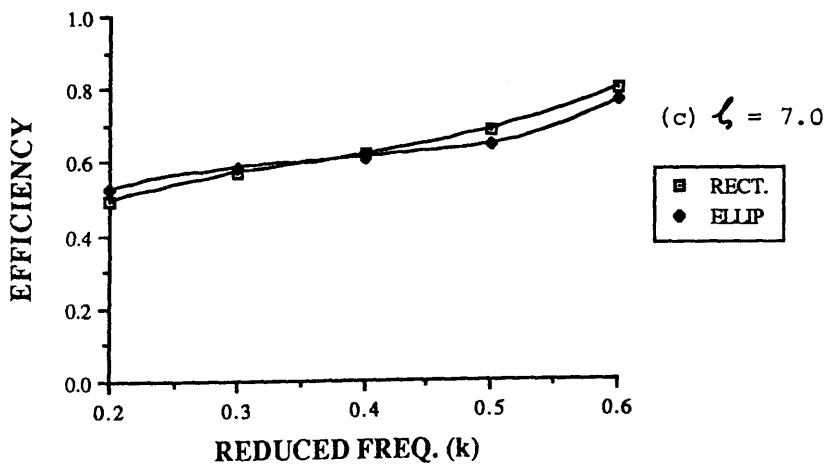
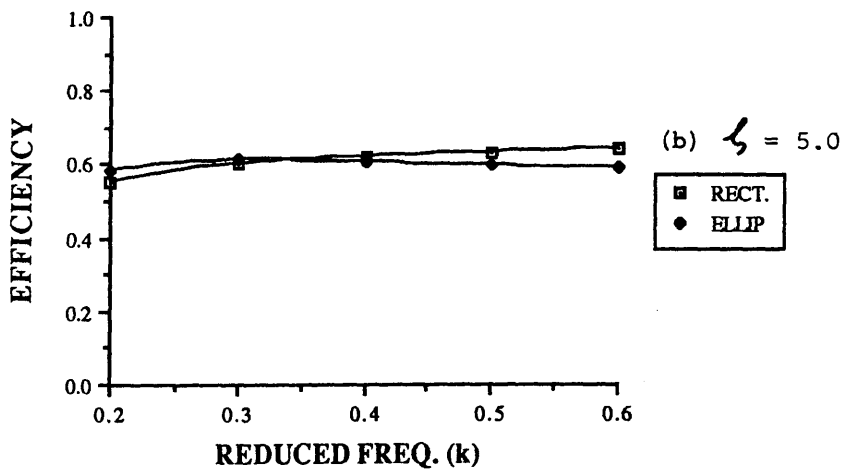
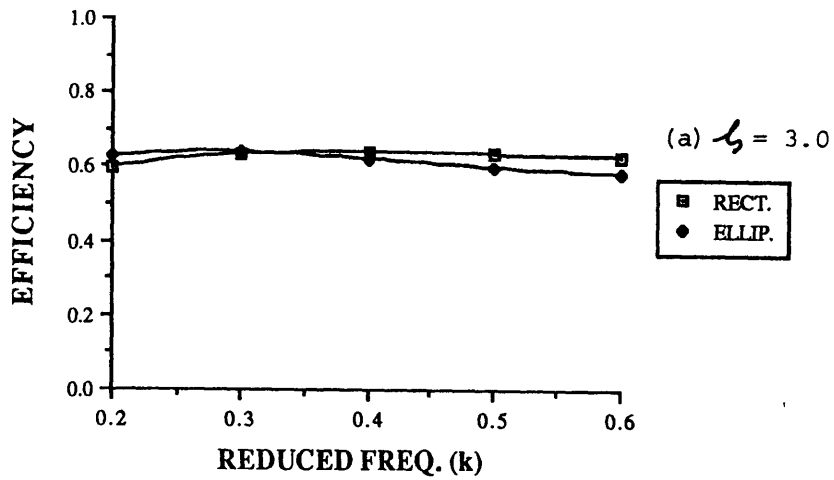
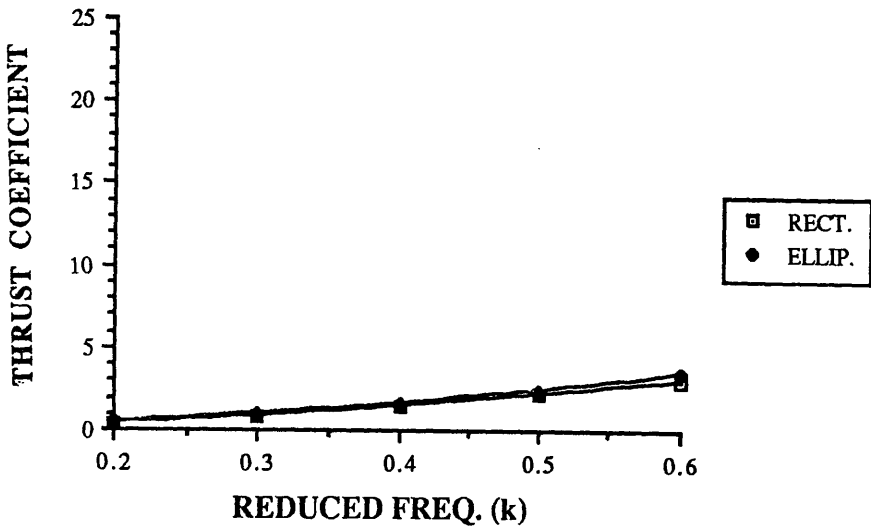
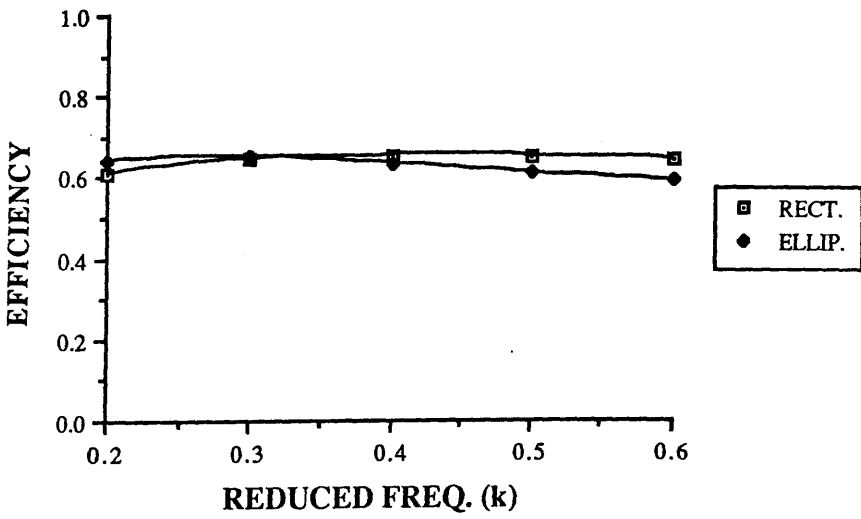


Fig. 5.10 Propulsive Efficiency for Rectangular and Elliptical Foils : $\zeta = 12.0$,
AR= 4.0



(a) Propulsive Thrust Coefficient



(b) Efficiency

Fig. 5.11 The Performance for Different Foil Shape; $\xi = 6.0$, $\zeta = 3.0$, AR=4.0

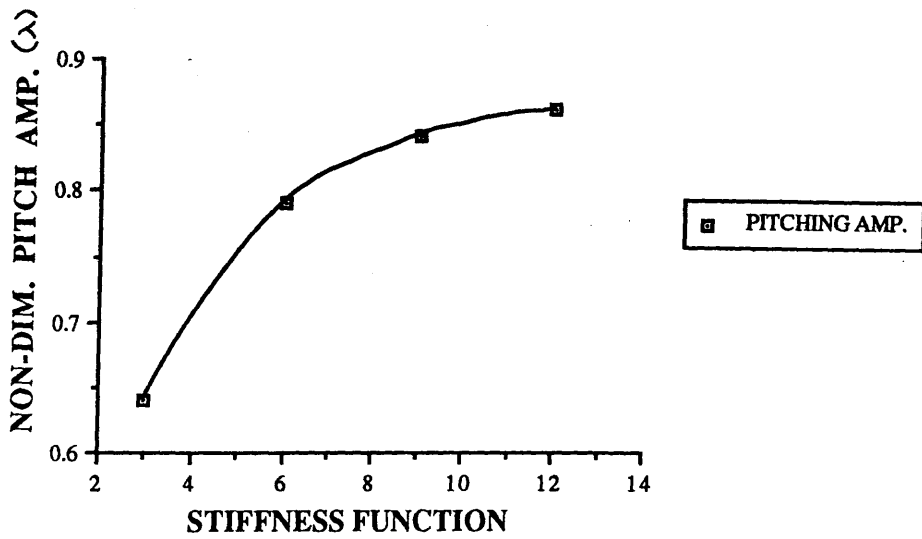
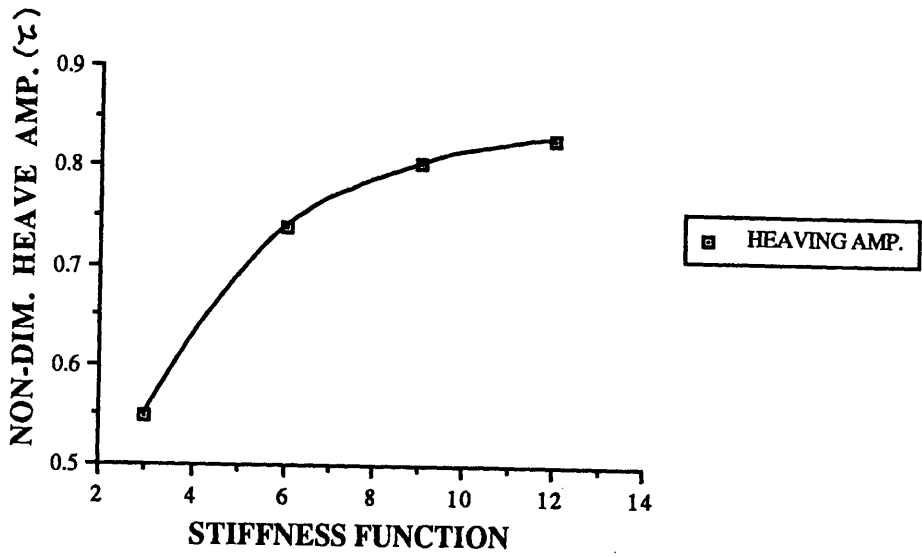
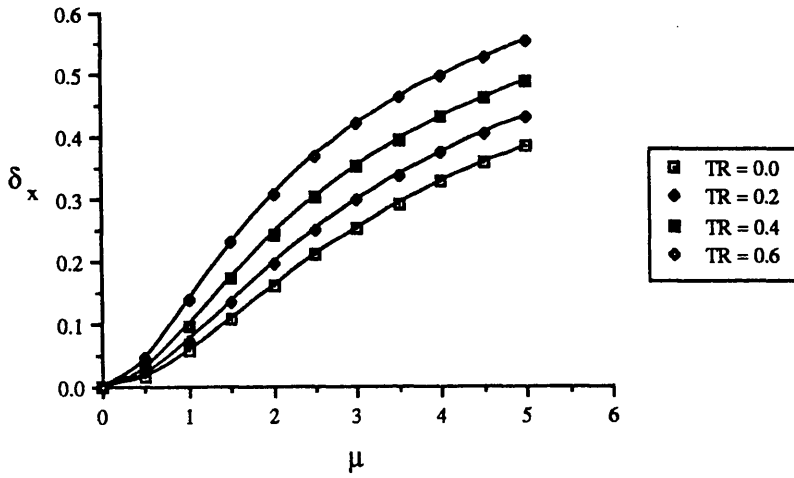
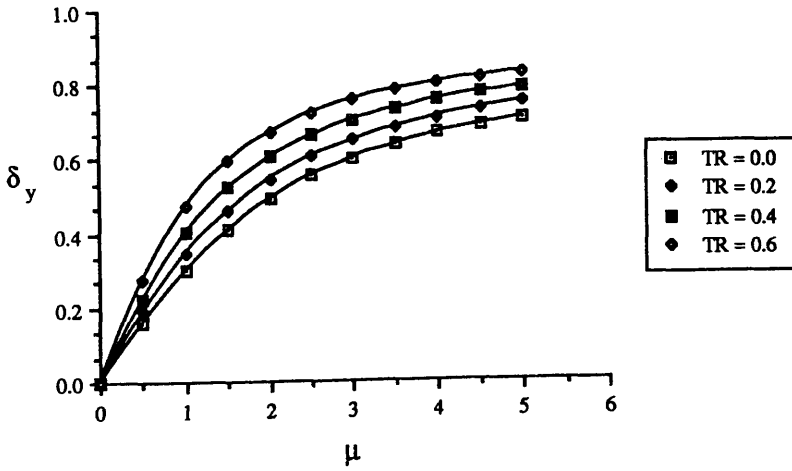


Fig. 5.12 The Amplitudes of Heave & Pitch for different Stiffness Functions

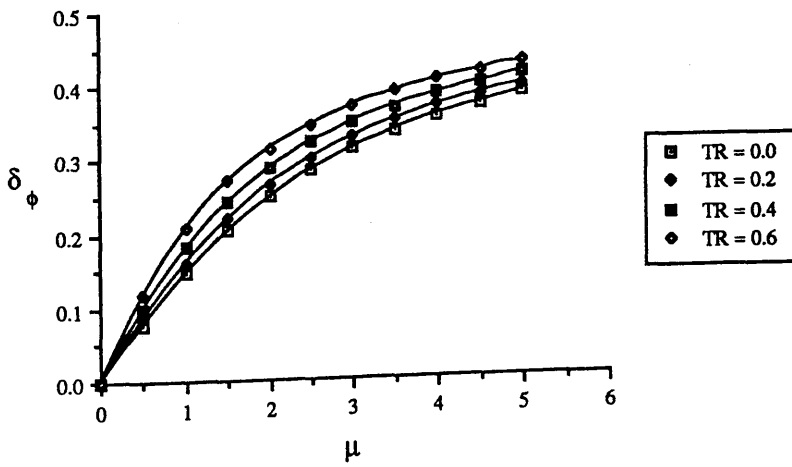
$\zeta = 3.0, k=0.6$ and $AR= 4.0$



(a) Tip Deflection in X - Direction



(b) Tip Deflection in Y- Direction



(c) Tip Deflected Slope

Fig. 5.13 The Tip Deflections for Different Taper Ratios

CHAPTER 6

THE MODEL AND TEST RIG FOR A FLEXIBLE FIN PROPELLER

1.0 INTRODUCTION

An experimental program was an important part of this study. A model of a flexible fin propeller was designed and built together with an integral force dynamometer and driving mechanism. The aim of the rig design was to produce a sinusoidal angular oscillation at the pivot to drive the flexible fin propeller model. This test rig was complex; it was built in the workshop of the Hydrodynamics Laboratory, University of Glasgow, and it took approximately one year of a technician's time to complete. The construction drawings are presented in Appendix I. Functions of individual components of the rig were tested and confirmed. In this chapter, the design and function of the test rig is presented. The methods of measuring the output thrust and input power are described.

2.0 THE DESIGN OF THE TEST RIG AND THE MODEL

A general arrangement of the test rig and model is presented in fig. 6.1. A corresponding diagrammatic arrangement is shown in fig. 6.2. It was made up of :

- (i) a driving unit;
- (ii) sinusoidal oscillator;
- (iii) wire and pulley system;
- (iv) three bar system;
- (v) propulsive thrust measuring arm;
- (vi) flexible bar and foil clamp; and,
- (vii) an enclosing strut.

2.1 The Driving Unit

The driving unit is presented in Drg. No. 011, Appendix I (fig. 6.3). The prime mover was a 3 kW A. C. motor (fig. 6.3 {1}) with a variable speed frequency control device to control its rotation speed. A reduction gear (7.8 to 1) (fig. 6.3 {2}) was used. A flexible coupling was fitted between the A. C. motor and the reduction gear box. An intermediate shaft (40 mm diameter) was used to connect the reduction gear and the double flanges (fig. 6.3 {3}) of the sinusoidal oscillator. The shaft supported all the weight of the double flanges and the tilting moment caused by the weight of flanges was counteracted by two self-aligning plumber blocks.

2.2 The Sinusoidal Oscillator

The design of the sinusoidal oscillator is shown in Drg. No. 007, Appendix I (fig. 6.4). Angular rotation from the double flanges was transferred to a sliding mechanism through a connecting pin. The objective of the first flange was to transfer rotation to the second flange. The second flange was a holed flange. The holes were in pairs (one opposite to the other), and named as A, B, C, D, E, and F. The connecting pin to the sliding block was mounted on one of the holes while a counter weight was secured opposite to it. The counter weight was used to even out vibration caused by the unbalanced weight of the connecting pin and the sliding block. The holes were located at different locations with different distances to the centre of the flange. Changing the distances gave different oscillating amplitudes.

The sliding block was made of phosphor bronze (see fig. 6.4). Phosphor bronze liners (3mm thickness) were applied to the contact areas of the sliding mechanism. The central oscillating part could be detached from the frame. Therefore liners could be repaired and renewed in case of wear. Grease was applied to reduce friction between the contact areas. Fabricated eyes (see Drg. No. 007, sheets 7 and 8 of 9) were mounted at the ends of the vertical bars of the oscillator. The eyes were

connected to a wire and pulley system. The eye of the lower end connection was fitted with a swivel joint. The tension of the wire was increased by screwing down the fabricated eye with the swivel joint. Lock nuts were used to fix the positions of the fabricated eyes and keep the wire under tension.

2.3 The Wire and Pulley System

The linear sinusoidal oscillation was transformed into an angular sinusoidal oscillation using a wire and pulley system. The wire was connected to the oscillator and formed a closed loop. It was clamped by three small clamps on each pulley to stop slip between the wire and pulleys. Therefore the linear displacement of the oscillator was transferred into an angular displacement. Phosphor bronze bushes were used to reduce friction between the pulleys and their axles. Grease nipples were fitted on the axles for lubrication.

2.4 The Three Bar System

The lower pulley was welded on to the upper oscillating arm (CD) of a three bar system, which is shown in drawing Drg. No. 006. The lower oscillating arm of this system is the pivot of the flexible fin propeller model (Drg. No. 003). The pivot was made of stainless steel. The connections between bars are shown in drawings Drg. No. 005 and 009. Since the lengths of the upper and lower oscillating bar were the same (170 mm), the angular oscillation of the pulley was copied down to the pivot. Phosphor bronze bushes and washers were fitted at the contact areas of moving parts above water and grease was applied to lower down the friction. Phosphor bronze was not applicable for conditions under water because of corrosion. A nylon material (Nylatron) was chosen for the under water bushes. Stainless steel shafts were used for those moving parts under water. The pivot was supported by two stainless steel supporting brackets mounted on the propulsive force measuring arm (see Drg. No. 004).

2.5 The Propulsive-Force-Measuring-Arm

The propulsive-force-measuring-arm was an L-shaped bar. The stainless steel pivot was supported at its lower end. The force generated by the oscillating foil acted on the pivot and hence on this L shaped bar. The arm was supported by a hinge (point D, fig. 6.2). The upper horizontal arm is the support for the load cell (see Drg. No. 008), which will be discussed in section 4. A solid mild steel bar (75 mm x 55 mm) was mounted on the supporting platform (Drg. No. 11, sheet 1 of 3) to provide a machined flat surface for the mounting of the other side of the load cell. Problems of welding distortion from the fabricated supporting frame were overcome by machining the surface of this mild steel bar.

2.6 The Flexible Bars and Foil Clamp

The ends of the flexible bars were sandwiched for reinforcement between metal plates. One end of the flexible bar was sandwiched with stainless steel plates and plugged into the slot of the pivot, as shown in Drg. No. 003. Two grub screws were used to hold the flexible bar in position and minimize vibration due to the clearance between the sandwiched end and the pivot. The other end of the flexible bar was sandwiched with aluminum plates and was connected to an aluminum foil clamp (Drg. No. 002). The function of this clamp was to hold the foil and connect it to the flexible bar. The clamp was split into two halves. Two screws were used to provide the clamping force. Since Poly-Vinyl-Chloride (PVC) was more easy to cut to shape, two PVC blocks were cut to shape to hold the foil. A soft rubber lining was used to provide a soft surface to clamp onto the foil. The aluminum clamp held the PVC block and the PVC block clamped the foil through the soft medium.

2.7 The Enclosing Strut

Part of the propulsive force measuring arm and the three bar system was located under water level; this part was enclosed by a PVC strut. The strut was faired to reduce

eddy flow around the foil. The design of the strut is presented in Drg. No. 012. The upper portion of the rear end was removable for the installation of the test rig. There were slots to lock this removable portion onto the main fairing strut. The strut was towed by a tee-bar which was mounted on a rectangular tube and was clamped onto the carriage.

3.0 FUNCTIONS OF INDIVIDUAL COMPONENTS OF THE TEST RIG

The test rig was assembled at the dock area of the testing tank in the Hydrodynamics Laboratory. The rig was supported on the sub-carriage with the whole rig out of the water. The functions of individual components were checked.

3.1 The Conversion From Linear Displacement into Angular Displacement

The sliding mechanism of the sinusoidal oscillator was connected to the holed flange through a connecting pin, as described in section 2.2. The amplitudes of the linear oscillation of the oscillator were controlled by plugging the connecting pin into different holes of the holed flange. The distances between the centre of holes to the centre of the flange were different for each pair of holes. These distances defined the amplitude of the linear sinusoidal oscillation and are set out in table 6.1:

<u>Hole</u>	<u>Distance from the Centre of Hole to Centre of Flange (mm)</u>
A	29.7
B	37.1
C	44.5
D	51.9
E	59.3
F	66.8

Table 6.1 The Distances of Centres of Holes to the Centre of Flange

This linear displacement was transformed into an angular displacement by the wire and pulley system. The angular displacement (in radians) of the pulley was found by dividing the linear displacement by the distance between the centre of the groove of pulley to the centre of the pulley, as shown in Drg. No. 006. A linear sinusoidal oscillation with the connecting pin at hole A generated a sinusoidal angular oscillation with an amplitude of 20° . Similarly, hole B, C, D, E, and F generated angular oscillating amplitudes (θ_{Ao}) of 25° , 30° , 35° , 40° and 45° respectively.

Angular displacement (θ_A) was confirmed by checking the vertical displacement (x_d) at the connecting bar of the three bar system, as shown in fig. 6.5, where

$$x_d = 170 \cdot \sin \theta_A \quad - 6.1$$

The relationship between the holes of the holed flange, angular oscillating amplitude and vertical displacement (x_d) were as listed in table 6.2,

<u>Holes</u>	<u>Angular Displacement</u> <u>at Pivot</u>	<u>Calculated Vertical</u> <u>Displacement (x_d)</u>	<u>Measured</u> <u>Displacement</u>
A	20°	58.1 mm	57.0 mm
B	25°	71.8 mm	73.0 mm
C	30°	85.0 mm	86.0 mm
D	35°	97.5 mm	97.0 mm
E	40°	109.3 mm	109.0 mm
F	45°	120.2 mm	120.0 mm

Table 6.2 The Relationship Between the Holes, Angular Oscillating Amplitude and x_d

Linear displacements (x_d) were measured and compared to the design values, as shown in the above table. Good agreement was found. The average error in terms of the angular amplitude at the pivot was less than 0.5° .

3.2 The Angular Sinusoidal Oscillation

The angular sinusoidal oscillation was also checked. A linear variable differential transformer (LVDT) was used to record the oscillation. The wire of the LVDT was mounted onto the upper hinge of the three bar system, as shown in fig. 6.5. When the upper bar CD was horizontal, the wire length from the centre of the pulley to the hinge was (l_s). At a specified instant of time (t), the bar CD was at an angle of (θ_A) to the horizontal. The relationship between l_t , l_o , & l_s is

$$l_t = \sqrt{l_o^2 + l_s^2}, \quad - 6.2$$

where $l_s = 2172$ mm and $l_o = 170$ mm. Therefore l_t was a constant and

$$(\theta_t + \theta_A) = \tan^{-1} \left(\frac{l_s}{l_o} \right) \quad - 6.3$$

was also a constant. The movement was recorded through the LVDT as (Δl) where

$$l_x = l_s - \Delta l \quad - 6.4$$

From the cosine rule,

$$l_x^2 = l_o^2 + l_t^2 - 2l_o l_t \cos \theta_t \quad - 6.5$$

therefore

$$\theta_t = \cos^{-1} \left(\frac{l_o^2 + l_t^2 - l_x^2}{2 \cdot l_o \cdot l_t} \right), \quad - 6.6$$

and θ_A was found from eqn. 6.3 using eqn. 6.6.

The relationship between the recorded displacement (Δl) by LVDT and the oscillating angle (θ_A) was set up by using eqns. 6.2-6.6. Since the length l_s was large in comparison to Δl , the oscillating angle (θ_A) could be calculated as,

$$\theta_A \approx \sin^{-1} \left(\frac{\Delta l}{170} \right) \quad - 6.7$$

There was no significant difference between the two results estimated by eqns. 6.7 and 6.2-6.6. The time series of the oscillating angles (θ_A) were calculated from the time series records of Δl . The calculated oscillating angles were plotted against time and compared to a pure cosine function with an equal oscillating amplitude. Examples are shown in fig. 6.6 a and b. The corresponding oscillating amplitude for both figs. 6.6a and b was 45° . The rotation speed was 1.5 rads^{-1} (14.5 rpm) for fig. 6.6a and 3.3 rads^{-1} (31.6 rpm) for fig. 6.6b. The rotation speed of 1.5 rads^{-1} was the speed at which the system started to rotate. The output power from the A.C. motor at this rotation speed just overcame the friction of the system and the oscillation was not smooth. At higher rotation speeds, the output power was increased and the oscillation was smooth: a nearly pure sinusoidal angular oscillation was obtained (fig. 6.6b). From this test, a lower limit on rotation speed was applied for a pure sinusoidal oscillation. This limit was set at 2.1 rads^{-1} (20 rpm).

3.3 The Motion of the Connecting Bar (BC)

The whole test rig was set up according to a global axes system (horizontal and vertical axes). The three bar system was rotated to different positions. The connecting bar (BC) moved in and out, and up and down, as the upper oscillating arm (CD) oscillated (fig. 6.5). A spirit level was used to check the motion of bar (BC). The spirit level indicated that the bar (BC) remained vertical at all positions as the system oscillated.

4.0 THE DYNAMOMETER

4.1 Measurement of Propulsive Thrust

The propulsive thrust (F_H) generated by the flexible fin propeller was measured by the propulsive thrust measuring arm. This L-shaped rigid bar was supported by a hinge at D (fig. 6.2). The propulsive thrust (F_H) acting at the pivot generated an anti-clockwise moment ($F_H \cdot l_1$) at hinge D. This moment was counteracted by a force (F_{out}) acting on the horizontal bar of the measuring arm. This force (F_{out}) was measured by a load cell. The relation between the propulsive thrust (F_H) and the measured force (F_{out}) was as follows,

$$F_{out} = F_H \frac{l_1}{l_2} \quad - 6.8$$

There were six different positions to mount the load cell and hence six different values of l_2 (see Drg. No. 008). This allowed the propulsive thrust to be amplified by six different levels. Four positions were used here.

Equation 6.8 is true in ideal conditions. In practice, owing to the friction at the hinge and pivot, another factor (K_{out}) is included in eqn. 6.8, as

$$F_{out} = F_H \frac{l_1}{l_2} (1 - K_{out}) \quad - 6.9$$

The force was transferred from the pivot to the load cell and K_{out} represented the frictional effect on the force transmission through hinges. Calibrations were done to find the factors (K_{out}) for the different positions. Since it was a static calibration, this factor (K_{out}) represents the effect of static friction at the hinge (D) (fig. 6.2) and pivot on the transferring force from the pivot to the load cell. Both tension and compression were tested. Weight was applied to the pivot through a wire and pulley system, as

shown in fig. 6.7. The applied weights (F_H) were plotted against the measured weights (F_{out}) for both tension and compression and are shown in fig. 6.8 a and b. The moment arm of the applied weight was constant at 1200 mm. The results from these calibrations are shown in table 6.3.

Position	l_2 (mm)	l_1/l_2	K_{out} (Compression)	K_{out} (Tension)
1	600	2.0	0.12	0.12
2	500	2.4	0.12	0.11
3	400	3.0	0.16	0.13
4	300	4.0	0.19	0.17

Table 6.3 Results from the Calibration of the Propulsive Thrust Measuring Arm

The load range of the load cell used in this model test was 50 kg. Both tensile and compression forces could be recorded by this load cell. The maximum deflection at full load was 0.5 mm. This low deflection characteristic kept the factor (l_1/l_2) in eqn. 6.9 constant under a wide range of loading. In addition, the low deflection under loads resulted in a good dynamic response. Internal thermal compensation was installed in the load cell.

4.2 Measurement of Input Power

The input power was calculated by combining the moment applied to the pivot to drive the flexible fin propeller and the angular oscillating velocity at the pivot as

$$\text{Input power} = M_A \cdot \dot{\theta}_A \quad - 6.10$$

A) Angular Oscillating Velocity

As described in section 3.2, a LVDT was used to measure the changes in displacement of arm CD and, hence, calculate the angular oscillating angle (θ_A). Since

a nearly sinusoidal angular oscillation was confirmed, the relationship between the angle (θ_A) and its oscillating velocity at an instant of time (t) was,

$$\begin{aligned}\theta_A &= \theta_{Ao} \cos(\omega t) \\ \dot{\theta}_A &= -\theta_{Ao} \omega \sin(\omega t)\end{aligned}\quad - 6.11$$

The corresponding velocity at any instant of time could be obtained.

B) The Moment Applied to the Pivot

A load cell was installed in the vertical connecting bar (BC) of the three bar system near the upper hinge (C), as shown in fig. 6.9a. This load cell was the same type as the one used to measure propulsive thrust. Tensile and compression forces acting on this connecting bar (BC) were recorded through this load cell. As the bar BC had hinged ends and the load cell was mounted at the upper end, no significant bending moment acted on the load cell. This load cell could be damaged very easily by bending moment. Since it was confirmed that bar (BC) remained vertical at all positions within an oscillating cycle, the moment (M_A) applied to the pivot to drive the flexible fin propeller was calculated by the following relationship,

$$M_A = F_{in} \cdot l_3 \quad - 6.12$$

where l_3 = the horizontal distance between the bar (BC) and the pivot

$$= l_o \cos \theta_A \quad - 6.13$$

According to this relationship, the moment (M_A) applied to drive the model was calculated by using recorded values from the load cell and the LVDT. The input power to the whole system at an instant of time (t) was calculated by eqn. 6.10.

In practice, as with the measurement of propulsive thrust, the moment acting at the pivot is not exactly the same as the measured thrust (F_{in}) times the moment arm (l_3). A factor (K_{in}) was introduced in eqn. 6.12, as

$$M_A \cdot (1 - K_{in}) = F_{in} \cdot l_3 \quad - 6.14$$

A calibration was done to find this factor (K_{in}) in both tension and compression conditions. A rigid bar was connected to the pivot and weight was applied to the bar and this generated a moment acting at the pivot, as shown in fig. 6.9b. The three bar system was restrained and clamped at its neutral position ($\theta_A = 0$). Bar (CD) was clamped to a fixed structure. In the tension condition, weight was applied to the rigid bar through a pulley system. In the compression condition, weight was put on to the rigid bar directly. In both conditions, the moment arm was 700 mm from the pivot. The corresponding tension and compression forces were recorded by the load cell. Measured moments were calculated and plotted against applied moment, as shown in fig. 6.10a and b. The factors (K_{in}) in tension and compression conditions were found as 0.22 and 0.24, respectively. This meant that the moment recorded was about 77% of the actual moment (M_A) at the pivot.

4.3 The Friction Factors K_{out} and K_{in}

The calibrations mentioned in the previous sections were static calibrations. The friction involved in these calibrations was a static friction. In the model test, the measured forces were oscillating forces. Consequently, dynamic friction in the hinges and pivot should be considered in the force and moment transfer. At particular instants, the forces changed direction and static friction might occur. In addition, the hinges were all lubricated. The corresponding dynamic friction was expected to be smaller but not very much smaller than the static friction. In a simple frictional test, dynamic friction was found to be about 60% of static friction. Therefore the factors, K_{in} and K_{out} , used in calculating the propulsive thrust and the input power were taken as 60% of those

obtained from the static test. Propulsive thrust and efficiency were not particularly sensitive to these frictional corrections. Propulsive thrust obtained with a static friction correction is up to about 8% higher than that obtained with a dynamic friction correction. Similarly, the one without any friction correction is about 9% lower than the one with a dynamic friction correction. The propulsive efficiency with a static frictional correction and without any correction on friction is about 4% higher and 3% lower than the one with dynamic friction correction, respectively.

4.4 The Speed Tachometer

An AC frequency controller was used to control the rotation speed of the motor. Since an oscillating cycle is completed every rotation cycle at the output of the reduction gear box, the rotation speed is the same as the oscillating frequency.

Light reflective tapes, each of 5mm wide, mounted on the circumference of the rigid flange of the oscillator. Each piece of reflective tape was separated by black adhesive tape with equal divisions. An optical sensor was used to count the number of reflections per second and this was converted back into revolutions per minute. The rpm value was shown on a tachometer. By using this method, the required oscillating frequency was set for a test run.

5.0 CONCLUSIONS

A test rig and force dynamometer for the flexible fin propeller model was designed and built. The functions of its components and the quality of the sinusoidal angular oscillation at the pivot of model were checked. A lowest limit of oscillating frequency of 2.1 rads^{-1} was set for a nearly pure sinusoidal angular oscillation. The force dynamometer was calibrated and frictional factors were found.

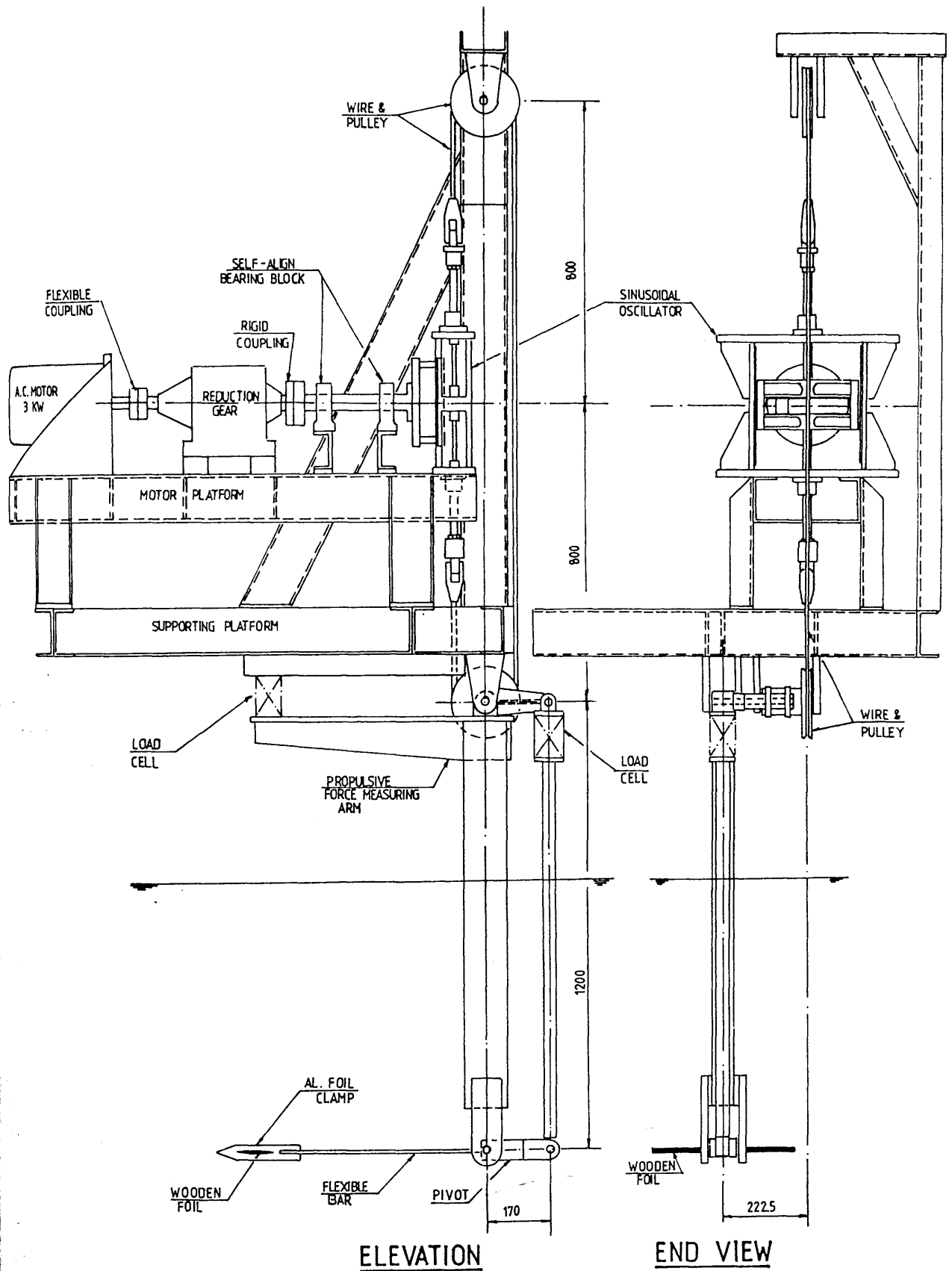
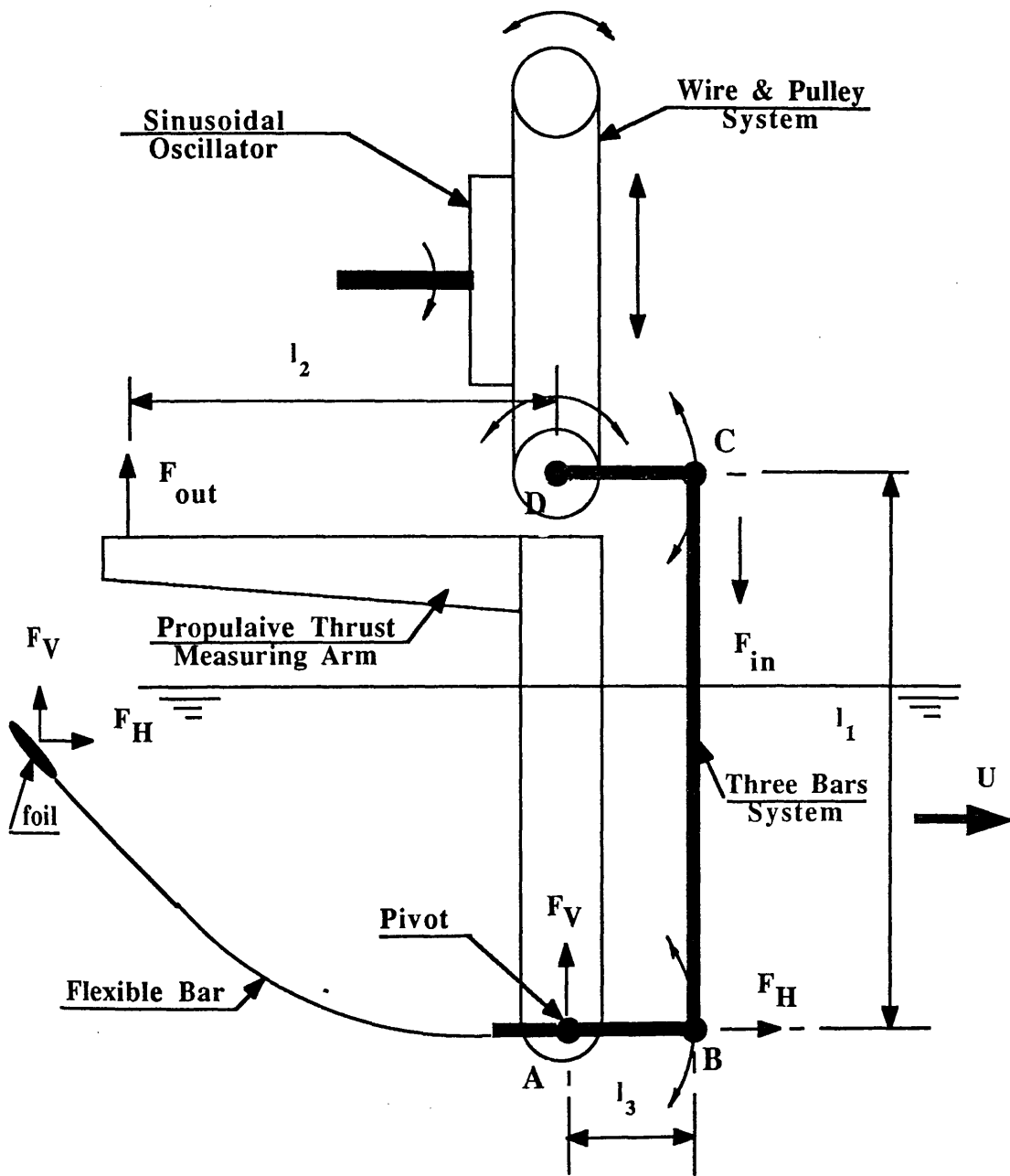


Fig. 6.1 GENERAL ARRANGEMENT OF THE FLEXIBLE FIN PROPELLER MODEL



**DIAGRAMMATIC ARRANGEMENT
OF
THE FLEXIBLE FIN PROPELLER MODEL**

Fig. 6.2

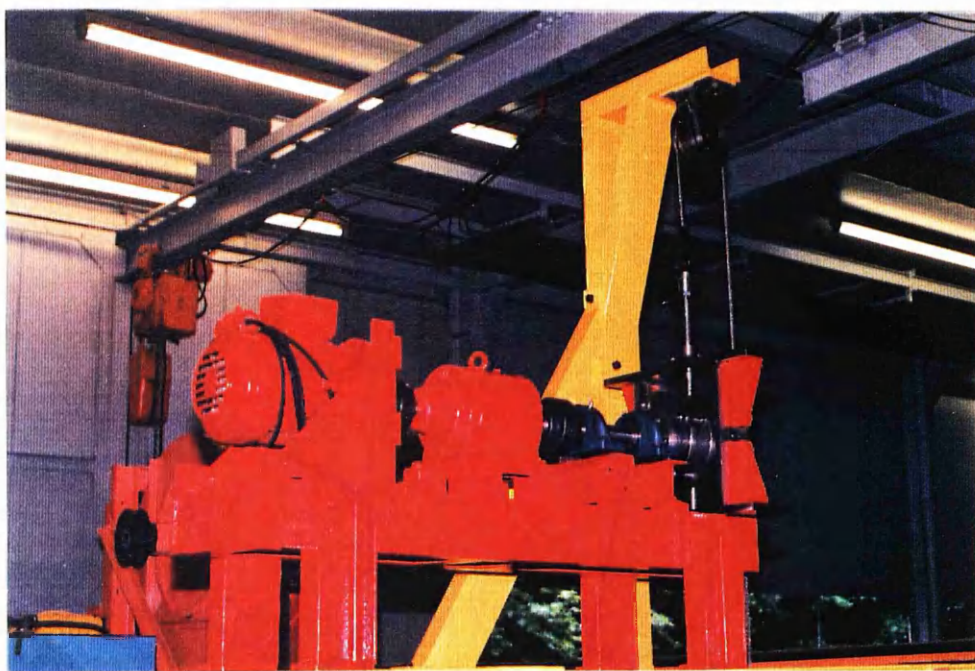


Fig. 6.3 The Driving Unit of the Test Rig

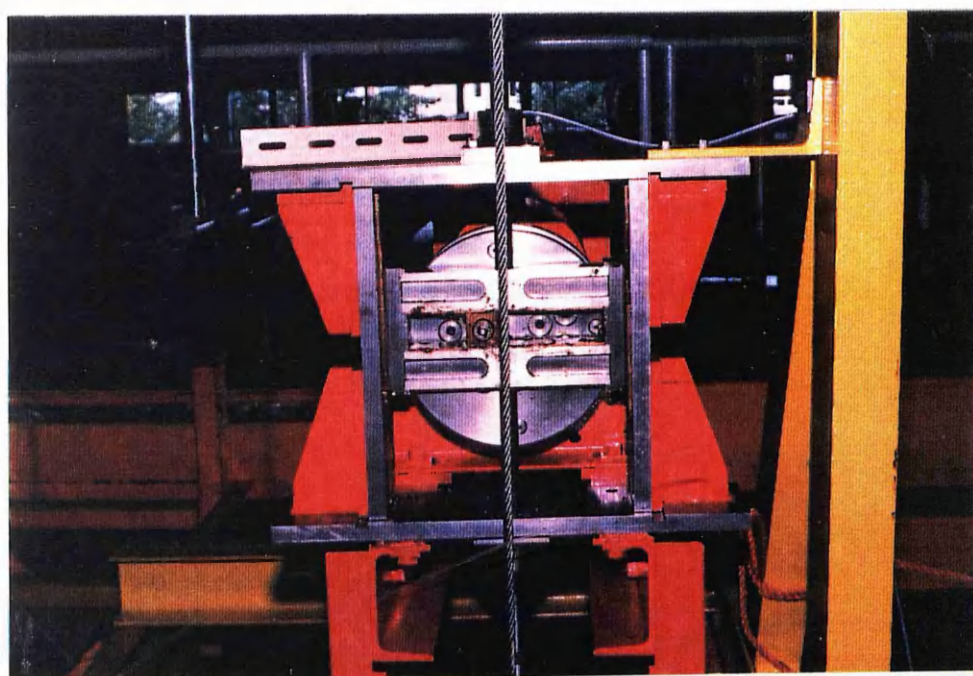
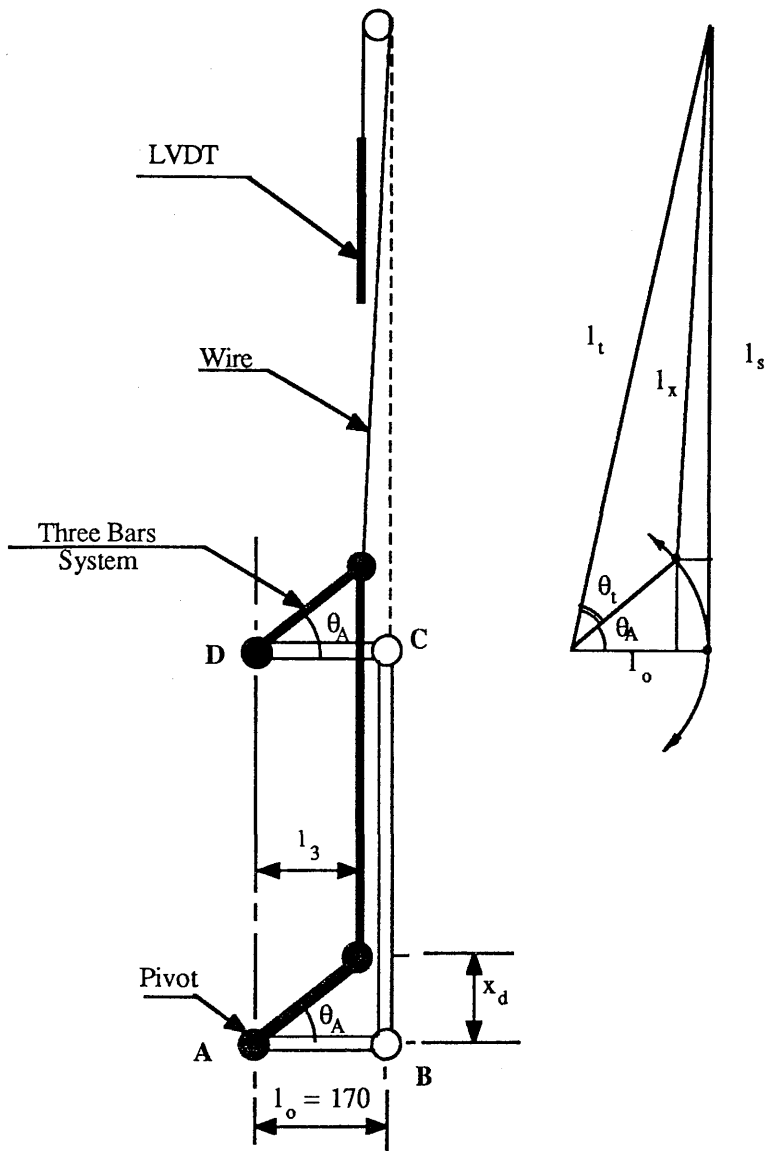
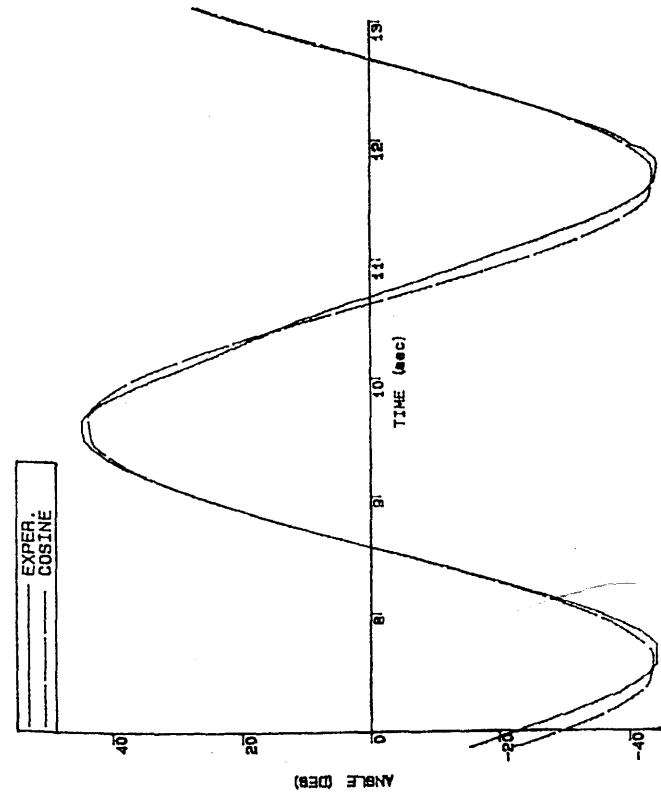


Fig. 6.4 The Sinusoidal Oscillator



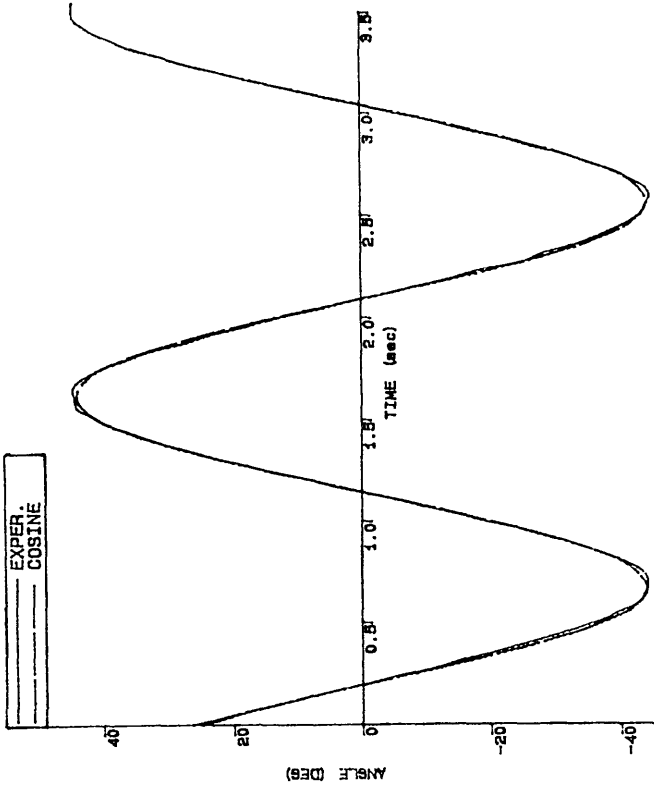
THE ARRANGEMENT OF THE LVDT FOR MEASURING THE ANGULAR OSCILLATING MOTION.

Fig. 6.5



ANGULAR OSCILLATION AT HOLE F
 ROTATING SPEED = 1.5 rad/s

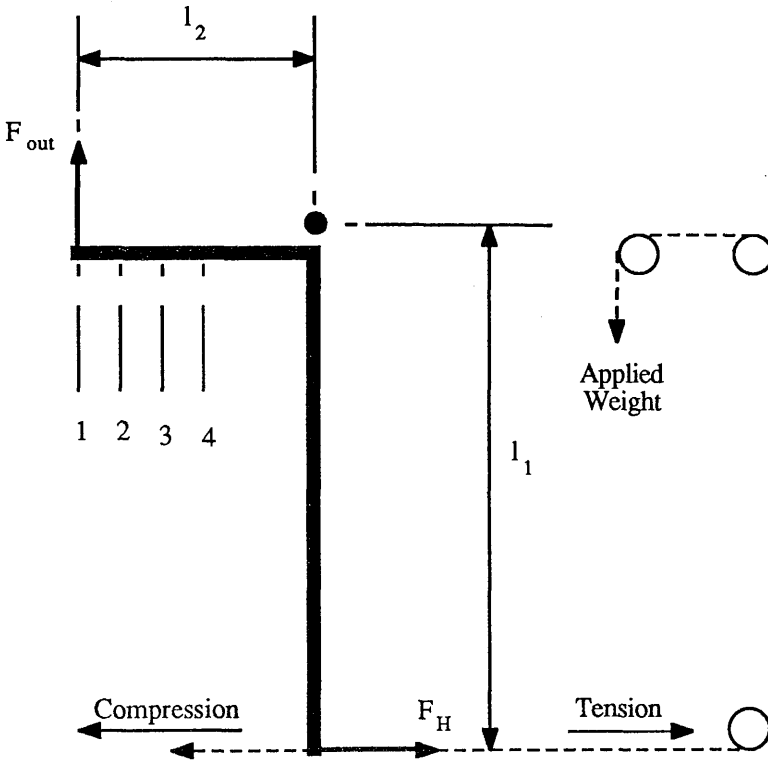
(a)



ANGULAR OSCILLATION AT HOLE F
 ROTATING SPEED = 3.3 rad/s

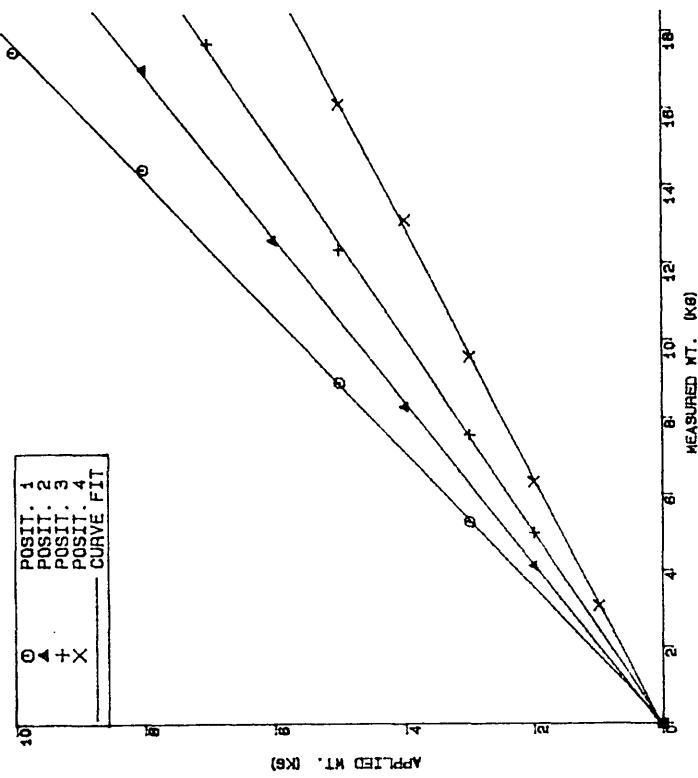
(b)

Fig. 6.6 Comparison of the Measured Angular Oscillation and The Cosine Function



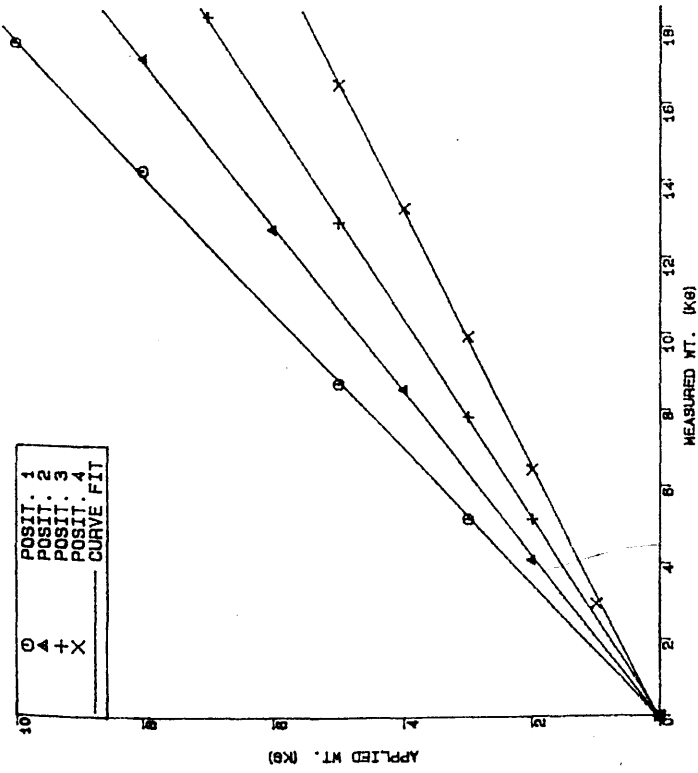
Arrangement of Calibration of the Propulsive Thrust Measuring Arm

Fig. 6.7



CAL. OF PROPULSIVE THRUST
MEASURING ARM (TENSION)

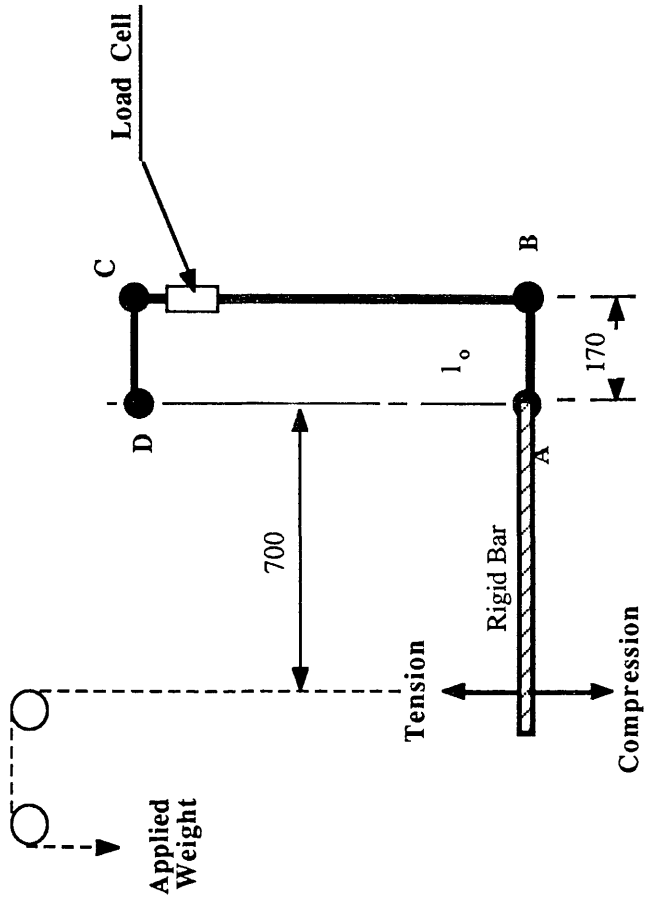
(a)



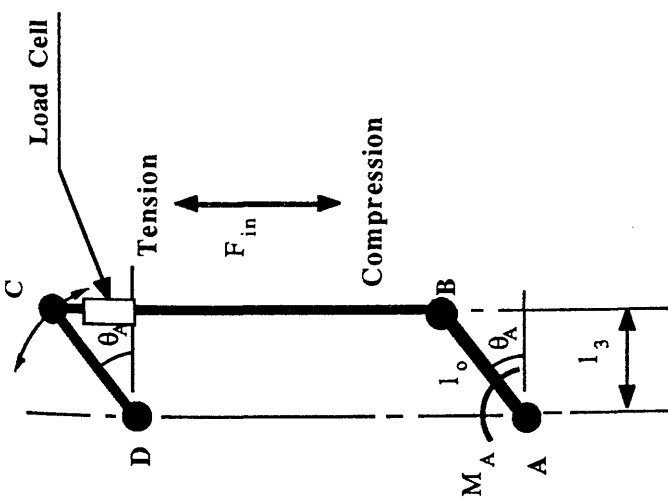
CAL. OF PROPULSIVE THRUST
MEASURING ARM (COMPRESSION)

(b)

Fig. 6.8 Calibration of Propulsive Thrust Measuring Arm

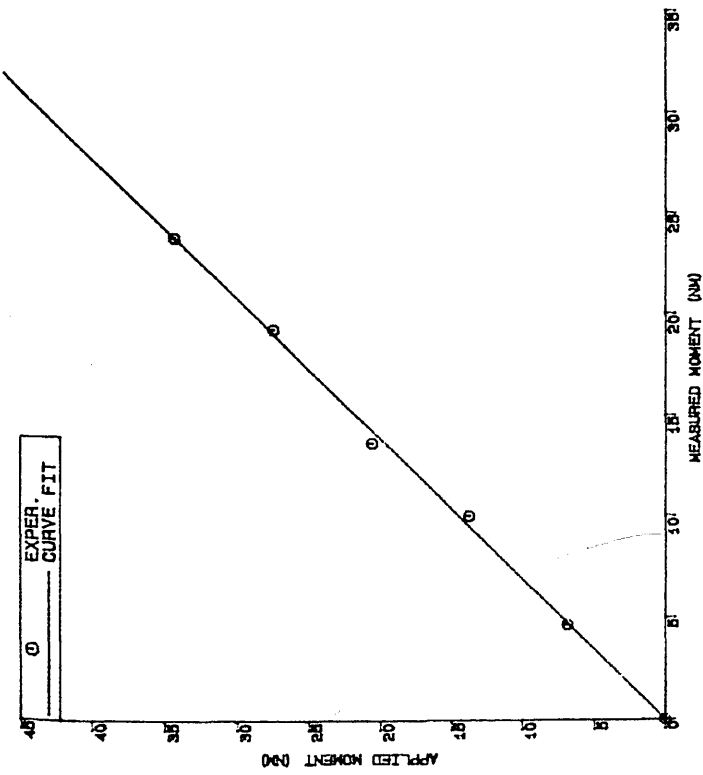


(a) The Measurement of the Input Power



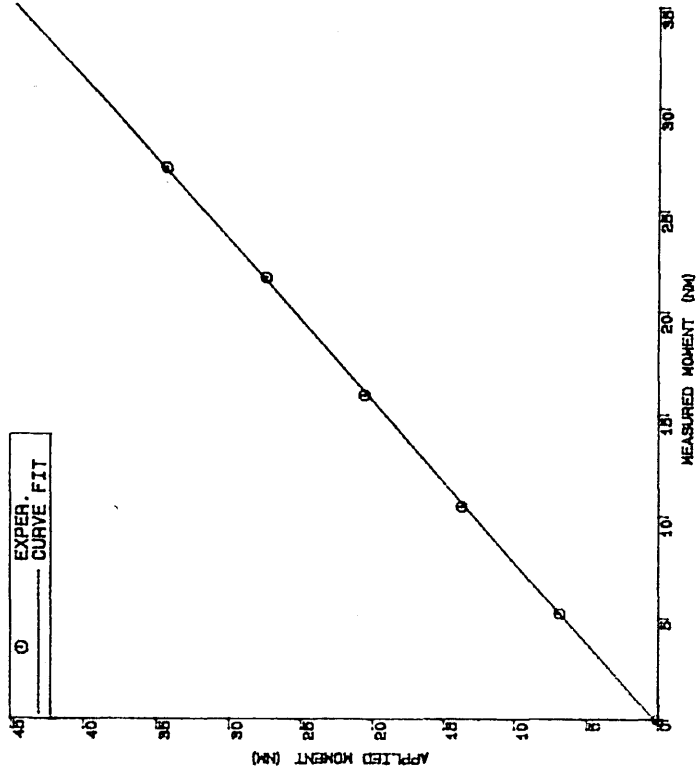
(b) Arrangement of Calibration of Input Thrust Measurement

Fig. 6.9



CAL. OF MEASUREMENT OF THE
MOMENT ACTING AT THE PIVOT

(a) Tension



CAL. OF MEASUREMENT OF THE
MOMENT ACTING AT THE PIVOT

(b) Compression

Fig. 6.10 Calibration of the Measured Moment Acting at the Pivot

CHAPTER 7

EXPERIMENTAL PERFORMANCE OF THE FLEXIBLE FIN PROPELLER

1.0 INTRODUCTION

In Chapter 5.0, a preliminary investigation of the performance of the flexible fin propeller, by using a theoretical model, was described. In order to investigate the ability and limitations of the theoretical model, an experimental study of the performance of the flexible fin propeller was carried out.

A flexible fin propeller model with a rectangular oscillating foil of aspect ratio 4.0 was tested in the Hydrodynamics Laboratory (tank 77m long x 4.6m wide x 2.4m water depth), at the Department of Naval Architecture and Ocean Engineering, University of Glasgow. The incoming flow velocity and frictional loss in the driving mechanism were investigated. The performance of the flexible fin propeller was tested in both forward and zero speed conditions. Experimental results are compared with theoretical results from a linearised mathematical model.

Propulsive thrust coefficient (C_T) of the propeller was found to increase by increasing the stiffness function (ξ), the angular oscillating function (ζ) and the reduced frequency (k); propulsive efficiency (η) increases as the stiffness function decreases. Maximum propulsive efficiencies around 0.7 are obtained when there is:

- low oscillating frequency ($k < 0.3$);
- low value of stiffness function (1.8); and,
- low value of angular oscillating functions (3.5).

In the zero speed condition, the propulsive thrust coefficient (C_{Tb}) decreases as oscillating frequency increases. It is shown that it is feasible to apply this flexible fin propeller to a small ship from the view point of its hydrodynamic performance.

2.0 THE FLEXIBLE FIN PROPELLER MODEL

The flexible fin propeller model is made up of a flexible bar and a foil, as shown in fig. 7.1. Two flexible bars were used to provide different stiffness functions and taper ratios. A rectangular foil was used in this experimental investigation. The details of the flexible bars and the foil are described in the following sub-sections.

2.1 The Bending Moduli of the Flexible Bars

Flexible bars for the model were purchased from Aquabattern. These bars are designed for sail battens and have a range of flexibilities. Three different grades of bars were ordered and coded as SO (green), ST (red) and XST (blue) by the manufacturer. However the mechanical properties of these bars were not known. The bending modulus (E) of these bars was one of the important parameters required in the study.

Two bars with different lengths (600mm and 1000mm) for each grade were purchased. The shorter one was used in testing the bending moduli. Here the shorter bars are coded with their grades as BAR-SO, BAR-ST and BAR-XST. All bars were the same in width (50mm) but different in thickness. The thickness distribution was stepped because of the manufacturing method and is shown in fig. 7.2. The thickness distribution is assumed to be linear.

A simple bending test was done to test these bars. These bars were clamped at one end and various vertical loadings were applied at the other end. The deflections in the x-direction (Δx) and in the y-direction (Δy) were measured, as shown in fig. 7.3. The results are presented in figs. 7.4a and b.

The program (FINBAR), which was based on the computation method described in section 4 of Chapter 4, was used to estimate the bending moduli of the flexible bars for the given thickness at both ends, lengths and loadings. The deflections based on the large deflection beam theory were computed with an estimated bending modulus for the given loading (F_V). The bending moduli were found by matching the computed deflections with the experimental deflections. The bending moduli were estimated through the whole range of loadings. The results are shown in table 7.1, 7.2 and 7.3 for BAR-SO, BAR-ST and BAR-XST respectively. Good agreement was found between the calculated deflections and the experimental results. The bending moduli of these grades of bar were found by combining the bending test results and computation based on large-deflection beam theory.

Timmins [1977] states that the modulus of unidirectional 'E'-glass (62% by volume) with Epoxy is about 35.8 GNm^{-2} . The bending moduli found are within the range of published moduli [Fibreglass Ltd 1977, Bose 1982] for unidirectional fibre-glass reinforced plastic.

2.2 The Flexible Bar

Two flexible bars were used to provide different flexibilities and taper ratios during the tests. These two bars were the longer bars 1000 mm and 50mm wide, but different in thickness. The grades of these bars according to the manufacturer were ST and XST. These bars were colour coded according to their stiffness as BAR-R (red for ST) and BAR-B (blue for XST) for soft and stiff respectively and distinct from the bars used for the bending moduli tests.

These bars were cut down to 660 mm in length to suit the model test and then sandwiched between metal plates at their ends for the connections at the pivot and foil clamp. The actual flexible section (L_o) was 500mm in length. The corresponding thickness of these two bars is plotted against distance from the pivot to the foil clamp and is shown in fig. 7.5. A linear variation in thickness was assumed and this is shown

by straight lines in this figure. The particulars of these bars are listed in the following table

	<u>BAR-R</u>	<u>BAR-B</u>
Thickness at Free End (t_1) mm	2.9	3.8
Thickness at Fix End (t_2) mm	4.2	5.1
Mean Thickness (t_m) mm	3.6	4.5
Taper Ratio (TR)	0.37	0.30
Bending Modulus (E) Nmm ⁻²	37.64×10^3	38.00×10^3
Mean Sectional Modulus (I_m) mm ⁴	1.90×10^2	3.69×10^2

Table 7.4 The Particulars of the flexible bars

2.3 The Foil

A wooden rectangular foil with an aspect ratio of four was used in this investigation. A NACA 16-012 wing section was chosen for the cross section of the foil. This NACA 16-series wing section is characterized by a small leading edge radius and uniform pressure distribution. This series of wing sections have proved useful for propellers [Abbott and Von Doenhoff 1959]. The section used in this investigation has minimum pressure at 60 % of the chord at zero angle of attack and a thickness to chord ratio of 0.12. The foil and wing section is shown in fig. 7.6 and the offsets of the cross-section are listed in table 7.5 .

3.0 DATA COLLECTION AND ANALYSIS

Four parameters were recorded during the tests: output propulsive thrust, input thrust, angular oscillation and rotation speed. The set up of this experiment is shown in fig. 7.7. The output thrust and input thrust were measured by load cells while angular rotation and rotation speed were recorded by a linear variable differential transformer (LVDT) and a speed tachometer respectively, as described in Chapter 6.

Four channels of data were recorded:

- i) channel 1 for collecting data from the load cell which measured the propulsive thrust;
- ii) channel 2 which recorded the input thrust from the load cell mounted on the three bar system;
- iii) channel 3 for measuring the angular oscillating motion through a LVDT; and,
- iv) channel 4 which recorded the signal from the tachometer for rotation speed.

The signals from four channels were fed to amplifiers and recorded on a pen recorder (W+W 500^{SP} signal processor).

When the system was operating, a high frequency vibration was recorded on channel 1, the load cell for measuring propulsive thrust. The load cell mount was a T-section cantilever, as shown in Drg No. 008. The pivot of the flexible fin propeller was supported at the lower end of the vertical column of the measuring arm. A high frequency vibration was generated as the system oscillated and this was enlarged at the free end of the cantilever where the load cell was mounted. This frequency of vibration was much higher than the operating frequency and it was removed by using a low pass filter. An example of the chart records for the experimental results is shown in fig. 7.8.

Signals from channel 1, 2 and 3 were collected by an IBM PC computer using a data collection package (PC500H). The pen recorder (W+W 500^{SP}) also acted as an analogue to digital converter. The sampling rate for data collection was a function of the number of channels used. In order to keep the sampling rate high, only data from these three channels were collected by computer. The maximum sampling rate for three channels was 20 Hz. The maximum oscillating frequency of this model test was 1.2 Hz. Therefore the minimum number of samples to describe an oscillating cycle at this maximum frequency was 23. The frequency of the propulsive thrust was twice that of the oscillating frequency of the whole system, as shown in section 4.3 of Chapter 3.

The number of samples to describe an oscillating cycle of the propulsive thrust was about 11. The sample rate of 20 Hz was the minimum acceptable rate.

The data files were transformed into ASCII digital files by using the package (PC500H). The data files could be transformed into three different formats: LOTUS 123; ASYST; and, DADiSP. Here, the data files were transformed into the format of DADiSP. After this transformation, a number of files were created from each data file, one for each of the channels which had been used. A typical file is shown in table 7.6. The header of these digital files represents the number of samples, the channel number, the time interval and a comment describing the file.

These ASCII data files were transferred to the main computer system (VAX 11/730) of the Hydrodynamics Laboratory using a program called KERMIT. A computer program (ANALFFP.FOR) was written to read these ASCII files and to plot the values on graphic terminals or a plotter. The user can choose a particular range of data for analysis. Propulsive thrust and corresponding input power were obtained by using the methods described in section 4 of Chapter 6. Frictional losses and their effect on propulsive thrust measurement, which are discussed in section 5 of this chapter, were taken into account in this program.

The oscillating frequency was measured from the chart records for the analysis. Since the paper advancing speed was 1.0 cm per second, the distance between peaks of the LVDT records was used to calculate the oscillating frequency.

The propulsive thrust coefficient (C_T) was calculated from the mean propulsive thrust as follows,

$$C_T = \frac{F_T}{\frac{1}{2} \rho U^2 S}, \quad - 7.1$$

where

$$F_T = \frac{\int_{t=0}^{t=N \cdot T} F_H \cdot dt}{N \cdot T}$$

The efficiency was calculated as follows,

$$\eta = \frac{\text{Output}}{\text{Input}} = \frac{\int_{t=0}^{t=N \cdot T} F_H \cdot U \cdot dt}{\int_{t=0}^{t=N \cdot T} M_A \cdot \dot{\theta}_A \cdot dt} \quad - 7.2$$

A number of complete cycles (N) were analysed from each run. A NAG routine (D01GAF) [NAG 1988] was used to do the numerical integration. This routine uses the third-order finite different formulae according to Gill and Miller [1972].

4.0 THE FLOW VELOCITY AROUND THE OSCILLATING FOIL

Part of the propulsive thrust measuring arm and the three bar system were located under water and these parts were covered by a surface piercing fairing strut. When the model and test rig advanced through calm water, the oscillation of the three bar system and the presence of the propulsive thrust measuring arm generated a disturbance to the incoming flow at the oscillating foil. The fairing strut was used to reduce this disturbance. However, the fairing strut also created a disturbance to the free stream flow and so the flow velocity at the position of the foil was investigated.

A current flowmeter system (STREAMFLO) was used to measure the flow velocity for this investigation. The flow meter was supplied by Nixon Instrumentation Limited. Two streamflow measuring probes, one a low speed probe and the other a high speed probe, were supplied. The low speed probe (type no. 413) is for a range of flow velocities from 0.02 ms^{-1} to 1.30 ms^{-1} . The high speed probe (type no. 414) is for a range of flow velocity from 0.60 ms^{-1} to 3.00 ms^{-1} . The measuring heads are

protected by a nickel plated bronze cage. The head consists of a five bladed rotor mounted on a hard stainless steel spindle. This spindle is supported on a smooth bearing. The friction is extremely low. When the rotor is immersed in an incoming fluid, the rotor rotates and the passage of the rotor past a gold wire tip slightly varies the measurable impedance between the tip and the tube. The frequency in Hz is calibrated against flow velocity in ms^{-1} . This frequency is then converted into a voltage output form and is displayed on an analogue indicator. This output was recorded on a pen recorder (W+W 500^{SP}) and also converted into digital values and stored in the IBM-PC using the data collection package PC500H.

In order to set up the relationship between output from the flow meter (in voltage) and free stream velocity, these two probes were first calibrated. The probes were mounted on the main carriage of the towing tank and run at different velocities. The incoming flow to the probe was undisturbed and free stream flow velocity was measured. The corresponding output voltage was recorded and the results are presented in fig. 7.9a and b. The results from the two probes were curve-fitted by using straight lines with equations as follows:

i) low speed probe,

$$\text{flow velocity } (\text{ms}^{-1}) = 0.04705 + 0.26134 * (\text{measured voltage});$$

- 7.3

ii) high speed probe,

$$\text{flow velocity } (\text{ms}^{-1}) = 0.00362 + 0.86509 * (\text{measured voltage}).$$

- 7.4

The low-flow velocity probe was used to study the flow velocity around the foil. The flow velocities at five points were measured. The location of these points are shown in fig. 7.10. These points were located at the leading edge of the foil in its neutral position when the flexible bar was not deflected and was horizontal. Since the span of the foil was 400 mm, these five points covered the whole span. The flow velocity investigation was done for four free stream flow velocities: namely, 0.3, 0.5,

0.7 and 0.9 ms⁻¹.

A turbulent wake existed behind the fairing strut. Eddies decreased as the distance from the centre line increased. Mean flow velocities at these points were found and plotted against free stream velocities. The results are shown in fig. 7.11a and b. The corresponding flow velocity profiles across the span are shown in fig. 7.12. The flow velocity drops at locations close to the centre line (point C). The differences in flow velocity between the centre (C) and the tips (A & E) increases as the free stream velocity increases. Mean flow velocities at point A and E are over 90% of the free stream velocities. The mean flow velocity across the whole span of the foil was found by integrating the flow velocity profiles and divided by the span. The results are plotted against the free stream velocity and are plotted in fig. 7.13. The results were fitted to a second order polynomial,

$$Y = -0.04377 + 0.99534 X - 0.19226 X^2 \quad - 7.5$$

where Y = the mean incoming flow velocity to the foil, and
X = the free stream velocity.

5.0 FRICTIONAL LOSS TEST

Energy was spent to drive moving parts and overcome mechanical friction in the test rig. The lower end of the three bar system was connected to the pivot which was supported by the propulsive thrust measuring arm. The measured values of the propulsive thrust were masked by the influence of the oscillation of the three bar system. These two points were investigated.

The flexible bar and the rectangular foil were removed from the test rig. The system was operated over a range of oscillating frequencies from 2.1 rads⁻¹ to 7.3 rads⁻¹ (i.e. 20 rpm to 70 rpm). Three angular oscillating amplitudes (θ_{Ao}) were tested: these were 20°, 30° and 40° at holes A, C and E of the holed flange (see section 3.1 of

Chapter 6).

An example of records from different channels is shown in fig. 7.14. The effect of oscillations of the three bar system on the measurement of propulsive thrust is shown by the signal recorded through channel one. At the hinge point D of the propulsive thrust measuring arm (fig. 6.2), a clockwise moment was induced by a downward motion of the bar (BC). As a result, a compression force was measured by the load cell on the propulsive thrust measuring arm. Similarly a tensile force was measured for an upward motion of the bar (BC). This influence mainly comes from friction in the hinges and acceleration of the bars. A mean propulsive thrust was calculated from these measured values and is shown in fig. 7.15. The mean propulsive thrusts were all found to be negative. As shown in fig. 7.14, the negative values recorded by channel one are higher than the positive ones.

The input power to overcome friction and drive the system was also calculated. The results of input power for angular oscillating amplitudes at hole A, C and E are shown in figs. 7.16a, b and c. Both propulsive thrust and input power were curve-fitted to polynomial equations, as shown in the figures. The equations were used to calculate the intermediate values. These values were deducted from those measured in the performance tests, which are described in the following sections.

6.0 THE PERFORMANCE OF THE PROPELLER AT FORWARD SPEEDS

In this experiment, the performance of the flexible fin propeller at forward speeds was investigated for a range of reduced frequencies at different stiffness functions (ξ), angular oscillating functions (ζ), and taper ratios (TR).

6.1 Testing Conditions

In the present study, three different angular oscillating amplitudes were tested using different holes in the holed flange. Hole A, C and E were used to obtain an oscillating amplitude (θ_{Ao}) of 20° , 30° , and 40° respectively and the corresponding angular oscillating functions (ζ) were 3.5, 5.2 and 7.0.

The experiments were performed at three different free stream velocities of 0.4, 0.6 and 0.8 ms^{-1} for each flexible bar. The corresponding mean incoming flow velocities (U) to the foil were calculated by using eqn. 7.5 as 0.3, 0.5 and 0.6 ms^{-1} . The mean sectional moduli (I_m) were used to calculate the stiffness functions (ξ). The corresponding stiffness functions are listed in the following table.

	<u>BAR-R</u>	<u>BAR-B</u>
$U = 0.6 \text{ ms}^{-1}$	1.8	3.5
$U = 0.5 \text{ ms}^{-1}$	3.1	6.0
$U = 0.3 \text{ ms}^{-1}$	6.8	13.4

Table 7.7 The Stiffness Functions (ξ) for Different Flexible Bars
with Different Incoming Velocity

6.2 Net Propulsive Thrust and Input Power

The measured propulsive thrusts were masked by the effect of the oscillation of the three bar system as found in the investigation of frictional loss. The values measured from the performance test were compared to those from the frictional loss tests. The values recorded in the frictional loss test can be regarded as a fluctuating datum line for values measured in the performance test. An example is shown in fig. 7.17a and the net values are plotted in the fig. 7.17b. The mean propulsive thrust from the performance test was reduced by the value measured during the frictional loss tests. Similarly, the input power from the performance test was also corrected by the

corresponding result from the frictional loss test. The corresponding efficiency (η) was calculated from the net values of propulsive thrust and the input power.

6.3 Propulsive Thrust Coefficient

In this section, the experimental results are compared with theoretical results. These theoretical predictions were calculated by using the method described in chapter 4. The propulsive thrust coefficients at different angular oscillating functions (ζ) and stiffness functions for BAR-R (i.e. TR = 0.37) and BAR-B (i.e. TR = 0.30) are shown in fig. 7.18 and 7.19. The symbols in the figures are experimental results while the lines are theoretical predictions.

The experimental propulsive thrust coefficient was increased by increasing the stiffness functions and the angular oscillating functions. The same tendency was predicted by the theoretical model. From the theoretical model, it is found that the propulsive thrust is not sensitive to small changes in taper ratio of the flexible bar, as shown in section 5.2 Chapter 5. In this experiment, there were two conditions with similar stiffness functions but different taper ratios. The corresponding stiffness functions were 3.5 and 3.1 with a taper ratio of 0.3 and 0.37 respectively. In order to investigate the effect of taper ratio on propulsive thrust, the experimental results of these two conditions were re-plotted in fig. 7.20. There is no practical difference between these two different taper ratios.

In fig. 7.21a, the experimental results at a high reduced frequency of 0.6 are plotted against the stiffness functions to demonstrate the effect of stiffness of the bar. Since the effect of taper ratio on propulsive thrust is not significant, the results from two different taper ratios are plotted together. These results were curve-fitted into a second order polynomial equation to find intermediate points. At this high reduced frequency, the increment of the propulsive thrust coefficient is 70% as the stiffness function increases from 3.0 to 6.0 for corresponding angular oscillating functions. When the stiffness function is increased from 9.0 to 12.0, the propulsive thrust

coefficient increases by 20%. The effect of stiffness function on the propulsive thrust decreases as the stiffness function goes up. This was also found when using the theoretical model, as shown in section 5.1 of Chapter 5. The curved-fitted results from fig. 7.21a were plotted against the angular oscillating function (ζ) and are shown in fig. 7.21b. For a range of stiffness functions from 3.0 to 12.0, there is a mean increment in propulsive thrust of 30% by increasing the angular oscillating functions from 3.0 to 5.0. A greater improvement of 60% in propulsive thrust is obtained by increasing the angular oscillating function from 5.0 to 7.0.

The overall agreement between the experimental results and the theoretical predictions is good when the angular oscillating function is small. Figures in which the vertical scale of figs. 7.17a and 7.18a are enlarged and shown in figs. 7.22a & b. Since the flexibility of the connecting bar tends to reduce the oscillating amplitude (fig. 5.9), the best agreement was obtained with the lowest stiffness functions. For higher angular oscillating functions and high reduced frequencies, the theoretical predictions on the propulsive thrust coefficient are higher than the experimental ones. This is attributed to non-linear effects. The linearising assumption fails at these oscillating amplitudes. Flow separation may occur on the surface of the foil when the oscillating function is high and the propulsive thrust is reduced. This results in dynamic stall [McCroskey 1977, 1981 and 1982]. A recent review on dynamic stall was carried out by Carr [1988]. In addition, propulsive thrust is affected by viscous drag which is not allowed for in the theory.

The experimental results show a higher propulsive thrust than the theoretical predictions when the angular oscillating function is low (3.5) and the incoming flow velocity was 0.3 ms^{-1} . The corresponding stiffness functions were 6.8 and 13.4 for BAR-R and BAR-B respectively. The recorded propulsive thrust magnitudes were small at a slow incoming flow velocity and a small angular oscillating amplitude. Small changes in measurement are enlarged by the non-dimensional coefficients in these two cases.

Owing to the disturbance generated by the fairing strut, the incoming flow velocity to the foil was not uniform across the span and a mean flow velocity was used in the analysis. Part of the discrepancy between experiment and theory is attributed to this factor.

6.4 Propulsive Efficiency

Propulsive efficiencies are shown in figs. 7.23 and 7.24 for BAR-R and BAR-B, respectively. Higher propulsive efficiencies were found for lower values of stiffness function. The same tendency was found using the theoretical model.

When the angular oscillating function is small at 3.5 and the bar is flexible with a stiffness function of 1.8, the experimental propulsive efficiency drops slightly at high reduced frequency. Propulsive efficiencies are around 0.7 at low reduced frequencies, below 0.3, and about 0.6 for higher reduced frequencies. The aspect ratio of the rectangular foil used in this model test was 4.0. Higher propulsive efficiency is expected by increasing the aspect ratio. From the theoretical prediction, shown in 5.3 of Chapter 5, the propulsive efficiency is increased by 22% by increasing the aspect ratio from 4.0 to 10.0. The propulsive efficiency drops for higher values of the stiffness function. At this small angular oscillating function (ζ), the efficiency is not sensitive to the change of stiffness function (ξ) for a low reduced frequency. However, the increase of stiffness function decreases the propulsive efficiency for high reduced frequencies.

At higher values of the angular oscillating functions, the oscillating amplitude is large and propulsive efficiency is over predicted by the theoretical model. Non-linear terms, such as viscous effects and dynamic stall, become more dominant in this area. The general pattern of experimental results agrees with the theoretical propulsive efficiency at an angular oscillating function of 5.2. The experimental efficiency is about 70% of the theoretical one for a flexible bar with a stiffness function of 1.8. For a higher stiffness function of 3.5, the percentage is about 60%. This percentage drops as

the stiffness function goes up. The range of propulsive efficiency at this angular oscillating function is from 0.2 to 0.5 for stiffness functions between 1.8 to 13.4.

For a higher angular oscillating function of 7.0, the discrepancy between the theoretical and experimental propulsive efficiency is large. The linearised assumption has failed completely in this condition. The experimental propulsive efficiency is found to be between 0.15 to 0.4. The propulsive efficiency is not sensitive to the changes in reduced frequency.

The effect of taper ratio on propulsive efficiency was investigated experimentally using two different testing conditions. The same conditions as for the propulsive thrust coefficient were used. An example of the corresponding efficiencies is plotted in fig. 7.25. There is practically no difference between these two different taper ratios. The same conclusion was drawn from the investigation using the theoretical model.

The best agreement between the theoretical predictions and the experimental results is obtained at the lowest stiffness function and lowest angular oscillating amplitudes. During the model test, the oscillating amplitude of the foil was smaller for a flexible bar than a stiff bar. The same phenomenon was also found by using the mathematical model. A linearised assumption is applied in the theoretical model and the theoretical prediction is more applicable to a small amplitude oscillation. As the problem is linearised in the theoretical model, the wake behind the oscillating foil is assumed to be a thin surface without thickness and the wake surface lies on the neutral axis. However this is not true at high angular oscillating functions with large oscillating amplitudes. The non-uniform incoming flow velocity across the span also affects the experimental results.

The experimental propulsive efficiency is low at high angular oscillating functions and hence at large oscillating amplitudes. From the view point of efficiency, development should be concentrated on small amplitude oscillations at low angular

oscillating functions. In section 8 of the present chapter, the generated propulsive thrust at low angular oscillating function is shown to be enough to propel a ship at the required speed. In this particular area, the linearised assumption is applicable and the agreement between the experimental and theoretical results is satisfactory.

7.0 THE PERFORMANCE OF THE FLEXIBLE FIN PROPELLER AT ZERO SPEED

The model was tested for a range of oscillating frequencies in calm water at zero speed (the bollard pull condition). The aim of this experiment was to investigate the initial propulsive thrust when a ship starts from rest.

The model was tested with the flexible bar (BAR-R) over a range of oscillating frequencies from 2.0 to 7.5 rads^{-1} and three different angular oscillating functions (ζ) of 3.5, 5.2 and 7.0. As the forward speed was zero in this condition, the corresponding propulsive thrust coefficient (C_{Tb}) is defined as,

$$C_{Tb} = \frac{F_{Tb}}{\frac{1}{2}\rho (L_o\omega)^2 S} \quad - 7.6$$

The results are plotted against oscillating frequency and are shown in the fig. 7.26a. Similarly, BAR-B was also used to test the performance in this condition for a range of oscillating frequencies from 2.0 to 4.5 rads^{-1} at three different oscillating functions. The corresponding results are shown in fig. 7.26b.

The propulsive thrust coefficient (C_{Tb}) decreases as the oscillating frequency increases. Increasing the angular oscillating amplitude also increases the propulsive thrust coefficient (C_{Tb}). The magnitudes of the bollard pulls generated by BAR-R are shown in fig. 7.27. The propulsive thrust increases with increases in the oscillating frequency. This is because the propulsive thrust is a function of oscillating frequency. The propulsive thrust is also sensitive to changes of oscillating amplitude. As the force

system acting on the flexible bar increases as the oscillating frequency increases, the deflections of the flexible beam increase and hence the oscillating amplitude decreases. This was observed during the experiments and the changes of amplitude were large in response to the changes of frequency. In the region of high oscillating frequency, between 6 to 7.5 rads⁻¹, the propulsive thrust becomes more constant and slightly reduced at the highest frequency. The effect of oscillating frequency and oscillating amplitude on the propulsive thrust in this condition cancel each other.

When the oscillating frequency is 4.5 rads⁻¹, the propulsive thrust generated by the flexible bar (BAR-R) at an angular oscillating function of 5.2 is about 50% higher than the one generated when $\zeta = 3.5$. An increment of 48% is obtained by increasing the angular oscillating function from 5.2 to 7.0. At the same oscillating frequency with a more stiff bar (BAR-B), a higher improvement in propulsive thrust is obtained by increasing the angular oscillating function. The propulsive thrust increases 63% by increasing the angular oscillating function from 3.5 to 5.2 and 72% for an angular oscillating function increase from 5.2 to 7.0.

The propulsive thrust generated by the flexible bar, BAR-R, at this bollard pull condition are compared with the thrust generated with a forward speed, where the mean incoming flow (U) is 0.6 ms⁻¹, when $\zeta = 3.5$, in fig. 7.28. At low oscillating frequency, the differences in propulsive thrust between the two conditions are small. The difference is larger when the oscillating frequency is high. At a high oscillating frequency of 7.5 rads⁻¹, the propulsive thrust generated in the zero speed condition is about 65% of the one generated with $U = 0.6$ ms⁻¹.

8.0 FULL SCALE PROPELLER

The application of a rotary foil propeller to a small ship was discussed in [Bose 1987 and Bose & Lai 1989]. The experimental results of the present investigation are used to examine the application of a flexible fin propeller. The same example used by Bose [1987] and Bose & Lai [1989] is adopted in the present study. A small ship with

$L_{PP} = 66.0\text{m}$ is considered in this example. The beam and depth of the ship are 10.5 m and 5.2m, respectively. The operating draft is 4.2m. The diameter of the existing screw propeller is 2.65m. The wake fraction is assumed to be 0.11 and the corresponding speed of advance is 5.5 ms^{-1} . The thrust power at a service speed of 12 knots and the required thrust were estimated to be 470 kW and 85 kN respectively for a vessel of these proportions, by using Holtrop and Mennen's [1982] method .

From the experimental results, a flexible fin propeller with a stiffness function of 1.8 and an angular oscillating function of 3.5 oscillating at a reduced frequency of 0.26 generates a propulsive thrust coefficient of 0.8. The corresponding propulsive efficiency is 0.7. The required foil area is about 6.85 m^2 (say, span = 5.3 m and chord = 1.3 m). The required span is about half of the beam of the ship. When the reduced frequency is 0.26, the corresponding oscillating frequency is 2.2 rads^{-1} (21 rpm). The length of the flexible bar is (L_o) 6.5 m and the angular oscillating amplitude is 20° (0.35 rad). From the theoretical prediction, the non-dimensional heaving amplitude (τ) of the oscillating foil is 0.71 in this condition. The corresponding heaving amplitude (y_o) in this case is 1.6m and the swept height of the foil is 3.2 m. It is about 20% larger than the diameter of the existing screw propeller. However, it is only 60% of the depth and within the operating draft of the ship. This shows that from the hydrodynamic performance point of view, the application of a flexible fin propeller is feasible.

9.0 CONCLUSIONS

A flexible fin propeller model was tested at forward speed and in the bollard pull condition. The experimental results of propulsive thrust coefficient and efficiency for different stiffness functions, angular oscillating functions, reduced frequencies and taper ratios have been presented in this chapter. By using the experimental results, the application of a flexible fin propeller to a small ship is discussed. The following conclusions are drawn from the investigation.

- 1) Similar general trends are found between the experimental results and theoretical

predictions. The following common trends are obtained in both experiment and theory:

- (a) the experimental propulsive thrust coefficient increases as the stiffness function, angular oscillating function and reduced frequency increase;
 - (b) the stiffness effect of the connecting bar on the propulsive thrust is larger when the stiffness function is low; and,
 - (c) the propulsive efficiency is higher at lower values of the stiffness function.
- 2) The agreement between theory and experiment of both propulsive thrust coefficient and efficiency is good when the angular oscillating function is small and the stiffness function is low.
 - 3) The rate of increase in propulsive thrust with stiffness of the connecting bar is decreased when the stiffness function is high. At a high reduced frequency of 6.0, the propulsive thrust coefficient increases by 70% for an increase in stiffness function from 3.0 to 6.0. When the stiffness function increases from 9.0 to 12.0, a smaller improvement of 20% in propulsive thrust is obtained.
 - 4) The increment in propulsive thrust is increased by increasing the angular oscillating function. There is a mean rise of 30% in propulsive thrust by increasing the angular oscillating function from 3.0 to 5.0 for a range of stiffness function between 3.0 and 12.0 at a reduced frequency of 0.6. When the angular oscillating function increases from 5.0 to 7.0, the propulsive thrust is increased by 60%.
 - 5) High efficiencies around 0.7 were found in this set of experiments for : low reduced frequency ($k < 0.3$); angular oscillating function of 3.5; stiffness function of 1.8. The theory suggests an improvement in propulsive efficiency can be obtained by increasing the aspect ratio from 4.0 to 10.0.
 - 6) The propulsive thrust coefficient (C_{Tb}) in the bollard pull condition increases as the

angular oscillating function increases and decreases as the oscillating frequency increases. However, the actual thrust generated is increased by increasing oscillating frequency. In the region of high oscillating frequency, between 6 to 7.5 rads^{-1} , the propulsive thrust becomes more constant and slightly reduced at the highest frequency.

- 7) For low oscillating frequencies, the bollard pull is slightly less than the propulsive thrust at a forward speed of 0.6 ms^{-1} but this reduces to two-thirds times the thrust value as the oscillating frequency is increased.
- 8) Geometrically and hydrodynamically, it is possible to use a flexible fin propeller for a small ship. The required thrust can be generated at small oscillating amplitude and high efficiency. For these conditions, the linearised assumption in the theory is valid.

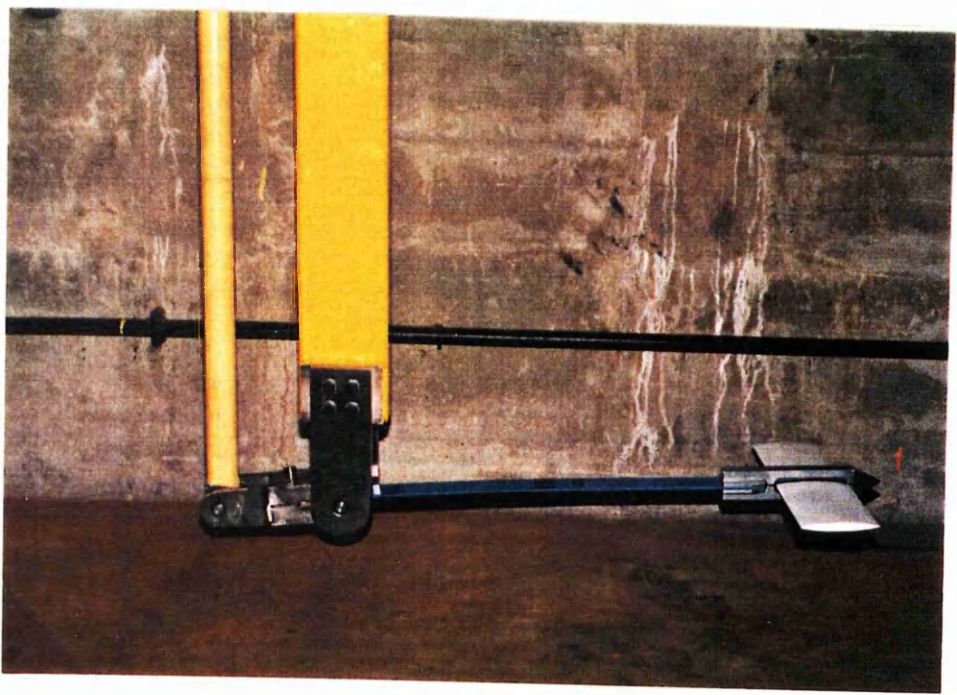


Fig. 7.1 The Flexible Fin Propeller Model

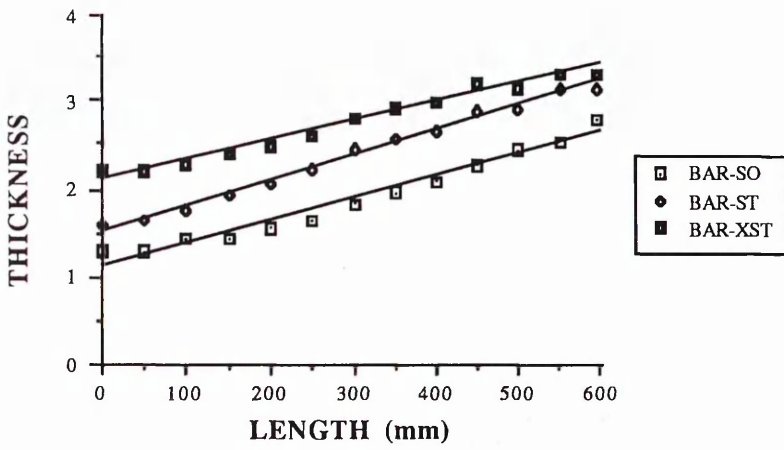


Fig. 7.2 Thickness Distribution of BAR-SO, BAR-ST and BAR-XST

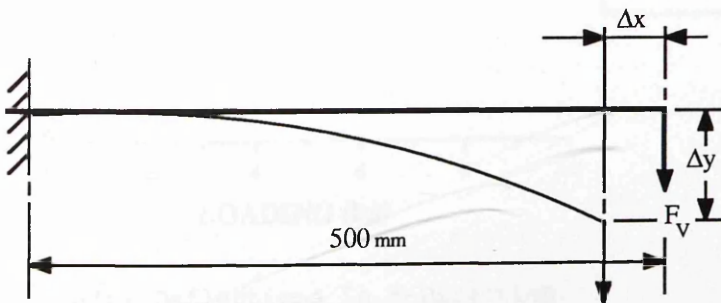
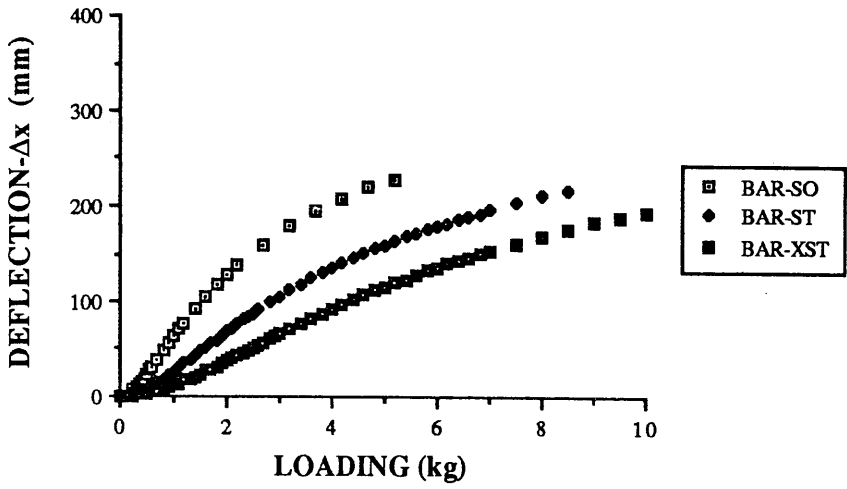
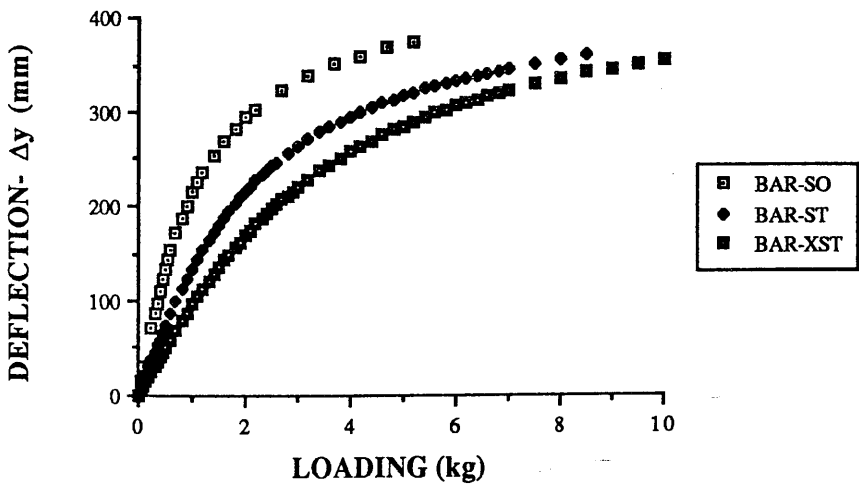


Fig. 7.3 Deflection of a Flexible Cantilever



(a) Deflections in X-Direction



(b) Deflections in Y-Direction

Fig. 7.4 Deflections Measured in the Bending Test

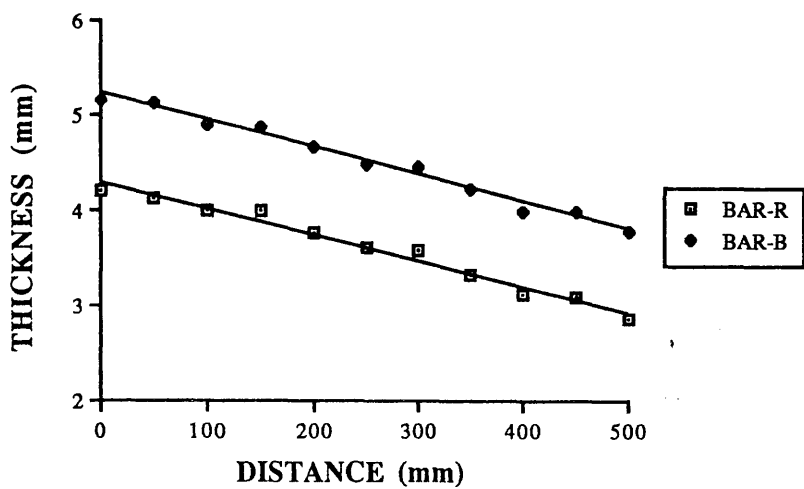
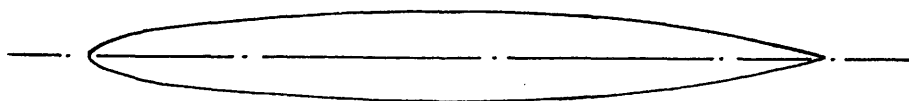


Fig. 7.5 Thickness Distribution of BAR-R and BAR-B



SECTION A-A (NACA-16-012)
(Scale = 1:1)

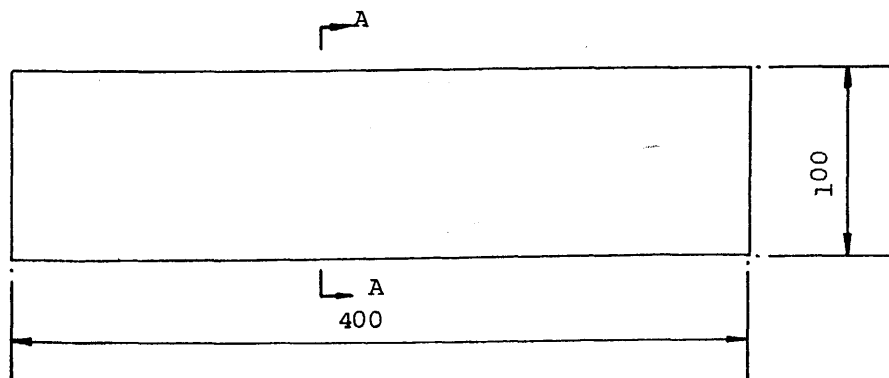


Fig. 7.6 The Foil for The Flexible Fin Propeller Model
(Scale = 1:4)

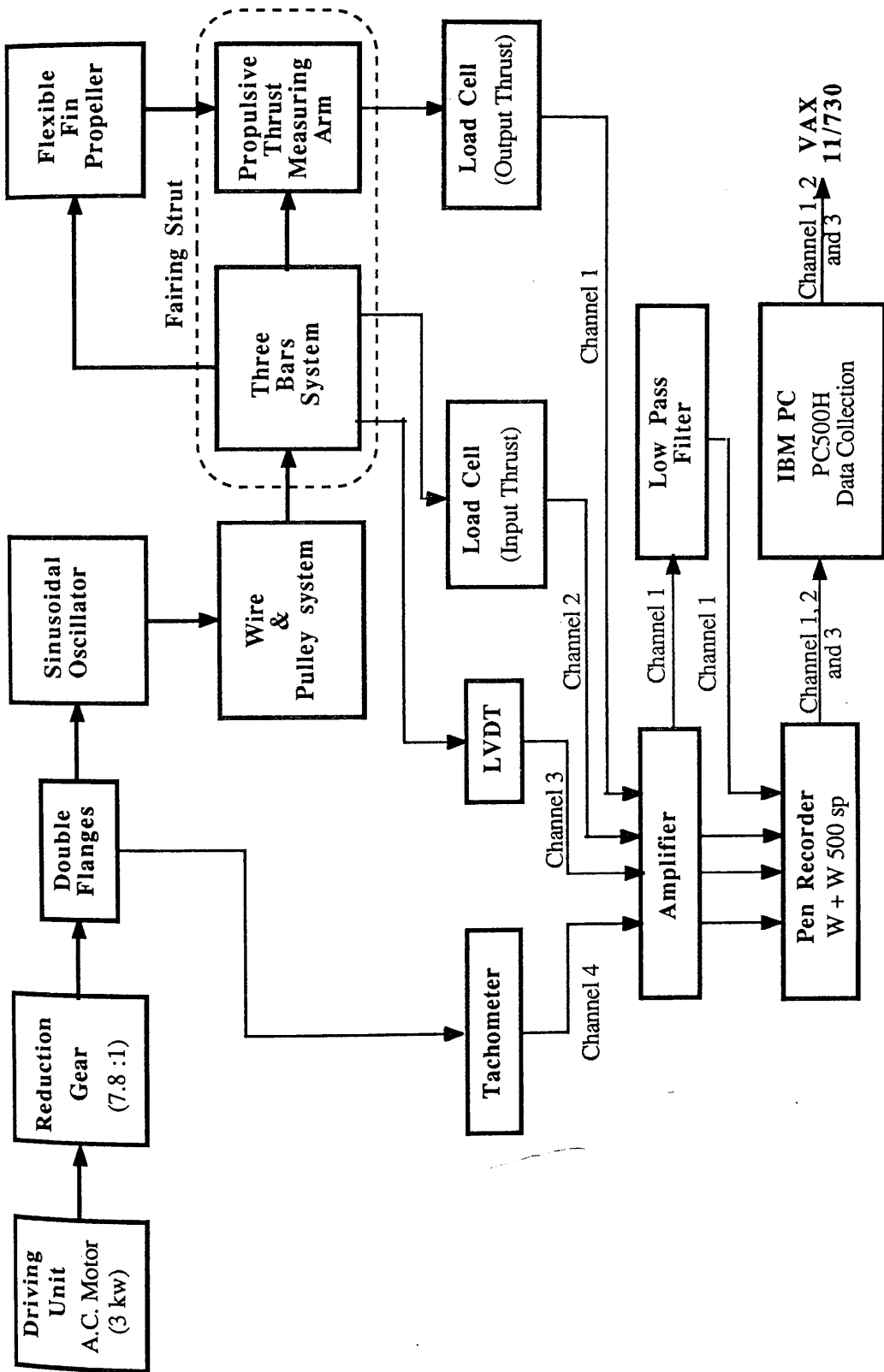


Fig. 7.7 THE DIAGRAMMATIC ARRANGEMENT OF THE FLEXIBLE FIN PROPELLER MODEL TEST

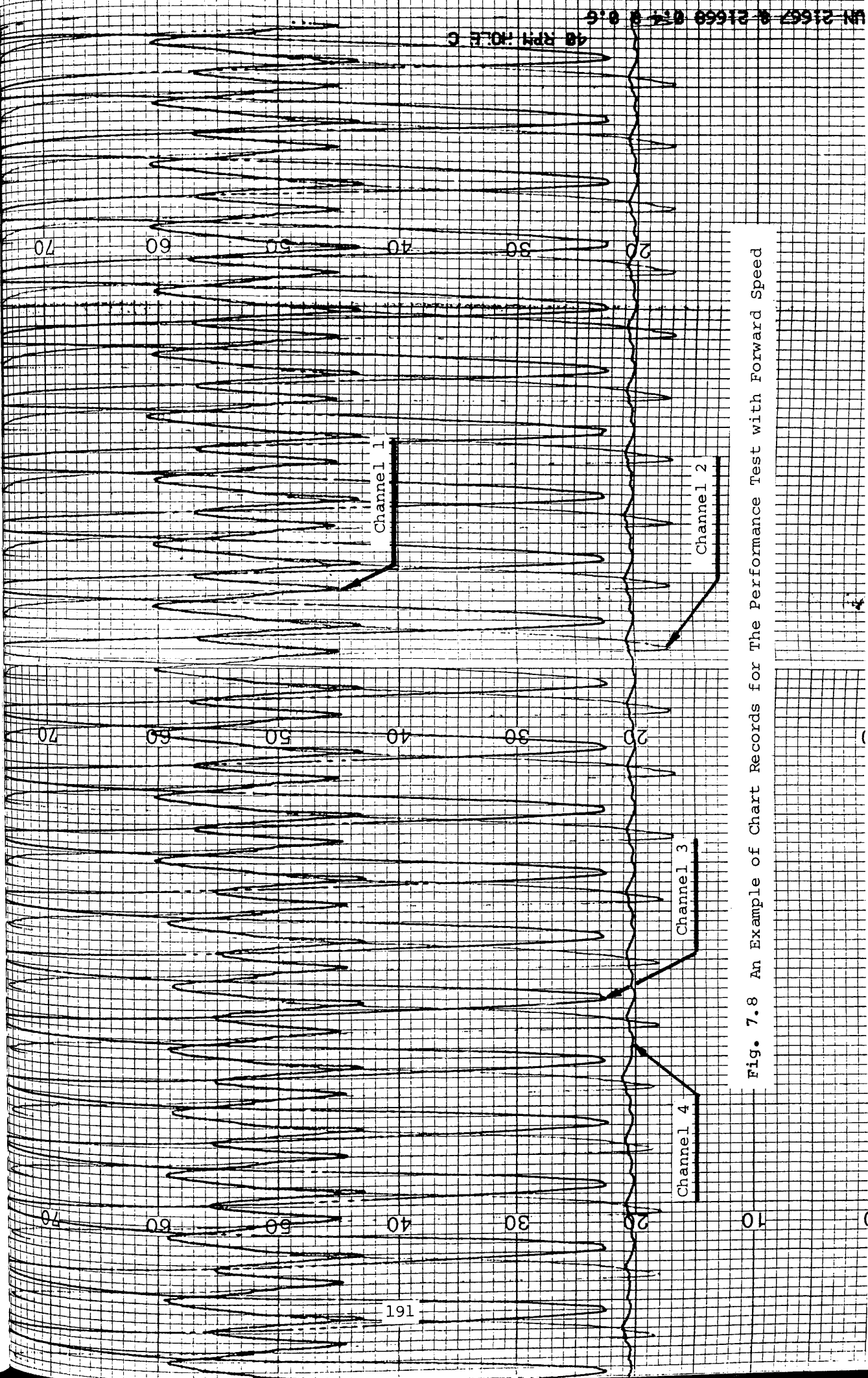
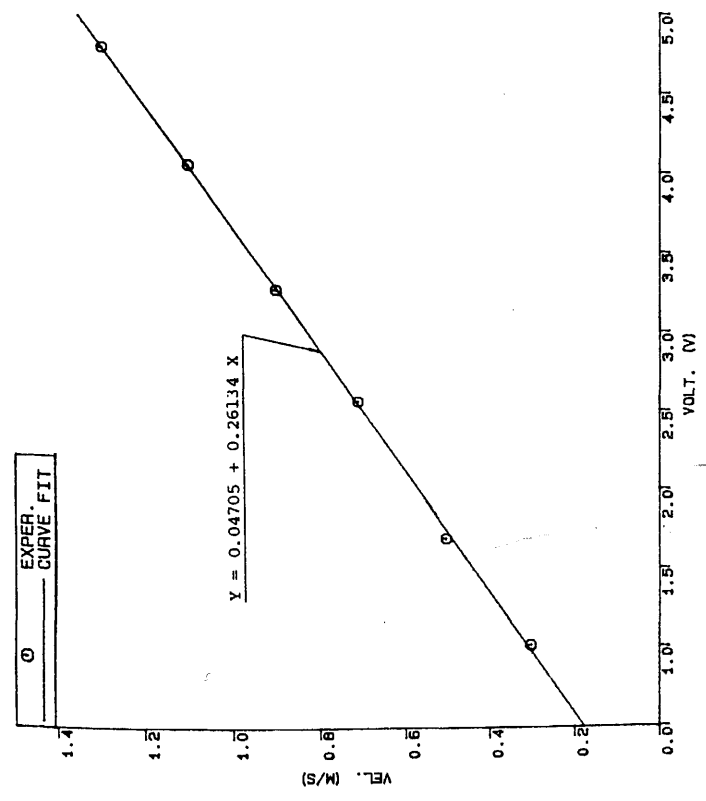
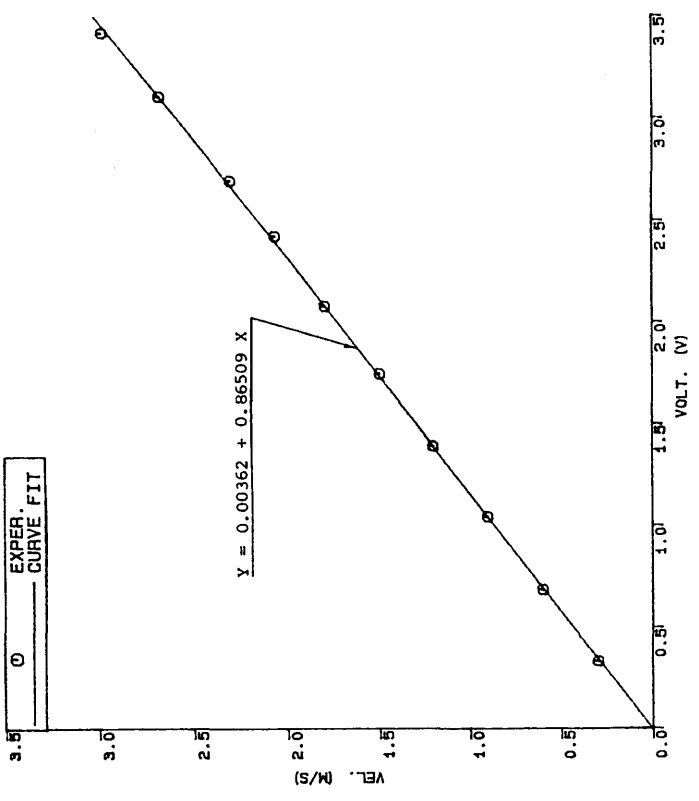


Fig. 7.8 An Example of Chart Records for The Performance Test with Forward Speed



CALIBRATION OF THE LOW SPEED
FLOW METER

(a)



CALIBRATION OF THE HIGH SPEED
FLOW METER

(b)

Fig. 7.9 Calibration of The Flow Meter (STREAMFLO)

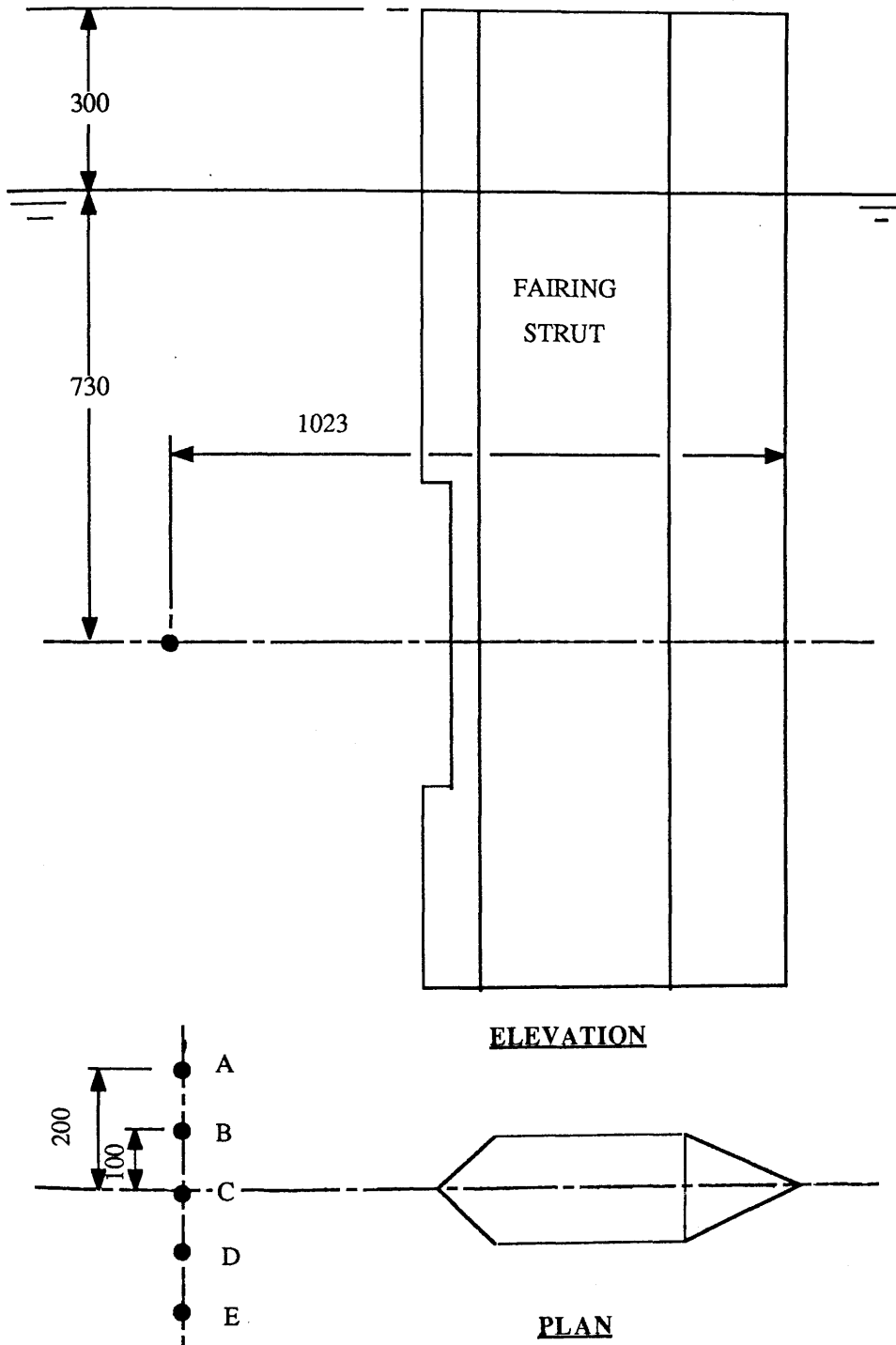
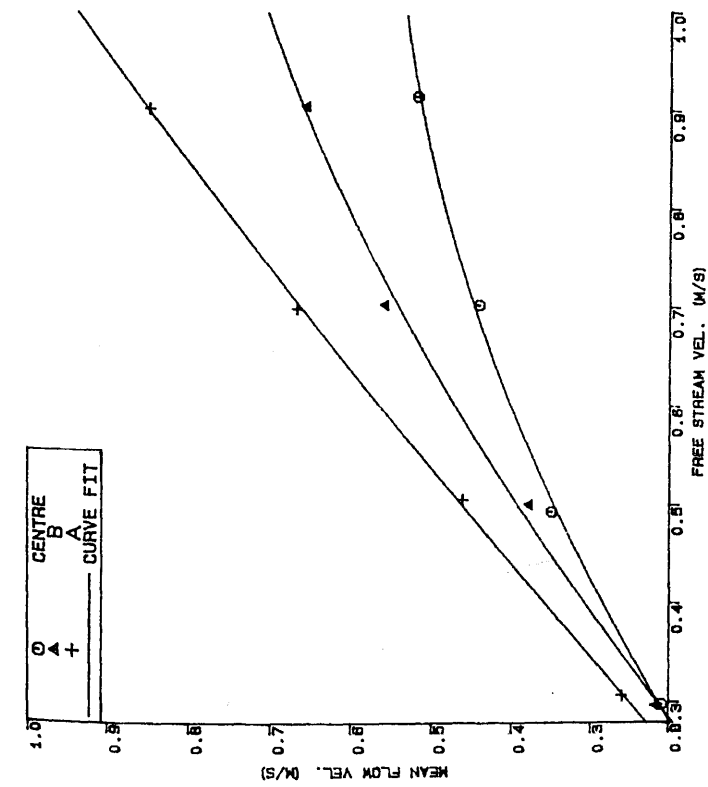
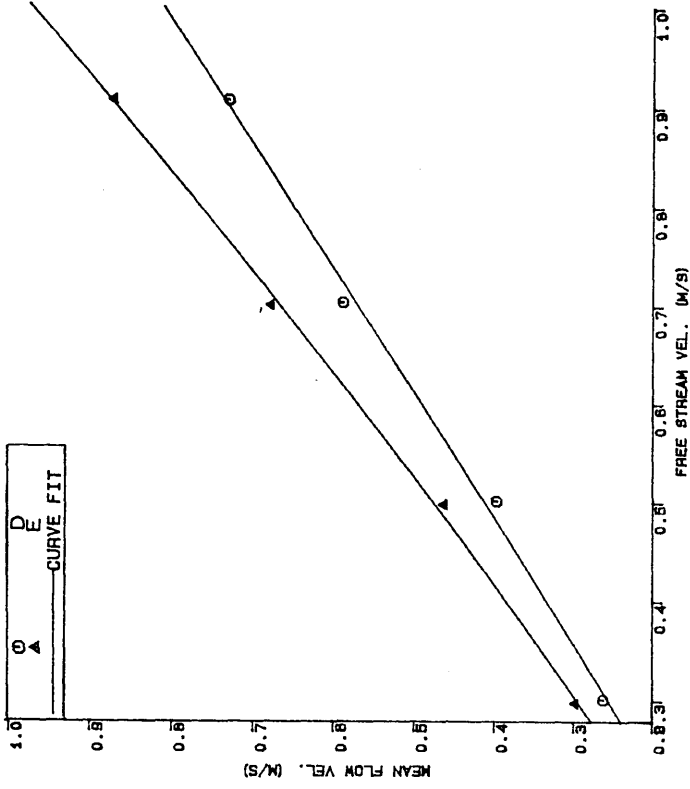


Fig. 7.10 FIVE POSITIONS FOR FLOW VELOCITY CALIBRATION



FLOW VEL. BEHIND THE FAIRING

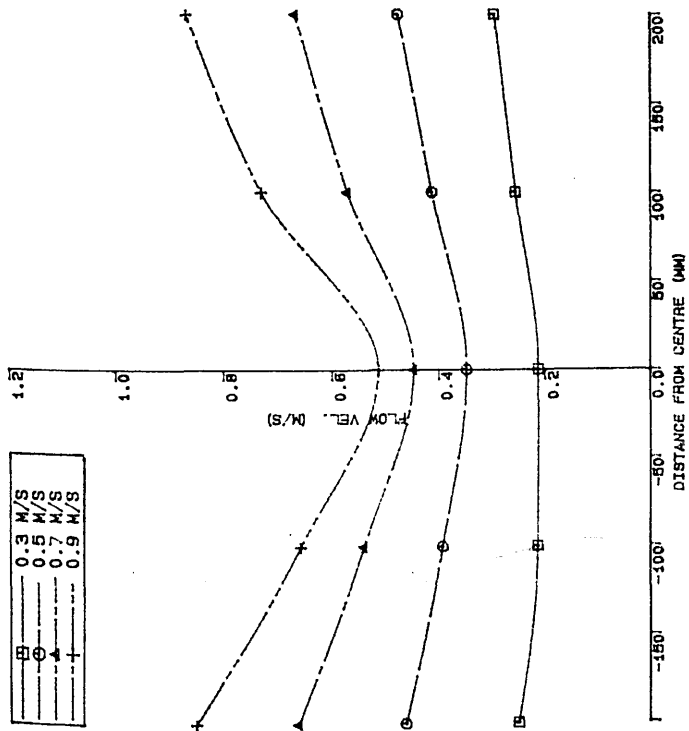
(a)



FLOW VEL. BEHIND THE FAIRING

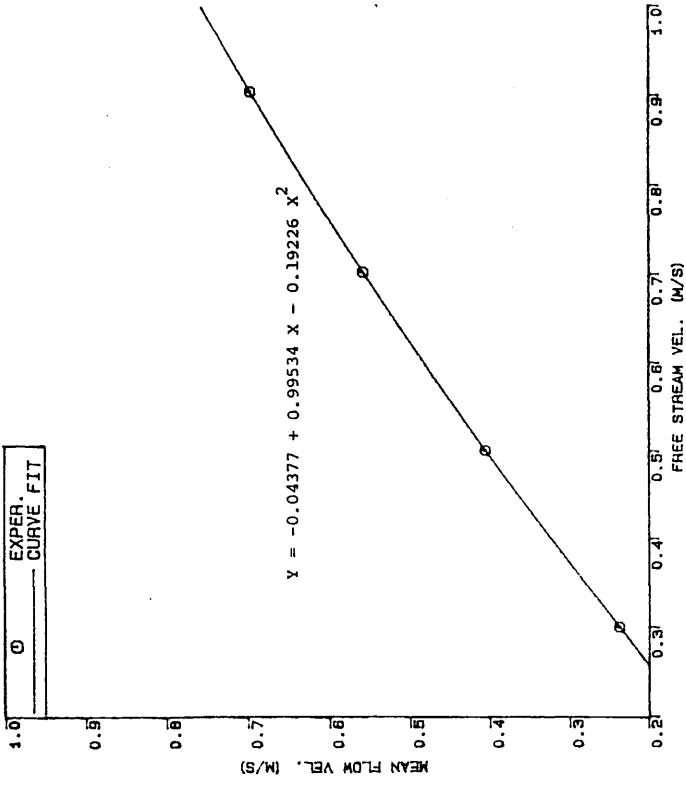
(b)

FIG. 7.11 Flow Velocity Behind The Fairing Strut



FLOW VELOCITY PROFILE BEHIND
THE FAIRING STRUT

Fig. 7.12



MEAN FLOW VEL. BEHIND THE FAIRING STRUT
Vs
FREE STREAM VEL.

Fig. 7.13

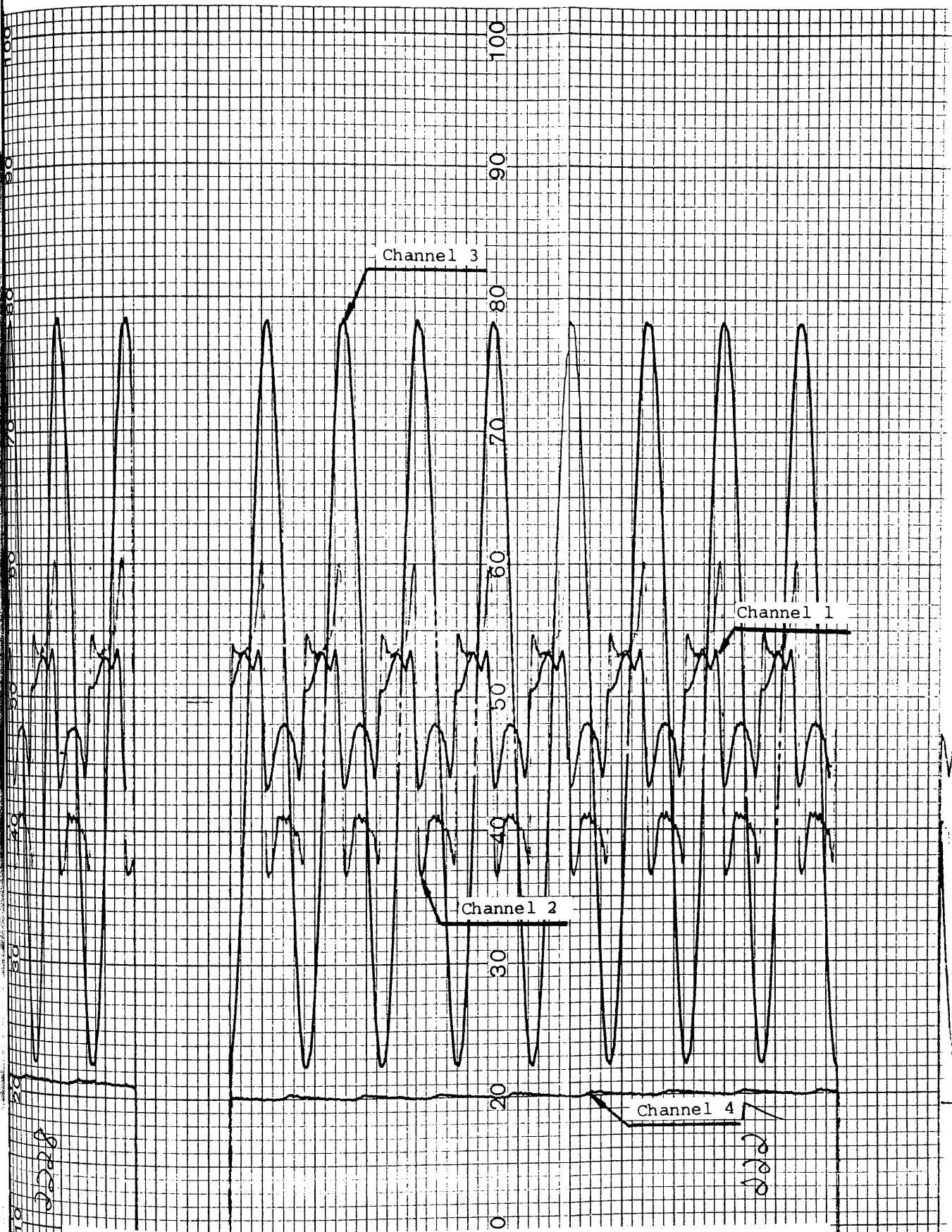
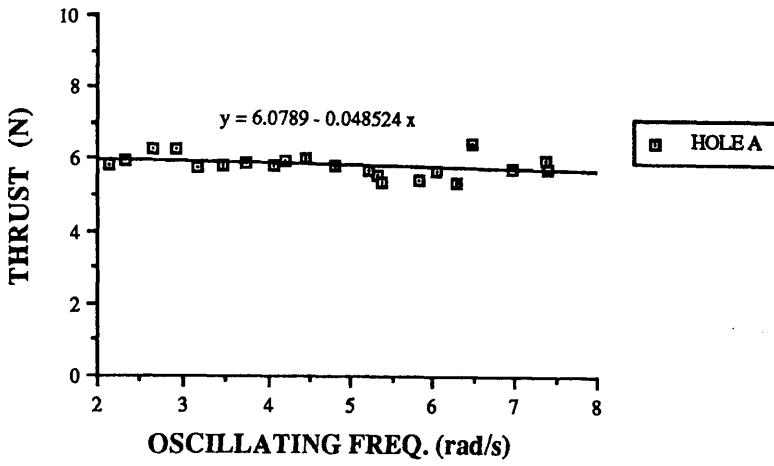
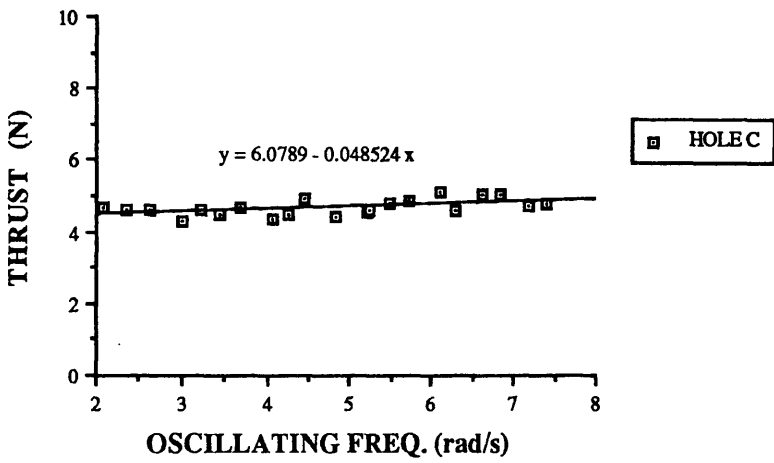


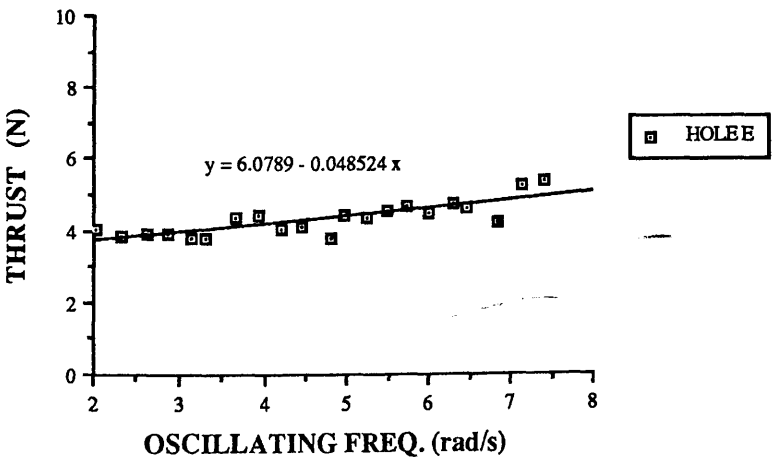
Fig. 7.14 An Example of Chart Records for the Frictional Loss Test



(a)

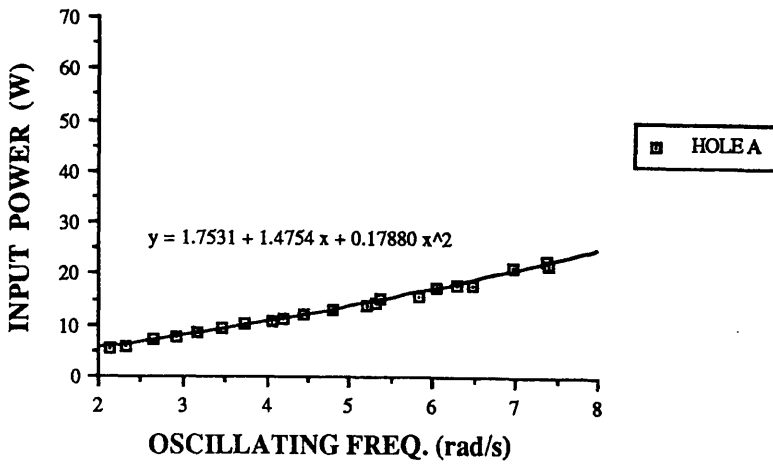


(b)

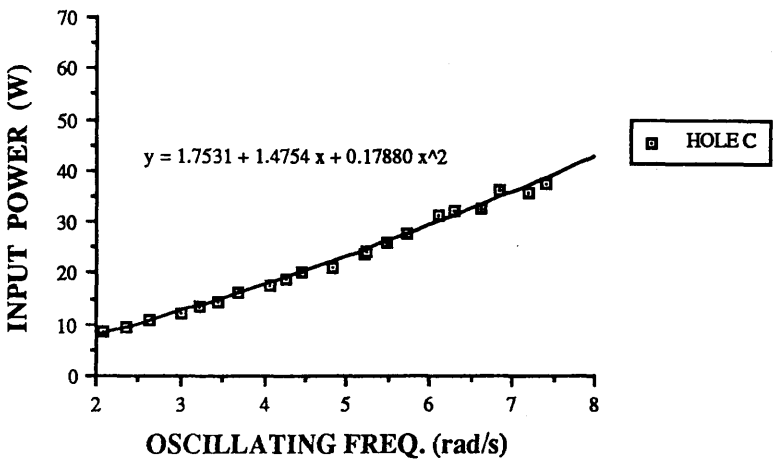


(c)

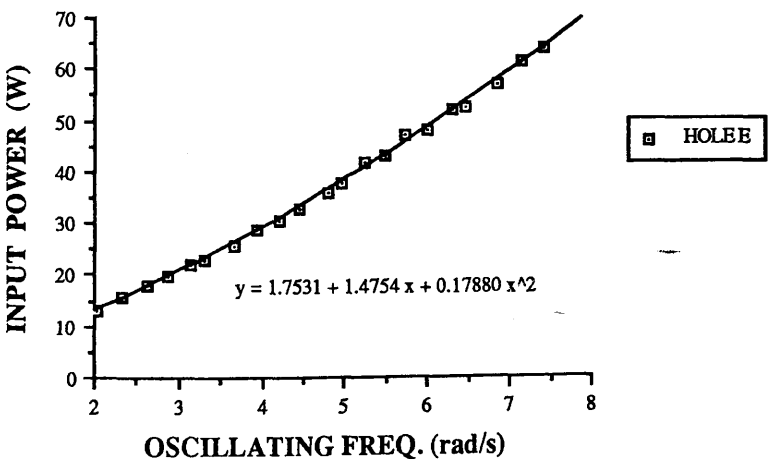
Fig. 7.15 Mean Propulsive Thrust Recorded in the Frictional Loss Test



(a)



(b)



(c)

Fig. 7.16 Mean Input Power Measured in Frictional Loss Test

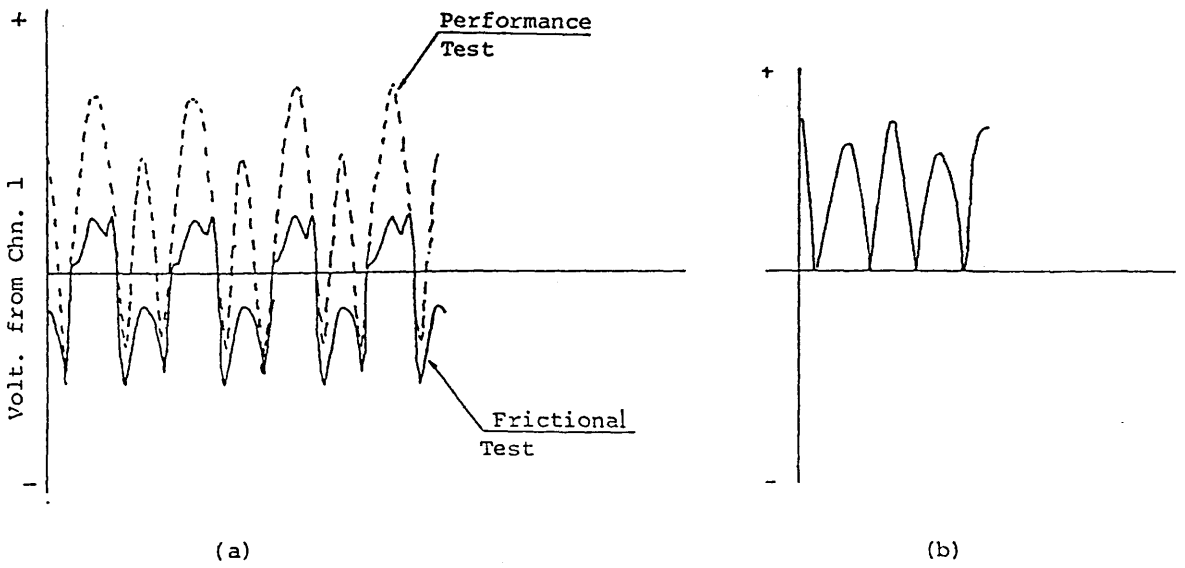


Fig. 7.17 Comparison of the Records of Propulsive Thrust Between The Performance Test and The Frictional Loss Test

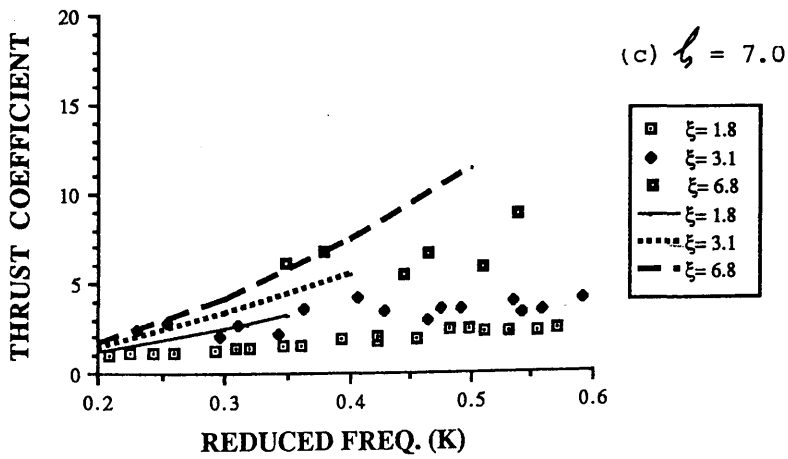
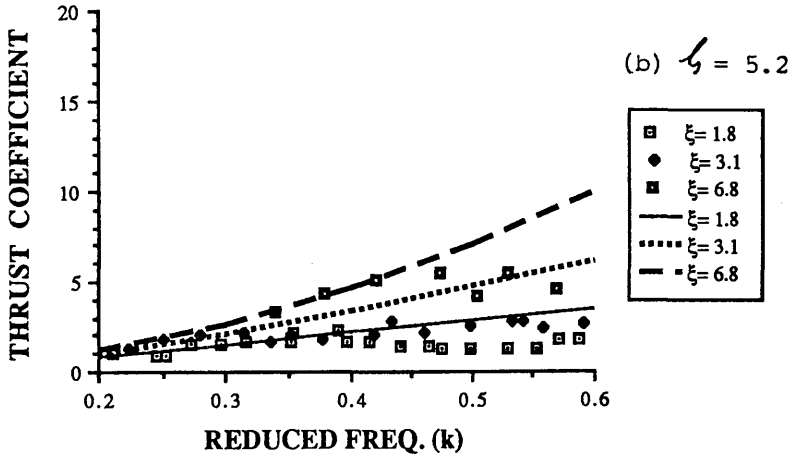
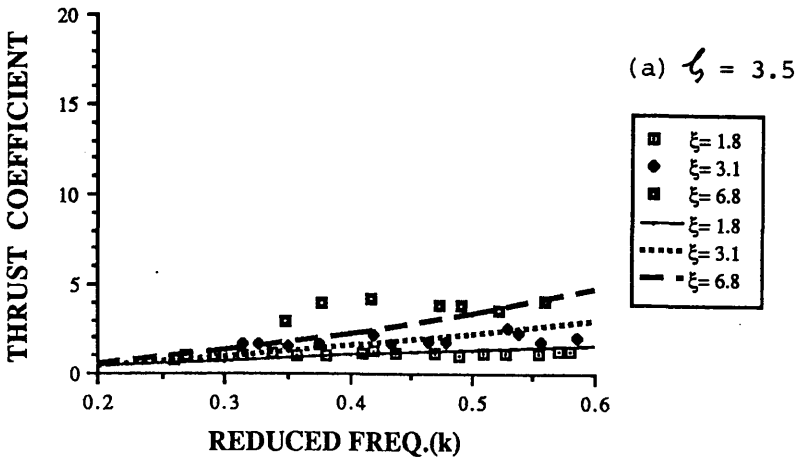


Fig. 7.18 The Propulsive Thrust Coefficient for Different Stiffness Functions where : Aspect Ratio = 4.0, Taper Ratio = 0.37

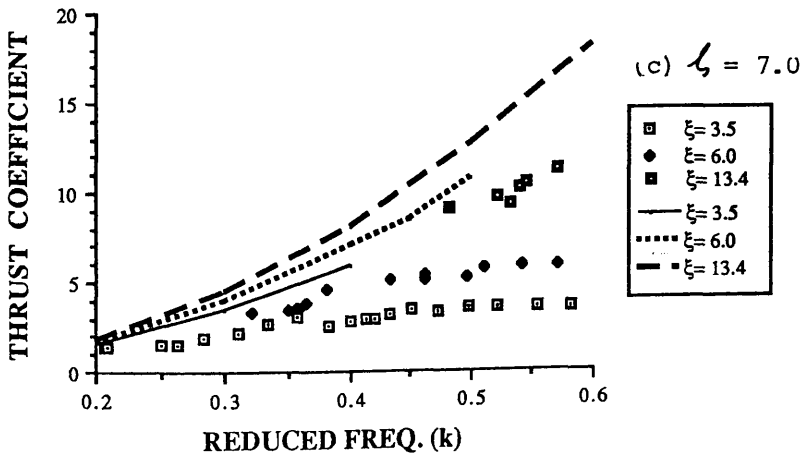
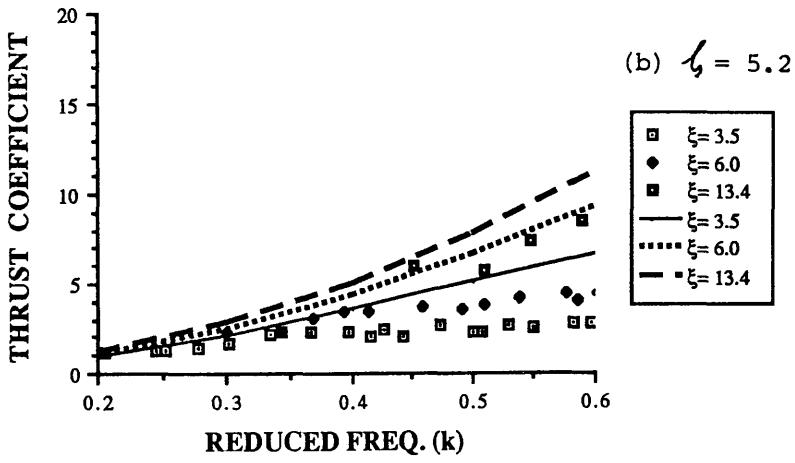
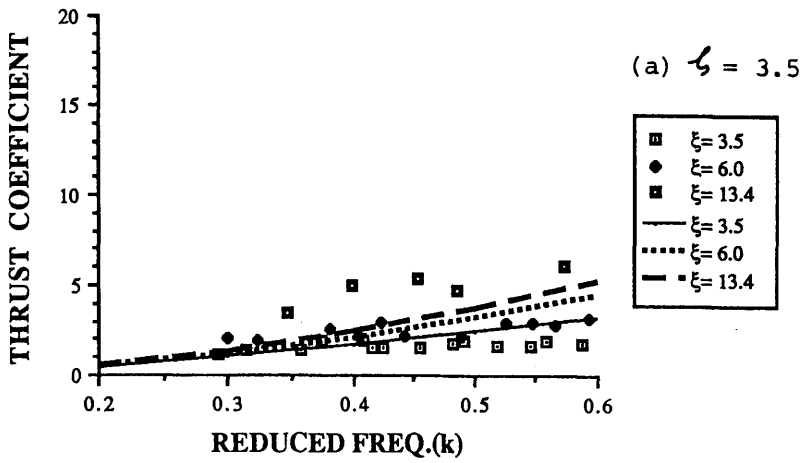


Fig. 7.19 The Propulsive Thrust Coefficient for Different Stiffness Functions where : Aspect Ratio = 4.0, Taper Ratio = 0.30

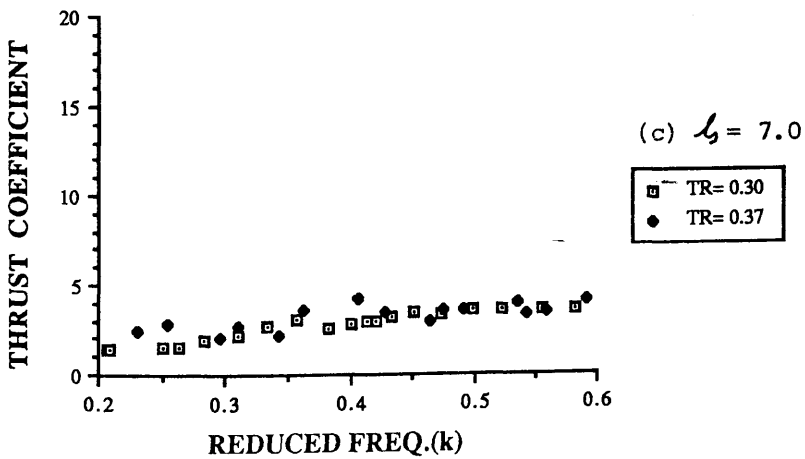
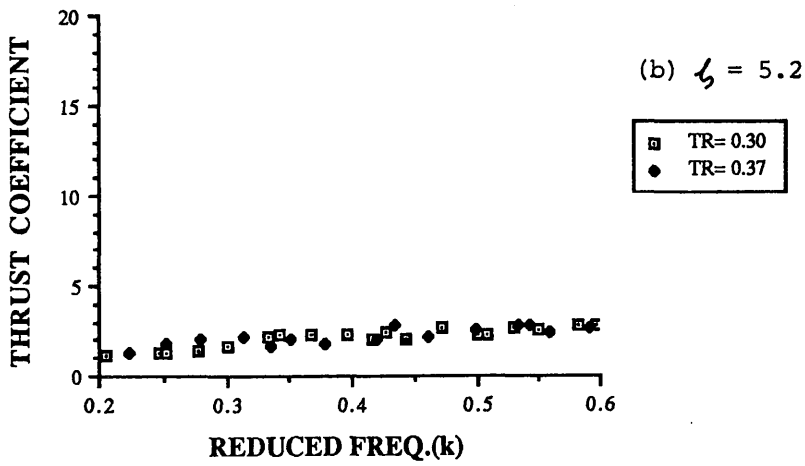
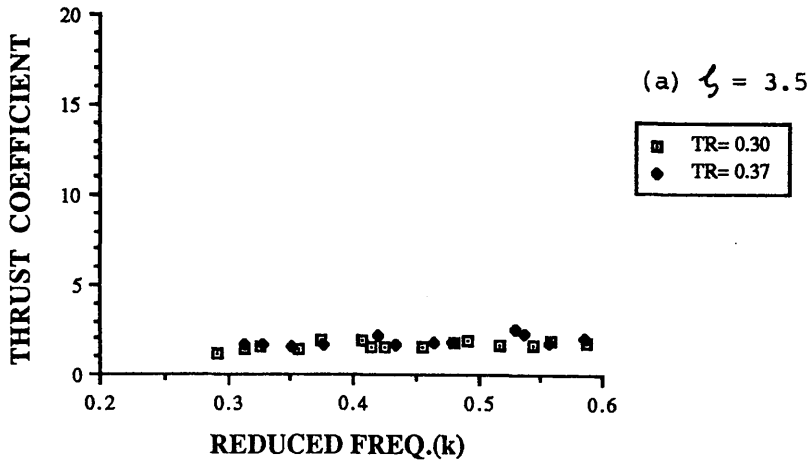
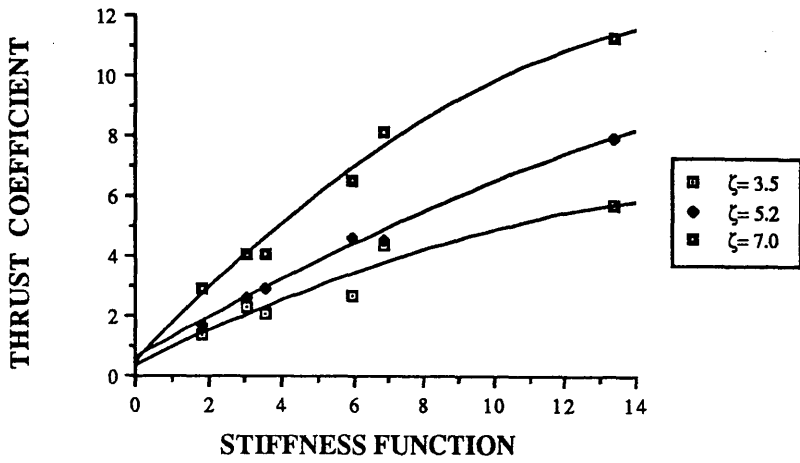
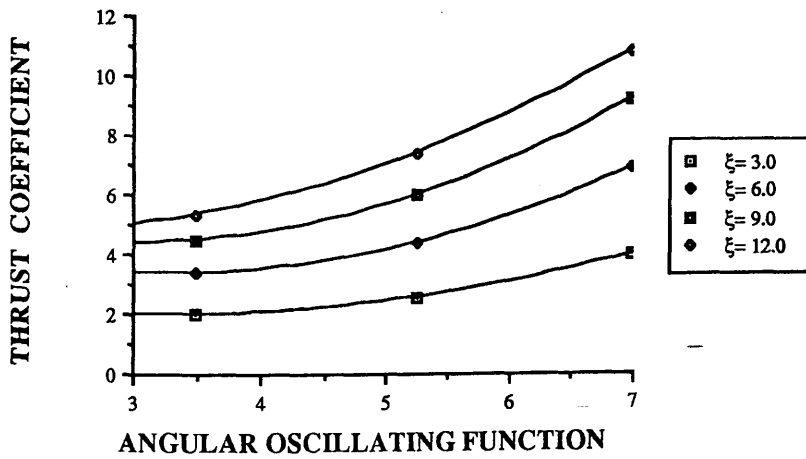


Fig. 7.20 Comparisons of Propulsive Thrust Coefficient for Different Taper Ratios with Similar Stiffness Functions



(a) The Propulsive Thrust Coefficient for Different Stiffness Functions when $k = 0.6$



(b) The Propulsive Thrust Coefficient for Different Angular Oscillating Function when $k = 0.6$

Fig. 7.21

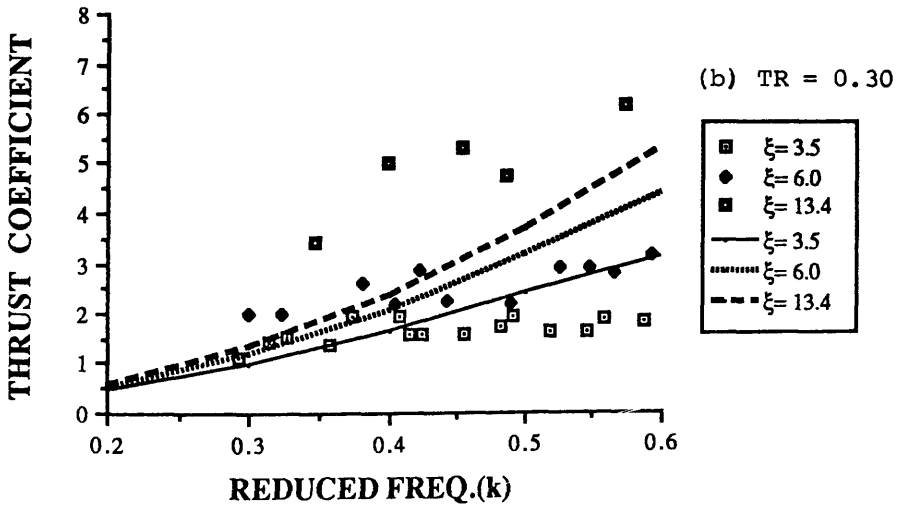
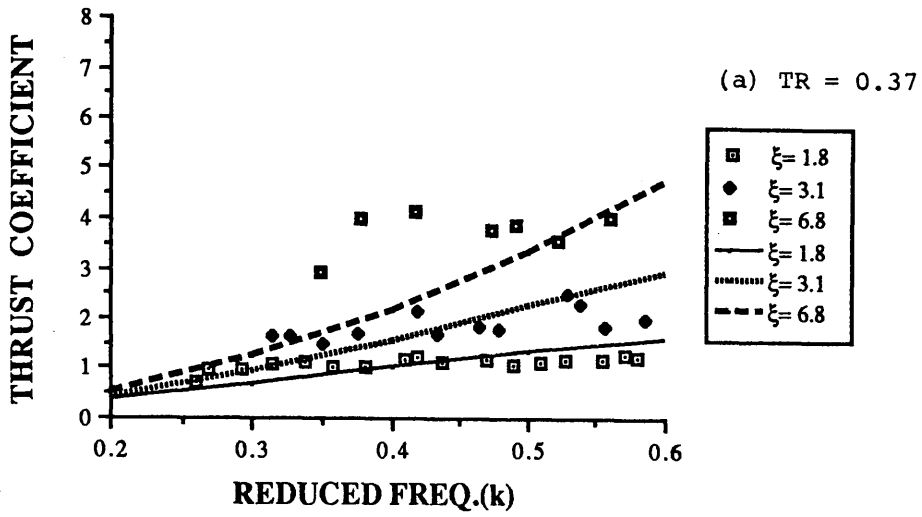


Fig. 7.22 The Propulsive Thrust Coefficient for Different Stiffness Functions where : Aspect Ratio = 4.0, $\zeta = 3.5$

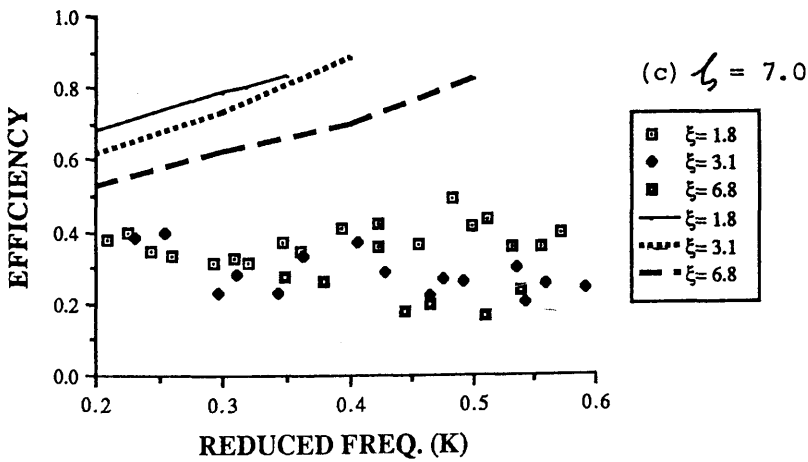
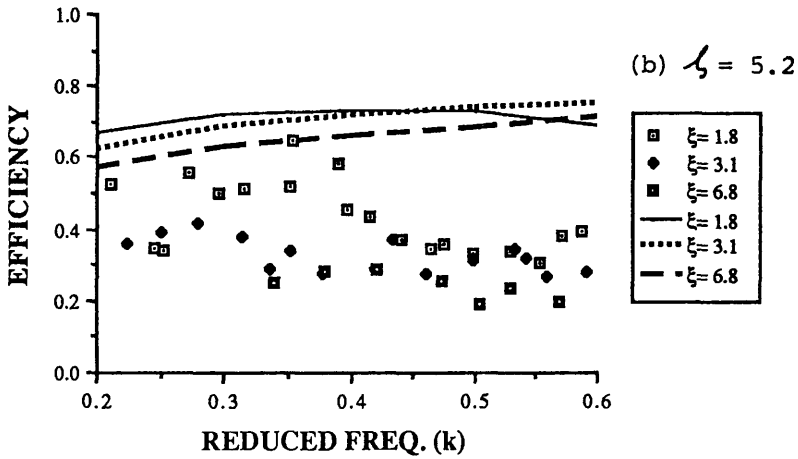
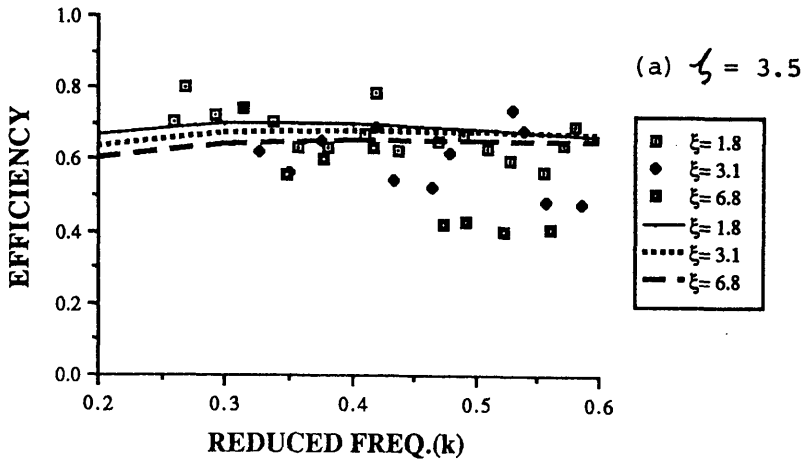


Fig. 7.23 The Propulsive Efficiency for Different Stiffness Functions where : Aspect Ratio = 4.0, Taper Ratio = 0.37

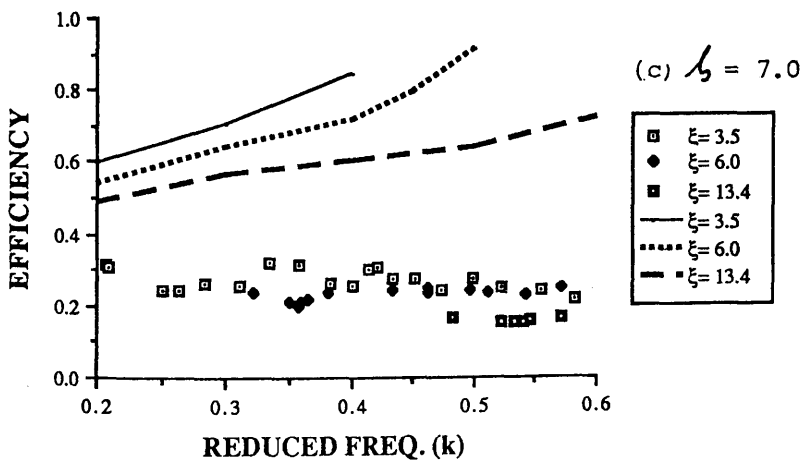
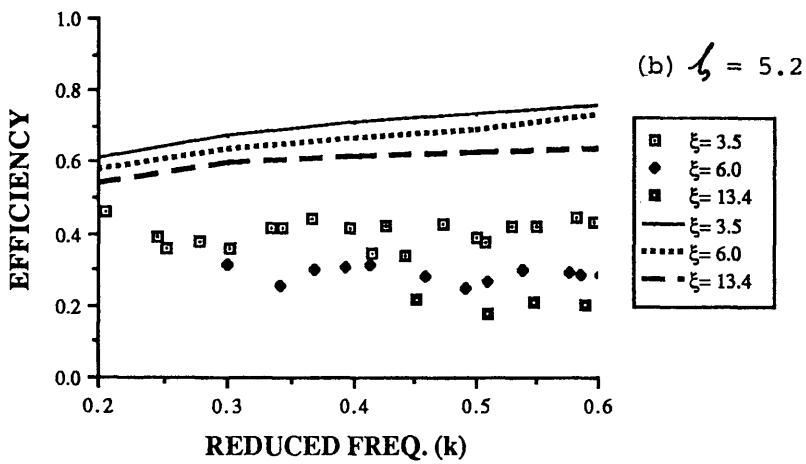
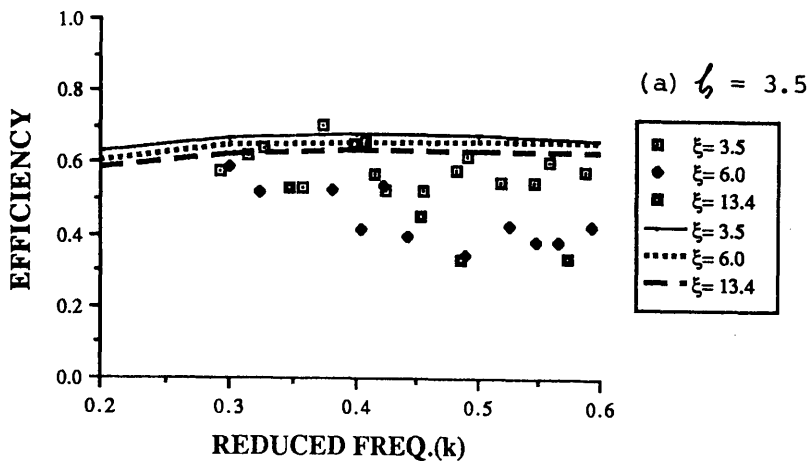


Fig. 7.24 The Propulsive Efficiency for Different Stiffness Functions where Aspect Ratio = 4.0, Taper Ratio = 0.30

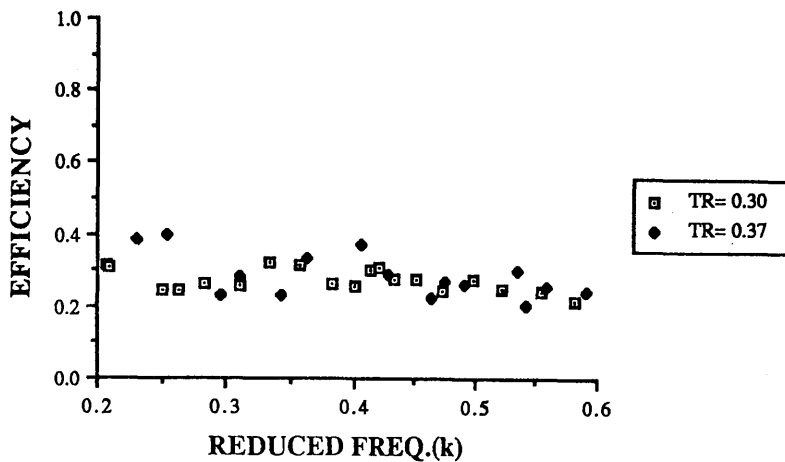


Fig. 7.25 Comparison of Propulsive Efficiency for Different Taper Ratios with Similar Stiffness Function when $\zeta = 7.0$

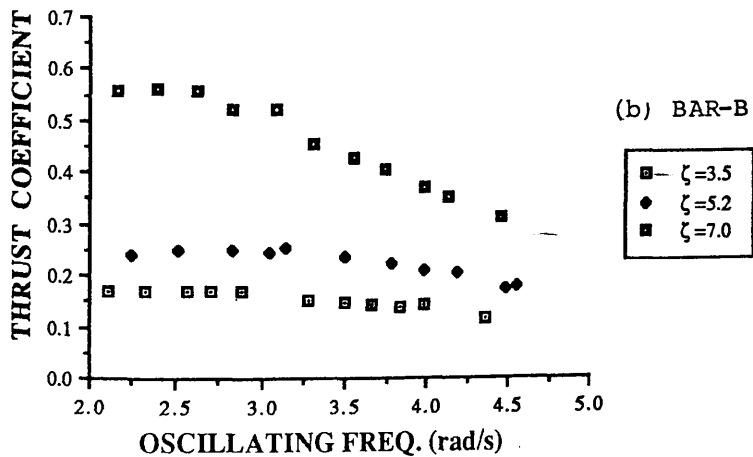
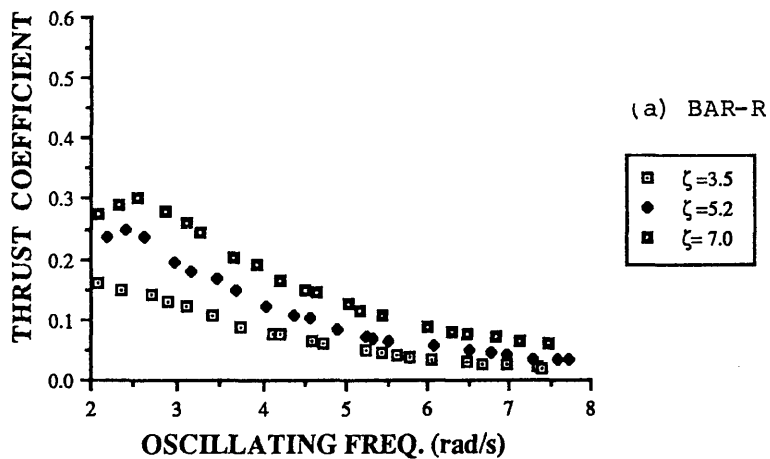


Fig. 7.26 The Propulsive Thrust Coefficient in Bollard Pull Condition

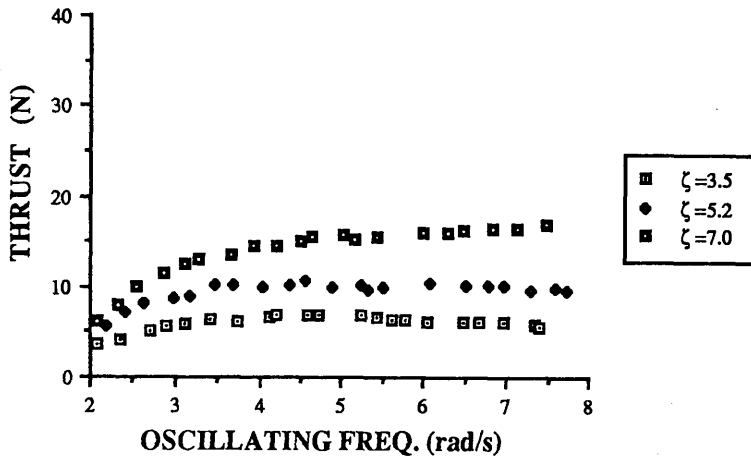


Fig. 7.27 The Propulsive Thrust Generated in Bollard Pull Condition by BAR-R

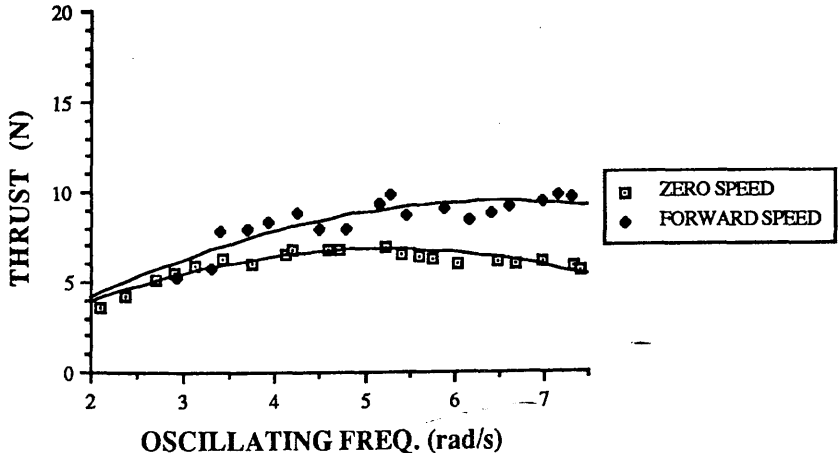


Fig. 7.28 Comparison of Propulsive Thrust Between Bollard Pull Condition and Forward Speed Condition

F_V (Kg)	ΔY_E (mm)	ΔX_E (mm)	$E \times 10^9$ (N/m ²)	ΔY_C (mm)	ΔX_C (mm)	$\Delta X_C - \Delta X_E$ (mm)
EXPERIMENT				COMPUTED		ERROR
0.05	14.4	0.0	37.5	14.4	0.3	0.3
0.10	30.1	0.0	35.9	30.1	1.2	1.2
0.25	72.0	6.5	36.3	72.1	6.9	0.4
0.30	86.4	9.0	35.7	86.4	10.0	1.0
0.40	111.3	16.0	35.6	111.3	16.7	0.7
0.50	133.5	23.0	35.6	133.5	24.2	1.2
0.70	170.7	39.5	35.8	170.8	40.2	0.7
0.90	201.2	56.0	35.8	201.3	56.7	0.7
1.20	235.2	78.1	36.3	235.2	79.2	1.1
1.40	253.7	92.2	36.3	253.7	93.5	1.3
1.80	282.4	117.0	36.2	282.4	118.6	1.6
2.20	303.2	138.0	36.3	303.2	139.5	1.5
2.70	323.4	160.0	36.0	323.4	162.1	2.1
3.70	350.3	194.5	36.0	350.3	196.2	1.7
4.20	359.8	207.0	36.0	359.8	209.3	2.3
4.70	368.8	221.0	35.4	368.9	222.5	1.5

Mean Bending Modulus = $35.97 \times 10^9 \text{ N/m}^2$

The Standard Deviation = $0.395 \times 10^9 \text{ N/m}^2$

Table 7.1 THE ESTIMATED BENDING MODULUS OF FLEXIBLE BAR (SO)

F_V (Kg)	ΔY_E (mm)	ΔX_E (mm)	$E \times 10^9$ (N/m ²)	ΔY_C (mm)	ΔX_C (mm)	$\Delta X_E - \Delta X_C$ (mm)
	EXPERIMENT			COMPUTED		ERROR
0.10	15.5	0.5	37.2	15.5	0.3	0.2
0.20	30.7	1.8	38.1	30.7	1.2	0.6
0.30	45.9	3.8	37.4	45.9	2.8	1.0
0.40	60.2	6.0	37.2	60.2	4.8	2.0
0.50	74.3	8.8	37.3	74.3	7.3	1.5
0.70	100.3	15.0	38.0	100.3	13.4	1.6
0.90	123.9	22.5	37.3	123.9	20.6	1.9
1.20	154.0	34.8	37.3	154.0	32.2	2.6
1.40	172.4	43.0	37.7	172.4	40.7	2.3
1.80	202.5	60.0	37.6	202.5	57.0	3.0
2.20	227.2	77.0	37.7	227.2	73.0	4.0
2.80	255.6	98.8	37.2	255.6	94.3	4.5
3.40	278.4	119.0	37.4	278.4	114.3	4.7
4.20	300.6	141.5	38.2	300.7	136.2	5.3
5.40	324.9	168.0	38.3	324.9	163.1	4.9

Mean Bending Modulus = $37.64 \times 10^9 \text{ N/m}^2$

The Standard Deviation = $0.41 \times 10^9 \text{ N/m}^2$

Table 7.2 THE ESTIMATED BENDING MODULUS OF FLEXIBLE BAR (ST)

F_V (Kg)	ΔY_E (mm)	ΔX_E (mm)	$E \times 10^9$ (N/m ²)	ΔY_C (mm)	ΔX_C (mm)	$\Delta X_E - \Delta X_C$ (mm)
EXPERIMENT				COMPUTED		ERROR
0.15	15.3	0.8	38.3	15.3	0.3	0.5
0.30	30.4	1.5	38.3	30.4	1.1	0.4
0.45	45.3	2.9	38.3	45.3	2.6	0.3
0.60	59.7	4.5	38.3	59.7	4.5	0.0
0.80	78.5	7.8	37.7	78.5	7.9	0.1
1.10	104.8	14.0	38.1	104.8	14.1	0.1
1.40	127.8	21.5	38.0	127.8	21.2	0.3
1.70	149.4	29.0	38.3	149.4	29.2	0.2
2.10	174.9	40.2	38.3	174.9	40.5	0.3
2.60	202.7	55.0	38.2	202.7	55.3	0.3
3.20	229.4	71.5	37.7	229.3	72.0	0.5
3.80	251.9	88.0	37.8	251.9	88.4	0.4
4.60	275.8	107.2	37.9	275.8	108.3	1.1
5.80	302.5	132.5	38.0	302.5	134.1	1.6
7.50	329.9	162.5	38.1	329.9	165.1	2.6

Mean Bending Modulus = 38.0×10^9 N/m²

The Standard Deviation = 0.41×10^9 N/m²

Table 7.3 THE ESTIMATED BENDING MODULUS OF FLEXIBLE BAR (XST)

Distance from the Leading Edge (mm)	Offset (mm)
0.00	0.0
1.25	1.3
2.50	1.8
5.00	2.5
7.50	3.0
10.00	3.5
15.00	4.1
20.00	4.7
30.00	5.4
40.00	5.9
50.00	6.0
60.00	5.8
70.00	5.3
80.00	4.2
90.00	2.5
95.00	1.4
100.00	0.1

Table 7.5 The Offset table for the Wing Section NACA-16-012

CHAPTER 8

STRESS ANALYSIS AND MATERIAL SELECTION FOR THE FLEXIBLE BAR

1.0 INTRODUCTION

The stress acting on the flexible bar of the flexible fin propeller is investigated in this Chapter. It is essential to prove that the idea of a flexible fin propeller is structurally possible and a stress analysis plays a vital part in the study of the application of this type of propeller in real life.

From large deflection beam theory, the bending moment at each point along the bar is estimated and hence the bending stress is found. A compressive stress, which is introduced by the force component parallel to the beam axis, also contributes to the total working stress. Since a long flexible bar is considered, the working stresses are dominated by the bending stresses. Two non-dimensional parameters, stress function and thickness function, are established to study the stress level.

A series of parametric studies has been carried out and these are discussed in this chapter. The effect of different parameters, such as : reduced frequency; angular oscillating function; stiffness function; taper ratio; aspect ratio; rectangular and elliptical foils; and, thickness function on the stress function have been studied.

The working stress of a full scale propeller example has been calculated. Material selection has been carried out by using Ashby's method and fibre reinforced materials are selected. The working stress of the full scale propeller example is used to discuss the application of glass fibre, carbon fibre and hybrid fibre reinforced plastics. A fatigue life study on the application of these fibre composites has also been carried out using published results.

The stress function increases as the reduced frequency and the angular oscillating function increases. Increase of taper ratio decreases the stress function. There is no significant difference in stress function for different aspect ratios. Higher stress functions are found in a propeller with an elliptical foil than that with a rectangular foil. The stress function is directly proportional to the thickness function. Hybrid glass/carbon fibre reinforced plastic is a promising, cost-effective material and provides suitable mechanical properties and fatigue strength for a full scale propeller.

2.0 OUTLINE OF THE THEORETICAL APPROACH

In Chapter 4, the theoretical model of the flexible fin propeller and large-deflection beam theory were described. By solving the second order differential equation (eqn 4.19), the change of curvature ($d\phi/d\sigma$) at different locations along the beam is calculated, as shown in section 4.0 of Chapter 4. Euler's "Law of Elastica" is applied and the bending moment is calculated from the change of curvature :

$$EI \frac{d\phi}{d\sigma} = M \quad - 8.1$$

The stress (f) is calculated from

$$\frac{M}{I} \bar{y} = f \quad - 8.2$$

In addition to the bending stress, the force component which is parallel to the X_T -axis of the instantaneous body-axis system (fig. 4.1) introduces a compressive stress in the flexible bar. The subroutine (BEAM) of the program (MAIN) was modified to calculate the stress at different points. The beam is divided into a number of segments and points are located at the ends of segments. A minimum of 50 segments is used. The stress distribution is investigated at the dynamic equilibrium condition as for the study on the hydrodynamic performance. An example of stress distribution

along the beam within an oscillating cycle is shown in fig. 8.1. The vertical axis-f, horizontal axis- σ and axis-T show the stress, location of beam and time respectively. High bending stress occurs at the pivot while a low stress occurs at the free end which is connected to the foil.

In section 5 of this chapter, fibre composite material is found to be promising for manufacture of the beam. One of the main properties of this type of material is lightness in weight. Because of this, the stress induced by the vibration of the mass of the beam is neglected in this approach.

The maximum stress (f_{\max}) within an oscillating cycle is calculated. The direct compressive stress is very small in comparison to the bending stress and is less than 0.2%. The shear stress in the bending cantilever is calculated. Generally, a long flexible bar with high slenderness ratio is used in the flexible fin propeller and the shear stress is negligibly small.

As the bending stress dominates the maximum working stress, a stress function is established with reference to eqn. 8.2. The maximum bending moment is a function of (qL_o) and the non-dimensional factor $\frac{M}{qL_o}$ is constant for different scales of propeller. With reference to eqn. 5.1, this non-dimensional factor can be transformed to

$$\frac{M}{qL_o} = \frac{ML_o}{EI\xi} \quad - 8.3$$

For the same stiffness function, the factor $\frac{ML_o}{EI}$ is a constant for different scales. In order to non-dimensionalise the maximum stress, the left hand side of eqn 8.2 is non-dimensionalised as

$$\frac{ML_o}{EI} \cdot \frac{\bar{y}}{L_o} = \frac{M\bar{y}}{I} \cdot \frac{1}{E} = \frac{f}{E} \quad - 8.4$$

Therefore a non-dimensional parameter, stress function (Λ), is established as,

$$\Lambda = \frac{f_{\max}}{E} \times 10^3 \quad - 8.5$$

In order to apply the stress function to different scales, an additional non-dimensional parameter to govern the \bar{y} value in eqn. 8.2 is required between different scales. Since a rectangular cross section is investigated here, the \bar{y} value is half of the thickness. This non-dimensional parameter is termed thickness function :

$$\vartheta = \frac{t_m}{L_o} \times 10^3 \quad - 8.6$$

3.0 PARAMETRIC STUDIES AND DISCUSSION

Stress functions have been calculated for a rectangular foil with an aspect ratio of 4.0 and a range of :

stiffness function (ξ) from 3.0 to 12.0 with an increment of 3.0;
reduced frequency (k) from 0.2 to 0.6; and,
angular oscillating function (ζ) from 3.0 to 7.0 with an increment of 2.0.

The predictions are shown in fig. 8.2. The effect of taper ratio (TR) between 0.0 and 0.6 with an increment of 0.2 was studied for two stiffness functions of 6.0 and 12.0 and is presented in fig. 8.3 and 8.4 respectively. The effect of aspect ratio was investigated for aspect ratios of 4.0, 7.0 and 10.0 as shown in fig. 8.11. In addition, the effect of rectangular and elliptical foil shapes on the maximum stress was studied for an aspect ratio of 4.0 and is presented in fig. 8.12. These investigations were carried out for a thickness function of 10. The effect of thickness function was also studied and is shown in fig. 8.13.

3.1 The Effect of Reduced Frequency

Since the force system is a function of oscillating frequency and increases as the frequency increases, maximum stress is increased by increasing the reduced frequency, as shown in fig. 8.2. When the angular oscillating function is 3.0 (fig. 8.2a), the stress is doubled by increasing the reduced frequency from 0.2 to 0.6 when the stiffness function is 3.0. For the same angular oscillating function with a stiffness function of 12.0, the stress level at a high reduced frequency of 0.6 is about 2.5 times higher than the one at a low reduced frequency of 0.2.

3.2 The Effect of Angular Oscillating Function

The stress function increases as the angular oscillating function increases. As an example, the condition with a high stiffness function of 12.0 is used here for discussion. The stress functions at reduced frequencies of 0.2, 0.4 and 0.6 are plotted against the angular oscillating function in fig. 8.5. The stress at an angular oscillating function of 7.0 is approximately twice that of the one at an angular oscillating function of 3.0 for all investigated reduced frequencies .

3.3 The Effect of Stiffness of the Flexible Bar

Fig. 8.2 shows that the stress function decreases as the stiffness function increases. For a given foil at constant advance speed, a higher stiffness function means a higher section modulus (I) and the corresponding stress level is lowered. The stress functions for different reduced frequencies of 0.2, 0.4 and 0.6 are plotted against stiffness function for a low angular oscillating function of 3.0 in fig. 8.6. The gradient of the curves in fig. 8.6 decreases as the stiffness function increases. This is similar to the effect of stiffness function on propulsive thrust. The mean stress function drops about 60% when the stiffness function is increased from 3.0 to 12.0.

3.4 The Effect of Taper Ratio

The effect of different taper ratios of the flexible cantilever have been investigated for two different stiffness functions of 6.0 and 12.0 and the results are presented in figs. 8.3 and 8.4 respectively. A bar with linear variation in thickness is considered here and the section modulus of the cross section at the pivot is greater than that at the free end. Since the maximum bending is located at the pivot, the maximum stress level drops as the taper ratio increases. The stress at the end connected to the foil increases as the taper ratio increases. However, the stress at this free end is low compared to that at the pivot. The stress distributions along the flexible bar within an oscillating cycle for two different taper ratios of 0.0 and 0.6 are shown in fig. 8.7. The stress distribution along the bar is linear when the cross-section is constant. For a bar with linear variation in cross-section, the stress distribution is non-linear. An example is shown in fig. 8.8 where the stress distribution along the bar for $TR=0.0$ is compared to the one with $TR = 0.6$.

When the angular oscillating function is 3.0, the stress functions for reduced frequencies of 0.2, 0.4 and 0.6 are shown in fig. 8.9. The stress functions of bars with stiffness functions of 6.0 and 12.0 are shown in fig. 8.9a and b respectively. The percentage drop in stress by increasing the taper ratio from zero is presented in fig. 8.10. This percentage is not sensitive to change of reduced frequency. The percentage drop in a stiff bar ($\xi=12.0$) is slightly higher than in a soft bar ($\xi=6.0$). The mean percentage drops by increasing the taper ratio from 0.0 to 0.2, 0.4 and 0.6 are 17% , 30% and 40% respectively for a stiffness function of 12.0 and 15%, 28% and 38% for a stiffness function of 6.0.

3.5 The Effect of Aspect Ratio and Foil Shape (Rectangular & Elliptical)

Three different aspect ratios of a rectangular foil of 4.0, 7.0 and 10.0 with a stiffness function of 12.0 were investigated. The difference in stress function between different aspect ratios is small and an example is shown in fig. 8.11.

The stress functions of rectangular and elliptical foils with aspect ratio 4.0 are calculated at a stiffness function of 12.0. The stress of the bar for an elliptical foil is higher than the rectangular one. The difference increases as the reduced frequency increases. The trend is the same for different angular oscillating functions. An example is shown in fig. 8.12. When the angular oscillating function is 3.0, the stress of the bar for an elliptical foil is 45% greater than the one for a rectangular foil at a reduced frequency of 0.2. At the same angular oscillating function and higher reduced frequency of 0.6, this percentage is increased to 52%.

3.6 The Effect of Thickness Function

The section modulus of the flexible bar is governed by the stiffness function (ξ). For the same section modulus (I), the thickness of the bar can be different and hence \bar{y} can also change. Therefore the stress level can be changed. The effect of different thickness functions on stress was investigated for both constant cross-section bars and bars with different taper ratios. Examples are shown in fig. 8.13. In fig. 8.13a, the stress function for different thickness function is presented for a condition with constant cross-section where: $TR=0.0$; $k=0.2$; $\xi=3.0$; $\zeta=3.0$; and the foil is rectangular with $AR=4.0$. In fig. b, the stress function is presented for a condition with a linear variation in cross-section where : $TR = 0.6$; $k=0.2$; $\xi=12.0$; $\zeta=3.0$; the foil is rectangular with $AR=4.0$. In both cases, a linear relationship between the thickness function and stress function is found where the stress function is directly proportional to the thickness function. The stress functions presented in previous sections were calculated at a thickness function of 10.0. Therefore the stress function for other thickness functions can be found using the property of direct proportionality.

A low thickness function implies a low stress function. However, a low thickness function may not be practical. Since a flat bar is considered here, the corresponding section modulus is

$$I_m = \frac{w t_m^3}{12}$$

- 8.6

For the same section modulus, breadth (w) is inversely proportion to the cube of the decrease in thickness (t_m). If the breadth of the bar is too large, it makes a significant disturbance to the flow. In order to keep this influence low, the breadth of the bar should be kept within a reasonable size and a low thickness function may not be practical. The breadth of the flexible bar will be discussed further in the next section.

4.0 FULL SCALE PROPELLER

The example used in section 8.0 of Chapter 7 is also applied here to study the working stress in a full scale propeller. The stiffness function and taper ratio in this example are 1.8 and 0.37. The corresponding bending modulus is $37.64 \times 10^9 \text{ Nm}^{-2}$. The propeller operates at a reduced frequency of 0.26. In the model scale, the thickness function was 7.1 and corresponding calculated stress function was 1.60.

For the full scale propeller, the foil is rectangular with an area of 6.85 m^2 (say span = 5.3 m and chord = 1.3 m) and the speed of advance is 5.5 ms^{-1} . The length of the flexible bar is approximately 10% of the ship length at 6.5 m. At a stiffness function of 1.8 and a bending modulus of $37.64 \times 10^9 \text{ Nm}^{-2}$, the corresponding mean section modulus is $4.2 \times 10^{-4} \text{ m}^4$. At a thickness function of 7.1, the corresponding mean thickness is 0.046 m. In order to achieve the required section modulus, the calculated breadth of the flexible bar is 51.5 m. This breadth of bar is about nine times the span of the foil and is not realistic. The breadth of the bar is taken as 10% of the span of foil in order to reduce the influence on the flow. The breadth of the beam is 0.53m and the requisite mean thickness is 0.212 m. The thickness function is increased from 7.1 to 32.6 and the stress function is increased to 7.37. The corresponding stress is 278 Nmm^{-2} .

5.0 THE MATERIAL OF THE FLEXIBLE BAR

The above analysis of hydrodynamic performance and working stress gives a guide line to the selection of material for the flexible bar of the propeller. There are over 50,000 materials available. Ashby [1989] divides these into six different classes as : metals; polymers; elastomers; ceramics; glasses; and, composites. The full menu of materials should be considered in the selection of materials. In fig. 8.14, the moduli of different materials are plotted against their corresponding strengths; log scales are used.

The required materials should have high strength and low stiffness (low modulus (E)). Therefore a high ratio of strength to modulus is required. A line with a slope of 0.01 is plotted on fig. 8.14 to show the ratio of strength to modulus. Higher ratios are to the right of the line, lower ratios to the left.

Elastomers have the highest strength to modulus ratio. However, they are very flexible and their moduli are low. The propulsive thrust decreases as the stiffness of the bar decreases as shown in chapters 5 and 7. In order to meet the stiffness to generate sufficient propulsive thrust, the cross section of the bar for a material with low modulus will be large and impractical. For the flexible bar of a full scale propeller, a material with reasonable stiffness and strength is required. Materials with a modulus which is higher than $20 \times 10^9 \text{ Nmm}^{-2}$, are a reasonable choice. The materials in the top right hand corner of fig. 8.14 may be promising choices.

These materials are engineering ceramics, titanium alloys, fibre reinforced plastics and glasses. Engineering ceramics and glasses provide a high compressive strength and very low tensile strength. In the case of the flexible fin propeller, both tensile and compressive stresses are applied to the flexible bar. Titanium alloy is an expensive material and is unlikely to be economically viable. Therefore the materials left are fibre reinforced plastics. In addition, if the foil is made of composite material, the flexible bar and the foil can form a single unit and so eliminate losses related to the pod assembly.

The most common fibres used are glass, carbon and Kevlar fibre. The compressive strength of Kevlar fibre reinforced plastic is comparatively weak and is about one quarter of its tensile strength [Bose 1982]. Since both tensile stress and compressive stress act on the bar, Kevlar fibre reinforced materials are not considered here.

One of the main properties of fibre reinforced material is anisotropy. The best mechanical properties occur when the orientation of fibre is in the same direction as the principal working stress. For example, the tensile modulus and tensile strength of random, orthogonal and unidirectional arrangements of glass fibres [Parkyn 1970] are plotted against glass content by weight and shown in fig. 8.15a and b respectively. The mechanical properties of unidirectional glass fibre reinforced plastics are listed in the following table:

Tensile Strength (Longitudinal)	$1.10 \times 10^3 \text{ Nmm}^{-2}$
Tensile Strength (Transverse)	$0.02 \times 10^3 \text{ Nmm}^{-2}$
Tensile Modulus (Longitudinal)	$40.00 \times 10^3 \text{ Nmm}^{-2}$
Tensile Modulus (Transverse)	$10.00 \times 10^3 \text{ Nmm}^{-2}$
Poisson's Ratio (Longitudinal)	0.30
Poisson's Ratio (Transverse)	0.06

Note : Longitudinal is in the same direction as the fibres. Transverse is the direction which is perpendicular to the direction of the fibres with 50% glass by volume.

Table 8.1 Mechanical Properties of Unidirectional Glass Fibre Reinforced Plastic with 50% by Volume (Paton, 1974)

As a bending cantilever is under consideration here, the stresses are mainly in one direction. Theoretically, unidirectional fibre reinforced plastics with a high warp to

weft fibre ratio are applicable here. The weft takes the stresses induced by Poisson's ratio.

The flexible bar considered in this study is a flat bar and suitable for a laminate composite with unidirectional fibre reinforcement.

5.1 Glass Fibre Reinforced Plastics

The example presented in section 4.0 is used here for discussion. The material used in this example is a unidirectional fibre E-glass with epoxy resin. The maximum working stress in this example, as shown in section 4.0, is 278 Nmm^{-2} . The flexural strength of this unidirectional glass reinforced plastic [Bose 1982] is 1000 Nmm^{-2} . The corresponding safety factor is about 3.6 by comparing the working stress and the flexural strength.

In glass-reinforced plastic, fatigue damage commences with debonding separation between the fibre and resin matrix. Resin cracks occur in resin-rich areas. Then cracks appear on those fibres parallel to the direction of the applied force. The final stage is separation. Smith and Owen [1968] studied the fatigue of a chopped strand mat (CSM) - polyester laminate and their result is reproduced in fig. 8.16. Debonding damage appears at a low stress level. The modulus is reduced by the onset of debonding [Smith and Owen 1968] and the stiffness of the flexible bar will decrease. Hence the propulsive thrust generated by the propeller is reduced.

Parkyn [1970] collected fatigue strength data from a number of published results between late 1950 to late 1960. Parkyn [1970, table 18.2] presented 20 fatigue strength results for 'E'-glass reinforced plastic with chopped strand mat reinforced laminates, woven rovings fabric reinforced laminates and unwoven reinforced laminates. The ratio of fatigue strength at a life time of 10^7 cycles to the ultimate strength is between 0.2 to 0.3. Here, this ratio is presented in a histogram as shown in fig. 8.17. A similar range of the ratio of fatigue strength to ultimate strength is shown

by Gibbs & Cox [1960].

Timmins [1977] presents the fatigue S-N curve for a unidirectional 'E' glass (62% glass by volume) with epoxy resin and is reproduced in fig. 8.18 for discussion. In order to take into account uncertainties in practical operating conditions of this type of propeller, a safety factor, say 1.5, is applied to the fatigue life study. In this early stage, a constant safety factor is applied. A sophisticated reliability analysis [Throft-Christensen and Baker 1982] may be required for a more detailed design. The working stress with a safety factor 1.5 is 417 Nmm^{-2} . The corresponding number of cycles for failure are 4.6×10^4 cycles (fig. 8.18). In this example, the oscillating frequency is 21 RPM and the corresponding working life is about one and half days continuous running.

Glass reinforced plastics can be adversely affected by unfavourable environmental conditions. Long term immersion in water may cause reduction in strength. However a flexible water-proof top coat, such as paint or polythene, can be applied to cover the bar and protect it from water absorption.

5.2 Carbon Fibre Reinforced Plastics

Carbon fibre is the other type of fibre commonly used in engineering. This type of composite is relatively insensitive to wet conditions at normal temperature. There are two main types of carbon fibre [eg. Gill 1972] : high strength fibre and high modulus fibre. Both types of fibres are considered here.

a) High Modulus Fibre Reinforced Plastic :

Fatigue effects of high modulus carbon fibre reinforced plastic are low [Broutman and Krock 1974]. Owen and Morris [1970] present the flexural fatigue strength for unidirectional high modulus carbon fibre reinforced plastic in fractions of ultimate flexural stress and is reproduced in fig. 8.19 for discussion. The upper line is

the log mean life while the lower line is the lower bound below which failures are unlikely to occur. At 10^7 cycles, the ratio of fatigue strength to ultimate flexural strength is 0.8 and 0.7 for the upper and lower lines respectively.

Mechanical properties [BP Advanced Materials Ltd. 1989] of a high modulus carbon fibre 'Torayca' M46J carbon fibre (60% carbon by volume) with 120° cure epoxy (from BP Advanced Materials Ltd.) is used here. Its flexural strength and modulus are 1310 Nmm^{-2} and $235,000 \text{ Nmm}^{-2}$. As in the previous section, the required section modulus for the condition in the example is calculated based on the stiffness function 1.8 and the given flexural modulus. The breadth of the bar is fixed as before at 10% of the span (i.e. 0.53 m). Then the calculated thickness function is 17.5 and the working stress is 968 Nmm^{-2} . At the same stiffness function, the high flexural modulus of the bar results in a high working stress. The safety factor on flexural strength was taken as 1.35. If a safety factor of 1.5 is applied in the fatigue life study as before, the corresponding stress is higher than the flexural strength and the beam would fail.

Interlaminar shear fatigue may be more troublesome for high modulus carbon fibre reinforced plastic. The working shear stress of the bar in the example is calculated and found to be only about 20% of the interlaminar shear fatigue stress at 10^6 cycles [Owen and Morris 1972]. Since a long flexible flat bar is considered here, the slenderness ratio is very high : around 200. The bending stress is much higher than the shear stress and dominates the fatigue picture.

b) High Strength Fibre Reinforced Plastic

Unidirectional high strength carbon fibre reinforced plastic is considered here. The mechanical properties of three high strength fibre composite products which are 'Torayca' T300B [BP Advanced Materials Ltd. 1989], SP313 [Robert 1977] and T300/F178 [Robert 1977], are listed in the following table :

Composite :	'Torayca' T300B	SP313	T300/F178
Fibre :	T300B	T300	T300
Curing Resin System:	120°C Epoxy	177°C Epoxy	232°C Polyimide
Fibre Content (in Vol.) :	0.6	0.6	0.6
Tensile Strength (Nmm ⁻²) :	1280	1370	1080
Tensile Modulus (Nmm ⁻²) :	130 x10 ³	140 x10 ³	140 x10 ³
Compressive Strength (Nmm ⁻²) :	-	1085	1241
Compressive Modulus (Nmm ⁻²) :	-	137 x10 ³	125 x10 ³
Flexural Strength (Nmm ⁻²) :	1750	1384	1407
Flexural Modulus (Nmm ⁻²) :	130 x10 ³	122 x10 ³	116 x10 ³

Table 8.2 Mechanical Properties of High Strength Carbon Fibre Reinforced Plastics

The mechanical properties of SP313 is used as an example for this investigation. According to the given flexural modulus, the required section modulus of the flexible bar in the example using SP313 material is calculated. As the breadth of the bar is fixed, the thickness function of the bar is found to be 22.0 and the corresponding working stress is 608 Nmm⁻². The corresponding safety factor is 2.3 by comparing the working stress to the flexural strength.

The experimental results of fatigue behaviour of SP313 are presented by Robert [1977] and are reproduced in fig. 8.20. Here, results are curve-fitted to find the mean values as shown in fig. 8.20. As with the previous section, a safety factor of 1.5 is applied in the fatigue investigation and the stress is 911 Nmm⁻². The corresponding fatigue life is 2.9×10^7 cycles (fig. 8.20). At an oscillating frequency of 21 RPM, the fatigue life is about two and half years continuous running.

The interlaminar shear fatigue behaviour of high strength carbon fibre reinforced plastic is better than glass fibre and high modulus carbon fibre reinforced plastics and is shown by Owen and Morris [1972]. The shear fatigue stress of high strength fibre is about 3 times that of high modulus fibre at 10^6 cycles.

5.3 Hybrid Fibre Reinforced Plastics

Another form of composite material commonly used are hybrid composites, in which a lay up is reinforced with two types of fibres. The hybrid material provides combined advantages of the different fibres and is believed to be a more cost-effective utilization of expensive materials. In principal, two or more different types of fibre can be used in the hybrid composite. The most common hybrid materials are glass-carbon, glass-Kevlar and Kevlar-carbon. There are different ways to combine different fibres to form a hybrid, as follows :

- a) sandwich : one material is sandwiched between two layers of another;
- b) interply : alternate layers of two different materials;
- c) intraply : tows of two different types of fibres are mixed in regular or random manners;
- d) intimately mixed hybrids : fibres are mixed in a completely random manner.

The main property of hybrid materials is the improvement of toughness of a high modulus material (e.g. carbon fibre), HMM, by mixing with low modulus material (e.g. glass), LMM. Kretsis [1987] presents a review of the mechanical properties of hybrid composites. The stress-strain behaviour is significantly improved by the mixture of two different materials. The initial behaviour of the hybrid material follows the high modulus fibre. Fracture in HMM occurs at low strain values and further loading is carried by the LMM. If the bonding is good, HMM still carries loading through the bonding. The failure strain of the HMM is enhanced in hybrid material and this effect is termed the ' hybrid effect'.

The flexural modulus can be controlled by using different ratios of two fibres. In addition, the flexural modulus can be reduced by arranging the stiffer fibre laminate near to the neutral axis of the beam [Kretsis 1987]; this increases the strength to

modulus ratio and is suitable for the requirements of a flexible fin propeller. Other designs of laminate may be possible but more research would be needed to find these.

Different fibres have different fatigue behaviour. Since fatigue is primarily strain dependent, the behaviour is dominated by the HMM. Lubin [1982] reports the fatigue behaviour of hybrid materials of glass-carbon, which consists of balanced laminates of 0° , $\pm 45^\circ$ and 90° oriented plies, with different glass to carbon ratios and is reproduced in fig. 8.21. The fatigue life of a hybrid composite is equivalent to that of a pure carbon fibre reinforced plastic and is substantially greater than a pure glass reinforced plastic. In fact, the glass fibre is restricted from being strained by the stiff carbon fibre and the behaviour is dominated by the carbon fibre. A series of S-N curves for carbon-Kevlar hybrid composites with different fibre ratios of carbon to Kevlar are shown by Curtis [1987]. The increase in Kevlar content increases the slope of the S-N curve. However, the fatigue behaviour is still dominated by the carbon fibre at a ratio of 1:1 and the slope is still rather flat.

By comparing the ultimate flexural strength to the working stress, the glass reinforced plastic beam possesses a higher safety factor than the one with carbon fibre owing to the high stiffness of the carbon fibre reinforced plastics. However, high strength carbon fibre composite shows a much better fatigue life than that with glass fibre. Carbon fibre is expensive [Timmins 1977]. The price of standard unidirectional high strength carbon fibre with 120° C curing epoxy resin prepreg is about 2.3 times that of E-glass fibre prepreg [Canning 1989]. In case of fabric prepreg, the cost of the prepreg with carbon fibre is about six times that with E-glass fibre [Canning 1989]. The hybrid composites of glass-carbon provide a more cost effective material with lower modulus than the pure carbon fibre but keep the good fatigue behaviour of carbon fibre.

6.0 CONCLUSIONS

The working stress of the flexible bar has been calculated by using the theoretical model described in Chapter 4. A series of parametric studies were carried out. A full scale example has been discussed. Material selection has been carried out based on the stress analysis. The following conclusions are drawn from this investigation.

- 1) The compressive stress induced by the force component parallel to the beam axis is small compared to the bending stress and is less than 0.2%. Owing to this, the working stress is found to be proportional to the bending modulus at a constant stiffness function and the same ratio of thickness to length of the flexible bar. Since the slenderness ratio of the bar used for a flexible fin propeller is high, a low shear stress is found.
- 2) Increases of reduced frequency and angular oscillating function increase the working stress of the bar. At a low value of angular oscillating function of 3.0, the stress function at a reduced frequency of 0.2 is twice that for a reduced frequency of 0.6 for a low stiffness function of 3.0. At the same angular oscillating function with a high stiffness function of 12, the stress function at low reduced frequency of 0.2 is 2.5 times the one at 0.6. The working stress at a low angular oscillating function of 3.0 is approximately doubled by increasing this function to 7.0.
- 3) The stress function drops as the stiffness function rises. The effect of stiffness function on the working stress decreases as the stiffness function increases. The mean stress function decreases 60% when the stiffness function is increased from 3.0 to 12.0.
- 4) The stress decreases by increasing the taper ratio of the flexible bar. The mean

decrease in stress function by increasing the taper ratio from 0.0 to 0.2, 0.4 and 0.6 is 17% , 30% and 40% respectively for a stiffness function 12.0 and slightly lower at a lower stiffness function.

- 5) The difference in stress function for different aspect ratios is small.
- 6) Higher stress is obtained from a flexible fin propeller with an elliptical foil than that with a rectangular foil. The difference is greater at high reduced frequencies .
- 7) The stress function increase is directly proportional to the increase of thickness function. This is for both conditions: constant cross-section and linear variation in cross-section.
- 8) Fibre reinforced plastic is found to be a promising material for the bar of a flexible fin propeller. Unidirectional fibre reinforced material with high warp to weft fibre ratio is suitable for the manufacture of the flexible beam of this type of propeller.
- 9) By comparing the flexural strength to working stress in the example, glass fibre reinforced plastic has the highest safety factor of 3.6 against breaking stress. The corresponding safety factors of high strength and high modulus carbon fibre are 2.3 and 1.35 respectively.
- 10) In the fatigue life study, high strength carbon fibre reinforced plastic possesses the best fatigue life which is two and half years continuous running in the example with a factor of 1.5 applied to include the uncertainty in operating conditions. The corresponding fatigue life of glass reinforced plastic in this condition is about one and half days continuous running. The stress of high modulus carbon fibre reinforced plastic with a factor of 1.5 is higher than the steady flexural strength. Both glass and high modulus carbon fibre reinforced plastic are impractical.

- 11) Carbon fibre reinforced plastic is more expensive than glass fibre. The price for unidirectional high strength carbon fibre with epoxy resin prepreg is about 2.3 times that of 'E' glass fibre. For fabric prepreg, the cost of prepreg with high strength carbon fibre is about six times the one with 'E' glass.

- 12) Hybrid glass/carbon fibre composite is a more cost-effective material for the flexible bar. These materials provide a lower modulus than pure carbon fibre and a higher strength than pure glass fibre and good fatigue strength. At present, the most practical way to achieve a working flexible fin propeller on a ship is to use a hybrid composite.

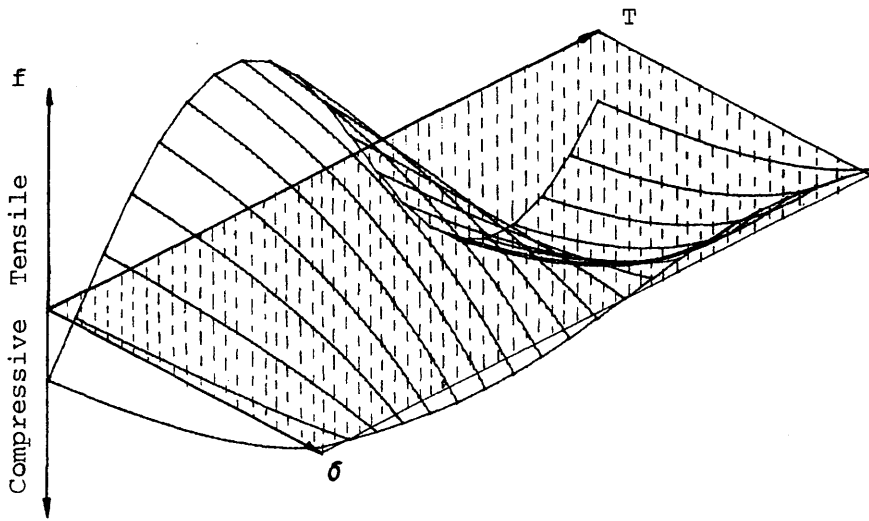


Fig. 8.1 Stress Distribution Along the Flexible Bar within an Oscillating Cycle

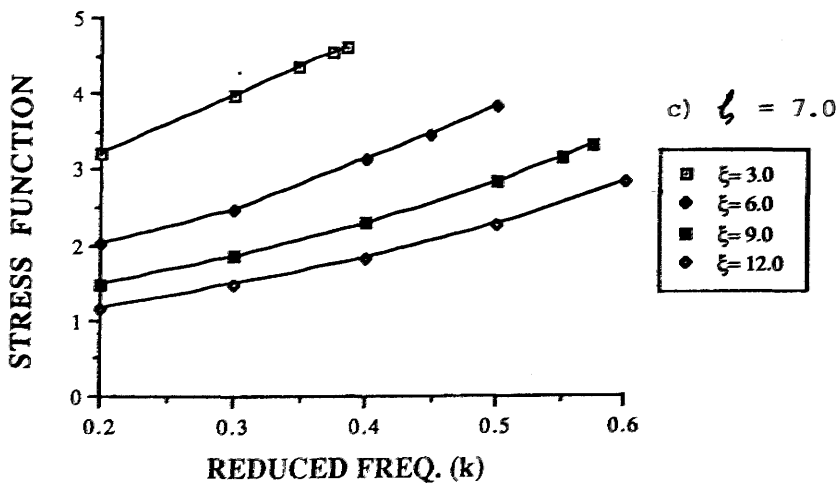
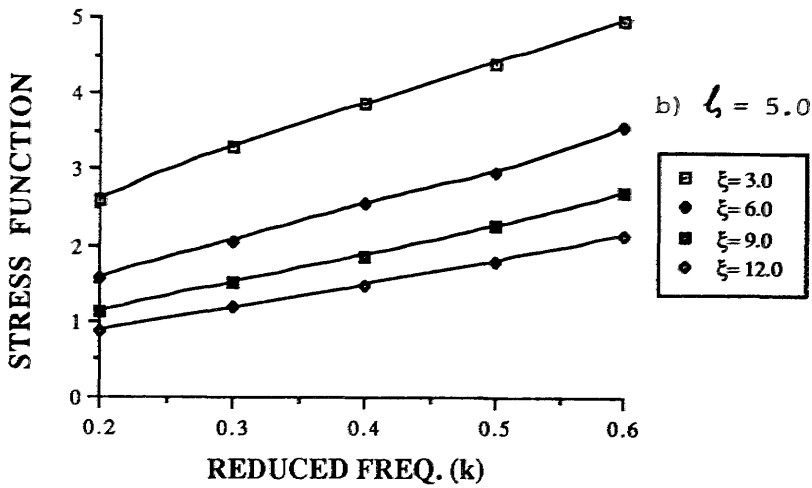
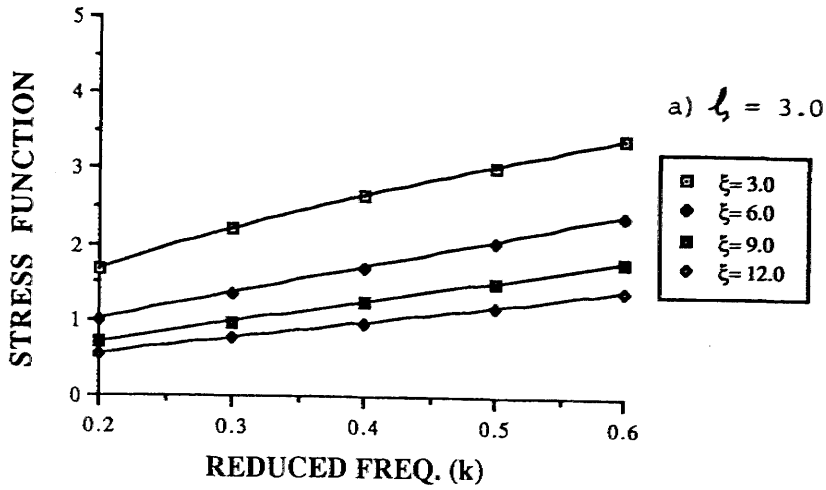


Fig. 8.2 Stress Function for Different Stiffness Function : AR= 4.0

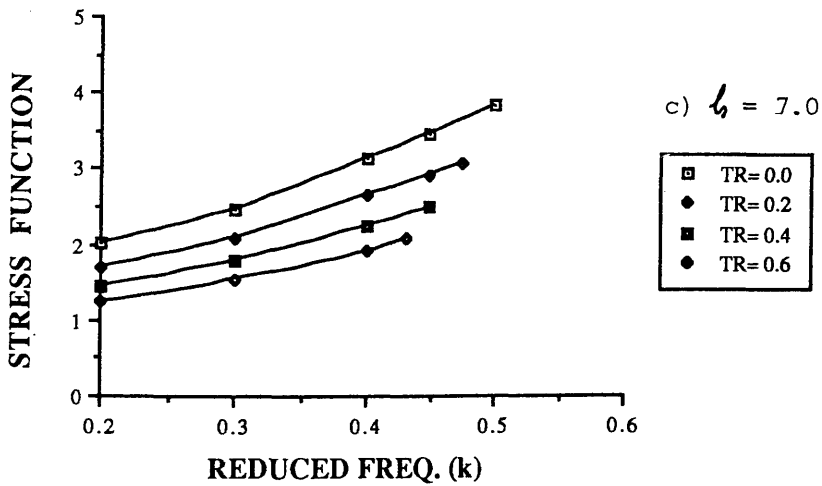
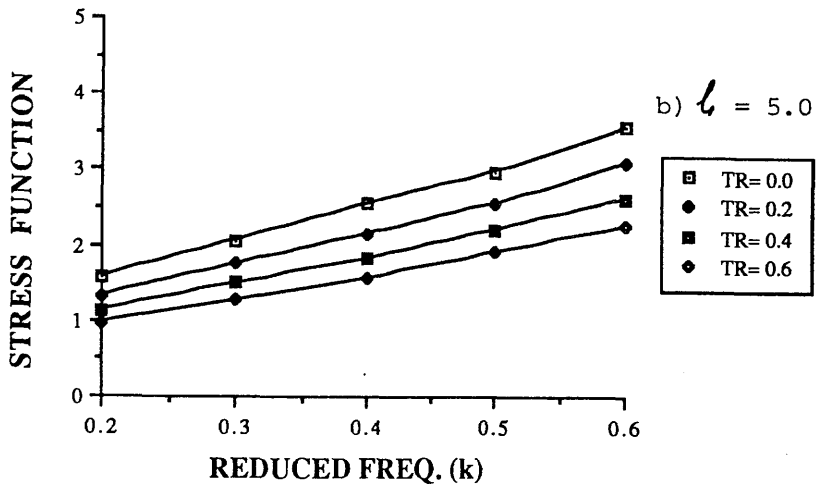
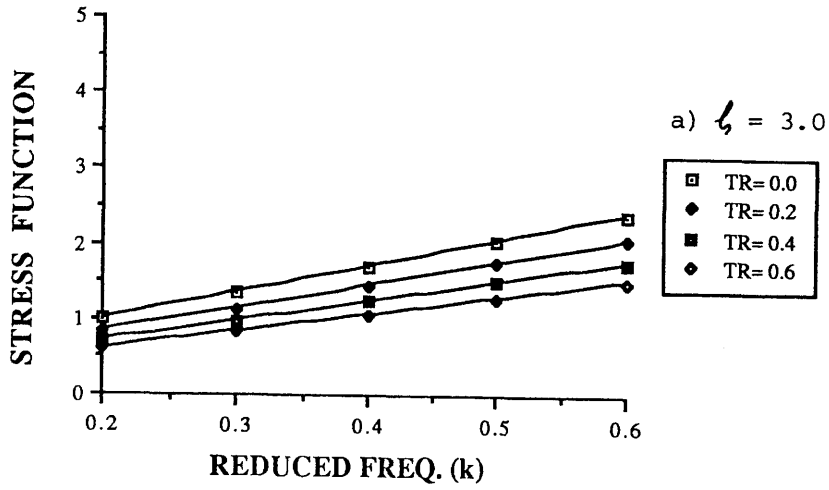


Fig. 8.3 Stress Function for Different Taper Ratios : AR = 4.0, $\zeta = 6.0$

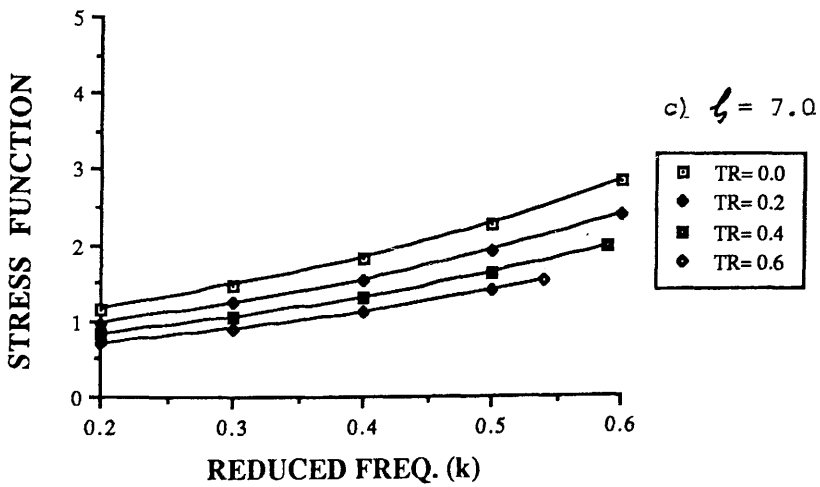
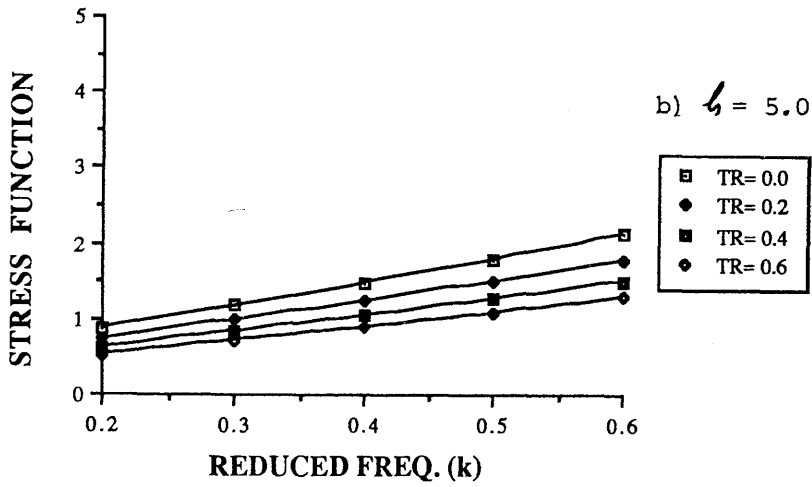
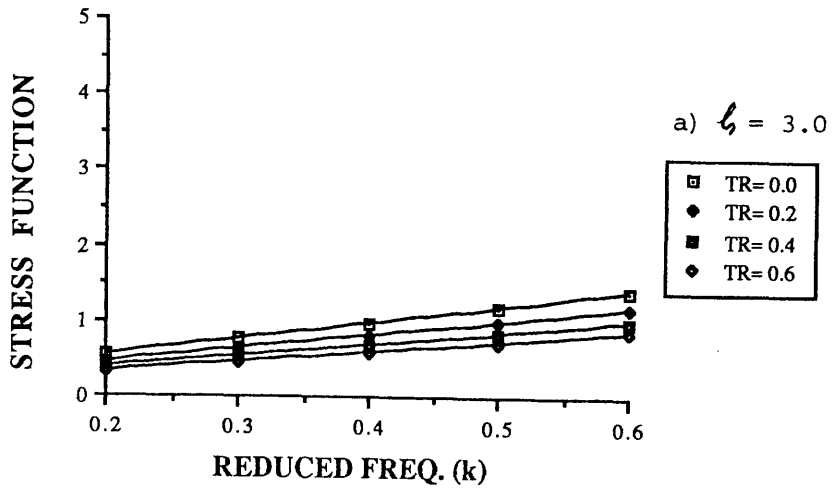


Fig. 8.4 Stress Function for Different Taper Ratios : AR = 4.0, $\zeta = 12.0$

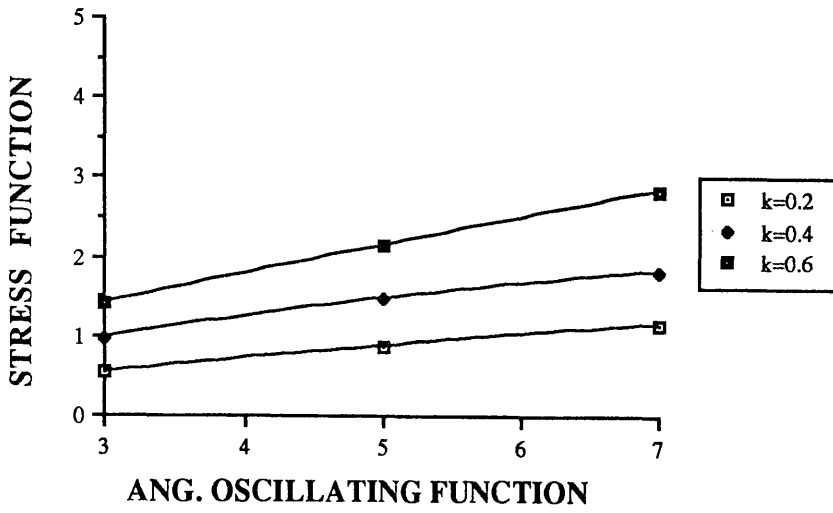


Fig. 8.5 Stress Function for Different Angular Oscillating Functions : $\xi = 12.0$

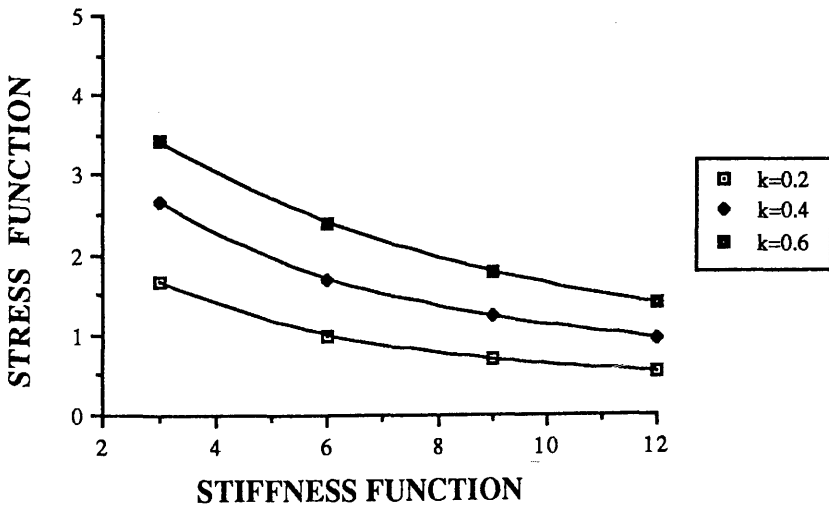
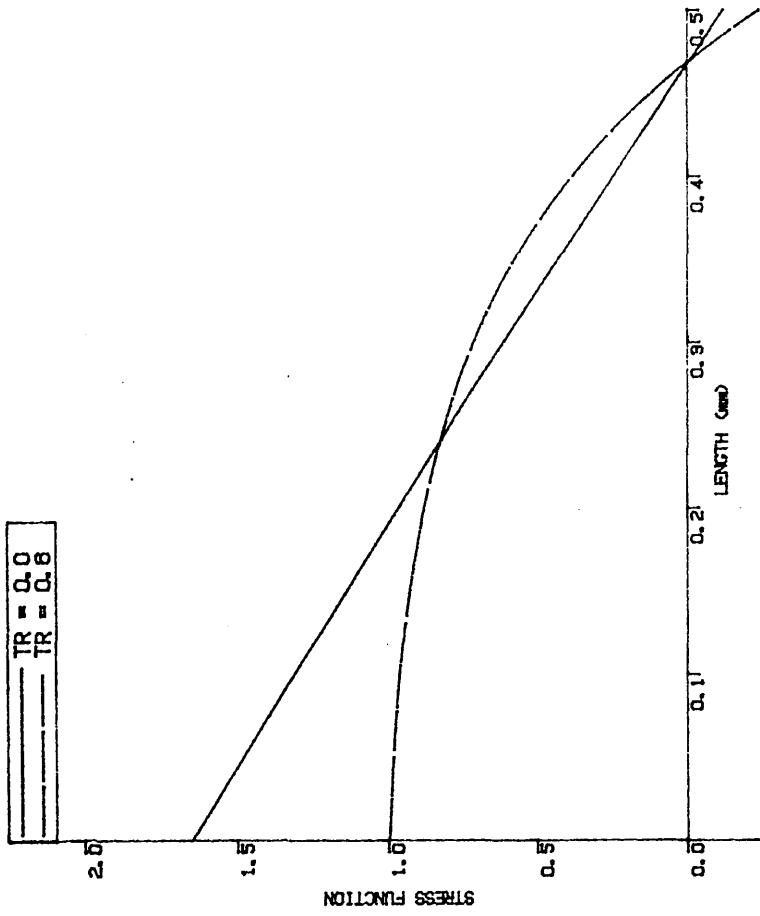
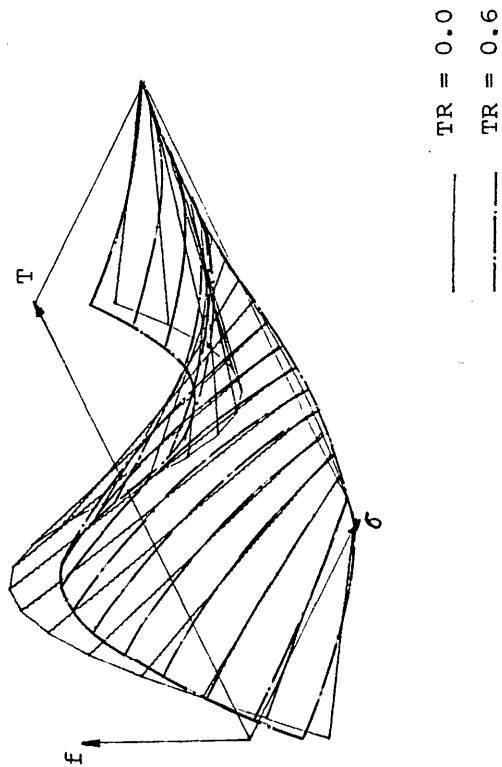


Fig. 8.6 Stress Function for Different Stiffness Functions : $\delta = 3.0$



Stress Distribution Along Flexible Bars

Fig. 8.8



Comparison of Stress Distribution Along Bars with Constant Cross-Section (TR=0.0) and Linear Variation in Thickness (TR=0.6)

Fig. 8.7

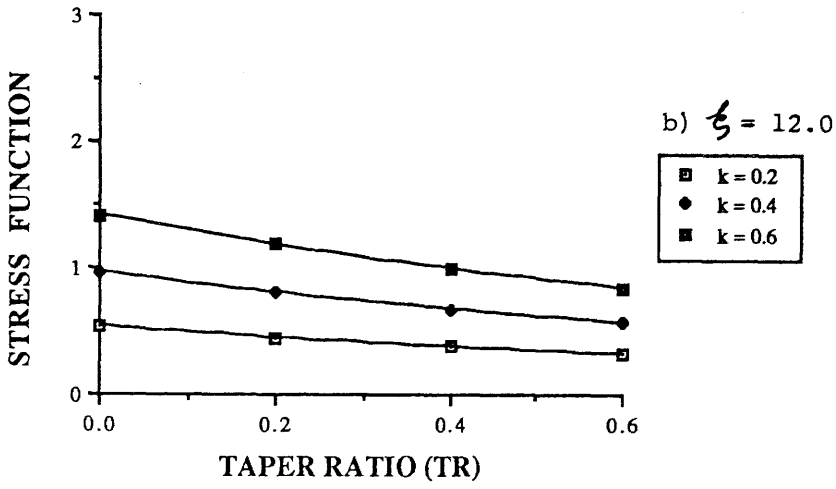
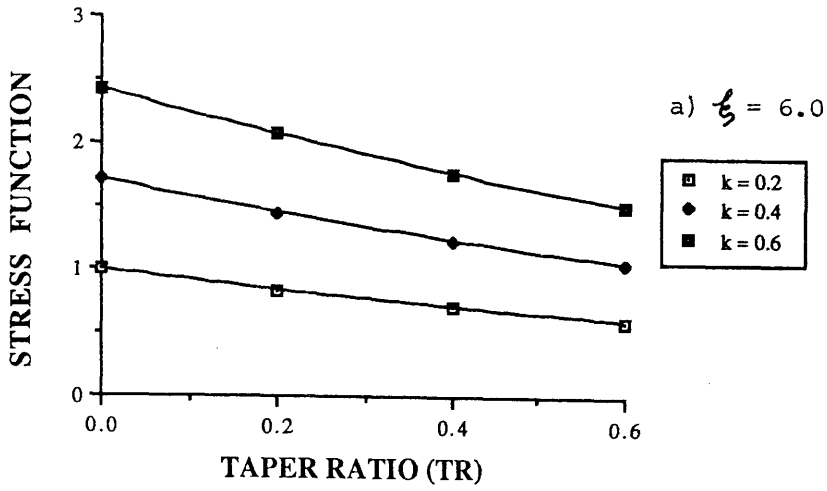


Fig. 8.9 Stress Function for Different Taper Ratios : $\xi = 3.0$

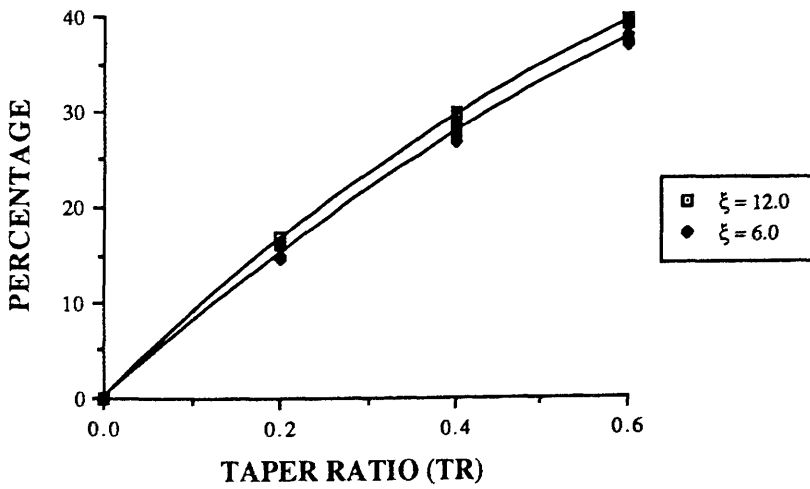


Fig. 8.10 The Percentage of Stress Function Drops for Different Taper Ratios

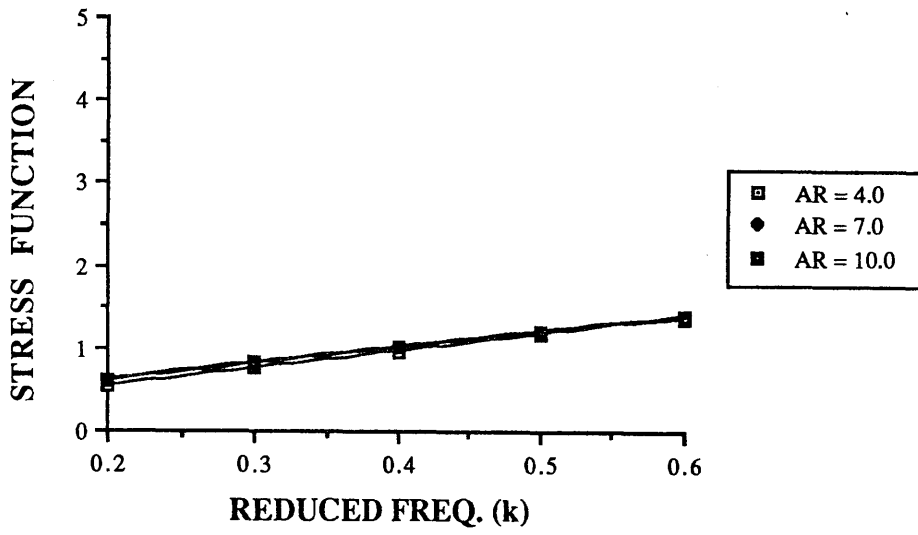


Fig. 8.11 Stress Function for Different Aspect Ratios : $\xi = 12.0, \eta = 3.0$

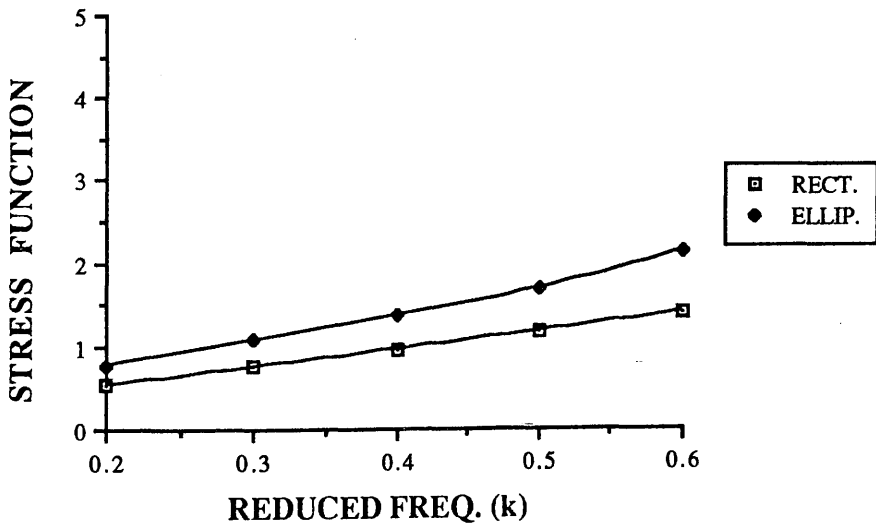
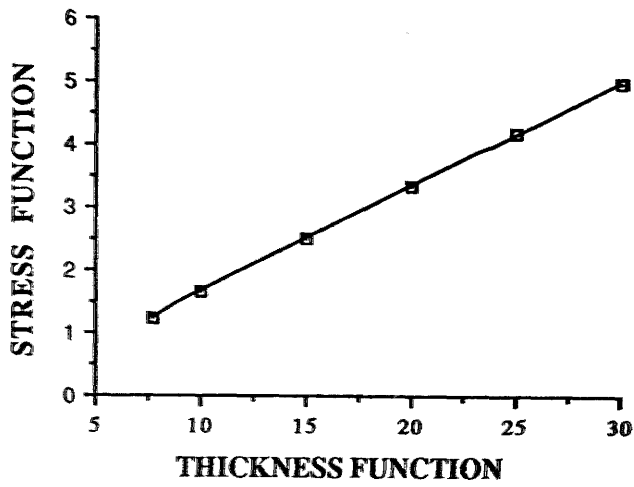
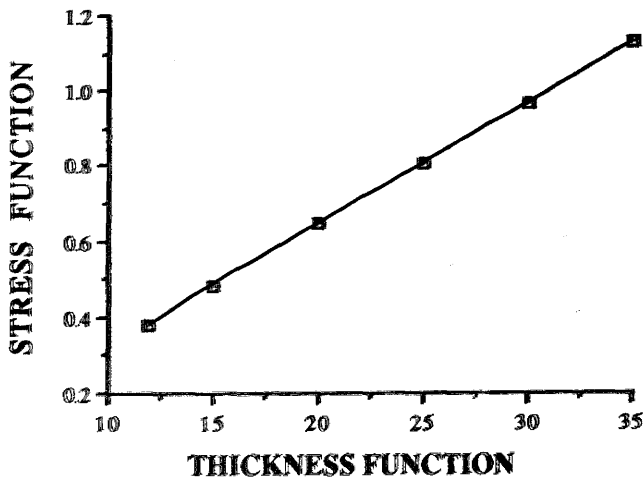


Fig. 8.12 Stress Function for Rectangular & Elliptical Foils : $\xi = 12.0, \eta = 3.0$

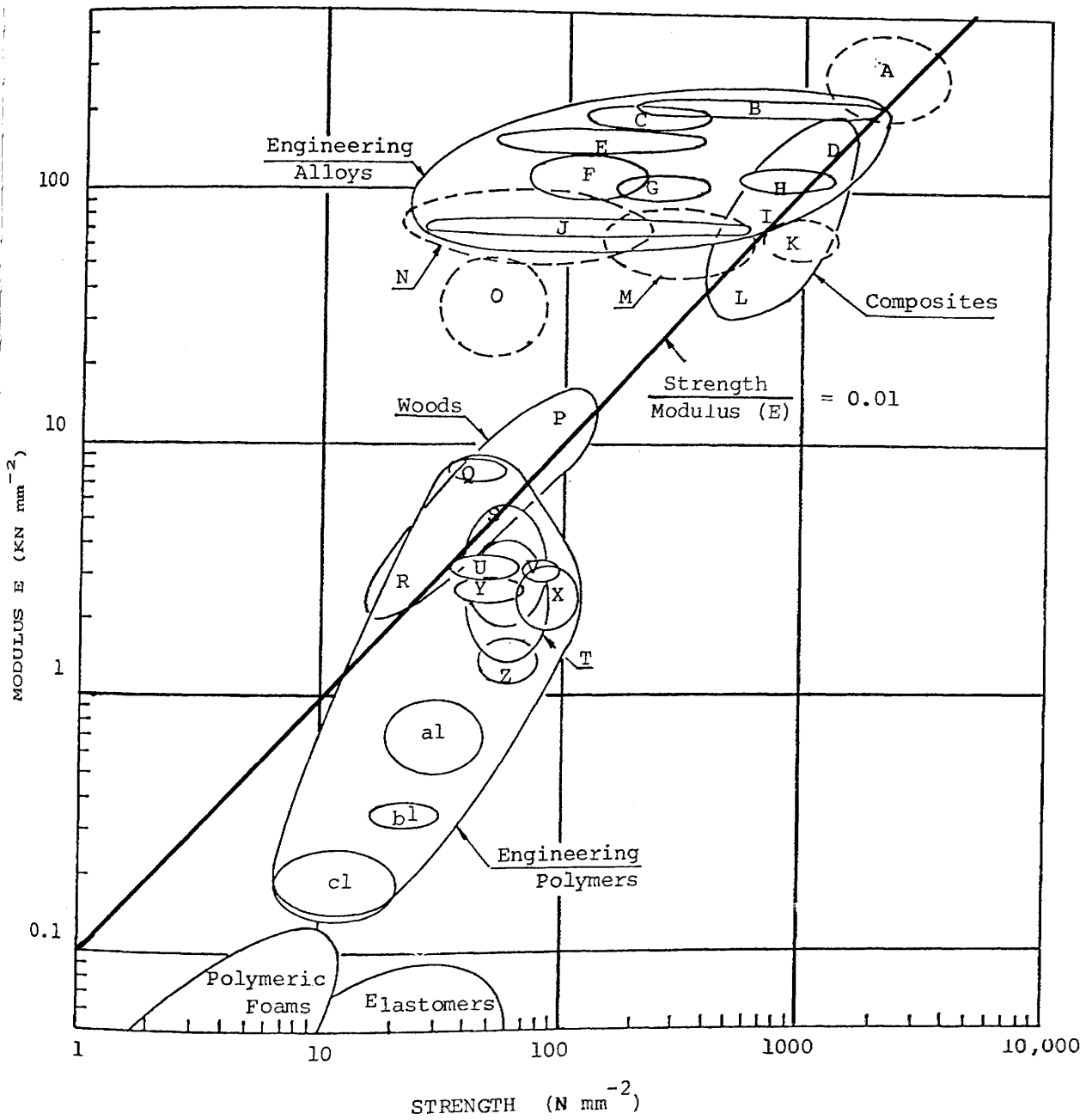


a) $TR = 0.0$



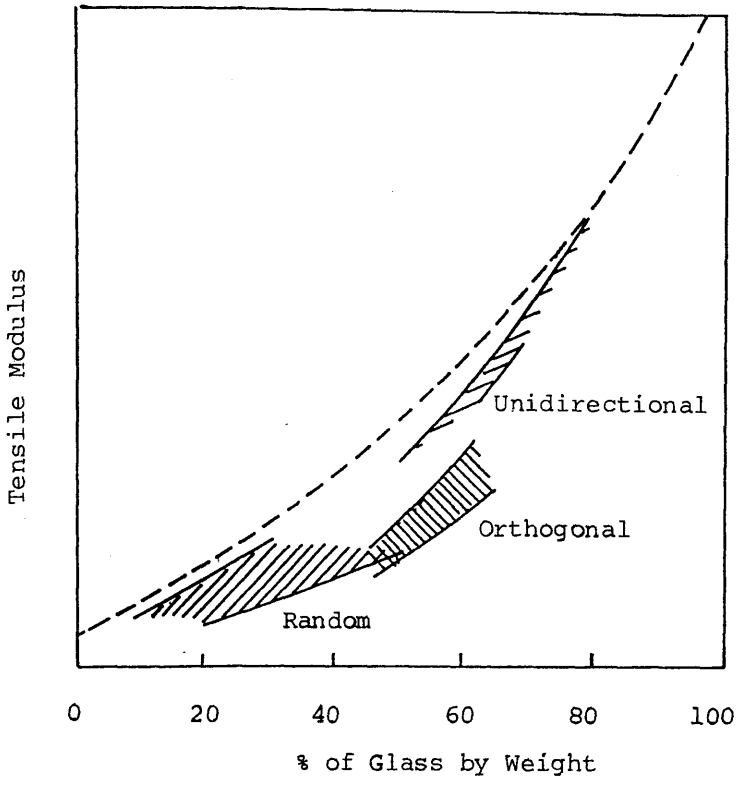
b) $TR = 0.6$

Fig. 8.13 Stress Function for Different Thickness Functions : $k = 0.2$,
 $b = 12.0$ $h = 3.0$

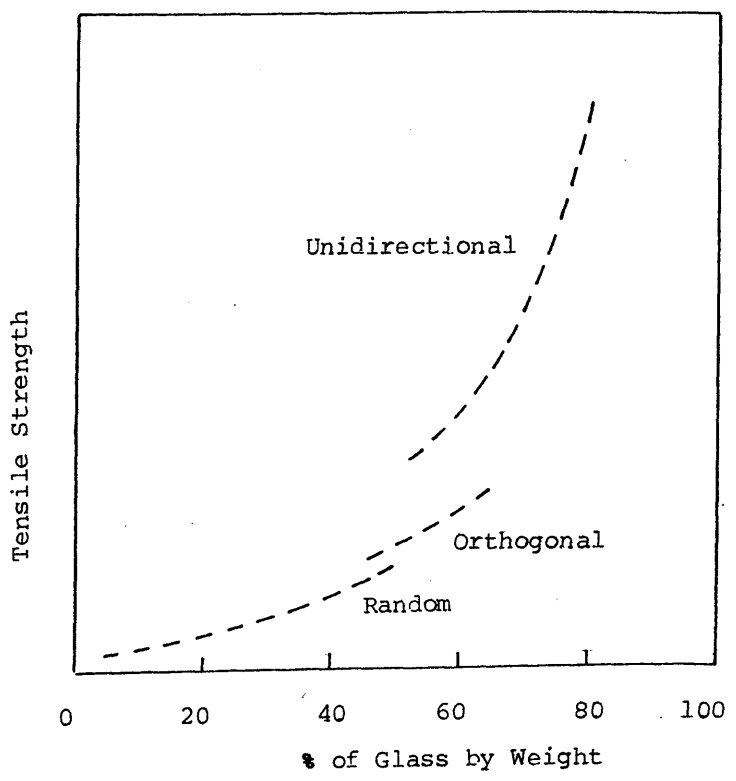


- | | | | | | |
|---|---------------------------------|---|--------------------------------|----|------------|
| A | Engineering Ceramics (Comp.) | K | Glasses (Comp.) | T | Polyesters |
| B | Steel | L | Glass Fibre Reinforced PLastic | U | PS |
| C | Ni Alloy | M | Brick Pottery (Comp.) | V | PMMA |
| D | Carbon Fibre Reinforced Plastic | N | Rock & Stone (Comp) | X | Nylons |
| E | Cast Iron | O | Cement and Concrete (Comp.) | Y | PVC |
| F | Cu Alloy | P | Oak, Ash & Pines | Z | PP |
| G | Zinc Alloy | Q | PF | a1 | HDPE |
| H | Ti Alloy | R | Balsa | b1 | PIFE |
| I | Kevlar Fibre Reinforced Plastic | S | Epoxies | c1 | LDPE |
| J | Al Alloy | | | | |

Fig. 8.14 Material Selection Chart : Modulus (E) Vs Strength (Ashby 1989)



(a) Tensile Strength Vs Glass Content



(b) Tensile Modulus Vs Glass Content

Fig. 8.15 Comparison between Different Fibre Arrangements in GRP (Parkyn, 1970)

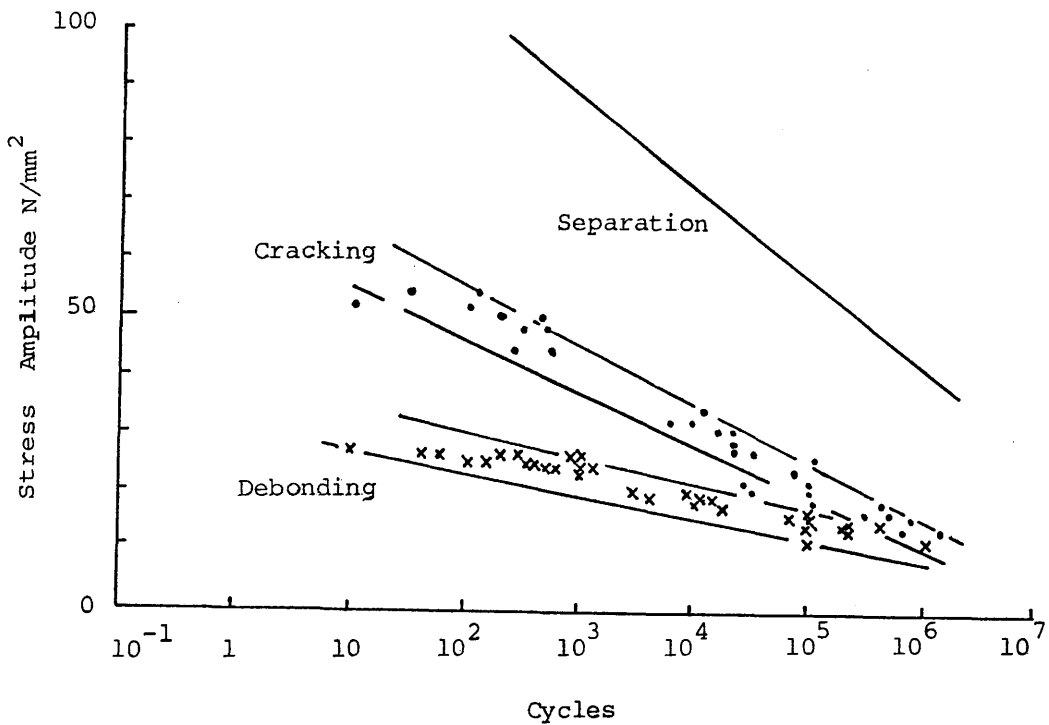


Fig. 8.16 The Fatigue S-N Diagram for Various Stages of Failure in Chopped Strand Mat - Polyester Resin Laminate (Smith and Owen, 1968)

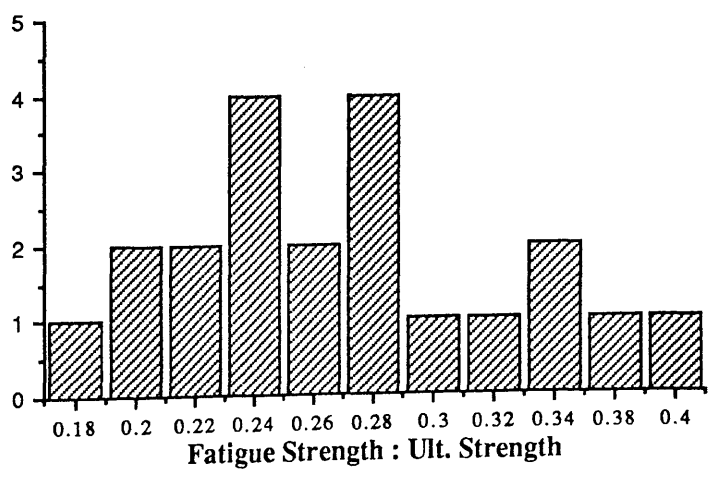


Fig. 8.17 The Histogram of the Ratio of Fatigue Strength at 10⁷ cycle to Ultimate Strength for 20 Published Results (Parkyn, 1970)

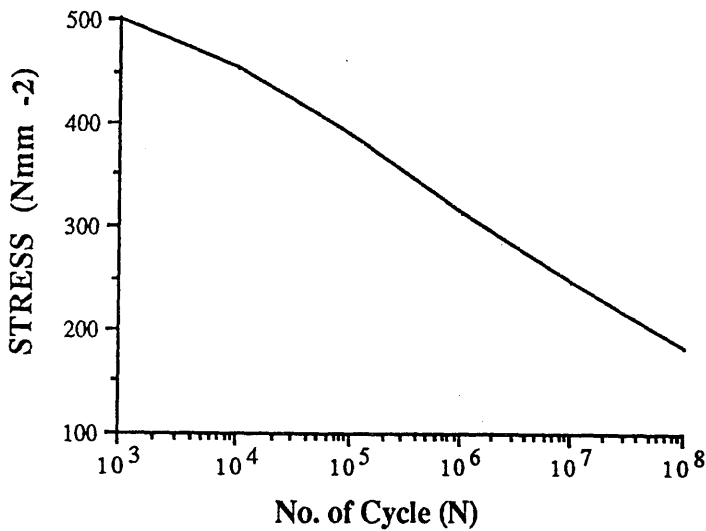


Fig. 8.18 Fatigue Strength S-N Diagram for Unidirectional 'E' Glass (62% by Vol.) with Epoxy (Timmins 1977)

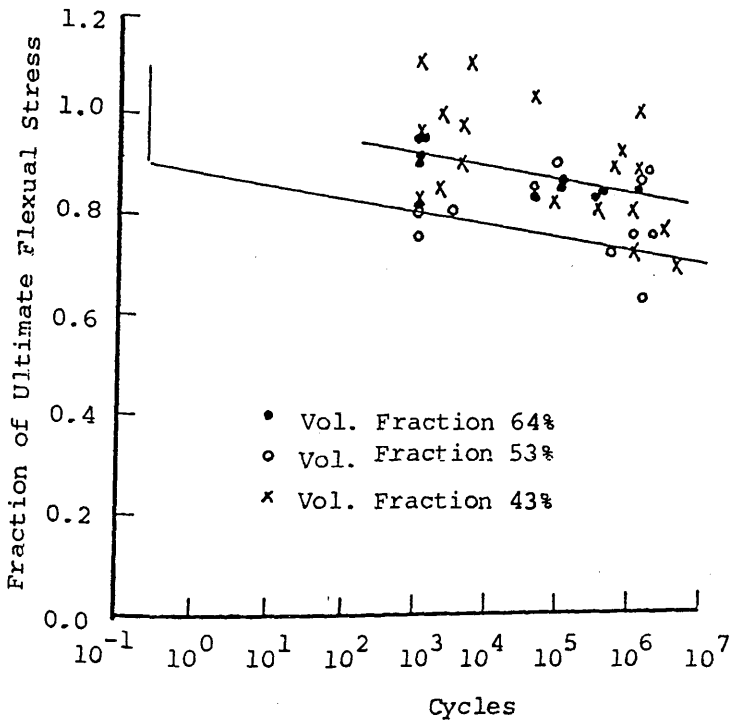


Fig. 8.19 Normalised Flexural Fatigue Results for Unidirectional, High Modulus Carbon Fibre with Polyester Resin. (Owen and Morris, 1970)

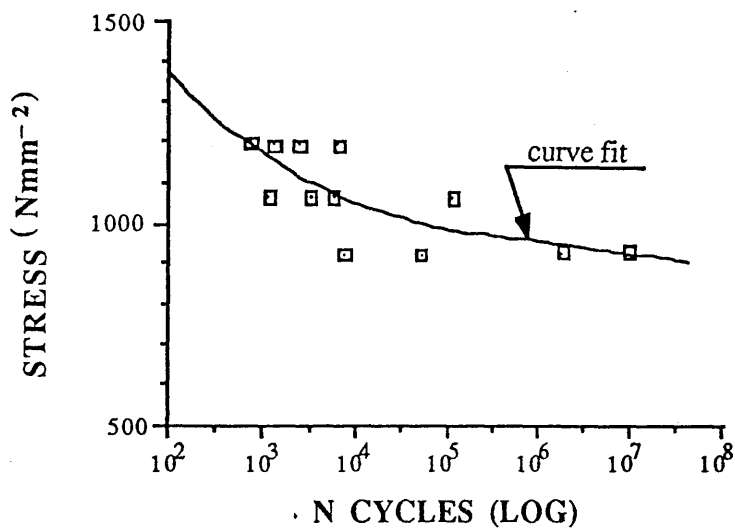


Fig. 8.20 Fatigue Behaviour of Unidirectional High Strength Carbon Fibre Reinforced Plastics (SP313) (Robert, 1977)

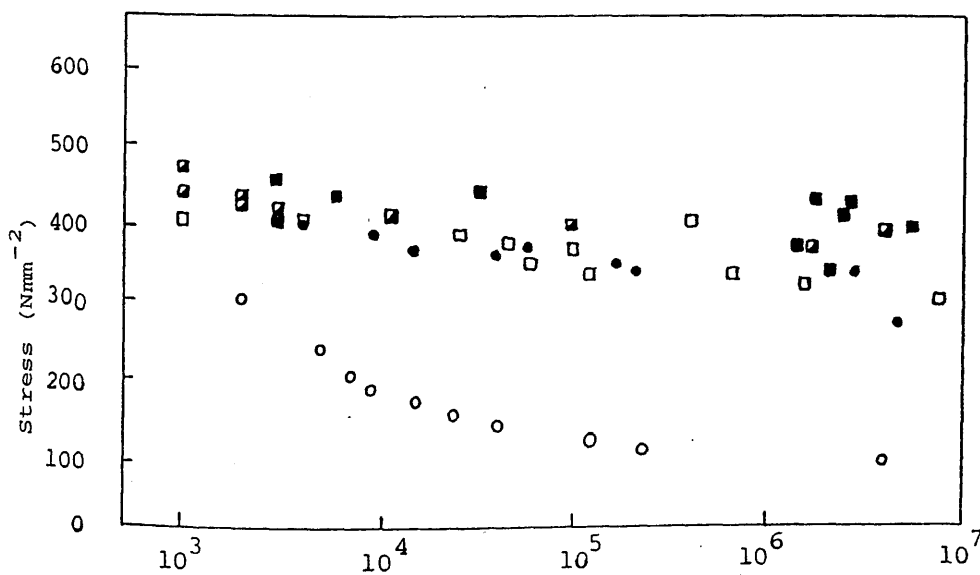


Fig. 8.21 Comparison of the Fatigue Behavior of Quasi-isotropic Carbon/Glass Hybrid Composites (Lubin, 1982)

Glass ○, Carbon ●, Glass to Carbon ratio : 1:1 □, 1:2 ■, 1:3 ■

CHAPTER 9

ON WAVE PROPULSION WITH A FLEXIBLE FIN PROPELLER

1.0 INTRODUCTION

In the world's oceans, there are many natural energy sources. One of the most widely distributed energy sources is wave energy. Inventors have proposed different devices to convert wave energy to other forms of energy : electricity and energy for ship propulsion. Dolphins are well known to be able to surf in the crest of waves or the bow wave of a ship [Woodcock 1951, Lang 1974]. This wave surfing is a good example of the use of wave energy for locomotion in the natural world.

As far back as 1895, Linden obtained a U. K. patent [Linden 1895] for converting wave energy into propulsive thrust with a flexible flap mounted at the stern of a ship as shown in fig. 9.1. Isshiki et al. [1984] mentioned that Linden had tried his device on a 13 foot boat. However, not much attention was paid to wave propulsion until early 1970. Wu [1972] showed theoretically that it is feasible to extract energy by an oscillating foil in waves. In the early 1980s, a wave motor was invented by Jakobsen [1982 and 1983]. This device comprises a supporting structure which was adapted to be connected to a vessel and extended downward. At the end of the supporting structure, an aerofoil shaped blade is fitted, as shown in fig. 9.2 and the foil heaves and pitches as the vessel heaves and pitches. In order to keep the angle between the blade and the path of the foil small and more effective, an arrangement of springs is used. A similar development with springs and a blade was also developed in Japan by Isshiki [1982]. This spring and foil system was fitted to a ship model (fig. 9.3) and tested and the results were reported by Nagahama et al. [1986]. A more sophisticated theoretical model for propulsion of a two-dimensional oscillating foil in waves is described by Grue et al. [1988]. This reference also showed that energy in waves can be absorbed by an oscillating foil near to the free surface.

In this chapter, the use of a flexible fin propeller as a wave propulsion device is described. The flexibility of the bar provides a spring effect. The propeller is fixed at the stern of a vessel extending horizontally aft and no power is input to the system. The vessel heaves and pitches in response to waves. The motion of the ship induces an oscillating motion at the foil through the flexible connecting bar and propulsive thrust is generated. Composite material may be used for the flexible bar and the foil and a monocoque structure could be formed. Since the oscillation of the foil is controlled by the flexible bar, the system is simpler than both Jakobsen's and Isshiki's designs and may be more economically viable.

To obtain a quick confirmation of the feasibility of this idea, a 0.33m yacht model was purchased and tested in the small tank of the Hydrodynamics Laboratory. A simplified flexible fin propeller was fitted at the stern. The model was tested with and without the propeller for different wave conditions. The model advanced in waves with the propeller and drifted back when the propeller was removed. This is described in section 2.0.

After this design of a flexible fin propeller for wave propulsion was confirmed, a larger scale model test was performed in the main testing tank of the laboratory. A flexible fin propeller model was connected to the stern of a model of a three-quarter ton racing yacht model and this was tested in head seas with a range of different frequencies and forward speeds and two different depths of submergence of the propeller. The resistance and motion of the model were measured with and without the propeller. The propulsive thrust was calculated. Results are compared and discussed in section 3.0. Reduction in motion and resistance were found near to the resonance area.

2.0 THE DEMONSTRATION TEST

2.1 The Model and The Experimental Apparatus

A 0.33m yacht model was used in this demonstration test. The principal dimensions of this model are listed as follows:

L_{WL}	=	0.333 m
Beam	=	0.094 m
Draft (without Keel)	=	0.033 m
Depth (without Keel)	=	0.045 m
Displacement	=	0.548 kg

Table 9.1 Dimensions of the 0.33m Yacht Model

A flexible fin propeller was connected to the transom of the yacht model (fig. 9.4). A rectangular aerofoil shaped fin was used. The particulars of this fin were,

Span (s)	=	0.060 m
Chord (c)	=	0.020 m
Thickness ratio (t/c)	=	0.150
Aspect Ratio (AR)	=	0.333

Table 9.2 Dimensions of the Blade

The blade was connected to the transom through a flexible flat bar with a length of 0.055 m.

The test was conducted in the demonstration tank, which is 3.00 m in length, 0.75 m in breadth and 0.13 m in depth. The arrangement is shown in fig. 9.5. The tank is fitted with a simple wave maker and a beach. The model was tested in waves. A

wave probe was used to measure the wave profile, which was recorded in an IBM-PC and chart recorder. From these measurements, the wave frequency and the wave amplitude were found. Two pointers were mounted at the side of the tank one metre apart. The time of travel between these pointers was used to measure the speed of the yacht model.

2.2 Results and Discussion

The model was tested with and without the flexible fin propeller in different wave conditions. The model heaved and pitched in waves. When the flexible fin propeller was mounted on the model, the motion of the model induced oscillations of the flexible fin propeller. The oscillating foil generated propulsive thrust and propelled the model and it advanced through waves. On the other hand, when the propeller was removed from the model, the yacht drifted backwards in head seas as a result of the wave drift force and the drag caused by the mean horizontal velocity of water particles in waves, which is known as 'Stoke drift' [Lighthill 1978, Lamb 1932]. The speed of model was measured in both conditions. The highest measured advance speed was 0.032 ms^{-1} and the corresponding Froude number was 0.018.

Since a simple wave generator was used in the demonstration tank, the wave amplitudes and frequencies could not be controlled separately and so wave slope ($\Theta = a_o/\lambda$) is used to present the results. Speeds of the model (U) are normalised by the maximum horizontal surface velocity in the wave ($a_o \omega_w$). The model was tested throughout a range of wave slopes between 0.001 and 0.010. Results from both conditions (with and without the flexible fin propeller) are shown in fig. 9.6a where the lines are the best fit to the points. By comparing these two curves, the net values are shown in fig. 9.6b. The non-dimensional speed (v) increases as the wave slope decreases.

3.0 THE EXPERIMENTAL INVESTIGATION OF WAVE PROPULSION WITH A FLEXIBLE FIN PROPELLER

3.1 The model

A yacht model was used in this investigation. This model was a one-fifth scale model of a three-quarter ton racing yacht which was designed according to the International Offshore Rule, 1975 [ORC. 1975] by Castro [1977]. The principal particulars of the model are listed in the following table.

L_{OA}	2.016 m
L_{WL}	1.616 m
B_{max}	0.728 m
B_{WL}	0.552 m
Draft (with Keel)	0.106 m
Draft (without keel)	0.056 m
Displacement	38.387 kg

Table 9.3 Principal Particulars of the 3/4 ton Yacht Model

A flexible fin propeller model was connected at the stern of the yacht model as shown in fig. 9.7. The foil was a wooden rectangular foil with NACA-16-012 section and an aspect ratio of 4.0 (span = 0.4m, chord = 0.1m) (as in section 2.3 of Chapter 7). The flexible bar was also supplied by Aquabatter and was graded as SO (green). The corresponding bending modulus was tested and described in section 2.0 of Chapter 7. This was a flat bar of 50 mm width and its thickness distribution is shown in fig. 9.8. The flexible length of the bar was 500 mm. The main particulars are listed below

Thickness at Free End (t_1) mm	2.3
Thickness at Fixed End (t_2) mm	3.6
Mean Thickness (t_m) mm	3.0
Taper Ratio (TR)	0.46
Bending Modulus (E) Nm ⁻²	35.97×10^9
Mean Sectional Modulus (I_m) m ⁴	1.07×10^{-10}

Table 9.4 The Particulars of the flexible bar

A tee-shaped fixed supporting bracket was mounted on the bottom of the yacht near the stern, as shown in fig. 9.9. The fixed end of the flexible bar of the propeller model was mounted below this tee-shaped bracket. A distant piece was inserted in this bracket. By changing this distant piece, the depth of submergence of the flexible fin propeller was changed. The supporting bracket and distant pieces were made of high strength plastic, nylatron, to minimize their weight.

3.2 The Set Up of the Experiment and Analysis

The model was towed by the main carriage with a pendulum type force dynamometer to measure resistance. Two LEDs were mounted on the model 1.6 m apart, as shown in fig. 9.10. One was near the bow while the other was near the stern. Two selspot cameras were used to record the vertical motions of these two LEDs. A dynamic wave probe was mounted on the carriage to measure the encounter wave profile. The diagrammatic arrangement of the test is shown in fig. 9.11.

A sum and difference unit was used to sum up and find the difference of the signals from the two LEDs. The heaving response was found by taking the mean of these two signals. The difference of these two signals was divided by 1.6 m and the pitching angle was found by taking the arc tangent of this value.

Signals from the sum and difference unit and the dynamic wave probe were recorded in a pen recorder and in an IBM-PC computer. An example is shown in fig. 9.12. The maximum sampling rate of the previous data collection package (PC500H) as described in section 3.0 of Chapter 7 was comparatively slow. Both hardware and software had been improved by the time this test was done. A 24 channel, 12-bit analogue to digital converter (AIP-24) from Blue Chip Technology was fitted in the IBM-PC. The maximum sampling rate of this converter is high; from 1800 samples per second for one channel to 250 samples for 24 channels. Data was collected by a data collection package (AIP-Logger from Blue Chip Technology) and directly stored in ASCII files with LOTUS 123 format. In these experiments, the sampling rate was 32 samples per second. As with the previous experiment, the results were transferred to a VAX 11/730 for analysis.

Three fixed capacitance wave probes were mounted on a bridge near the wave maker and used to measure the wave profile across the tank. These wave probes were mounted at locations of half span, 2/3 span and 1/4 span across the tank width. Signals were stored in the VAX 11/730. The incoming wave profile measured by these fixed wave probes was analysed from the chart records. An example is shown in fig. 9.13.

Spectral analysis was done to analyse the signals from the LEDs and the dynamic wave probe. A subroutine (SPECTRUM.FOR) was written to transform a time data series into a frequency spectrum. The amplitudes of heave, pitch and of the waves were found from the frequency spectrum. The output of the subroutine is a spectrum which shows the amplitude of the oscillating components for different frequencies (NAG routine (G13CBF) was used).

The input to this subroutine is a set of time series data with a regular time interval and the output is a spectrum showing the amplitudes of oscillating components at their oscillating frequencies. A test of the time series data and its spectrum is shown in fig. 9.14. This signal consists of two oscillating components together with a steady offset as shown in the following equation,

$$\text{Value} = 2.5 \sin(\omega_1 t) + 3.5 \cos(\omega_2 t) + 2.0$$

$$\text{where } \omega_1 = 2.5 \text{ rad s}^{-1} (0.398 \text{ Hz}) \quad - 9.1$$

$$\omega_2 = 3.5 \text{ rad s}^{-1} (0.716 \text{ Hz})$$

The spectrum (fig. 9.12b) shows the amplitudes of the different oscillatory components. The value at zero frequency gives the value which is equal to twice that of the mean steady drift value. This factor of two only exists at the zero frequency owing to the form of the Fast-Fourier Transformation. Spectra of heave, pitch and encounter waves in the example shown in fig. 9.12 are shown in fig. 9.15a, b, and c respectively.

3.3 The Non-Dimensional Parameters

The results are presented in non-dimensional form. The following parameters are employed in the present study.

- 1) Froude Number (Fr) :- This parameter is the non-dimensional ratio of advance speed to the square root of the length of the waterline (L_{WL}).

$$Fr = \frac{U}{\sqrt{g L_{WL}}} \quad - 9.2$$

- 2) Heave Coefficient (S_3) :- The heave amplitude (Z_o) of the model is non-dimensionalised by the incoming wave amplitude (a_o).

$$S_3 = \frac{Z_o}{a_o} \quad - 9.3$$

- 3) Pitch Coefficient (S_5) :- The pitch amplitude (ϕ_o) is normalised by the wave amplitude and the length of waterline of the model.

$$S_5 = \frac{\phi_o}{a_o} \cdot L_{WL} \cdot 10^3 \quad - 9.4$$

- 4) Wave Frequency Coefficient (ω_c):- The wave frequency is presented in a non-dimensional form as

$$\omega_c = \frac{\omega_w^2}{g} \cdot L_{WL} \quad - 9.5$$

- 5) Encounter Wave Coefficient (ω_{ec}):- As with the wave frequency coefficient, the encounter frequency is presented in a non-dimensional form.

$$\omega_e = \frac{\omega_{cw}^2}{g} \cdot L_{WL} \quad - 9.6$$

where the encounter frequency in head seas is

$$\omega_{cw} = \omega_w + U \frac{\omega_w^2}{g} \quad - 9.7$$

- 6) Encounter Wave Length Ratio (λ_c): The wave condition is also presented in form of encounter wave length (λ_e) to the length of waterline (L_{WL}).

$$\lambda_c = \frac{\lambda_e}{L_{WL}} \quad - 9.8$$

where

$$\lambda_e = \frac{2\pi g}{\omega_{cw}^2} \quad - 9.9$$

- 7) Propulsive Thrust Coefficient (C_T):- The thrust coefficient used in chapters 5 and 7.0 is also employed here.

3.4 Testing Conditions

In the present study, the yacht model was tested in waves with and without the flexible fin propeller model. The test was performed in head seas with a range of wave frequencies between 0.4 and 1.3 Hz and the corresponding wave frequency coefficients are from 1.0 to 11.0. Three advance speeds of 0.5, 0.7 and 1.3 ms^{-1} were tested. The equivalent Froude numbers are 0.13, 0.18 and 0.33. The depth of submergence of the flexible fin propeller during these tests was equal to the chord length (100mm) of the foil. An additional depth of submergence of 1.5 chord length (150mm) was tested at the same range of wave frequencies with a Froude number of 0.18.

3.5 Motion Response of the Model in Waves

The motion response of the yacht model for three different Froude numbers of 0.13, 0.18 and 0.33 are presented in figs. 9.16, 9.17 and 9.18 respectively. The amplitudes of heave and pitch with and without the flexible fin propeller are shown in figs a and b respectively.

The natural frequencies of heave and pitch of the yacht model were found from tests. These two frequencies were very close to each other at 6.4 rads^{-1} . The peaks of heave and pitch motions were found near to the resonance zone where the encounter wave frequency was close to this natural frequency and the encounter wave length ratio near one. Nagahama [1986] also showed this reduction in motion around the resonant frequency. When the Froude number and the wave frequency coefficient were 0.13 and 4.2 respectively, the motion responses were large and the limit of the two guides (fig. 9.10) were exceeded and no reliable measurement was taken.

The amplitudes of heave and pitch of the yacht model without the flexible fin

propeller are compared to those with the propeller. When the flexible fin propeller model was fitted, the amplitudes of heave and pitch around the resonance zone were reduced. At low Froude numbers of 0.13 and 0.18 and around the peak response, experimental results showed that the pitch responses were reduced by about one-third with the flexible fin propeller fitted (fig. 9.16b and 9.17b) The results also showed that the amplitudes of heave and pitch were reduced by 40% at a low Froude number of 0.13 (fig. 9.16a). During the model test, the frequency corresponding to the peak of motion response of model was either not spotted on or the motion exceeded the limit of guides when the frequency was spotted on. Therefore the maximum reduction in motion response cannot be quoted and the figures mentioned here are conservative and higher values are expected. The effect of a flexible fin propeller on improving the ship motion around the resonance zone decreases as Froude number increases.

At frequencies outside the resonance zone, the differences in motion responses of the yacht model with and without the flexible fin propeller are small. At high encounter wave length ratio, the amplitudes of heave and pitch at low Froude number were slightly increased by fitting the flexible fin propeller (fig. 9.16).

3.6 Resistance of the Model and Propulsive Thrust Generated by the Flexible Fin Propeller in Waves

The resistance of the model in waves and corresponding propulsive thrust coefficients for three Froude numbers are shown in figs. 9.19 to 9.21. The model test was first conducted without the flexible fin propeller fitted. The resistance of the yacht model was measured. Then the flexible fin propeller was fitted and the total resistance of the propeller and the yacht was measured. This measured resistance comprises the resistance of the yacht model, the resistance of the propeller, the propulsive thrust generated by the propeller and the change of resistance owing to the change of ship motion. The resistance of the yacht model is compared to that of the yacht model with the flexible fin propeller and the difference was calculated. The difference is regarded as the apparent propulsive thrust generated by the propeller and is presented in the form of

a propulsive thrust coefficient (figs. b of 9.19 to 9.21).

The tests were conducted over a range of wave frequencies. The waves were generated by a plunger type wave maker driven by a hydraulic system with electronic control. The wave maker was set to give a similar wave amplitude for different wave frequencies. However, it is practically impossible to generate the same wave amplitude for different wave frequencies from the present control device.

The resistance of the model in waves comprises the calm water resistance and the added resistance due to waves. The added resistance is proportional to the square of wave amplitude [Maruo 1957]. The calm water resistances at three Froude numbers were tested. The added resistance of the model in waves was found by subtracting the calm water resistance from the total resistance. The added resistance at a selected height close to the mean of all the experimental wave heights at different wave frequencies is computed by multiplying the added resistance by the square of the ratio of the selected wave height to the measured wave height. The total resistance of the model corresponding to the selected wave amplitude is calculated by adding this computed added resistance to the calm water resistance. The selected wave amplitude of the test was 25 mm and equal to one quarter of the chord length of the foil. Both presented resistances and thrust coefficients were calculated at this mean wave amplitude. Since the model was a one-fifth scale model, the corresponding sea condition for this wave height is realistic.

At low Froude numbers of 0.13 and 0.18, the peak resistances of the yacht model without the propeller were found in wave frequencies where the peaks of motion response were obtained (figs. 9.16, 9.17, 9.19a and 9.20a). At higher Froude numbers, the peak resistances were found at higher wave frequencies than that of the peak motion responses (figs. 9.18 and 9.21a). At all three Froude numbers, the wave frequencies corresponding to peak resistances of the model with propeller were higher than those of the yacht model only.

A reduction in total resistance was obtained near the resonance zone after fitting the flexible fin propeller when the encounter wave length ratio was around 1.0. Similar trends were shown by Nagahama et al. [1986]. From the experimental results, a high thrust coefficient of 0.5 was found at a low Froude number of 0.13. The total resistance was reduced by half by fitting the propeller. For the studied range of wave frequencies ($\omega_c = 1.0$ to 11.0), the percentage of wave frequencies where positive thrust was generated to the whole study range, decreases from 60 % to 15% as the Froude number increases from 0.13 to 0.33. It is believed that positive propulsive thrust would occur for all wave frequencies when the Froude number is low enough. This was also shown in the demonstration test where the highest Froude number was ver low.

When the wave frequency coefficient is higher than 4.0, the thrust coefficient decreases as the Froude number increases. In other words, for a given ship and wave condition where the wave frequency coefficient is higher than 4.0, increase in advance speed decreases the thrust coefficient.

3.7 The Effect of Depth of Submergence of the Flexible Fin Propeller

The depth of the propeller mounting was changed in this study. The propeller was moved to 1.5 chord length below the water line in this study. Since the ballast and the propeller mounting were changed, the yacht model with and without the propeller at a Froude number of 0.18 were tested again for the full range of wave frequencies. The corresponding motion response and resistance are shown in figs. 9.22 and 9.23. In order to highlight this effect, the thrust coefficients of the two depths of submergence of the propeller are plotted together.

The effect of the flexible fin propeller on the reduction of motion response and resistance around the resonance zone was reduced by increasing the depth of submergence. At an encounter wave frequency coefficient of 7.7, the percentages of reduction in motion response and resistance for the two depths of submergence are

shown in the following table.

	Depth of submergence of the flexible fin propeller	
	1.0 c	1.5 c
reduction in heave amplitude	21%	4%
reduction in pitch amplitude	37%	20%
reduction in resistance	35%	14%

Table 9.5 Reduction in Motion Response and Resistance

At the same encounter frequency coefficient, the thrust coefficient was reduced by two-thirds by increasing the depth of submergence from one chord length to 1.5 chord lengths (fig. 9.23).

4.0 CONCLUSIONS

The feasibility of using a flexible fin propeller as a wave propulsion device has been examined and the following conclusions are drawn.

- 1) When the flexible fin propeller was fitted on the 0.33m yacht model, the model advanced in waves. The model drifted back in waves when the flexible fin propeller was removed. The highest measured advance speed in this demonstration test was 0.032 ms^{-1} and the equivalent Froude number was 0.018. The idea of using a flexible fin propeller to convert wave energy into propulsive energy was successfully demonstrated.
- 2) When the wave length is close to the length of the water line, reductions in amplitudes of heave and pitch are obtained by use of a flexible fin propeller. A 40% reduction in heave motion was obtained at a low Froude number of 0.13. At Froude numbers of 0.13 and 0.18, the measured amplitudes of pitch reduced by one-third. Higher reduction is expected at the peak motion response.

- 3) The differences in motion response between the model with and without the flexible fin propeller are small outside the resonance zone. At a low Froude number of 0.13 and high encounter wave length ratio, the amplitude of heave was increased slightly by fitting the flexible fin propeller.
- 4) As with the motion response, the resistance is reduced in the resonance area by mounting the propeller. High propulsive thrust coefficients are generated by the propeller at low Froude numbers. The highest measured thrust coefficient is 0.5 with a reduction in resistance of 53%.
- 5) The band width of wave frequencies where resistance was reduced decreases as the Froude number increases. The percentages of these wave frequencies to the full studied range drops from 60% to 15% by increasing the Froude number from 0.13 to 0.33.
- 6) In a wave condition with a wave frequency coefficient higher than 4.0, the thrust coefficient generated by the flexible fin propeller of a ship decreases as the advance speed increases.
- 7) The reduction in both motion response and resistance decreases as the depth of submergence of the foil increases. At an encounter frequency coefficient of 7.7, the thrust coefficient was reduced by two-thirds by increasing the depth of submergence from one chord length to 1.5 chord lengths.

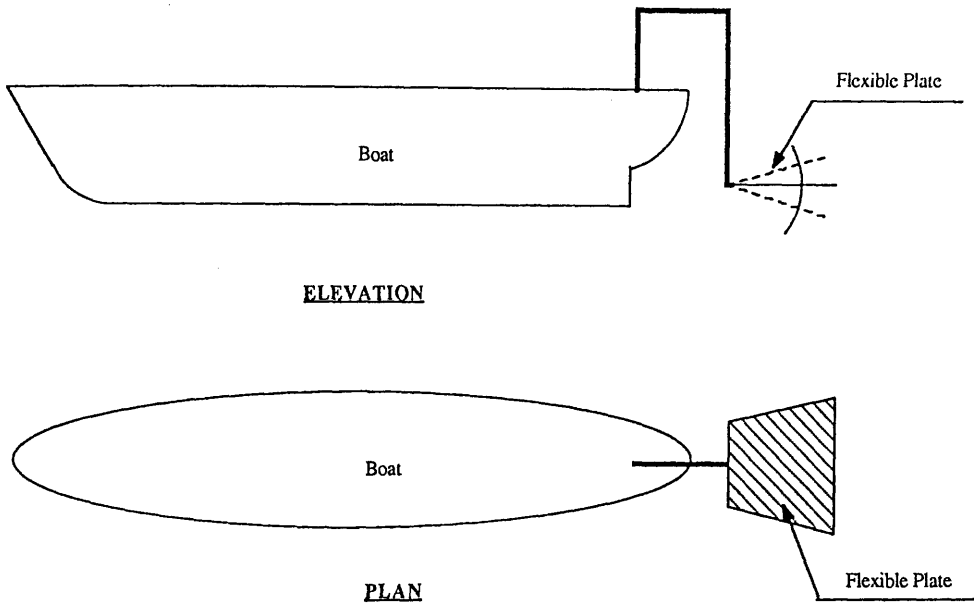


Fig. 9.1 LINDEN'S WAVE PROPULSION DEVICE

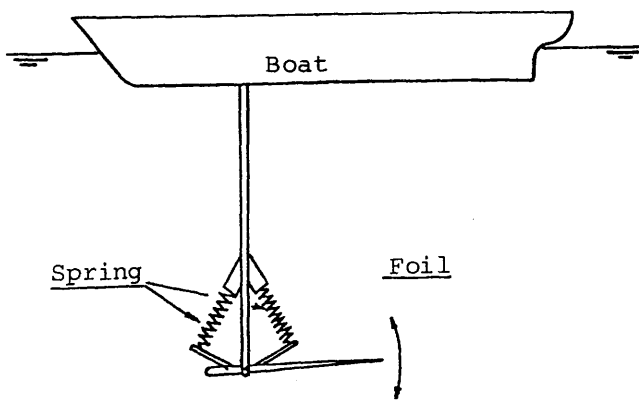


Fig. 9.2 Jakobsen's Wave Motor

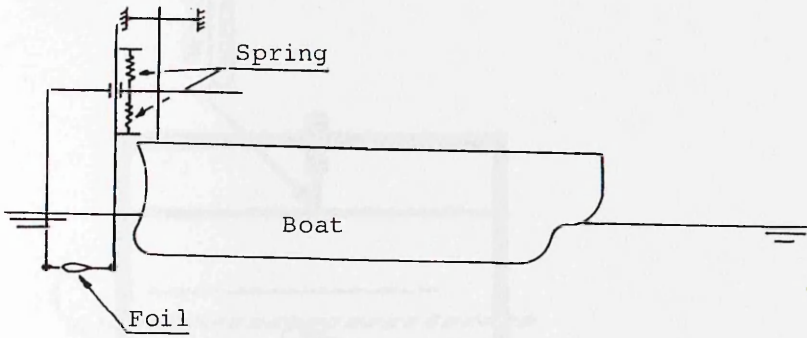


Fig. 9.3 The Ship Model with the Springs and Foil System

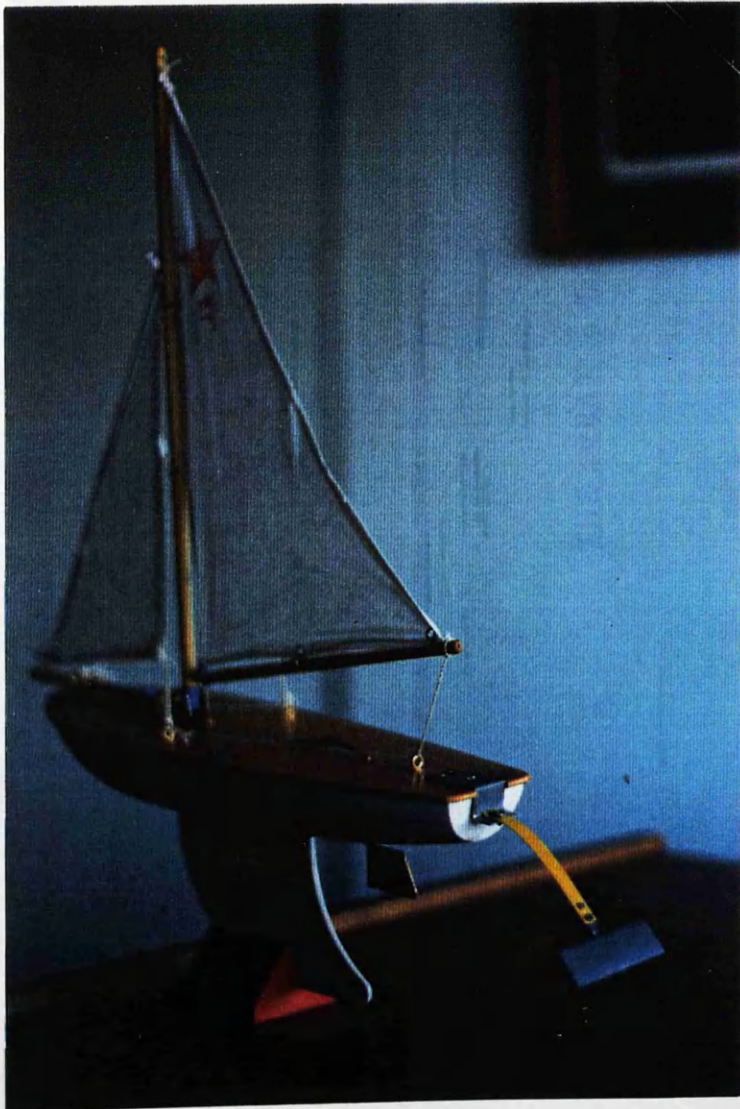
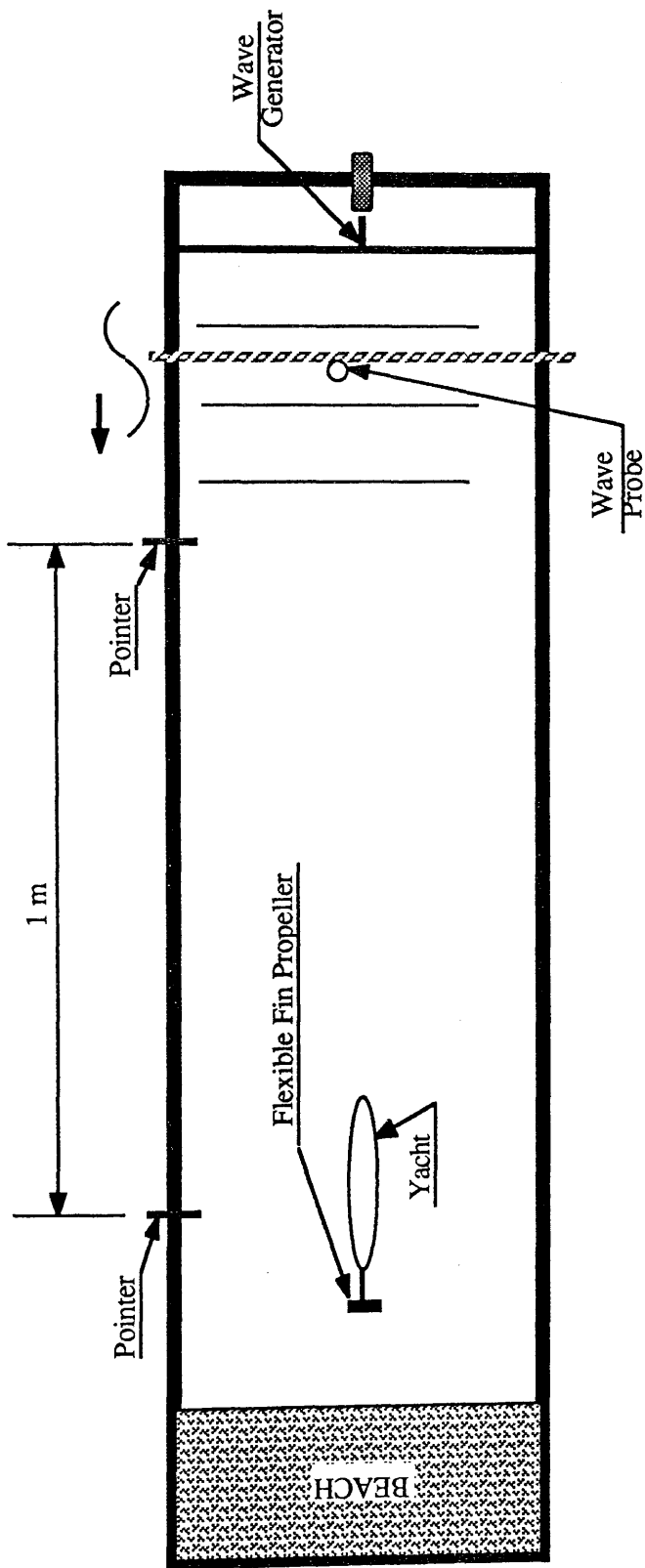


Fig. 9.4 The 0.33m Yacht Model with Flexible Fin Propeller



THE ARRANGEMENT OF THE MODEL TEST

Fig. 9.5

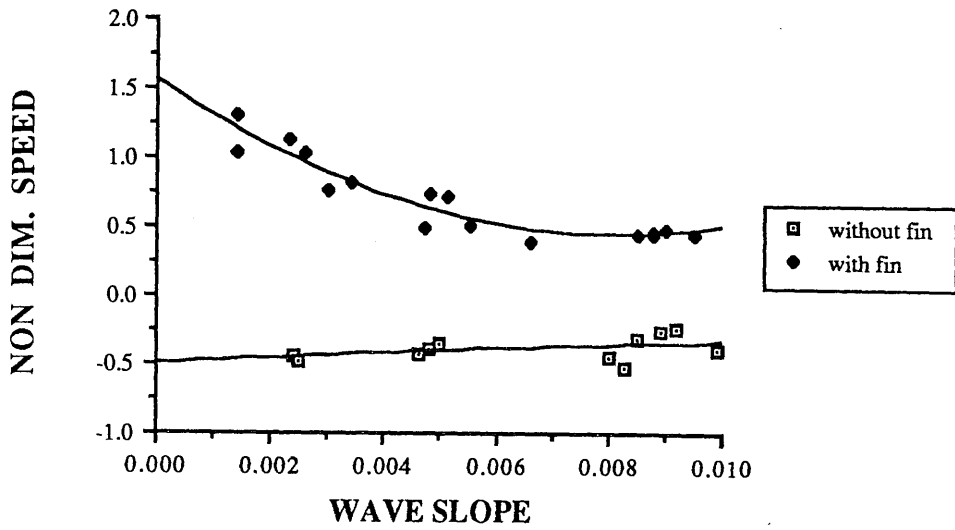


Fig. 9.6a The Speed of Model with and without Flexible Fin Propeller

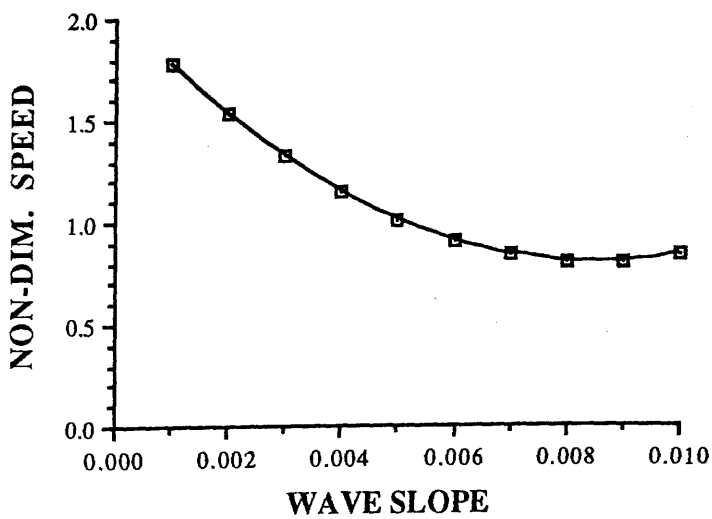


Fig. 9.6b The Net Speed of the Model

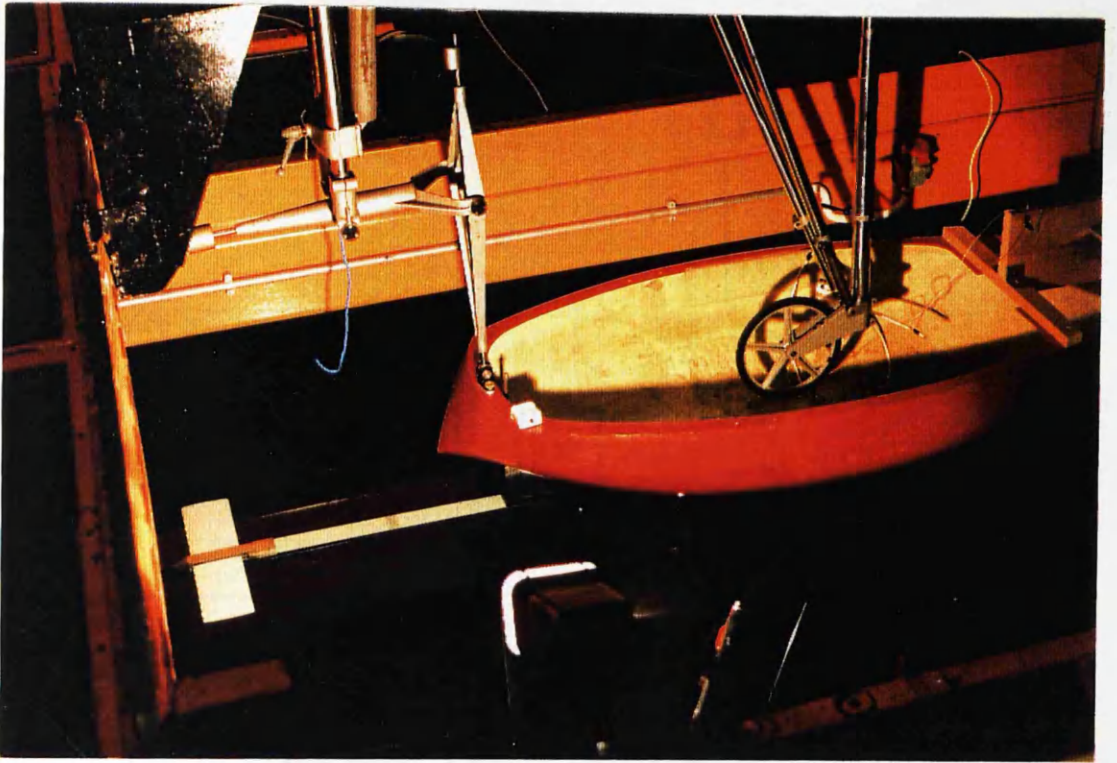


Fig. 9.7 The Three Quarter Ton Racing Yacht Model with Flexible Fin Propeller

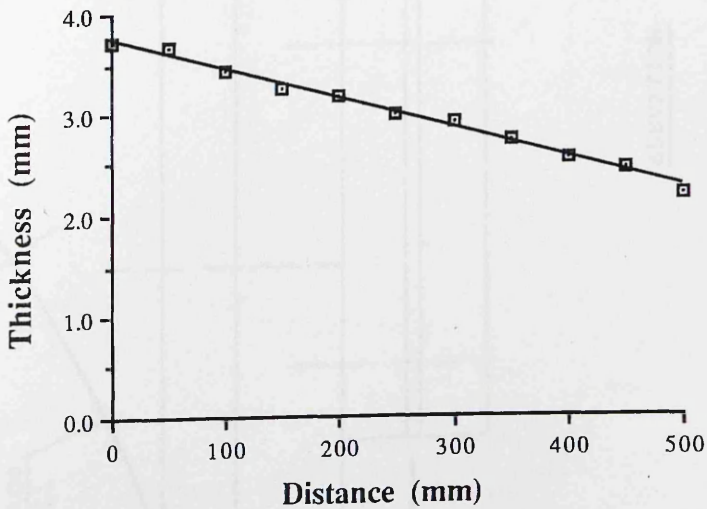


Fig. 9.8 The Thickness Distribution of the Flexible Bar

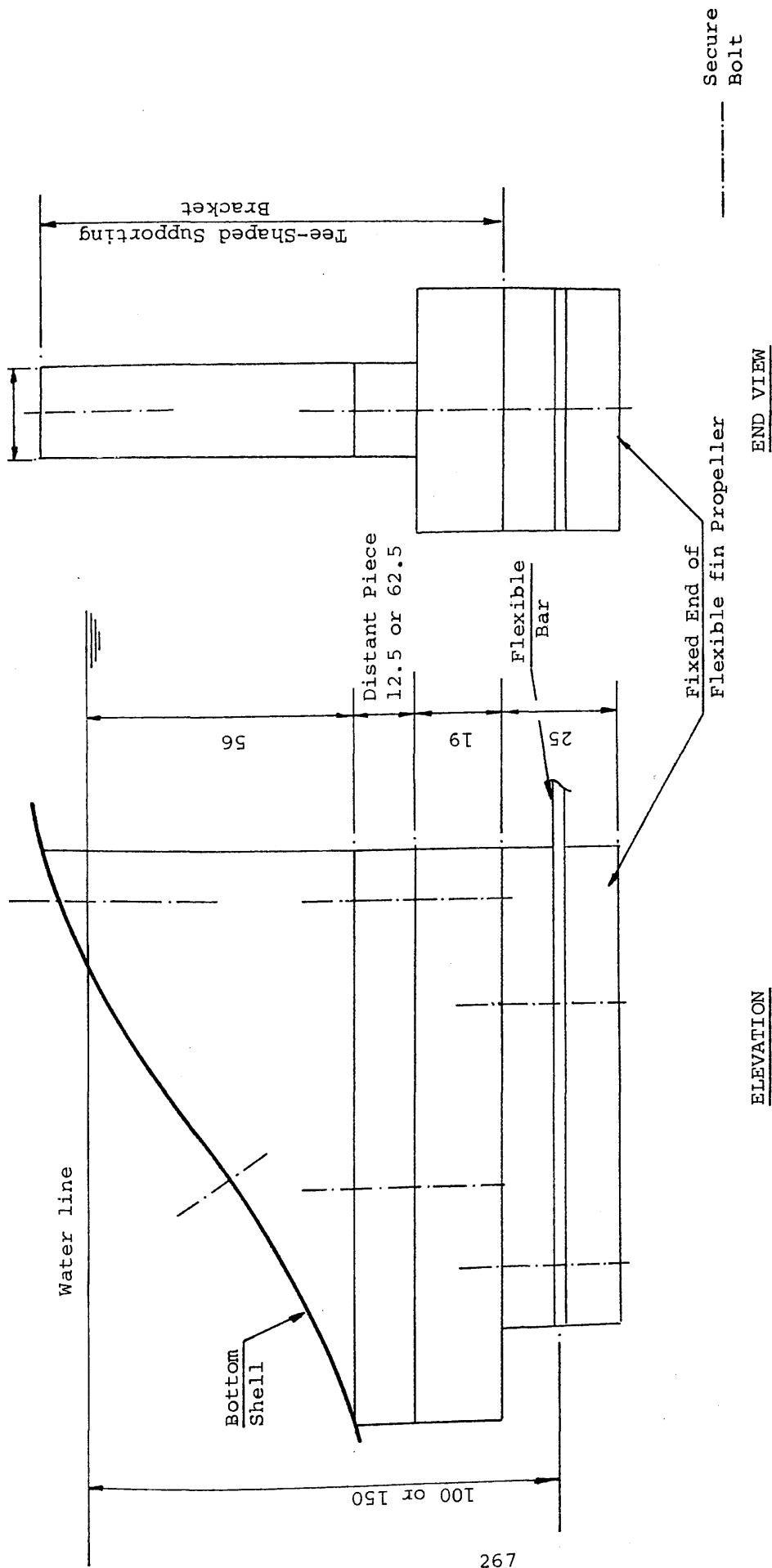


Fig. 9.9 THE ARRANGEMENT OF THE MOUNTING OF THE FLEXIBLE FIN PROPELLER

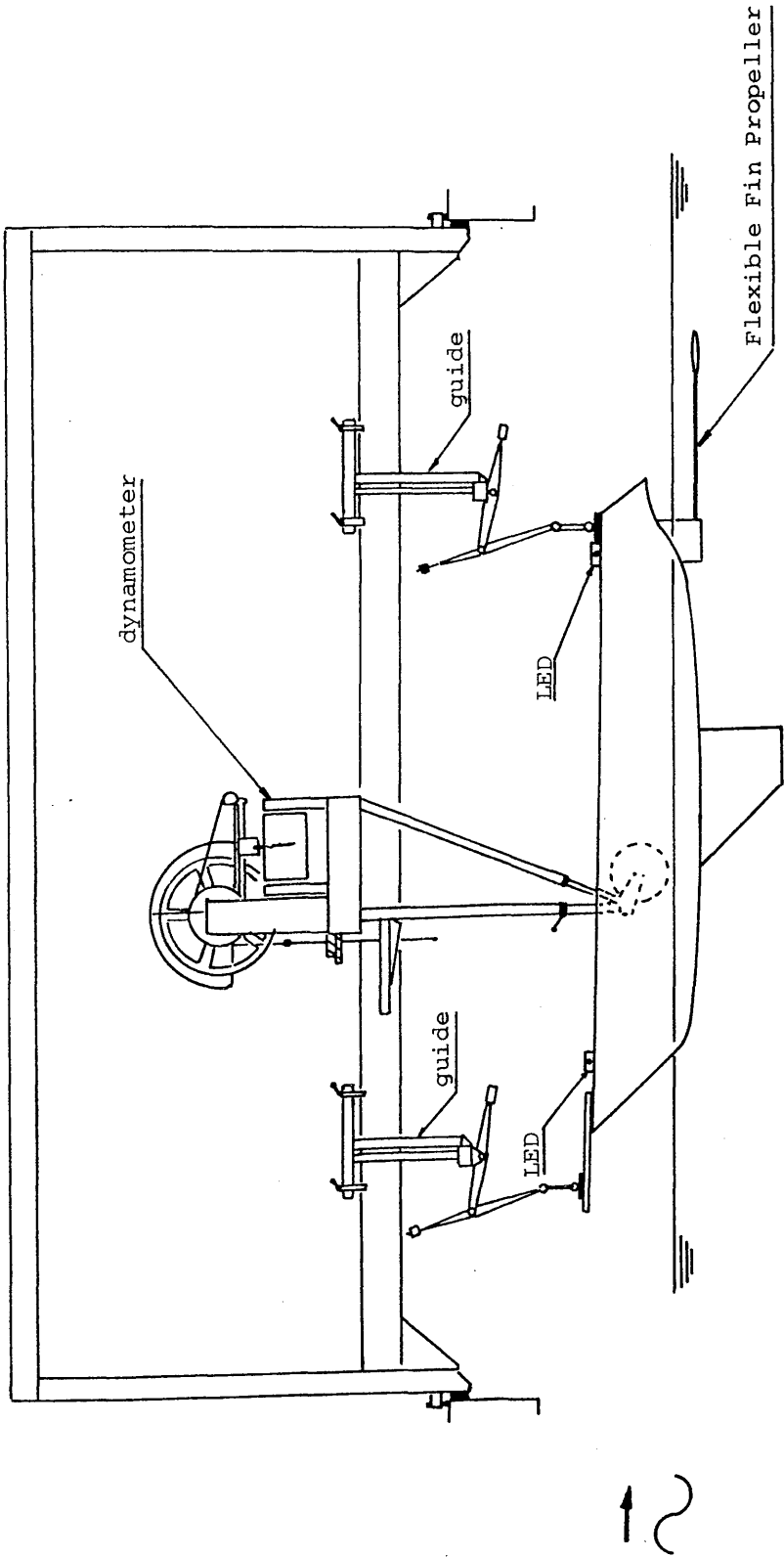


Fig. 9.10 The General Arrangement of The Model Test

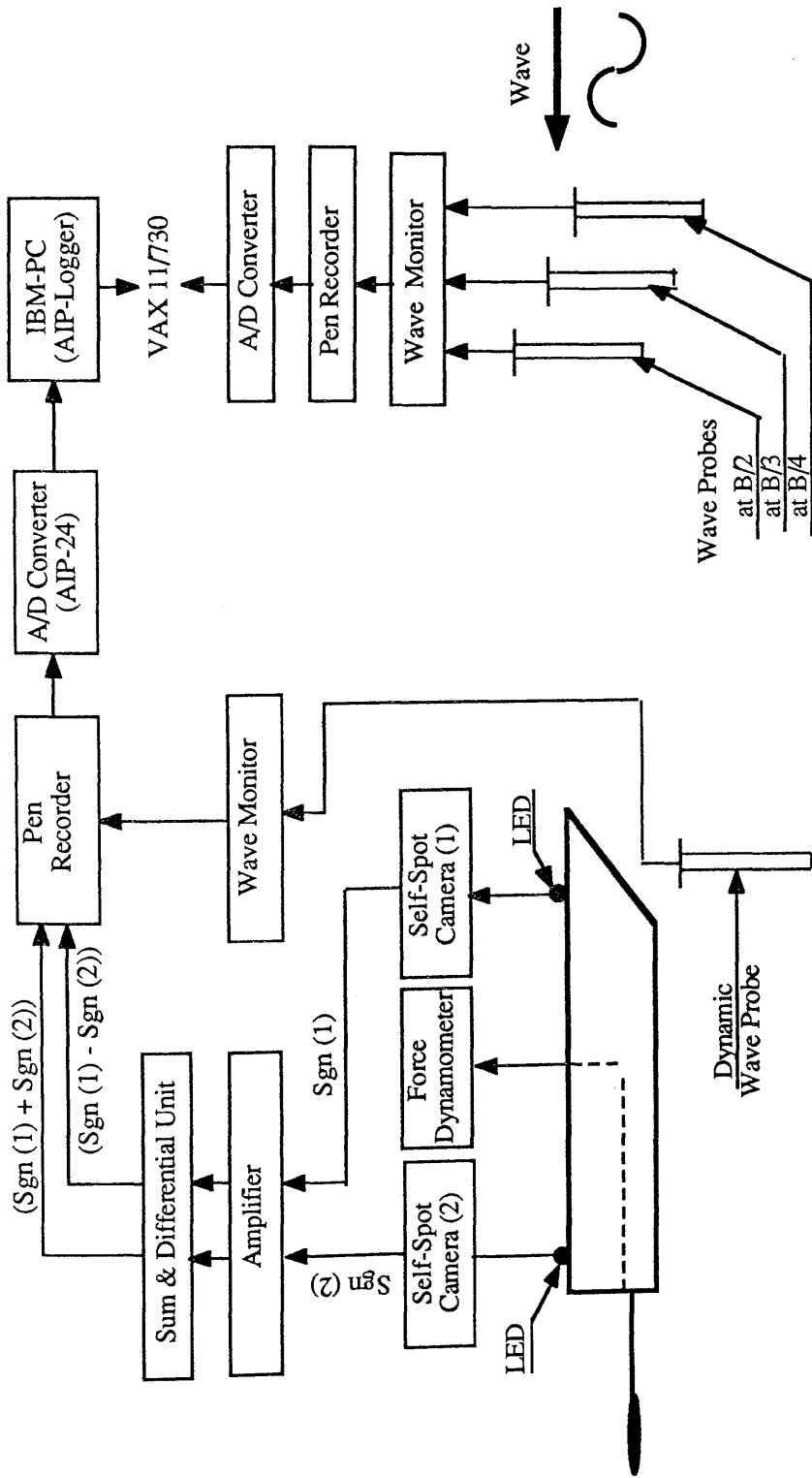


Fig. 9.11 THE DIAGRAMMATIC ARRANGEMENT OF THE WAVE PROPULSION TEST

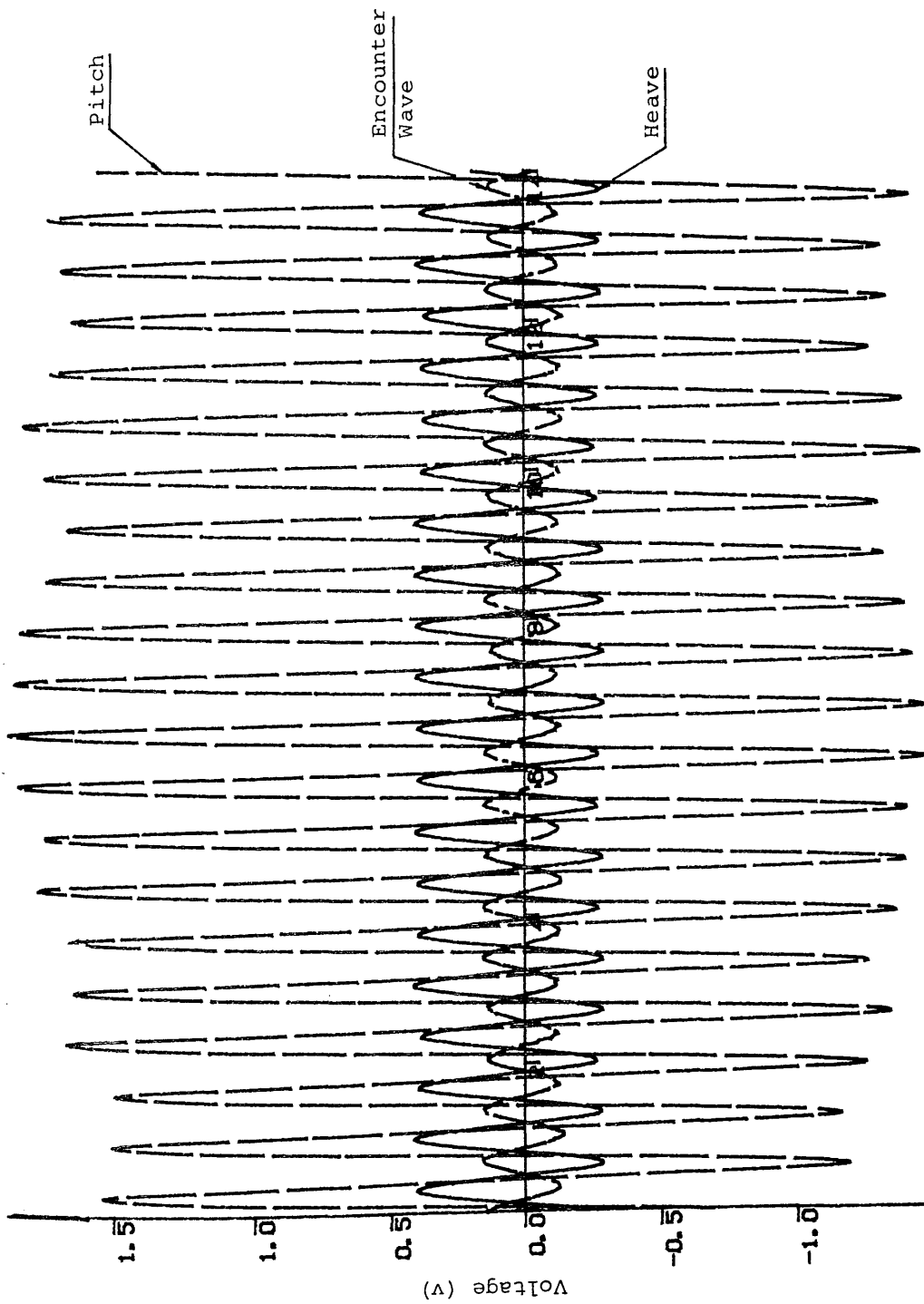


Fig. 9.12 Example of Times Series Records of Motion Response and Encounter Wave

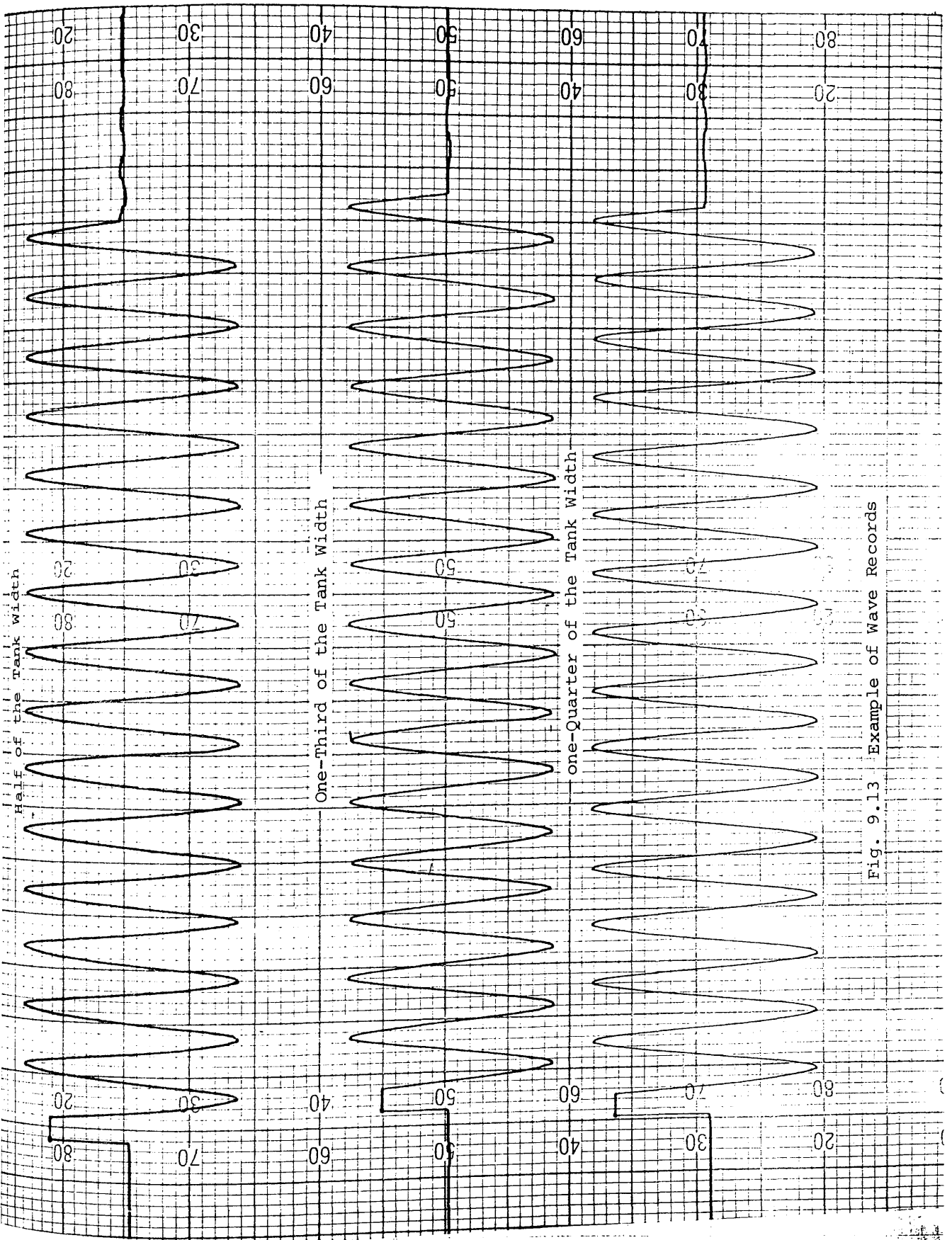
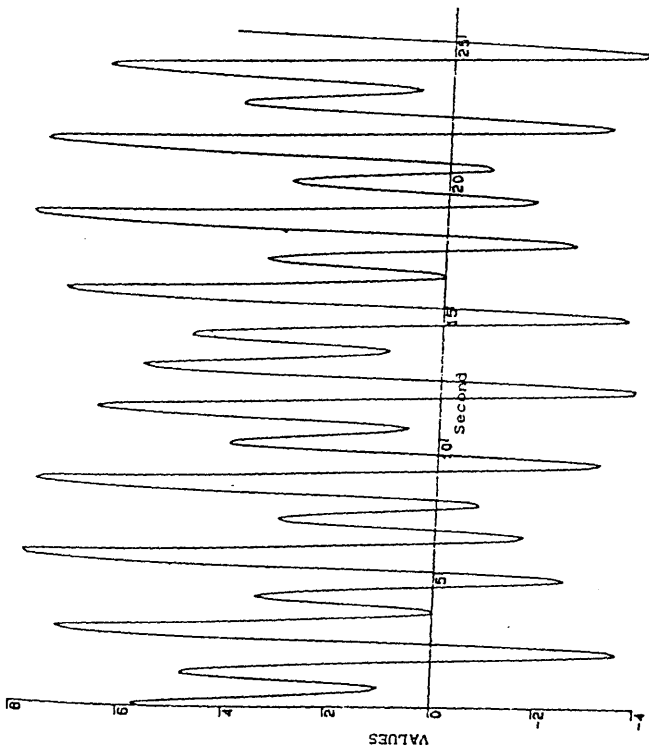
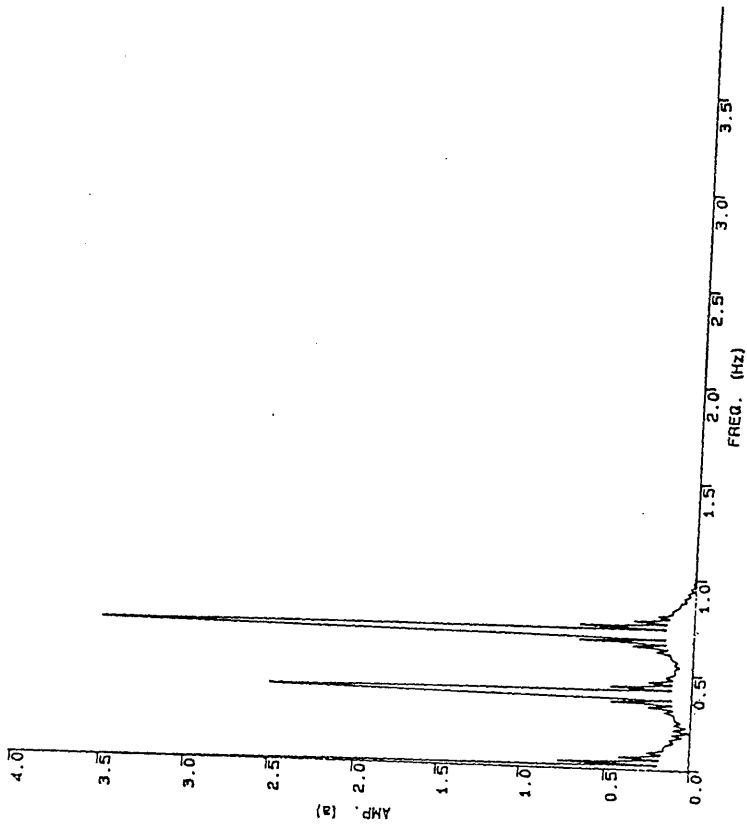


Fig. 9.13 Example of Wave Records



$$\text{Value} = 2.5 \times \sin(2.5\pi t) + 3.5 \times \cos(4.5 \times \pi t) + 2.0$$



SPECTRUM

Fig. 9.14 Time Series Data and Its Frequency Spectrum

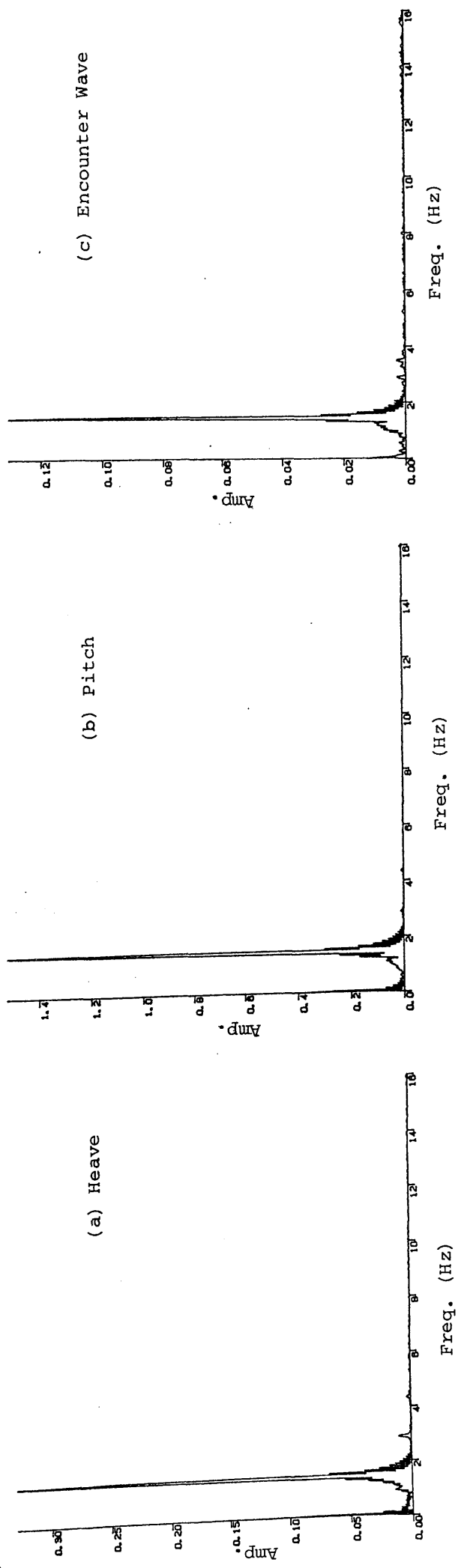
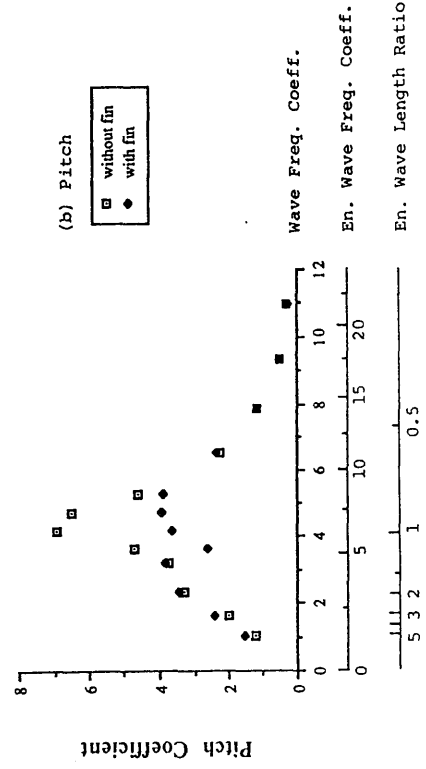
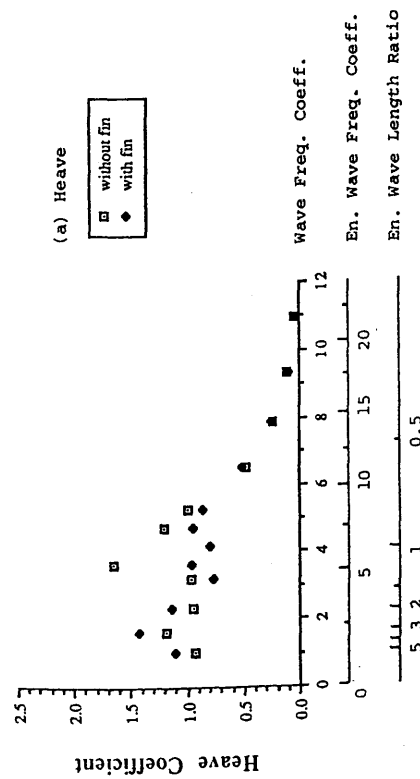
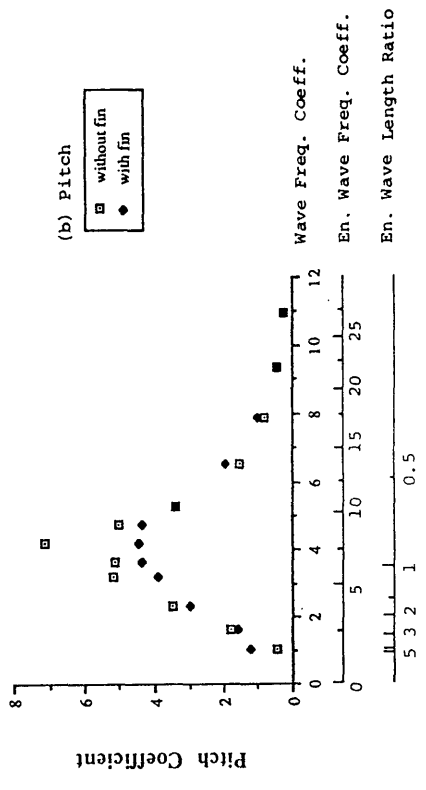
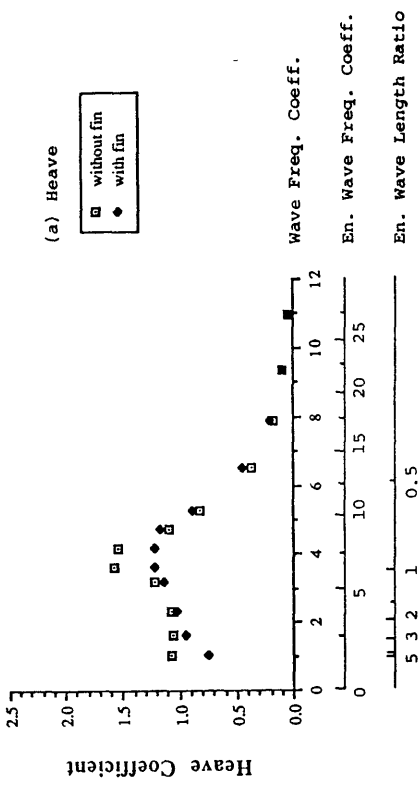


Fig. 9.15 Example of Frequency Spectra of Motion Response and Encounter Wave



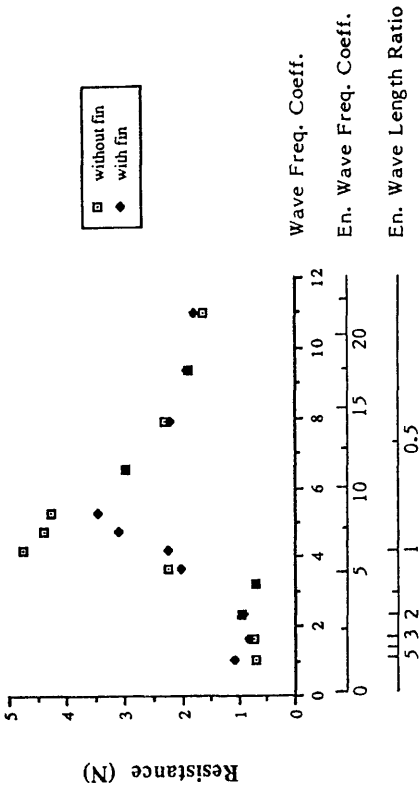
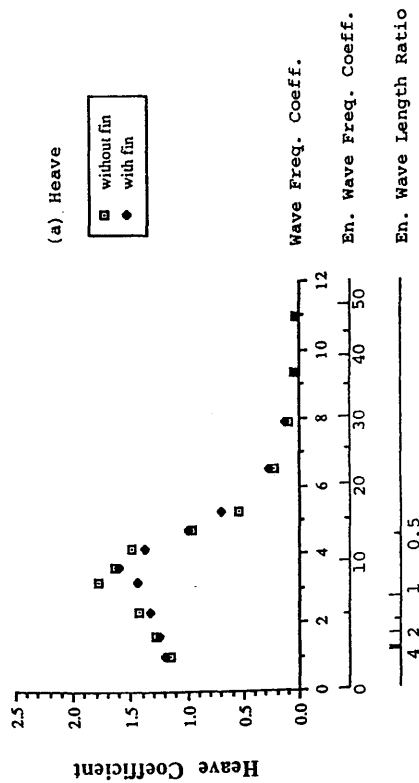
The Motion Response of the Model in Head Sea ($Fr = 0.13$)

Fig. 9.16

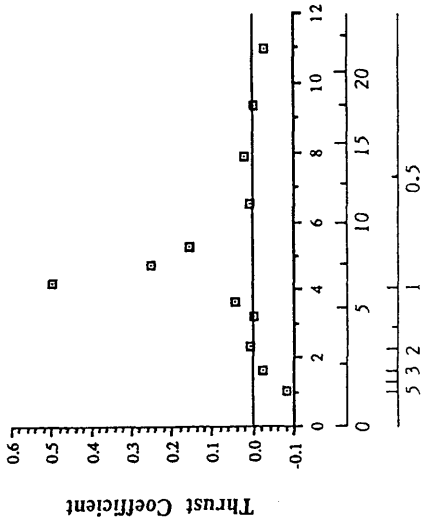
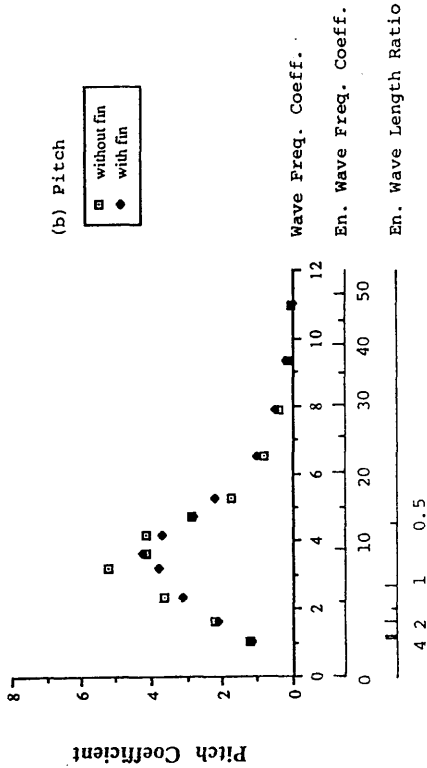


The Motion Response of the Model in Head Sea ($Fr = 0.18$)

Fig. 9.17



(a) The Resistance of the Model in Head Sea ($Fr = 0.13$)

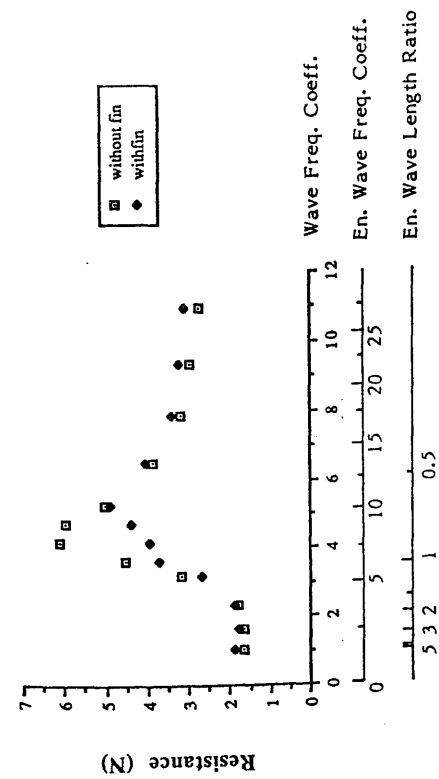


(b) Propulsive Thrust Coefficient ($Fr = 0.13$)

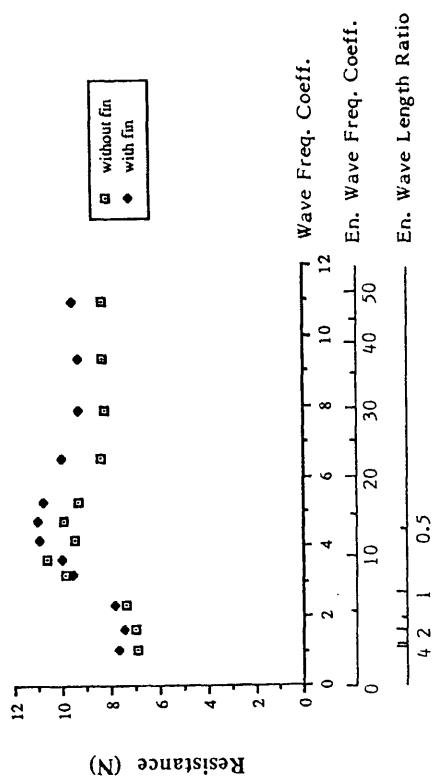
The Motion Response of the Model in Head Sea ($Fr = 0.33$)

Fig. 9.18

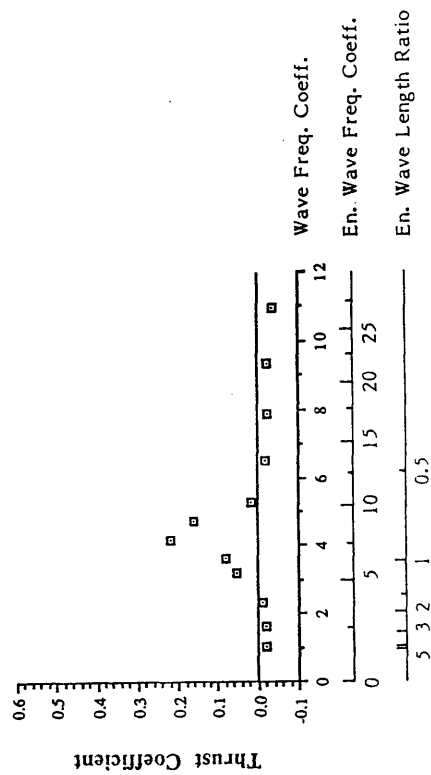
Fig. 9.19



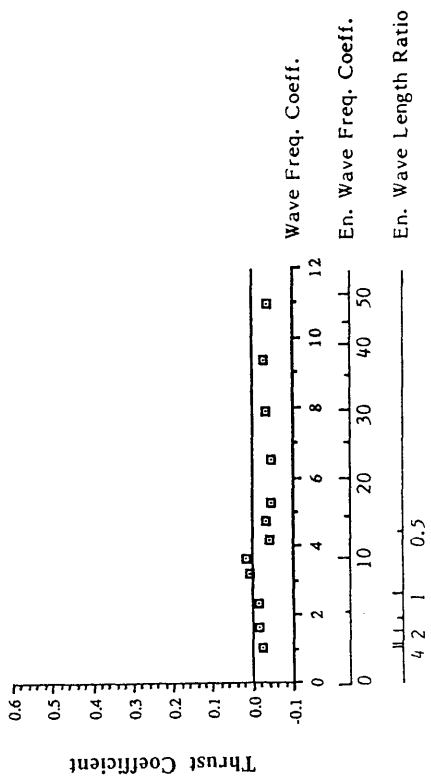
(a) The Resistance of the Model in Head Sea ($Fr = 0.18$)



(a) The Resistance of the Model in Head Sea ($Fr = 0.33$)



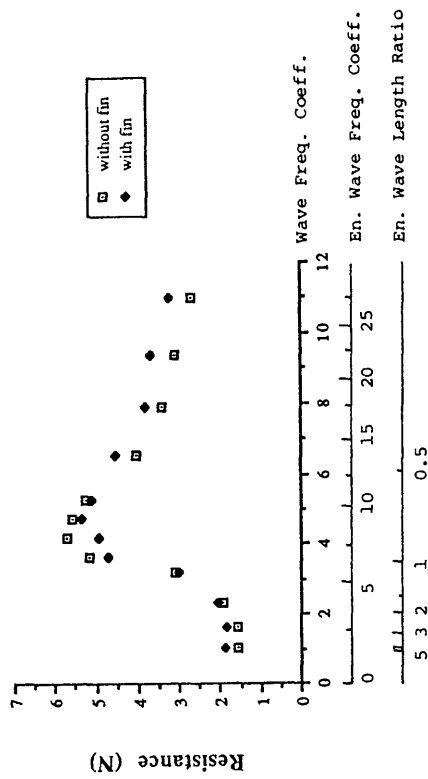
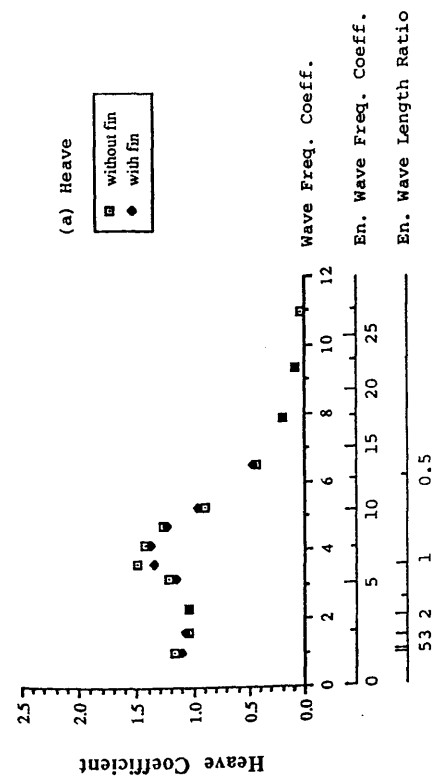
(b) Propulsive Thrust Coefficient ($Fr = 0.18$)



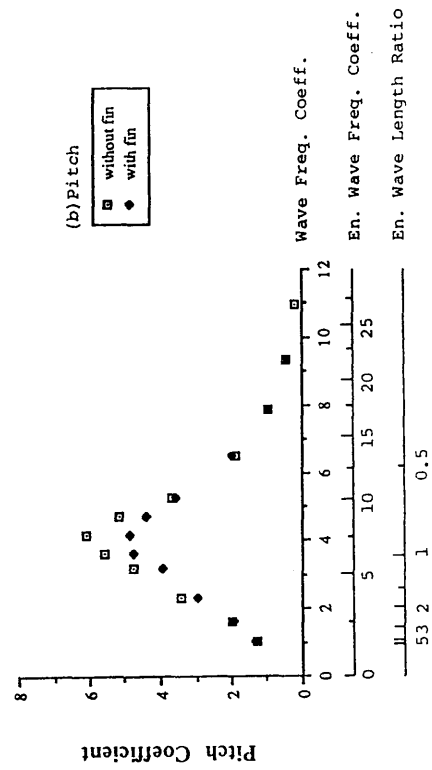
(b) Propulsive Thrust Coefficient ($Fr = 0.33$)

Fig. 9.20

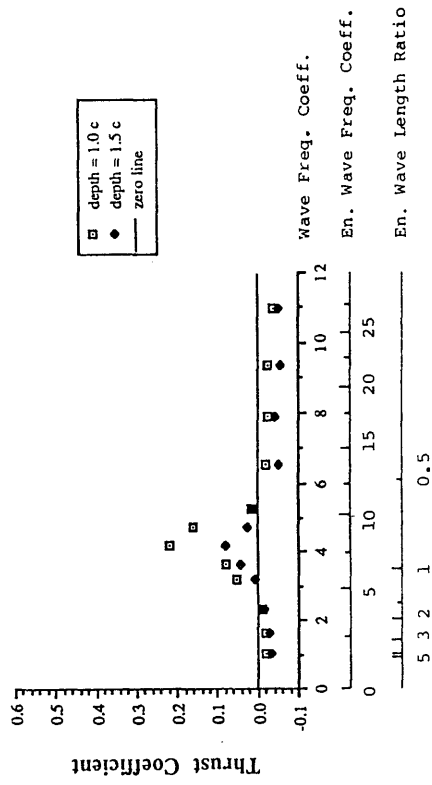
Fig. 9.21



(a) The Resistance of the Model in Head Sea
Fr = 0.18, Depth = 1.5 c



The Motion Response of the Model in Head Sea, Fr = 0.18 ,
Depth = 1.5 c



(b) Propulsive Thrust Coefficient, Fr = 0.18
Fig. 9.23

PART III

A ROTARY FOIL PROPELLER

A rotary foil propeller is investigated in this part. This propeller is a multi-bladed propeller where blades with high aspect ratio are mounted on a rotating drum. The foil oscillates about its own axis while the whole drum rotates and this results in heaving and pitching motion of the blades. A three bladed propeller was tested in forward and reverse operating conditions and in the zero speed condition. Results are discussed and presented in Chapter 10.

CHAPTER 10

EXPERIMENTAL PERFORMANCE OF A TROCHOIDAL PROPELLER WITH HIGH ASPECT RATIO BLADES

1.0 INTRODUCTION

In Chapter 3, the propulsive thrust generated by an oscillating foil over a cycle is presented. The oscillatory behaviour of the force system is a common problem in foil propulsion systems. A rotary foil propeller with a number of oscillating blades moving with phase lags to each other is an alternative design which reduces the oscillatory nature of the force system. Oscillating vertical forces are a bi-product of the force system of oscillating foils and these may induce unpleasant vertical ship motions. As with the propulsive thrust, this oscillating vertical thrust can also be evened out with these multi-bladed propellers.

Open water tests on vertical axis trochoidal propellers have been performed at the Marine Research Institute (MARIN), the Netherlands [van Manen 1966], and the David Taylor Research Centre (DTRC), U.S.A [Dickerson & Dobay 1975]. Four bladed propellers with an effective aspect ratio (AR_e) 6.7 and maximum blade pitch angles (β_{max}) of 26.4°, 30.0°, 34.8°, 41.8° and 53.1° were tested at MARIN. The maximum efficiency was found to be around 0.7. At DTRC, six bladed propellers with effective aspect ratio 5.7 and maximum pitch angles of 17.5°, 30.0°, 36.9° and 44.4° were tested. In both reports [Van Manen 1966 and Dickerson 1975], this type of propeller was suggested to have application on high speed craft.

A multiple stream-tube momentum theory was applied to study the performance of a trochoidal propeller with high aspect ratio blades, designated rotary foil propeller by Bose [1987]. In this theoretical model, a quasi-steady foil theory with a three-dimensional correction was used. Bose [1987], predicts efficiencies higher than 0.7

for a propeller with high aspect ratio blades over a range of maximum pitch angles between 10° and 60° .

An experimental investigation of this rotary foil propeller was carried out to obtain more reliable performance information. A three bladed model with an effective aspect ratio of 10 was designed at Glasgow University by Bose [1986] and built in the workshop of the Hydrodynamics Laboratory. The model was tested in the main tank and two sets of experiments were conducted.

In the first set of tests, the driving torque needed to overcome the friction within the model was found to be high. As this frictional torque was a high percentage of the total driving torque, the torque associated with the hydrodynamic forces was masked and accuracy was lost. In addition, the records from the first set of experiments show that there was a stiffness within the rotating mechanism. The model was opened up for examination. A high point was found in the contact area between the supporting bearing and the aluminum alloy hub, as shown in fig. 10.1. To rectify these two problems, the supporting nylon bearing was removed. Also a groove was found on the aluminum alloy hub, at the connection between the rotating drum and the static drum. This had been cut by the oiltight seal when the hub rotated. The friction between the oiltight seal and the rotating hub was reduced by increasing the depth of the groove. The first set of tests is reported in detail by Lai & Bose [1988]. The model was retested. The results presented in this chapter are mainly from the second set of experiments.

The experimental study consisted of an investigation into the frictional loss, the flow velocity around the propeller blades, the performance of the propeller at different advance ratios (J) operating in the forward and reverse direction and the performance of the propeller at zero speed. The experimental results from the above investigations are presented alongside the theoretical predictions from the multiple stream tube theory [Bose 1987].

2.0 THE PROPELLER MODEL AND DYNAMOMETER

The mechanical arrangement of the propeller model is shown in fig. 10.1. The rotary foil propeller model is a three bladed propeller. These aerofoil shaped blades are mounted on a rotating drum which is driven by a motor through a reduction gear enclosed by a static drum with an oil bath. The static drum and rotating drum are enclosed by a wooden propeller boat. The model is mounted at midships and the outer surface of the rotating drum was flush with the starboard side of the boat. The blades operate outside of the boat as shown in fig 10.2. The boat provides a steady fluid flow around the propeller blades. The model was mounted on its supporting frame (fig. 10.3) which was fixed on the propeller boat (fig. 10.4). The static and rotating drums were completely free from the propeller boat and no direct contact to the boat was made by the model.

The blades heave, pitch and surge as the propeller rotates as shown in fig. 10.5. A sliding mechanism [Bose and Lai 1989] in the rotary drum controls the pitch angle of the blades such that the pitch angle follows the slope of a trochoidal curve and is given by

$$\beta = \tan^{-1} \left\{ \frac{\sin \beta_{\max} \cos \theta_R}{1 + \sin \beta_{\max} \sin \theta_R} \right\} \quad - 10.1$$

where β_{\max} is the maximum blade pitch angle which occurs at an angle of $\theta_R = -\beta_{\max}$ and $(\pi + \beta_{\max})$, a blade position of β_{\max} below the horizontal through the propeller axis. In this propeller model, the maximum pitch angle (β_{\max}) was 20° .

The blades were tapered about their quarter-chord position, as shown in fig. 10.6. The blade sections were NACA 16 series without camber and the thickness ratio was 0.12 to 0.21 from tip to root. The geometrical aspect ratio of the blades was 5. Since one end was mounted on the drum, there is an image effect and the effective aspect ratio (AR_e) was 10. The radius of the blade rotation was 0.1 m.

Hydrodynamic forces acting on the propeller consist of a thrust acting at the propeller axis and a torque acting about this axis. There is also a lift force at the propeller axis although this was not measured. Components of thrust or lift from the propeller blades which act away from the line of the propeller axis are resolved into a thrust or lift at the propeller axis and a torque about the axis. Two sets of strain gauges, 0.7 m and 0.5 m above the propeller axis, were mounted on an aluminium box section supporting beam (fig. 10.3) to measure bending moments induced by the propulsive thrust. The propulsive thrust was found from the average value of these two measured bending moments.

The power absorbed by the propeller was calculated from the measured torque and rotation speed. Driving torque was measured by strain gauges mounted on the driving shaft (fig. 10.3). The signal was transmitted through silver-plated slip rings with silver-graphite brushes. The shaft speed was measured by an optical speed tachometer, as described in the section 4.4 of Chapter 6, where reflection tapes were mounted on the coupling of the drive shaft. A one to four reduction gear was installed; the propeller rotation speed was a quarter of the recorded one. The model was driven by a 3 kW three-phase A. C. motor, the speed of which was regulated by an electronic A. C. variable speed control.

3.0 DATA COLLECTION AND ANALYSIS OF EXPERIMENTAL RECORDS

The diagrammatic arrangement of the test is shown in fig. 10.7. Five channels were used to record : bending gauge no. 1 (0.7 m above the propeller axis); bending gauge no. 2 (0.5m above the propeller axis); torque gauges; flow velocity; and tachometer. A low pass filter was used to filter out high frequency noise in the strain gauge signals. Records were taken on a chart recorder and on an FM tape recorder (RACAL STOR 7) as a back up.

Signals from the bending gauges and torque gauge were also stored in an IBM-PC. The maximum number of channels which can be collected with this system is eight. As described in section 3.0 of Chapter 7, the pen-recorder (W+W 500^{SP}) also acted as an analogue to digital converter; maximum sampling rate for three channels was 20 Hz; data stored in IBM-PC was transformed into ASCII format and transferred to a VAX 11/730 for analysis. The shaft speed and flow speed were analysed by hand from the chart records.

4.0 FLOW VELOCITY AT THE PROPELLER

Owing to the presence of the propeller boat, the flow around the propeller was disturbed and the flow velocity at the propeller was different to that of the free stream. Therefore a flow velocity calibration was carried out to set up the relationship between the free stream velocity and the flow velocity at the propeller.

A pitot tube was used to measure the flow velocity. A differential pressure transducer, which cancels the effect of static pressure by taking the difference of pressure acting on the front and rear surfaces of the transducer, was used to measure the pressure changes in the pitot tube. In order to relate the output voltage from the transducer to the actual flow velocity, the pitot tube was mounted on the carriage to measure the free stream velocity. The calibration results are shown in fig. 10.8. The results were curve fitted into two equations. For those output voltages smaller than 1.8 V, the relationship of the flow velocity (Y) to the output voltage (X) was,

$$Y = -0.1116X^2 + 0.6200X - 0.1768 \quad - 10.2$$

For those output voltages greater than or equal to 1.8 V, the relationship of flow velocity to output voltage is,

$$Y = -0.0116X^2 + 0.2634X + 0.4936 \quad - 10.3$$

The propeller boat was symmetrical and the flow was assumed to be symmetrical. The flow velocity on the port side was calibrated. In this way, the disturbance from the propeller on the flow velocity was not included. The flow velocities of these three points were measured at the same depth of submergence as the propeller axis. Their locations are shown in fig. 10.9. The calibration results of these three points were curve fitted and are shown in fig. 10.10. By using the curve fitted equations, the actual flow velocity profiles at the propeller for different free stream flow velocities are shown in fig 10.11.

The flow velocity at the propeller is slightly higher than the free stream flow velocity. The flow velocity at the propeller is stable and constant (fig. 10.11).

5.0 FRICTIONAL LOSS TESTS

For this frictional loss test, the water level of the tank was lowered down and the model was kept out of the water. The model was tested in air to find the required torque at different rotation speeds to overcome the mechanical friction within the mechanism, gears, bearings and seals. In such a way, the hydrodynamic effects were not included in the measurements. After an initial run-in period, the results were stable.

The primary support of the rotating drum was from bearings between the mild steel mandrill and the hub fig 10.1. As described in the introduction, a nylon bearing was removed in the second series of tests to lower the frictional losses. This reduced the friction by 35% compared to the one measured in the first set of tests [Lai and Bose 1988]. However, the oiltight seal was essential to avoid oil leaks from the static drum and was not removed. Water was poured onto the oiltight seal during the test to simulate the situation when the model was in water.

The investigation was done for both forward and reverse rotations of the propeller over a range of shaft speeds between 200 rpm and 1000 rpm. The equivalent rotation speeds of the propeller were from 5.2 rads^{-1} to 26.2 rads^{-1} which was one-

quarter of the shaft speed. The results are shown in fig. 10.12. The lines are the best-fit values.

The frictional loss in reverse was less than that in forward rotation when the shaft speed was below 760 rpm. At higher rotation speeds, the frictional losses are nearly the same in both conditions.

6.0 PROPELLER PERFORMANCE TESTS IN FORWARD MOTION

In this experiment, the performance of the propeller at forward speeds was investigated. The model was run towards the wave maker in calm water (from left to right in fig. 10.2) at various speeds while the propeller rotated in a clockwise direction at various rotation speeds. The test covered a range of advance ratios (J) from 0.38 to 9.0, where

$$J = \frac{U\pi}{\Omega R} \quad - 10.4$$

These values were achieved by changing the shaft rotation speed from 200 to 1000 rpm and the carriage speed from 0.3 to 1.5 ms^{-1} . Owing to the large propeller boat, the maximum model speed was limited to 1.5 ms^{-1} . At higher speeds, the model generated high waves and water spilled out of the tank. Propulsive thrust and torque are presented as non-dimensional coefficients; these are listed below.

1) Thrust coefficient (T_c) :- the measured thrust (T) is non-dimensionalised by the propeller rotation speed (Ω), radius of rotation of the blades (R) and the propeller swept area ($A_s = 2R s$)

$$T_c = \frac{T}{\rho \Omega^2 R^2 A_s} \quad - 10.5$$

2) Torque Coefficient :- as with the thrust coefficient, the measured torque

(Q) is also non-dimensionalised by the rotation speed, radius of blade rotation and the swept area.

$$Q_c = \frac{Q}{\rho \Omega^2 R^3 A_s} \quad - 10.6$$

The efficiency (η) is given by

$$\eta = \frac{TU}{\Omega Q} = \frac{T_c J}{Q_c \pi} \quad - 10.7$$

6.1 The Propulsive Thrust Coefficient

The propulsive thrust coefficient in forward motion is shown in fig. 10.13. The experimental result increased from 0.17 to 0.25 as J is increased but dropped to zero at an advance ratio of 8.0. Experimental thrust coefficients are higher than the theoretical ones for advance ratios below 7.0. At a low advance ratio around one, the experimental results were 70% higher than the theoretical ones. The peak value of the experimental results was obtained at a slightly lower advance ratio of 5.0 than that of the theoretical peak value.

In the multiple stream-tube theory, a quasi-steady assumption is applied. The lift and drag of the propeller blades at each instant of time are taken to be equal to those of a hydrofoil in steady flow at a similar angle of attack. In reality, the changing circulation around the blades leads to vortices being shed into the wake which influence the lift force generated by the blades. The leading edge suction force is also ignored in this theoretical model. The effect of unsteadiness increases as the oscillation frequency and rotation speed of the propeller increases. Therefore, a large discrepancy would be expected at high rotation speeds and low advance ratios. In addition, the effect of steady stall is applied in the theory. In unsteady conditions, dynamic stall would be obtained at a different angle of attack than that of steady stall and this results in higher maximum lift

coefficients as the angle of attack increases [McCroskey 1981]. Sophisticated two-dimensional unsteady lifting foil theories with blade to blade interference are presented by Mendenhall and Spangler [1973] and Potze [1986]. However, a linearised unsteady foil theory would not account for the dynamic stall either.

In spite of these shortcomings, good agreement in curve forms is found between experiment and theory.

6.2 The Driving Torque Coefficient

In fig. 10.14, the total torque coefficient and the frictional torque coefficient are presented. The frictional torque is presented in the form of the best-fit curve to the experimental results. The hydrodynamic torque was estimated by taking the difference between these two results and is presented in fig. 10.15. At high advance ratios, a large proportion of the torque was frictional torque. Since the hydrodynamic torque was estimated by taking the difference of two large experimental values, there is a lot of scatter, especially at higher advance ratios. The theoretical prediction is also shown in fig. 10.15a for comparison. The hydrodynamic torque coefficients were curve-fitted by a fourth degree polynomial equation using a least squares method (fig. 10.15b), in order to eliminate the scattering effect and show the mean values.

The differences between the theoretical and experimental results are very similar to those for the propulsive thrust coefficient. Despite these and the scatter, a reasonable agreement in shape is found between the experimental and theoretical curves.

6.3 The Propulsive Efficiency

The propulsive efficiency (η) was estimated by using the thrust coefficient and hydrodynamic torque coefficient shown in figs. 10.13 and fig. 10.15. The results are shown in fig. 10.16 with the theoretical predictions [Bose 1987]. In order to eliminate the effect of the scatter of torque coefficients on the efficiency, the curve-fitted values

(fig. 10.15b) were used to calculate the efficiency. There is good agreement over the range of advance ratios from 0.0 to 6.0. Maximum peak propulsive efficiency was around 0.8. However the efficiency dropped slightly faster than the theoretical prediction for the higher advance ratios. The propulsive efficiency reduced to zero around an advance ratio of 8. This corresponds to the value at which the propulsive thrust coefficient (fig. 10.13) also drops to zero.

7.0 PROPELLER PERFORMANCE TEST IN REVERSE MOTION

Twin propellers may be used in an actual application [Bose 1987] and a steering couple could be generated by running one propeller in reverse. Therefore, the ability of the propeller to provide a reverse propulsive thrust is important for this reason as well as for driving the ship in reverse. The model was run towards the slatted beach with different advance speeds (from right to left in fig. 10.2) and rotation speeds were in the reverse direction (anti-clockwise rotation). The test was similar to the one described in section 6.0. The sharp trailing edge of the blade was the leading edge in this reverse test; therefore the blades become slightly swept back and the pitching axis of the blade was at the three-quarter chord point instead of the quarter-chord point. The test covered a range of advance ratios from 0.65 to 8.0. The theoretical values for calm water with forward motion are also presented for comparison.

7.1 The Propulsive Thrust Coefficient

The propulsive thrust coefficient in reverse motion are shown in fig. 10.17. Although the peak is not clearly defined, similar values are found for thrust coefficients in both reverse and forward operating conditions. (fig. 10.13). The thrust coefficients increase from 0.16 to 0.28 as the advance ratio increases from 0.7 to 7.0 (though one value is higher than 0.28) and drop to zero as the advance ratio increases further.

7.2 The Driving Torque Coefficient

The total torque coefficients, which were recorded in the experiments, are compared with the frictional loss torque coefficient in reverse motion and presented in fig. 10.18. The corresponding hydrodynamic torque coefficients are shown in fig. 10.19. The hydrodynamic torque coefficients are higher than those for forward speed. The coefficients increase from 0.45 to a value about 1.0 and the scatter is comparatively less than for forward motion.

7.3 The Propulsive Efficiency

The propulsive efficiency in reverse motion was calculated from the results shown in figs. 10.17 and 10.19 and is presented in fig. 10.20. In response to the higher hydrodynamic torque, the peak propulsive efficiency is approximately 20% lower than that in the forward operating condition.

8.0 PROPELLER PERFORMANCE AT ZERO SPEED

The object of this test was to investigate the available initial thrust (bollard pull) and the required torque to start a vessel from a stationary position. The model was tested with different rotational speeds at zero speed in calm water. Tests were carried out for propeller rotation speeds from 6.5 rads^{-1} (62 rpm) to 19.0 rads^{-1} (180 rpm).

The propulsive thrust coefficients (T_C) in the bollard pull condition are shown in fig 10.21. The thrust coefficient is around 0.1 over the whole range of rotation speed although it increases slightly with speed. Since the coefficient is nearly constant and the propulsive thrust has been divided by the square of the rotation speed, a higher propulsive thrust is obtained by increasing the rotation speed.

In this bollard pull condition, the inflow velocity is induced primarily by the angular rotation of the propeller with a secondary effect coming from the oscillation of

the propeller blades on the flow. Hence the flow velocity is tangential to the motion of the blade. As a result, the angle of attack of the blades does not change rapidly with the rotation speed at each angular blade position. For a given angle of attack, the force acting on the blades are proportional to the square of the inflow velocity. Since the thrust is normalised by this square term, the thrust coefficient is almost independent of the rotation speed.

The hydrodynamic torque coefficients in the bollard pull condition are shown in fig. 10.22. This torque coefficient reduces with the rotation speed from 0.65 to 0.45 over the rotation speed ranges of this test.

9.0 FULL SCALE PROPELLER

Bose [1987] uses the theoretical results to discuss the application of this type of propeller to a small ship. A large span of propeller, over twice the beam of the ship, was shown to be required and is not practical. Bose & Lai [1989] use the experimental results to look at the application of this propeller to a small ship.

The small ship used in the discussion is with 66.0 m in length between perpendiculars, 10.5 m in breadth and 5.2 m in depth. The existing propeller diameter is 2.65 m and the service speed is 12 knot with a required thrust power of 470 kW. A wake fraction of 0.11 was assumed and the corresponding speed of advance is 5.5 ms^{-1} .

From the experiment, a thrust coefficient of 0.25 and an efficiency of 0.7 can be obtained at an advance ratio of 5.0. The required swept area of the propeller was re-examined by using these experimental results. The required swept area (A_s) of the propeller can be found by combining eqn. 10.4 and 10.5 where,

$$A_s = \left(\frac{1}{\rho \pi^2} \frac{T}{U^2} \right) \frac{J^2}{T_c} \quad - 10.8$$

The term in the brackets is a function of the service conditions while the other term outside the brackets describes the propeller characteristics. In this example, the required swept area is 28 m^2 . The radius of the blades' rotation is taken as 2.65 m, the same as the existing diameter of the screw propeller. The required span is 10.6 m or about the beam of the ship. The effect of Reynolds number and hence the scale effect was not included in this full scale study. The maximum Reynolds number in the test was about 10^5 while that of the full scale propeller is about 10^7 .

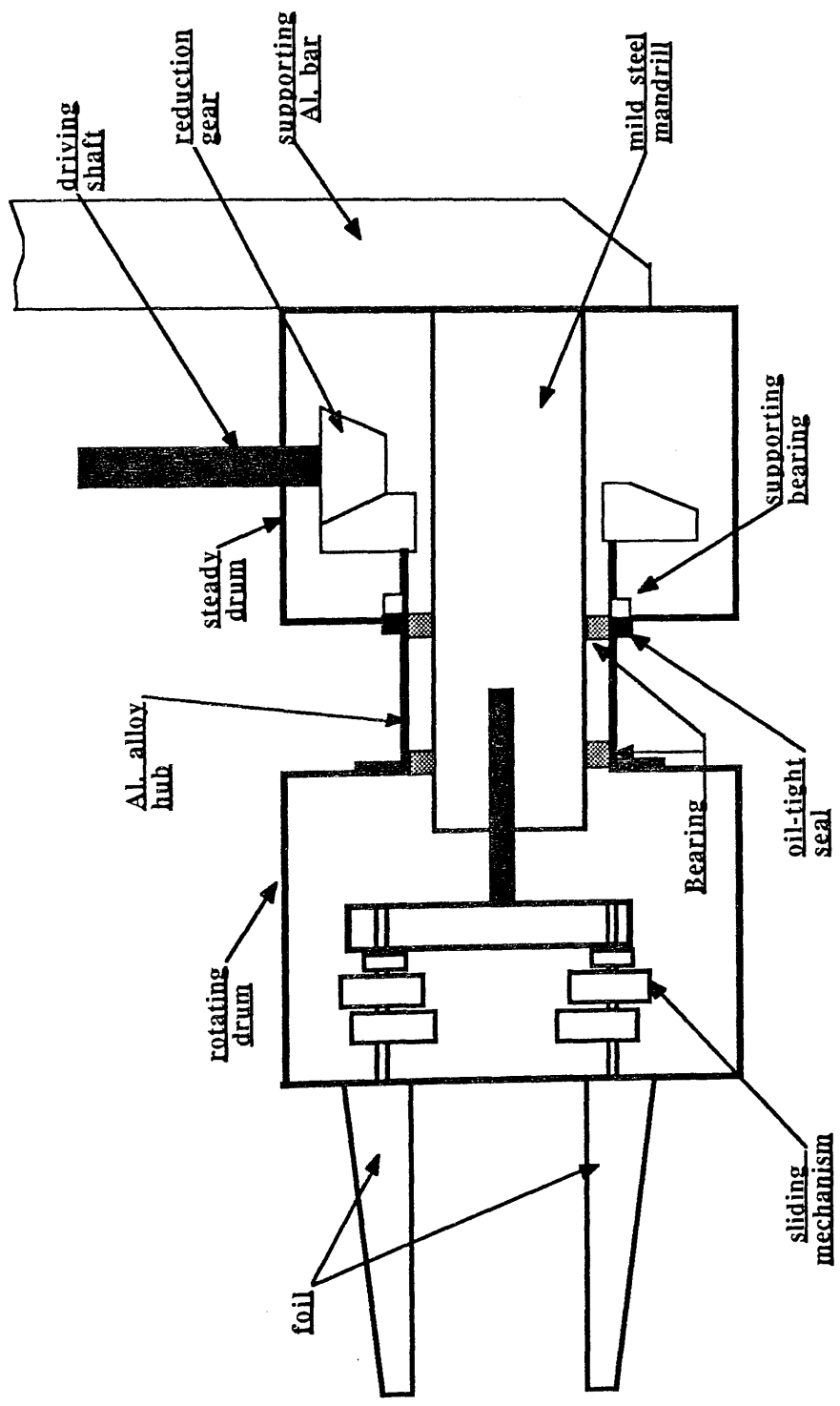
10.0 CONCLUSIONS

Experimental investigations were done on the performance of a trochoidal propeller model with high-aspect ratio blades. The propulsive thrust coefficient, hydrodynamic torque and efficiency are presented. These investigations include the conditions with: forward and reverse motion; and zero speed (bollard-pull). The following conclusions are drawn from the present study.

- 1) In forward motion, the experimental results of propulsive thrust coefficient increased from 0.17 to 0.25 as the advance ratio increased from 0.4 to 5.0 and reduced to zero when the advance ratio further increased to 8.0. For advance ratios below 7.0, higher thrust was found in the experiment than the theoretical model. Unsteady effects and dynamic stall become important at low advance ratios. From the experimental results, the range of advance ratio with positive thrust was up to 8.0 and slightly lower than that predicted by the multiple stream tube theory. The forms of the curve were similar for both the theoretical and experimental results.
- 2) The curve-fit of experimental hydrodynamic torque coefficients in the forward motion showed that this coefficient increased from 0.45 to 0.6 by increasing the advance ratio from 0.4 to 5.0 and decreased to zero at an advance ratio of 9.0. As with the thrust coefficient, the experiment showed a higher torque at low advance

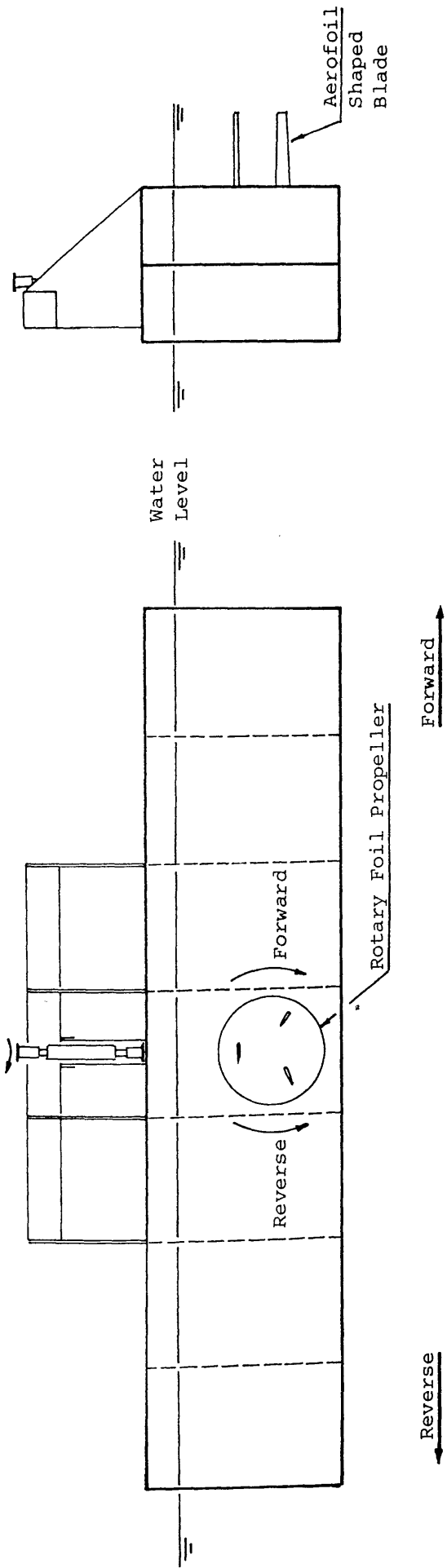
ratio than the theory.

- 3) The experimental peak efficiency found in the forward motion was about 0.8 and occurred at an advance ratio of 6.0. The effect of the underprediction of thrust and torque cancelled each other and good agreement with the theoretical prediction was obtained in a range of advance ratio between 0.0 and 6.0. As with the thrust coefficient the experimental efficiency dropped to zero at an advance ratio of 8.0.
- 4) Similar magnitudes of propulsive thrust were found in both forward and reverse motion. Higher hydrodynamic torque was obtained in the reverse motion than in forward motion and the peak efficiency was 20% lower.
- 5) In the zero speed condition, the thrust coefficient was about 0.1 and increased slightly as the rotation speed increased. Higher thrust was generated at higher rotation speed. The torque coefficient reduced from 0.65 to 0.45 over a range of propeller rotation speed between 6.5 rads^{-1} (62 rpm) and 19 rads^{-1} (180 rpm).
- 6) In future developments, the internal friction loss of the propeller should be reduced to maintain the high overall efficiency and to minimise problems with hydrodynamic torque measurement.
- 7) Large swept area is required to generate sufficient thrust for propulsion. In small ships, the span of the blades would be as large as the ship beam.



MECHANICAL ARRANGEMENT OF ROTARY FOIL PROPELLER MODEL

Fig. 10.1



ELEVATION

END VIEW

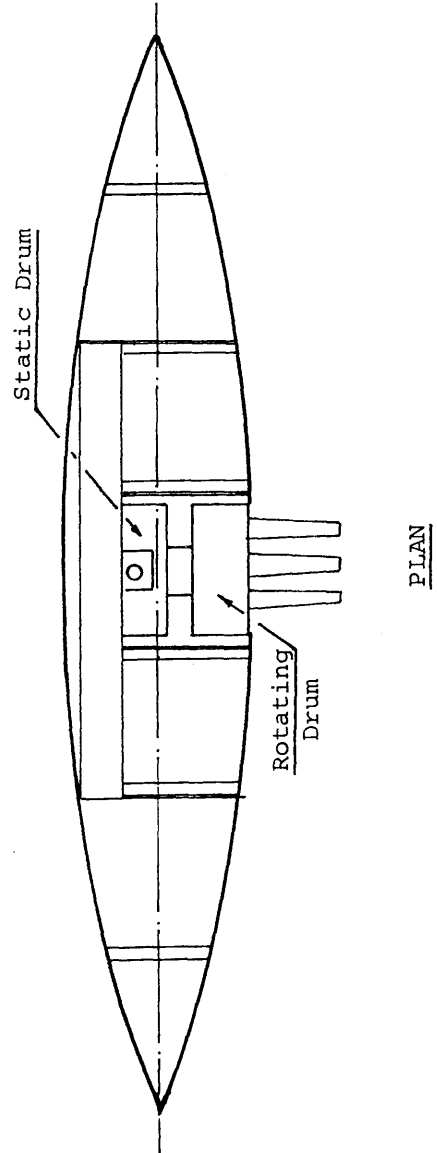


Fig. 10.2 Propeller Boat

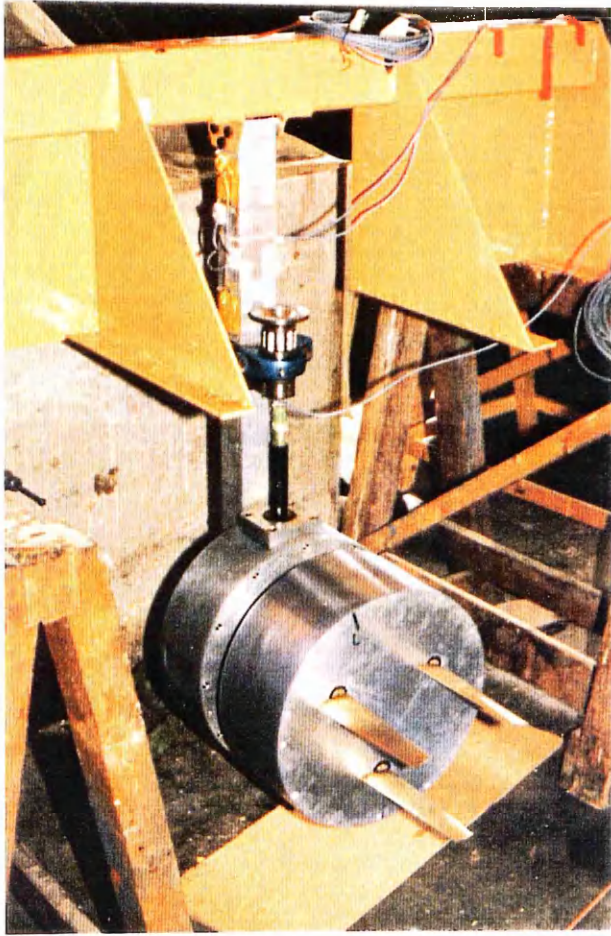


Fig. 10.3 The Rotary Foil Propeller Model and the Supporting Frame

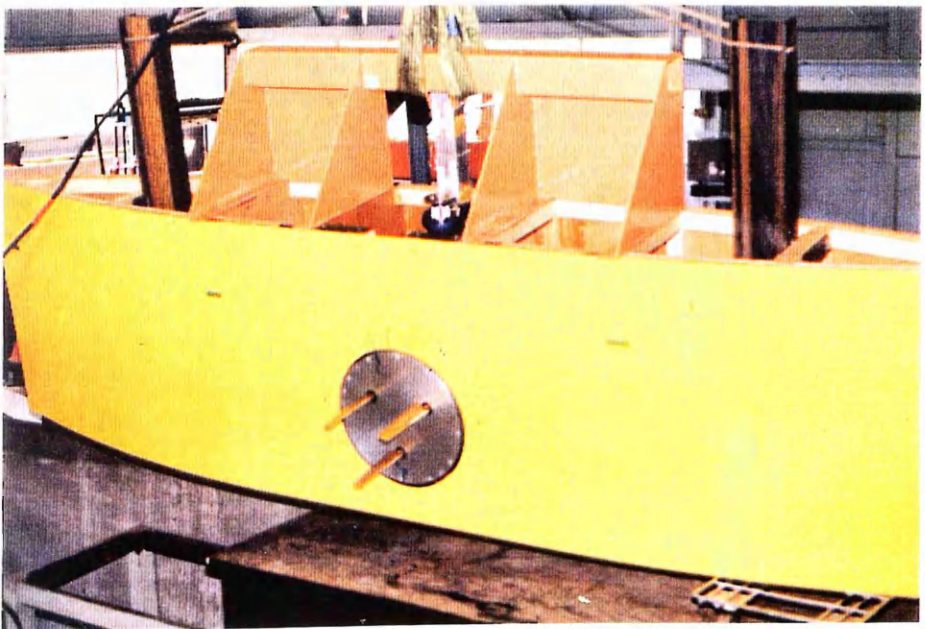


Fig. 10.4 The Rotary Foil Propeller Model with the Propeller Boat

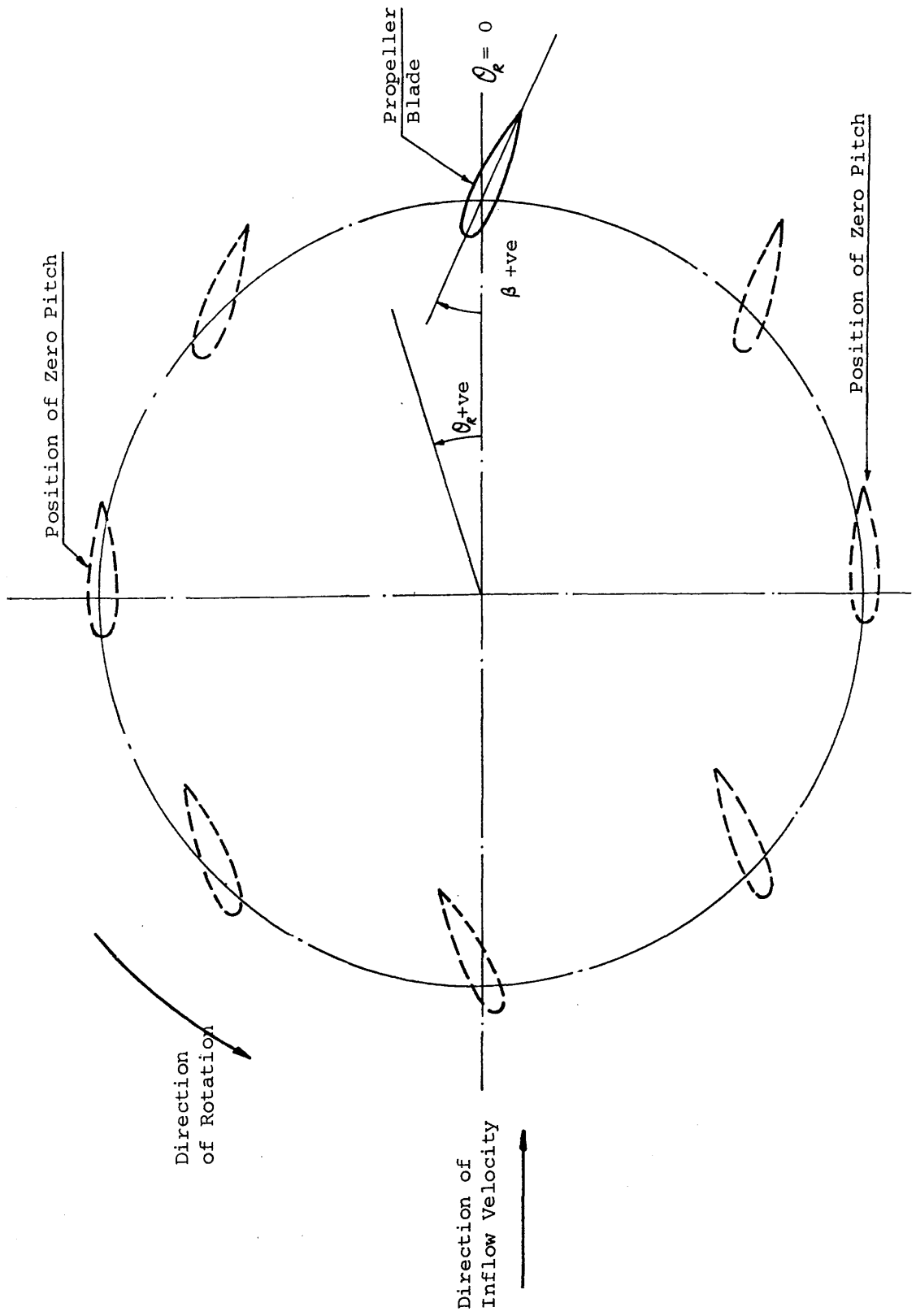
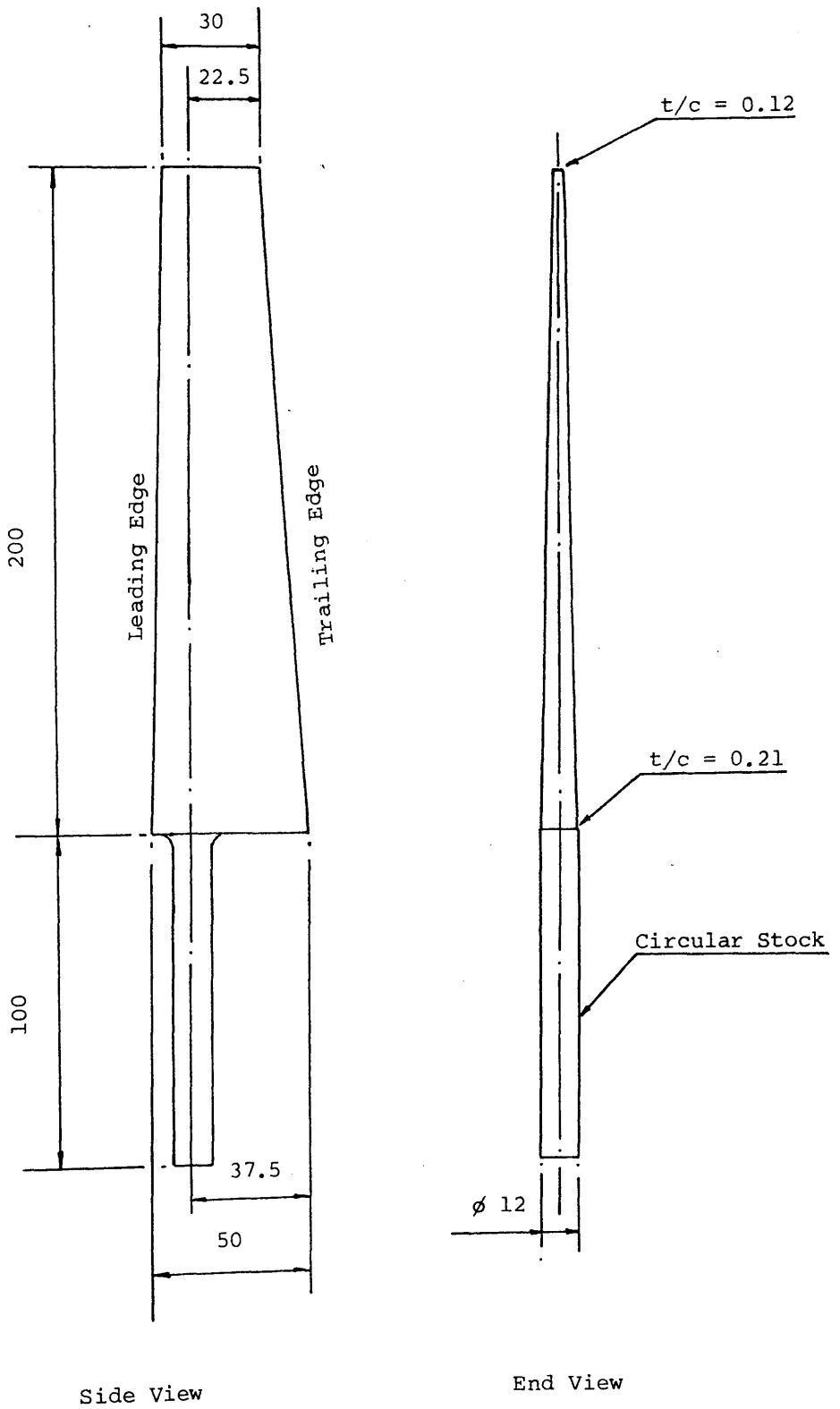


Fig. 10.5 Side View of Propeller Depicting the Form of the Blade Oscillation



Side View

End View

Fig. 10.6 Rotary Foil Propeller Blade (Blade Section : NACA - 16 Series)

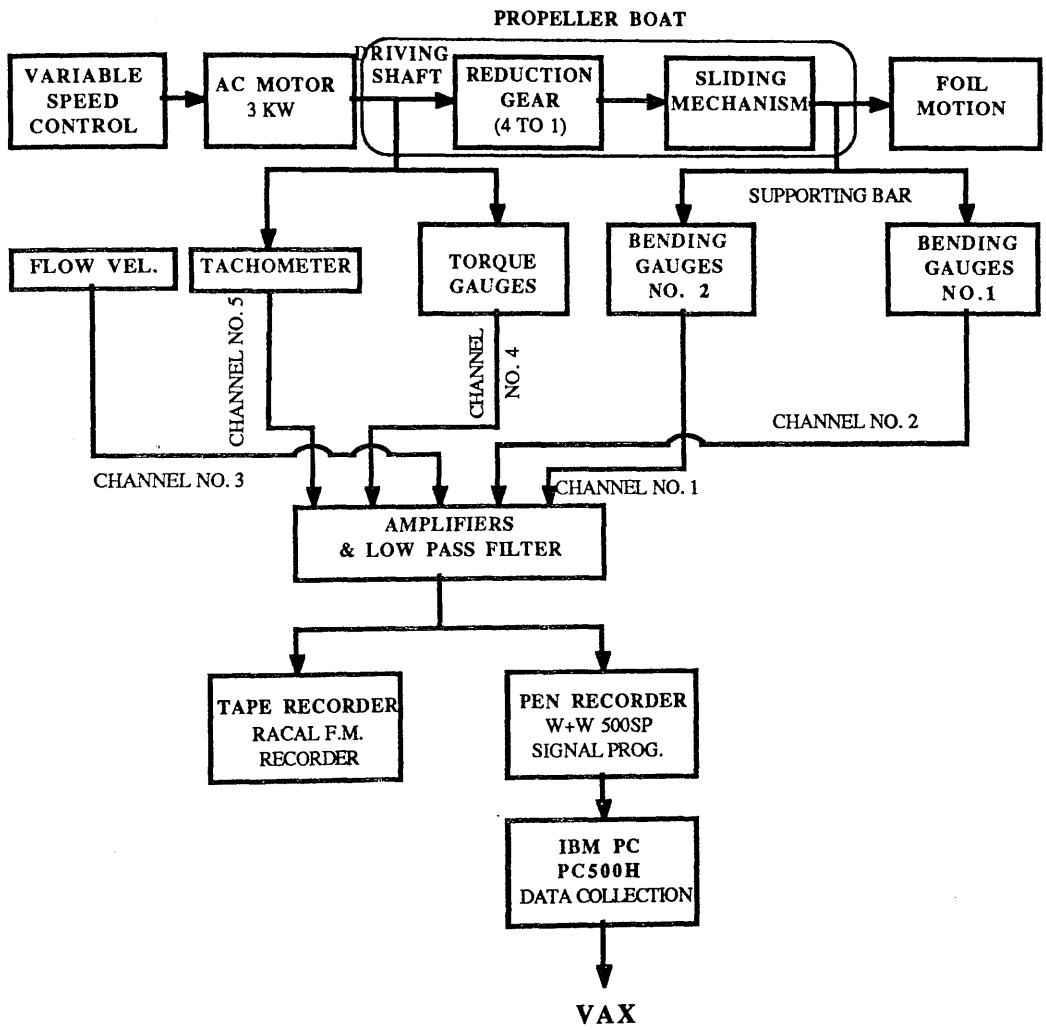
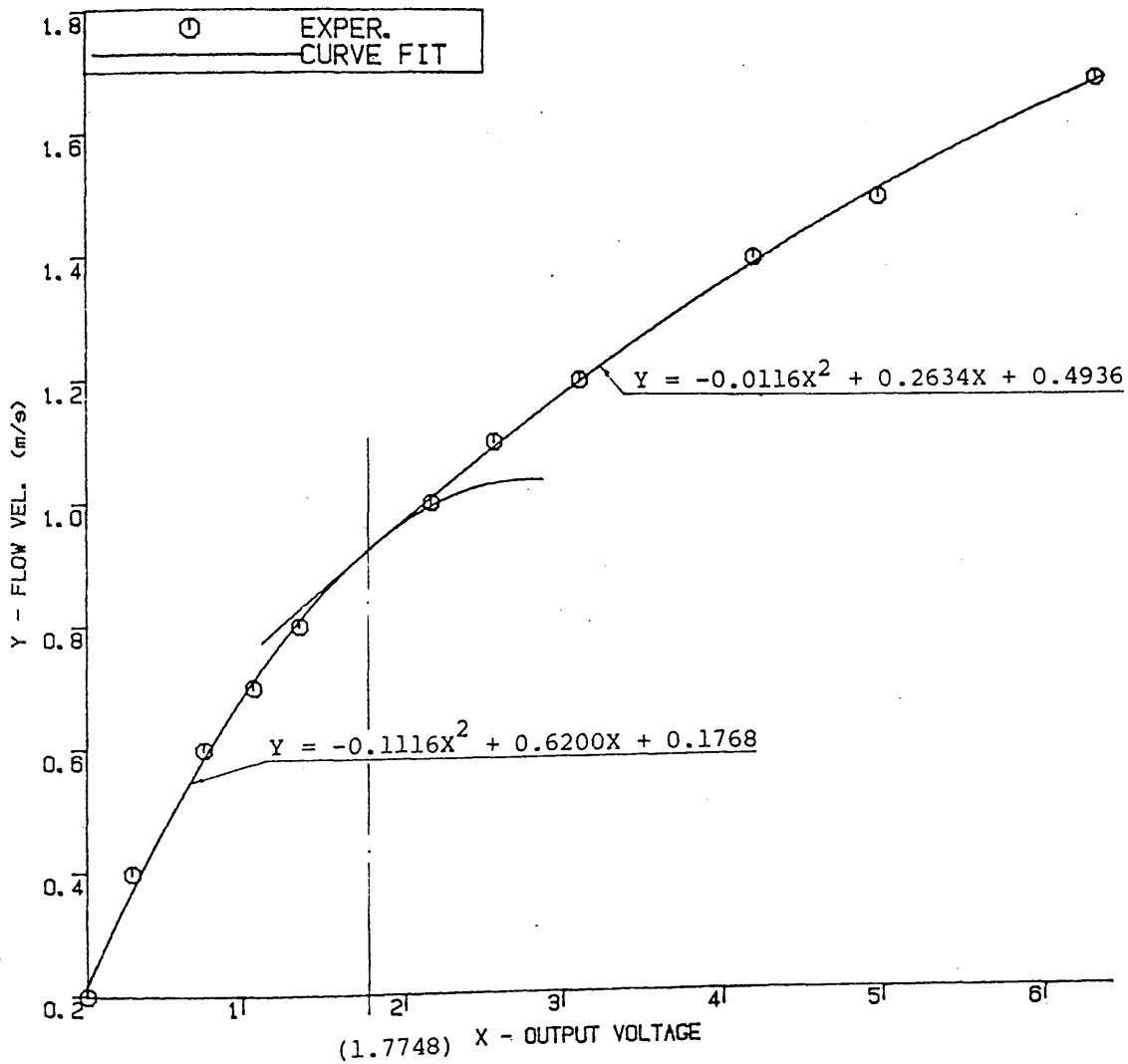


Fig. 10.7 THE DIAGRAMMATIC ARRANGEMENT OF THE ROTARY FOIL PROPELLER MODEL TEST



THE FLOW VEL. CALIBRATION
(output volt. VS flow vel.)

Fig.10.8

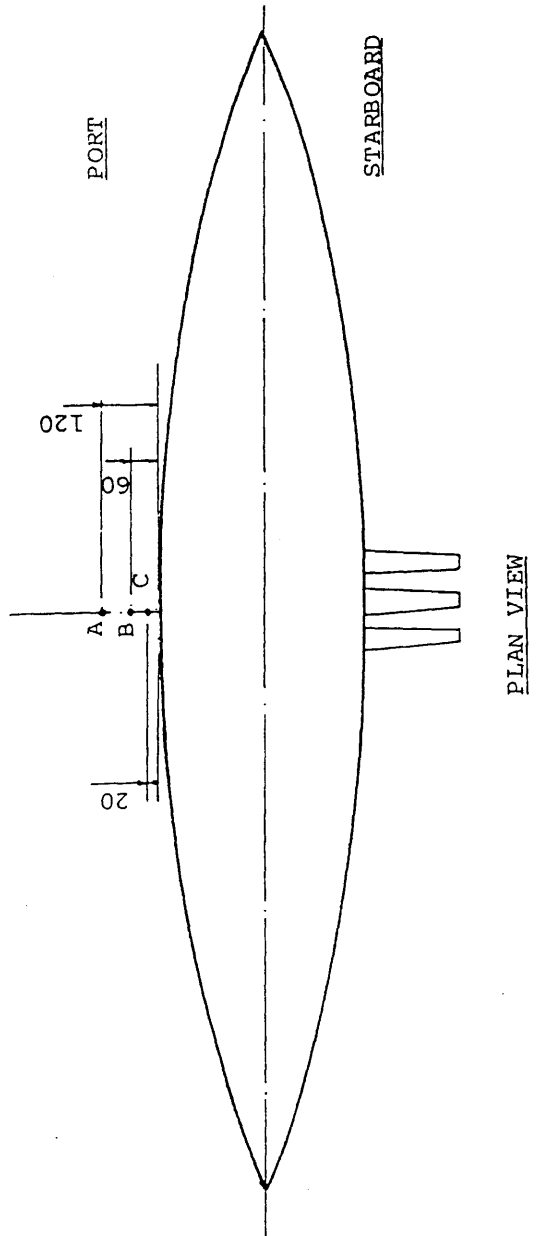
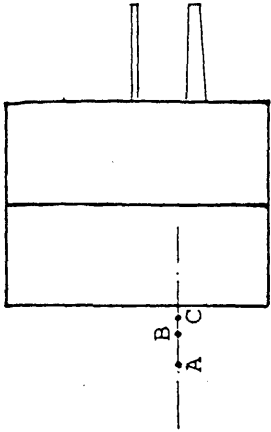
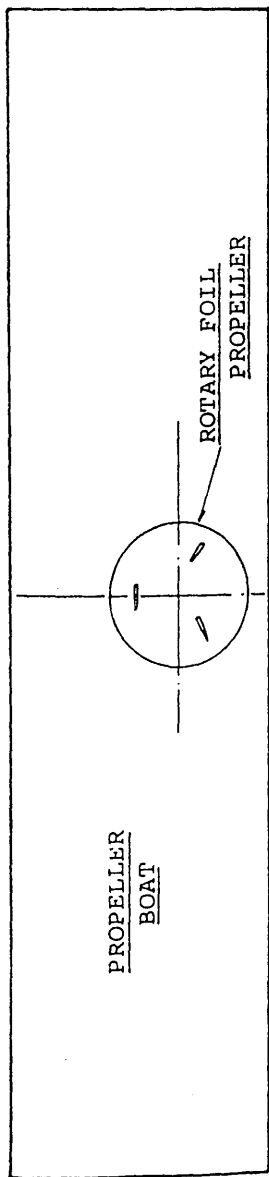
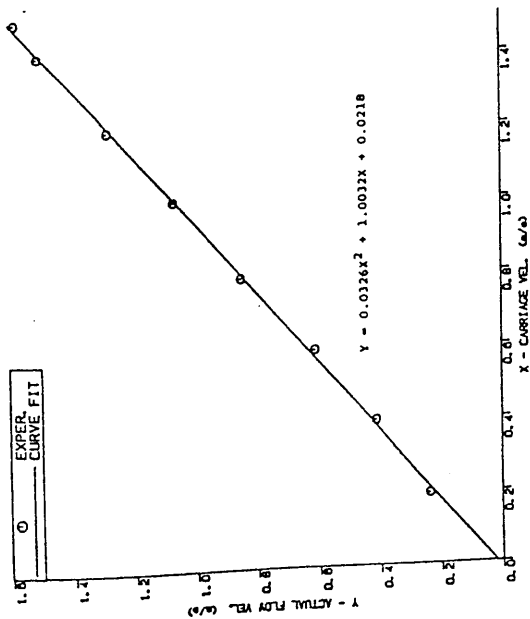
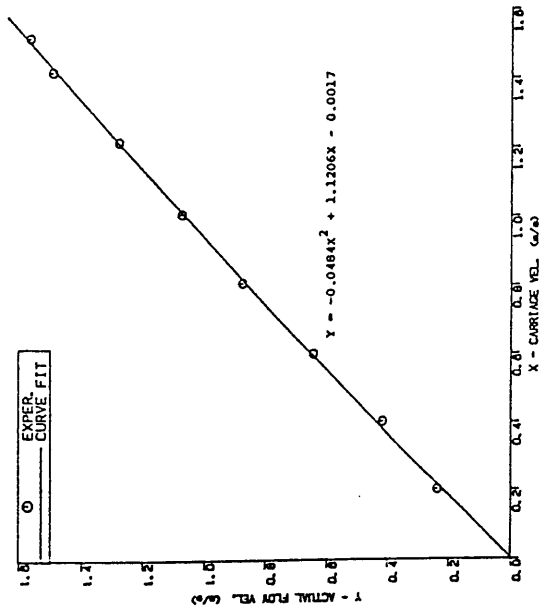


Fig. 10.9 The Location of The Points for Flow Vel. Calibration



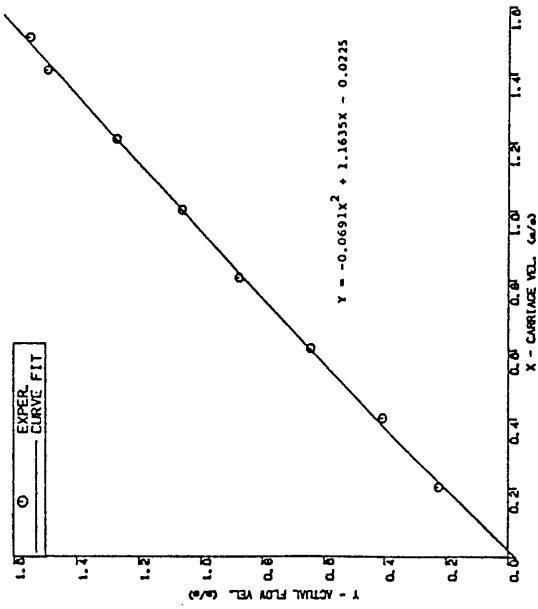
THE ACTUAL FLOW VEL. AT
20mm FROM THE HULL

(a)



THE ACTUAL FLOW VEL. AT
60mm FROM THE HULL

(b)

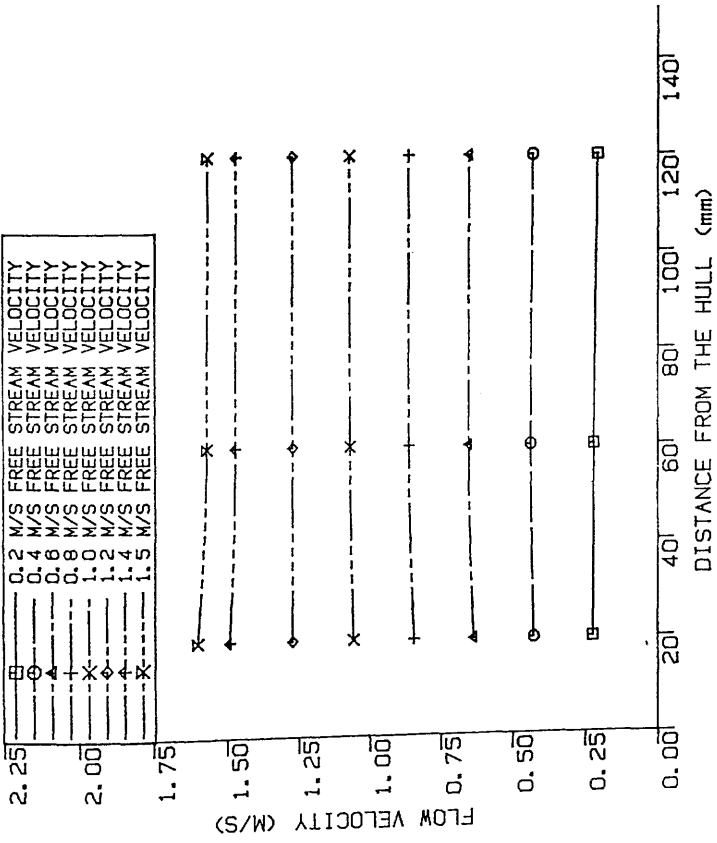


THE ACTUAL FLOW VEL. AT
120mm FROM THE HULL

(c)

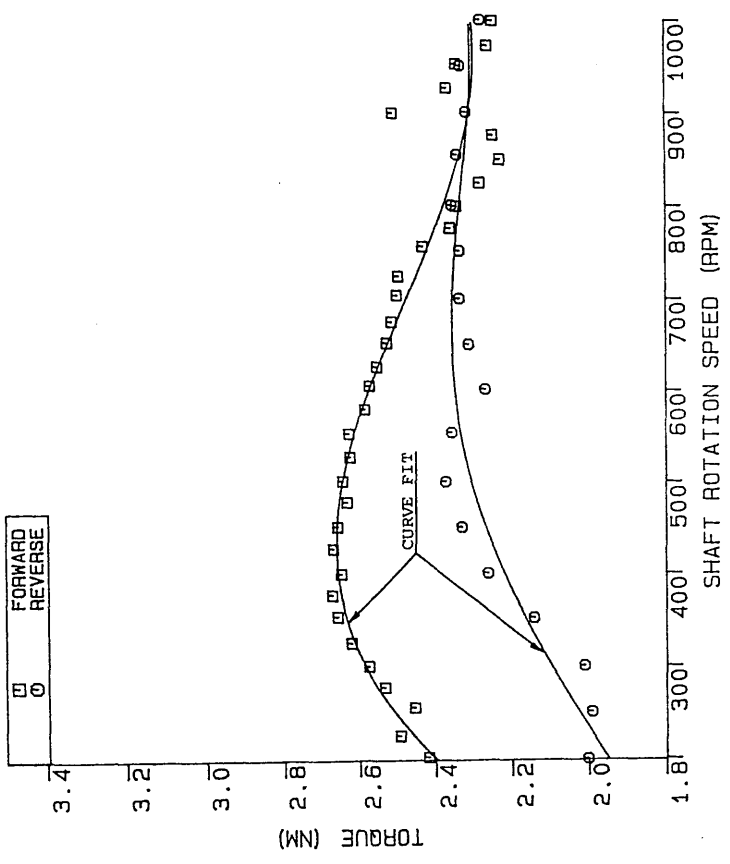
The Relationship Between the Actual Flow Velocity and the Free Stream Velocity

Fig. 10.10



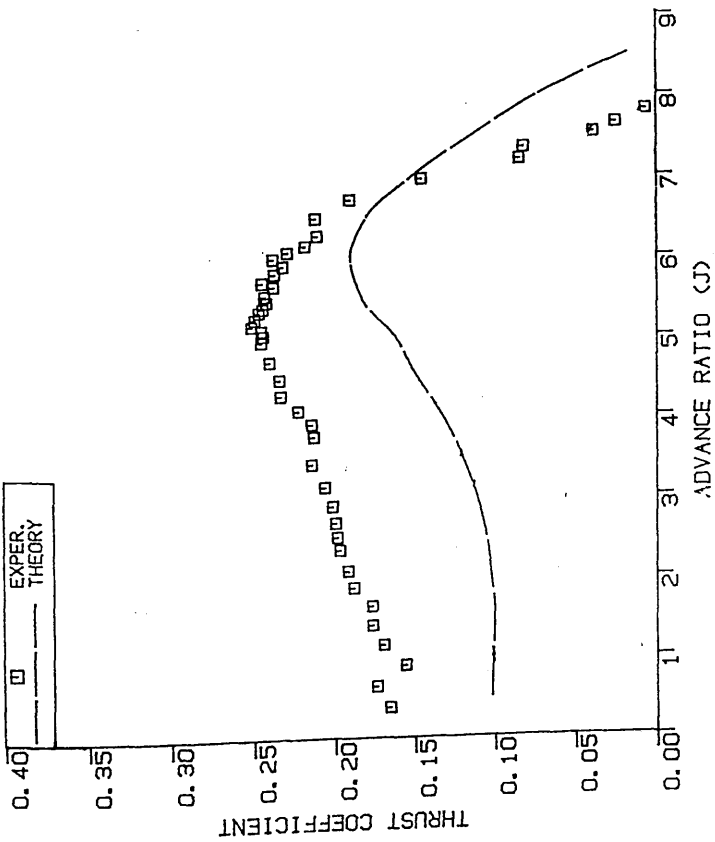
Flow Velocity Profile Alongside Propeller Boat at Propeller Axis Position

Fig. 10.11



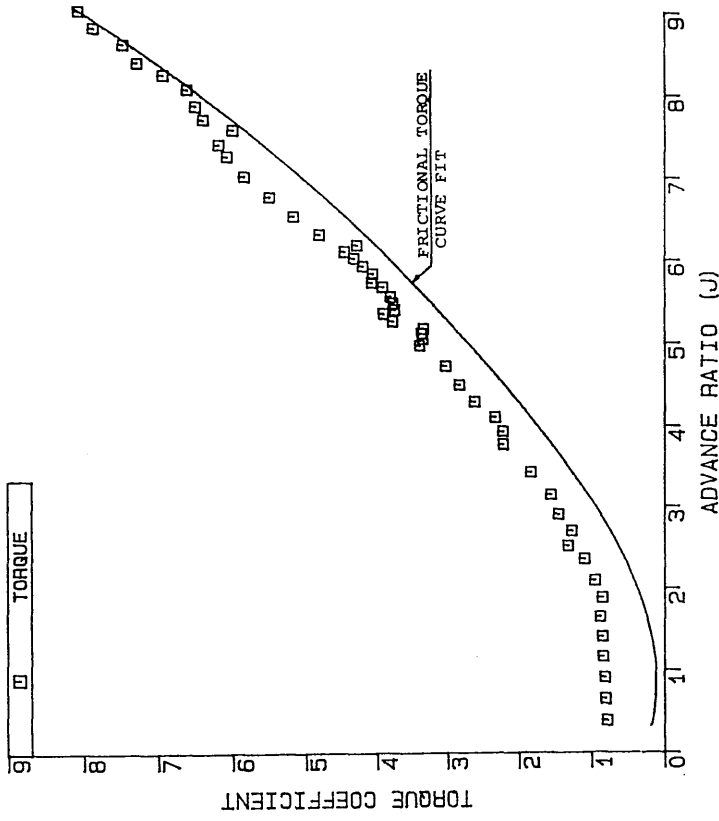
Torque Associated with Frictional Losses Within Propeller Model

Fig. 10.12



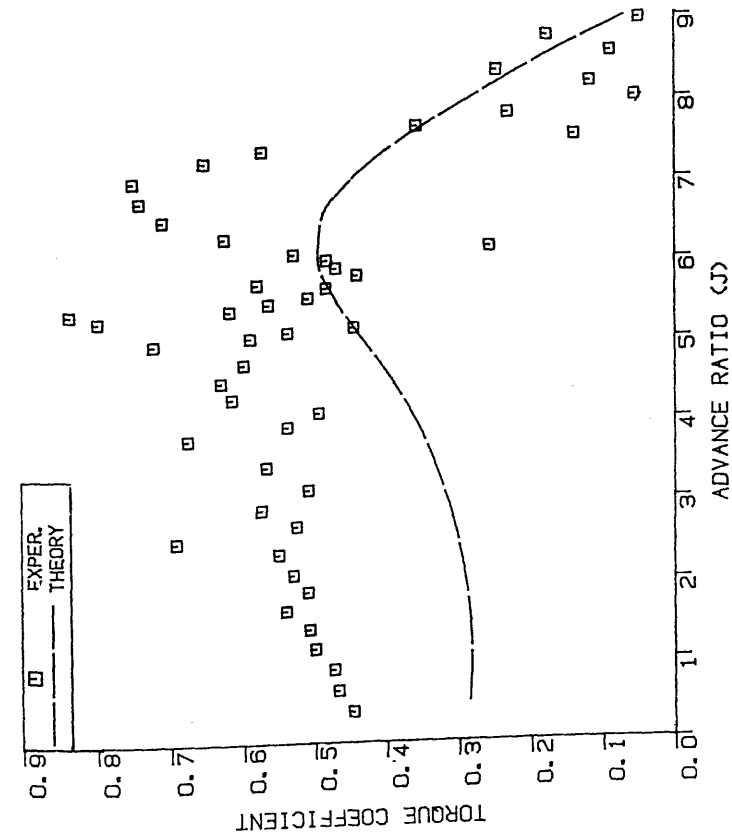
Thrust Coefficient of Propeller Operating at Forward Speed

Fig. 10.13

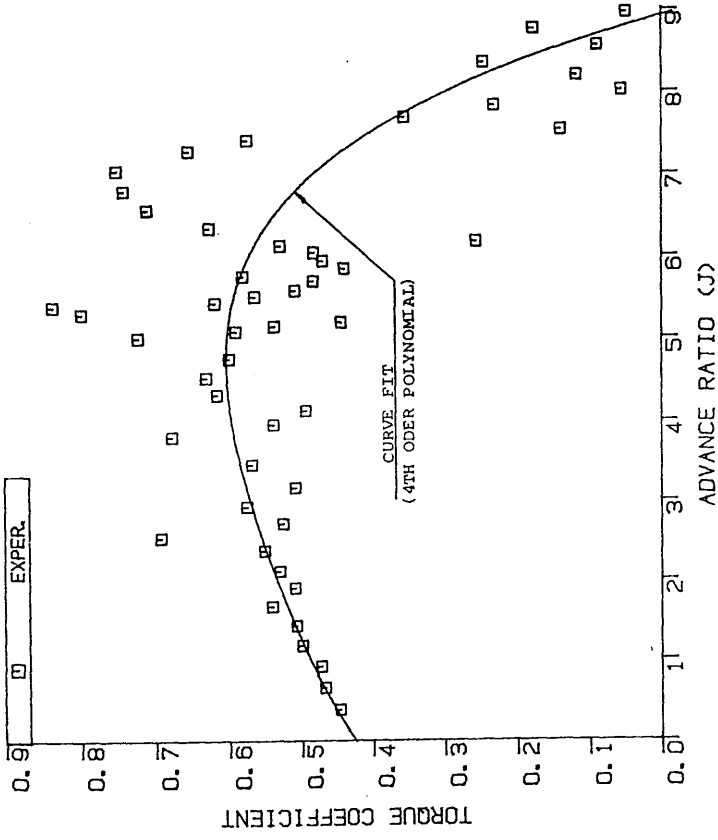


Total and Frictional Torque Coefficients of Propeller Operating at Forward Speed

Fig. 10.14



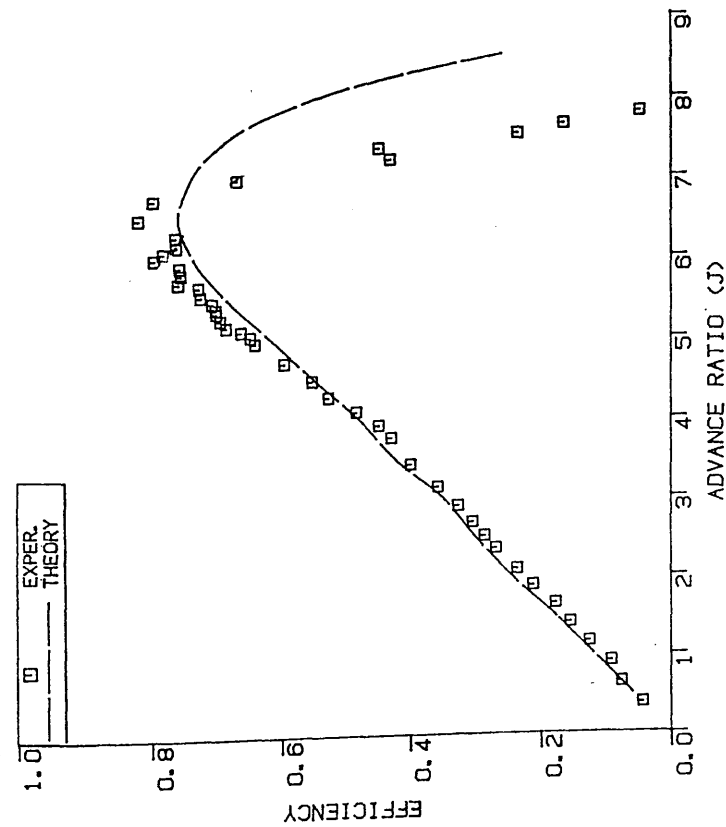
(a)



(b)

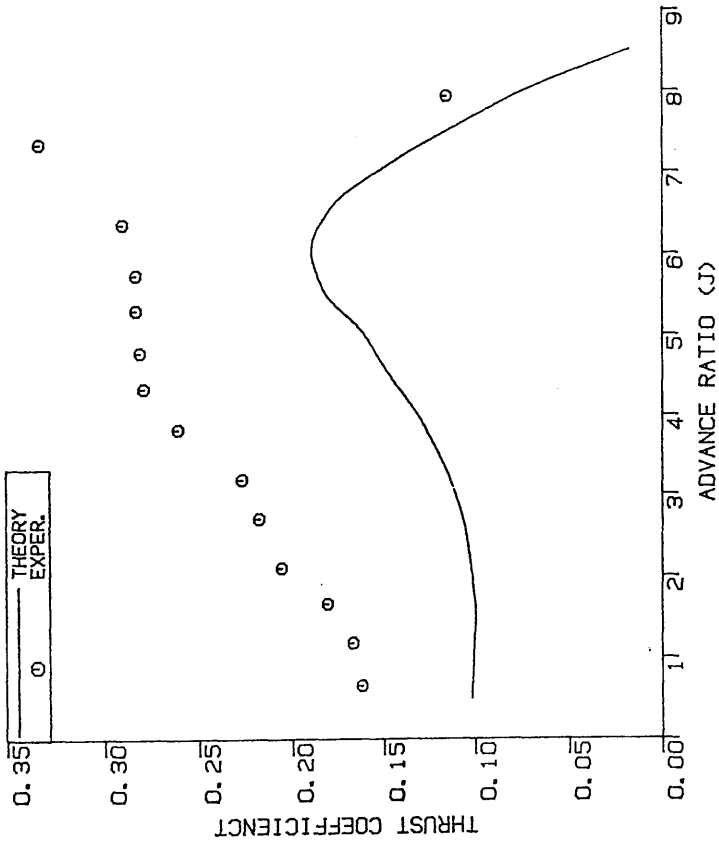
Torque Coefficient of Propeller Operating at Forward Speed

Fig. 10.15



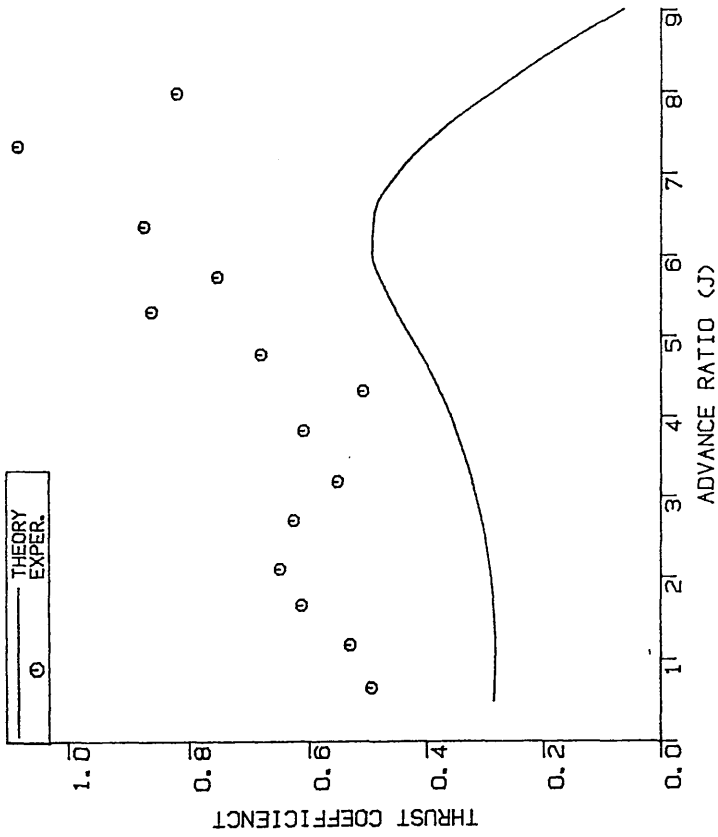
Efficiency of Propeller Operating at Forward Speed

Fig. 10.16



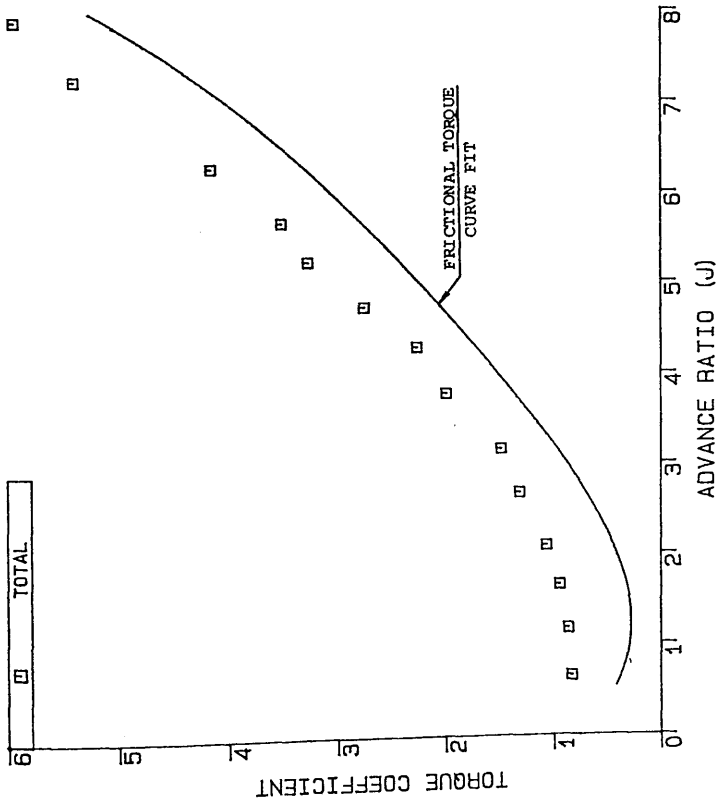
Thrust Coefficient of Propeller Operating in Reverse

Fig. 10.17



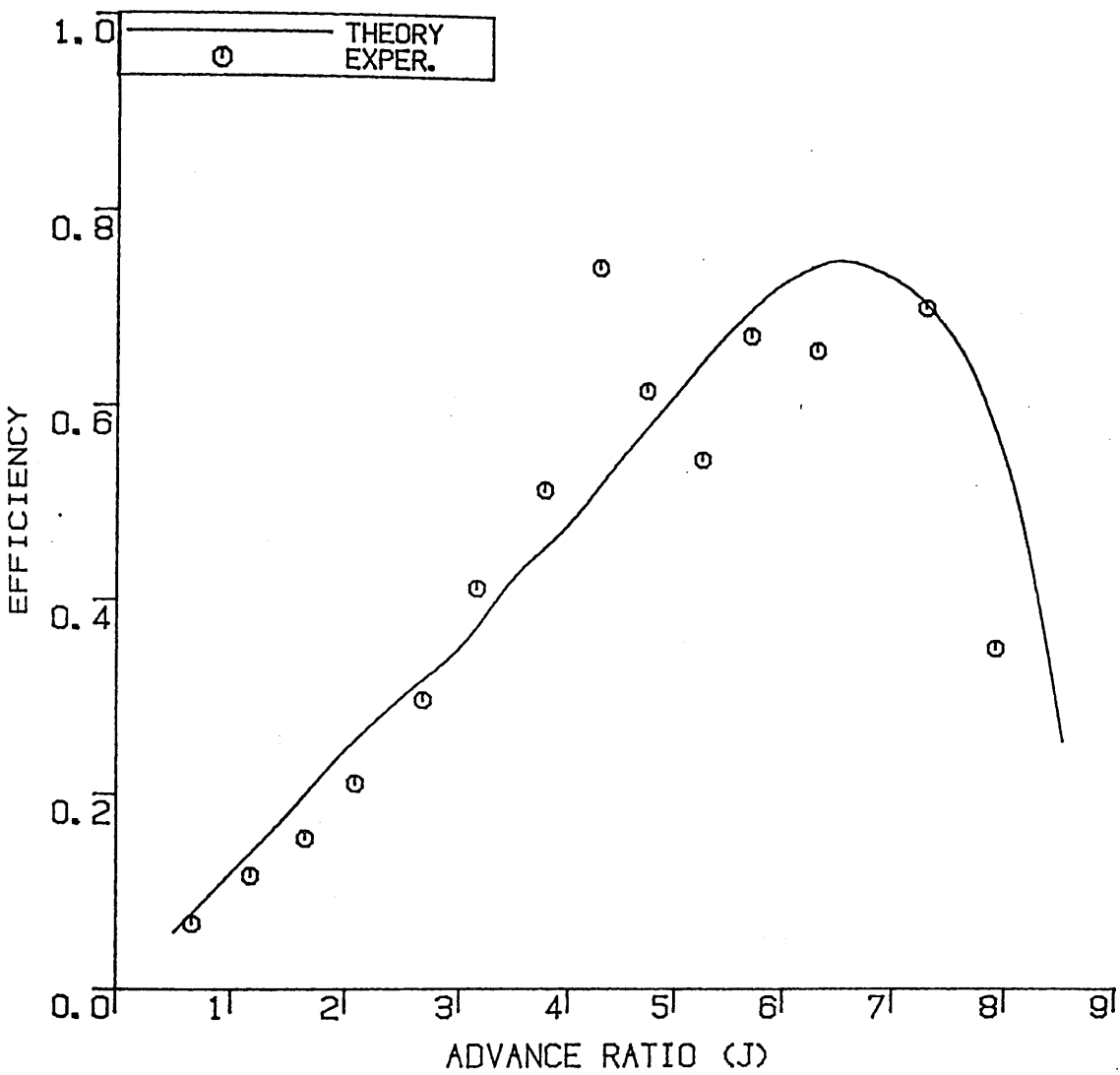
Torque Coefficient of Propeller Operating in Reverse

Fig. 10.19



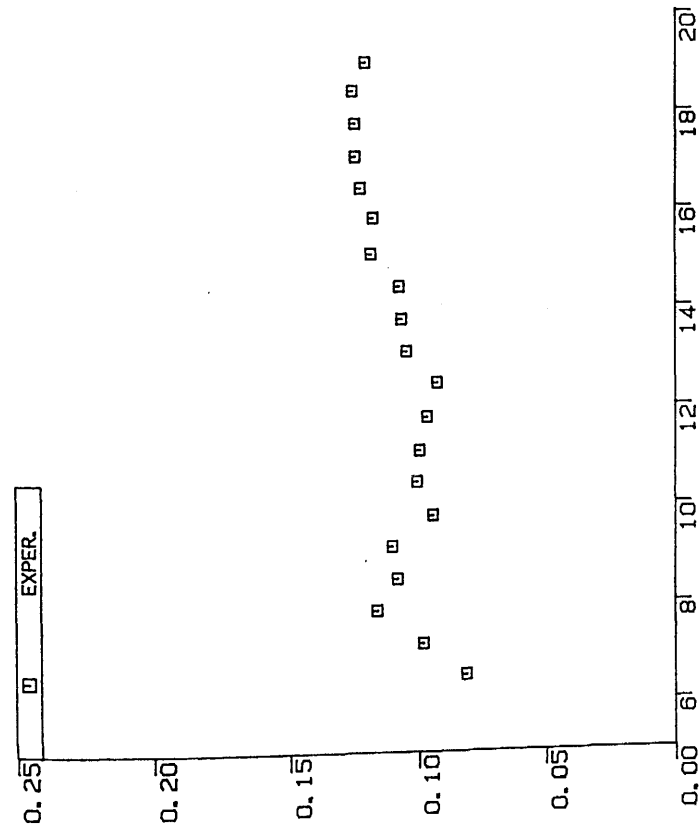
Total and Friction Torque Coefficients of Propeller Operating in Reverse

Fig. 10.18



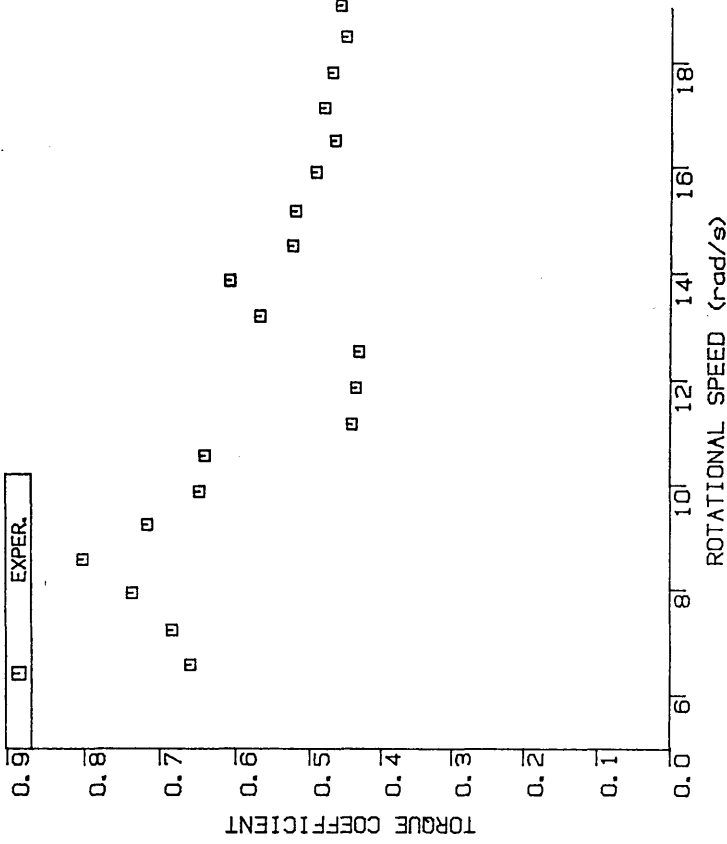
Efficiency of Propeller Operating in Reverse

Fig. 10.20



Thrust Coefficient of Propeller at Zero Speed

Fig. 10.21



Torque Coefficient of Propeller at Zero Speed

Fig. 10.22

PART IV

APPLICATION OF OSCILLATING FOIL PROPELLER

&

GENERAL CONCLUSIONS

The practical application and economic studies of oscillating foil propellers in actual marine service life have been done and described in the Chapter 11. The main conclusions of the present work have been drawn in the Chapter 12 and the future development is also proposed.

CHAPTER 11

APPLICATION OF OSCILLATING FOIL PROPULSION

1.0 INTRODUCTION

In previous chapters, the performance of two-dimensional oscillating foil propellers, flexible fin propellers and rotary foil or trochoidal propellers have been investigated. In this chapter, the practical application of these oscillating foil propellers to different ships has been investigated. Both theoretical and experimental results are used in the studies of the practical application of these oscillating foil propellers to full scale ship examples.

In chapters 7 and 10, experimental results have been applied to the design of full scale propellers for a 66 metre ship. The study is extended here for four different ships including the 66 metre ship. Three of them have similar Froude numbers, though they are of different sizes, while the other one is a high speed craft. Three types of oscillating foil propellers are designed for these four ships. The required hull form and the arrangement of these propellers is also discussed in this chapter. The natural frequency of the flexible fin propeller is calculated and compared to its operating frequency.

The ultimate practicality of applying oscillating foil propulsion depends on a solution to the problems of their driving mechanisms, as pointed out by Sherer [1968]. In this chapter, the required driving mechanisms of three oscillating foil propellers are designed and discussed. A simple driving mechanism is designed for the flexible fin propeller and a motion close to a sinusoidal angular oscillation is generated. This is the simplest driving mechanism among these three types of propeller [Lai, McGregor & Bose 1989a].

The oscillating foil propeller is an alternative propulsion system to the conventional screw propeller. A comparative economic analysis can provide one element in a judgement as to whether oscillating foil propulsion can be competitive with the conventional system. It is very difficult to make an accurate economic comparison between any type of foil propulsion and conventional screw propulsion. In most cases, the design of the ship lines especially in the after-body has to be altered in order to accommodate the foil mechanism. Such a change will alter the ship resistance characteristics, its construction cost and may affect the cargo carrying capability. These changes can produce both economic gains and losses and are impossible to assess without a very detailed investigation. For example, any significant change in the after-body lines is likely to be assessed as more expensive by a shipbuilder, since his staff have to go on a learning curve on how to construct the new design economically.

There are other considerations which are listed as follows.

- a) Ship Motions :- The modified ship lines will alter the motion characteristics and the action of the the foil propellers on motions will differ from screw propellers. Generally, they will provide an increased damping especially in pitch.
- b) Machinery Fit :- The machinery of conventional screw propulsion requires to be fitted at a point sufficiently forward of the stern in order to accommodate the large sized engines involved in slow or medium speed diesels. A connecting shaft between the power units and the propeller is also required. With a foil propeller, the drive mechanisms have to be changed. In some cases, the mechanisms would require a larger internal volume with in the ship and, in some cases, a smaller internal volume. Again, it would be necessary to do an extended study on different machinery fits in order to make an exhaustive analysis.
- c) Noise :- For naval ship vessels, the noise generated by propellers is of considerable concern and part of this noise is hydromechanical in nature. There is great interest in propulsion systems which produce low noise. In this aspect, some aspects of foil propellers could be beneficial.

- d) **Reliability** : - A ship owner is greatly concerned to avoid breakdowns which can lead to losses through cargo deterioration, tonnage cost, repair costs etc. Oscillating foil technology will need to go through a period of development to ensure the same level of reliability as existing screw propellers. In particular, the successful application of flexible fin propeller requires the use of new materials which are not common in the marine field at the present time and this will require a learning curve in how to design and fabricate the required element.

It has not been possible to go into all of these factors and the present analysis has been performed with the following assumptions.

- i) There is no change in ship hull cost and in its resistance characteristics.
- ii) There is no change in motion characteristics.
- iii) It will be possible to select a suitable machinery to drive the foil propeller.
- iv) The reliability, except where questions of fatigue life come into the design of flexible fin propeller, is the same for screw and foil propulsion. A partial allowance has been made for this factor in terms of an increased maintenance cost in some cases.

In this chapter, the present value method is adopted in the economic analysis [Brealey & Myers 1984]. The present value of the fuel savings for the whole life time of the ships arising from the improvement of propulsive efficiency, are calculated using the present oil price [The Motor Ship 1989]. Breakeven costs, at which the present value of the fuel savings from improving propulsive efficiency is equal to the extra cost in the application of foil propulsion, are calculated for different interest rates, allowing for extra maintenance costs and variation in the oil price.

2.0 PARTICULARS OF SHIP EXAMPLES

Four ships, representing different groups, are studied to investigate the full scale application of oscillating foil propellers. The particulars of these ships are :

	SHIP-A	SHIP-B	SHIP-C	SHIP-D
Length Bet. Perp.(L_{PP}) m	66.0	121.9	200.0	50.0
Beam (B) m	10.5	16.8	32.0	12.0
Draft (D_T) m	4.2	6.7	10.0	3.15
Block Coefficient (C_B)	0.7	0.65	0.59	0.47
Displacement (tonnes)	2088	9196	38438	923
Service Speed (V) kn	12.0	17.0	25.0	25.0
Froude Number (Fr)	0.24	0.25	0.29	0.58
Wake Fraction* (w)	0.11	0.23	0.26	0.039
Thrust Deduction Fraction* (t)	0.18	0.14	0.17	0.054
Effective Power (P_E)* kW	440	2831	23063	8513
Thrust Power (P_T)* kW	470	2546	20721	8638
Required Propulsive Thrust, kN	85	378	2173	69

* definition of these terms is presented in [Brealey & Myers 1984]

Table 11.1 Principal Particulars of Ships

The service conditions of the first three ships correspond to similar Froude numbers. The fourth ship (SHIP-D) is a high speed craft with a high Froude number of 0.58. The information of SHIP-A is taken from Bose & Lai [1989]. SHIP-B is a series 60 parent model (model no. 4211W). The corresponding effective power has been estimated by using the © curve in Todd [1953]. The wake and thrust deduction fraction were estimated by using the Holtrop and Mennen method [1982]. From the effective power and the wake and thrust deduction fractions, the required propulsive thrust at the service speed was calculated. The required propulsive thrust and other particulars of SHIP-C and SHIP-D were estimated by using the methods of Holtrop and Mennen [1982] and Holtrop [1984] respectively.

3.0 FULL SCALE PROPELLERS

The results from previous studies on the performance of different types of foil propulsion are applied to investigate the feasibility of application on these four ships. In the sections concerning flexible fin and rotary foil propellers, model test results were used in the discussion. No allowance for the difference in Reynolds' numbers between model scale and full scale application has been included in the discussion.

3.1 Two-Dimensional Oscillating Propeller

The application of a two-dimensional oscillating foil propeller is investigated in this section. Here, the theoretical predictions in Chapter 3 are used and a two-dimensional oscillating foil propeller with the following operating conditions is chosen,

- 1) pitch lags heave by 90° ,
- 2) rotating centre at the three quarter-chord point,
- 3) a feathering parameter of 0.6, and
- 4) reduced frequency of 0.8.

Although lower reduced frequency gives higher efficiency, a high reduced frequency is required to generate the demanded propulsive thrust. From the theoretical results of Chapter 3, a propulsive thrust coefficient of 0.5 can be generated by the propeller in the above operating condition. The corresponding propulsive efficiency is 0.8. In this operating condition, the thrust contributed by the leading edge suction force is about half of the total thrust and flow separation due to the high leading edge suction force does not occur. The chord of the propeller is taken as about 2% of the ship length. The span of the foil is taken as 80% of the beam while the other 20% is reserved for the enclosing struts. The operating frequency is calculated from the chord length and the speed of advance. The heaving amplitude of the foil is found from the thrust coefficient once the oscillating frequency, area of the foil and the required thrust are known. From the given feathering parameter and the calculated amplitude of heave, the amplitude of

pitch is computed. The applications of oscillating foil propellers for the operating conditions of the four ships (table 11.1) was investigated and the particulars of propellers are listed in table 11.2.

	SHIP-A	SHIP-B	SHIP-C	SHIP-D
Span (s) m	8.4	13.4	25.6	9.6
Chord (c) m	1.5	2.5	4.0	1.0
Amplitude of Heave (y_0) m	0.87	1.52	2.37	0.6
Amplitude of Pitch (α_0) rad.	0.56	0.58	0.57	0.58
Oscillating Frequency (ω) rpm	56	41	36	189
Amp. Heave (y_0) / Half chord (b)	1.2	1.2	1.2	1.2

Table 11.2 Particulars of the Two-Dimensional Oscillating Propellers

The ratio of heaving amplitude to the half chord is 1.2 in the examples. Chopra [1976] shows that when the ratio of heaving amplitude to half chord is around 1.0, the linearised small-amplitude assumption used in the theory is justified. The swept heights of the foil are all less than the operating drafts in the examples. This type of propeller is also suitable for a high speed craft. The results show that it is feasible to apply the propeller to these different ship groups, at least from the hydrodynamic performance point of view.

3.2 Flexible Fin Propeller

In section 8 of Chapter 7, the application of a flexible fin propeller with a rectangular foil, on SHIP-A is discussed. It is shown that the thrust generated by the system can propel this ship at its service speed. The selection of material is discussed in Chapter 8 based on this example. In the present section, the investigation is extended to cover a wider range of ships. The results for the above four ships are presented together in this section for comparison.

The experimental results used in chapter 7 are also applied here. From the experiments, a flexible fin propeller, with a stiffness function of 1.8, taper ratio of 0.37 and angular oscillating function of 3.5 oscillating at a reduced frequency of 0.26 generating a propulsive thrust coefficient of 0.8 at an efficiency of 0.7, is chosen. The aspect ratio of the foil is 4.0. The corresponding non-dimensional heaving amplitude was predicted by the theory as 0.71.

From the thrust coefficient and the speed of advance, the required foil area is calculated and hence the span and chord of the foil are found for a given aspect ratio. The length of the flexible bar is assumed to be about 0.1 of the ship length and then the angular oscillating amplitude is calculated from the angular oscillating function. The heaving amplitude of the foil is calculated from the non-dimensional heaving amplitude. The operating frequency is calculated from the reduced frequency. The particulars of flexible fin propellers for these four ships are listed in table 11.3.

	SHIP-A	SHIP-B	SHIP-C	SHIP-D
Foil Area (S) m ²	6.9	20.3	58.3	11.2
Span (s) m	5.3	9.0	15.3	6.7
Chord (c) m	1.3	2.3	3.8	1.7
Length of the Bar (L _o) m	6.5	12.4	20.5	5.0
Angular Oscill. Amp. (θ _o) rad.	0.35	0.32	0.32	0.58
Oscillating Frequency (ω) rpm	21	15	12	37
Heave Amplitude (y _o) m	1.6	2.8	4.7	2.1
Span / Beam (s/B)	0.50	0.54	0.48	0.56
Swept height / Draft (2y _o /D _T)	0.76	0.84	0.94	1.26

Table 11.3 The Particulars of Flexible Fin Propellers

The spans of the foils in these examples are all less than the beam of the ship and the ratio of span to beam is around 0.5. The ratio of swept height to the operating draft increases as the ship size increases. In SHIP-C, the largest ship in this study, the

swept height is about the same as the operating draft. In the case of the high speed craft (SHIP-D), the swept height for the high required thrust is larger than the draft of the ship and is not practical. From the hydrodynamic performance point of view, it is feasible to apply the flexible fin propeller of aspect ratio 4 in the ships with low Froude number.

In Chapter 8, the stresses acting on the flexible bar of the propeller and its fatigue life were discussed. The application to SHIP-A has been used for discussion. High strength carbon fibre reinforced plastic (SP313 from 3M) shows a good strength and fatigue life. Here, this material (SP313) is also used to study the applications on SHIP-B and SHIP-C. The flexural strength and modulus of SP313 are 1384 Nmm^{-2} and $122 \times 10^3 \text{ Nmm}^{-2}$ respectively.

The stress function is predicted by the theory described in Chapter 8. At model scale with the design operating condition (which is stated in the early part of this section), the thickness function and the flexural modulus of the flexible bar are 7.1 and $37.64 \times 10^6 \text{ Nmm}^{-2}$ respectively; giving a stress function of 1.60. The required mean sectional modulus of the bar is calculated based on the given stiffness function, flexural modulus, advance speed, length of the flexible bar and foil area. The breadth of the flexible bar is restricted to 0.1 of the span of foil in order to limit the disturbance to the flow. The corresponding mean thickness of the bar is then calculated from the required section modulus. From this mean thickness, a new thickness function is computed. Since the stress function is linearly proportional to the thickness function, then

$$\Lambda_{\text{full scale}} = \Lambda_{\text{model}} \frac{\vartheta_{\text{full scale}}}{\vartheta_{\text{model}}} \quad - 11.1$$

The maximum working stress is then calculated and used to study the fatigue life. The particulars, working stress and fatigue life of the flexible bar of the propellers for different ships are shown in table 11.4.

The safety factor shown in the table is the ratio of the maximum working stress to the flexural strength of the high strength carbon fibre reinforced plastic (SP313). As in Chapter 8, the working stress is multiplied by 1.5 for the uncertainty in operation in estimating the fatigue life. The fatigue curve shown in fig. 8.20 is used in the fatigue life estimation. The life time shown in the table is for continuous running.

	SHIP-A	SHIP-B	SHIP-C	SHIP-D
Breadth of the Bar (w_b) m	0.53	0.90	1.60	0.67
Mean thickness (t_m) m	0.14	0.31	0.65	0.23
Taper Ratio (TR)	0.37	0.37	0.37	0.37
Length of the Bar (L_o) m	6.50	12.40	20.50	5.0
Thickness Function (ϑ)	22.05	24.65	31.81	45.24
Stress Function (A)	4.98	5.57	7.19	10.22
Max. Working Stress (Nmm^{-2})	608	680	877	1247.0
Safety factor	2.3	2.0	1.6	1.1
Fatigue Life *	2.5 years	1.0 day	14.0 min.	-

* the fatigue life is estimated based on the maximum working stress with a factor of 1.5 for uncertainty in operation.

Table 11.4 Particulars of the Flexible Bars of the Propellers

In order to keep the same stiffness function, the working stress on the flexible bar in the examples increases as the size of ship increases. In SHIP-B and SHIP-C, the fatigue life is short and not practical. For the high speed craft (SHIP-D), the working stress is high and the stress with a factor of 1.5 for the fatigue analysis is higher than the steady flexural strength. The situation can be improved by using a higher taper ratio. It is not recommended to increase the breadth of bar in order to lower the thickness function and hence the working stress because a wide bar will lead to an unacceptable disturbance to the flow. A hybrid composite lay-up may be designed to give high strength, low stiffness and hence long fatigue life. Here the application of flexible fin propeller is limited by the fatigue life to the small ship with low Froude number.

In Chapter 5, theoretical predictions showed that a higher efficiency can be obtained for a foil with a higher aspect ratio. The performance of a propeller with an aspect ratio 10 foil is predicted by using the theory shown in Chapter 4. The previous operating condition is applied where

- (i) stiffness function (ξ) = 1.8,
- (ii) angular oscillating function (ζ) = 3.5,
- (iii) taper ratio (TR) = 0.37, and
- (iv) reduced frequency (k) = 0.26.

In this condition, a flexible fin propeller with an aspect ratio of 10 can generate a thrust coefficient of 0.5 and the corresponding efficiency is 0.8. Here, application to SHIP-A is presented. The following particulars of the flexible fin propeller has been designed using the theoretical method.

	SHIP-A
Foil Area (S) m ²	11.15
Span (s) m	10.56
Chord (c) m	1.06
Length of the Bar (L _o) m	6.5
Angular Oscill. Amp. (θ_o) rad.	0.28
Oscillating Frequency (ω) rpm	26
Heave Amplitude (y_o) m	1.16
Span / Beam (s/B)	1.0
Swept height / Draft ($2y_o/D_T$)	0.55
Breadth of the Bar (w_b) m	1.05
Mean thickness (t_m) m	0.14
Taper Ratio (TR)	0.37
Thickness Function (ϑ)	21.54
Stress Function (Λ)	4.6
Max. Working Stress (Nmm ⁻²)	564
Safety factor	2.45
Fatigue Life	over 7 years

Table 11.5 Particulars of the Flexible Fin Propeller with Aspect Ratio of 10

The span of the foil is slightly larger than the beam of the ship. In Chapter 7, the thrust coefficient and efficiency in the model test for the propeller model with aspect ratio 4 is slightly higher than the theoretical prediction in this operating condition. If this is applicable to the case of aspect ratio 10, the estimated foil area could be smaller than that shown in table 11.5 and the situation with regard to oversize would be improved.

The stress function of the propeller with aspect ratio 10 is 7% lower than that with aspect ratio 4. As the span of the foil with an aspect ratio 10 is large, the breadth of the flexible bar is larger than that with an aspect ratio of 4. For the same stiffness function and hence required mean sectional modulus, the corresponding thickness function is lowered and hence the stress function is lowered. A significantly longer fatigue life is obtained for the propeller with aspect ratio 10 than that with an aspect ratio of 4 in the application for SHIP-A. For the other ship examples, although lower stress is obtained for the propeller with aspect ratio 10 than that with aspect ratio 4.0, the fatigue life is still not long enough to be practical.

This study shows that high aspect ratio is desirable from the view point of high efficiency and fatigue life. The upper limit of aspect ratio occurs around 10.0 for a practical application where the required span is about the beam of the ship.

3.3 Rotary Foil Propeller

The application of a three bladed rotary foil propeller on SHIP-A was discussed in Chapter 10 by using experimental results. Here, as with the flexible fin propeller, the study is extended to cover a wider range of ships.

The experimental results show that a propulsive thrust coefficient (T_c) of 0.25 can be generated by a three bladed propeller with an effective aspect ratio (AR_e) of 10 and a pitching amplitude of 0.35 rad (20°) operated at an advance ratio (J) of 5.0. The propulsive efficiency is 0.7. The swept area of propeller which is defined as the span of

the foil times the diameter of the blade rotation, is calculated from the given advance ratio, the corresponding thrust coefficient, required thrust and speed of advance in the design condition by using eqn. 10.8. The diameter of blade rotation is limited by the operating draft for most practical cases. The diameter of blade rotation for SHIP-A, SHIP-C and SHIP-D are the same as the respective diameters of the existing screw propeller. For SHIP-B, there is no given data on the existing diameter of screw propeller and the diameter of blade rotation is taken as 0.8 of the draft. Then the required span of the foil is found. The particulars of the propellers for these three ship examples are listed in table 11.6.

	SHIP-A	SHIP-B	SHIP-C	SHIP-D
No. of Blades	3	3	3	3
Effective Aspect ratio (AR_e)	10	10	10	10
Max. pitching angle (β_{max})	0.35	0.35	0.35	0.35
Swept Area (S) m ²	28.0	82.2	236.1	45.2
Radius of Blade Rotation (R) m	1.3	5.4	4.0	1.6
Span (s) m	10.6	15.3	29.5	14.0
Rotation Speed (Ω) rpm	24	15	14	46
R / L _{pp}	0.019	0.022	0.020	0.032
s / B	1.01	0.91	0.92	1.17

Table 11.6 The Particulars of Rotary Foil Propellers

For ships SHIP-A, SHIP-B and SHIP-C (those with low Froude Number), the ratio of radius of blade rotation to ship length is around 0.02. The span of the blades of the propellers for these ships is similar to the beam. In practice, space for the propeller mechanism is required. The total length of the span of the blades and the driving mechanism will be greater than the beam of the ship and will project out from the ship side and be impractical. In order to cope with the high required thrust of the high speed craft (SHIP-D), the span of the propeller itself is larger than the beam of the ship. To increase the thrust at the same swept area, a larger number of blades or higher pitching

angle may be required as pointed out by [Bose 1987].

The deep operating draft, large beam and strut spacing of SWATH ship configurations give better space to accommodate the oscillating foil propeller. Here the application of a rotary foil propeller to a high speed small SWATH ship is studied. The particulars of this example [Chun 1989] are given in table 11.7.

Overall Length	18.29 m
Overall Beam	9.96 m
Length of the hull	16.76 m
Max. Hull Diameter	1.01 m
Length of the Strut	17.22 m
Max. Strut Thickness	0.61 m
Hull Spacing Between Centre-Lines of Hull	7.77 m
Operating Draft	2.61 m
Service Speed	30.0 kn
Froude Number	1.20
Resistance	59.7 kN

Table 11.7 The Particulars of a SWATH Ship

At the propeller is located between the struts and not at the stern, the standard prediction method does not apply and the thrust deduction and wake fractions are assumed to be zero. The required thrust is the total ship resistance. The required swept area of the rotary foil propeller is 2.5 m^2 . If the swept height of the propeller is 25% of the operating draft then the radius of blade rotation is 0.32 m. The rotation speed is 289 rpm. The span of each of two propellers is about one quarter of the strut spacing which is feasible.

van Manen [1966] and Dickerson [1975] suggested the use of this type of propeller for high speed craft.

4.0 ARRANGEMENT OF OSCILLATING FOIL PROPELLERS FOR MONOHULLS

Layouts of oscillating foil propulsion systems for the conventional mono-hull ships are presented in figs. 11.1 to 11.4. A transom stern with a width equal to the beam of ship is proposed to provide maximum space to accommodate the span of the oscillating foils.

4.1 Two-Dimensional Oscillating Foil Propeller

Horizontal and vertical two-dimensional oscillating foil propulsion systems are shown in figs. 11.1 and 11.2. In the force system generated by the oscillating foil, an oscillating force parallel to the heaving motion is obtained as a by-product of propulsive thrust (Chapter 2). This vertical force can induce a pitch and heave motion of the ship. This unwanted oscillating force can be cancelled by foils heaving 180° out of phase. In the case of the horizontal foil system, the span of the foil could be separated into three small sections as shown in fig. 11.1 [Jakobsen 1988]. The span of each of the side foils is half of the central foil and the side foils heave 180° out of phase with the central foil so cancelling the oscillating force. According to Isshiki [1987], the motion response of the ship to the oscillating vertical force may be minimized, if the foil oscillates under the bottom of the stern of the ship, as shown in the stern arrangement of fig. 11.1 around station (e). The flat stern bottom provides a mirror image of the foil and cancels the vertical oscillating force. However, this may induce unwanted hull vibration. For steering, the foil and its enclosing struts could be rotated to generate the propulsive thrust at an oblique angle.

An oscillating foil system can be arranged vertically [Kubota et al. 1984] in the form of a twin foil system as shown in fig. 11.2. The foils of the port and starboard sides move 180° out of phase and the unwanted sideways oscillating forces cancel

each other. Steering moment can be generated when one of the foils (eg. port) generates a negative thrust while the other (eg. starboard) generates a positive thrust. In Chapter 3, it was shown that a negative thrust can be generated at some specified values of phase lag between the heaving and pitching of the foil. In addition, if one of the foils stops and is perpendicular to the direction of advance, the drag is maximum and also generates a significant amount of negative thrust. The flat bottom of the stern and a horizontal extension from the bottom of the skeg provide an enclosing effect to increase the effective aspect ratio (fig. 11.2). However increasing the number of foils increases the complexity of the driving mechanism and the cost. The proposed stern hull forms are presented in the form of a body plan with five different sections. The hull form presented is simplified to show the concept.

4.2 Flexible Fin Propeller

In fig. 11.3, a flexible fin propeller is fitted at the stern of a ship with a centre line rudder for steering. It is not practical to separate the foil into three different foils to cancel the unwanted oscillating force, as with the two dimensional oscillating foil propellers (fig. 11.1). This is because the aspect ratio of the foil is decreased giving lower propulsive efficiency and increased complexity of the driving mechanism. Side enclosing struts are not recommended to make the flow more two-dimensional, although this may solve the problem with low aspect ratio foils. Since the oscillation of the foil is controlled by a flexible bar, a slight rotation of the foil may be obtained in practical operating conditions and the foil could jam. This problem would be overcome by increasing the gap between the foil and the strut but the purpose of the strut is to avoid pressure leakage at the tip of foil and this will be lost. The mirror image provided by the flat bottom might minimize the motion induced by the oscillating force, as described in the previous section.

4.3 Rotary Foil Propeller

A schematic arrangement of a pair of rotary foil propellers fitted on a ship is shown in fig. 11.4. The propellers are fitted on the ship's centre skeg, where the control and power transmission are housed, as shown by Bose [1987].

As shown in Chapter 10, negative thrust can be generated by the propeller by rotating the drum in the reverse direction. A steering moment for manoeuvring may be generated by changing the direction of rotation for one of the propellers.

The oscillating vertical forces are almost cancelled by the use of several foils moving with phase differences to each other. This also evens out the propulsive force.

5.0 ARRANGEMENT OF AN OSCILLATING FOIL PROPELLER ON A SWATH SHIP

5.1 Two-Dimensional Oscillating Foil Propeller

For SWATH ships, there are some special configurations which demonstrate possible advantages for the oscillating foil propulsion system. These configurations involve

- (i) the side struts act as the end shielding struts,
- (ii) large hull separation provides for either large span of the foil or space for the required oscillating amplitude if a vertical arrangement is used,
- (iii) deeper draft, compared to conventional mono-hulls, also provides either larger space for the required oscillating amplitude or span if a vertical arrangement is applied.

In the application of a two dimensional oscillating foil propeller with a horizontal foil, the driving mechanism can be installed in the struts. For the vertical foil system, two horizontal struts are required to provide a shielding effect and also act as

bracings between the hulls. Although the bending stress at the deck and the vessel motions are reduced by these struts, the resistance is increased. The arrangement of this application is shown by Lai [1987].

5.2 Flexible Fin Propeller

In the case of a flexible fin propeller, the span of the foil should not project beyond the ship side. In this case, this gives an upper limit at an aspect ratio 10. Space to accommodate the foil is not a problem. In military applications of SWATH, the Froude number in the operating condition is usually high. The stress acting on the flexible bar is high for high speed craft and a short fatigue life results. However, some SWATH ships may operate at low Froude number [MacGregor et al. 1988]. There exists a possibility of jamming the foil between struts and care would need to be exercised in design and fabrication to avoid this.

5.3 Rotary Foil Propeller

The application of a rotary foil propeller to a high speed SWATH has been described in the previous section. The problem of requiring large span to generate the necessary propulsive thrust is solved with the large strut spacing as shown in fig. 11.5. In order to provide a flat surface for the propeller, D-shaped hulls are suggested as shown in the figure.

6.0 NATURAL FREQUENCY OF THE FLEXIBLE FIN PROPELLER

The natural frequency of the flexible fin propeller with aspect ratio 4.0 in the case of SHIP-A has been computed by using Myklestrad's method [Myklestad 1944; Bishop 1956] for a non-uniform tapered vibrating beam. The particulars of the flexible fin propeller are shown in tables 11.3 and 11.4.

The flexible fin propeller is modeled as an oscillating cantilever. The cantilever

is separated into a number of segments as shown in fig. 11.6. Each segment is replaced with a light beam having the same properties in flexure and carrying two equal masses at each end of the segment. These masses are equal to the mass of that segment. At a given oscillating frequency, the receptance at the fixed end is calculated, where

$$\text{Receptance} = \frac{\text{Deflected Slope}}{\text{Bending Moment}} \quad - 11.2$$

The reciprocal of the receptance is plotted against the oscillating frequency. For a cantilever with clamped-free ends, the deflected slope is zero at the fixed end and the reciprocal of receptance is infinity. A horizontal asymptote of the curve occurs at a natural frequency.

The flexible fin propeller in the example is separated into 6 segments (fig. 11.6). The mass and added mass of the foil is added on to the mass m_1 . The approximate added mass of a foil with finite aspect ratio [Martin 1963] is

$$\frac{AR}{\sqrt{1 + AR^2}} \rho \pi \left(\frac{c}{2}\right)^2 s. \quad - 11.3$$

In the present study, the mass and added mass of the flexible bar and the added mass of the foil have been taken into account. The mass of the foil is neglected at the moment. In fig. 11.7, the corresponding reciprocal of the receptance is presented. The natural frequency occurs at 5.27 rads^{-1} . The operating frequency is 2.1 rads^{-1} (21 rpm) and the natural frequency of the first mode is 2.5 times higher than the operating frequency.

Here, the variation in the mass of the foil is considered. The mass m_1 will be changed and so will the natural frequency. If a light fibre composite is used, the mass of foil will be small. The change of the natural frequency in responding to a change of mass of the foil is plotted in fig. 11.8. The natural frequency reduces by 6% to 4.94

rads⁻¹ with an increase in mass from zero to 1000 kg. The natural frequency is still 2.35 times higher than the operating frequency. Resonance will not occur during operation.

7.0 THE DRIVING MECHANISM

There are significant differences in the driving mechanism between these different types of propeller. In this section, the driving mechanisms of these propellers are discussed.

7.1 Two-Dimensional Oscillating Foil Propeller

Isshiki [1987] used a crank mechanism to drive an oscillating foil with low aspect ratio (fig. 11.9). Three rigid rods were used. The foil was connected to the driving disc by two rods while the third one was connected to a fixed pivot point. The third rod was used to restrict the motion of the foil while the others drove the foil. In order to demonstrate the motion, a second location is shown in chain dotted-lines. In the Norwegian Marine Technology Centre, another driving mechanism was used to drive a rectangular oscillating foil model [Lai 1988]. A vertical oscillating bar was connected to the rotating centre of the foil to provide heave motion while the pitch motion is provided by two springs as shown in fig. 11.10. The stiffness of the two springs must be the same to provide identical upward and downward pitching motion.

Both these mechanisms can be used to drive a two-dimensional oscillating foil propeller. All the driving mechanisms could be installed inside the enclosing strut. However, the rigid forward connecting bar of Isshiki's crank mechanism is an awkward arrangement. The mechanism applied in the Norwegian Marine Technology Centre is more suitable. In order to convert a rotation into a vertical sinusoidal oscillation, a sliding mechanism, such as the sinusoidal oscillator in Chapter 6, is necessary. Frictional losses may be large. Alternatively, the vertical reciprocating motion could also be provided by a special internal combustion engine with linear

explosion [Ohna 1987]. For more precise control in pitching motion, a more complicated driving mechanism is required.

7.2 Flexible Fin Propeller

The driving mechanism of the flexible fin propeller is simpler than those for the other two oscillating foil propellers. An angular oscillation with a specified oscillating amplitude at the pivot of a flexible fin propeller is the only required operation. In the model test, a complicated rig was used to generate a sinusoidal angular motion at the pivot. A simplified driving mechanism to provide an angular oscillation at the pivot is proposed in fig. 11.11. This angular oscillation is close to a sinusoidal oscillation. A right angle reduction gear is fitted to reduce the rotation speed. Water tight seals are fitted on the shaft at the pivot connecting the driving bar and the flexible fin propeller. A connecting bar is used to link the points D on the driving bar and B on the output of the reduction gear as shown in fig. 11.12. There are no sliding parts and low frictional losses are expected.

Let the radius of the rotation of B be r_d and the length of driving bar AD be r_p . First, consider the pivot (A) and the centre of the rotation of B on the same level, shown as solid line (ADB) in fig. 11.12. The amplitude of the angular oscillation (θ_{Ao}) is computed from the ratio of r_d and r_p where,

$$\theta_{Ao} = \sin^{-1} \left(\frac{r_d}{r_p} \right) \quad - 11.4$$

The vertical motion of the point D (i.e. $= r_p \sin \theta_A$) throughout an oscillating cycle is shown as the solid curve in fig. 11.12. From this motion, the oscillating angle at any time instant within an oscillating cycle is calculated. The computed oscillating angle throughout an oscillating cycle is compared to that of pure sinusoidal angular oscillation and is shown in fig. 11.13a. A large angular oscillating amplitude of 45° is chosen in this example to enlarge the difference. A significant difference is obtained in

the second half of the cycle.

In order to generate an angular oscillation close to a sinusoidal oscillation and keep the driving mechanism simple, the pivot is moved back from A to A' by $\frac{r_p}{2}(1 + \cos \theta_{Ao})$ as shown in chain-dot-line (A'D'B) in fig. 11.12. From the motion of the point D', the oscillating angle is computed and compared to that of sinusoidal oscillation (fig. 11.13b). The difference is small and may be neglected.

7.3 Rotary Foil Propeller

The driving mechanism of the rotary foil propeller in the full scale size will be very close to that of the model. As pointed out in Chapter 10, the frictional loss in the driving mechanism is significant. Every effort is required to lower the frictional loss and keep the overall efficiency high. In the model, high friction is obtained from the watertight seal. On a full size propeller, it is likely that a convention shaft seal (eg. Glacier Pilgrim 'Coastguard' System [Bunyan 1979]) could be applied and this may be expected to lead to low frictional losses. In the model, the sliding mechanism is made of phosphor bronze and is lubricated. As the sliding mechanism will be enclosed in a rotating drum, self-lubricating fabric liner materials, such as Uniflon [Rose Bearing 1978] and Faflon [Fafnir Bearing Division of Textron Inc. 1978], might be used. This type of material is available in a liner form and can be adhered onto the sliding surface. This material is designed for oscillation duty and is suitable for high loading, low speed and over a wide temperature range (eg. Uniflon from -75° to 120°) [Rose Bearing 1978]. More tests are required to test this on a prototype propeller.

8.0 WAVE PROPULSION WITH A FLEXIBLE FIN PROPELLER

In Chapter 9, when a passive flexible fin propeller is fitted on a yacht model, significant reductions in resistance and motion response of the model in waves have been found near to the resonance region, where the encounter wave length is close to the ship length. The reductions are more significant at low Froude numbers. The

feasibility of the application of wave propulsion with a passive flexible fin propeller as an auxiliary propulsion device is studied here.

The highest propulsive thrust coefficient measured in the model test (Chapter 9) was generated at a low Froude number of 0.13 with an encounter wave length ratio about 1.0. Here, a 20-metre yacht is considered. The speed corresponding to this low Froude number is about 3.5 knot. When the encounter wave length ratio (λ_c) is 1.0, the encounter wave frequency is 1.8 rads^{-1} . The equivalent wave frequency and wave period of the sea conditions are 1.4 rads^{-1} and 4.5 seconds. The mean wave height in the model test was 0.05 m and the equivalent wave height in this example is 0.618 m (2 ft), which is realistic.

Oceanographic scientists have recorded wave periods and heights and have presented these in the form of scatter diagrams for different areas. Draper and Herbert [1977] report the sea conditions in Scottish waters from visual observations. The information in the scatter diagrams is used for the present discussion. For example, if the 20-metre yacht is sailing around 5 miles East of Barra ($56^\circ 58' \text{ N}$ and $7^\circ 17' \text{ W}$), the observed sea condition with sea and swell data is presented in the form of a histogram where percentage of occurrence is plotted against the wave period, as shown in fig. 11.14. The highest percentage of occurrence is between 4 and 5 sec. At this wave condition, the flexible fin propeller generates high propulsive thrust coefficients and reduces the motion.

A passive flexible fin propeller with no direct input power can be fitted at the stern of the ship as shown in the fig. 11.15. A right-angle hinge could be used. The flexible fin propeller is flapped down and locked in place for a suitable sea condition. In a calm sea condition or wave frequency outside the resonance region, the resistance is increased by the propeller (Chapter 9) and it can be flapped up as shown in the dotted-lines in the figure and secured onto the rack. This arrangement is suitable for the head and following seas condition.

In beam and oblique seas, a twin passive oscillating fin propeller arrangements with propellers fitted on port and starboard side could be used. In this arrangement, rolling motion could also be used to oscillate the flexible fin propellers and generate propulsive thrust. The encounter frequency in oblique seas is

$$\omega_{ew} = \omega_w - U \frac{\omega_w^2}{g} \cos \beta_e \quad - 11.5$$

where β_e is the angle between the wave direction and the ship advance direction. Owing to the change in β_e , the favourable wave frequency in using wave propulsion will be changed and can be estimated by using eqn. 11.5.

9.0 ENGINEERING ECONOMY ON THE APPLICATION OF OSCILLATING FOIL PROPULSION

Oscillating foil propulsion is an alternative propulsion system to the conventional screw propeller. In order to make a choice between the conventional screw propeller and an oscillating foil propeller, an economic analysis is essential to the decision making process. The study is carried out on the four ship examples (SHIP-A, SHIP-B, SHIP-C and SHIP-D) as in section 2. The particulars of the existing screw propellers and engines in the examples are listed in the following table,

	SHIP-A	SHIP-B	SHIP-C	SHIP-D
Diameter of Propeller (m)	2.65	5.27	8.00	3.231
Rotation speed (rpm)	200	100	100	259
No. of Blades	4	4	4	4
Efficiency	0.66	0.69	0.65	0.70
Cost (£)*	12000	45000	240000	44000 (2 off)
Required BHP (kW)	753	3820	33300	12900
Fuel Consumption (g/kWh)	212	188	120	183

* Information from Stone Manganese Marine Limited [Patience 1989]

Table 11.8 The Particulars of Existing Screw Propellers and Engines

The efficiency of the existing screw propellers is estimated using the $B_p - \delta$ diagrams and the optimum efficiency is used. From the delivered power, the required engine brake horse power is estimated; engines with the specific fuel consumption shown are chosen from the Marine Engineers Review [1989]. The engines in the example are medium speed engines. With modern diesel engines, medium speed engines can be run on heavy fuel oil. More equipment, such as oil pre-heater and filters, is required in the oil treatment in using heavy fuel oil compared to marine diesel oil. However, marine diesel oil is 80% more expensive. Heavy fuel oil is commonly used in modern engines and its use has been assumed in this study. Therefore the analysis will be more conservative than that based on expensive marine diesel oil. The fuel oil price used in this study is the price at October 1989 [The Motor Ship 1989]. The mean oil price of heavy fuel oil is £62.0 per tonne.

The life time of the ships is assumed to be 15 years and the proportion of operating time is 50% each year. When the propulsive efficiency of an oscillating foil propeller is higher than that of the existing screw propeller, fuel cost per year is reduced and can be regarded as an incoming cash flow every year in the economic analysis. The fuel saving is

$$\text{Fuel Saving per year (£)} = (\text{Efficiency of oscillating foil propeller} - \text{Efficiency of existing screw propeller}) * \text{Engine brake horse power (kW)} * \text{Fuel consumption per hour kW} * \text{Fuel cost (£)} * 24 \text{ hour} * 183 \text{ days}$$

- 11.6

The method of net present value [Brealey & Myers 1984] is applied here for the investment decision. The cash flow every year within the life time of the ship is adjusted to present value. Since money earns interest and the future is less certain than the present, future cash flow is discounted to a lesser value in the present. The total present worth of fuel saving for a 15 year life time is

Present Worth = fuel saving per year at the present oil price * Series present worth factor (SPWF) for 15 years at an interest rate (int)

$$\text{where SPWF} = \frac{(1 - \text{int})^{15} - 1}{\text{int} (1 - \text{int})^{15}} \quad - 11.7$$

For a range of efficiency of oscillating foil propeller between 0.65 and 0.82, the net present value of fuel saving for 15 years with interest rates at 8%, 10% and 12% for the four example ships are shown in fig. 11.16. The fuel saving per year is calculated at the present fuel oil price and the future inflation is not included. Therefore the interest rate in the computation is a real discount rate [Brealey & Myers 1984, p. 90] where inflation is subtracted out from the nominal interest rate.

9.1 Two-Dimensional Oscillating Foil Propeller

Breakeven analysis is used in this economic study. In the breakeven condition, the cost of this type of propeller is found as follows,

$$\begin{aligned} \text{Cost of 2-D oscillating foil propeller} = & (\text{Fuel saving} - \text{Extra Maintenance cost}) + \\ & \text{Cost of existing screw propeller} \\ & - 11.8 \end{aligned}$$

The costs of the oscillating foil propeller, which includes the extra cost in the driving mechanism, for the four ships are presented as a percentage of their existing screw propeller cost in fig. 11.17 and results are presented with no extra maintenance costs for initial comparison.

As the driving system of a two-dimensional oscillating foil propeller is more complicated than that of a screw propeller, the maintenance cost is expected to be higher than that of a conventional screw propeller. Here, extra maintenance costs of 2.5% and 5% of the cost of existing screw propeller per annum are considered. The drops in the

breakeven cost at different extra maintenance costs and interest rates are presented as a percentage of the existing cost of the screw propeller and listed in table 11.9. The percentages are the same for different ships.

	<u>Interest Rate</u>		
	<u>8%</u>	<u>10%</u>	<u>12%</u>
Extra Maintenance Cost at 2.5%	21	19	17
Extra Maintenance Cost at 5.0%	43	38	34

Table 11.9 The Reduction in Breakeven Cost at Different Interest Rate and Different Extra Maintenance Costs

If extra maintenance cost is considered, the corresponding breakeven cost is found by subtracting the percentage presented in table 11.9 from that presented in fig. 11.17.

The driving mechanism of this type of propeller is more complicated than that of the screw propeller. Either a sliding mechanism or a new internal combustion engine with linear explosion is required. The total initial cost of a two-dimensional oscillating foil propeller and its driving mechanism is expected to be higher than that of a screw propeller. The cost of the oscillating propeller (the left-hand-side of eqn. 11.7) represents the sum of the extra cost in driving mechanism and the cost of the propeller.

Owing to the complexity of the driving mechanism, a frictional loss should be considered and results in a lower overall efficiency than the hydromechanical efficiency. In section 3.1, the two-dimensional oscillating foil propeller is applied on all four examples with a high hydromechanical efficiency of 0.8 predicted by the theory. An overall efficiency of 0.75, with 5% loss as allowance for the complexity of driving mechanism, is assumed. As an example in using the results presented in fig. 11.17 and table 11.9, when the interest rate is 8%, the breakeven cost at an overall efficiency of 0.75 with no extra maintenance cost for SHIP-A is 3.8 times that of the existing cost of the screw propeller (fig. 11.17). If the sum of the extra cost of the driving mechanism

and cost of the oscillating fin propeller is over 3.8 times the cost of existing screw propeller, there is no benefit in using this type of propeller on SHIP-A. If the extra cost of maintenance of 5.0% is considered, the maximum cost should not be higher than 3.4 times that of the cost of the existing propeller. A lower limit is obtained for higher interest rates. As with SHIP-A, the limits on the maximum cost for the other three examples are found. For reference purposes, those with no extra maintenance cost at different interest rates in the same condition are presented as a percentage of the cost of an existing screw propeller and listed in the table 11.10.

	<u>Interest Rate</u>		
	<u>8%</u>	<u>10%</u>	<u>12%</u>
SHIP-A	378	348	322
SHIP-B	304	281	263
SHIP-C	553	502	460
SHIP-D	381	350	324

Table 11.10 The Breakeven Prices of Oscillating Foil Propeller with an Overall Efficiency of 0.75 at Different Interest Rates

If an extra cost in maintenance is considered, the value listed in table 11.10 is reduced by that listed in table 11.9. If an extra maintenance cost at 5% is considered, the breakeven prices presented in fig. 11.10 are changed as follows.

	<u>Interest Rate</u>		
	<u>8%</u>	<u>10%</u>	<u>12%</u>
SHIP-A	335	310	288
SHIP-B	261	243	229
SHIP-C	510	464	426
SHIP-D	338	312	290

Table 11.11 The Breakeven Prices of Oscillating Foil Propeller with an Overall Efficiency of 0.75 at Different Interest Rates
(An Extra Maintenance Cost at 5% is included)

The breakeven cost depends on the fuel saving which is higher for vessels with a higher fuel consumption. Therefore the breakeven cost for SHIP-C and SHIP-D is

higher than for the other ships. With reference to table 11.9 and 11.10, if the extra cost of the driving mechanism and the propeller is less than or about twice that of the cost of the existing screw propeller, there is a benefit in applying the two-dimensional oscillating foil propeller on these examples even with highest interest rate and highest extra maintenance cost in the range of this study. This is true if a high overall efficiency of 0.75 or above is achievable. Low frictional losses are essential for application of this system.

The present oil price is used in this analysis. However fluctuations in the price of oil are significant. In the fig. 11.18, the breakeven cost with an overall efficiency of 0.75 and no extra maintenance cost are presented as a percentage of the cost of existing screw propeller for variations of the oil price. The changes in oil price are presented as a percentage of present oil price over the range between a 50% increase and a 60% decrease. If the extra cost of the driving mechanism plus the cost of the oscillating foil propeller is about twice that of the existing screw propeller, it is of no benefit to use this type of propeller if the oil price drops 60% for SHIP-A, SHIP-B and SHIP-D. Taking into account of an extra maintenance cost at 5%, the breakeven cost would be around 1.5 times that of the existing screw propeller. Owing to the high fuel consumption of SHIP-C, the breakeven cost is higher than double that of the existing screw propeller cost even if the oil price drops 60%.

On all the scenarios considered the two-dimensional oscillating foil propeller is economically attractive on all the ships at the present oil price provided that the propulsion system is of the order of twice that for the existing screw propeller.

9.2 Flexible Fin Propeller

In section 3.2 of this chapter, the fatigue life of the flexible fin propeller with aspect ratio 4 is about 2.5 years continuous running in the application on SHIP-A. Since the operating time is assumed to be six months per year, the actual life time in application is 5 years. In a 15 year life time, three propellers are required at the

beginning of the first, sixth and eleventh years.

Let the present cost of a flexible fin propeller be C_{FFP} . The present value of the three propellers will be

$$\text{Present value of three propellers} = C_{FFP} \left(1 + \frac{1}{(1 + \text{int})^5} + \frac{1}{(1 + \text{int})^{10}} \right).$$

- 11.9

As the driving system of the flexible fin propeller is not complicated, the costs of the driving mechanisms of a screw propeller and this type of propeller are assumed to be the same. Similarly, the cost of maintenance for the propulsion system using a flexible fin propeller is expected to be similar to that using the screw propeller. In the breakeven condition, the extra cost of using flexible fin propellers, which is the present value of three flexible fin propellers minus the cost of an existing screw propeller, is equal to the total fuel saving in the present value (fig. 11.16). The cost of each flexible fin propeller in the breakeven condition is calculated and presented as a percentage of the existing screw propeller for different efficiencies of oscillating foil propeller in fig. 11.19. At a specified propulsive efficiency, if the cost of the flexible fin propeller is higher than that at breakeven condition, it is better to use the conventional screw propeller.

Because of novelty of the system, it is difficult to give an accurate estimation on the cost of a flexible fin propeller at this stage of development. If fibre reinforced composite materials are applied in both foil and flexible connecting bar, the manufacturing process is simpler than that of a screw propeller. The cost of casting a screw propeller and machining the surface of blades is expected to be more expensive than that of the construction of a flexible fin propeller. Although high strength carbon fibre reinforced plastic is expensive, the alloy used in a screw propeller, which is made of Nikalium in this example, is also costly. In general, the cost of a flexible fin propeller is expected to be lower than the screw propeller for the same application.

In this example, the flexible fin propeller with aspect ratio 4.0 gives an efficiency of 0.7. Since the driving mechanism is simpler than the others, the overall efficiency is expected to be the same as the hydromechanical efficiency. If a flexible fin propeller gives a propulsive efficiency of 0.7, the corresponding breakeven price of a flexible fin propeller is about the same as that of screw propeller for the range of interest rates in this study at the present oil price (fig. 11.19). Since the cost of flexible fin propeller is expected to be cheaper than the screw propeller, a net saving is expected.

The net saving by using a flexible fin propeller is the difference in present value between the fuel saving and extra cost of using flexible fin propeller. For example if the cost of the flexible fin propeller is 75% of that of screw propeller, the net savings in present value by using a flexible fin propeller with efficiency of 0.7 at different interest rates and fluctuation of oil price are shown in fig. 11.20. In the present oil price, the net saving is around £7000 at an interest rate of 10%. This net saving is doubled when the oil price increases 50%. If the oil price drops below 50% of the present price, the net saving is close to zero and there is no benefit in changing to a flexible fin propeller.

A flexible fin propeller with aspect ratio of 10 has an efficiency of 0.8 and a fatigue life of over 7 years continuous running and so only one propeller is required in the 15 year life time. If this propeller, as described in section 3.2, is considered satisfactory, the breakeven costs are 5.3, 4.8 and 4.4 times the cost of existing screw propeller at interest rates of 8%, 10% and 12% respectively. If the cost of flexible fin propeller is assumed to be 75% of the existing screw propeller, the net savings with different interest rates are plotted against the fluctuation of oil price in fig. 11.21. The net saving with an interest rate of 10% is £50,000 at the present oil price. If the oil price drops 60%, the net saving decreases to £20,000 at the same interest rate. This is a very profitable scenario.

9.3 Rotary Foil Propeller

The economic analyse of the application of rotary foil propellers to the four ship examples are similar to that of two-dimensional oscillating foil propeller. Equation 11.7 is applicable to the study of the rotary foil propeller. Figure 11.17 still represents the breakeven cost of the rotary foil propeller for different efficiency and different interest rates with no extra maintenance cost. Table 11.9 is also used here for the consideration of extra maintenance costs. The complexity of the driving mechanism of the rotary foil propeller is similar to that of the two-dimensional oscillating foil propeller. As with the two-dimensional oscillating foil propeller, the sum of the extra cost of the driving mechanism and cost of the rotary foil propeller is expected to be higher than the cost of an existing screw propeller.

In section 3.3, a rotary foil propeller with a high hydromechanical efficiency of 0.7 is applied in the study. If a 5% loss in efficiency is assumed in the driving mechanism, as with the two-dimensional oscillating foil propeller, the overall efficiency is 0.65. The breakeven cost is either the same as or lower than that of the existing cost of a screw propeller (fig. 11.17). However it is expected that the cost of applying a rotary foil propeller is higher than that of a screw propeller. Therefore the cost is higher than that of the breakeven cost and there is no benefit in using a rotary foil propeller.

In chapter 10, the peak efficiency is around 0.8 as shown in fig. 10.16. The operating condition with efficiency 0.7 is chosen for the peak propulsive thrust coefficient to minimise the swept area. The number of blades should be increased in order to provide higher propulsive thrust and to use the operating condition with peak efficiency instead of peak thrust coefficient. Bose [1987] used a parameter, solidity, to represent the number of blades where

$$\text{solidity} = \frac{\text{no. of blades} \times \text{chord}}{\text{radius of rotation}} \quad - 11.10$$

The solidity of the operating condition in section 3.3 is 1.2 where mean chord length is

used. Bose [1987] shows that a drop of 3% in efficiency is obtained by increasing the solidity from 0.3 to 1.8 and the propulsive thrust varies more or less linearly with solidity at any given value of advance ratio. If a five bladed propeller is used, the solidity is 2.0. According to the theory, the peak efficiency drops less than 2% and the propulsive thrust coefficient increases 67% by increasing the solidity from 1.2 to 2.0. The experimental results of a three bladed propeller could be extended to predict the performance of a five bladed propeller by assuming that the theoretical predicted results are applicable. The peak efficiency was obtained at an advance ratio of 6.0 instead of 5.0 in the operating condition described in section 3.3. The experimental propulsive thrust coefficient for a three bladed propeller at advance ratio 6.0 is 0.24 (fig. 10.16) and the calculated thrust coefficient for a five bladed propeller is 0.4. The corresponding peak hydromechanical efficiency is 0.78. By using eqn. 10.8, the swept area of the propeller is estimated. The terms (J^2/T_c) in eqn.10.8 for the three bladed and five bladed propeller are 100 and 90 respectively. Since the other terms are the same in eqn. 10.8, the swept area of five bladed propeller is 10% less than that of three bladed one and hence the span of foil is less.

As with the previous economic analysis, a 5% loss is assumed for the allowance of frictional loss in the complicated driving mechanism and the overall efficiency of the five bladed propeller is 0.73. The breakeven costs of using a rotary foil propeller at an efficiency of 0.73 for the four example ships are found from fig. 11.17 and listed as follows,

	<u>Interest Rate</u>		
	<u>8%</u>	<u>10%</u>	<u>12%</u>
SHIP-A	317	293	273
SHIP-B	230	215	204
SHIP-C	465	425	391
SHIP-D	256	239	224

Table 11.12 The Breakeven Prices of Five Bladed Rotary Foil Propeller with an Overall Efficiency of 0.73 at Different Interest Rates

As with the two-dimensional oscillating foil propeller, if an extra maintenance cost is considered, the percentage presented in table 11.9 should be reduced from the breakeven cost. A pair of rotary foil propellers will be used in full scale applications and no steering rudder is required. The sum of the extra cost in the driving mechanism and the cost of propeller is expect to be higher than the conventional screw propeller. In addition, the maintenance cost is also expected to be increased.

For example, if the propeller is assumed to be 2.5 times the cost of the existing screw propeller and the extra maintenance cost per annum is assumed to be 5% of the cost of screw propeller, the breakeven costs of SHIP-B and SHIP-D are lower than 2.5 times the cost of screw propeller. The breakeven cost of SHIP-A is broadly the same as the assumed values. Therefore there is insufficient benefit in using a rotary foil propeller in these examples. For SHIP-C, a large fuel consumption is involved. The application of rotary foil propeller on SHIP-C is found to be economically viable. The oil price can drop up to 50% before the decision to use rotary foil propeller on SHIP-C becomes unfavourable.

10.0 CONCLUSIONS

The practical application of two-dimensional oscillating foil propellers, flexible fin propellers and rotary foil propellers on four full scale example ships with ship lengths of 66m, 120m, and 200m and a 50m high speed craft have been studied. The arrangement of the propeller, required hull forms, driving mechanism and economic performance have been investigated. The following conclusions are drawn from these studies.

1) Two-dimensional Oscillating Foil Propeller

The heaving amplitude of the foil in these examples is 1.2 times the half chord length with a span of 80% of the beam of the ships and a chord of 2% of the ship

length. The oscillating frequency is higher than that for the other two types of oscillating foil propellers.

The following conclusions may be drawn.

- a) The unwanted oscillating force which is parallel to the heaving motion, can be cancelled by introducing foils moving 180° out of phase. Also it is believed that a mirror effect may be produced by the flat bottom of the stern and the motion induced by this unwanted oscillating force is minimized.
- b) The foil of the propeller can be arranged horizontally or vertically.
- c) Steering moments may be generated by turning the whole system in the propeller with horizontal foil arrangement.
- d) In the vertical arrangement, one of the foils generates drag while the other generates propulsive thrust.
- e) A crank mechanism or vertical oscillating mechanism with two identical springs can generate the required motion of this type of propeller.
- f) Either a linear explosion internal combustion engine or a conventional engine with sliding mechanism can be used to generate the vertical oscillation.

Since the driving mechanism is more complicated than that of a conventional screw propeller, the sum of the cost of the driving mechanism and the cost of the propeller is expected to be higher than that of an existing screw propeller. The maintenance cost is also expected to be higher than that of a screw propeller. The breakeven cost of a two-dimensional oscillating foil propeller with an overall efficiency of 0.75 at an interest rate of 8% is 3.4 times the cost of an existing screw propeller for a 66 metre ship if an extra maintenance cost per annum of 5% of the cost of the screw propeller is allowed for. If the sum of the extra cost of the driving mechanism and the cost of propeller is assumed to be twice that of the cost of screw propeller, there is benefit in applying this type of propeller at present oil prices. If the oil price drops by 60%, the application is only beneficial on a ship with a large fuel consumption, e.g. a 200 metre ship, SHIP-C, at this assumed value.

2) Flexible Fin Propeller

Flexible fin propellers with aspect ratio four have been designed for the four example ships. The spans of the foil in these examples are all smaller than the beam of the ship. The swept height of the foil is within the operating draft in all ship examples except the 50m high speed craft. The fatigue life of the flexible fin propeller for the 66m ship, is about two and a half years, if it is made of high strength carbon fibre reinforced material. As the required thrust for other examples is higher, the stress acting on the propeller is also higher. A short fatigue life was found for these examples and this propulsion system is not practical. A detailed design of hybrid composite reinforced plastic is required to give a higher strength to flexure modulus ratio and to lower the working stress at the same flexibility.

In addition, a flexible fin propeller with aspect ratio 10 which provides a higher efficiency, has also been considered. The required span of the foil is about the same as the beam of the ship. Therefore the upper limit of the aspect ratio in practical application occurs at 10. The working stress is lowered by allowing a wider flexible bar with lower thickness ratio and a longer fatigue life which is increased three times in the case of the 66 m ship. However, the fatigue life on the other sample ships is still not long enough to be practical.

The natural frequency of the propeller is found to be much higher than the operating frequency. This natural frequency is not sensitive to the increment of the mass of the foil.

The required driving oscillation can be provided by a simple crank system which gives an angular oscillation which is close to pure sinusoidal oscillation. The unwanted oscillating force can be cancelled by the mirror image generated from the flat bottom at stern.

It is practical to apply the flexible fin propeller for wave propulsion as an auxiliary propulsion at head and following seas contain a preponderance of the required wave lengths for the resonance condition. The propeller can be hinged up out of the flow in unfavorable sea condition such as calm sea or when the wave frequency is outside the resonance zone. In beam and oblique seas, an arrangement with twin passive flexible fin propellers could be used.

In a 15 year life time, three flexible fin propellers with aspect ratio 4 are required for the 66m ship. The corresponding breakeven cost of a flexible fin propeller is about the same as that of the screw propeller for the range of interest rates in this study at the present oil price. Since the driving mechanism is not complicated, the maintenance cost and the cost of driving system is expected to be the same as that of existing screw propeller. Owing to the manufacturing process for a flexible fin propeller, the cost of this type of propeller is believed to be lower than that of a screw propeller. If the cost of a flexible fin propeller is 75% of that of the screw propeller, the application of a flexible fin propeller with an efficiency of 0.7 is beneficial on the 66 m ship in the present oil price. If the oil price drops 50%, there is no benefit in using the flexible fin propeller with an aspect ratio four.

In the case of a flexible fin propeller with aspect ratio 10, one propeller is required in a 15 year life time for the application of SHIP-A. The breakeven costs are about five times the cost of the existing screw propeller at an interest rate of 10%. If the cost of the flexible fin propeller is 75% of that of screw propeller, the net saving in the whole life time at the present oil price is £50,000. There is benefit even if the oil price drops 60% and the net saving is £20,000 at an interest rate of 10%. This is clearly an attractive economic and practical option.

This study shows that high aspect ratio is desirable from the view point of high efficiency, long fatigue life and economically viable. The aspect ratio of 10.0 is the upper limit in the practical application where the required span is about the beam of the ship. Foils with higher aspect ratio will project outside the ship beam and not be

practical.

3) Rotary Foil Propeller

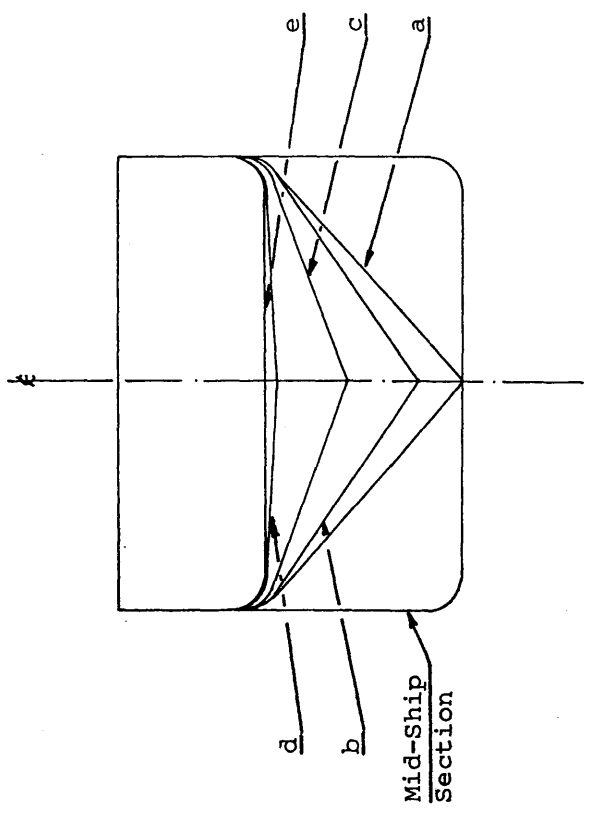
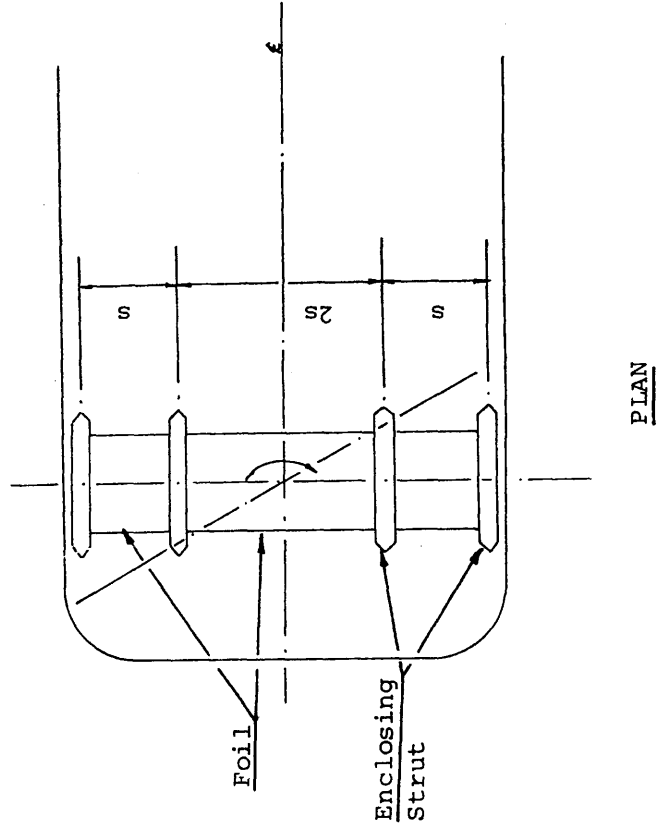
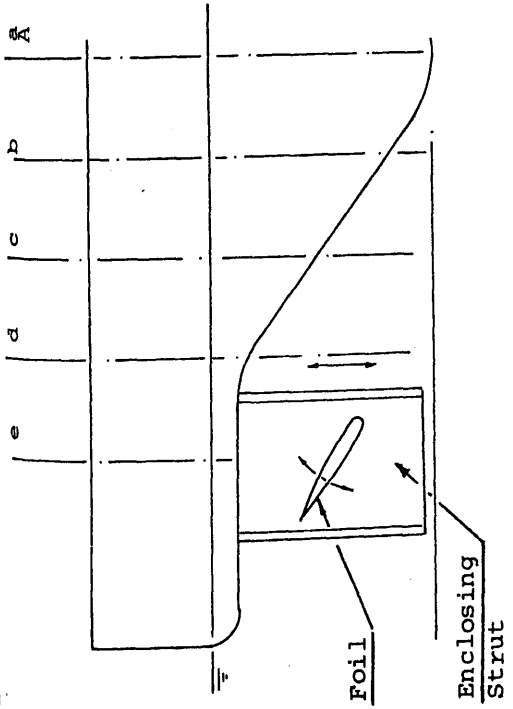
Three bladed rotary foil propellers with an effective aspect ratio of ten have been designed for the four example ships. The required span of the foil is close to the beam of the ship. For the high speed craft, the required span is 17% larger than the beam of the ship and not practical. Higher numbers of blades are required to increase the propulsive thrust and reduce the required span. Owing to the special configuration of the SWATH ship, the three bladed rotary foil propeller is found suitable to propel a high speed SWATH without this oversize problem.

The oscillating force generated by the propeller is evened out by foils moving with different phase shifts.

For full scale application, low frictional loss is important. If a 5% loss in the mechanical friction is assumed, the three bladed propeller with hydromechanical efficiency of 0.7 is not economically viable in all four example ships. A higher number of blades is required to make use of the peak efficiency instead of using the peak thrust coefficient. For a five bladed propeller with an overall efficiency of 0.73, the breakeven costs at an interest rate of 8% with no extra maintenance cost are about 3.2, 2.3, 4.7 and 2.6 times the cost of the existing screw propeller for SHIP-A, SHIP-B, SHIP-C and SHIP-D respectively. Owing to the complexity of the driving mechanism and two propellers are required in the application, the sum of extra cost in driving mechanism and the rotary foil propeller cost is expected to be higher than the existing cost of screw propellers. If the five bladed propeller is assumed to be 2.5 times the cost of the existing screw propeller and an extra maintenance cost per annum at 5% of the cost of screw propeller is considered, only application on the 200 m ship with high fuel consumption is beneficial at the present oil price. When the oil price drops 50%, there is no longer benefit in changing into rotary foil propulsion.

The key conclusions are summed up as following.

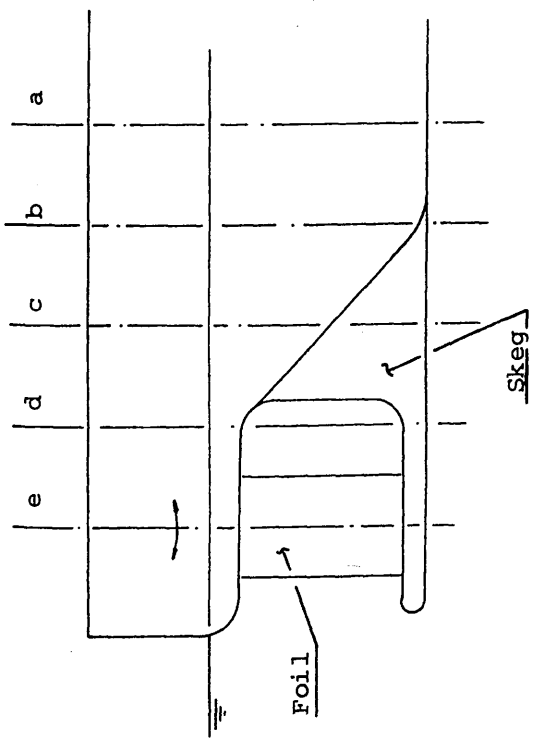
- 1) Application of a two-dimensional oscillating foil propeller is found suitable for whole range of ships, even for high speed craft, within this study.
- 2) Flexible fin propulsion is found suitable in application for ships up to about 2000 tonnes with a Froude number around 0.25.
- 3) Application of rotary foil propeller is found suitable for ships with a wide beam (eg. SWATH ship) to accommodate the span of the foils.



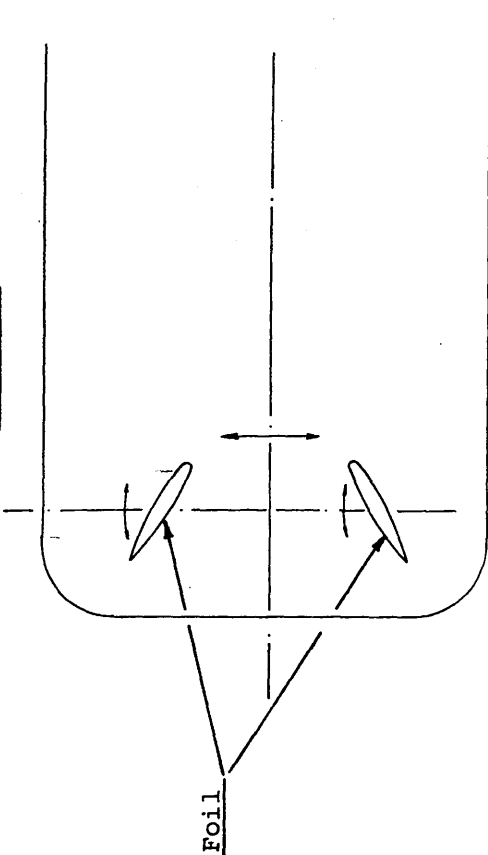
STERN BODY PLAN

The Arrangement of Two-Dimensional Oscillating Foil Propeller (Horizontal)

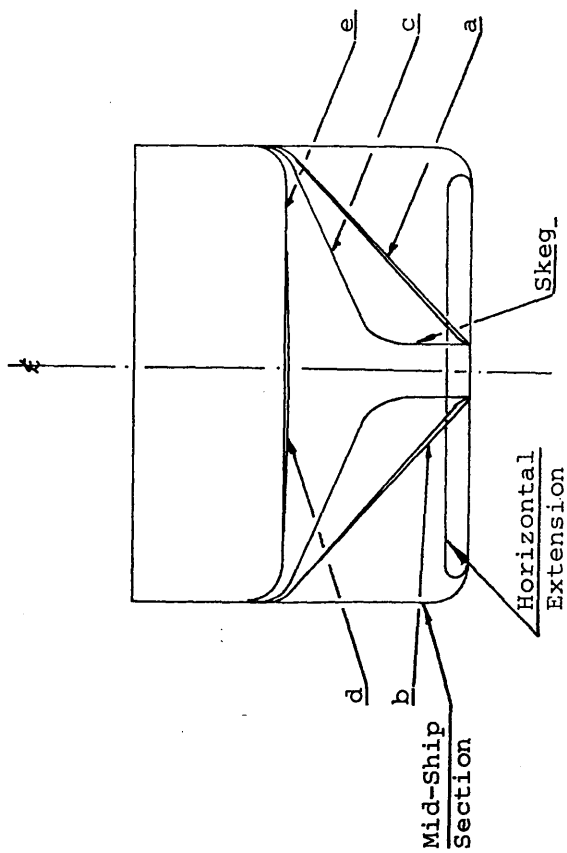
Fig. 11.1



ELEVATION



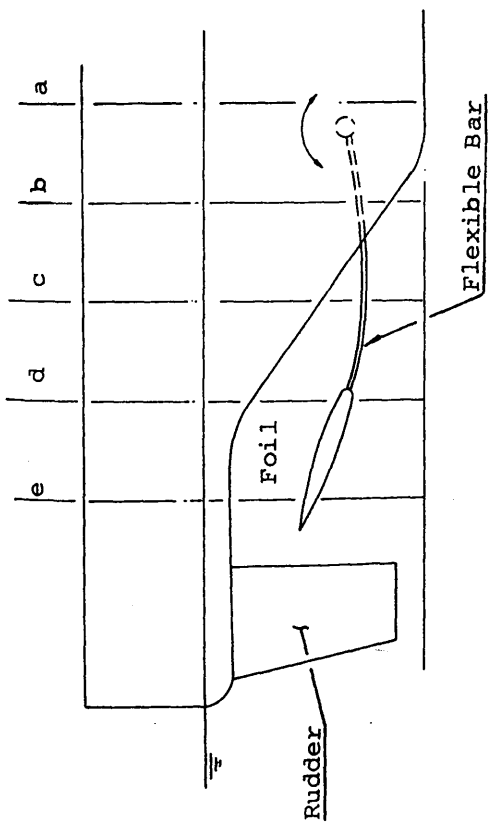
PLAN



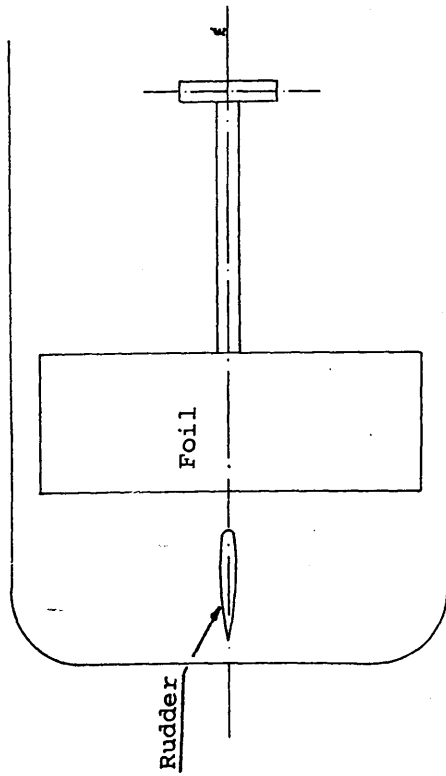
STERN BODY PLAN

The Arrangement of Two-Dimensional Oscillating Foil Propeller (Vertical)

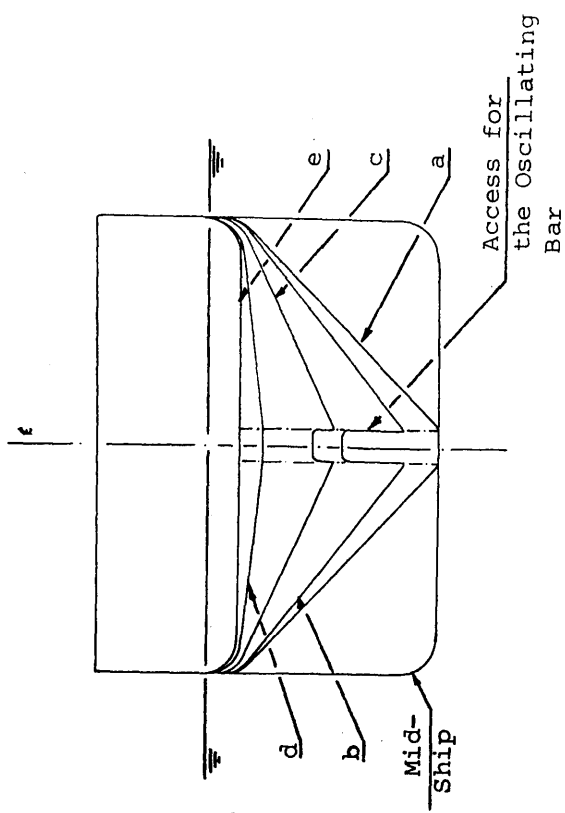
Fig. 11.2



ELEVATION



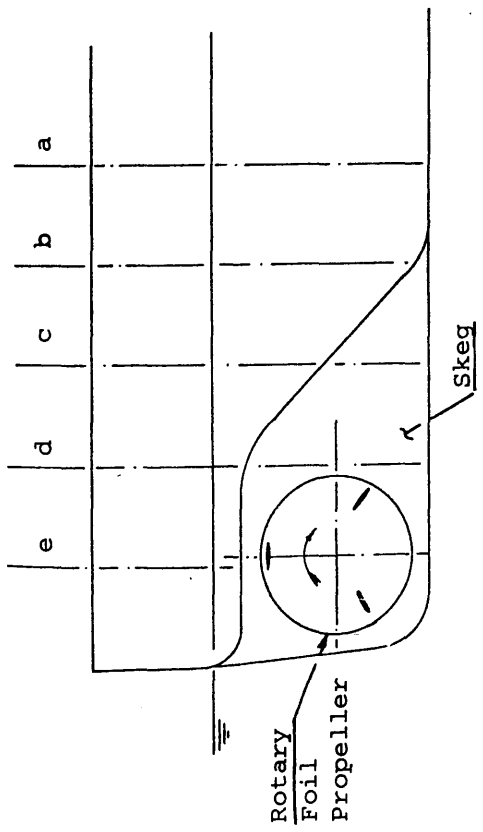
PLAN



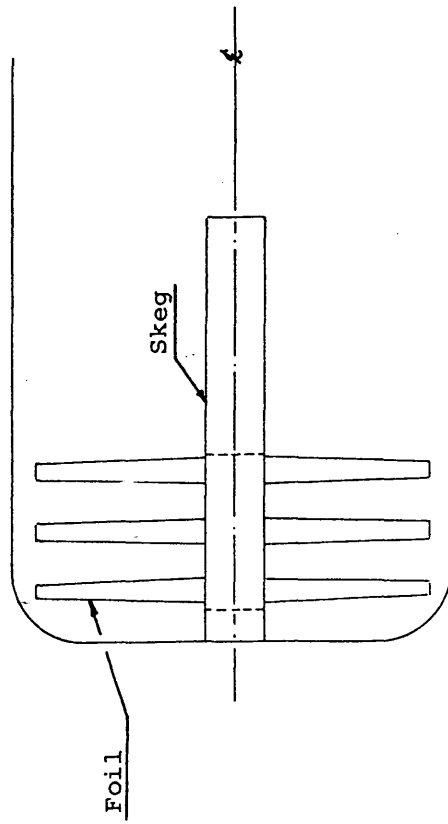
STERN BODY PLAN

The Arrangement of Flexible Fin Propeller

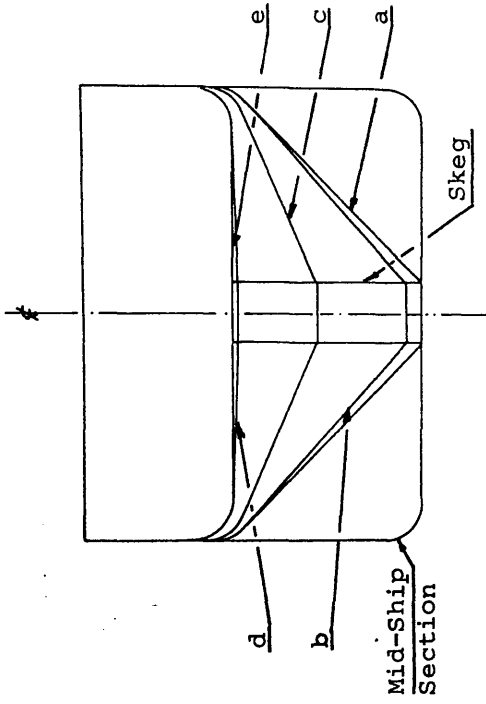
Fig. 11.3



ELEVATION



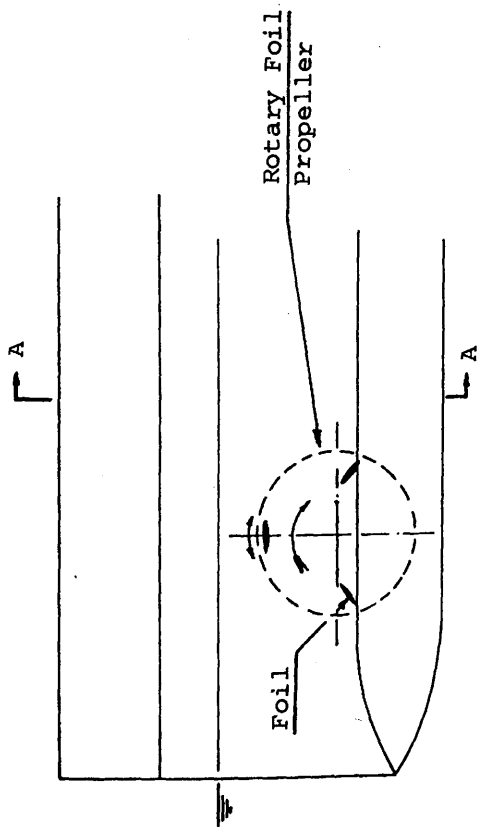
PLAN



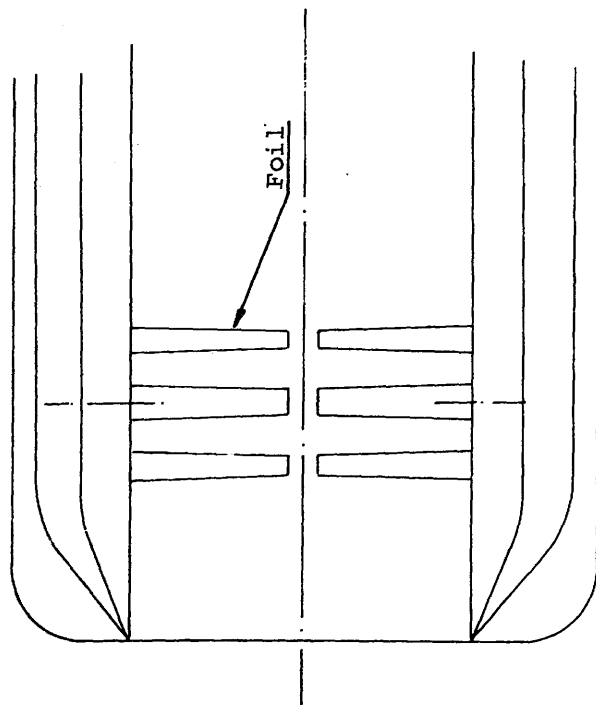
STERN BODY PLAN

The Arrangement of Rotary Foil Propeller

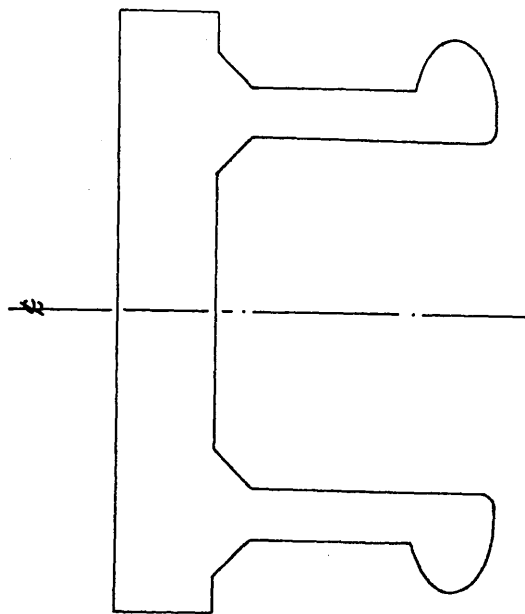
Fig. 11.4



ELEVATION



PLAN



SECTION A-A

The Arrangement of Rotary Foil Propeller
with SWATH

Fig. 11.5

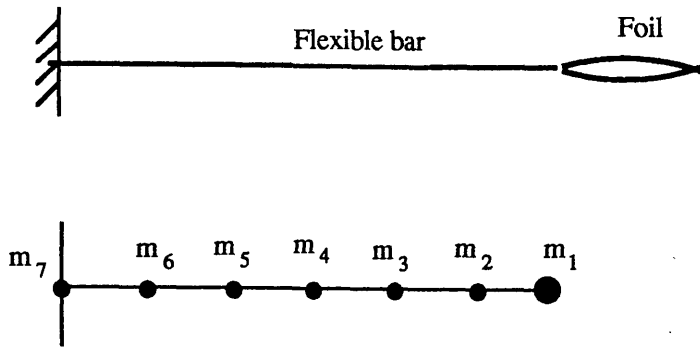


Fig. 11.6 Modeling of the Flexible Fin Propeller in Myklestad's Method

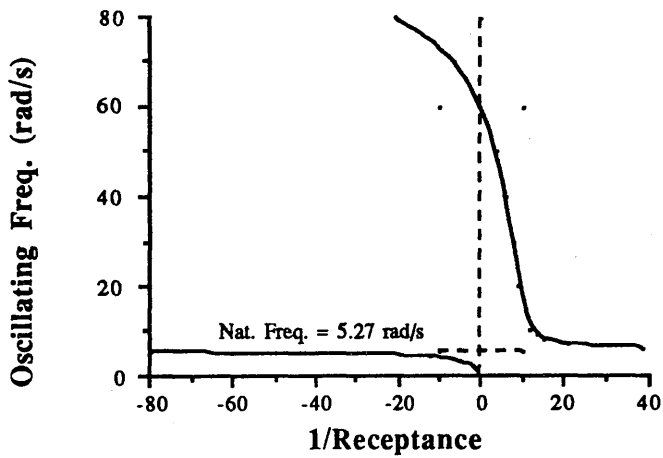
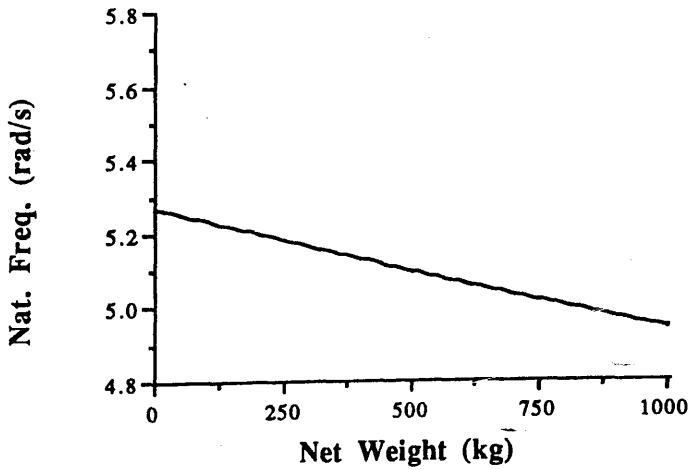


Fig. 11.7 Frequency Vs Reciprocal of Receptance Curve



11.8 The Change of Natural Frequency with Changes in the Net Weight of the Foil

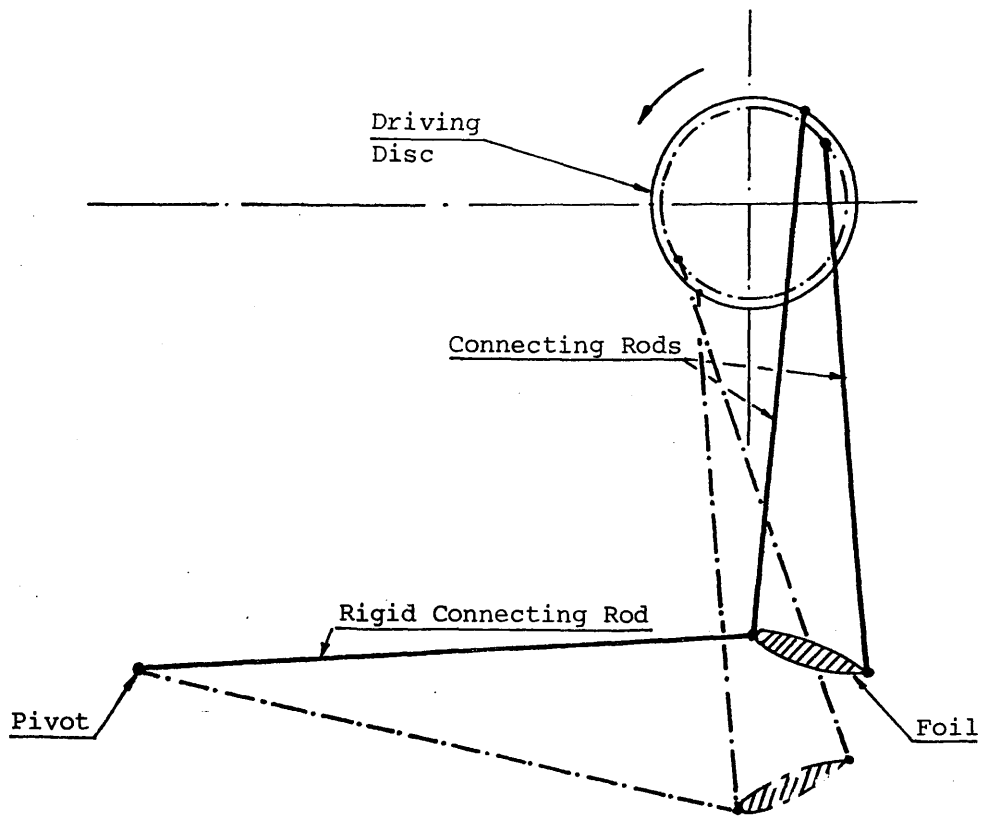


Fig. 11.9 Crank Mechanism of the Oscillating Foil (Isshiki, 1987)

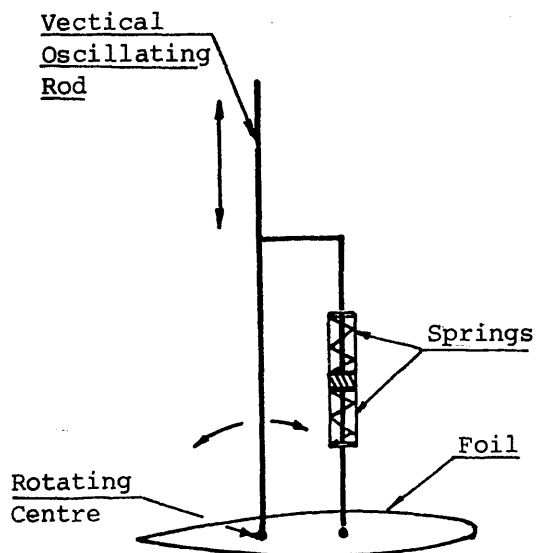
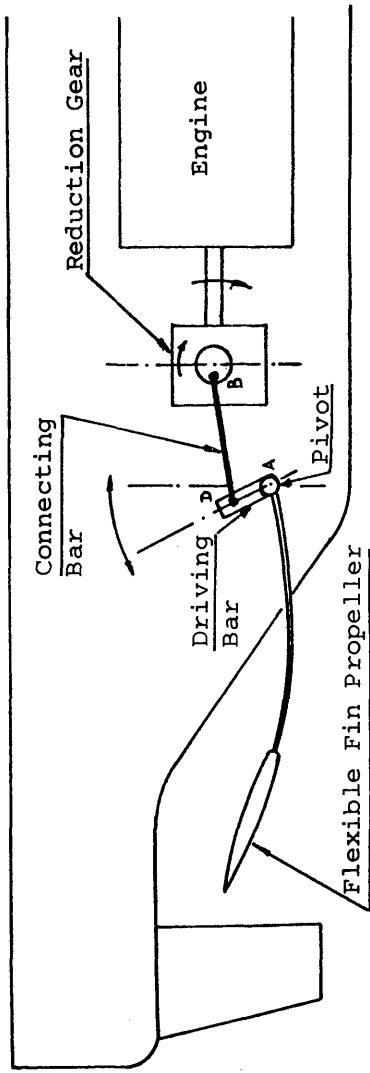
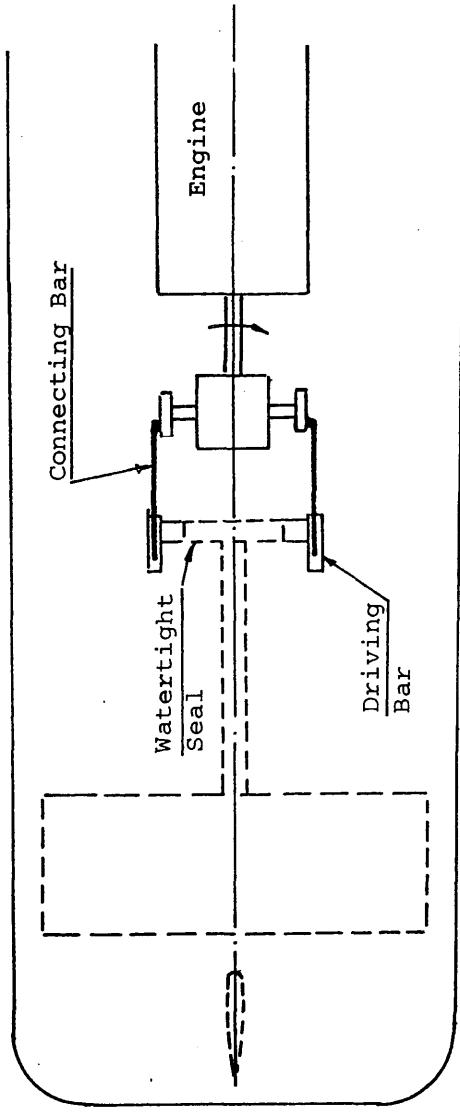


Fig. 11.10 Driving Mechanism of the Oscillating Foil Developed by Marine Technology Centre, Norway (Lai, 1988)



ELEVATION



PLAN

Fig. 11.11 The Driving Mechanism of Flexible Fin Propeller

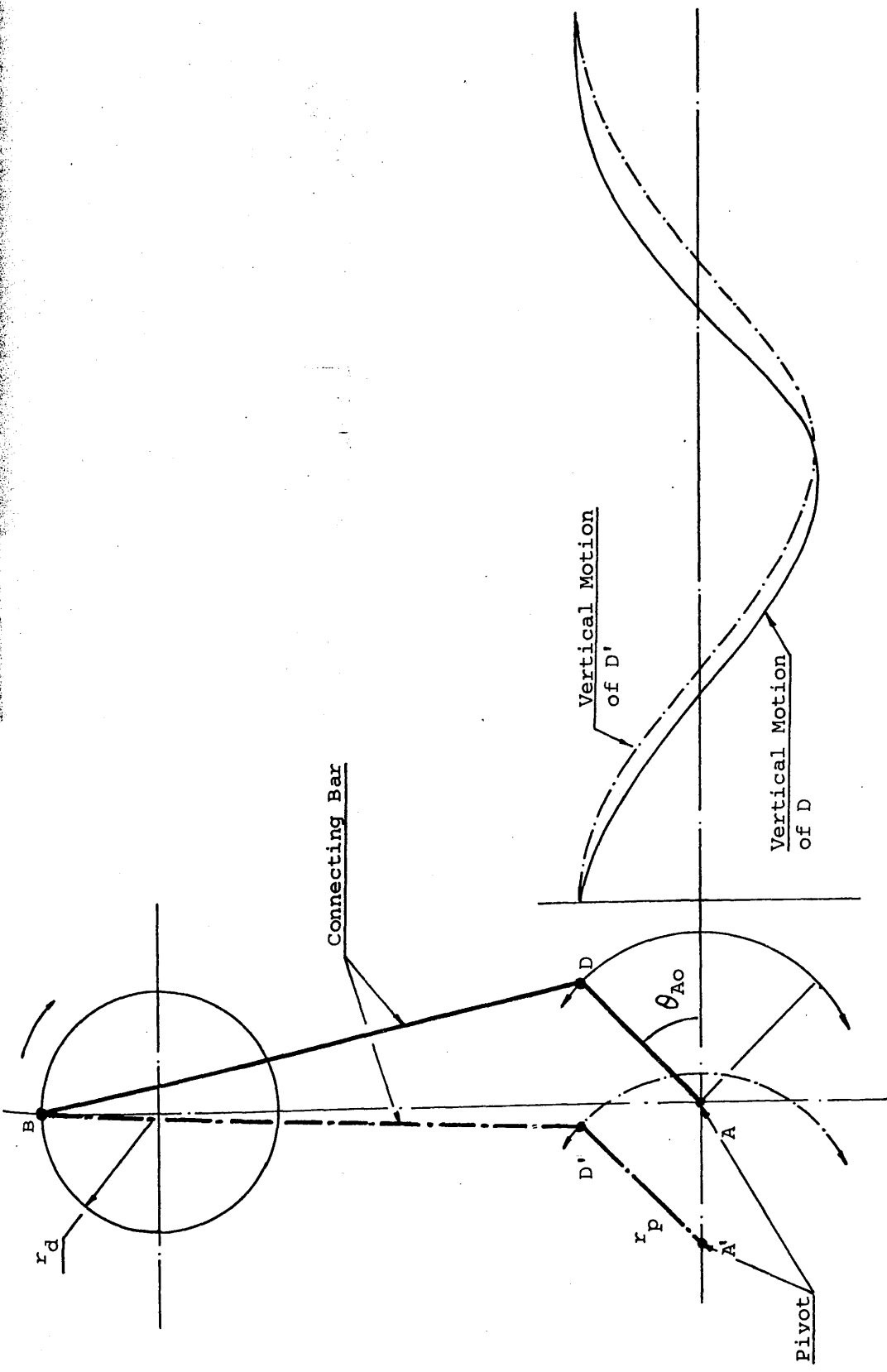


Fig. 11.12 The Oscillating Motion of the Driving Bar (DA) of Flexible Fin Propeller

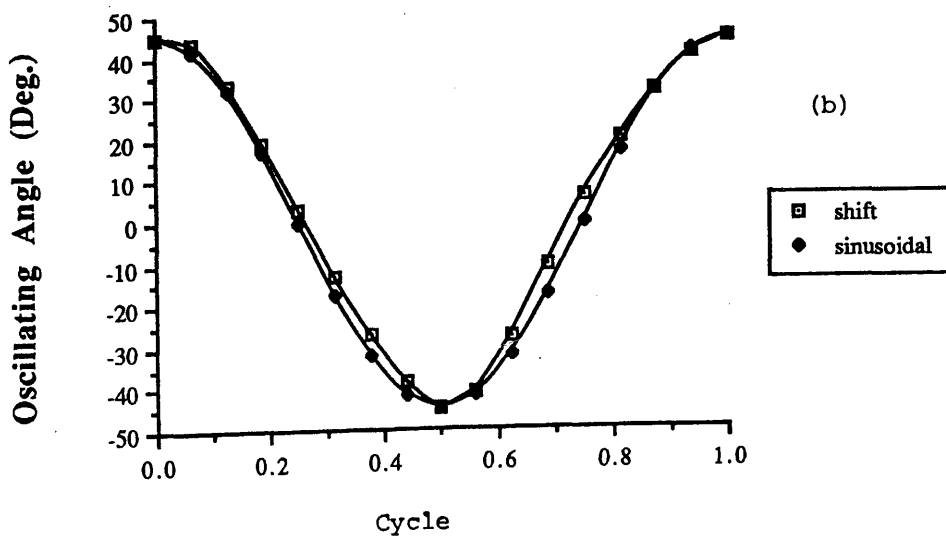
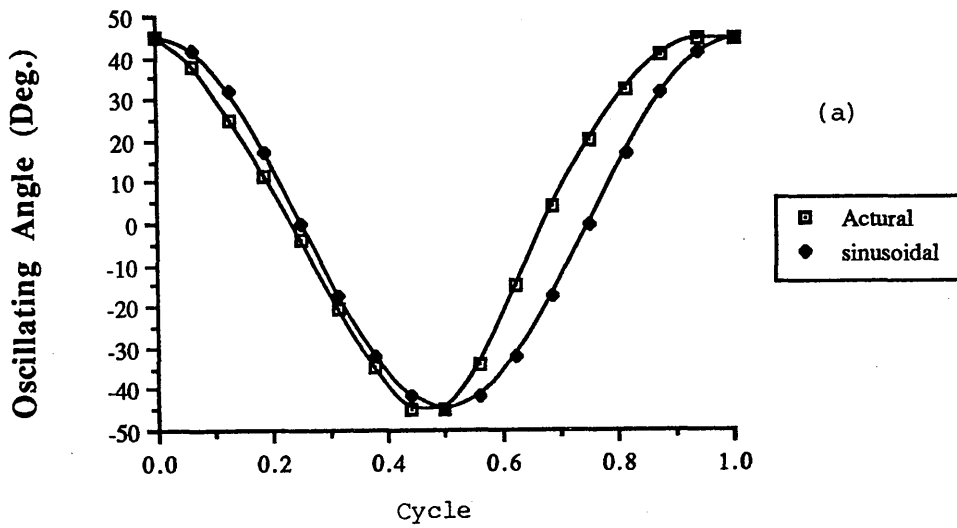


Fig. 11.13 Angular Oscillating Motion at the Pivot Generated by the Proposed Driving Mechanism

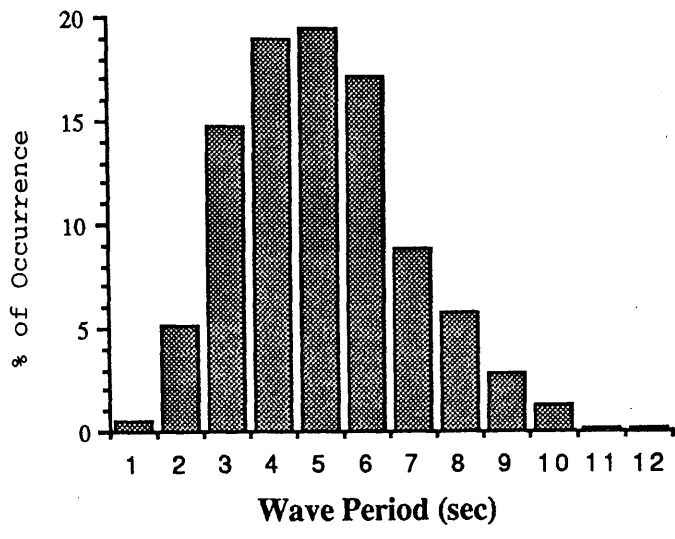


Fig. 11.14 Percentage of Occurrence of Wave Period (Sea + Swell) at 5 miles East of Barra

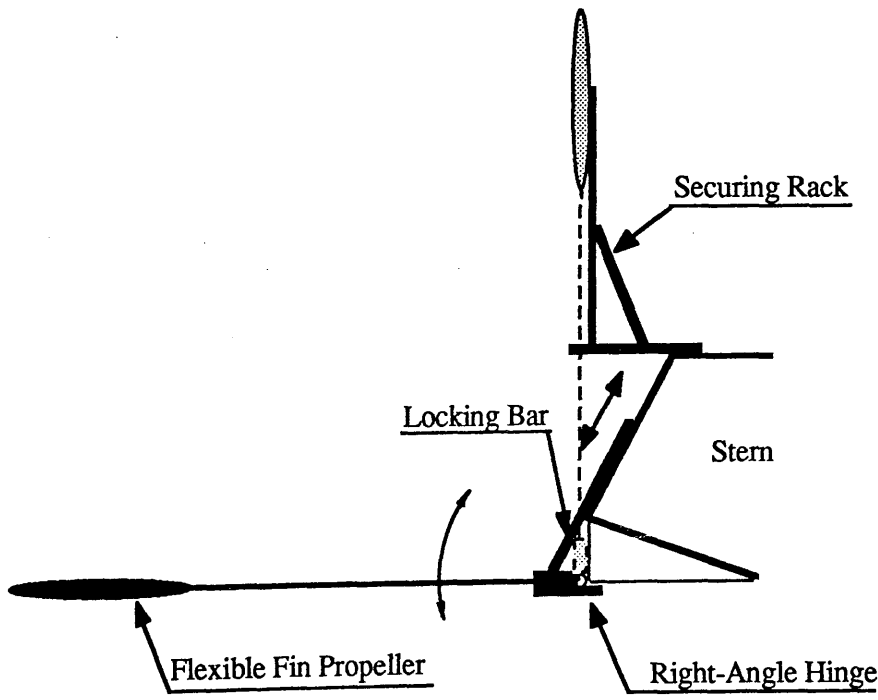


Fig. 11.15 The Arrangement of a Passive Flexible Fin Propeller at Stern

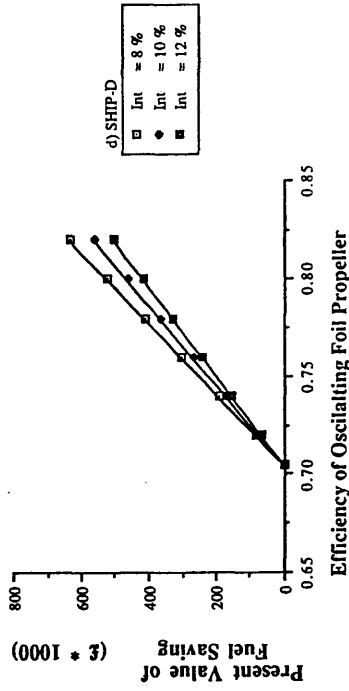
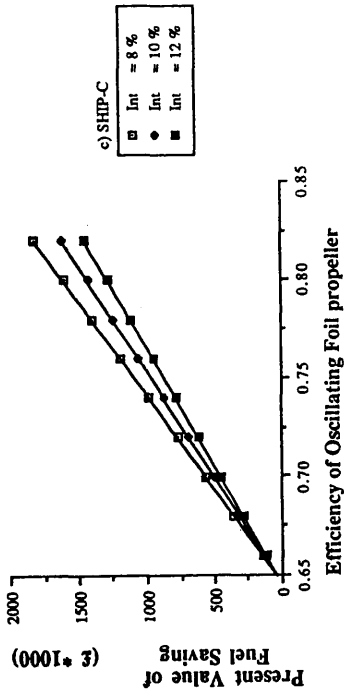
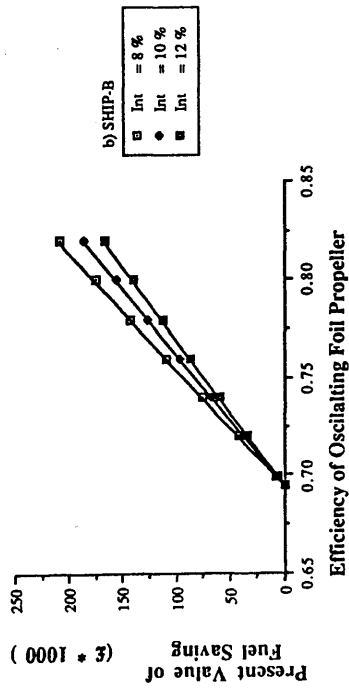
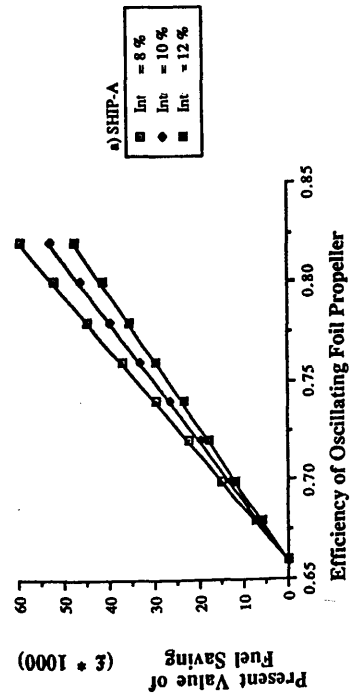


Fig. 11.16 The Present Value of Fuel Saving in a 15 Year Life Time

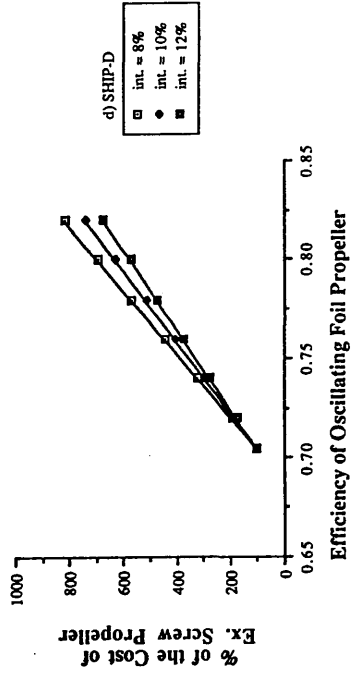
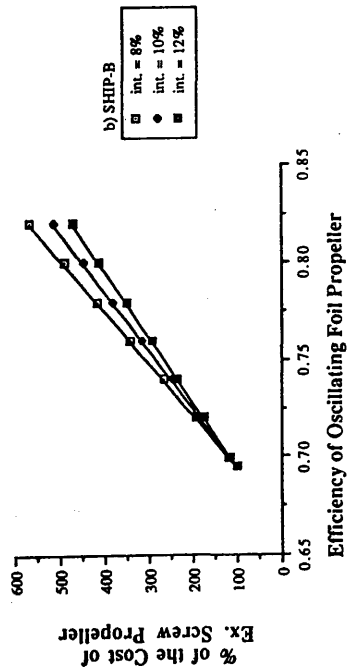
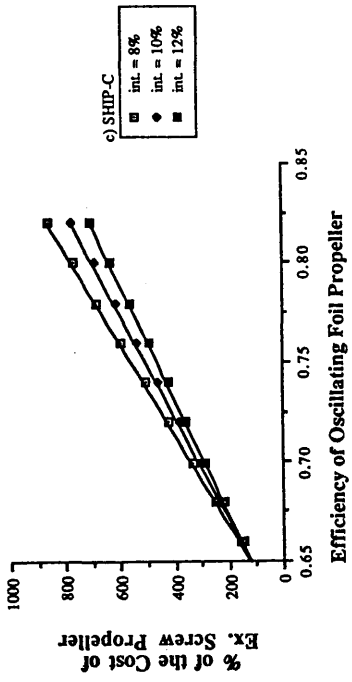
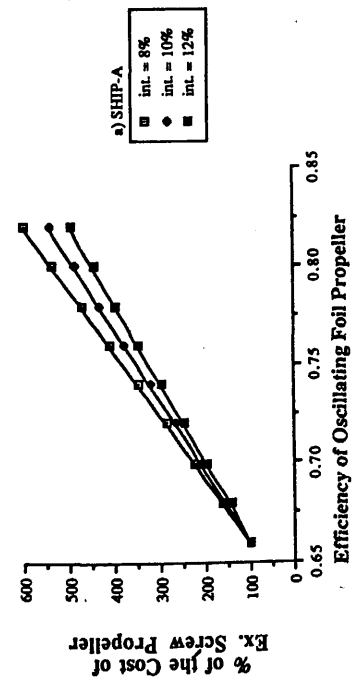


Fig. 11.17 The Breakeven Cost of the Oscillating Foil Propeller Presented in Percentage of the Cost of Existing Screw Propeller

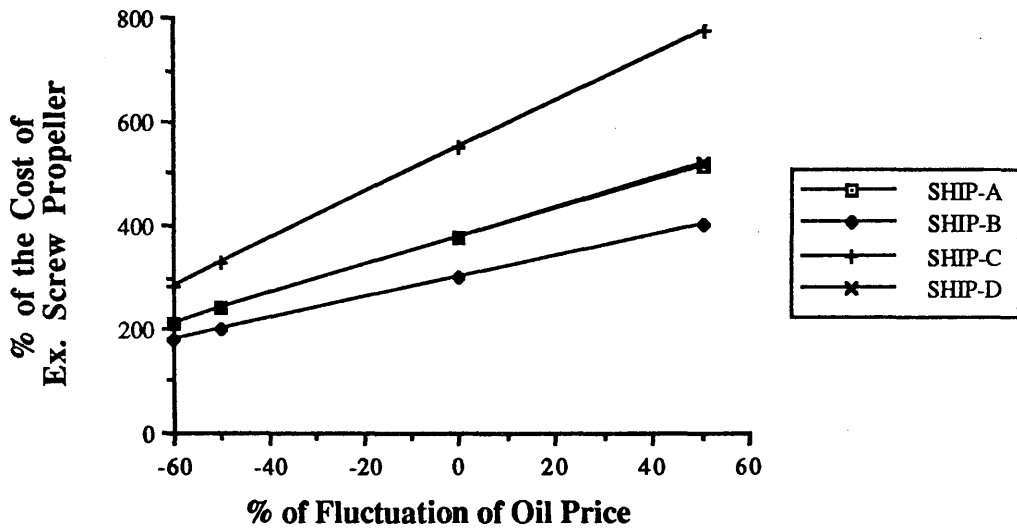


Fig. 11.18 The Breakeven Cost of the Oscillating Foil Propeller with the Fluctuation of Oil Price

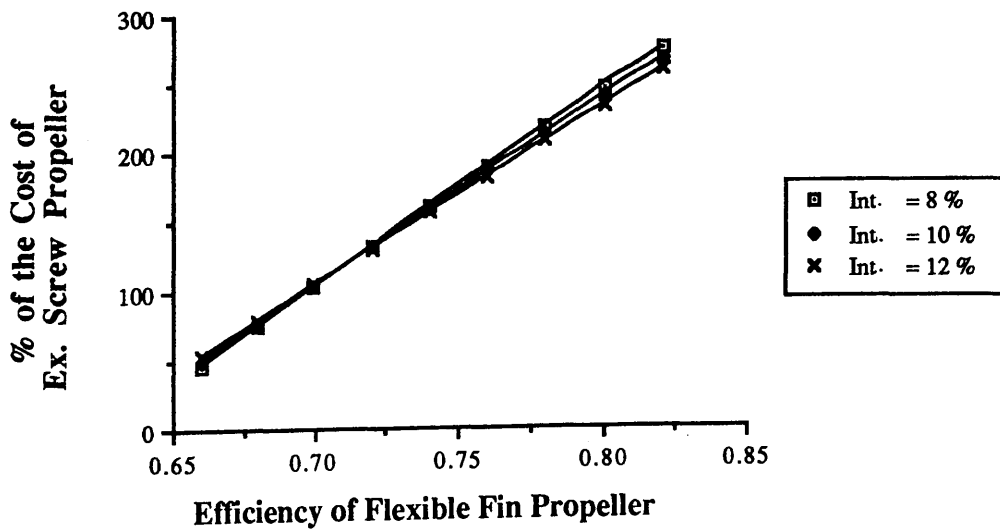


Fig. 11.19 The Breakeven Cost of the Flexible Fin Propeller at Different Interest Rates

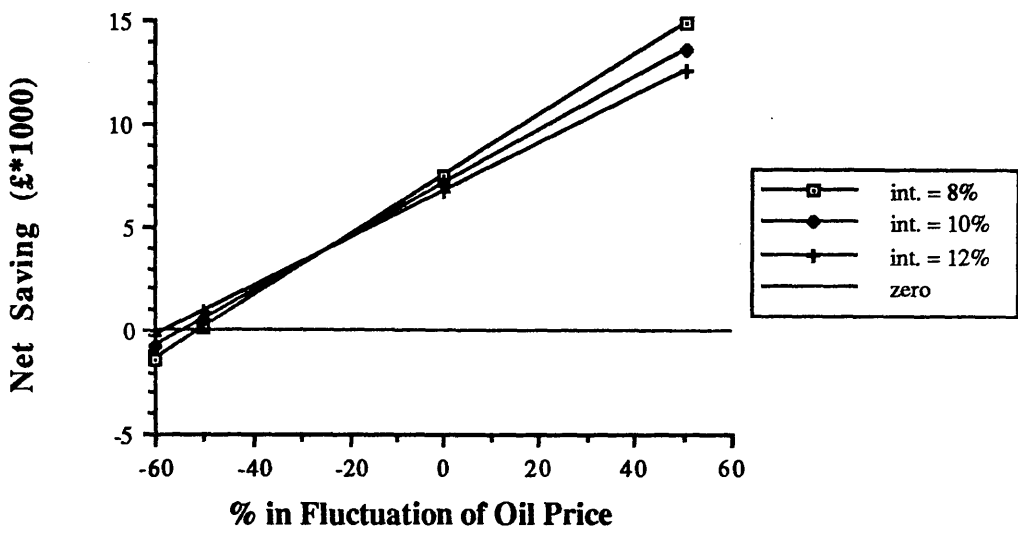


Fig. 11.20 The Net Saving of a Flexible Fin Propeller with Aspect Ratio 4.0 at 75% of the Cost of Existing Screw Propeller with Fluctuation of Oil Price

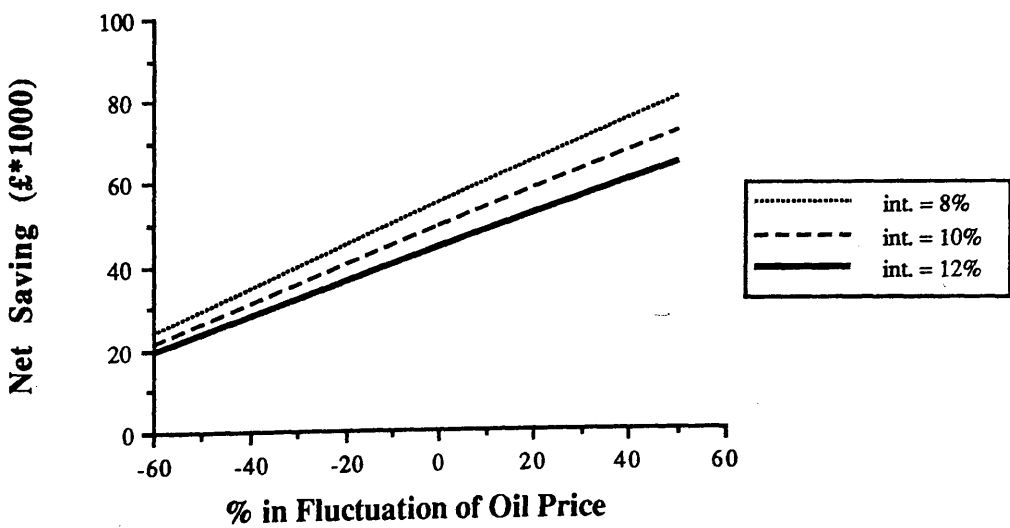


Fig. 11.21 The Net Saving of a Flexible Fin Propeller with Aspect Ratio 10.0 at 75% of the Cost of Existing Screw Propeller with Fluctuation of Oil Price

CHAPTER 12

GENERAL CONCLUSIONS

1.0 INTRODUCTION

Inspired by the study of fish swimming, three types of oscillating foil propulsion system have been studied: a two-dimensional oscillating foil propeller; a flexible fin propeller; and a rotary foil propeller. This thesis has been centred on the investigation of the use of these propellers for marine propulsion. The hydromechanical performance of these propellers has been investigated and the data generated is used in the studies relating to practical application and economics studies. Detailed conclusions have been drawn at the end of each chapter. In the present chapter, the main conclusions and recommendations are summarised and future developments are proposed.

2.0 TWO-DIMENSIONAL OSCILLATING FOIL PROPELLER

The force system acting on a two-dimensional oscillating foil has been examined. In spite of different approaches to the analysis, two-dimensional linearised unsteady foil theory results in the same equations for calculating the lift force and pitching moment.

When the phase lag between heave and pitch is around 90° , the variation of propulsive thrust is small for different locations of rotating centre. When the feathering parameter is high (above 0.4), negative propulsive thrust occurs at some phase lags. High efficiency is obtained at low oscillating frequencies (below 0.2) and the efficiency is close to 1.0, when the reduced frequency approaches zero. With a high feathering parameter (above 0.4), the efficiency is sensitive to the change of phase lag. High efficiency is centre in the region where the phase lag is around 90° for different

locations of the rotating centre.

For 90° phase lag, high propulsive thrust with high efficiency is obtained when the rotating centre is located close to the trailing edge. However, in this condition, the leading edge suction force is dominant in the propulsive thrust and flow separation may occur. When the rotating centre is located aft of the three quarter chord point, the efficiency increases as the feathering parameter increases.

The propulsive thrust oscillates at a frequency twice that of the oscillating frequency. At some conditions, the system produces drag within part of an oscillating cycle. In order to avoid the system producing drag, the rotating centre should be located between the mid-chord and the three-quarter-chord point.

The optimum performance is expected to occur for:

- (i) phase lags around 90° ;
- (ii) low reduced frequency below 0.2;
- (iii) high values of feathering parameter; and
- (iv) a location of rotating centre between the mid-chord and the three-quarter-chord point and best around three-quarter-chord point.

Although high efficiency is obtained at low reduced frequency, higher reduced frequencies are required to generate sufficient thrust for ship propulsion without resort to propellers with very large swept areas.

Three ships of different sizes operating at a Froude number around 0.25 and a high speed craft have been used in studying the application of this propeller and its economic of operation. The heaving amplitude of the foil in these examples is 1.2 times the half chord length, where the assumption of linearity is applicable, with a span of 80% of the beam of the ship and a chord of 2% of the ship length. From the application studies, the following main conclusions were drawn.

- (a) The oscillating frequency is higher than the other two types of oscillating foil propellers.
- (b) It is possible to cancel the unwanted oscillating force which is parallel to the heaving motion, by introducing foils moving 180° out of phase or possibly by using the image effect from the flat bottom of the stern.
- (c) The foil of the propeller can be arranged horizontally or vertically.
- (d) Steering moments can be generated by the system.
- (e) A crank mechanism or vertical oscillating mechanism with two identical springs can generate the required motion of this type of propeller. A linear explosion internal combustion engine or a sliding mechanism with a conventional engine can be employed to generate the vertical oscillation.
- (f) Application of a two-dimensional oscillating foil propeller is found suitable for whole range of ships, even for high speed craft, within this study.

Since the driving mechanism is more complicated than that of a conventional screw propeller, the sum of the cost of the driving mechanism and the cost of the propeller is expected to be higher than that of an existing screw propeller and so is the maintenance cost. Assuming a life time of 15 years with an overall efficiency of 0.75 at an interest rate of 8% and an extra maintenance cost per annum at 5% of the cost of a screw propeller, the breakeven costs of two-dimensional oscillating foil propellers are over 2.5 times the cost of existing screw propellers for the four example ships. If the sum of the extra cost of the driving mechanism and the cost of the propeller is assumed to be twice that of the cost of screw propeller, then there is benefit in applying this type of propeller at the present oil price of £62 per tonne. If the oil price drops by 60%, there is only benefit in applying the propeller to a ship with a large fuel consumption, eg. the 200 metre SHIP-C, under the above conditions.

3.0 FLEXIBLE FIN PROPELLER

The theoretical model of a flexible fin propeller has been established by combining linearised unsteady lifting foil theory with large deflection beam theory. Three dimensional unsteady lifting functions, which are based on mathematical solutions, have been applied in the foil theory. The published results from the numerical solution of Chopra's unsteady lifting foil theory and Lan's unsteady quasi-vortex-lattice method are shown to be in good agreement with the present method. The tip deflections computed using this method combined with large deflection beam theory are the same as those calculated by using the Frish-Fray method, in which elliptical function are applied in the solution. The present method has been extended to cover flexible bars with linear variation in thickness but constant in width. A flexible fin propeller model with a rectangular foil, of which the aspect ratio is 4, and different flexible bars were tested in the Hydrodynamics Laboratory.

From the studies of the hydromechanical performance, the following conclusions are drawn .

- (a) Propulsive thrust generated by the flexible fin propeller increases as the stiffness of the beam, the reduced frequency and the angular oscillating amplitude increase.
- (b) Propulsive efficiency decreases as the stiffness increases.
- (c) Efficiency is improved significantly by increasing the aspect ratio of the foil.
- (d) Neither propulsive thrust nor efficiency are sensitive to the change in taper ratio of the flexible bar.
- (e) A flexible fin propeller with an elliptical foil generates higher propulsive thrust coefficients than that with a rectangular foil. Higher efficiency is obtained by using an elliptical foil at lower reduced frequencies and vice versa at high reduced frequencies.
- (f) Small oscillating amplitudes at low values of the angular oscillating function are recommended for practical propellers. From the experiment, high efficiency is obtained at low angular oscillating function and sufficient propulsive thrust for

ship propulsion is generated.

- (g) An efficiency of 0.7 was obtained from the experimental results of a flexible fin propeller model with aspect ratio 4.0. In this region, the agreement between experimental and theoretical results is satisfactory and the linearised assumption is applicable.
- (h) A flexible fin propeller with high oscillating amplitudes requires a deep draft for operation and is not practical.
- (i) In the bollard pull condition, the propulsive thrust increases as the oscillating amplitudes and frequency increase.

The maximum working stress acting on the flexible bar increases as the reduced frequency and angular oscillating function increase. Increase of stiffness and taper ratio of the flexible bar decrease the maximum working stress. Higher stresses occur in a flexible fin propeller with an elliptical foil than that with a rectangular foil. For a given section modulus, increasing the thickness of the beam increases the stress. The flexible bar requires a material with high strength to flexural modulus ratio. High strength carbon fibre reinforced plastic possesses the required fatigue strength and mechanical properties. In addition, hybrid carbon-glass fibre reinforced plastic is a promising material for this application with better cost efficiency, suitable mechanical properties and fatigue strength.

The feasibility of using a passive flexible fin propeller to convert wave energy into propulsive thrust has been confirmed. Motion response and the required thrust from the main propulsion system of a yacht model in waves was reduced significantly in the resonance region, where the encounter wave length is roughly equal to the ship length, with the flexible fin propeller model fitted. The reduction in both motion response and resistance decreases as the depth of submergence of the propeller increases. The effect of the flexible fin propeller on reduction in motion response and required thrust decreases as the forward speed increases.

As with the two-dimensional oscillating foil propeller, four example ships have

been used in the study of application and economics. Propellers with aspect ratios 4.0 and 10.0 have been considered. The span of the propeller with aspect ratio 10.0 is around the same as the beam of the ship. The stress acting on the flexible bar and its fatigue life are very important parameters in these studies. When high propulsive thrust is required as for the large ship or high speed craft, the stress acting on the bar is high and its fatigue life is short when the stiffness function is sufficiently low to maintain high propulsive efficiency. At a stiffness function of 1.8, the application on a 66m ship has been shown to be practical. If a detailed design of a hybrid fibre reinforced plastic bar with higher strength to flexural modulus ratio is to be used, the stress acting on the bar would be lowered and a better fatigue life could be obtained. High aspect ratio slightly decreases the stress acting on the bar owing to the increase of span of the foil and the consequent the width of the bar.

The operating frequency of the flexible fin propeller is much lower than its natural frequency and resonance is not expected. A simple crank mechanism is proposed to drive the flexible fin propeller.

In a 15 year life time, three flexible fin propellers with aspect ratio 4 are required for the 66m ship. The corresponding breakeven cost of flexible fin propeller is about the same as that of the screw propeller for the range of interest rates in this study at the present oil price (£62 per tonne). As the driving mechanism is not complicated, the maintenance cost and the cost of the driving system is expected to be similar to those for an of existing screw propeller. Owing to the simplicity of the manufacturing process of the flexible fin propeller, the cost of this type of propeller is believed to be lower than that of a screw propeller. If the cost of a flexible fin propeller is 75% of that of a screw propeller, application of a flexible fin propeller with an efficiency of 0.7 is beneficial on the 66 m ship in the present oil price. If the oil price drops 50%, there is no benefit in using the flexible fin propeller with an aspect ratio of four.

In the case of a flexible fin propeller with aspect ratio 10, one propeller is required in a 15 year life time for the application of SHIP-A. The breakeven costs are

about five times the cost of the existing screw propeller at an interest rate of 10%. If the cost of the flexible fin propeller is judged to be 75% of that of the existing screw propeller, the net saving in the whole life time at the present oil price is £50,000. There is benefit even if the oil price drops 60% and the net saving is then £20,000 at an interest rate of 10%.

This study shows that high aspect ratio is desirable from the view point of high efficiency, long fatigue life and economic viability. The aspect ratio of 10.0 is the upper limit in the practical application where the required span is about the beam of the ship. The foil with higher aspect ratio will project outside the ship beam and not be practical.

The optimum design of a flexible fin propeller is expected to be with,

- i) low angular oscillating function,
- ii) high aspect ratio with an upper limit at 10.0, and
- iii) a cost effective material with higher strength to modulus ratio, good fatigue strength and mechanical properties (eg. hybrid fibre composite)

Application of a flexible fin propeller is found suitable for ships up to about 2000 tonnes with a Froude number around 0.25.

4.0 ROTARY FOIL PROPELLER

Experimental investigations on a three bladed trochoidal propeller model with high aspect ratio were carried out. The propulsive thrust and driving torque measured in the experiment with forward speed are higher than those predicted by the multiple stream tube theory at low aspect ratio. This is attributed to unsteady effects and dynamic stall which occurs at low advance ratios instead of the steady stall assumed in the theory. In forward operating conditions, the peak propulsive thrust has been obtained at an advance ratio of 5.0 while a high efficiency of 0.8 occurred at an advance ratio of 6.0. Similar curves of thrust were obtained in both reverse and forward

conditions. However, higher driving torque was required in the reverse operating conditions and the peak efficiency dropped by 20%. The propulsive thrust increases as the rotation speed increases in the bollard pull condition.

In the study of the application of the three bladed rotary foil propeller on the four ship examples, the required span of the propeller is approximately the same as the beam of ship. For high speed craft, the required span is 17% larger than the beam of the ship and is not practical. The oversize problem can be overcome by using a higher number of blades or increasing the pitching angle. Owing to the special configuration of SWATH ships, the three bladed propeller is found to be suitable for a SWATH ship even if the service speed is high.

High frictional loss occurred in the model and the overall efficiency was low in the model tests. For the full scale application, it is likely that the high frictional loss can be reduced by using conventional shaft seals as used for screw propellers and a self lubricating fabric liner on the sliding surfaces.

For full scale application, low frictional loss is important. If a 5% loss in the mechanical friction is assumed at full scale, the three bladed propeller with an hydromechanical efficiency of 0.7 is not economically viable in any of four example ships. A higher number of blades is required to make use of the peak efficiency instead of using the peak thrust coefficient. For a five bladed propeller with an overall efficiency of 0.73, at an interest rate of 8%, with no extra maintenance cost, the breakeven costs are about 3.2, 2.3, 4.7 and 2.6 times the cost of the existing screw propeller for SHIP-A, SHIP-B, SHIP-C and SHIP-D respectively. Owing to the complexity of the driving mechanism and because two propellers are required in the application, the sum of extra costs in the driving mechanism and propeller cost is expected to be higher than the existing cost of a screw propeller. If the five bladed propeller is assumed to be 2.5 times the cost of the existing screw propeller and an extra maintenance cost per annum of 5% of the cost of screw propeller is considered, only application on the 200 m ship with high fuel consumption is found to benefit from

the application of a rotary foil propeller at the present oil price. When the oil price drops 50%, there is no longer a benefit in changing to rotary foil propulsion.

The key design recommendation is to apply a propeller with a higher number of blades than three and a five bladed propeller is suggested. Application of rotary foil propeller is found suitable for ships with a wide beam (eg. SWATH ship) to accommodate the span of the foils.

5.0 FUTURE DEVELOPMENTS

On finishing the present work, the following aspects are felt to be the next steps required for further development.

- (1) In the present work, open water performance has been investigated. In the future, an investigation on the interaction between the hull form and the oscillating foil propeller is essential to set down the optimum relationship between the ship parameters and the parameters of the oscillating foil propeller. The hull efficiency associated with using an oscillating foil propeller is expected to be different from that of a screw propeller and needs to be investigated.

Two-Dimensional Oscillating Foil Propeller

- 2) In order to get more reliable data and confirmation of the linearised theory, experimental investigation on the performance of the two dimensional oscillating foil propeller is desirable. The proposed driving mechanism with spring system can be applied to drive the model.
- 3) The manoeuvring characteristics of a vessel fitted with fin propulsion system could be examined.

Flexible Fin Propeller

- 4) For the flexible fin propeller, the development should be concentrated on different foil shapes, especially the lunate shape, with experimental and theoretical approaches. The present flexible fin propeller can be refined by using a flexible (or partially flexible) foil in both chordwise and spanwise directions with a spring-loaded hinge at the connection of the flexible bar and the foil. The foil might be made of a flexible material.

- 5) A detailed investigation of hybrid fibre reinforced plastics are desired with a view to find a suitable combination of fibres to produce the required mechanical properties and fatigue strength for the flexible beams. Available test data on mechanical properties, especially on fatigue strength, of different hybrid materials is limited and experimental investigation is required.

- 6) The present work has established the general characteristics of the design of using flexible fin propellers for wave propulsion. Optimisation of the application of flexible fin propeller to wave propulsion should be carried out, for example, different foil shapes and flexibilities of bars.

REFERENCES

- Abbott, I. H. and von Doenhoff, A. E. (1959) "Theory of Wing Sections", Dover Publications, Inc., New York.
- Ahmadi, A. R. and Widnall, S. E. (1985) "Unsteady Lifting-Line Theory as a Singular-perturbation Problem", J. Fluid Mech., vol. 153, p 59-81.
- Ahmadi, A. R. and Widnall, S. E. (1986) "Energetics and Optimum Motion of Oscillating Lifting Surface of Finite Span", J. Fluid Mech., vol. 162, p. 261-282.
- Antoni, G. (1913) "Blade or Fish Tail Propeller and Submarine Boat", U. S. Patent No. 1050090.
- Ashby, M. F. (1989) "Material Selection in Conceptual design", Material Science and Technology, Vol. 5, p 517-525 (also the Materials '88 Conference "Materials and Engineering Design", May, 1988)
- Barten, H. J. (1944 & 1945) "On the Deflection of a Cantilever Beam", Quart. J. of Applied Math., vol. 2, p. 168-171. and vol. 3 , p. 275-276 (correction).
- Berman, M. and Gothberg, S. (1985) " Experimental Investigation of the Propulsive Characteristics of the Foil Propeller", Institute of Ship Hydromechanics, Chalmers Technical University, Goteborg (in Swedish).
- Biot, M. A. (1940) " Some Simplified Methods in Airfoil Theory ", J. Aero. Sc. 9., p. 186-190
- Bishop, K. E. and Drucker, D. C. (1945) " Large Deflection of Cantilever Beams", Quart. J. of Applied Math., vol. 3, p. 272 -275.
- Bishop, R.E.D. (1956) "Myklestad's Method for Non-uniform Vibrating Beams - No.1 & No. 2", The Engineer, Dec., p 838-840 and p 874-875.
- Bjelovucic, M. S. (1907) "Improvement in Propellers for Water and Aerostatic Vessels", U.K. Patent No. 26884.
- Bose, N. (1982) " Hydrofoils - Design of a Wind Propelled Flying Trimaran", Ph. D. Thesis, Dept. of Naval Architecture and Ocean Engineering, University of Glasgow.
- Bose, N. (1986) "Drawings of the Rotary Foil Propeller Model", Hydrodynamics

- Laboratory, Dept. of Naval Arch. and Ocean Eng., the University of Glasgow.
- Bose, N. , Ferguson, A. M. and McGregor, R. C. (1986) "Flexible Fin Propeller - Case for Support (for application of SERC Grant)" Marine Technology Centre, University of Glasgow, Project No. 1G91.
- Bose, N. (1987) "Rotary Foil Propeller", Paper of Ship Research Institute, Ministry of Transport, Tokyo, Vol. 24, No. 5.
- Bose, N. and Lai, P. S. K. (1989) " Experimental Performance of a Trochoidal Propeller with High Aspect Ratio Blades", Marine Technology, Vol.26, No. 3, p 192-201.
- Bose, N. and Lien, J. (1989) " Propulsion of a Fin Whale (Balaenoptera Physalus) : Why the Fin Whale is Fast Swimmer", Proc. of Royal Society, B 237, p 175-200.
- BP Advanced Materials Limited (1989) "Data Sheet, R23, 120°C Cure Epoxy Preregs System", Material Systems.
- Brealey, R. and Myers, S. (1984) "Principles of Corporate Finance", McGraw-Hill Book Company.
- Broutman, L. J. and Krock, R. H. (1974) " Composite Materials, Vol. 5 'Fracture and Fatigue' ", Academic Press.
- Brown, G. I. (1986) "Lateral Thrust Drive for Watercraft", U.S. Patent No. 4568290.
- Bunyan, T. W. (1978) "Development and Service Performance in Propeller and Shafting Connections", 47th Andrew Laing Lecture, North East Coast Institution of Engineers and Shipbuilders, Vol. 95, p. 19-28.
- Canning, M. S. (1989), Private Communication, BP Advanced materials Limited, Materials Systems.
- Carr, L. W. (1988) "Progress in Analysis and Prediction of Dynamic Stall", J. Aircraft, vol. 25, p. 6-17.
- Castro, A. M. E. (1977) " In Search of Zero Leeway", M. Sc. Thesis, Dept. of naval Architecture and Ocean engineering, University of Glasgow.
- Cheng, H. K. (1975) " On the Lifting - Line Theory in Unsteady Aerodynamics", Proc. Symp. Unsteady Aerodynamics, U. of Arizona, p. 719-739.
- Cheng, H. K. and Murillo, L.E. (1984) " Lunate-Tail Swimming Propulsion as a

- Problem of Curved Lifting Line in Unsteady Flow, Part 1 Asymptotic Theory", *J. Fluid Mech.*, Vol. 143, P. 327-350.
- Chopra, M. G. (1974a) "Lunate-Tail Swimming Propulsion", *Proc. of Symp. on Swimming and Flying in Nature*, Vol 2, p 635-650.
- Chopra, M. G. (1974b) "Hydromechanics of Lunate -Tail Swimming Propulsion ", *J. Fluid Mech.*, vol 64, pp 375-391.
- Chopra, M. G. (1976) "Large Amplitude Lunate-Tail Theory of Fish Locomotion", *J. Fluid Mech.*, vol. 74, p. 161-182.
- Chopra, M. G. and Kambe, T. (1977) " Hydrodynamics of Lunate-tail Swimming Propulsion. Part - 2 ", *J. Fluid Mech.* vol. 79, pp 49-69.
- Chun, H. H. (1989) Private Communication, YARD fellow, Dept. of Naval Architecture and Ocean Eng., University of Glasgow.
- Comstock, J. P. (1977) "Principles of Naval Architecture", *The Society of Naval Architectures and Marine Engineers*, New York.
- Curtis, P. T. (1987) "A Review of the Fatigue of Composite Materials", Royal Aircraft Est. Tech. Report 87031.
- Davies, D. E. (1965) "Calculation of Unsteady Generalised Airforces on a Thin Wing Oscillating Harmonically in Subsonic Flow" *Aero. Research Council, R & M No. 3409*.
- Dickerson, M. C. and Dobay, G. F. (1975) "Experimental Performance of the Some high-Pitch Cycloidal Propellers", *NSRDC Report No. SPD-399-01*, David Taylor Research Centre.
- Draper, L and Herbert, J. P. (1977) "Visual Wave Observations in Scottish Waters 1968- 1976", *Institute of Oceanographic Science*.
- Drishler, J. A. (1956) " Calculation and Compilation of the Unsteady -Lift Functions for a Rigid Wing subjected to Sinusoidal Gusts and to Sinusoidal Sinking Oscillations" *NACA TN 3748*.
- Dumpleton, O. W. (1986) " Efficient Ship Programme - Fuel Efficiency Study ", DOTI no. SM1, Report No. 981, Marine Design Consultants Limited.
- Durand, W. F. (Editor), von Karman, T. and Burgers, J. M. (1943) " Aerodynamic Theory (Vol II), General Aerodynamic Theory - Perfect Fluids ".

- Fafnir Bearing Division of Textron Inc. (1978) "Technical Information on Aircraft Control and Rod End Bearings"
- Fibreglass Ltd. (1977) "Properties of Fibreglass Thermoset Composites", Information Sheet FIS1052.
- Fierstine, H. L. and Walters, V (1968) " Studies in Locomotion and Anatomy of Scombroid Fishes" Mem. South Calif. Acad. Sci., vol. 6, p. 1-31.
- Frisch-Fay, R. (1961) " A New Approach to the Analysis of the Deflection of Thin Cantilevers", J. Appl. Mech., vol. 28, p. 87-90.
- Frisch-Fay, R. (1962) "Flexible Bars", Butterworth and Co. Ltd.
- Fung, Y. C. (1969) " An Introduction to The Theory of Aeroelasticity ", Dover Publications, Inc. New York.
- Gearhart, W. S. and McBride, M. W. "Performance Assessment of Propeller Boss Cap Fin Type Device", Proc. of 22nd American Towing Tank Conference, St. John's, Newfoundland, Canada.
- Gibbs and Cox, Inc. (1960) " Marine Design Manual for Fiberglass reinforced Plastics", McGraw-Hill Book Co..
- Gill, P. E. and Miller, G. F. (1972) " An Algorithm for the integration of Unequally Spaced Data", The Computer Journal, Vol. 15, No. 1, p. 80-83.
- Gill, R. M. (1972) "Carbon Fibres in Composite Materials", London Iliffe Books.
- Glauert, H. (1929) "The Force and Moment on an Oscillating Aerofoil", British A. R. C., R. & M. No. 1242.
- Glauert, H (1942) " The Elements of Aerofoil and Airscrew Theory ", Cambridge University Press.
- Gray, J. (1936) "Studies in Animal Locomotion VI, The propulsive Powers of the Dolphin", J. Exp. Biol. vol 13, p 192-199.
- Gray, J. (1968) " Animal Locomotion ", Weidenfeld and Nicolson.
- Grue, J., Mo, A. and Palm, E. (1988) "Propulsion of a Foil Moving in Water Waves", J. Fluid Mech., vol. 186, p. 393-417.
- Hoar, W. S. and Randall, D. J. (1978) "Fish Physiology, Volume VII, Locomotion", Academic Press.
- Holtrop, J. and Mennen, G. G. J. (1982) " An Approximate Power Prediction

- Method", *Int. Shipbuilding Progress*, Vol. 29, p. 166-170.
- Hotrop, J. (1984) " A Statistical Re-Analysis of Resistance and Propulsion Data", *Int. Shipbuilding Progress*, Vol. 31, p. 272-276.
- Hotchkiss, D. V. (1947) " Improvements Relating to the Propulsion of Watercraft and Aircraft", U.K. Patent No. 588953.
- International Offshore Rule (1975) - Mark III by ORC.
- Isshiki, H. (1982) "A Theory of Wave Devouring Propulsion (1st Report)", *J. of the Soc. of Naval Architects of Japan*, vol 151, p. 54-64.
- Isshiki, H., Murakami, M. and Terao, Y. (1984) "Utilization of Wave Energy into Propulsion of Ships - Wave Devouring Propulsion", *Proc. of 15th Symp. on Naval Hydrodynamics*, National Academy Press, Washington, D.C.
- Isshiki, H. and Murakami, M. (1986) " Wave Power Utilization into Ship Propulsion", 5th OMAE Symposium, Tokyo.
- Isshiki, N., Hashimoto, K. and Morikawa H. (1987) "Studies on Fin Ship Propelled by Oscillating Horizontal Tail Fin", *Int. Marine Engineering Conference*, Shanghai, China, 1-8.
- Jakobsen, E. (1981) "The Foil Propeller, Wave Power for Propulsion", *Proc. of 2nd Int. Symp. on Wave & Tidal Energy*, Cambridge, U. K.
- Jakobsen, E. (1982) " Wave motors", Uk. Patent, GB 2009069B.
- Jakobsen, E. (1983) " Wave Motor Especially for Propulsion of Boats", UK Patent, GB 2045708B.
- Jakobsen, E. (1988) Private Communication, The Wave Control Company, Norway.
- James, E. C. (1975) "Lifting Line Theory for an Unsteady Wing as a Singular Perturbation Problem", *J. Fluid Mech.* vol. 70, 1975, p 735 -771.
- Jones, R. T. (1940) " The Unsteady Lift of A wing of Finite Aspect Ratio ", *NACA Report No. 681*.
- Jones, W. P. (1943) " Theoretical Air-Load and Derivative Coefficients for Rectangular Wings ", *Aeronautical Research Council, R & M No. 2142*.
- Jones, W. P. (1945a) " Aerodynamic Forces on Wings in Simple Harmonic Motion ", *Aeronautical Research Council, R & M No. 2026*.
- Jones, W. P. (1945b) " Aerodynamic Forces on Wings in Non-Uniform Motion ",

Aeronautical Research Council, R & M No. 2117.

- Katz, J. and Weihs, D. (1978) "Hydrodynamic Propulsion by Large Amplitude Oscillation of an Airfoil with Chordwise Flexibility", *J. Fluid Mech.* (1978), Vol. 88, part 3, p. 485-497.
- Kretsis, G. (1987) "A Review of the Tensile, Compressive, Flexural and Shear Properties of Hybrid Fibre-Reinforced Plastics", *Composites*, Vol. 18, No. 1, p. 13 - 23.
- Kubota, A., Kudo, T., Kato, H. and Yamaguchi, H. (1984) "Study on Propulsion by Partially Elastic Oscillating Foil (2nd Report) - Numerical Simulation by Singularity Distribution Method and Evaluation of Scope for Application to Ship Propulsion ", *J. of Soc. of Naval Architect of Japan*, Vol. 156, p 95-104 (in Japanese).
- Kudo, T., Kubota, A., Kato, H. and Yamaguchi, H. (1984) " Study on Propulsion by Partially Elastic Oscillating Foil (1st Report) - Analysis by Linearized Theory", *J. of Soc. of Naval Architects of Japan*, vol. 156, p. 85 - 94 (in Japanese).
- Kyozuka, Y., Kurahashi, M. and Koterayama, W. (1988) " Hydrodynamic Forces Acting on an Oscillating Wing in Uniform Flow", *Transactions of the West-Japan Society of Naval Architects*, Vol. 76, p 85-96.
- Lai, P. S. K. (1987) "A Note on Foil Propulsion Systems", Department of Naval Architecture and Ocean Engineering, University of Glasgow.
- Lai, P. S. K. (1988) "Visiting Report - Wave Control Company and Marine Technology Centre of University of Trondheim, Norway", File 4/1, 6/June, Dept. of Naval Arch. and Ocean Eng., University of Glasgow.
- Lai, P. S. K. (1988a) " Studies of a Two-Dimensional Linearized Unsteady Foil Theory", Report No. NAOE-88-27, Dept. of Naval Arch. and Ocean Eng., University of Glasgow.
- Lai, P. S. K. (1988b) " Studies of the Propulsive Thrust and the Hydromechanical Efficiency of a Two Dimensional Oscillating Foil "Report No. NAOE-88-32, Dept. of Naval Arch. and Ocean Eng., University of Glasgow.
- Lai, P. S. K. (1988c) " The Design of the Flexible Fin Propeller Model and the Testing Rig", Report No. NAOE-88-38, Dept. of Naval Arch. and Ocean Eng.,

University of Glasgow.

- Lai, P. S. K. (1989) "Theoretical Studies of the Performance of Flexible Fin Propellers", Report No. NAOE-89-15, Dept. of Naval Arch. and Ocean Eng., University of Glasgow.
- Lai, P. S. K. (1989a) "Experimental Studies of the Performance of the Flexible Fin Propeller", Report No. NAOE-89-16, Dept. of Naval Arch. and Ocean Eng., University of Glasgow.
- Lai, P. S. K. and Bose, N. (1988) " Experimental Studies of Rotary Foil Propeller (Part one)", Report No. NAOE-88-06, Dept. of Naval Arch. and Ocean Eng., University of Glasgow.
- Lai, P. S. K. and McGregor, R. C. (1989) " Flexible Fin Wave Propulsion ", Report No. NAOE-89-17, Dept. of Naval Arch. and Ocean Eng., University of Glasgow.
- Lai, P. S. K., McGregor, R. C. and Bose, N (1989) " Experimental Investigation of Oscillating Foil Propellers", Proc. of 22nd American Towing Tank Conf., St. John's, Newfoundland, Canada.
- Lai, P. S. K., McGregor, R. C. and Bose, N (1989a) " On the Flexible Fin Propeller", 4th Int. Symp. on Practical Design of Ships and Mobile Units (PRADS' 89) Varna, Bulgaria.
- Lamb, H. (1932) "Hydrodynamics", Cambridge University Press.
- Lan, C. E. (1974) " A Quasi-Vortex-Lattice Method in Thin Wing Theory", J. of Aircraft, Vol. 11 No. 9 p. 518-527.
- Lan, C.E. (1979) " The Unsteady Quasi-Vortex-Lattice Method with Applications to Animal Propulsion", J. Fluid Mech., Vol. 93, part 4, p. 747-765.
- Lang, T. and Dcybell, D. (1963) " Porpoise Performance Tests in a Sea-Water Tank", NAVWEPS Report 8060.
- Lang, T. G. (1974) "Speed, Power and Drag Measurements of Dolphins and Porpoises", Proc. of Sym. on Swimming and Flying in Nature, vol. 2, p. 553-572.
- Lawrence, H. R. (1951) " The Lift Distribution on Low Aspect Ratio Wings at Subsonic Speeds", J. of Aero. Sci., Vol. 18, No. 10, p 683-695.

- Lawrence, H. R. and Gerber, E. H. (1952) "The Aerodynamic Forces on Low Aspect Ratio Wings Oscillating in an Incompressible Flow", *J. of Aero. Sci.*, Vol.19, No. 11, p769-781.
- Lighthill, M. J. (1960) "Note on the Swimming of Slender Fish", *J. Fluid Mech.*, vol 9, p. 305-317.
- Lighthill, M. J. (1969) "Hydromechanics of Aquatic Animal Propulsion", *Ann. Rev. Fluid Mech.*, vol. 1, p. 413-446.
- Lighthill, M. J. (1970) "Aquatic Animal Propulsion of High Hydromechanical Efficiency", *J. Fluid Mech.*, vol. 44, part 2, pp.265-301
- Lighthill, M. J. (1971) "Large -Amplitude Elongated-Body Theory of Fish Locomotion" *Proc. of Royal Society, B* 179, p125-138.
- Lighthill, M. J. (1973) "On the Weis-Fogh Mechanism of Lift Generation", *J. of Fluid Mech.* Vol. 60, p. 1-17.
- Lighthill, M. J. (1977) "Aquatic Animal Locomotion", *Trans. of N. E. Coast Inst.* vol 93, No. 6, p 127-135.
- Lighthill, M. J. (1978) "Waves in Fluids", Cambridge University Press.
- Linden, H. (1895) "Improved Combination with Floating Bodies, of Fins Adapted to Effect Their Propulsion" U. K. Patent No. 14630.
- Lubin, G. (1982) "Handbook of Composites".
- Lunde, J. K. (1982) "A Theoretical Hydrodynamic Investigation of the Foil Propeller", Report Sh-114-82, Gothengurg.
- MacGregor, J. R., Bose, N. and Small, G. (1988) "Design and Construction of a Small Waterplane Twin Hull (SWATH) Fishing Vessel", *World Sym. on Fishing Gear and Fishing Vessel Design*, St. John's, Canada.
- McCroskey, W. J. (1977) "Some Current Reseach in Unsteady Fluid Dynamics - the 1976 Freeman Scholar Lecture", *Trans. of ASME*, March p. 8-38.
- McCroskey, W. J. (1981) "The Phenomenon of Dynamic Stall", *NASA Tech. Memo.* 81264.
- McCroskey, W. J. (1982) "Unsteady Airfoils", *Ann. Rev. Fluid Mech.*, vol. 14, p. 285-311.
- Marine Engineers Review (1989) "Directory of Marine Diesel Engines", *J. of Inst. of*

Marine Engineers.

- Martin, M. (1963) "The Stability Derivatives of a Hydrofoil", Hydronautics, Inc., Tech. Report 001-10.
- Maruo, H. (1957) "The Excess Resistance of a Ship in a Rough Sea", Inter. Shipbuilding Progress, Vol. 4, p. 337-345.
- Mendenhall, R. M. and Spangler, S. B. (1973) "Theoretical Analysis of Cycloidal Propellers", Report No. NEAR TR-53, Nielsen Engineering and Research, Inc.
- Mitchell, T. P. (1959) "The Nonlinear Bending of Thin Rods" , J. Appl. Mech., vol. 26, p. 40 - 43.
- The Motor Ship (1989), "Bunkers", October, p. 8.
- Myklestad, N. O. (1944) "A New Method of Calculating Natural Modes of Uncoupled Bending Vibration of Airplane Wings and Other Types of Beams", J. of Aeronautical Sciences, vol. 11, No.2, p. 153 - 162.
- NAG Fortran Library Manual (1988) Mark 12, vol. 1, The Numerical Algorithms Group Ltd.
- Nagahama, M., Murakami, M. and Isshiki, H. (1986) " Effect of a Foil Attached to a Ship in Waves", Hitachi Zosen Shipbuilding Tech. Report Vol 47, No. 3-4.
- Ohna, B. E. (1987) "Internal Combustion Engine", U. S. Patent No. 4700667.
- Owen, M. J. and Morris, S. (1970) "An Assessment of the Potential of Carbon Fibre Reinforced Plastics as Fatigue Resistant Materials" 25th Ann. Tech. Conf. Reinforced Plastics/Composites Division, The Society of the Plastics Industry, Washington, D.C.
- Owen, M. J. and Morris S. (1972) " Some Interlaminar Shear Fatigue Properties of Carbon Fibre Reinforced Plastics", Plastics and Polymers, p. 209-216.
- Parkyn, B. (1970) "Glass Reinforced Plastics", London Iliffe Books.
- Patience, G. (1989) Private Communication, Stone Manganese Marine Limited.
- Paton, W. (1974) " Materials Design Factors in Reinforced Plastics", Reinforced Plastics: Technolgy and Design, Paper No.2, National Engineering Laboratory.
- Peachey, J. H. (1981) "Oscillating Fin Propulsion in Water", M. Sc. Thesis, University of Liverpool.
- Potze, W. (1986) "On Optimum Sculling Propulsion", J. of Ship Research, Vol. 30,

No. 4, pp. 221-241.

Prandtl, L. (1936) " Theorie Des Flugzeugtragflügels im Zusammendruckbaren Medium", Luftfahrtforschung, Bd. 13, Nr. 10, p. 313-319.

Ramsay-Whale, N. (1980) "Boat Propulsion and Steering Device", U. K. Patent No. 2044705.

Richardson, J. R. (1960) "A Method for Calculating the Lifting Forces on Wings (Unsteady Subsonic and Supersonic Lifting-Surface Theory)", Aero. Research Council, R & M No. 3157.

Robert, D. (1977) " Development of Engineering Data on Advanced Composite Materials", University of Dayton Research Institute, Report No. AFML-TR-77-151.

Robinson, A. and Laurmann, J.A. (1956) " Wing Theory", Cambridge at the University Press.

Rose Bearing (1978) "Technical information on Aircraft Series"

Ruys, A. W. (1966) " A Comparison of Some Published Results of Tests on Vertical Axis Propellers", Int. Shipbuilding Progress, Vol. 13, No. 148, pp. 399-401.

Scherer, J. O. (1968) "Experimental and Theoretical Investigation of Large Amplitude Oscillating Foil Propulsion System ", Hydronautics Inc. Tech. Report, 662-1.

Schlichting, H and Truckenbrodt, E (translated by Ramm, H.J.) (1979) "Aerodynamics of the Airplane", McGraw-Hill International Book Company.

Scott B. (1978) " Resin, Fibreglass and Foam Information", Unitex Marine Ltd.

Seames, A. E., Conway, H. D. and Ithaca, N. Y. (1957) " A Numerical Procedure for Calculating the Large Deflections of Straight and Curved Beams", J. Appl. Mech., vol. 24, p. 289-294.

Seide, P. (1984) "Large Deflections of a simply Supported Beam Subjected to Moment at One End", J. of Applied Mechanics, Vol. 51, p. 519-525.

Smith, T. R. and Owen, M. J. (1968) "The Progressive Nature of fatigue damage in GRP ", 6th Int. R. P. Conference, British Plastic Federation Paper 27.

Strekalov, S. D. (1986) "Fin-Type Propeller of Ship", USSR Patent No. 529104.

Theodorsen, T. (1935) "General Theory of Aerodynamic Instability and the Mechanism of Flutter" NACA TR 496.

- Thoft-Christensen, P and Baker, M. J. (1982) " Structural Reliability and its Applications", Springer-Verlag, Berlin.
- Timmins, P. F. (1977) " A Feasibility Study of Fibre Reinforced Plastics for Use in the Spring Industry", Designing with Fibre Reinforced Materials, I. Mech. E. Conference Publications.
- Tipaldi, A. (1980) "Water Craft Propulsion", U. K. Patent No. 2049594.
- Todd, F. H. (1953) " Some Further Experiments on Single Screw Merchant Ship Forms - Series 60", SNAME Trans., Vol.61, p. 516-589.
- Tsutahara, M and Kimura, T. (1987) "An Application of Weis-Fogh Mechanism to Ship Propulsion", J. of Fluid Eng., Vol. 109, p. 107-113.
- Unitex Marine Limited (1989) Private Communication on "Aqueon Inner Space Vehicle".
- van Manen, J. D. (1966) "Results of Systematic Tests with Vertical Axis Propellers", Int. Shipbuilding Prog., Vol.13, No. 148, pp. 399-401.
- Videler, J. and Kamermans, P. (1985) " Differences Between Upstroke and Downstroke in Swimming Dolphins", J. of Experimental Biology, vol 119, p. 265 - 274.
- von Karman, T and Sears, W. R. (1938) "Airfoil Theory for Non-uniform Motion" J. Aero. Sc., Vol. 5, No. 10, pp.379 - 390.
- Wagner, H. (1925) "Dynamischer Auftrieb von Tragflugeln", Zeitschr. f. Angew Math. U. Mech. Bd. 5, p 17.
- Warner, N. S. (1963) "Boat Propulsion and Steering Device", U.S. Patent No. 3110283.
- Watson, G. N. (1922) "A Treatise on Theory of Bessel Functions", Cambridge University Press.
- Weis-Fogh, T. (1973) "Quick Estimates of Flight Fitness in Hovering Animals, Including Novel Mechanism for Lift Production", J. Exp. Biol., vol. 5, p 169-231.
- Wilmott, P. (1988) "Unsteady Lifting-Line Theory by the Method of Matched Asymptotic Expansions", J. of Fluid Mech., vol. 186, p 303-320.
- Woodcock, A. H. (1951) "Wave Riding Dolphins", J. Exp. Biology, vol. 28, p. 215-

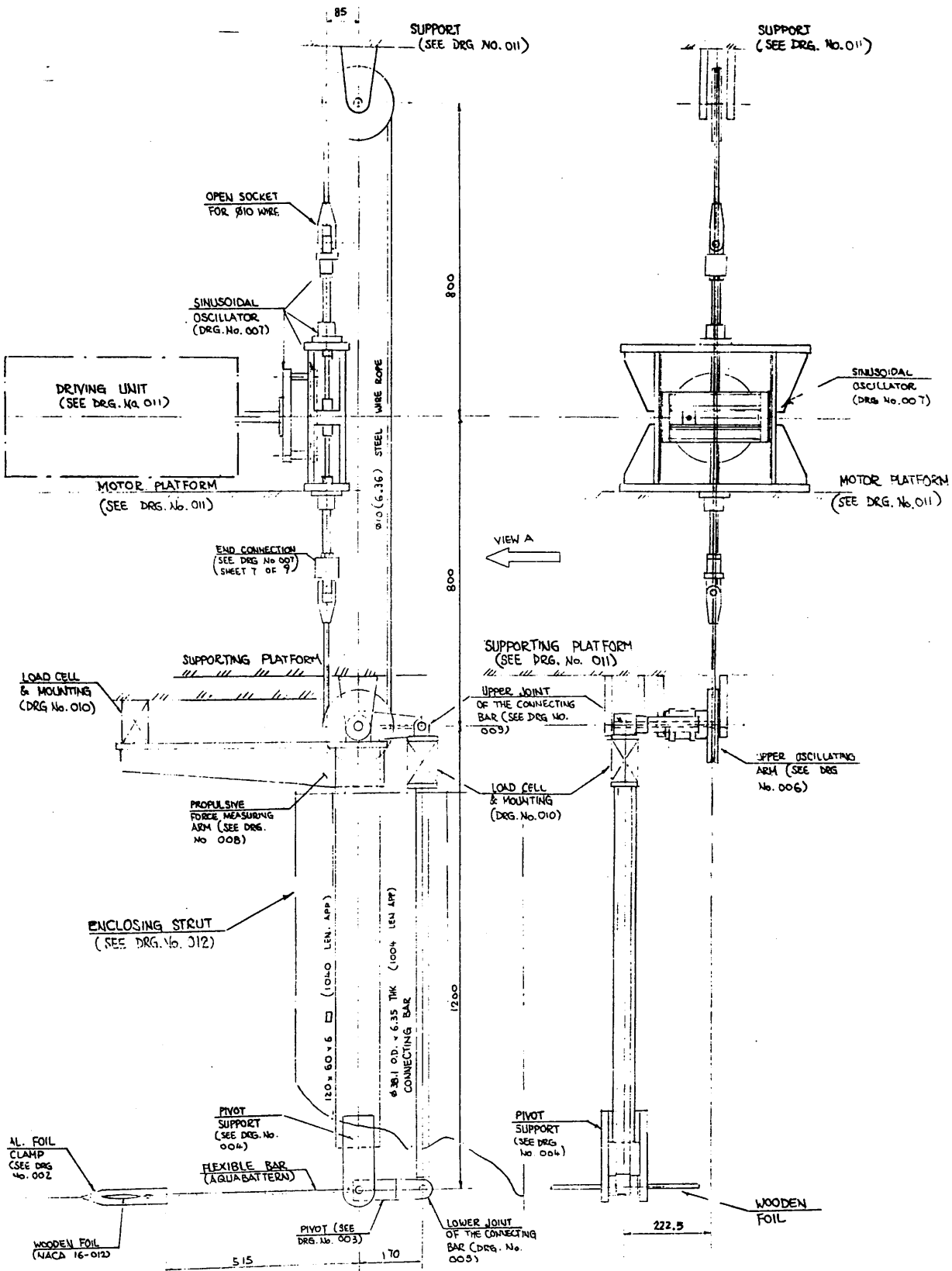
- Wu. T. Y. (1971a) " Hydrodynamics of Swimming Propulsion : Part I, Swimming of a Two-Dimensional Flexible Plate at Variable Forward Speeds in Inviscid Fluid", J. of Fluid Mech., Vol. 46, p 337-355.
- Wu. T. Y. (1971b) " Hydrodynamics of Swimming Propulsion : Part II, Some Optimum Shape Problems", J. of Fluid Mech., Vol. 46, p 521-544.
- Wu. T. Y. (1971c) " Hydrodynamics of Swimming Propulsion : Part III, Swimming and Optimum Movements of Slender Fish with Side Fins", J. of Fluid Mech., Vol. 46, p 545-568.
- Wu, T. Y. (1972) "Extraction of Flow Energy by a Wing Oscillating in Waves", J. of Ship Research, vol. 16, no. 1, p. 66-78.

APPENDIX I

**CONSTRUCTION DRAWINGS OF THE TEST RIG OF THE FLEXIBLE
FIN PROPELLER MODEL**

Designed by : P. S. K. Lai

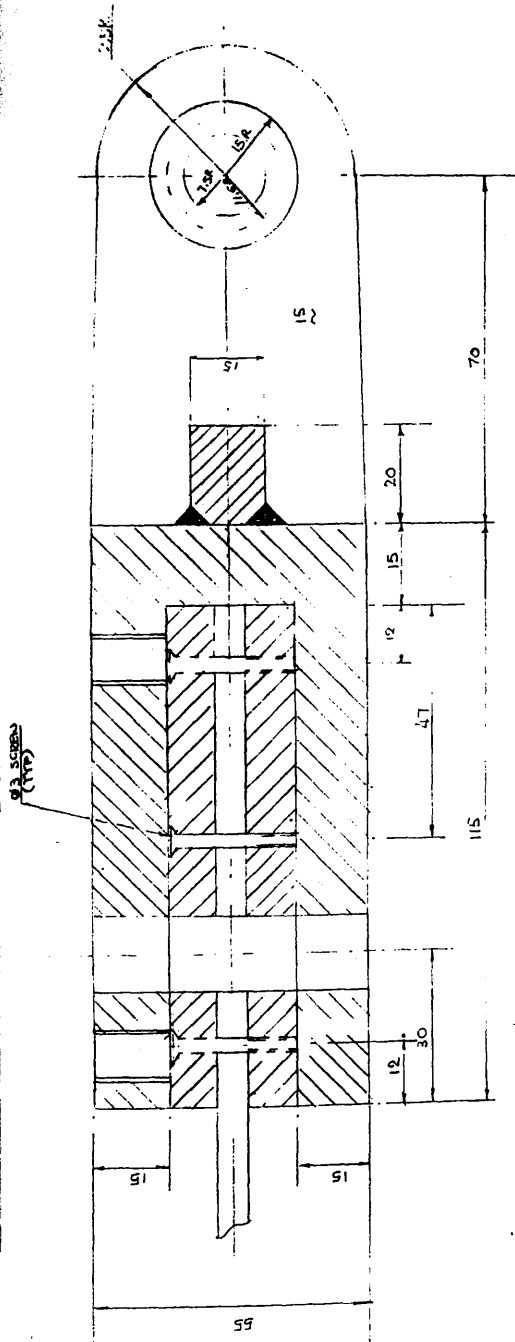
Drawn by : P. S. K. Lai



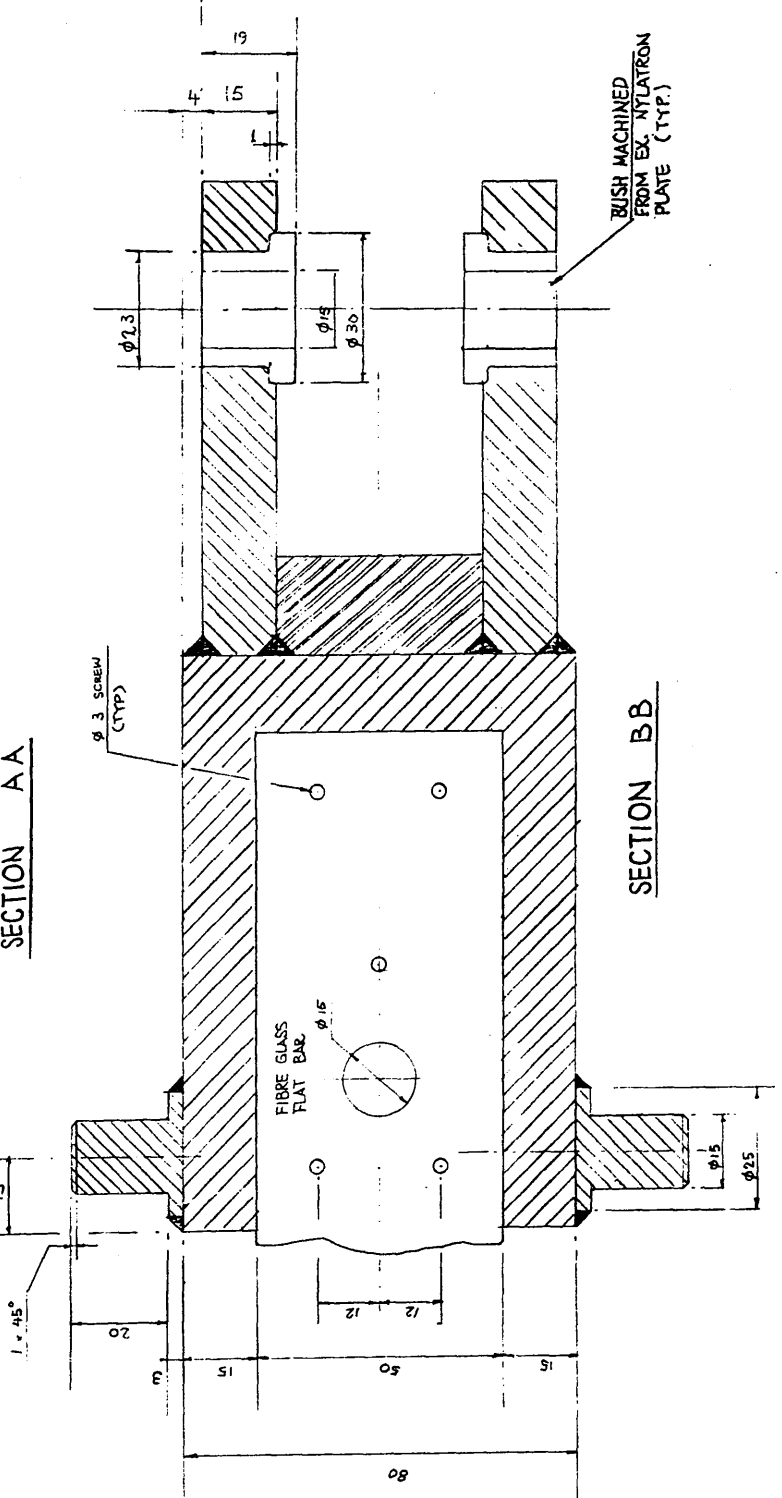
ELEVATION OF THE
ARRANGEMENT OF THE
FLEXIBLE FIN PROPELLER
MODEL

VIEW A

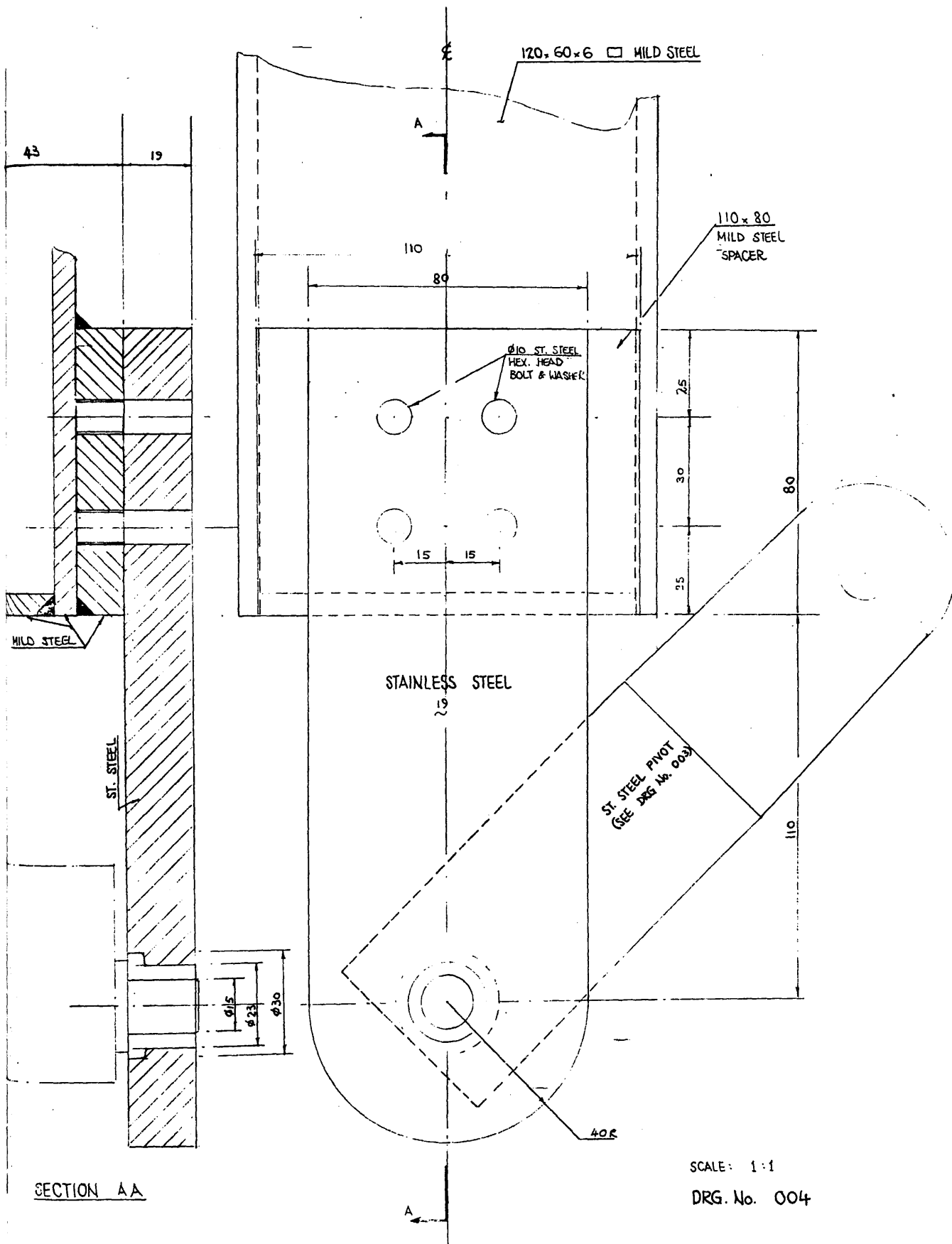
SCALE 1:10
DRG. No. 001



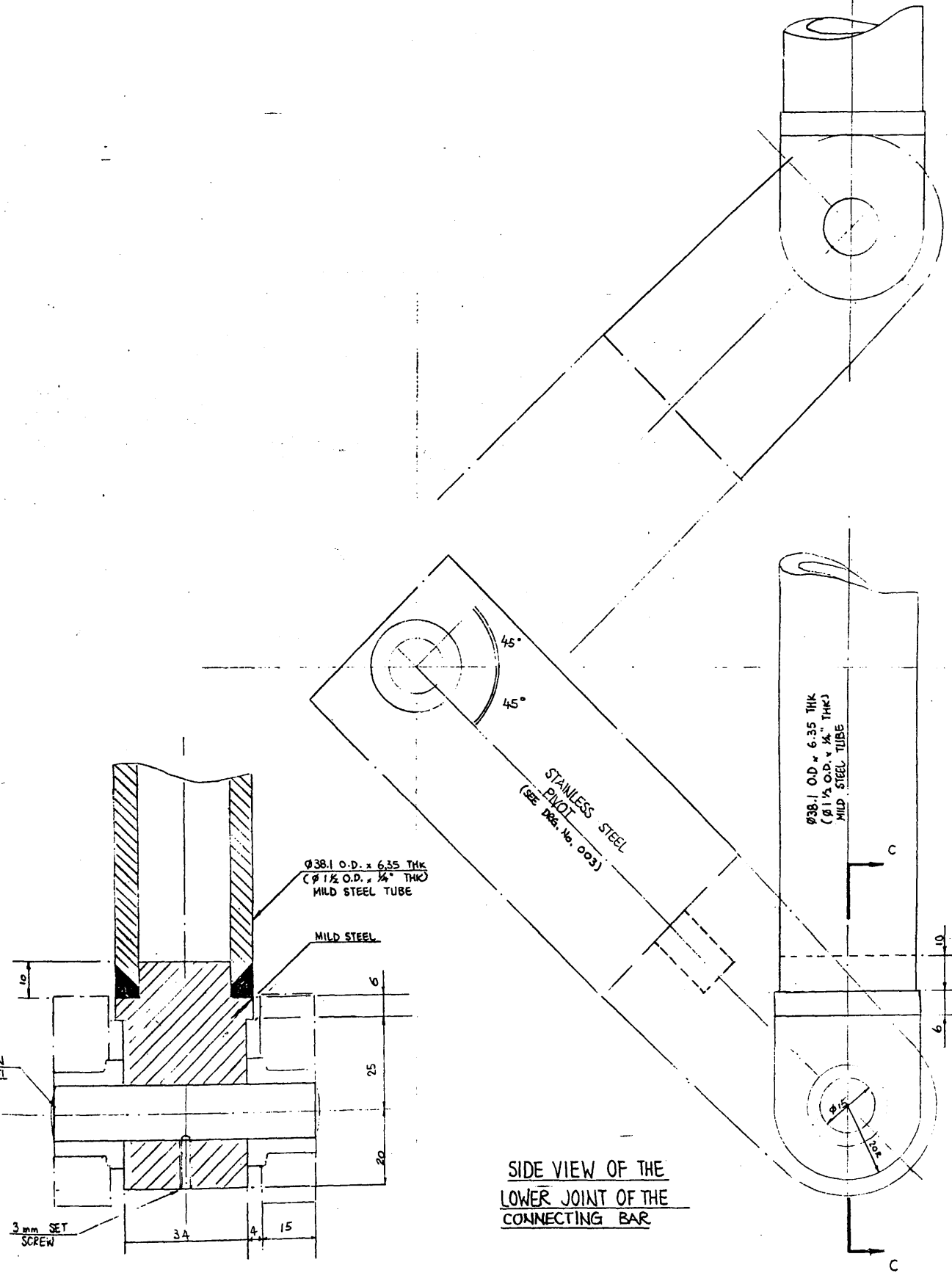
SECTION AA



SECTION BB



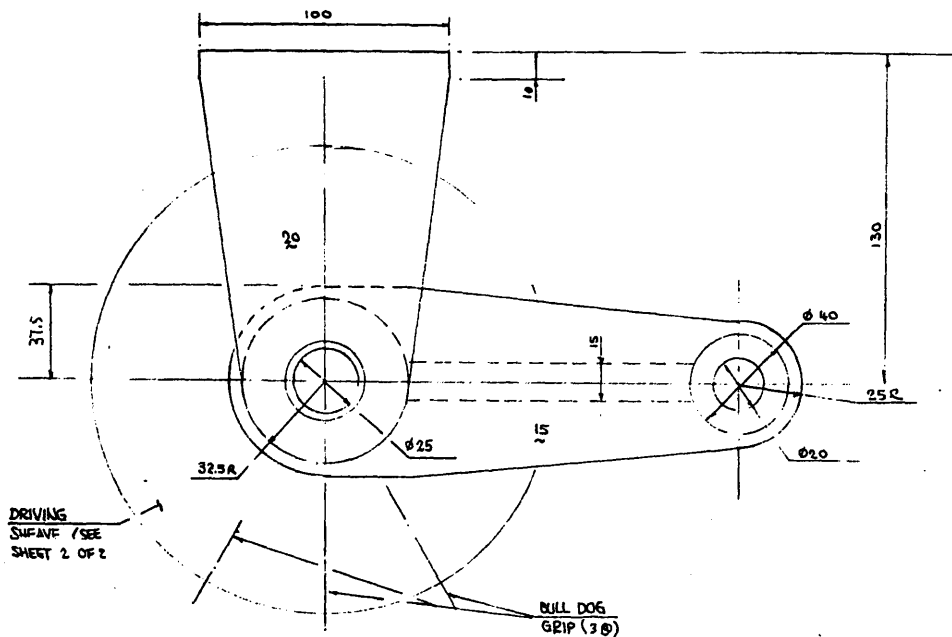
SIDE VIEW OF THE PIVOT SUPPORT



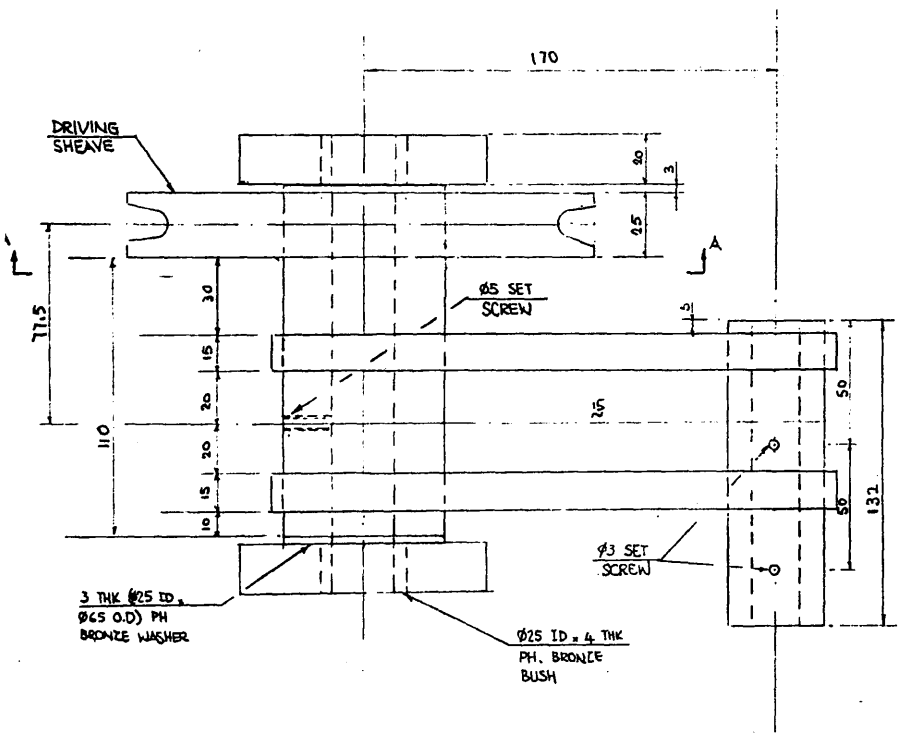
SECTION C C

SIDE VIEW OF THE LOWER JOINT OF THE CONNECTING BAR

SCALE 1:1
DRAWING No. 005

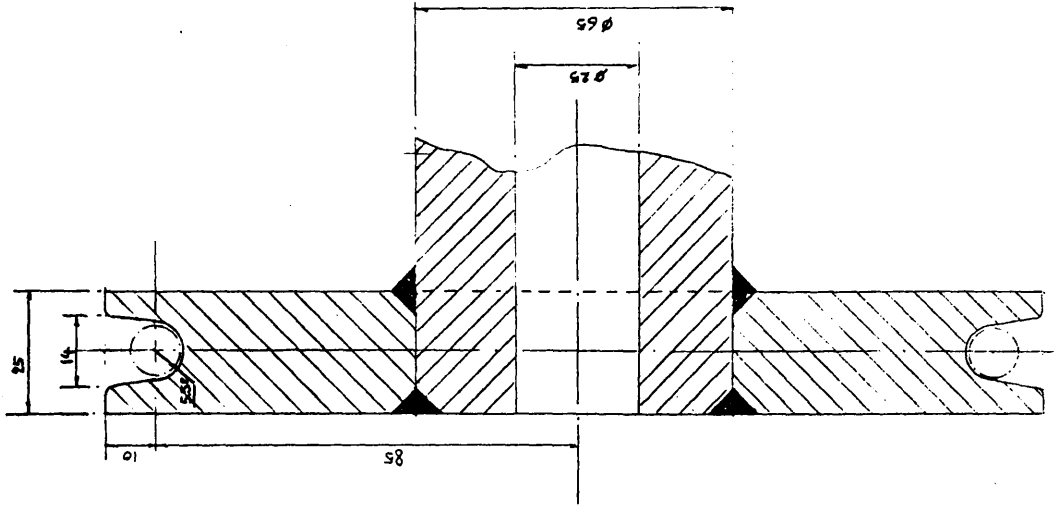


ELEVATION

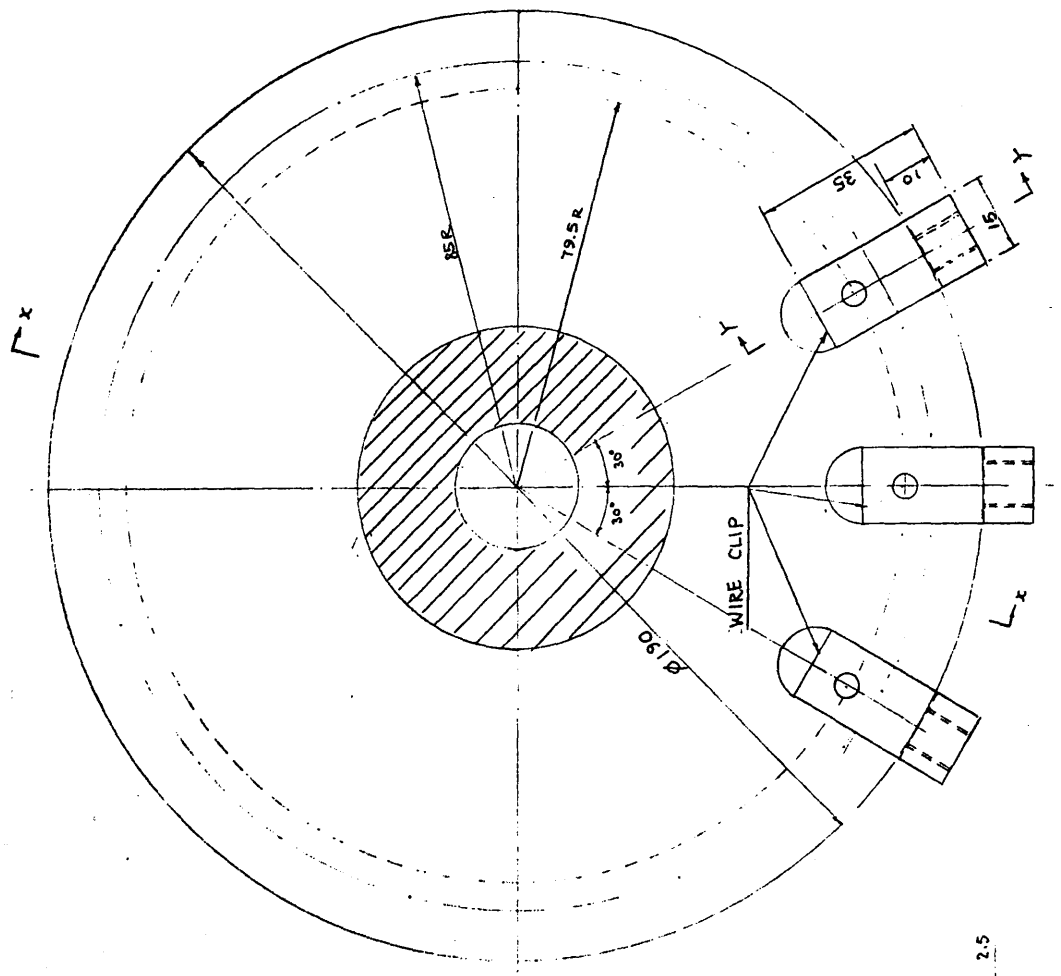


PLAN VIEW OF UPPER OSCILLATING ARM

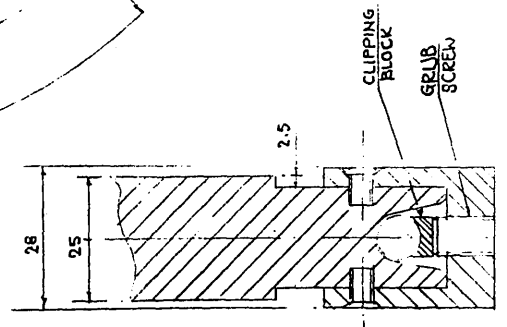
SCALE 1:2
 DRG No. 006
 SHEET 1 OF 2



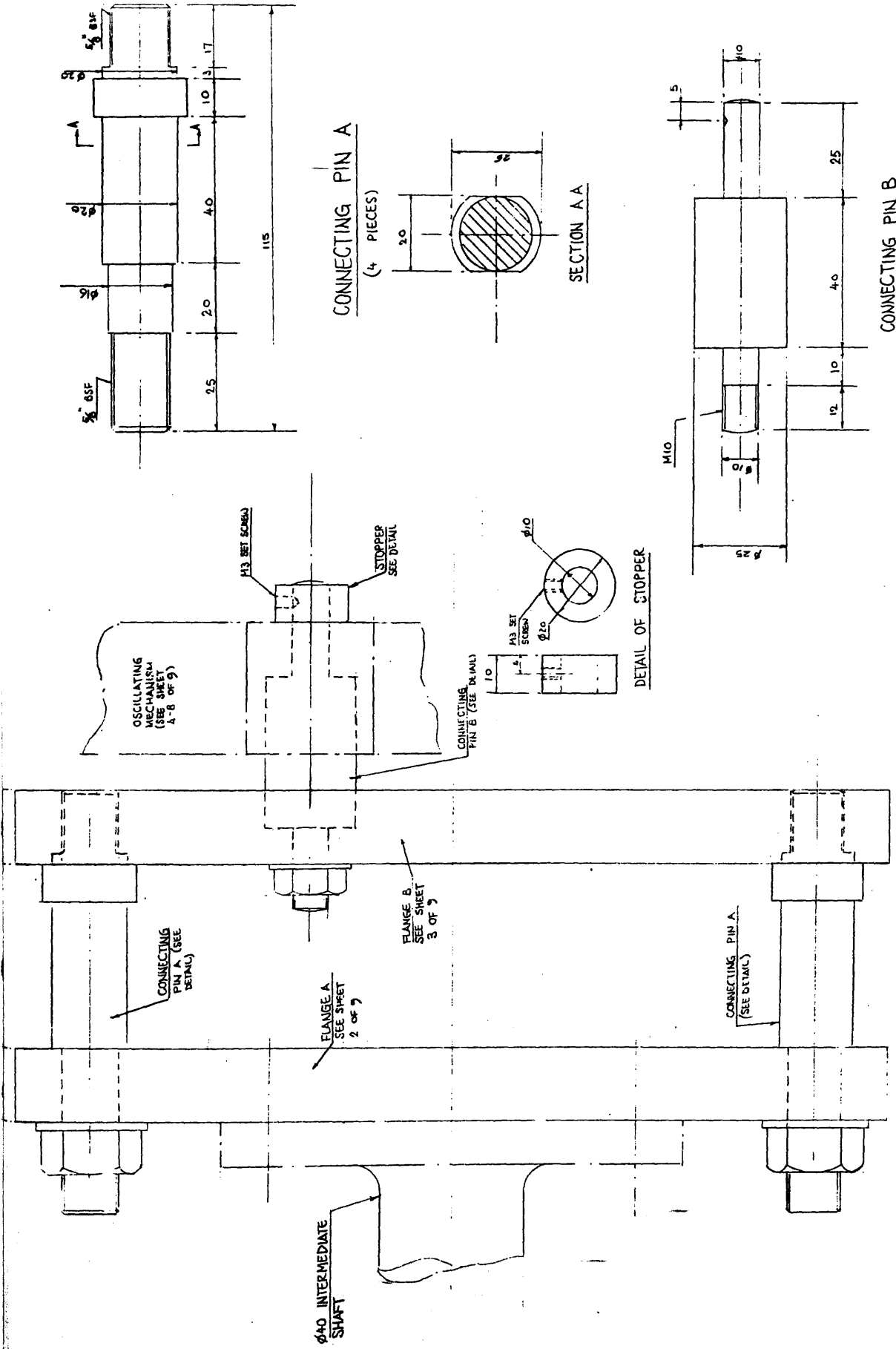
SECTION XX



SECTION A A

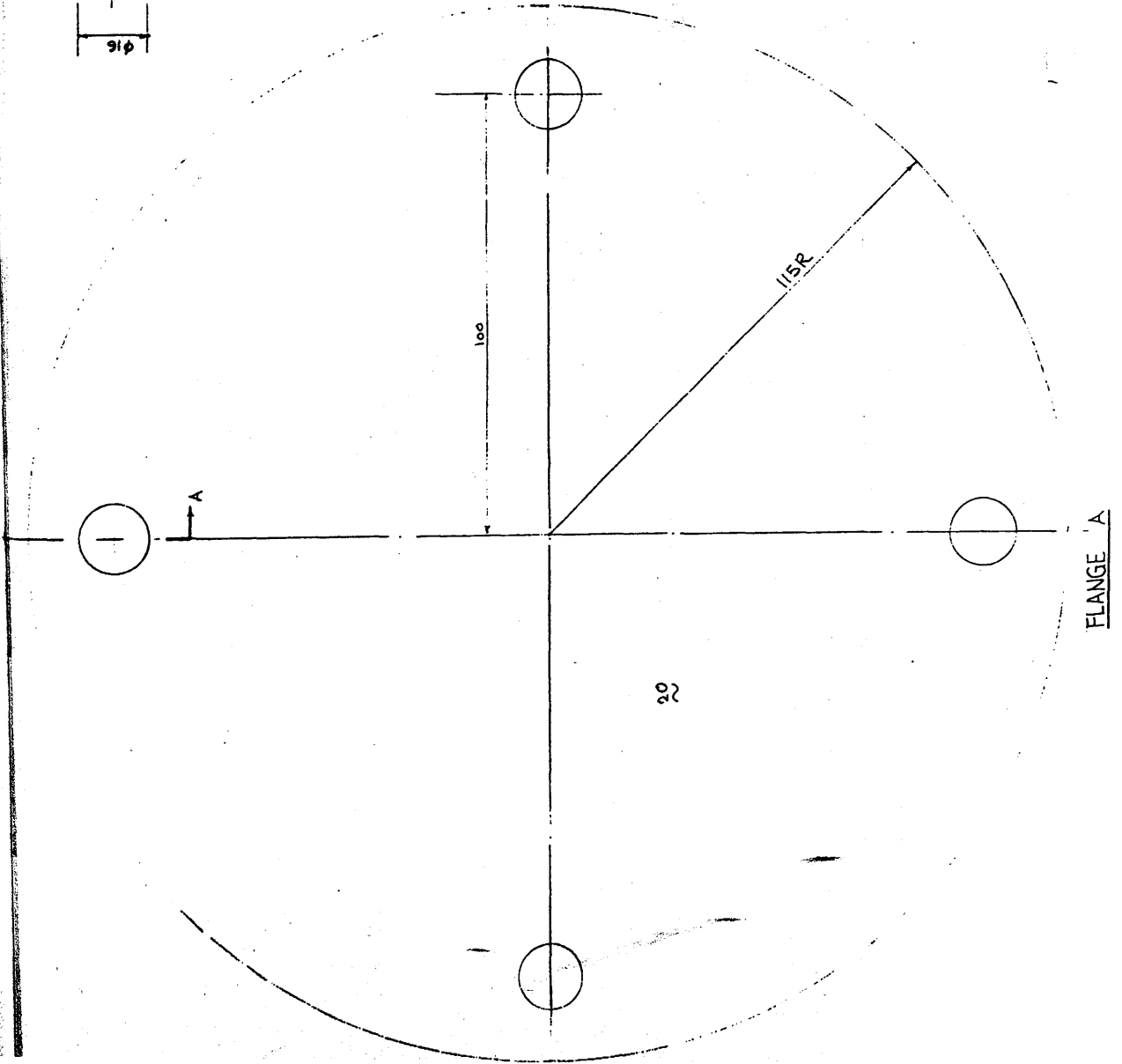
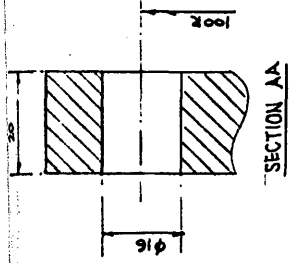


SECTION Y Y

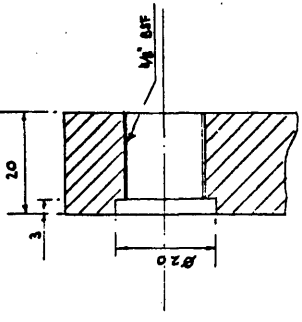


SIDE VIEW OF DRIVING FLANGES

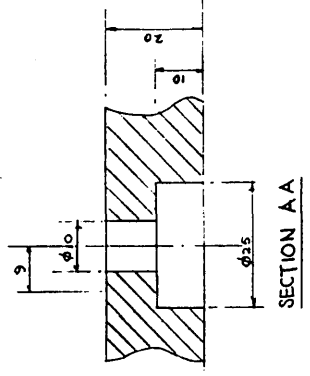
SCALE : 1:1
 DRG. No. 007
 SHEET 1 OF 9



22



SECTION BB



SECTION AA

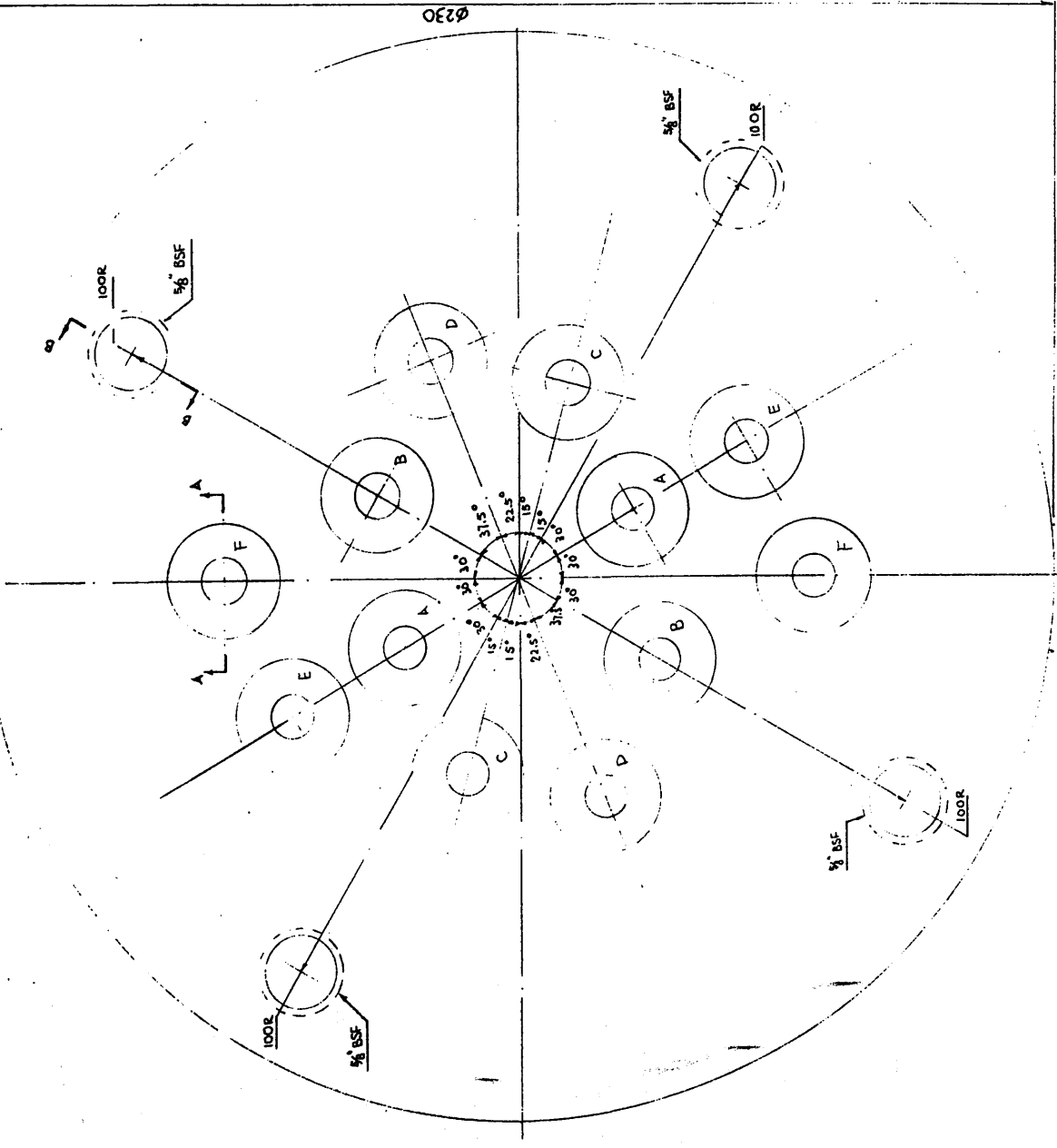
DISTANCE FROM CENTRE
OF HOLE TO THE CENTRE
OF THE FLANGE (mm)

HOLE

HOLE	DISTANCE FROM CENTRE OF HOLE TO THE CENTRE OF THE FLANGE (mm)
A	29.6106
B	31.0882
C	44.5055
D	51.9235
E	59.3412
F	66.7588

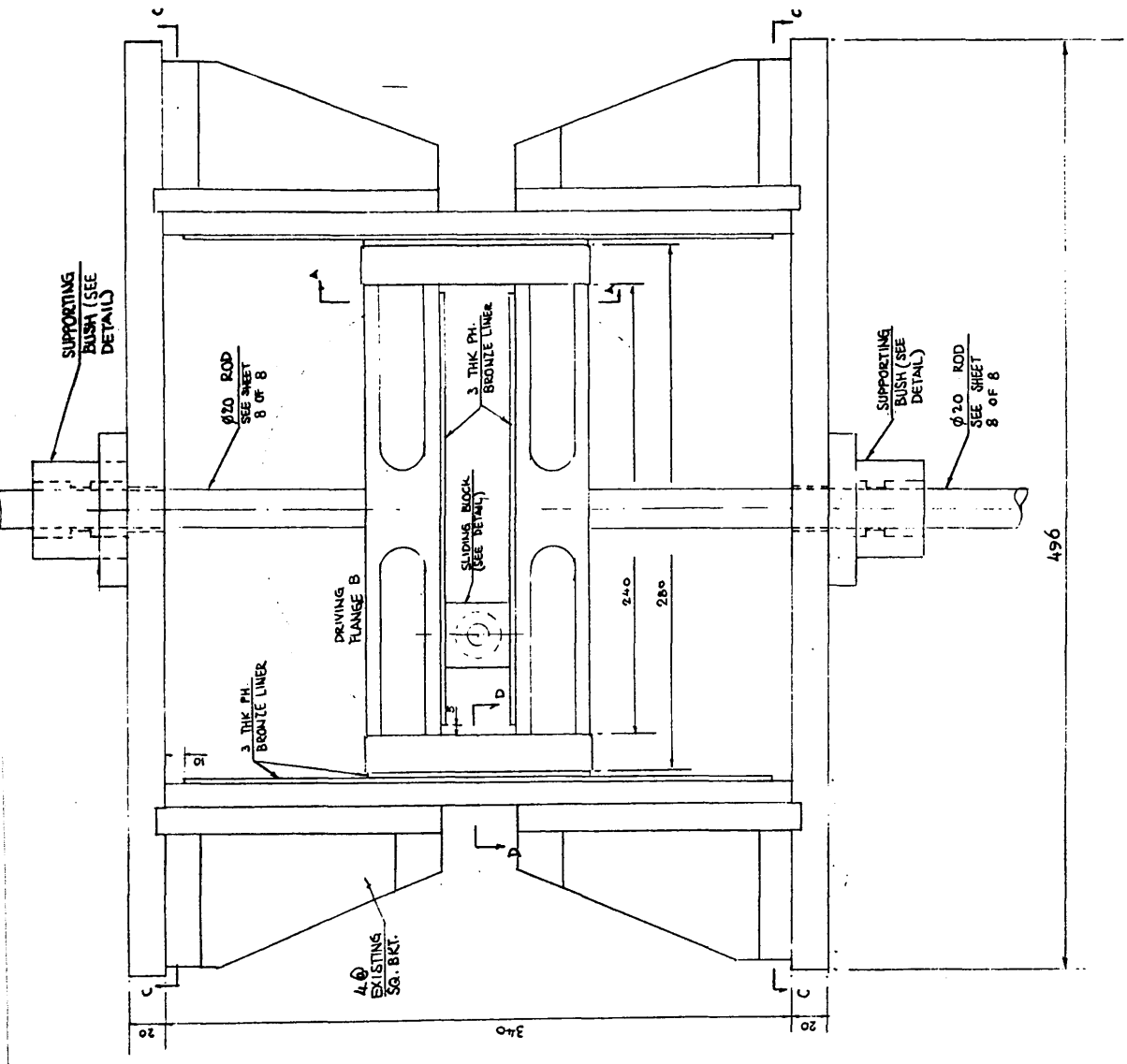
SCALE : 1 : 1

DRG No. 007
SHEET 3 OF 9

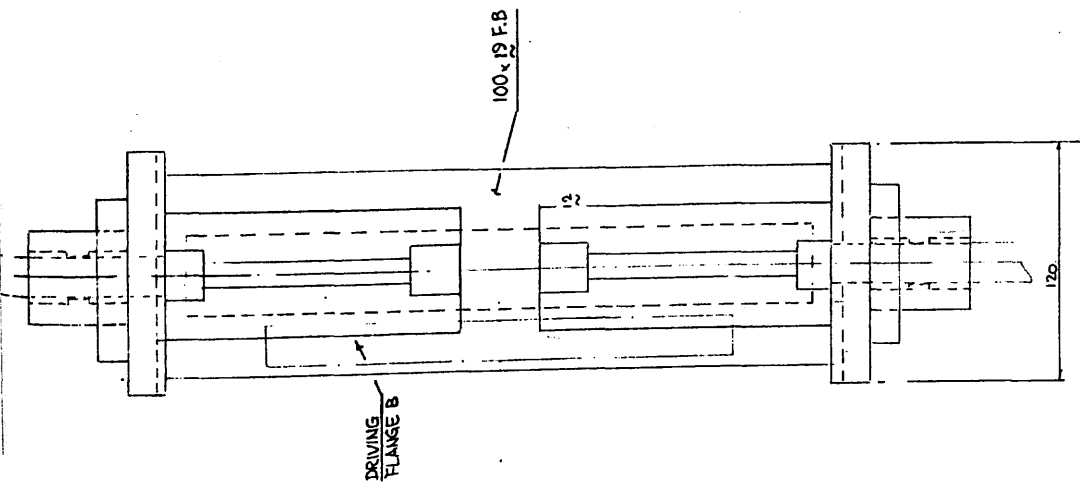


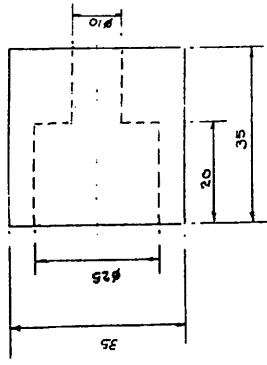
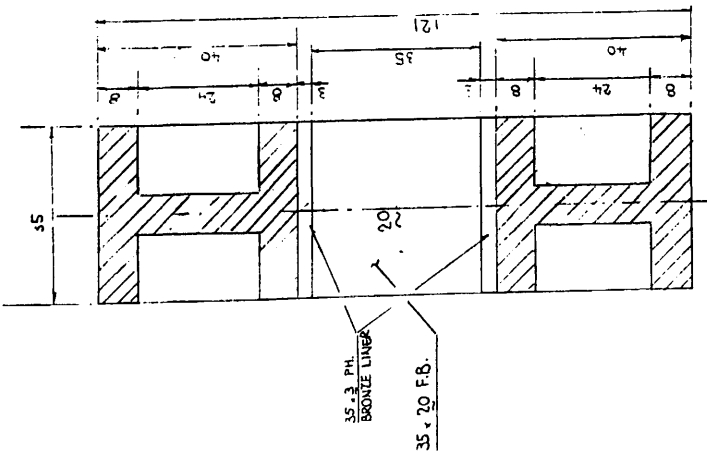
FLANGE B

FRONT VIEW OF THE SINUSOIDAL
 OSCILLATOR

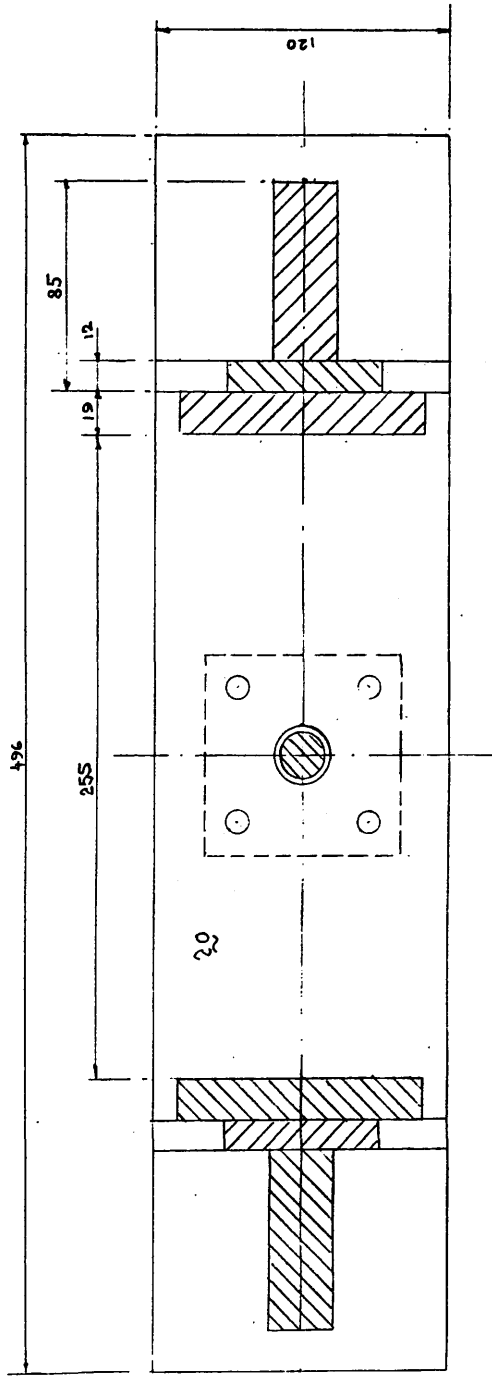
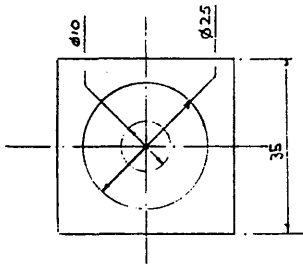


SIDE VIEW



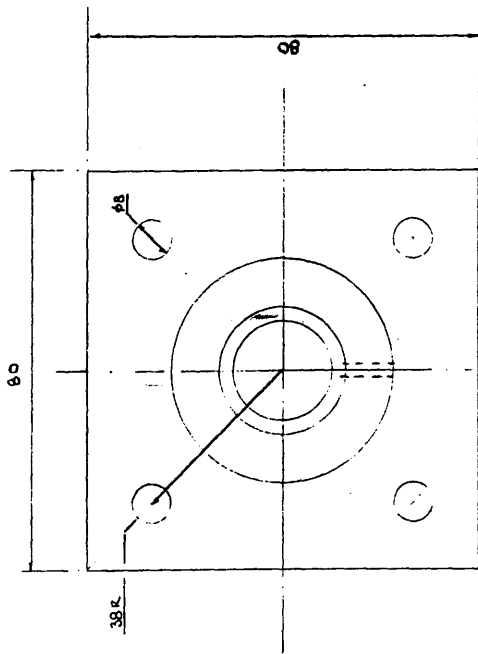
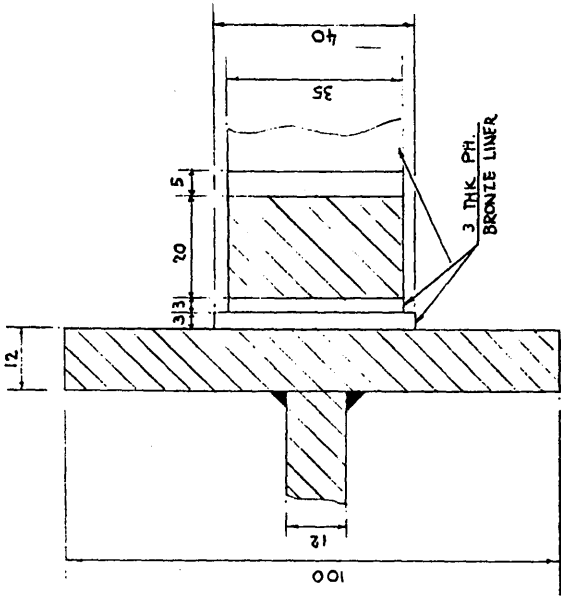
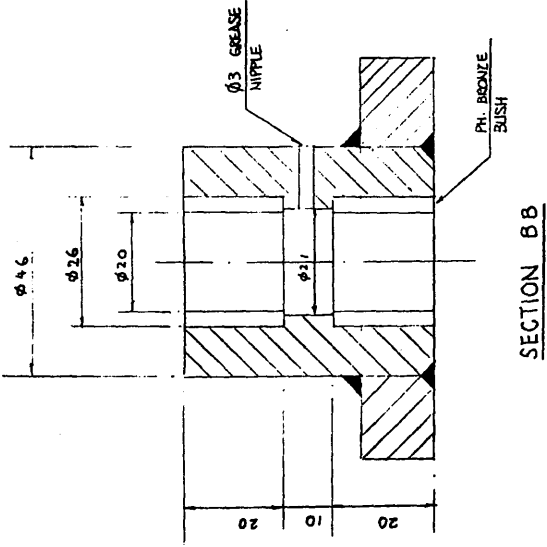
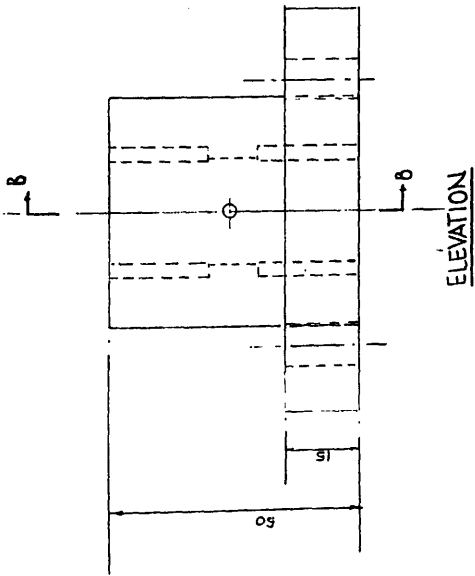


END VIEW OF
SLIDING BLOCK
(PH. BRONZE)

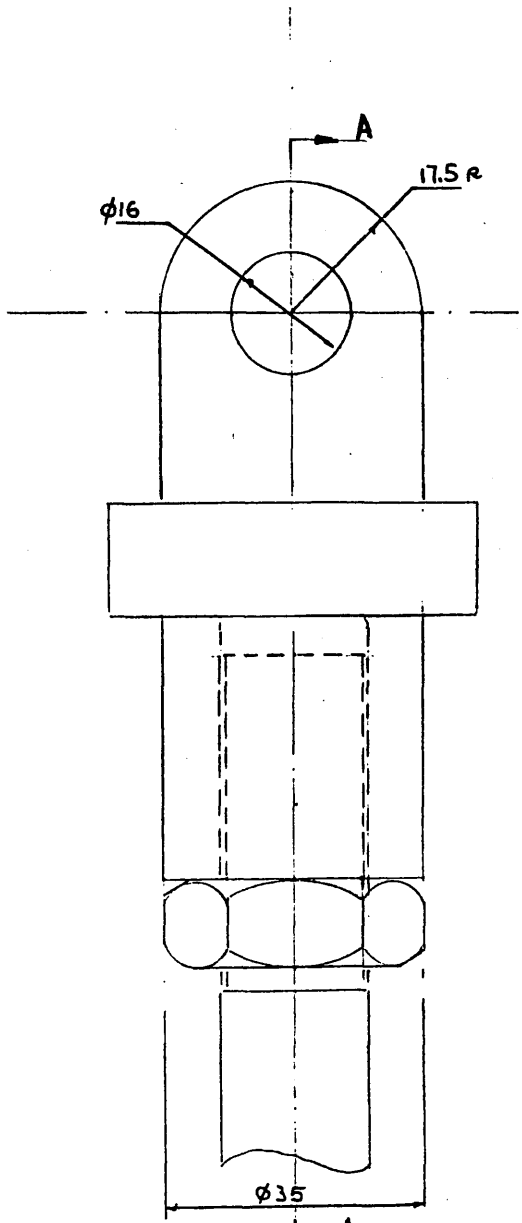


SECTION C C
(SCALE 1:1)

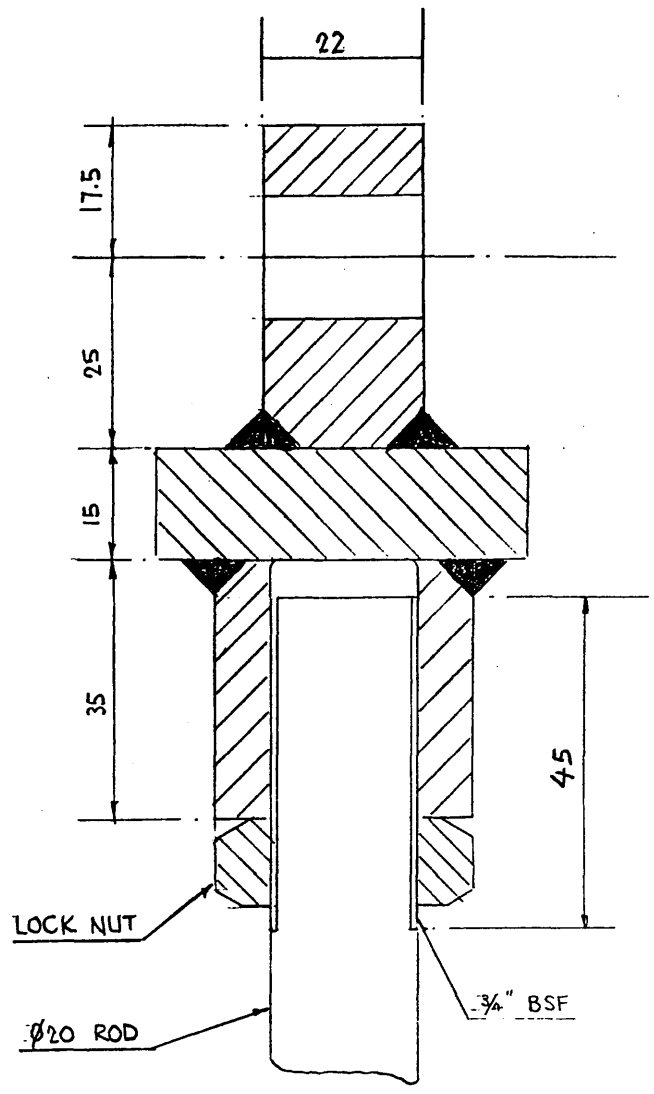
SCALE : AS SHOWN
DRG No. 007
SHEET 6 OF 9



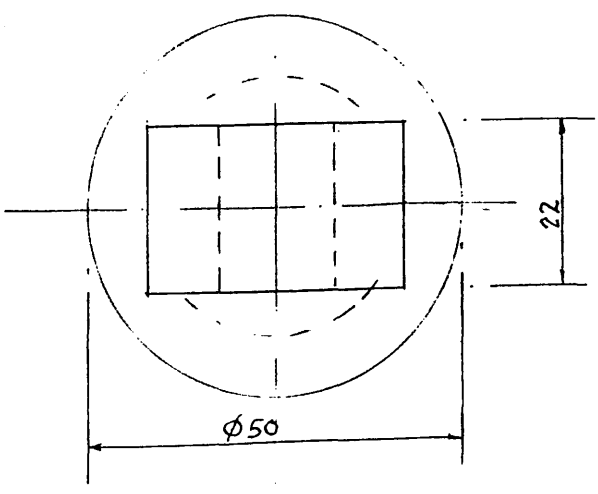
SCALE : 1:1
 DRG No. 007
 SHEET 6 OF 9



SIDE VIEW



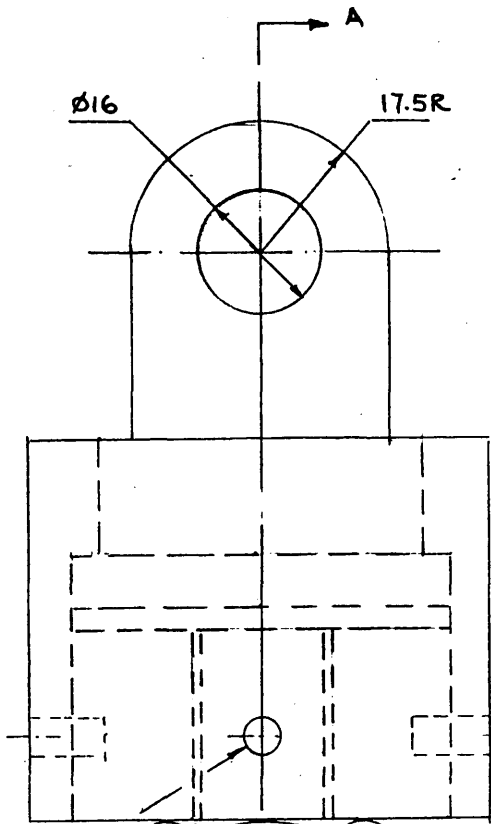
SECTION AA



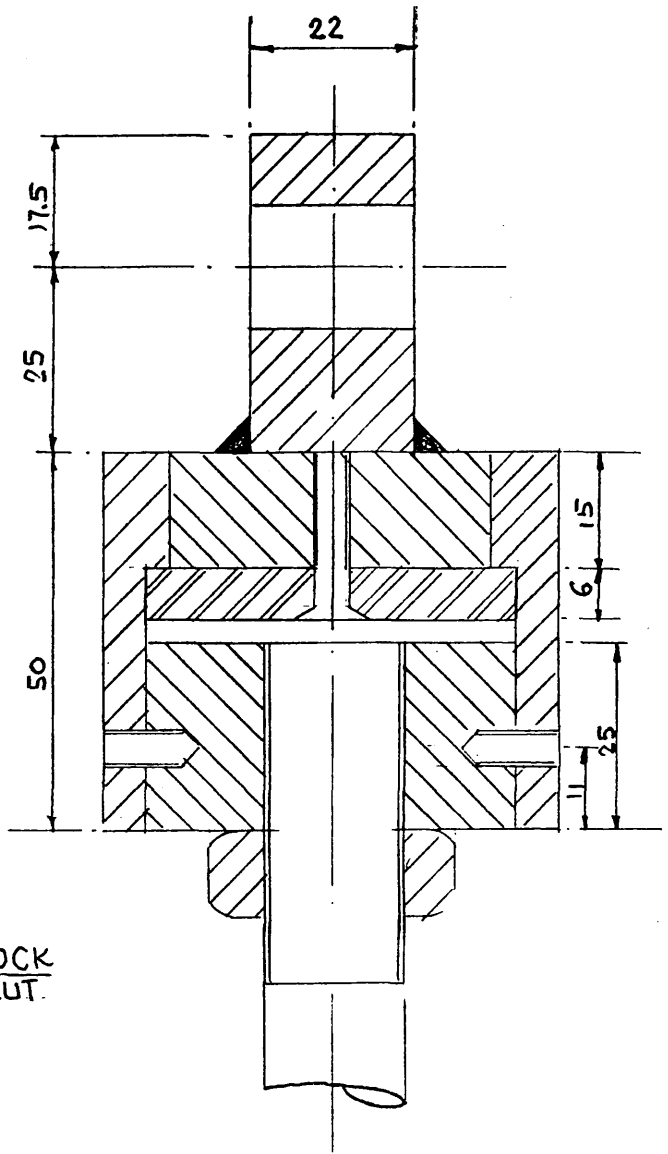
PLAN VIEW

THE UPPER END CONNECTION
OF THE OSCILLATING BAR

SCALE 1:1
DRG. No. 007
SHEET 7 OF 9



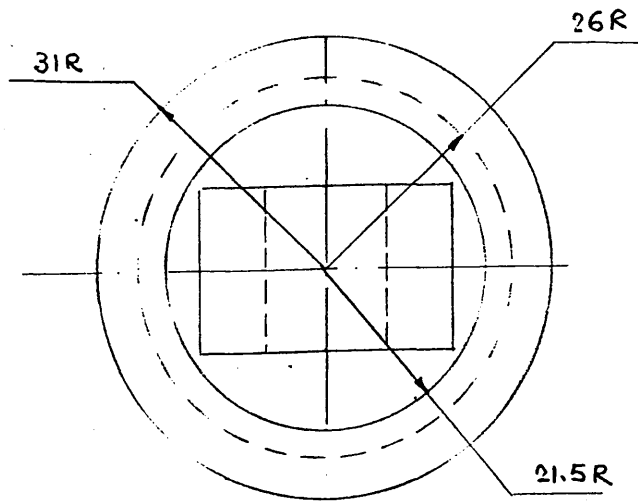
SIDE VIEW



SECTION A-A

4 @ GRUB
SCREW

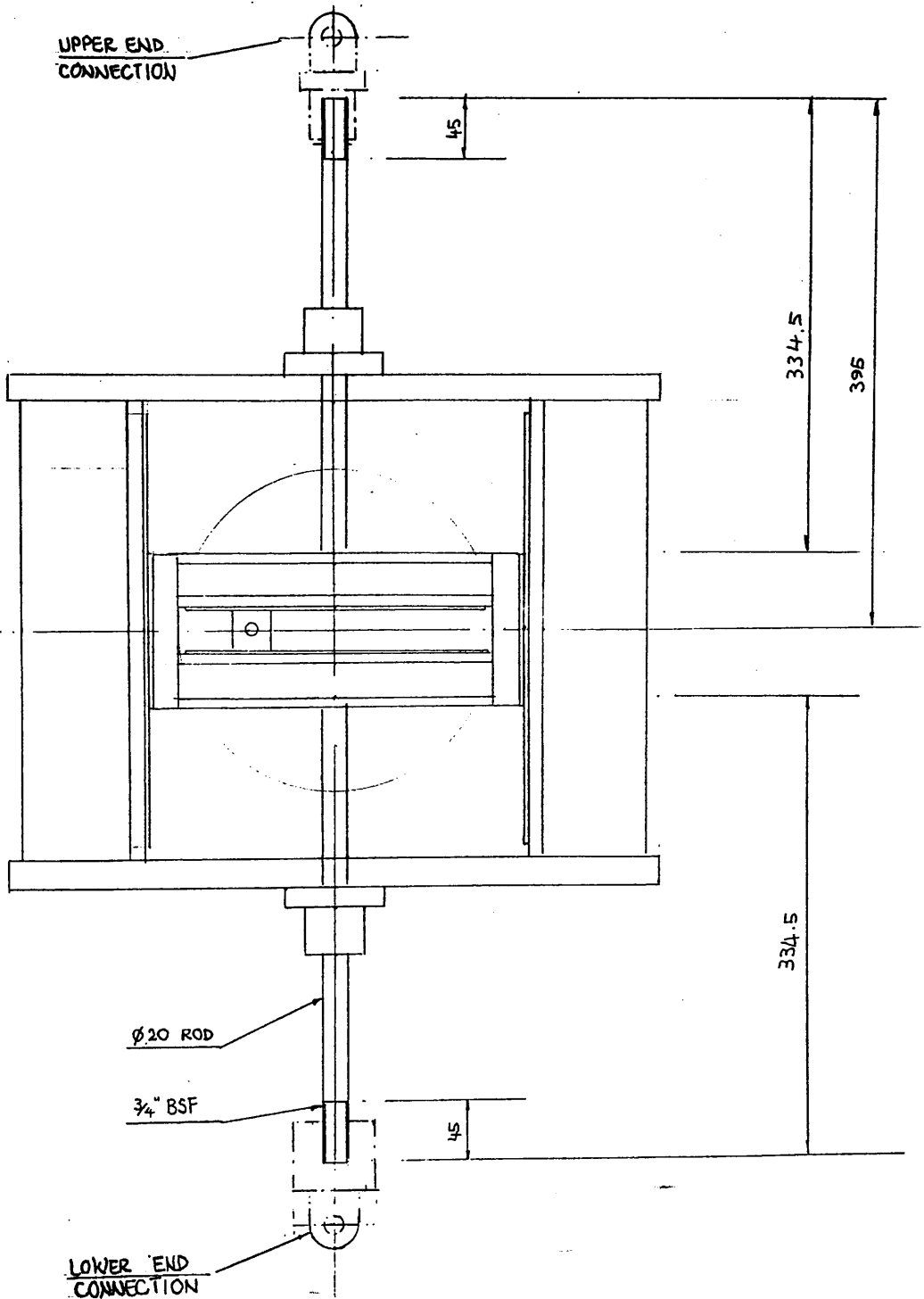
LOCK
NUT.



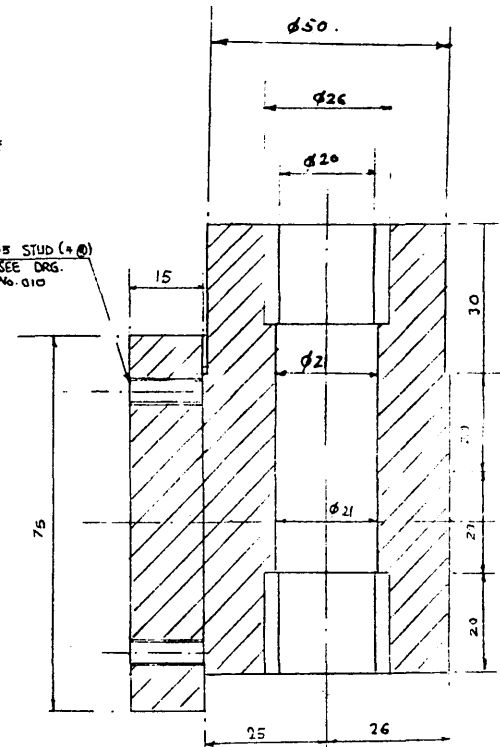
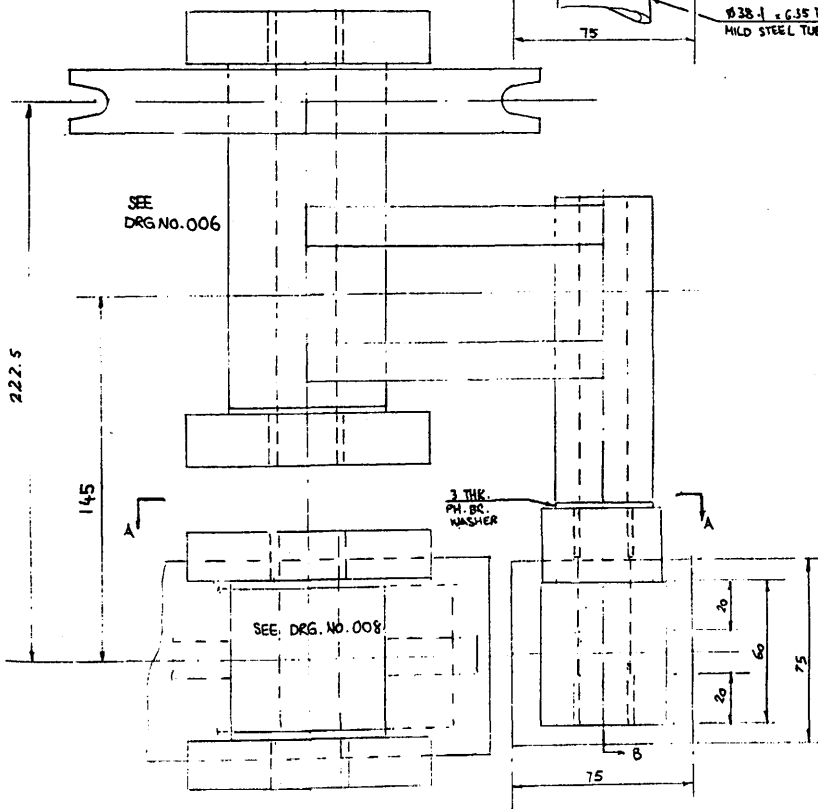
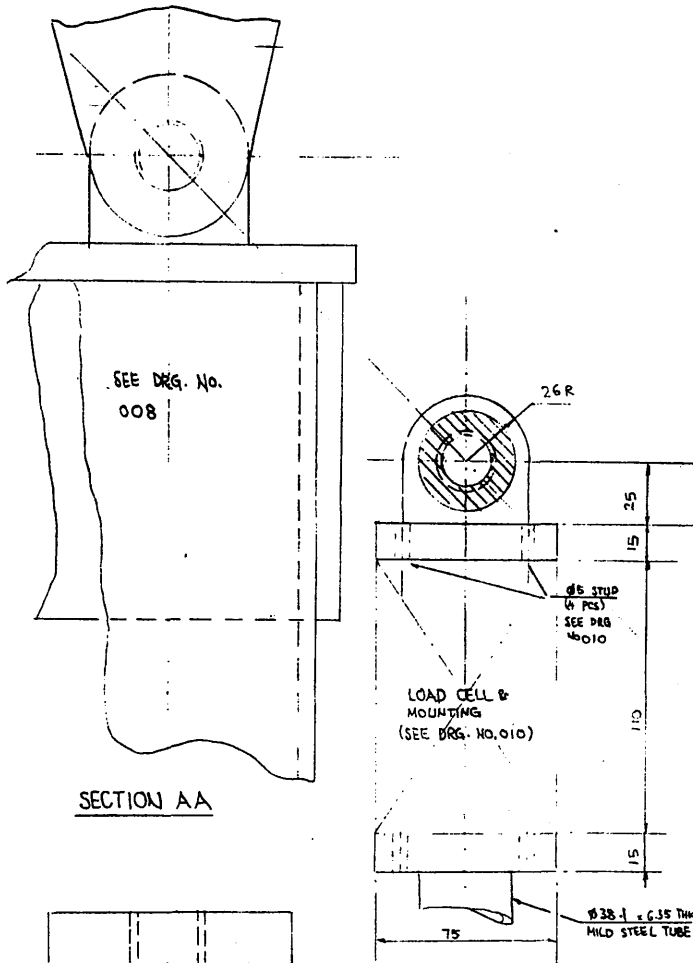
PLAN VIEW

THE LOWER END CONNECTION
OF THE OSCILLATING BAR

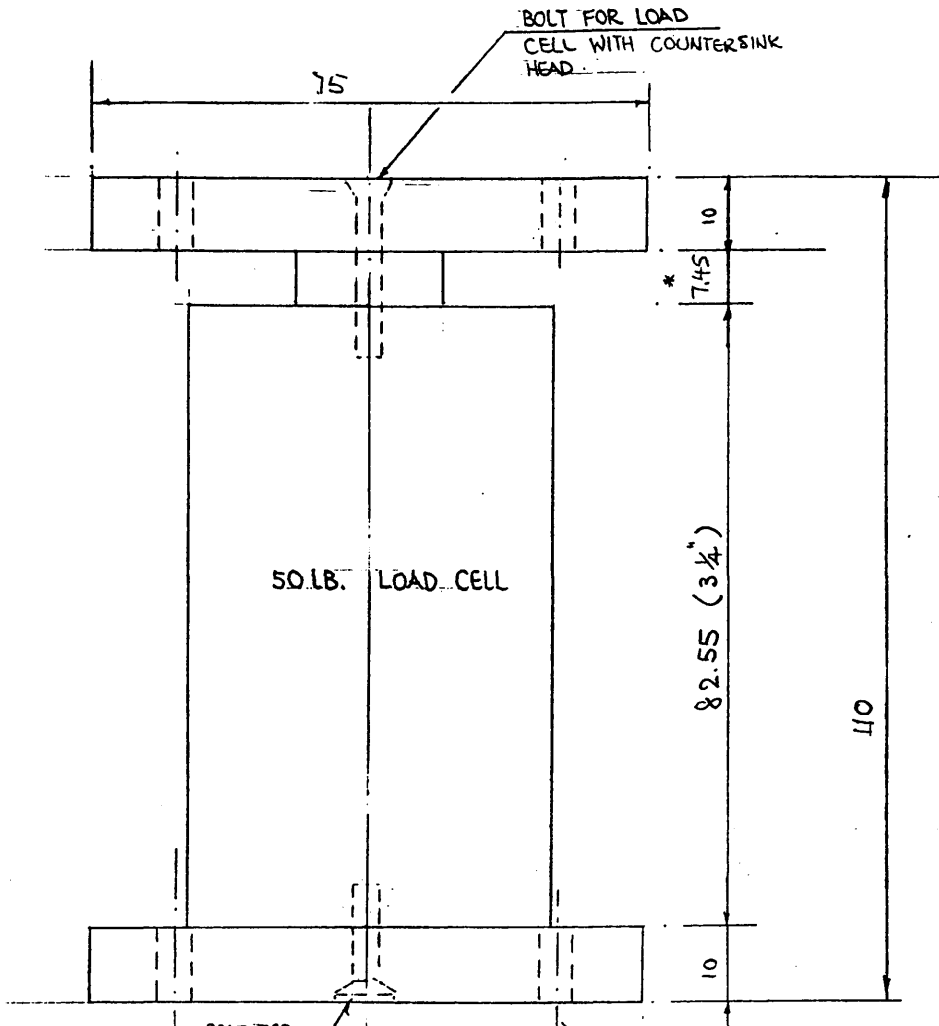
SCALE 1:1
DRG. No. 007
SHEET 8 OF 9



SCALE 1:5
 DRG No. 007
 SHEET 9 OF 9



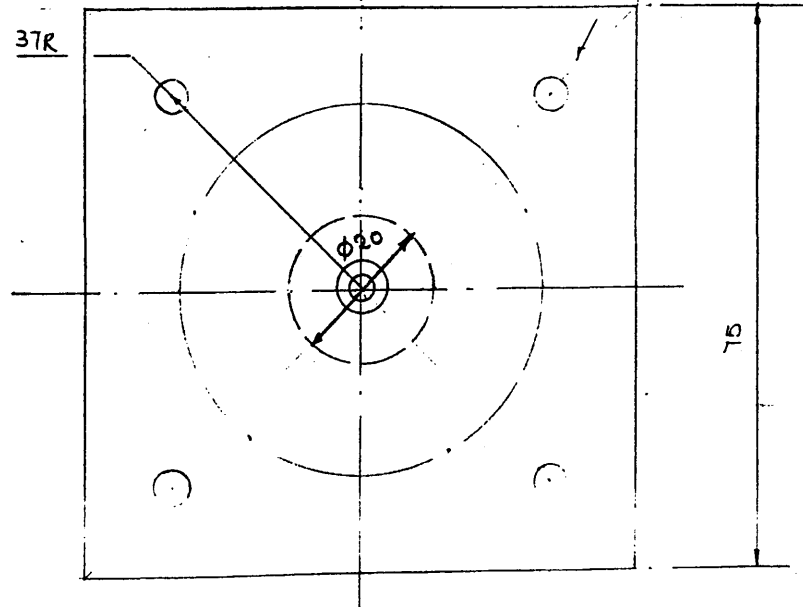
SCALE : AS SHOWN
DRG No. 009



* DIMENSION SHOULD BE CHECKED

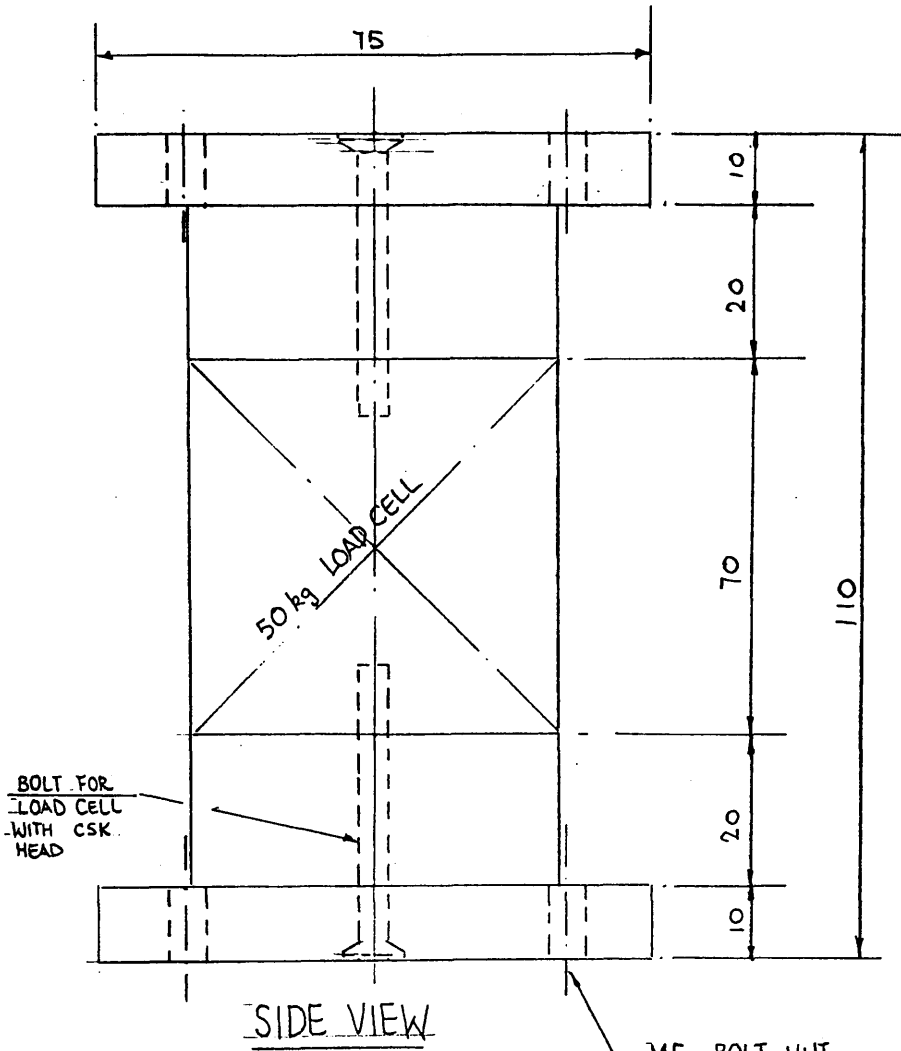
BOLT FOR LOAD CELL WITH CSK.
SIDE VIEW

M5 BOLT, NUT & WASHER (4 PCS)

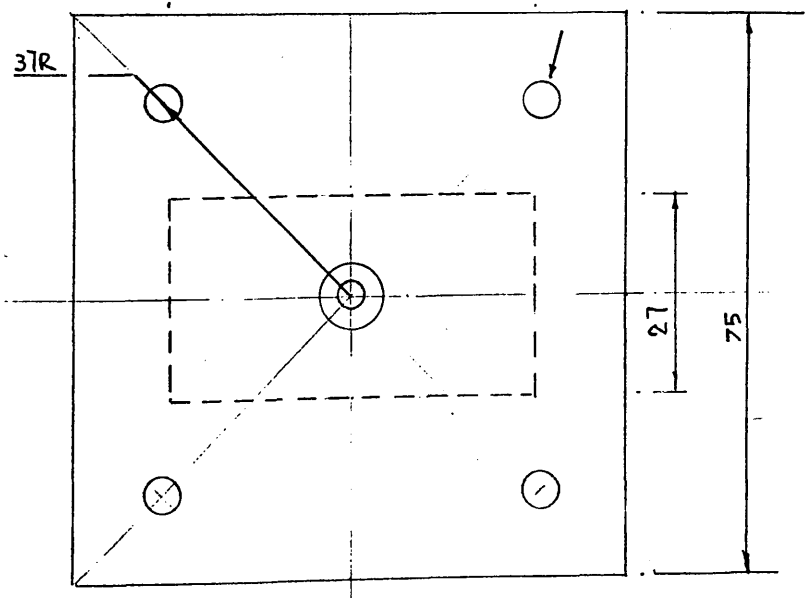


PLAN VIEW OF THE 50 LBs LOAD CELL MOUNTING

SCALE : 1:1
DRG. No. 010
(SHEET 1 OF 2)

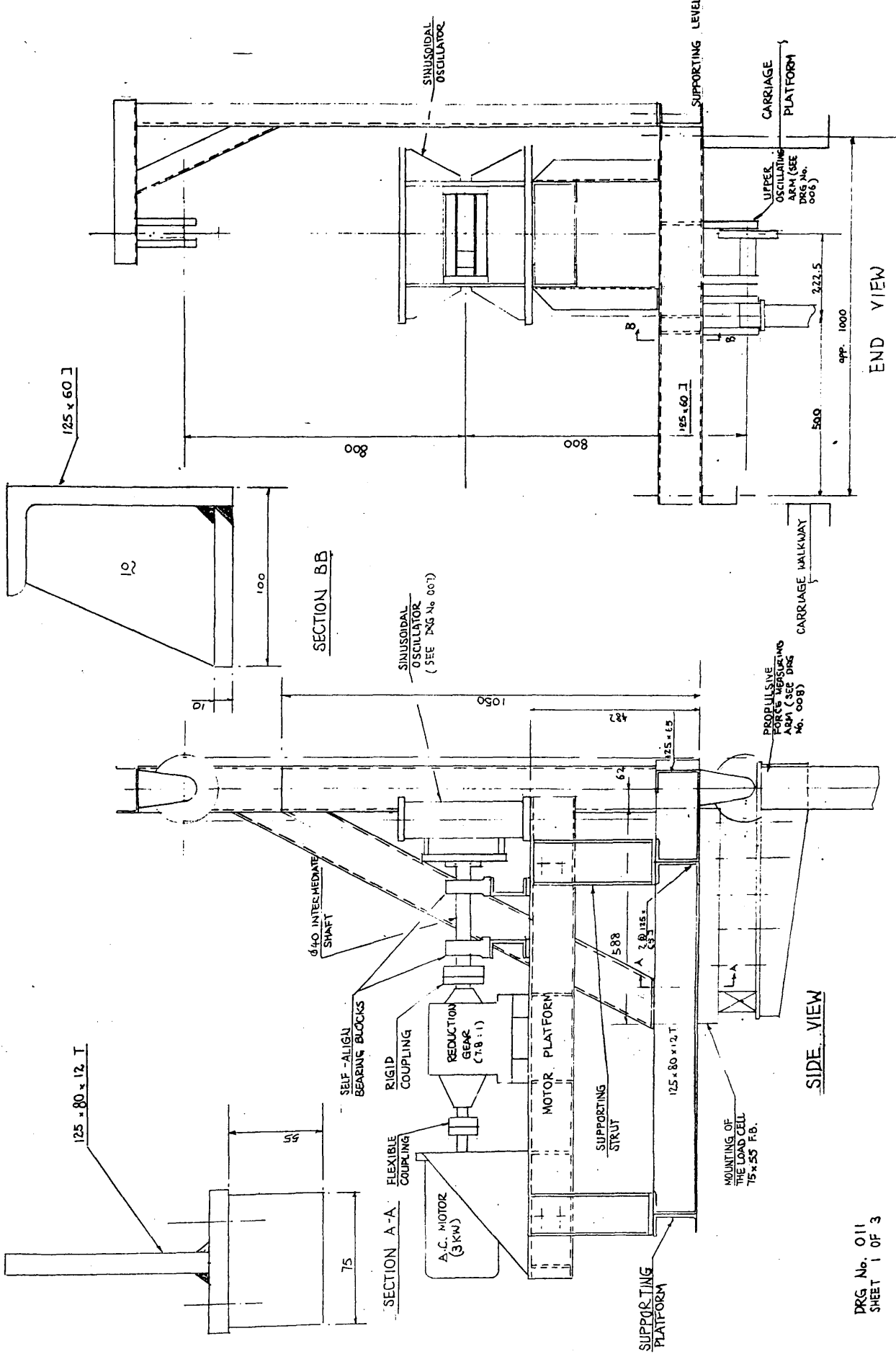


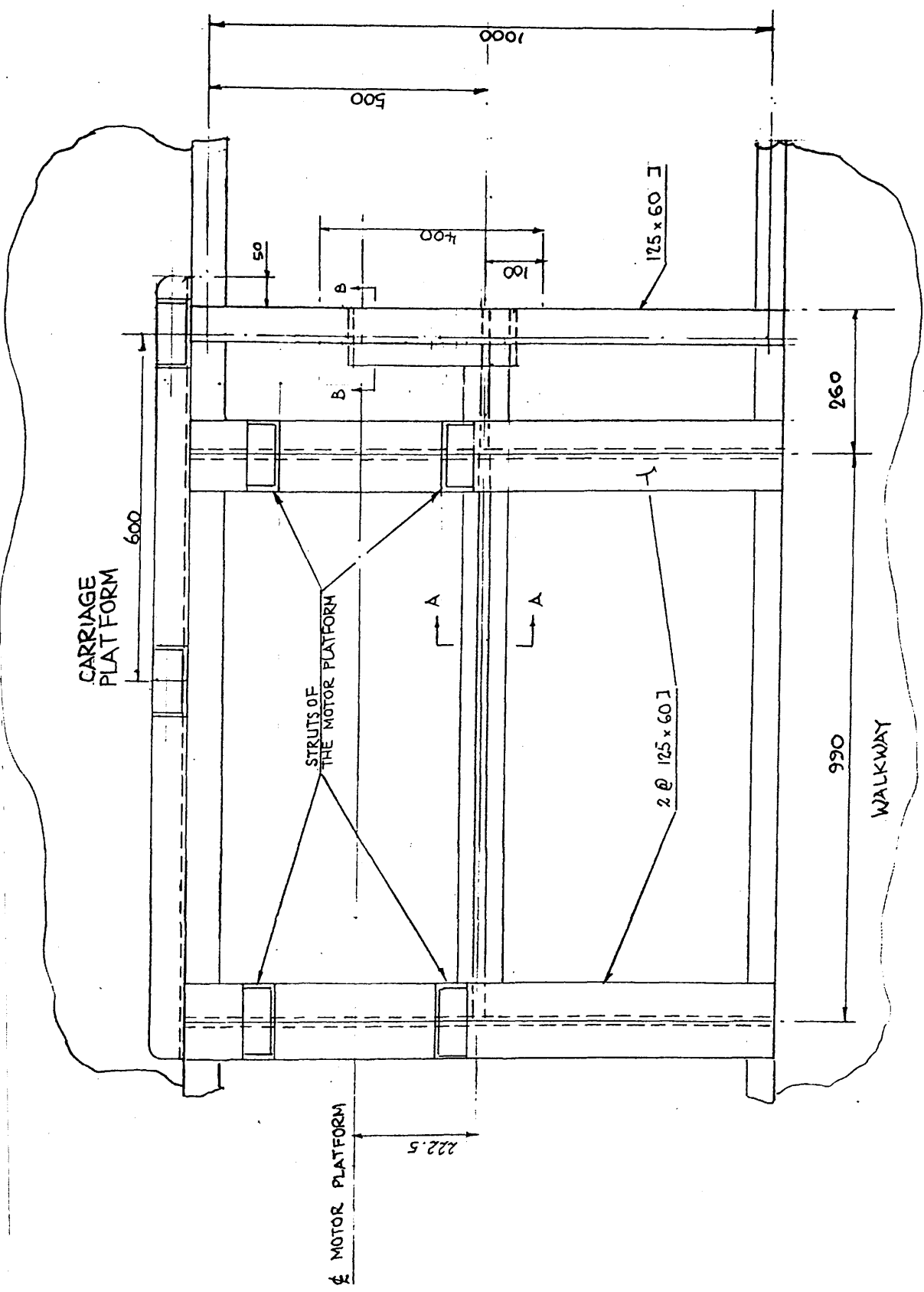
M5 BOLT, NUT & WASHER (4 PCS)



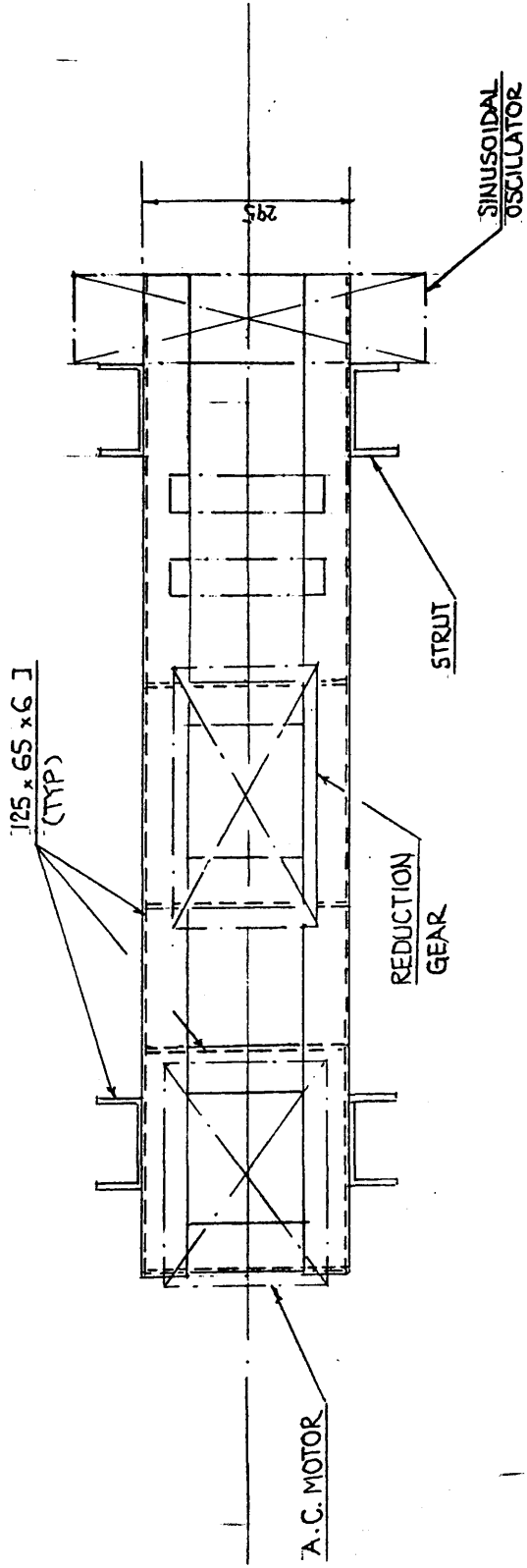
PLAN VIEW OF THE 50 KG LOAD CELL MOUNTING

SCALE 1:1
 DRG. No. 010
 (SHEET 2 OF 2)

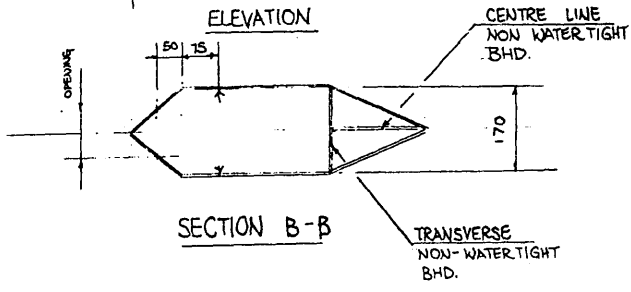
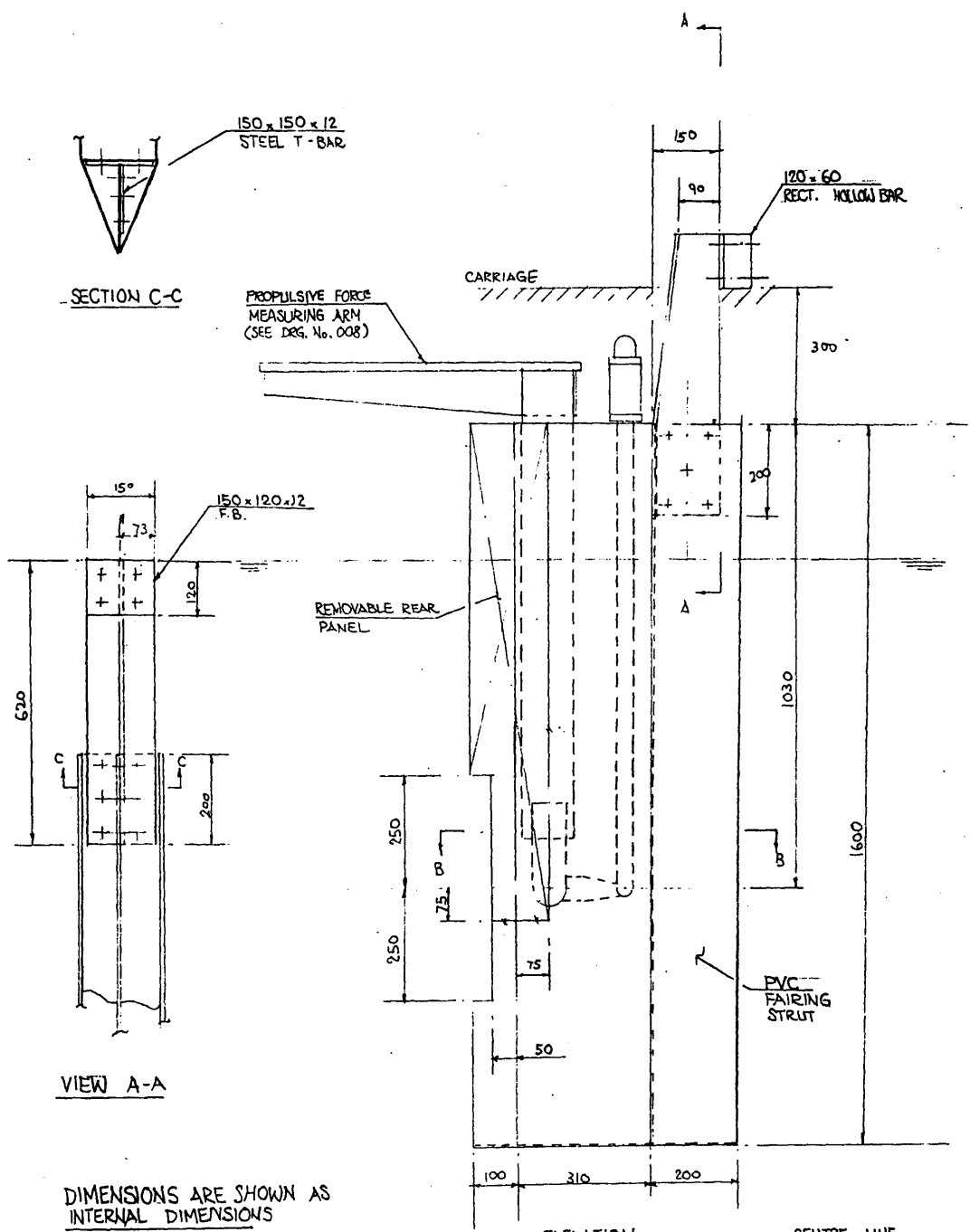




SUPPORTING PLATFORM



MOTOR PLATFORM



FAIRING STRUT

GLASGOW
UNIVERSITY
111